Adding ammonia during Fischer-Tropsch Synthesis: Pathways to the formation of N-containing compounds.

by

Christian de Vries

A thesis presented for the degree of
Doctor of Philosophy

Centre for Catalysis Research
Department of Chemical Engineering
University of Cape Town
July 2017

Supervisor: **Prof. M. Claeys**
Co-supervisor: **Dr. M. Petersen**

ACKNOWLEDGEMENTS

Even though I am the sole author of this document, getting to the end-line was by no means an individual effort! I made a mental note to thank Johan Landsman and Le Roux v/d Westhuizen, should I ever reach this goal. If you did not come to my rescue 10 years ago, this achievement would have been a daydream.

My supervisor, Prof. Michael Claeys is a world leader in the field of Fischer-Tropsch synthesis. My co-supervisor, Dr. Melissa Petersen, is a world leader in theoretical calculations of the Fischer-Tropsch synthesis. This definitely made things extremely challenging, but by standing on the shoulders of giants I was able to achieve so much more. Thank you for your hard work and patience through these many years! It was invaluable to have my initiation of the laboratory by the infamous Dr. Nico Fischer, vielen dank! Discussions with Prof. Eric van Steen wasn't easy but it kept you on your toes and steered you in the right directions. Lee-Anne Kallam, without your help I would have been in so much trouble. Graham Inggs, you don't know how much all the help means! The Chem Eng people are just rock solid, thanks for the good times (Illy, Cindy, Nabeel, Doreen, Claire, Wess, Sancha, Joe, Dirk, Steven, Marc, Waldo, Chantel, Liezel, Rachel, Nothando, Zandile etc).

Thanks to all my friends (Skip, Heindes, GB, Masjien, Wendy, Big Rod etc.) who stuck with me through the tough times. My brothers and sisters, in particular Ettie that became my slave when things got out of hand! Thank you to my new family for all your support in the USA!

You saw me battle a blocked reactor, stuck with me stuck in a chair for a VERY long time - there are no words to express the gratitude Theresa B. Feltes!

I would like to dedicate all the sweat and tears that went into this manuscript to Edmond and Miriam de Vries. For my parents who never had the opportunities but always act selflessly to improve the lives of others, this is a small token of my appreciation.

Synopsis

The Fischer-Tropsch synthesis (FTS) process, better known for its ability to produce synthetic fuel via the hydrogenation of CO, has shown potential to produce valuable chemicals when ammonia is added to the feed. In this work certain aspects of the pathway to the formation of N-containing compounds that form when NH_3 is added during FTS, using mostly iron based catalysts is investigated. In addition, the effect this has on the FTS reaction itself is evaluated. To achieve this goal, both theoretical and experimental techniques are used in this study.

The CO adsorption and dissociation reactions are assumed to be important elementary reactions for many proposed FTS pathways. In the theoretical part of this thesis, spin-polarized periodic density functional theory (DFT) calculations are employed to study aspects of the initial stage of the pathway on a model Fe(100) surface. Considering the formation of N-containing hydrocarbons, one would assume that NH_3 initially adsorbs and dissociates on the catalyst surface, which could take place in the presence of CO. The surface chemistry of these adsorbates is well studied both experimentally and theoretically, but their co-existence has not yet been evaluated on model Fe surfaces. Initially a platform is generated by calculating the individual potential energy surfaces (PES) for the decomposition of CO and NH_3 on Fe(100) at a coverage of $\theta = 0.25$ ML. These calculations provided the basis for comparing the adsorption and dissociation profiles of CO and NH_3 on the Fe(100) surface via the use of the same computational methodology, and importantly making use of the same exchange correlation functional (RPBE) for both adsorbates. Furthermore, it was desired to evaluate the kinetics and thermodynamics of the NH_3 decomposition on the Fe(100) surface at relevant temperatures and pressures (by combining the DFT results with statistical thermodynamics) to better understand the role of NH_x surface species involved in the pathway to the formation of the N-containing compounds on a model catalyst surface. The DFT results that are reported for the individual decomposition PES for CO and NH_3 were generally found to be in close agreement with what has been reported in previous DFT studies and deduced experimentally for the relevant adsorption and decomposition pathways. The resulting Gibbs free energies for the PES suggests that NH_2 may be kinetically trapped on the Fe(100) surface at a coverage of $\theta = 0.25$ ML and the reaction

conditions (T = 523 K and $p^*_{NH_3}$ = 0.2 bar) where NH_3 is co-fed with synthesis gas during FTS. The individual adsorptions of CO and NH_x (with x = 3, 2, 1, 0) were compared to their coadsorbed states, by calculating the heat of mixing (ΔE_{mix}) and the activation barriers (E_a) for CO dissociation in the presence and absence of the NH_x surface species on the Fe(100) surface. Similar to the individual adsorption of NH_3, the 0 K regime inherent to DFT calculations is bridged by calculating the Gibbs free energy of mixing for CO + NH_3 on Fe(100) at higher temperatures. Both repulsive and attractive interaction energies were calculated for the various coadsorbed states (CO + NH_x on Fe(100)) and similarly some configurations resulted in an energetically favored or unfavored heat of mixing. The activation barrier for CO dissociation was lowered when coadsorbed with NH_3 and NH_2, and raised when coadsorbed with NH and N. With all the coadsorbed structures the CO dissociation reaction became more endothermic. Previous experimental studies have shown a concomitant reduction in oxygenate selectivity with an increase in the selectivity for N-containing compounds, when NH_3 is added during FTS. It is well-known that oxygenates undergo secondary reactions when using iron-based catalysts in FTS. In addition, the catalyst used in aforementioned studies (precipitated Fe/K) are active for the amination reactions of oxygenates. It is therefore hypothesized that some oxygenates produced via the primary FTS pathway are converted to N-containing compounds via a secondary reaction. The experimental part of this thesis is therefore aimed at testing this hypothesis. A base case study included a comparison between a Fe-catalyzed slurry phase FTS reaction and a FTS reaction with all parameters remaining unchanged, except for the addition of 1 vol % NH_3 to the syngas (CO + H_2) feed. The activity (CO and H_2 conversion) data collected did not reveal any appreciable loss in the rate of the FTS reaction when 1 vol % NH_3 was added and steady state was reached (, that is after 48 hours time on stream (TOS)). A slower carburization period was however observed when comparing the CO conversion during the first 24 hours TOS, and further supported by the slow increase in CO_2 selectivity during the same period. The use of two-dimensional gas chromatography (GC × GC-TOF/FID) allowed for the discovery of a formation of a range of secondary and tertiary amines, not reported in previous studies. The expected loss in oxygenate selectivity was observed and further probed by co-feeding 1-octanol with the feed (CO + 2 H_2 + 1 vol % NH_3) via a saturator. These results clearly indicated a significant loss in oxygenate formation as a result of secondary conversion to N-containing compounds. Questions regarding the stability of aliphatic nitriles prompted the co-feeding of nonanitrile under similar conditions. The results obtained after co-feeding nonanitrile, suggests that nonanitrile is readily converted to secondary and tertiary amines and that the ratios of aliphatic alcohols and nitriles are close to equilibrium. The use of CO_2 as carbon source, the investigation of the product spectrum at higher space velocities and the use of Rh-based catalysts, when NH_3 is added during FTS were included in shorter studies. The combination of these results, adds to the knowledge pool for the case where NH_3 is present in the FTS regime, as a poison or reactant. Additional information regarding the path to the formation of N-containing compounds was obtained via the detailed analysis of the product spectra with two-dimensional gas chromatography and the subsequent co-feeding reactions. The results obtained via co-feeding reactions, can be used to devise strategies to increase the selectivity of the desired N-containing compounds.

Contents

List of Figures

List of Tables

NOMENCLATURE

Process terms

FTS	Fischer-Tropsch synthesis
HTFT	high temperature Fischer-Tropsch synthesis
KE	Kölbel Engelhardt (synthesis)
LPG	liquefied petroleum gas
LTFT	high temperature Fischer-Tropsch synthesis
syngas/synthesis gas	$CO + H_2$
WGS	water-gas-shift (reaction)

Laboratory reactor related

CSTR	continuously stirred tank reactor
FBR	fixed bed reactor
GHSV	gas hourly space velocity
NTP	normal temperature and pressure
SPR	slurry phase reactor

Chromatography related

FID	flame ionization detector

GC	gas chromatograph
GC×GC	comprehensive two-dimensional gas chromatography
TCD	thermal conductivity detector
TOF	time-of-flight (detector)

Catalyst characterization

AAS	atomic absorption spectroscopy
ICP	inductively coupled plasma (spectroscopy)
PXRD	powder X-ray diffraction
TEM	transmission electron microscopy
TPD	temperature programmed desorption
TPR	temperature programmed reduction
WAXS	wide angle X-ray scattering
XAFS	X-ray fine structure spectroscopy

Surface science terms

AES	Auger electron spectroscopy
LEED	low energy electron diffraction
UHV	ultra high vacuum
UPS	ultraviolet photo-electron spectroscopy

Greek notations (exp.)

α	chain growth probability
θ	Bragg angle

Theory terms

E_a	activation energy
E_{ads}	adsorption energy
E_{cut}	kinetic cut-off energy
E_{xc}	exchange-correlation energy (functional)
CASTEP	Cambridge serial total energy package
DFT	density functional theory
GGA	generalized gradient approximation
HF	Hartree-Fock (theory)
HOMO	highest occupied molecular orbital
LUMO	lowest unoccupied molecular orbital
MEP	minimum energy path
ML	monolayer
NEB	nudged elastic band (method)
PAW	projector augmented wave (method)
TST	transition state theory
USPP	ultrasoft pseudo potentials
VASP	Vienna *ab initio* software package
ZPE	zero point vibrational energy
ZPEV$_c$	correction for the zero point vibrational energy

Greek notations (theory)

ω	lateral interaction
ψ	wave function
ρ	electron density
θ	surface coverage (fractional)

Chapter 1

Introduction

The Fischer-Tropsch synthesis (FTS) is a well-known reaction and industrial process due to its ability to produce fuels from inexpensive starting material (e.g. coal, natural gas, biomass and even waste material). These sources are converted to synthesis gas/syngas ($CO + H_2$), which is then reacted over a catalyst to form mainly aliphatic hydrocarbons. Industrially, Co- and Fe-based catalysts are used, with the choice of catalyst pending on the nature of the feed and/or the desired product. As an example, Fe-based catalysts can be operated at lower H_2/CO ratios in the feed due to a higher water-gas-shift (WGS) activity, they are more resistant to poisons in the feed and generate more olefins and oxygenates in the product spectrum when compared to Co-based FTS catalysts [1, 2]. The focus of this thesis departs to some extent from the conventional FTS reactions, by looking at the case where NH_3 is present in the synthesis gas during Fe-catalyzed FTS reactions. This concept of deliberately adding NH_3 during FTS has received attention in the past as a potential alternative route for the production of valuable N-containing hydrocarbons [3–5] and it was recently revisited by Claeys and Roessner [6–10]. Ammonia is however grouped with the FTS catalyst poisons [11], which particularly presents problems for biomass-derived syngas, where ca. 0.1 - 1.4 vol % NH_3 typically has to be removed prior to FTS reactions [12]. In this work, several aspects of the presence of ammonia in the iron-based FTS, are approached via two discrete techniques:

- Use of spin-polarized, periodic density functional theory (DFT) calculations to investigate the individual and coadsorption of CO and NH_x (with $x = 3, 2, 1, 0$) on a model Fe(100) surface (*Theoretical*).

- Evaluation of the performance of NH_3 addition during Fe-based FTS in a slurry phase reactor and use of additional co-feeding reactions to study the pathway to the formation of the N-containing compounds (*Experimental*).

Both studies are aimed at studying the possible changes when NH_3 is involved in the pathway to product formation, but the two systems under study are vastly separated by their respective scales and complexities. Theoretically, it is desired to shed light on the elementary reactions at the initial and final stages of the pathway to the formation of the FTS products and N-containing compounds on a model iron surface. CO adsorption and dissociation are assumed to be important elementary reactions during the initiation stage, when considering the proposed primary FTS pathways [13]. In this thesis it is desired to investigate the influence that NH_x ($x =$ 3, 2, 1, 0) has on these key elementary reactions for CO on a Fe(100) model surface. In addition, at the final stage of the pathway to the formation of N-containing compounds, elementary reactions that involve a combination of typical FTS surface species and an NH_x (with $x = 3, 2, 0$) surface species were proposed [6, 9, 10]. Since the NH_x surface species that are involved is merely speculative, periodic DFT calculations combined with statistical mechanics are thus employed in this work to gain an improved understanding of the decomposition of NH_x on the Fe(100) surface. The individual surface chemistry [14–16] of CO and its respective coadsorptions with H [17], S [18] and K [19] on the Fe(100) facet has been studied via spin-polarized DFT calculations to improve the understanding of these elementary reactions in the presence of co-reactants, poisons and promoters. Due to the importance of the ammonia synthesis reaction, experimental [20] and theoretical studies of NH_3 on the Fe(100) have been reported previously [21]. Sufficient literature is thus available for comparison with the DFT results presented in this work. Initially a model Fe(100) surface is optimized, and subsequently used for calculating the individual potential energy surfaces (PES) for the adsorption and decomposition of CO and NH_3 on the Fe(100). These results are compared with the above mentioned theoretical studies, and where possible with available experimental results. Moreover, the NH_3 decomposition pathway is evaluated at higher temperatures and pressures through the use of the harmonic transition state theory (TST) and statistical thermodynamics, which allows for the discussion of possible NH_x surface species present at the final stage of the formation of the N-containing compounds. In Chapter 6, a comparison is made between the individual adsorption profiles with the coadsorbed state

($CO + NH_x$) by calculating the heat of mixing (ΔE_{mix}) and the changes in activation barriers ($E_a/\Delta E_a$) for the CO dissociation reaction. Based on these results, the implications for the initiation steps in FTS are discussed.

In earlier experimental studies, the use of slurry phase reactors, when deliberately adding NH_3 to syngas during FTS was ruled out due to the low selectivity for N-containing compounds [3]. Sango et al. [9, 10] however recently revisited the use of a slurry phase reactor, by adding NH_3 during FTS over a potassium promoted Fe-based catalyst. They studied changes in the reaction while varying the concentration of NH_3 in the inlet between 0 - 35 vol %. At high NH_3 partial pressures (i.e. high NH_3 concentrations) a high concentration of aliphatic nitriles was observed, in addition to higher selectivities for primary amines and amides. The increase in NH_3 concentration did however lead to a decline in FTS activity, in particular at very high NH_3 partial pressures. Another important observation was a decline in oxygenate selectivity, which corroborated the results from similar reactions conducted in a fixed bed reactor, reported by Henkel [6]. The pathway to oxygenate formation in FTS when using Fe-based catalysts involves complex termination reactions that can follow primary or secondary reaction routes [2, 13, 22]. Based on the knowledge that oxygenates can undergo secondary reaction during FTS, and that Fe-based catalysts are active for amination reactions [23], it is hypothesized in this work that oxygenates formed via primary routes can re-adsorb on the catalyst surface to subsequently be converted to N-containing compounds via secondary reactions. In the experimental part of this thesis, a similar reaction setup as that of Sango [9] is used, in order to reproduce the reported loss in oxygenate selectivity. A direct comparison of the FTS activity, product selectivities, and spent catalysts was made between reactions conducted with and without 1 vol % NH_3 addition (Chapter 7), which allowed for a base case study that was not included in Sango's work. The analyses of the organic FTS product spectrum were performed via the use of comprehensive two-dimensional gas chromatography (GC×GC-TOF/FID) and on-line gas chromatography (GC-FID), which allowed for an improved understanding of the formation of the N-containing compounds. The concomitant loss of oxygenates with the production of the N-containing compounds was probed via co-feeding of an oxygenate (1-octanol) via a saturator with the feed ($CO + 2\ H_2 + 1$ vol % NH_3) during the reaction conducted in a slurry phase reactor in Chapter 8. In addition, nonanitrile was co-fed with a similar feed ($CO + 2\ H_2 +$

1 vol % NH_3) to evaluate the stability of these N-containing compounds during the NH_3 co-feeding FTS reactions. Furthermore, in Chapter 9, (1) the use of CO_2 as carbon source, (2) the evaluation of the product spectrum at higher space velocities (3) and the use of a Rh-based (Rh/Al_2O_3) catalyst is investigated. The results obtained in both the theoretical and experimental studies and its implications on the FTS and possible pathways to the formation of N-containing compounds are concluded in the relevant chapters, but a general summary is given in Chapter 10. Recommended future studies based on the results acquired in this thesis are summarized in Chapter 11.

REFERENCES

[1] E. van Steen and M. Claeys, Chem. Eng. Technol. 31 (2008) 655–666.

[2] M.E. Dry, Chapter 3 in Fischer-Tropsch Technology - Chemical concepts used for engineering purposes (Stud. Surf. Sci. Catal.), Vol. 152, Elsevier Science & Technology Books, 2004.

[3] R.B. Anderson, The Fischer-Tropsch synthesis, Academic Press, Inc., Orlando, 1984.

[4] W. Röttig, Catalytic hydrogenation of carbon monoxide with addition of ammonia or methylamine, US - 2,821,537 (1958).

[5] H. Kölbel and J. Trapper, Angew. Chem. Int. Ed. 5 (1966) 843–844.

[6] R. Henkel, The influence of ammonia on Fischer-Tropsch synthesis and formation of N-containing compounds, Ph.D. thesis, Carl von Ossietzky Universität (2012).

[7] M. Claeys, E. van Steen, A. Rausch and F. Roessner, A process for the production of hydrocarbons including olefins from synthesis gas, WO 2009/127950 A2 (2011).

[8] M. Claeys, E. van Steen, T. Sango and F. Roessner, A process for the production of nitrogen or phosphorous containing compounds from synthesis gas, WO 2009/127942 A2 (2011).

[9] T. Sango, N-containing compounds from ammonia co-feed to the Fischer-Tropsch synthesis, Master's thesis, University of Cape Town (2013).

[10] T. Sango, N. Fischer, R. Henkel, F. Roessner, E. van Steen and M. Claeys, Appl. Catal., A 502 (2015) 150–156.

[11] C.H. Bartholomew, Appl. Catal. A: General 212 (2001) 17–60.

[12] W. Torres, S. Pansare and J. Goodwin, Catalysis Reviews 49 (2007) 407–456.

[13] M. Claeys and E. van Steen, Chapter 8 in Fischer-Tropsch Technology - Basic Studies (Stud. Surf. Sci. Catal.), Vol. 152, Elsevier Science & Technology Books, 2004.

[14] D.C. Sorescu, D.L. Thompson, M.M. Hurley and D.C.F. Chabalowski, Phys. Rev. B: Condens. Matter 66 (2002) 035416–1–13.

[15] T.C. Bromfield, D.C. Ferré and J.W. Niemantsverdriet, ChemPhysChem 6 (2005) 254–260.

[16] P. van Helden, Initial steps of the Fischer-Tropsch synthesis on Fe(100): The role of hydrogen, Ph.D. thesis, University of Cape Town (2008).

[17] P. van Helden and E. van Steen, J. Phys. Chem. C 112 (2008) 16505–16513.

[18] D. Curulla-Ferré, A. Govender, T.C. Bromfield and J.W. Niemantsverdriet, J. Phys. Chem. B 110 (2006) 13897–13904.

[19] D.C. Sorescu, Surf. Sci. 605 (2011) 401–414.

[20] M. Grunze, F. Bozso, G. Ertl and M. Weiss, App. Surf. Sci. 1 (1978) 241–265.

[21] S.C. Yeo, S.S. Han and H.M. Lee, J. Phys. Chem. C 118 (2014) 5309 – 5316.

[22] E. Iglesia, Appl. Catal. A: General 161 (1997) 59–78.

[23] T. Mallat and A. Baiker, Handbook of Heterogeneous Catalysis - Amination Reactioins, Wiley-VCH, Weinheim, 1997.

Chapter 2

Literature Review

The Fischer-Tropsch Synthesis

Introduction

Fischer-Tropsch technology is an important industrial process, which transforms inexpensive starting material, such as coal, natural gas or biomass into clean fuels and chemicals. The FTS process makes use of synthesis gas ($CO + H_2$), which is generally produced via gasification or reforming processes. Subsequently, the complex "non-trivial" surface polymerization FTS reaction converts the synthesis gas to longer chain products [1, 2]. A variety of aliphatic (and aromatic) products, including paraffins, olefins, oxygenates and waxes can be produced during FTS. The research interest has fluctuated over the last 90 years due to socio-economic considerations as well as environmental constraints. However, the knowledge that has been acquired has led to the design of sophisticated catalysts and reactor systems, which makes the FTS a versatile reaction [3]. In this section an overview of the history of the process and the main and side reactions is given. In addition, the most important variables for the process are discussed, in particular those which highlight the important aspects that relate to the case where NH_3 is present in the synthesis gas.

FTS History

Two German researchers, Franz Fischer and Hans Tropsch, investigated the hydrogenation of CO over transition metal-based catalysts, and in 1925 reported the formation of longer chain length hydrocarbons at atmospheric pressure [4]. Following their discovery [5], they were involved in the elucidation of the mechanism and development of the process, and hence the process was attributed the name Fischer-Tropsch synthesis. If the relevant resources (e.g. coal or natural gas) are available, the FTS provides an alternative to the use of crude oil reserves and distantiation from the complexity of oil trading. Industrial application of the FTS was initiated in Germany during 1935 and lasted up to the end of World War Two [4, 6]. Towards the end of the war (ca. 1942-1950) the Hydrocarbon Research Inc. (HRI) developed a plant in Brownsville, Texas [7]. This natural gas based plant was shut down just before it reached design capacity due to an increase in the price of natural gas and concurrent discoveries in the Middle East [4, 7]. South Africa, due to political reasons and availability of inexpensive coal, was driven to be independent of oil trade and started developing its own FTS technology. During 1950, SASOL (South African coal and oil refineries) brought their first plant on-line. They installed circulating fluidized bed (CFB) reactors based on the reactors used in Texas [6]. Today, SASOL operates coal and gas-based plants in Secunda and Sasolburg, as well as in Qatar and further international expansion plans are being considered [8, 9]. PetroSA makes use of CFB technology to operate their 20 000 bbl/day plant in Mosselbay, South Africa. Shell is involved with the middle distillate synthesis (SMDS) plants in Bintulu, Malaysia and Ras Laffan, Qatar, which produce 15 000 and 140 000 bbl/day respectively [10]. Various proposals for future FTS plants in China, Australia, Indonesia, Russia, Argentina and Egypt have been proposed by various institutions [9].

The FTS reaction(s)

The FTS has been termed a “non-trivial” surface polymerization reaction, where syngas ($CO + H_2$) is converted to longer-chain hydrocarbons (see Eq. 2.1) [2]. The reaction is catalyzed by various transition metal-based catalysts (e.g. Fe-, Co-, Ni-, Ru-, Rh-based catalysts). Due to economic and selectivity constraints, only Fe- and Co-based catalyst are utilized industrially. In addition to the surface polymerization reaction (Eq. 2.1), the WGS (Eq. 2.2) and the

Boudouard (Eq. 2.3) reactions takes place. These reactions are discussed below.

The Fischer-Tropsch reaction: The overall FTS reaction, which includes the hydrogenation of carbon monoxide and subsequent coupling and desorption reaction(s) to produce linear and branched long-chain hydrocarbons, is highly exothermic. This feature is an important aspect in the design and operation of the process. Variation of the temperature of operation leads to a considerable shift in the product spectrum and has thus led to the separation of the two modes High Temperature Fischer-Tropsch synthesis (HTFT) and Low Temperature Fischer-Tropsch synthesis (LTFT). HTFT usually operates at temperatures ranging between 320 and 350 ℃, LTFT temperatures ranges between 220 and 250 ℃ and both are operated at elevated pressures (20 to 30 bar).

$$n\,CO + 2n\,H_2 \rightarrow (-CH_2-)_n + n\,H_2O \tag{2.1}$$

$$(\Delta H_{rxn,\,523\,K} = -158.5\,kJ/mol\,of\,CO\ \ \text{for n=1})$$

The Water-Gas-Shift reaction: When making use of an iron-based catalyst, the WGS reaction becomes important, especially at higher temperatures. The reaction can thus be utilized to shift a hydrogen poor syngas into an 'in-situ' hydrogen enriched gas. The synthesis gas obtained via gasification of coal or biomass generally has low syngas ratios (H_2/CO < 2). This is one of the reasons why an iron-based catalyst would be preferred over cobalt for biomass and coal-orientated FTS processes [11].

$$CO + H_2O \rightleftharpoons CO_2 + H_2 \tag{2.2}$$

$$(\Delta H_{rxn,\,523\,K} = -39.5\,kJ/mol\,of\,CO)$$

The Boudouard reaction: The surface reaction $2\,CO \rightleftharpoons C + CO_2$ is thermodynamically favored at FTS conditions, but does not readily take place when sufficient H_2 gas is present [12]. The Boudouard reaction can contribute to iron carbide formation when using iron-based catalysts during FTS.

$$2\,CO \rightleftharpoons C + CO_2 \tag{2.3}$$

$$(\Delta H_{rxn,\,523\,K} = -172.9\,kJ/mol\,of\,CO)$$

The Kölbel-Engelhardt Synthesis

Driven by an improved understanding of the WGS reaction, the so-called Kölbel-Engelhardt (KE) synthesis was developed [4]. In this reaction (Eq. 2.4) water is used as the source of hydrogen.

$$3n\,CO + n\,H_2O \rightleftharpoons C_nH_{2n+2} + 2n\,CO_2 \tag{2.4}$$

$$(\Delta H_{rxn} = -244.5\,kJ/mol)$$

Kinetic experiments (see Ref. [4]) have shown that an intermediate hydrogen producing step occurs (via the WGS reaction), and thus eliminates the need for its direct production. Stochiometrically, the KE synthesis can be regarded as the FT reaction, combined with multiple WGS reactions.

Versatility of the FTS reaction

The product spectrum obtained from FTS is complex since the products generally vary in chain length and functional groups. There are many variables that have an influence on the product spectrum. In Table 2.1, a summary of the possible effect on chain length, branching, product selectivies for olefins, alcohols and methane (S_{Olefin}, S_{ROH}, S_{CH_4}) and carbon deposition as a consequence of changing variables (temperature, pressure, H_2/CO ratios, conversion, space velocities and alkali content) is given (as sourced from Ref. [8]). In the experimental section of this thesis, a specific set of variables is used to study the pathway of formation of N-containing compounds. In principle, the variables for manipulating the FTS can be used in future studies, in conjunction with the findings of this thesis, to optimize the desired selectivities of N-containing compounds.

When considering the way in which the chain length of the products is influenced, the chain growth probability (α) serves as a valuable indicator. The value for α is mathematically expressed in equation 2.5 and can be extracted from the slope of the plot of $log(W_n/n)$ over n (see Ref. [12] and references therein).

$$log(W_n/n) = nlog(\alpha) + K \tag{2.5}$$

Table 2.1: van der Laan [8] summarizes the influence of certain parameters on chain growth, chain branching, the selectivities (S_x) of selected organic products and carbon deposition.

Parameter	Chain length	Branching	S_{Olefin}	S_{ROH}	S_{CH_4}	C-deposition
Temperature	↓	↑	*	↓	↑	↑
Pressure	↑	↓	*	↑	*	↓
H_2/CO	↓	↑	↓	↓	↓	↑
Conversion	*	*	↓	↓	↑	↑
Space velocity	*	*	↑	↑	*	↓
Alkali content	↑	↓	↑	↑	↑	↓

Indicators (↑, ↓ and *) represents incline, decline or complex relation when increasing parameter.

where W_n is the mass fraction of products with a carbon number n and K is a constant.

In Table 2.2, an example is given of a typical FTS product spectrum as well as the chain growth probabilities (α) that can be expected when using cobalt or iron-based catalysts in either slurry phase or fluidized bed reactors at the relevant temperatures. This data was taken from the work of Dry in Ref. [12]. Considering the changes in the selectivies for the FTS products, one can see how the product formation is significantly influenced by the choices of these parameters.

Iron-based FTS catalysts

Iron- and cobalt-based catalysts are currently the only commercially applied catalysts. The choice of catalyst is governed by a combination of the economic considerations (e.g. price of metal) and the desired final product (e.g. wax, jet fuel, diesel). As mentioned before, iron-based catalysts are preferred for coal-derived synthesis gas and they are potentially the ideal catalyst for biomass-derived synthesis gas. This is due to the higher resistance to poisons and high WGS activity, which allows for the use of synthesis gas with lower H_2/CO ratios [11]. Iron-based FT catalysts are typically promoted with potassium, which improves catalyst activity and promotes chain growth as well as the WGS activity [12, 13]. Importantly, potassium promotion also leads to improved selectivities of valuable chemicals, such as olefins and oxygenates. Iron-based catalysts can be further modified with copper, which acts as a reduction promoter, and

Table 2.2: Typical product distributions observed when using different industrial FTS catalysts, reaction temperatures and reactor systems. Data is taken from Ref. [12]

FT product spectra at 20 bar

Catalyst	Cobalt	Iron	Iron
Reactor type	Slurry	Slurry	Fluidized
Temperature °C	220	240	340
% Selectivities on C atom basis			
methane (CH_4)	5	4	8
ethene (C_2H_4)	0.05	0.5	4
ethane (C_2H_6)	1	1	3
propene (C_3H_6)	2	2.5	11
propane (C_3H_8)	1	0.5	2
1-butene (C_4H_8)	2	3	9
n-butane (C_4H_10)	1	1	1
C_5 - C_6	8	7	16
C_7 - 160 °C	11	9	20
160 - 350 °C	22	17.5	16
+350 °C	46	50	5
Total water soluble oxygenates	1	4	5
ASF alpha value (α)	0.92	0.95	0.7

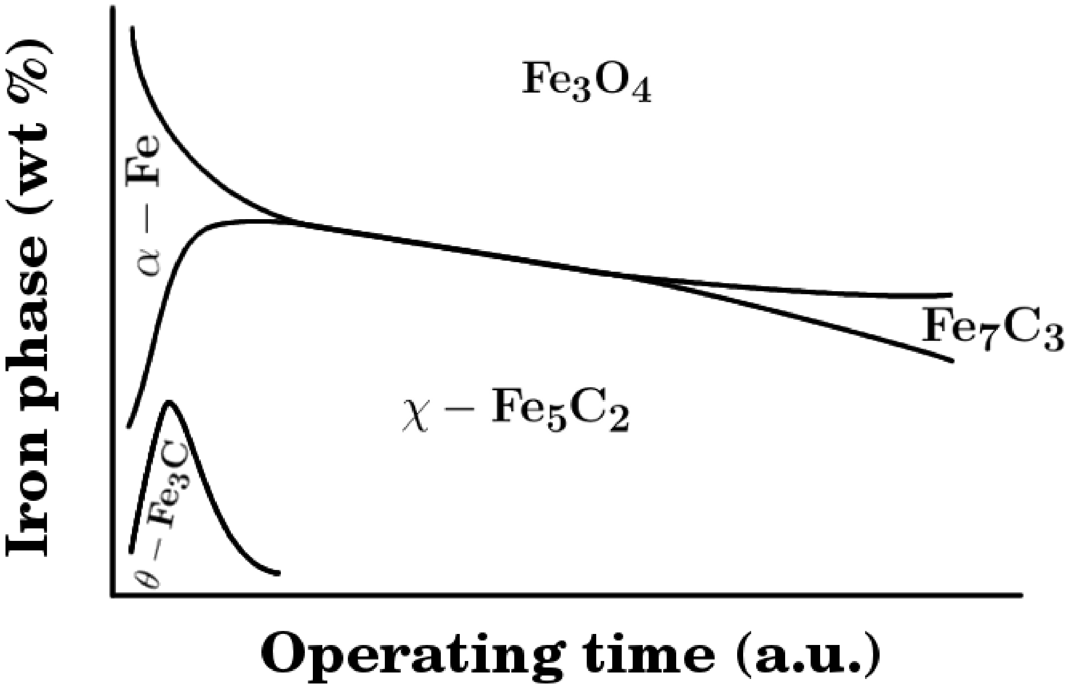

Figure 2.1: Depiction of the phases present during FTS as a function of time on stream. Adapted from [14]

structural promoters such as silica, which is used in the low temperature "Ruhrchemie" catalyst [12, 13]. Dry [14] reported changes of catalyst phase composition as a function of time on stream for a reduced high temperature Fe-based FT catalyst as shown in Figure 2.1. These phase transformations have also been observed during the initial stages of low temperature FTS when CO_2 was used as a carbon source [15]. A set of in-situ techniques, including in-situ X-ray Absorption Fine Structure Spectroscopy (XAFS), wide angle X-ray scattering (WAXS), X-ray Diffraction (XRD) and Raman Spectroscopy were used to study the active phase of iron-based catalysts during FTS [16–18]. These studies revealed that, depending on the pretreatment followed (reduction via H_2 or syngas ($CO + H_2$)), a combination of $\alpha - Fe$, $\gamma - Fe$, $\theta - Fe_3C$, $\varepsilon - Fe_2C$, $\varepsilon' - Fe_{2.2}C$, $\chi - Fe_5C_2$ and Fe_3O_4 can exist as bulk phases after FTS. Furthermore it was shown in these studies that a large fraction of the catalyst can exist as amorphous carbide phases. These results would suggest that the active phase during FTS is a form of iron-carbide, with the Hägg caride, $\chi - Fe_5C_2$ often observed as the main phase. It is however not clear what the exact active phase is for iron-based catalysts during FTS.

FTS catalyst deactivation

Apart from the activity and selectivity, the lifetime of a catalyst plays a pivotal role in the choice and design of a catalytic process [6]. It is inevitable that all catalysts are exposed to some mode of poisoning, which leads to a decline in catalytic activity [19]. The costly catalyst thus has to be replaced or, if possible, regenerated after a certain time spent on-line. It is therefore important to gain a fundamental understanding of the mechanisms of poisoning, and in doing so acquire information that could be used to minimize or, if possible, reverse the deactivation. Considering the origin of the reactant (i.e. synthesis gas from natural gas, coal or biomass) and products (H_2O, CO_2, aliphatic and aromatic organic compounds), the Fischer-Tropsch process is prone to several forms of deactivation [19]. Reaction with the products H_2O and CO_2 can lead to oxidation of the active bulk phase to a less or non-active phase (e.g. conversion of Fe_5C_2 to Fe_3O_4). In certain cases, CO has the potential to form inorganic complexes (e.g. $Ni(CO)_4$ [20]) and subsequently leach metal particles from the surface. The carbonaceous products (e.g. aromatic hydrocarbons) can build up on the catalyst surface, thus blocking active sites and in addition result in plugging of the reactor. Gases that contain electronegative atoms (e.g. H_2S, NH_3), are present in coal- or biomass-derived synthesis gas and can interact with the metal surface. The use of biomass derived synthesis gas has been indicated as an important alternative source of energy and fuel in the United States of America (USA) (see Figure 2.2, [21]), which necessitates extensive knowledge of the "cut-off" concentrations for N- and S- containing synthesis gas [11].

The effects of S-containing volatile compounds have been evaluated to a large extent for FTS [4, 22–26]. Bartholomew and Bowmen [22] evaluated the effect of sulfur poisoning by adding 0.5 - 8.0 ppm levels of H_2S to synthesis gas during FTS, when using a K-promoted and borated iron catalyst supported on silica in a differential reactor ($T = 227$ ℃, $P = 1.01$ bar, $H_2/CO = 2.0$). Based on their results, they concluded that below 2 ppm addition of H_2S, only monolayer sulfides form, whereas bulk sulfides are likely to form at higher concentrations (2.0 - 8.0 ppm H_2S). In addition, they showed that in-situ poisoning was more detrimental to the catalyst than pre-sulfiding the iron-based catalyst. Furthermore, boride seemed to act as deterrent for S poisoning. Chaffee et al. [23] evaluated the potential of a series of prepared and commercially available FT catalysts to resist H_2S (300 ppm) poisoning in a fixed bed reactor ($T \rightarrow$ based on desired CO conversion, P = 21.0 bar, $H_2/CO = 2.0$, gas hourly space velocity (GHSV) ca. 800-1000 ml/g_{cat}/hr). Deactivation of all catalysts was observed at these concentrations of H_2S, however the addition of Mn significantly (by two orders of magnitude) improved the iron-based catalyst's resistance to H_2S poisoning. The authors argued that a fast S-exchanging reaction between manganese and sulfur ($MnO + S \leftrightarrow MnOS$), resulted in protection of the active iron-based catalyst. In contrast to the detrimental effects of S, the promotional effects have been demonstrated when S is incorporated ex-situ (e.g. pre-sulfided iron-based catalysts) in low concentrations [27–30]. Bromfield and Coville [27] added varied amounts (500 - 20000 ppm) of Na_2S to a precipitated iron catalyst and observed increased FTS activity of up to four times, when lower (500 - 5000 ppm) concentrations of Na_2S were added. The highly sulfided (20000 ppm) catalyst reduced rapidly to α-Fe, which seemed to retard the carburization process during the initial stages of the FT reaction (fixed bed reactor (FBR), T = 250 ℃, P = 8.0 bar, $H_2/CO = 2.0$, GHSV = 400/800 ml/g_{cat}/h). It was concluded that the carbide phase is the active phase for FTS in their catalysts, the formation of which was suppressed by the highly sulfided α-Fe. Wu et al. [28] reported low methane selectivities (2.0 - 2.9 %) and high C_{5+} selectivities upon the addition of 150 ppm of SO_4^{-2} when preparing their iron-based catalyst from a ferrous sulfate precursor (FBR/continuous stirred-tank reactor (CSTR), T = 250/260 ℃, P = 20.0 bar, $H_2/CO = 2.0/0.67$, GHSV ca. 2.0 Nl/g_{cat}/hr). Torres-Galvis et al. [29, 30] recently reported on the novel preparation of a catalyst consisting of Fe-nanoparticles, promoted with Na and S and supported on α-alumina or carbon nanofibers. These catalysts were shown to produce a selectivity of up to 60 wt % C_{2-4} olefins during their FTS catalyst testing (FBR, T = 340/350 ℃, P = 1/20 bar, $H_2/CO = 1$, GHSV = 10500/3000 ml/g_{cat}/h).

Proteins, DNA, RNA, chlorophyll, alkaloids and porphyrins all contain nitrogen which lead to high content of NH_3 (c.a. 0.1 - 1.4 vol %) found in synthesis gas obtained via gasification of biomass [31]. However, even though NH_3 is grouped as a FTS catalyst poison, fewer studies [25, 32, 33] exist that evaluate the tolerability of FTS catalysts against NH_3 poisoning. To test the influence of several biomass-derived synthesis gas impurities on FTS activity, Borg et al. [25] introduced 23 combinations of impurity elements (e.g. Na, Ca, Cl) to a cobalt-based catalyst by an incepient wetness procedure. This study included the in-situ addition of 4 ppm of NH_3 during FTS (FBR, T = 170 ℃, P = 20 bar, $H_2/CO = 2.1$, GHSV →depended on

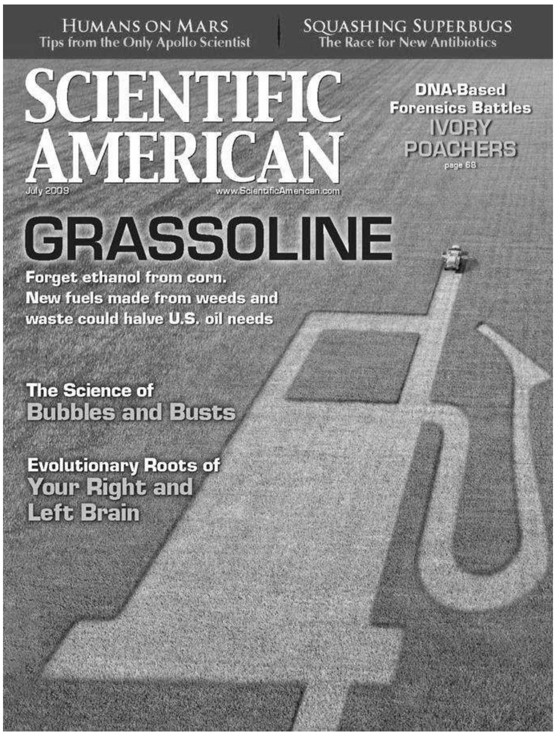

Figure 2.2: Biomass-derived synthesis gas has significant potential for alternative fuel source in the USA. (Figure from July, 2009 copy of **Scientific America** [21])

catalyst/experiment), and no appreciable decline in activity was observed. Pendyala et al. [32] added between 1-1200 ppmw NH_3 during FTS, when using a cobalt-based catalyst (CSTR, T = 220 ℃, P = 19 bar, SV = 5 SL/g_{cat}/h). A constant loss of ± 5 % in CO conversion was observed at all concentrations. At higher concentrations a decrease in methane selectivity and increase in C_{5+} hydrocarbons selectivity was observed. Sango et al. [33–35] added between 0 - 35 vol % NH_3 during FTS with an iron-based catalyst for the purpose of producing valuable N-containing chemicals (slurry phase reactor, T = 270 ℃, P = 4 bar, H_2/CO = 2, GHSV = 2250 ml/hr/g_{cat}). They found minimal de-activation when using "low" (2 vol%) concentrations of NH_3 in the reactant stream. After a certain period (i.e. after 10 vol % NH_3 addition) of the reaction, the NH_3 addition was terminated which showed that activity could be recovered to some extent (see Appendix C Figure C.14).

The addition of NH_3 during Fischer-Tropsch Synthesis

Introduction

In this section the literature for the reaction where NH_3 is added as a reactant with synthesis gas ($CO + H_2$) during FTS, to produce valuable N-containing compounds is discussed (see Eq. 2.6 for the formation of amines). Producing chemicals in this way is not a novel concept, but is not a widely studied reaction [4].

$$n\,CO + 2n\,H_2 + NH_3 \rightleftharpoons C_nH_{2n+1}NH_2 + 2n\,H_2O \tag{2.6}$$

$$(\Delta H_{rxn} = -39.2\,kcal/mole\;amine)$$

However, literature in the form of patents and theses provide invaluable information. A thorough review of all forms of relevant publications is given and should provide an improved understanding of the current state-of-the-art. In addition, a discussion of the practical and economic aspects of the process, in particular the relative value of the N-containing compounds when compared to the normal FTS product spectra, is reported.

Economic incentive

To gain insight into the economic value of the N-containing compounds that are produced when NH_3 is added during FTS, the prices of some common petroleum products and FTS chemicals are compared. A full description of these values is given in Appendix A, and only the summary of the results is presented here. In Figure 2.3 prices for petroleum products, olefins, oxygenates and N-containing compounds are compared on the basis of their value in U.S. dollar per pound. This figure clearly shows that the values for the N-containing compounds are significantly higher than “fuels” in the same carbon number range, and even higher than the typical chemicals (olefins, oxygenates) produced from FTS. This is due to the fact that the starting materials for the production of N-containing compounds are in fact usually oxygenates or olefins. Therefore, ammonia co-feeding during the FTS provides a potential route to directly produce these N-containing compounds from inexpensive starting materials.

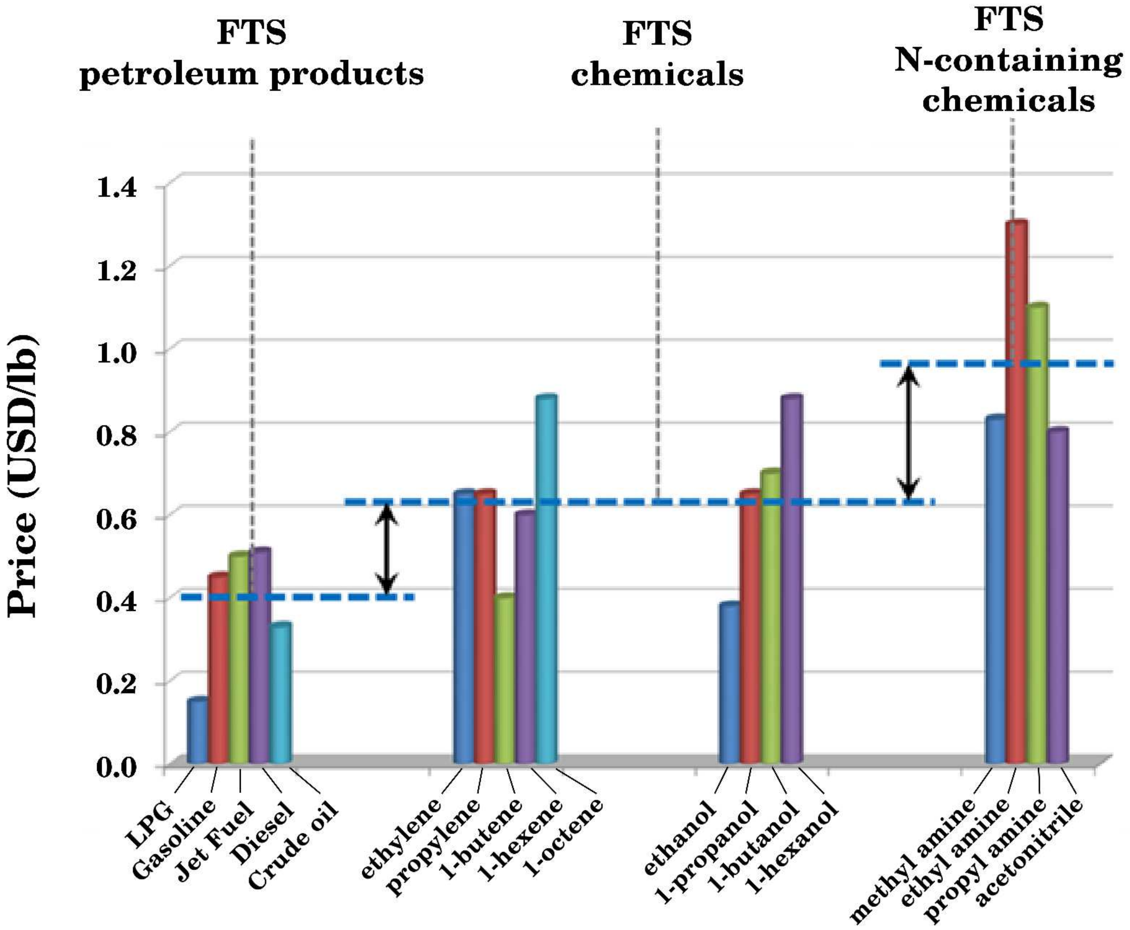

Figure 2.3: A comparison of the prices of various FTS petroleum products (e.g. LPG, jet Fuel), FTS chemicals and N-containing compounds.

Patent literature

Considering the economic incentive, most literature pertaining to this work is presented in the form of patents or patent applications [36–38]. The earliest example of an attempt to produce valuable chemicals in this way was published by Clark [36] who filed a patent in 1947 (published in 1950). He reported efforts to design a process (see Figure 2.4), where both FTS products (paraffins/olefins) and the primary amines, which are formed during the reaction upon ammonia co-feeding, could be isolated. Cobalt- and iron-based catalysts were tested at differentn temperature ranges (182-221 and 282-326 ℃ respectively). These reactions were conducted in a reactor "suitable for FTS", with a 2:1 H_2/CO ratio, a total pressure of 10 bar and varying space velocities (GHSV = 2400 - 4200 ml/g_{cat}/h). The major difference between the two examples given was the observation that N-containing organic compounds were present in the product wax when using the cobalt-based catalyst. In addition, he reported the formation of ammonium carbonate present in the water phase, which has relevance for the results presented in this work. No clear quantitative data with respect to the product spectra were given by Clark [36].

During the 1950's Röttig [37] published a patent claiming an improved process for the production of N-containing compounds via FTS. When adding methyl amine or NH_3 with synthesis gas during FTS over a copper and/or potassium promoted iron-based catalyst a yield of 12 - 17 % primary amines as well as 30 - 39 % linear alcohols was obtained. In the examples given, water gas (i.e. syngas generated via passing steam over coke) containing 2 % NH_3 was passed over an iron-based catalyst in a fluidized bed reactor. A syngas conversion (CO + H_2) of 55-65 % was achieved at temperatures ranging between 183 - 193 ℃, at a space velocity of GHSV = 6000 ml/g_{cat}/h and a total pressure of 30 bar. No major differences could be deduced from the results given, where the major variables were the catalyst promoters (Cu and K). A closer investigation shows a slightly higher ratio for the N-containing compounds compared to the linear alcohols when using the catalyst that contained no potassium. Claeys et al. [38] recently filed a patent, where they show how an increase in ammonia concentration (0 - 35 vol % NH_3 added to synthesis gas) results in an increase in selectivity of N-containing compounds. This trend was also observed for the formation of aliphatic nitriles. Bartley et al. [39] reported on the selective production of various N-containing compounds (including secondary and tertiary C_{1-2} amines) when pumping 24 ml/hr of NH_4OH during FTS reactions ("Berty-type reactor", T =

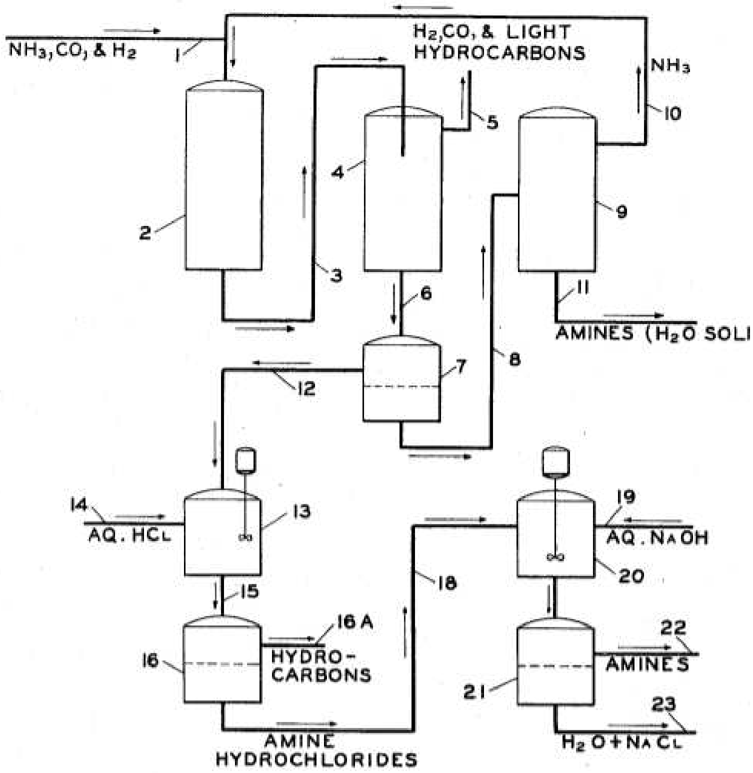

Figure 2.4: Process designed by Clark [36] for the production and separation of primary amines via the addition of NH_3 during FTS

300 ℃, P = 69 bar, H_2/CO = 1:1, GHSV = 9000 ml/g_{cat}/hr) conducted with a rhodium-iron based catalyst.

The extensive evidence for the production of N-containing compounds via FT technology has led to a number of academic studies discussed below.

Academic literature

The collaborative effort of the University of Cape Town and the Carl von Ossietzky Universität in Oldenburg (Germany) has generated an additional knowledge base for conducting these reactions on laboratory scale [34, 40, 41]. The present study is a continuation of the work conducted by Sango [34, 35], who evaluated the FTS product selectivity and activity as a function of increased ammonia concentrations (0 - 35 vol %) as the only parameter varied. A precipitated iron-based catalyst was used in a slurry phase reactor at low temperature FT reaction conditions (T = 250 ℃, P = 5.0 bar, CO/H_2 = 2.0 , GHSV = 2250 ml/g_{cat}/hr). At lower concentrations (2 and 5 vol %) the dominant N-containing compounds were primary amines. An increase in NH_3 concentration led to an increase in aliphatic nitriles, which is an industrially sought chemical. A patent was published on the work [38].

The oxygenate and N-containing compound content in the C_{1-20} fraction before and after 10 vol % NH_3 was added is summarized in Table 2.3. An important observation was a concomitant decrease in oxygenate selectivity with increased selectivity for the desired products (the N-containing compounds) (see Table 2.3). This led to the proposition that oxygenates precursors lead to the formation of N-containing compounds. Alternatively, some of the primarily formed oxygenates could be consumed via secondary reactions to yield N-containing compounds.

Sango [34] included calculations of Gibbs free energies ($\Delta G_{f,500K}$ (kJ/mol_{CO})), for linear aliphatic alkanes, alkenes and selected O- and N-containing compounds as a function of carbon number (see Figure 2.5) for the reaction where NH_3 is added as reactant. (Thermodynamic data used in these calculations were obtained from Daubert et al. [42].) Even though the FTS is governed by kinetics [4], these thermodynamic calculations serve as a valuable tool in determining the relative stability of different compound classes and therefore the feasibility of their formation. The major conclusion in this regard, is that it is thermodynamically feasible for N-containing compounds to form, to approximately the same extent of the FT oxygenates at

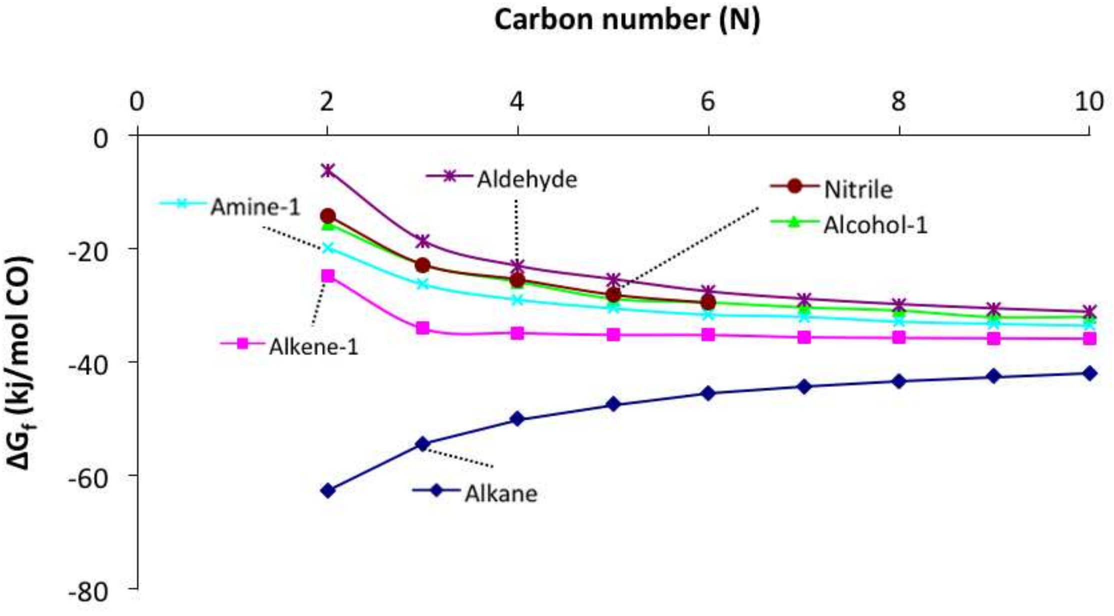

Figure 2.5: Comparative calculation of the Gibbs free energy of formation for a set of linear alkanes, alkenes and selected O- and N-containing compounds. Adapted from [34] (Data used in calculations from [42]

Table 2.3: Content of oxygenates and N-containing compounds (given in C wt %) reported by Sango et al. [35] for the C_{1-20} fraction at steady state and after 24 hrs of 10 vol % NH_3 addition during FTS. (slurry phase reactor, T = 250 ℃, P = 5.0 bar, $CO/H_2 = 2.0$, GHSV = 2250 ml/g_{cat}/hr)

	NH_3 conc. (vol%)	
Conc. (C%)	**0**	**10**
Alcohols	6.6 ± 0.13	1.9 ± 0.04
Aldehydes	4.7 ± 0.09	0.1 ± 0.01
Carboxylic acids	0.3 ± 0.01	n/a
Methyl-ketones	4.8 ± 0.10	4.8 ± 0.10
Amines	n/a	7.0 ± 0.14
Nitriles	n/a	2.6 ± 0.05
Amides	n/a	2.2 ± 0.04
Sum	16.4	18.6

the conditions that was considered in aforementioned calculations. It is interesting to note that linear nitriles and alcohols have similar $\Delta G_{f,500K}$-values, and would thus be present in equimolar quantities if this reaction was in equilibrium at 500 K. The role of the catalyst is inevitably to manipulate the “natural” rates of reactions, which thus necessitates kinetic evaluations.

The effects of NH_3 addition (p_{NH_3} = 0.0 and 0.2 bar) during FTS, when using bulk iron- and cobalt-based catalysts, for fixed bed operation were further probed by Henkel [41] (T = 270 ℃, P = 4.0 bar, $H_2/CO = 2.0$, GHSV = 1920 ml/hr/g_{cat}). During the NH_3 co-feeding FTS reactions that was conducted using Fe-based catalysts with no K content, the addition of NH_3 led to higher catalyst activities, chain growth probabilities and selectivity for olefins, which led the author to suggest that NH_3 could play a similar promotional role as K does in Fe-catalyzed FTS. Similar to the work of Sango [34, 35] a link between the oxygenates and N-containing compounds was observed. Henkel [41] showed that the molar values of the N-containing compounds compensated, quantitatively, for the loss of molar values of the oxygenates. This further indicates the conversion of oxygenates to N-containing compounds without the loss to the paraffins. The N-containing compounds formed during these reactions were predominantly primary

amines and aliphatic nitriles, with smaller quantities of amides and formamides.
The analysis of the products produced during Fe-based FTS is inherently problematic due to the large distribution in the chain lengths of the products and the presence of the different classes of products (i.e. olefins, paraffins, oxygenates and aromatics) which could in turn be either branched or linear. To isolate and quantify the oxygenates is even more complex, considering the different functional groups that can be present present i.e. -OH, $-COCH_3$, -CHO and COOH. Similarly, the difficulties in the analysis of the N-containing compounds were highlighted in the NH_3 co-feeding studies of both Henkel [41] and Sango [34], which could be expected considering the similarities of the functional groups in the N-containing compounds i.e. $-NH_2$, -N and $CONH_2$. The advent of comprehensive two-dimensional gas chromatography (GC×GC-TOF/FID) has recently shown superior ability to separate and quantify oxygenates obtained from Fe-based catalysed FTS reactions [43–45]. This technique could thus be ideally suited for the analysis of such a complex system of compounds formed when NH_3 is co-fed during FTS.

Kölbel Engelhardt conditions

Not too long following the discovery of the direct synthesis of N-containing compounds via the addition of NH_3 during FTS, Kölbel and Trapper conducted similar experiments using an iron-based catalyst (Fe:Cu:K = 100:0.2:0.34 wt %), but instead of H_2, used steam (H_2O) as reactant (see Section 2.1.4) [4, 46–49]. They report the ability to produce up to 25 wt.% primary amines, which was the chief compound formed when NH_3 was added during FTS in a fixed bed reactor (T = 200 - 250 °C, P = 11 bar, $H_2O/CO = 0.33$, 0.9 - 1.1 % NH_3, GHSV = 350 - 370 Sl/l_{cat}/h) [4, 46, 47]. The reaction for the formation of primary amines via the KE route can be expressed as shown in Eq. 2.7

$$3n\,CO + n\,H_2O + NH_3 \rightleftharpoons C_nH_{2n+1}NH_2 + 2n\,CO_2 \tag{2.7}$$

$$(\Delta H = -52.2n\,kcal/mole\,amine)$$

In addition, Kölbel et al. [48, 49] showed the potential of incorporating various groups of N-containing compounds (e.g. piperidine, pyrrolidine; see Figure 2.6) under similar reaction conditions. It was concluded that the use of slurry phase reactors (CSTR) was not suitable for these types of reactions [4].

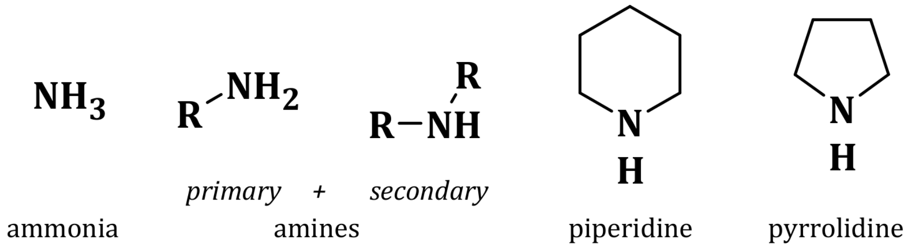

Figure 2.6: Apart from the addition of NH_3, Kölbel and Trapper [47] explored and succeeded in the incorporation of various N-containing compounds.

Amination reactions

The amination reaction generally refers to the insertion of an amino group into an organic compound [50] and it may be closely linked to the pathway of N-containing compounds when NH_3 is co-fed during FTS. Amination reactions describe a broad set of reactions, which are normally used to refer to the conversion of oxygenates (e.g. aldehydes, alcohols) to N-containing organic compounds. It is known that an iron-based catalyst, similar to the catalyst used in previous NH_3 co-feeding FTS reactions [34, 41], is active for the amination reaction [50]. Furthermore, in the previous work where NH_3 was co-fed during FTS [34, 41], a dramatic loss in oxygenates selectivity was observed, suggesting that the N-containing compounds form through the detriment of the oxygenates. If one considers the high probability of oxygenates to undergo secondary reactions during Fe-based FTS [7, 51], it is fair to assume that the N-containing compounds evolve via similar pathways. For the amination reaction where a linear aliphatic alcohol is converted to a linear aliphatic amine of the same carbon chain length, the following hypothetical pathway can be constructed:

$$ROH + * \rightleftharpoons ROH^* \tag{2.8}$$

$$ROH^* + * \rightleftharpoons R^* + OH^* \tag{2.9}$$

$$NH_3 + * \rightleftharpoons NH_3^* \tag{2.10}$$

$$NH_3^* + * \rightleftharpoons NH_2^* + H^* \tag{2.11}$$

$$R^* + NH_2^* \rightleftharpoons RNH_2 + 2* \tag{2.12}$$

(Please note that this pathway can be constructed in several different configurations. This proposed pathway is employed to aid the discussion.)

Considering the hypothetical pathway with reactions 2.8 - 2.12, it can be seen that amines could form via primary and/or secondary pathways. Reactions 2.8 - 2.12 would thus be considered as a conversion of a primarily produced FTS oxygenate to a N-containing compound via a secondary reaction. Competition between the reverse reactions 2.8 and 2.9 and the forward reaction 2.12 could explain the loss of oxygenates via a primary route. The latter reaction is, to some extent, easier to test as a possible sink for oxygenates via co-feeding the oxygenate. The extent to which this conversion takes place as a primary or secondary route is not known. In fact, the possibility of converting a primarily produced FTS oxygenate to form N-containing compounds via a secondary route is only hypothesized [34, 35, 41].

Primary FTS pathways

The Fischer-Tropsch reaction pathways are characterized by a network of possible elementary reactions. These individual bond cleaving and formation reactions can in turn be catalyzed by more than one catalytic site. Depending on the catalyst of choice, the bulk of the catalyst can range from interstitial metals (e.g. Fe_2C or Fe_3O_4) to pure metals (e.g. Co or Rh) which are typically supported on metal oxides (e.g. Al_2O_3 or SiO_2). In the case of Fe-based FTS reactions, a combination of these bulk phases co-exists. If one now adds the complexity of variable operating conditions such as pressure, temperature and reactor system, it becomes easy to see why several aspects of the FTS mechanism are not fully understood. However, it should be noted that extensive research in this field has allowed numerous pathways to be proposed. The most relevant and widely accepted pathways will be discussed shortly (several good reviews are available [4, 7, 52] for the interested reader). Experimental (and theoretical efforts) have aided an improved description of the FTS pathways to product formation (see Ref. [52] and references therein). These mechanisms are regarded as primary routes to product

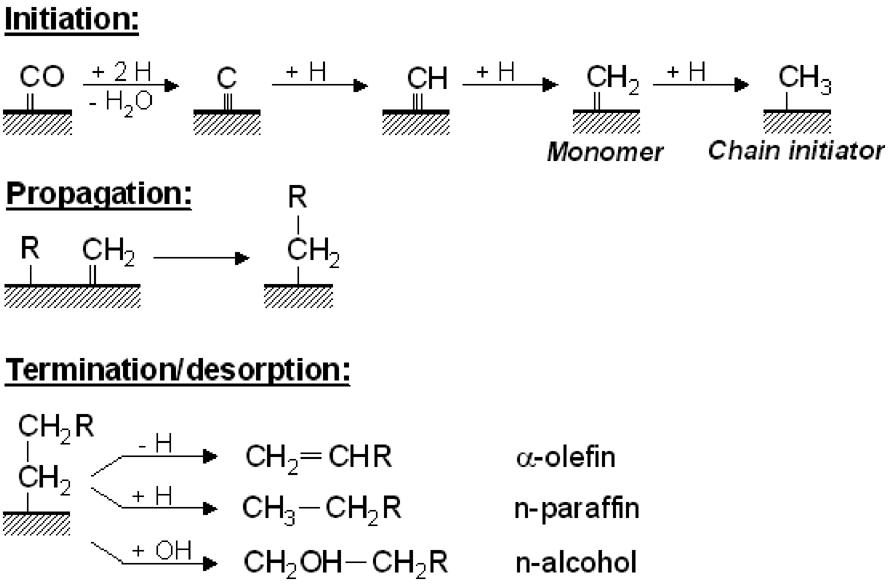

Figure 2.7: The carbide or alkyl mechanism. Adapted from [52].

formation, i.e. n CO and $2n$ H_2 molecules undergo one sequence of a "non-trivial surface polymerization" reaction to yield a long-chain hydrocarbon [1]. It is important to define the similarities, differences and requirements of the most widely accepted reaction pathways (e.g. carbide, CO insertion or enol mechanism).

The carbide (or alkyl) mechanism

The so-called carbide or alkyl mechanism (see Figure 2.7) is generally the most accepted pathway [4, 7, 8, 17, 52–54]. For this pathway it is assumed that CO adsorbs on the metal surface where the C$-$O bond is cleaved to generate surface C^* and O^* species. These adsorbates are subsequently hydrogenated to form the surface species CH^*, CH_2^*, CH_3^* or OH^*. In the formulation of the carbide mechanism, CH_3^* further acts as the chain initiator and CH_2^* as the monomeric surface species. Chain growth is thus achieved via continuous insertion of the monomer (CH_2^*) into the growing chain (R^*). The carbide mechanism does not provide adequate information regarding the formation of oxygenates.

The Enol mechanism

The enol mechanism, proposed by the Storch et al. [55], is based on the formation of an oxygen-containing enol surface species that initiates the surface polymerization reaction (see Figure 2.8). These enol species, in addition, are involved in the propagation of the chain via a condensation reaction where H_2O is eliminated. The primary products formed are oxygenates and α-olefins, while paraffins are thought to occur via an alternate mechanism or secondary hydrogenation of the olefins.

The CO insertion mechanism

The CO-insertion mechanism, fully developed by Pichler and Schulz [56], involves a CO insertion reaction that resembles those well-known in homogeneous catalysis. The adsorbed CO^* thus acts as the monomer, that is continuously inserted into a growing alkyl chain. The alkyl chain is initiated via the formation of a methyl (CH_3^*) surface species. The termination steps allow for the formation of α-olefins and paraffins similar to the 'alkyl' mechanism. The formation of oxygenates follows from several possible steps which involve an acyl intermediate. The formation of oxygenates are best described via the CO insertion mechanism. Considering all the advantages and disadvantages of the various reaction mechanisms, Hinderman et al. proposed that more than one mechanism may be at play in order to account for the complexity of the FT product spectrum.

Current views on primary FTS pathways

Since the FTS pathway is complex and to a large extent unresolved, several studies are frequently conducted in order to improve the understanding (or extend the conversation) of the FTS pathway. Some recent studies will be highlighted. Ojeda et al. [57] combined kinetic FTS tests (using Fe- and Co-based catalysts in a fixed bed reactor) and self-consistent DFT calculations (on Fe(110) and Co(0001) model systems) to probe mechanistic details of monomer formation via direct or H-assisted CO activation. That is, they compared the direct CO bond breaking process (as it is classically assumed to occur in various proposed mechanisms) with a pathway where CO instead initially reacts with H adsorbates to form an intermediate (e.g. formyl ("HCO")) surface species, that is subsequently decomposed to CH + OH units. Both

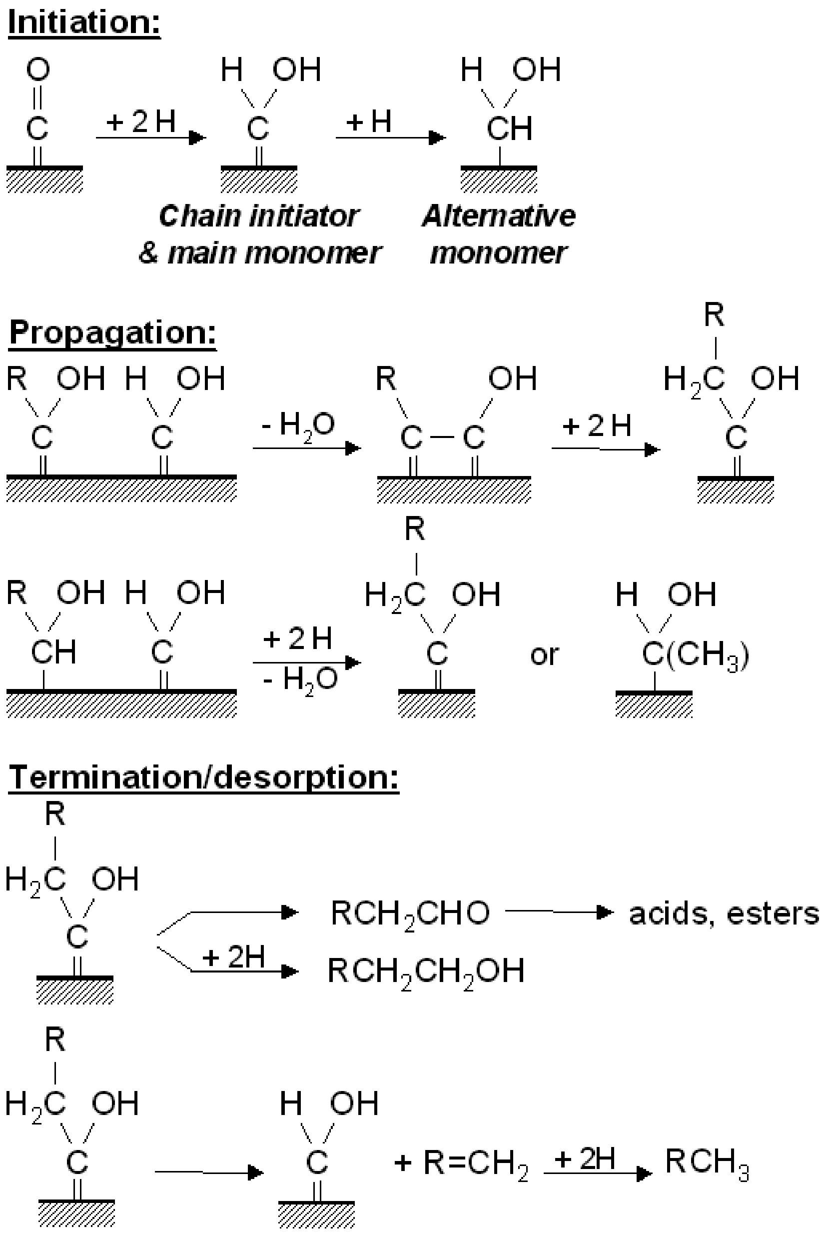

Figure 2.8: The enol mechanism. Adapted from [52].

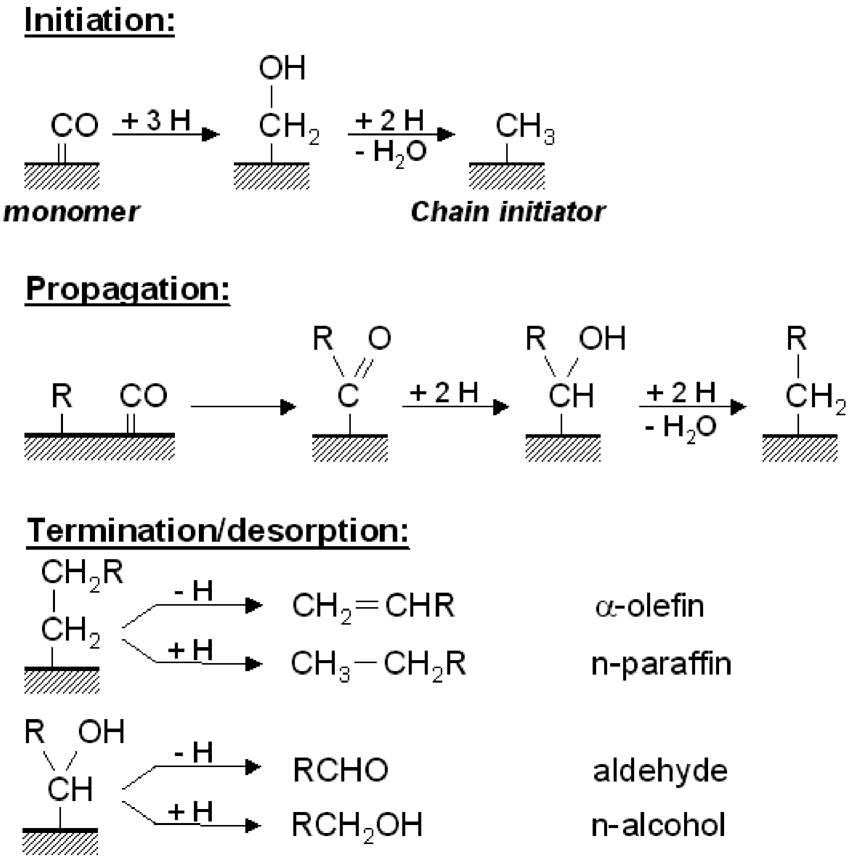

Figure 2.9: The CO insertion mechanism. Adapted from [52].

their experimental and theoretical results clearly showed that direct CO dissociation plays a minor role in monomer formation, and that the alternate route, the formation of C_1 units via H-assisted pathways would be energetically favored.

Secondary FTS pathways

Secondary reactions of the FTS refer to the set of reactions where some of the reactants (e.g. α-olefins, oxygenates) that were produced during a primary FTS reaction (as discussed in previous sections) are converted to secondary FTS products (e.g. internal olefins, paraffins). These reactions can play a pivotal role in shaping the product spectrum observed. In particular, when a longer residence time allows “lingering” of the primary products in the vicinity of the catalyst to further undergo secondary reactions. The most common and more thoroughly studied secondary reactions are those of the α-olefins and will briefly be discussed before introducing secondary reactions of oxygenates, which are important aspects of the work discussed throughout the experimental part of this thesis.

Secondary reactions of α-olefins

α-Olefins are primary products of the FTS that can re-adsorb on the catalyst surface to be hydrogenated to the corresponding paraffins, initiate further chain growth or undergo isomerization [52]. Schulz and Claeys [59] co-fed a range of C_{2-11} α-olefins during FTS with a cobalt-based catalyst in a gradientless slurry phase reactor to investigate their secondary reactions, and importantly, their chain length dependence at various reaction conditions. The chain length dependencies of the secondary hydrogenation and incorporation reactions observed during co-feeding reactions could be correlated with the base case FTS experiments where no α-olefins were added. They ascribed the chain length dependencies to be mainly due to solubility of the olefins in the liquid reaction product (see Figure 2.10). Claeys [60] conducted a similar set of α-olefin co-feeding FTS experiments with an Fe-based catalyst, which illustrated that these secondary reactions are also at play during FTS reactions where Fe-based catalysts are used.

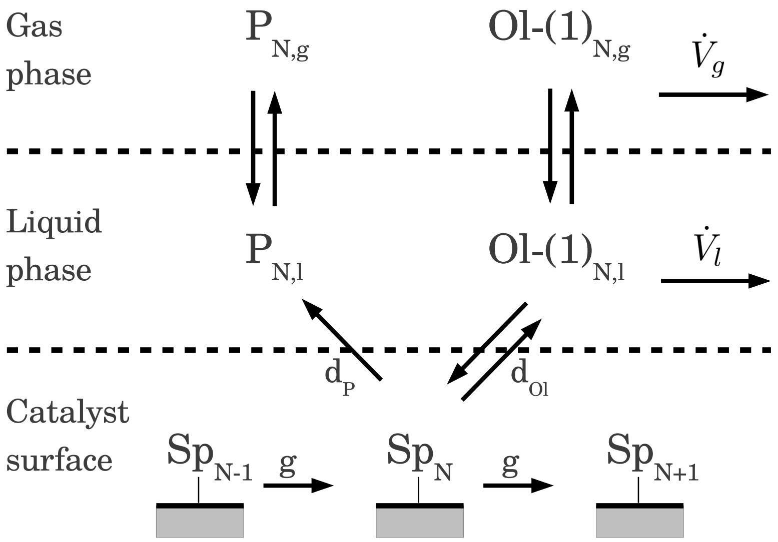

Figure 2.10: Schematic of the secondary reactions of olefins. Schulz and Claeys [59] co-fed a range α-olefins (Ol-1) during FTS that shed light on the secondary reactions of these compounds. (SP = surface bonded species; P = end product; N = carbon number;$\dot{V}$ = flow rate; g/l = gas or liquid phase)

Secondary reactions of oxygenates

As early as 1948, Emmett and co-workers realized the value of adding trace amounts of ^{14}C labeled compounds to study mechanistic aspects of the FTS reaction [61]. Since separation science and mass spectrometry were still in their development stages, following the radio-activity of a co-fed compound and its effects on the FTS product distribution proved to be fruitful [62]. In order to elucidate oxygenate formation they co-fed ^{14}C-labeled C_{1-4} linear- and iso-alcohols, CO_2 and gaseous formaldehyde [63–65]. They found that ethyl, n-propyl and isobutyl alcohols initiated chain growth while incorporation of isopropyl alcohol was limited. Davis et al. studied several aspects of the FTS mechanism, and in particular oxygenate formation/decomposition, by co-feeding labeled compounds [66–71]. Tau et al. [69] co-fed ^{14}C-labeled 1-pentanol and 1-hexanol, labeled in the α and β carbon positions respectively, during FTS conducted in a slurry phase reactor over Fe-based catalysts (T = 260 ℃, p = 7 bar, $H_2/CO = 1.2$, GHSV = 180 ml/hr/g_{cat}). Their data corroborated the potential for incorporation of linear alcohols [63–65] and indicated that these oxygenates can undergo dehydration and decarboxylation via the evolution of H_2O and CO_2 respectively to yield mainly paraffinic linear hydrocarbons. The authors suggested that the preference for paraffins as opposed to the commonly observed dominant product α-olefin formed during FTS shows that a parrallel mechanism is at play for the secondary reactions of 1-ROH and that linear alcohols are not a significant intermediate during Fe-based FTS. A separate study conducted by Tau et al. [70] reports on the results when co-feeding ^{14}C-labeled tracer amounts of the terminal 1-propanol and internal 2-propanol during Fe-based FTS (T = 264 ℃, p = 6.8 bar, GHSV = 180 ml/hr/g_{Fe}). Similar findings were reported with regards to incorporation, dehydration and decarboxylation of the co-fed alcohols, with 2-propanol being much less reactive than 1-propanol (1-3 % vs 10-20 % incorporation respectively). It was also shown that 1-propanol undergoes dehydrogenation in order to establish an equilibrium concentration ratio between the alcohol/ketones and aldehydes. In three separate reactions, Snel and Espinoza [72] co-fed dimethyl ether (DME), diethyl ether (DEE) and acetaldehyde during FTS (T = 270 ℃, p = 20 bar, $H_2/CO = 0.5$, GHSV = 1000 ml/hr/g_{cat}) conducted in a fixed bed micro-reactor over an Fe-based catalyst. After the addition of DME, a short period was observed where activity and selectivity deviated from the normal FTS reaction. After this period however, higher activity and similar chain growth probabilities were observed when compared to the reaction with no co-feeding. In contrast, the co-feeding of DEE immediately led to a slightly higher activity and similar chain growth patterns observed before co-feeding. The addition of DEE affected a pronounced increase in the formation of 1-butene. These results led the authors to suggest that DME, in a slower reaction compared to DEE, forms surface products that are similar to that involved in the regular FTS pathways. Acetaldehyde seemed to lower the activity, disturb the chain growth probability patterns and FTS product selectivities (of oxygenates and hydrocarbons) after co-feeding commenced.

Cairns [51] co-fed a range of C_8-oxgyenates during FTS (T = 300 ℃, P = 18 bar, GHSV = 3900 ml/hr/g_{cat}, $H_2/CO_2/CO$ = 4:1:1) in a Berty reactor using an Fe-based catalyst (Fe/K - 100:2 (g/g)) to shed light on the secondary reactions of oxygenates. Three FTS reactions were conducted where the oxygenates 1-octanol, octanal and octanoic acid were respectively combined with the synthesis gas after 48 hours time on stream (TOS) through the use of a saturator. When co-feeding 1-octanol during FTS an increase in the formation of octanal and octanoic acid was observed (see Figure 2.11). Similarly, the addition of octanal or octanoic acid leads to an increase in the formation of 1-octanol and octanoic acid/octanal respectively. These observations were ascribed to the close interaction of these oxygenates, potentially via an acyl surface intermediate. Apart from the interrelation of these three oxygenates, increases in the C_9 methyl ketone and 2-nonanol were observed. A fourth co-feeding experiment, with the C_9 methyl ketone showed that this compound is unreactive for conversion, other than to the corresponding secondary alcohol, 2-nonanol.

When considering possible secondary reactions (see reactions 2.13 - 2.18), Cairns [51] included a set of thermodynamic calculations to investigate the feasibility of these reactions at FTS conditions. Thermodynamically it was revealed that many of these secondary reactions were close to equilibrium when comparing the observed quantities with those calculated. From these results it was concluded that certain C_8-oxygenates readily undergo secondary reactions during FTS when using an Fe-based catalyst [51]. The order of reactivity based on the co-feeding reactions were octanal > octanoic acid > 1-octanol.

$$RCOOH + H_2 \rightleftharpoons R'COCH_3 + H_2O \tag{2.13}$$

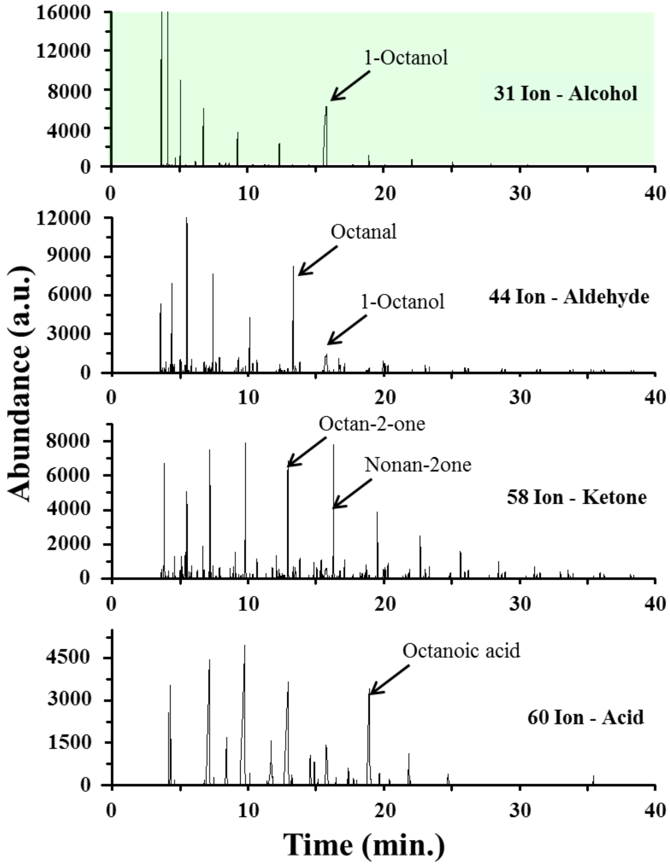

Figure 2.11: Cairns [51] co-fed oxygenates, including octanol during FTS. By extracting unique molecular ion fragments he could evaluate the role of the secondary reactions 2.13 to 2.18.

$$RCHO + H_2 \rightleftharpoons ROH \tag{2.14}$$

$$ROH \rightleftharpoons RCOCH_3 + H_2 \tag{2.15}$$

$$RCHO \rightleftharpoons R'COCH_3 \tag{2.16}$$

$$ROH + H_2O \rightleftharpoons RCOOH + 2H_2 \tag{2.17}$$

$$RCHO + H_2O \rightleftharpoons RCOOH + H_2 \tag{2.18}$$

Pathways to N-containing compounds

Considering the link between oxygenates and N-containing compounds observed by Sango [34, 35] and Henkel [41], one would presume that the final stages of the pathway involve reactions with oxygenated surface species or their precursors with NH_x^* surface species. Such pathways have been proposed [34, 47] and are discussed in the following subsection. In addition, it is known that secondary reactions of oxygenates readily take place on Fe-based catalysts [7, 51]. It can furthermore be shown (see Section 2.2.6) that the amination reactions represent a similar pathway to the route where primary produced FT oxygenates can be converted to N-containing compounds via a secondary pathway. Pathways proposed for amination reactions are therefore discussed further in Section 2.5.2.

Pathways to N-containing compounds proposed based on NH_3 co-feeding during FTS results

Based on previous amination and NH_3 co-feeding during FTS experiments, several pathways to the formation of N-containing compounds have been postulated. Sango [34, 35] co-fed (0 - 35 vol%) NH_3 during FTS in a slurry phase reactor using an iron based catalyst (T = 250 ℃, P = 5.0 - 8.0 bar, $H_2/CO = 2.0$, GHSV = 2250 ml/g_{cat}/h) and observed a concomitant

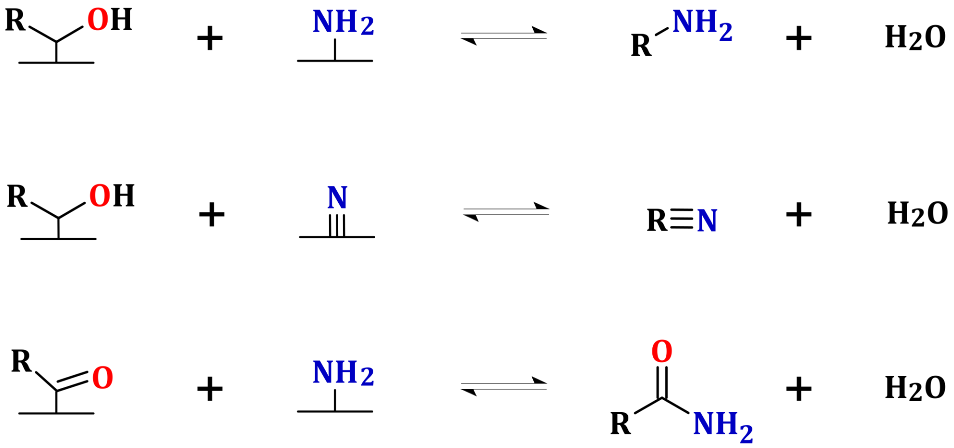

Figure 2.12: Pathways to the formation of several N-containing compounds proposed by Sango [34] based on results from co-feeding NH_3 during FTS experiments.

decrease in oxygenate selectivity with an increase in N-containing compounds. Based on these observations he put forward possible mechanism where NH_x^*-surface species (NH_2^*, N^*) react with oxygen-containing surface species during the final elementary step to produce primary aliphatic amines, amides and nitriles (see Figure 2.12). Henkel [41] co-fed NH_3 during FTS (T = 270 ℃, P = 4.0 bar, $H_2/CO = 2.0$, GHSV = 2250 ml/g_{cat}/h) in a fixed bed reactor using Fe-based (Fe/K - 100:0 and 100:2 (g/g)) catalysts. Based on the selectivities of the FTS products, he ruled out the possibility of α-olefins reacting in secondary reactions to form N-containing compounds. The selectivities for the formation of oxygenates during FTS with and without NH_3 addition, implied a direct link between the oxygenates and N-containing compounds. The results obtained in these reactions did not allow Henkel [41] to comment on the extent to which the N-containing compounds form due to a suppression of intermediate for primary oxygenate formation or consumption of the primary oxygenates via a secondary reaction. Henkel therefore suggested that the pathway to N-containing compounds could either follow the pathways proposed by Sango [34] or those proposed for amination reactions.

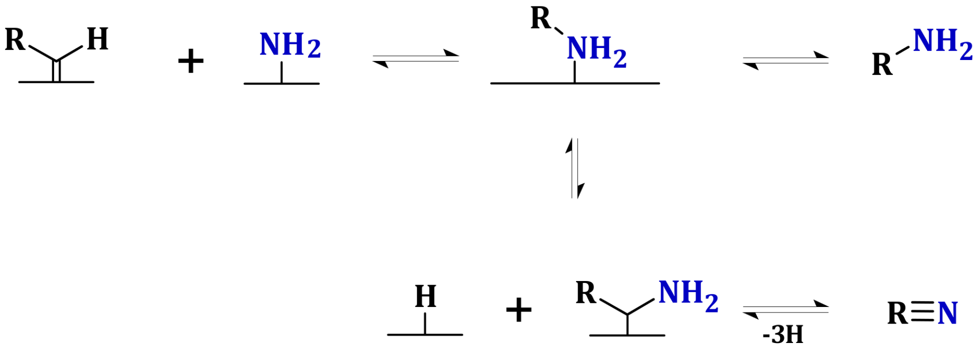

Figure 2.13: Pathways to the formation of several N-containing compounds proposed by Jones et al. [73] based on results from amination reactions.

Pathways to N-containing compounds based on amination reactions

In Figure 2.13, a simplified version of the pathway to the formation of N-containing compounds via amination reactions, as proposed by Jones et al. [73] is illustrated by the schematic. For simplicity the decomposition of oxygenate to surface alkylidene is omitted in order to highlight the final desorption steps. The surface alkylidene interacts with NH_2^*, which can then desorb as an amine or alternatively isomerize to have the α-carbon bonded to the surface. The formation of the aliphatic nitriles is then given by a further dehydrogenation step.

Rausch [40] studied the amination of ethanol over a Co-based catalyst and proposed similar pathways to the formation of N-containing compounds. Here however, the pathways are slightly altered in that, the oxygen-containing surface species interacts with NH_3^* via the evolution of H_2O to yield an intermediate, which subsequently desorbs to give the relevant N-containing compound (see Figure 2.14).

The pathways proposed for the formation of N-containing compounds via primary or secondary (i.e. amination) reactions of oxygenates suggest the incorporation of either NH_3, NH_2 or N in the final step. It is therefore not known which of these NH_x^*-surface species would kinetically and thermodynamically be available for reaction with the surface species.

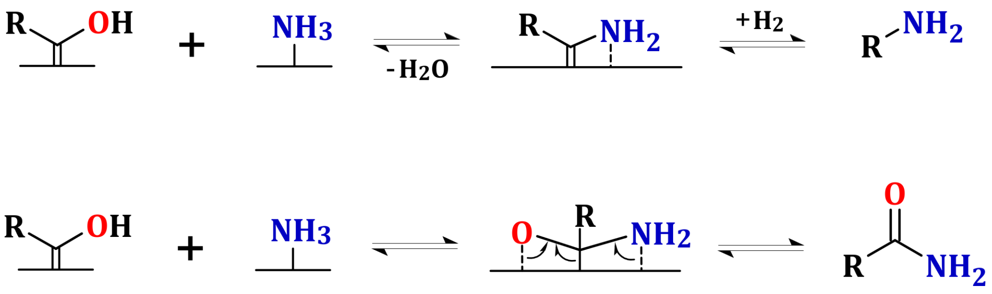

Figure 2.14: Pathways to the formation of several N-containing compounds proposed by Rausch [40] based on results from co-feeding NH_3 during FTS experiments.

Understanding fundamental principals from model iron surfaces

Choice of a model Fe surface

The addition of NH_3 as a reactant raises several questions that are ideally approached via fundamental studies, e.g. theoretical calculations or surface science experimentation. For example, it is of interest to know what the most abundant surface species of NH_x would be on the catalytic surface. Furthermore, the way that these NH_x surface species influence the FTS pathway can be probed via fundamental studies. The active phase for Fe-based catalysts used in FTS is still heavily debated in literature, and hence the choice for the ideal model surface during Fe-based FTS is even more complex.

In order to use a surface that mimics what is believed to be the active catalyst surface (e.g. a cleaved Hägg carbide surface), one should consider a model surface that perhaps contains subsurface C atoms. This was however not possible within this work a for a few reasons. Firstly, within the framework of the entire project (in particular at the onset), the computational expense needed to conduct such a study was not feasible. Secondly, it was preferable to have some correlation to surface science experiments, which is most likely be non-existent for the coadsorption of CO and NH_x on an Fe-carbide surface. Furthermore, numerous ultra high vacuum (UHV) surface science experiments and DFT studies have been conducted on the low Miller

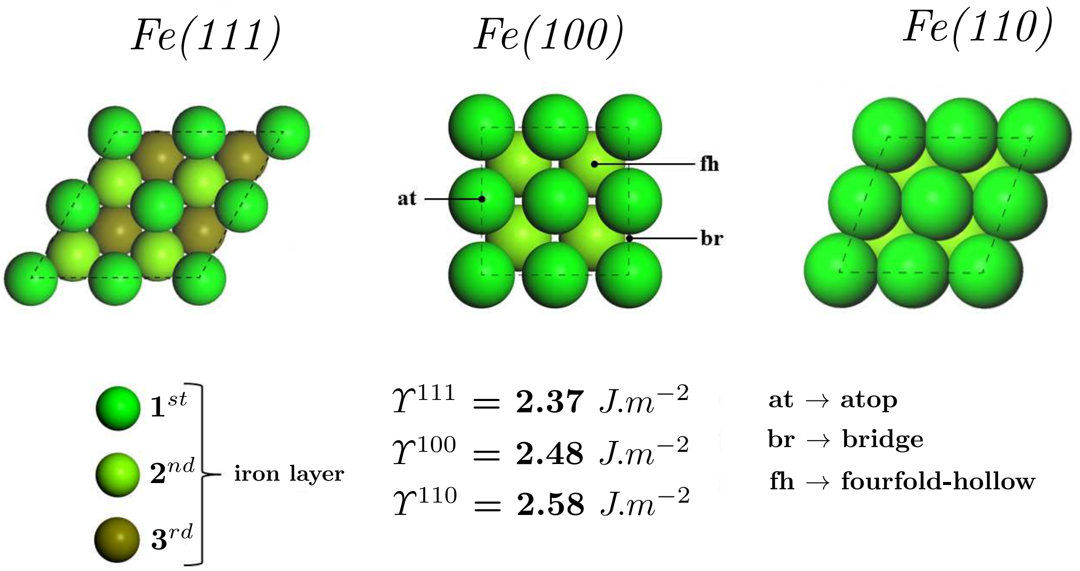

Figure 2.15: A top view of the Miller indices (111/100/110) on bcc iron are given to illustrate the more ”open” and ”closed” catalytic surfaces. Surface energies are taken from Ref. [89]

indices (111/100/110) of bcc iron, to study various aspects of the FTS mechanisms, in particular on the Fe(100) surface [53, 57, 74–82].j In other words, even though FT reactions on a metallic surface is to some extent fictitious, many studies exists that allows for a depiction of the FTS pathway on an Fe(100) surface, which would could serve as a way to bring this particular study into context. In addition, the studies of elementary reactions involved in the NH_3 synthesis and decomposition reactions have benefited from similar approaches on the Fe(100) surface [83–88].

The Fe(100) is more open than the Fe(110) surface and more compact than the Fe(111) and thus provides an ideal intermediate catalytic surface (see Figure 2.15). In a series of spin-polarized DFT calculations of low Miller index Fe surfaces, Blonski and Kenja [89] determined that the Fe(100) surface is very stable and is assumed to be exposed based on the Wulff construction of a model Fe nanocrystal. In the following sections and subsections the literature of CO adsorption and dissociation as well as $NH_x \pm H$ reactions on model Fe surfaces are reviewed. Based on the aforementioned discussion and the model surface used for the theoretical part of this thesis, the studies pertaining to the Fe(100) surface are highlighted in the subsequent sections.

NH_3 synthesis on model iron surfaces

Ammonia plays an integral role in the fertilizer industry and is employed directly or indirectly as starting material for numerous specialty chemicals [90] (e.g. pharmaceuticals, explosives and cleaning products). Since the advent of the Haber-Bosch process, in which molecular nitrogen and hydrogen are converted to ammonia over metal (eg. Fe and Ru) based catalysts, the interaction of ammonia with metal surfaces has attracted immense attention [91]. The first elementary step in the mechanism of the reaction is the dissociative adsorption of N_2, which is assumed to be the rate limiting step [92]. This is followed by three consecutive hydrogenation steps to produce ammonia as an adsorbate, which is finally desorbed to afford gaseous ammonia. Considering the industrial drive for ammonia production, a rich history of fundamental studies on model iron surfaces exists, which has been directed towards elucidating the rate limiting step. The initial work of Paul Emmett [93] and Hugh Taylor [94] was followed by a series of ultra high vacuum (UHV) experiments conducted by Gerhard Ertl and co-workers [85, 86, 95]. His group employed several surface science techniques to study the interaction of NH_x species with the lower Miller indices surfaces Fe(110), (100) and (111) [85, 86, 91, 95]. Considering its order of reactivity for the NH_3 synthesis reaction [83], Fe(111) > (100)> (110) [91], many studies were aimed at elucidating aspects of the N_2 dissociation reaction (the rate limiting step) on Fe(111) [96–98]. Mortensen et al. [84] calculated adsorption energies and structures for nitrogen atom adsorption on the Fe(111), (100) and (110) surfaces using DFT and finds the Fe(100) surface to be ~ 0.70 eV more stable than the Fe(111) and Fe(110) surfaces in this regard. This is due to the availability of fourfold hollow sites on the Fe(100) surface. The structure that Mortensen et al. [84] calculated at $\theta_N = 0.50$ ML (i.e. a 50 % surface coverage) were similar to the c(2 × 2) structure experimentally (LEED) determined by Imbihl et al. [85] for N adsorbed on Fe(100).

NH_3 decomposition on model iron surfaces

Apart from the ammonia synthesis reaction, other industrial applications are drivers for a fundamental understanding of the decomposition mechanism over iron based catalysts. As an example, the concept of using NH_3 for storage of H_2 in fuel cell applications has attracted attention [99–101]. An important application related to this study, is the decomposition of NH_3 on iron-based catalysts, which are being considered for the removal of NH_3 from biomass-derived synthesis gas [31]. It should be borne in mind that Boisen et al. [101] recently showed that the optimal ammonia synthesis catalyst (e.g. Fe based catalyst) would not be the optimal decomposition catalyst. Regardless of this finding, several fundamental studies have focused on the decomposition of NH_3 on model Fe surfaces. By means of UPS, AES, LEED, thermal desorption and work function measurements Grunze et al. [86] characterized molecularly adsorbed ammonia and its decomposition on Fe(111) and Fe(100) surfaces. They found the adsorption energies for NH_3 to be between 0.43 and 0.52 eV (10-12 kcal/mol) and the highest activation barrier to be that of $NH_2 \rightarrow$ NH + N with E_a = 0.80 eV on the Fe(100) surface. Cheng et al [87] used a theoretical approach that combined DFT and the tight binding extended Hückel method to investigate the nitriding mechanism at Fe(100), Ni(100) and Cr(100) surfaces. This methodology was restricted due to the level of theory and only allowed them to estimate binding energies and follow nitriding trends between the transition metal surfaces. They calculated the binding energies for NH_3 to be $\Delta E_{ads} \sim$ -1.40 eV on Fe(100), which deviates significantly from the experimentally determined value (0.43 - 0.52 eV [86]). Yeo et al. [88] recently evaluated the mechanism of the catalytic decomposition of NH_3 on Fe(100) via spin-polarized periodic DFT calculations. Their adsorption energy for NH_3 on Fe(100) was more accurate (ΔE_{ads} = -0.92 eV), but still deviates from the experimentally determined adsorption energy by ca. 0.40 - 0.50 eV. The highest activation barrier calculated by Yeo et al. for the sequential dehydrogenation of NH_3 on the Fe(100) surface, was that of NH_2 decomposing to NH + H with E_a = 1.14 eV. Other cluster [99, 102] and bulk phase [100, 103] DFT calculations have focused on the adsorption of NH_3 on model Fe surfaces, but these values range between -0.36 eV and -0.92 eV which was shown to be influenced significantly by the choice of exchange-correlation functional used in the calculations [103]. Mckay et al. [103] used periodic DFT calculations to extensively study the behavior of NH_x ± H atoms on an Fe(211) surface. The high activation barrier (E_a = 1.40 eV) that was calculated for the dehydrogenation reactions ($NH_2 \rightarrow$NH + H) was later questioned by the experimental work (AES,TPD and LEED) of Iyngaran et al. [104] who studied the hydrogenation reactions of N over Fe(111). When starting with an Fe(111) surface covered with θ = 0.61 ML N and exposing it to 0.6 mbar H_2(g) at various temperatures, the activation barriers extracted were experimentally determined as E_a = 0.16 eV [104].

The literature based on the DFT studies for NH_3 adsorption and decomposition on model iron surfaces serves as valuable data to be used as comparison for future studies. There is however a need to address some differences in the DFT calculated results and those obtained experimentally. In addition, for the purpose of the formation of N-containing compounds during FTS, it would be interesting to speculate on the most abundant NH_x surface species at elevated temperatures and pressures. DFT data can readily be used within the transition state theory (TST) and statistical mechanics to predict thermodynamic and kinetic behaviour for the decomposition of NH_x on metal surfaces at relevant reaction conditions [105].

CO adsorption on model Fe surfaces

The discussion of primary FTS pathways (see Section 2.3) highlights the importance of these elementary reactions of CO in the FTS. In Figure 2.16 a schematic representation for the production C_2 hydrocarbon formation via the carbide mechanism is given. Govender [53] evaluated a similar route in her calculations and finds that the CO dissociation reaction is the rate limiting step on the Fe(100) surface. The potential energy surface would surely change if hydrogen assisted CO dissociation [57, 78], stepped surfaces or a combination thereof are considered. However, considering the information available for direct CO dissociation and the novelty of CO coadsorption with NH_x (x = 3, 2, 1, 0), the DFT calculations considered in this work is focused on the effects the NH_x adsorbates have on the direct CO adsorption and dissociation reactions on the Fe(100) surface.

The CO adsorption and dissociation on the Fe(100) surface has been studied via several UHV techniques including TPD, XPS, HREELS and AES [106–113]. TPD experiments indicates that CO adsorbs sequentially into adsorption states denoted as α_1, α_2 and α_3 at low temperatures (< 300 K) [106, 107]. CO takes on the atop, bridge and fourfold hollow configurations for α_1, α_2 and α_3 adsorption states respectively. The α_3-CO has been identified to be the precursor for CO dissociation [107] and has a very low CO stretching vibrational mode (1210 cm^{-1}) as evidenced by HREELS experiments [108, 109]. In addition, it has been shown that CO in this configuration is tilted and makes a 45 ± 10 degree angle with the surface, which indicates additional π-bonding between CO and the surface [107, 108]. Increased π-bonding is further supported by UPS data for CO adsorption on Fe(100), which showed extensive re-hybridization

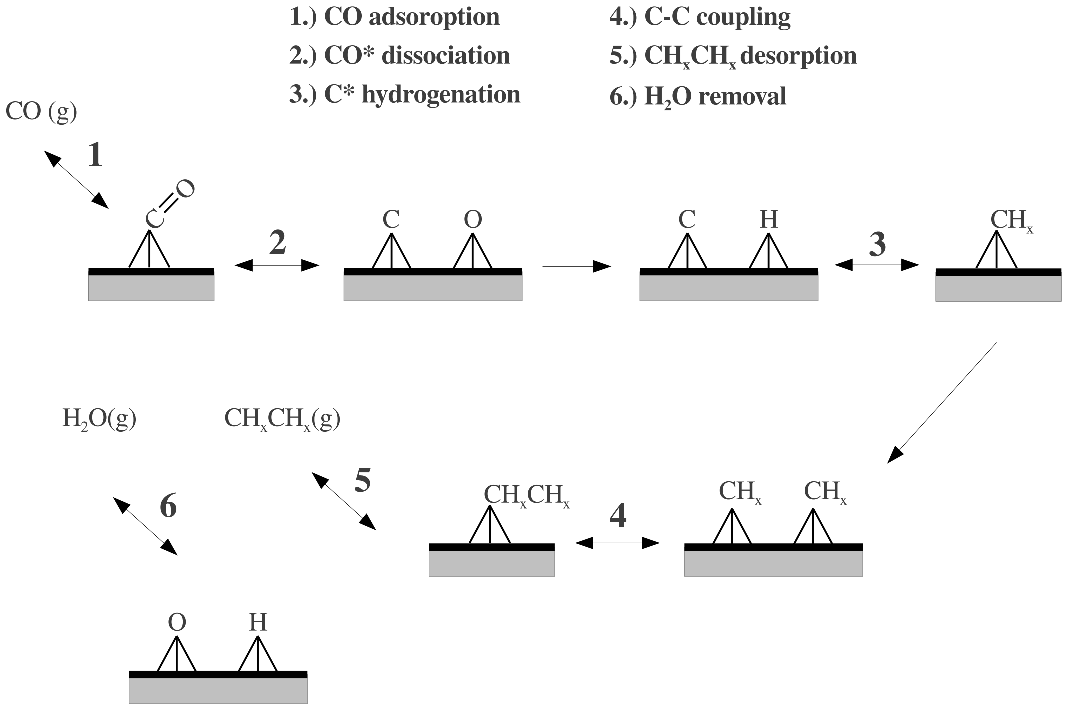

Figure 2.16: A schematic of the important elementary reactions that has been considered on the Fe(100) and other surfaces.

for the α_3-CO state [109]. At 440 K the α_3-CO dissociates into the C and O adatoms. The CO dissociation reaction was shown (via TPD experiments) to displace the α_3-CO molecules to lower co-ordinated sites and in doing so, it triggers the desorption of the remaining α_3-CO at 440 K [113]. Furthermore, from TPD experiments, a peak (β) at 800 K suggests that the C and O adatoms recombine and desorb at this temperature.

The direct CO adsorption and dissociation reactions on the Fe(100) surface have been studied in detail by periodic DFT methods [76, 81, 82], and provide a good platform for comparing results from this thesis. Sorescu [81] used plane wave based DFT with the PBE functional and showed that CO can adsorb on the Fe(100) surface in five possible configurations (atop, bridge, tilted bridge, fourfold hollow and fourfold tilted). The fourfold tilted configuration, that corresponds to the experimentally determined α_3-CO, was calculated to have an adsorption energy between $\Delta E_{ads} = -1.90$ and -2.02 eV (-43.8 and -46.7 kcal/mol) and an activation barrier in the range of $E_a = 1.06$ - 1.22 eV (24.5 - 28.2 kcal/mol). Bromfield et al. [82] performed similar DFT calculations, using the RPBE functional, and found the adsorption energy of α_3-CO to be $\Delta E_{ads} = -2.56$ eV and an activation barrier of $E_a = 1.16$ eV. Their study however included a vibrational analysis of CO on the Fe(100) surface, which was ultimately used to show which of the adsorbates were at a local minimum on the PES [82].

CO + X (X = H, S, O, K) adsorption on Fe(100)

CO adsorption and dissociation is influenced by dissociated fragments from the FTS reactants (H, C, O), as well as promoters such as K and poisons like S. If a co-adsorbate is present on the surface, the electronic structure of the surface is manipulated, which influences the adsorption of CO on the metal surface [114]. For example, if sulfur is present on a metal surface it transfers electrons away from the surface, while the opposite is true when potassium is present on the surface [114]. In addition, if these adsorbates are in close proximity, attractive or repulsive lateral interactions can exist between the adsorbates. Sulfur is usually removed from the synthesis gas as it is regarded as a poison, while potassium is added to an iron-based catalyst to promote the reaction [12]. The way certain coadsorbates influence CO on a model Fe(100) surface has been investigated via experimental and theoretical techniques [76, 79, 107, 115–118].

A combination of TPD [115] and EELS [116] experiments have demonstrated that hydrogen blocks the fourfold hollow sites for CO adsorption on Fe(100), but that the surface species (CO + H) does not segregate into separate phases. Further EELS analysis conducted by Merril and Madix [117] indicated that CO has a weakening effect on the Fe-H bond and shifts the H-surface atom within the fourfold hollow site to a lower ligancy (three-fold) adsorption state. This weakening of the H-bond led the authors to conclude that the weakened H-bonding facilitates H-transfer for further reaction with adsorbed alkyl groups [117]. Van Helden and Van Steen [76] made use of spin-polarized DFT calculations and report that (both stabilizing and de-stabilizing) electrostatic interactions exists between H and CO, when co-adsorbed on Fe(100) with $\theta_{CO} = 0.25$ and 0.50 ML. By calculating the heat of mixing ΔH_{mix} using the methodology proposed by Ciobica et al. [119], van Helden and van Steen [76] showed that the instability of the compressed, individually adsorbed CO and H leads to thermodynamically stable mixed phases.

The coadsorption of CO and K ($\theta_K < 1.0$ ML) was investigated via TPD, XPS and UPS experiments by Cameron [120]. The TPD experiments were indicative of a lower activation barrier for the CO dissociation reaction and the α_3-CO desorption occurred at lower temperatures with increasing K coverage. When adsorbing CO on a K modified Fe(100) surface, the HREELS spectra contained a band at ca. 950 cm^{-1}, which the author [121] interpreted as CO adsorbed in a K modified α_3 state. Sorescu [80] conducted a plane-wave DFT study of CO coadsorbed with K on the Fe(100) surface and calculated a significant increase in adsorption energy (stabilization $\sim$ 0.10 - 0.50 eV) upon K coadsorption, which was dependent on K-coverage and the distance between coadsorbates. In addition, at $\theta_K = 0.25$ and 0.50 ML a drop in the activation energy for CO dissociation of 0.24 - 0.27 eV (5.5 - 6.2 kcal/mol) and 0.34 eV (7.8 kcal/mol) respectively was reported.

The AES and LEED experiments used to study the coadsorption of CO with O and CH_3S on the Fe(100) surface indicated that these adsorbates limit the amount of CO adsorbed onto the surface [118]. Moon et al. [107] investigated the adsorption and dissociation of CO on a clean and sulfur added Fe(100) surface using XPS and TPD and reported that S inhibits the CO dissociation reaction by blocking the fourfold hollow sites needed for the dissociated C and O adatoms. Curulla-Ferré et al. [79] used DFT to study the adsorption and dissociation of CO on sulfur pre-covered surfaces with a Fe(100)-S-p(2 × 2) configuration at a sulfur coverage θ_S

= 0.25 ML and a Fe(100)-S-c(2 × 2) configuration at a coverage with $\theta_S = 0.50$ ML. Only minor changes were calculated for the activation barriers for CO dissociation in the presence and absence of the S* adatoms, but a change in the sign of the reaction were calculated. That is, the exothermic CO dissociation on a clean Fe(100) [81, 82] surface was calculated to be slightly endothermic when S was present on the Fe(100) surface.

CO + NH$_x$ (x = 3, 0)

NH_3 is usually classified as a poison for the FTS reaction [19], which demands its removal from synthesis gas. Fe-based catalysts has been proposed as the ideal metal-based catalysts for biomass-derived synthesis gas that contains high quantities of NH_3 [11, 31]. Moreover, the deliberate addition of NH_3 has shown promise for the production of valuable N-containing compounds [34, 38, 41] when using Fe-based catalysts. To date however, no theoretical or experimental studies have been reported on the co-adsorption of CO and NH_x on model Fe surfaces. Considering the broader role of CO and NH_3 as products or reactants in various catalytic reactions (e.g. Haber-Bosch reaction and FTS), the coadsorption of these adsorbates have been studied on other model metal surfaces. The interaction between CO and NH_3 has been studied via UHV surface science and theoretical approaches on Ru(100) [122–124], Rh(100) [125, 126], Pd/Mo(110), Pd(111)/Mo(110) [127] and Pt(111) [128]. Sasaki et al. [122] investigated the co-adsorption of CO and NH_3 by LEED, TPD and HREELS experiments and showed that exposing a Ru(100) surface, pre-covered with CO, to NH_3 leads to the formation of ordered mixed layers with (2 × 2) periodicity. Furthermore, the HREEL spectra obtained by Sasaki et al. [122] indicated tilting of the axis between the adsorbed NH_3 and the surface normal. Akhter et al. [124] used TPD and HREELS to study the interactions between donor-acceptor molecules (CO, NH_3, PF_3) on Ru(100). Based on the HREELS results, the authors ascribes the attractive interaction between adsorbates with opposite dipoles, such as the CO + NH_3 system, to charge transfer between the co-adsorbates. The co-adsorption of CO and NH_3 on Pd_{1ML}/Mo(110) and Pd(111)/Mo(110) surfaces were found to result in mixed phases with attractive interactions between CO and NH_3, based on the LEED, TPD and HREELS results reported by Xu and Goodman [127]. These authors however ascribe this observation to both $d - \pi^*$ charge transfer and dipole-dipole interactions between co-adsorbed CO + NH_3 on these mono- and multilayer palladium on molubdinum surfaces. On the Rh(100) surface, van Bavel et al. [126] combined TPD, LEED and Monte Carlo simulations to quantify the lateral interactions between CO and N. At high N and CO coverage on Rh(100), repulsive lateral interactions of $\omega^{NN}_{CO-N} = 0.20$ eV (19 kJ/mol, with ω^{NN}_{CO-N} the interaction energy for next nearest neighbors) were deduced. Curulla Ferré et al. [125] were able to confirm and shed further light on the TPD experimental results [126] via their DFT calculations for CO and N co-adsorbed on Rh(100). In the DFT study [125] they showed that the pairwise additive potential approximation can be used to calculate the perturbation of the adsorption energy of CO by the presence of co-adsorbed N. The strongest lateral repulsive interaction were calculated within short range to be $\Phi^{CO-N} =$ -0.296 eV for CO and N.

REFERENCES

[1] H. Schulz, K. Beck and E. Erich, Vol. 36 of Stud. Surf. Sci. Catal., Elsevier, Amsterdam, 1988.

[2] E. van Steen and H. Schulz, Appl. Catal., A 186 (1999) 309–320.

[3] A.P. Steynberg, Chapter 1 - Introduction to Fischer-Tropsch Technology, in: A.P. Steynberg and M.E. Dry (Eds.), Fischer-Tropsch Technology, Vol. 152 of Stud. Surf. Sci. Catal., Elsevier, 2004, pp. 1 – 63.

[4] R.B. Anderson, H. Kölbel and M. Rálek, The Fischer-Tropsch synthesis, Academic Press, Orlando, 1984.

[5] F. Fischer and H. Tropsch, Brennstoff-Chem. 7 (1926) 97.

[6] M. Dry, Catal. Today 71 (2002) 227–241.

[7] B.H. Davis, Catal. Today 141 (2009) 25–33.

[8] G.P. van der Laan and A. Beenackers, Cat. Rev. - Sci. Eng. 3 - 4 (1999) 255–318.

[9] M.E. Dry and A.P. Steynberg, Chapter 5 - Commercial FT Process Applications, in: A.P. Steynberg and M.E. Dry (Eds.), Fischer-Tropsch Technology, Vol. 152 of Stud. Surf. Sci. Catal., Elsevier, 2004, pp. 406–481.

[10] Shell, Pearl GTL (March 2016).
URL `http://www.shell.com.qa/en/products-services/pearl.html`

[11] E. van Steen and M. Claeys, Chem. Eng. Technol. 31 (2008) 655–666.

[12] M.E. Dry, Chapter 3 - Chemical concepts used for engineering purposes, in: A.P. Steynberg and M.E. Dry (Eds.), Fischer-Tropsch Technology, Vol. 152 of Stud. Surf. Sci. Catal., Elsevier, 2004, pp. 196–257.

[13] M.E. Dry, Catalysis - Science and Technology, Berlin Heidelburg:Springer-Verlag, 1981.

[14] M. Dry, Chemtech (1982) 744.

[15] T. Riedel, H. Schulz, G. Schaub, K.W. Jun, J.S. Hwang and K.W. Lee, Top. Catal. 26 (2003) 41–55.

[16] E. de Smit, A.M. Beale, S. Nikitenko and B.M. Weckhuysen, J. Catal. 262 (2009) 244–256.

[17] E. de Smit, Iron-based fischer-tropch synthesis: New insights from in-situ (micro)spectroscopy, diffraction and theory, Ph.D. thesis, Universiteit Utrecht, The Netherlands (2010).

[18] E. de Smit, F. Cinquini, A.M. Beale, O.V. Safonova, W. van Beek, P. Sautet and B.M. Weckhuysen, J. Am. Chem. Soc. 132 (2010) 14928–14941.

[19] C.H. Bartholomew, Appl. Catal., A 212 (2001) 17–60.

[20] W.M Shen, J.A. Dumesic and C.G. Hill, J. Catal. 68 (1981) 152–165.

[21] G.W. Huber and B.E. Dale, Sci. Am. 301 (2009) 52–59.

[22] C.H. Bartholomew and R.M. Bowman, Appl. Catal., A 15 (1985) 59–67.

[23] A.L. Chaffee, I. Campbell and N. Valentine, Appl. Catal., A 47 (1989) 253–276.

[24] Z. Liu, J. Zhou and B. Zhang, J. Mol. Catal. 94 (1994) 255–261.

[25] Ø. Borg, N. Hammer, Enger B.C., R. Myrstad, O.A. Lindvag, S. Eri, T.H. Skagseth and E. Rytter, J. Catal. 279 (2011) 163–173.

[26] D.E. Sparks, G. Jacobs, M.K. Gnanamani, V.R.R. Pendyala, W. Ma, J. Kang, W.D. Shafer, R.A. Keogh, U.M. Graham, P. Gao and B.H. Davis, Catal. Today 215 (2013) 67–72.

[27] T.C. Bromfield and N.J. Coville, Appl. Catal., A 186 (1999) 297–307.

[28] W. Wu, L. Bai, H. Xiang, Y. Li, Z. Zhang and B. Zhong, Fuel 83 (2004) 205–212.

[29] H.M. Torres Galvis, J.H. Bitter, C.B. Khare, M. Ruitenbeek, A. Iulian Dugulan and K.P. de Jong, Science 335 (2012) 835–838.

[30] H.M. Torres Galvis, A.C.J. Koeken, J.H. Bitter, T. Davidian, M. Ruitenbeek, A. Dugulan, Iulian Dugulan and K.P. de Jong, J. Catal. 303 (2013) 22–30.

[31] W. Torres, S.S. Pansare and J.G. Goodwin, Cat. Rev. - Sci. Eng. 49 (2007) 407–456.

[32] V.R.R. Pendyala, M.K. Gnanamani, G. Jacobs, W. Ma, W.D. Shafer and B. Davis, Appl. Catal., A 468 (2013) 38–43.

[33] M. Claeys, E. van Steen, T. Sango and F. Roessner, Process for the production of nitrogen or phosphorous containing compounds from synthesis gas (2013).

[34] T. Sango, Nitrogen-containing compounds from ammonia co-feed to the Fischer-Tropsch synthesis, Master's thesis, University of Cape Town, South Africa (2013).

[35] T. Sango, N. Fischer, R. Henkel, F. Roessner, E. van Steen and M. Claeys, Appl. Catal., A 502 (2015) 150–156.

[36] A. Clark, Process of synthesizing aliphatic amines (1950).

[37] W. Röttig, Catalytic hydrogenation of carbon monoxide with addition of ammonia or methylamine (1958).

[38] M. Claeys, E. van Steen, T. Sango and F. Roessner, Process for the production of nitrogen or phosphorous containing compounds from synthesis gas (2013).

[39] W.J. Bartley, Production of acetamides with rhodium-manganese catalysts (1981).

[40] A. Rausch, C-n-kopplungen an heterogenen kobalthaltigen katalysatoren, Ph.D. thesis, Carl von Ossietzky Universität, Germany (2008).

[41] R. Henkel, The influence of ammonia on fischer-tropch synthesis and formation of N-containing compounds, Ph.D. thesis, Carl von Ossietzky Universität, Germany (2012).

[42] T. Daubert, Physical and thermodynamic properties of pure chemicals: evaluated process design data, Taylor and Francis, Philadelphia, Pensilvania, USA, 1999.

[43] T. Grobler, M. Claeys, E. van Steen and M.J. Janse van Vuuren, Catal. Commun. 10 (2009) 1674–1680.

[44] R. van der Westhuizen, H. Potgieter, N. Prinsloo, A. de Villiers and P. Sandra, J. Chromatogr. A 1218 (2010) 3173–3179.

[45] R. van der Westhuizen, R. Crous, A. de Villiers and P. Sandra, J. Chromatogr. A 1217 (2010) 8334–8339.

[46] H. Kölbel and J. Trapper, Angew. Chem. Int. Ed. 4 (1965) 981.

[47] H. Kölbel and J. Trapper, Angew. Chem. Int. Ed. 5 (1966) 843–844.

[48] H. Kölbel, I. Abdulahad, S. Kanowski and M. Ralek, React. Kinet. Catal. Lett. 3 (1974) 267–270.

[49] H. Kölbel, I. Abdulahad and M. Ralek, Erdoel Kohle, Erdgas, Petrochem. Brennst.-Chem, 28(8) (1975) 385–388.

[50] T. Mallat and A. Baiker, Handbook of Heterogeneous Catalysis, Wiley-VCH, Weinheim, 2008.

[51] P. Cairns, Oxygenates in iron Fischer-Tropsch Synthesis: is copper a selectivity promoter?, Ph.D. thesis, University of Cape Town, South Africa (2008).

[52] M. Claeys and E. van Steen, Chapter 8 - Basic studies, in: A.P. Steynberg and M.E. Dry (Eds.), Fischer-Tropsch Technology, Vol. 152 of Stud. Surf. Sci. Catal., Elsevier, 2004, pp. 601–680.

[53] A. Govender, Towards a mechanism for the Fischer-Tropsch Synthesis on Fe(100) using Density Functional Theory, Ph.D. thesis, Technische Universiteit Eindhoven, The Netherlands (2010).

[54] N. Fischer, Preparation of nano and angstrom sized cobalt ensembles and their performance in the fischer-tropsch synthesis, Ph.D. thesis, University of Cape Town, South Africa (2011).

[55] H.H. Storch, N. Golumbic and Anderson R.B., The Fischer-Tropsch and Related Synthesis, John Wiley & Sons, New York, 1951.

[56] H. Pichler and H. Schulz, Chem. Ing. Tech. 42 (1970) 1162.

[57] M. Ojeda, R. Nabar, A.U. Niekar, A. Ishikawa and M. Mavrikakis, J. Catal. 272 (2010) 287–297.

[58] C.J. Weststrate, P. van Helden and J.W. Niemantsverdriet, Catal. Today.

[59] H. Schulz and M. Claeys, Appl. Catal., A 186 (1999) 71–90.

[60] M. Claeys, Selektivität, Elementarschritte und kinetische Modellierung bei der Fischer-Tropsch-Synthese, Ph.D. thesis, Unversität Fridericiana Karlsruhe, Germany (1997).

[61] J.T. Kummer, T.W. DeWitt and P.H. Emmett, J. Am. Chem. Soc. 70 (1948) 3632–3643.

[62] P.H. Emmett, Cat. Rev. - Sci. Eng. 7 (1972) 1–24.

[63] J.T. Kummer and P.H. Emmett, J. Am. Chem. Soc. 75 (1953) 5177–5184.

[64] J.T. Kummer, H.H. Podgurski, Spencer W.B. and P.H. Emmett, J. Am. Chem. Soc. 73 (1957) 564–570.

[65] K.H. Hall, R.J. Kokes and P.H. Emmett, J. Am. Chem. Soc. 79 (1957) 2983.

[66] L. Tau, R. Robinson, R.D. Ross and B.H. Davis, J. Catal. 105 (1987) 335–41.

[67] L. Tau, H. Dabbagh and B.H. Davis, Energy Fuels 4 (1989) 94–99.

[68] L. Tau, H. Dabbagh, S. Bao and B.H. Davis, Catal. Lett. 7 (1990) 127–140.

[69] L. Tau, H. Dabbagh and B.H. Davis, Energy Fuels 5 (1991) 174–179.

[70] L. Tau, H. Dabbagh, J. Halasz and B.H. Davis, J. Mol. Catal. 71 (1992) 37–55.

[71] A. Sarkar, R. Keogh, S. Bao and B.H. Davis, Catal. Lett. 120 (2008) 25–33.

[72] R. Snel and R.L. Espinoza, J. Mol. Catal. 54 (1989) 213–223.

[73] J.R. Jones, A.P. Sharrat, S.D. Jackson, L.F. Gladden and G. Webb, Synthesis and application of isotopic labeled compounds, Wiley & Sons, 1995.

[74] J.M.H. Lo and T. Ziegler, J. Phys. Chem. C 111 (2007) 13149–13162.

[75] J.M.H. Lo and T. Ziegler, J. Phys. Chem. C 112 (2008) 13681–13691.

[76] P. van Helden, Initial steps of the Fishcer-Tropsch synthesis on Fe(100): The role of hydrogen, Ph.D. thesis, University of Cape Town, South Africa (2008).

[77] P. van Helden and E. van Steen, J. Phys. Chem. C 112 (2008) 16505–16513.

[78] M.R. Elahifard, M.P. Jigato and J.W. Niemantsverdriet, ChemPhysChem 13 (2012) 89–91.

[79] D. Curulla-Ferré, A. Govender, T.C. Bromfield and J.W. Niemantsverdriet, J. Phys. Chem. B 110 (2006) 13897–13904.

[80] D.C. Sorescu, Surf. Sci. 605 (2011) 401–414.

[81] D.C. Sorescu, D.L. Thompson, M.M. Hurley and C.F. Chabalowski, Phys. Rev. B: Condens. Matter 66 (2002) 035416–1–13.

[82] T.C. Bromfield, D.C. Ferré and J.W. Niemantsverdriet, ChemPhysChem 6 (2005) 254–260.

[83] N.D. Spencer, R.C. Schoonmaker and G.A. Somorjai, J. Catal. 74 (1982) 129–135.

[84] J.J. Mortensen, M.V. Ganduglia-Priovano, L.B. Hansen, B. Hammer, P. Stoltze and J.K. Nørskov, Surf. Sci. 422 (1999) 8–16.

[85] R. Imbihl, R.J. Behm and G. Ertl, Surf. Sci. 123 (1982) 129–140.

[86] M. Grunze, F. Bozso, G. Ertl and M. Weiss, App. Surf. Sci. 1 (1978) 241–265.

[87] H. Cheng, D.B. Reiser, P.M. Mathias, K. Baumert and S.W. Dean, J. Phys. Chem. 99 (1995) 3715–3722.

[88] S.C. Yeo, S.S. Han and H.M. Lee, J. Phys. Chem. C 118 (2014) 5309–5316.

[89] P. Błoński and A. Kiejna, Surf. Sci. 601 (2007) 123–133.

[90] Barbara Elvers (Ed.), Ullmann's Encyclopedia of Industrial Chemistry, Seventh Edition, WILEY-VCH, 2006.

[91] G. Ertl, Angew. Chem. Int. Ed. Eng. 29 (1990) 1219–1227.

[92] P.H. Emmett, The physical basis for heterogeneous catalysis, Plenum Press, New York, 1975.

[93] P.H. Emmett and S. Brunauer, J. Am. Chem. Soc. 56 (1934) 35–41.

[94] H.S. Taylor and J.C. Jungers, J. Am. Chem. Soc. 57 (1935) 660–661.

[95] F. Bozso, G. Ertl, M. Grunze and M. Weiss, J. Catal. 49 (1977) 18–41.

[96] J.J. Mortensen, L.B. Hansen, B. Hammer and J.K. Nørskov, J. Catal. 182 (1999) 479–488.

[97] A. Logadottir and J.K. Nørskov, Surf. Sci. 489 (2001) 135–143.

[98] R.C. Egeberg, S. Dahl, A. Logadottir, J.H. Larsen, J.K. Nørskov and I. Chorkendorff, Surf. Sci. 491 (2001) 183–194.

[99] G. Lanzani and K. Laasonen, Int. J. Hydrogen Energy 35 (2010) 6572–6577.

[100] R.J. Lin, Li F.Y. and Chen H.L., J. Phys. Chem. C 115 (2011) 521–528.

[101] A. Boisen, S. Dahl, J.K. Nørskov and C.H. Christensen, J. Catal. 230 (2005) 309–312.

[102] S. Satoh, H. Fujimoto and H. Kobayashi, J. Phys. Chem. B 110(10) (2006) 4846–4852.

[103] H.L. Mckay, S.J. Jenkins and D.J. Wales, J. Phys. Chem. C 113 (2009) 15274–15287.

[104] P. Iyngaran, D.C. Madden, S.J. Jenkins and D.A. King, PNAS 108 (2011) 925–930.

[105] A. Logadottir and J.K. Nørskov, J. Catal. 220 (2003) 273–279.

[106] J. Benziger and R.J. Madix, Surf. Sci. 94 (1980) 119–153.

[107] D.W. Moon, D.J. Dwyer and S.L. Bernasek, Surf. Sci. 163 (1985) 215–229.

[108] D.W. Moon, S.L. Bernasek, D.J. Dwyer and J.L. Gland, J. Am. Chem. Soc. 107 (1985) 4363–4364.

[109] S.D. Cameron and D.J. Dwyer, Langmuir 4 (1988) 282–288.

[110] J.P. Lu, M.R. Albert and S.L. Bernasek, Surf. Sci. 217 (1989) 55–64.

[111] J.P. Lu, M.R. Albert and S.L. Bernasek, J. Phys. Chem. 94 (1990) 6028–6033.

[112] M.H. Nassir, B. Frühberger and D.J. Dwyer, Surf. Sci. 312 (1994) 115–123.

[113] M. Nassir, D.J. Dwyer and P. Kleban, Surf. Sci. 356 (1996) L429–L432.

[114] J.K. Nørskov, Prog. Surf. Sci. 38 (1991) 103–144.

[115] M.L Burke and R.J. Madix, Surf. Sci. 237 (1990) 20–34.

[116] P.B. Merril and R.J. Madix, Surf. Sci. 271 (1992) 81–84.

[117] P.B. Merril and R.J. Madix, Surf. Sci. 347 (1996) 249–264.

[118] T.T. Vink, O.L.J. Gijzeman and J.W. Geus, Surf. Sci. 150 (1985) 14–23.

[119] I.M. Ciobîcă, A.W. Kleyn and R.A. van Santen, J. Phys. Chem. B 107 (2003) 164–172.

[120] S.D. Cameron, Surf. Sci. 198 (1988) 315–330.

[121] J. Paul, Surf. Sci. 224 (1989) 348–358.

[122] T. Sasaki, T. Aruga, H. Kuroda and Y. Iwasawa, Surf. Sci. 240 (1990) 223–244.

[123] T. Sasaki, T. Aruga, H. Kuroda and Y. Iwasawa, Surf. Sci. 276 (1992) 69–85.

[124] S. Akhter, Y. Zhou and White J.M., J. Chem. Soc., Faraday Trans. 86 (1990) 2271–2275.

[125] D. Curulla Ferrè, A.P. van Bavel and J.W. Niemantsverdriet, ChemPhysChem 6 (2005) 473–480.

[126] A.P. van Bavel, M.J. Hopstaken, D. Curulla, J.W. Niemantsverdriet, J.J. Lukkien and P.A.J. Hilbers, J. Chem. Phys. 119:1 (2003) 524–532.

[127] C. Xu and D.W. Goodman, J. Phys. Chem. B 102 (1998) 4392–4400.

[128] J.T. Ranney, A.J. Franz and J.L. Gland, Surf. Sci. Lett. 384 (1997) L865–L868.

Chapter 3

Scope of the project

Introduction

In this chapter a summary is given of the scope of the project that aims to shed light on the pathway to the formation of N-containing compounds when NH_3 is added during Fischer-Tropsch synthesis (FTS). The questions discussed below stem from the literature review presented in Chapter 2 and were used to formulate the hypotheses, which directed the approach taken throughout this study.

Key questions

This work involves both theoretical calculations and experimental techniques, which were used to approach two different sets of questions. The first set of questions are of a fundamental nature and makes use of first principle calculations to look at the initial stages of the pathway to the formation of N-containing compounds, by paying particular attention to the adsorption of and coadsorption of CO and/or NH_3 on a model Fe(100) catalyst surface.

How does the adsorption and decomposition energy profiles of NH_3 and CO compare on an Fe(100) surface? The literature for NH_3 and CO decomposition on model Fe surfaces is abundant and their interactions with model Fe surfaces have been studied individually via several surface science experiments and theoretical techniques. A direct comparison of the respective potential energy surfaces (PES) for CO and NH_3 adsorption and decomposition on a model Fe(100) surface based on theoretical results reported in literature would however be complex and could lead to inaccurate comparisons. When periodic density functional theory (DFT) calculations are used to calculate these properties, it is important to note that the choice of computational methodology, in particular the exchange correlation energy can significantly influence the accuracy of the calculations. To achieve the ultimate goal, that is the analysis of the co-existence of these adsorbates ($CO + NH_x$) on the Fe(100) surface, it is thus imperative that a base case data set is generated where the same computational methodology is applied to investigate the individual decomposition reactions of CO and NH_3 on the Fe(100) facet. Moreover, the results obtained for the decomposition of NH_3 on the Fe(100) surface allow for the discussion of the role of NH_x surface species during the initial stages of the pathway.

Which of the NH_x adsorbates would be readily available for surface reactions on a model Fe(100) surface in the absence of other reactants?

Previous suggestions for the pathway to the formation of N-containing compounds include termination reactions where N, NH_2 or NH_3 combine with a FTS surface product (e.g. alkyl, acetyl). With the use of spin polarized periodic DFT calculations, it is possible to investigate the elementary reactions that would lead to the formation of these NH_x surface species, namely the decomposition reactions of NH_3. Furthermore, the application of statistical thermodynamics allows for the prediction of the feasibility of these elementary reactions approaching temperatures and pressures relevant to the actual process ($T = 523$ K and $P = 5$ bar).

Is it feasible for CO and NH_x to co-exist on a model iron catalyst surface?

It is generally accepted that CO has a strong bonding energy when compared to that of NH_3 on Fe surfaces. In addition, both adsorbates are “bulky” and contain electronegative atoms (i.e. N and O), which leads to the question: Can these adsorbates co-exist on a Fe(100) catalyst surface? If so, how does the NH_x surface species influence the important CO adsorption and dissociation reactions?

The second set of questions stem from aspects of the final stages of the pathway to the formation of N-containing compounds, and are approached via laboratory scale experimental techniques.

How does the presence of 1 vol % NH_3 in the syngas feed influence the FTS reaction?

NH_3 is classically grouped with FTS catalyst poisons, however, few studies exist that indicate how NH_3 directly influences FTS activity and selectivities. To this extent, it is of interest to know how the addition of 1 vol% NH_3 during FTS affects the activity of an Fe-based catalyst, the total product selectivities and the working catalyst. Here an advance is made from previous studies by directly comparing an NH_3-free and NH_3-added FTS reaction, and analyzing the organic product spectrum through the use of comprehensive two-dimensional gas chromatography (GC×GC-TOF/FID).

How is the formation of N-containing compounds associated with the loss of oxygenate selectivity?

From previous studies, it was proposed that N-containing compounds form to the detriment of the oxygenates. The intuitive assumption would be that this could be due to a competition between N/O-containing surface species at the final stages of the pathway. However, considering the facile secondary reactions of oxygenates and the fact that Fe-based catalysts are active for amination of oxygenates reactions, it is desired to know if it is in fact possible for amination reactions (or secondary conversion of primary oxygenates) to take place during FTS. The potential for these secondary reactions to occur during the reaction is tested by co-feeding 1-octanol with the feed (n CO + $2n$ H_2 + 1 vol % NH_3) through the use of a saturator.

Is it possible to use CO_2 as carbon source for the production of N-containing compounds?

It is well-known that CO_2 can be used in Fe-based FTS to produce petrochemicals. Since CO_2 is a greenhouse gas, the potential production of valuable chemicals through the use of CO_2 as the carbon source when NH_3 is added during FTS could additionally provide an alternative route for CO_2 mitigation. The use of CO_2 as carbon source is investigated by conducting Fe-catalyzed slurry phase FTS experiments and substituting CO with CO_2 in the gas feed (n CO_2 + $3n$ H_2 + 0/1 vol % NH_3).

Would a FTS catalyst with high oxygenate selectivity lead to high selectivities for N-containing compounds when NH_3 are co-fed during FTS?

Certain FTS based catalysts that are not industrially relevant, for example ruthenium or rhodium based catalysts are known to produce lower carbon number (C_1 - C_4) oxygenates in high selectivities during FTS. It could therefore be possible that the formation of (C_1 - C_4) N-containing compounds could form in higher selectivities when co-feeding of NH_3 with Rh-based FTS experiments, based on the assumption that these compounds share similar pathways to product formation. To evaluate this statement a 10 wt % Rh-Al_2O_3 catalyst is used in fixed bed NH_3 co-feeding FTS experiments.

Hypotheses

Based on the literature review and the key questions phrased in the previous section, the major hypotheses for this thesis are:

1. At certain coverages and conditions, NH_3 and CO can co-exist on a model Fe(100) surface.
2. Oxygenates that form during primary FTS reactions can be converted to N-containing compounds via secondary reactions when NH_3 are present in synthesis gas, for low temperature Fe-based FTS.
3. A feed containing CO_2, H_2 and NH_3 can lead to the formation of N-containing compounds during Fe-catalyzed FTS reactions.
4. Catalysts that yield high oxygenate selectivity are suitable for the production of N-containing compounds when NH_3 are co-fed during FTS.

Chapter 4

Methodologies

In Chapter 4 the theoretical techniques and experimental methodologies used throughout this thesis are presented.

The theoretical background of density functional theory is briefly discussed, by looking at the development of the Kohn-Sham equations, the role and importance of exchange-correlation functionals and the important theoretical aspects of modeling a periodic system. This is followed by a discussion of the general computational methodologies employed in the results (Chapters 5 and 6) of this work. This includes the description of the calculation of the optimized bulk phase system, adsorption energies, vibrational modes, transition state structures and activation energies.

In the experimental section of this Chapter, the catalyst preparation and characterization procedures and the results thereof are presented. Furthermore, the setup and operation of the slurry phase and fixed bed reactors that was used to obtain the results presented in Chapters 7, 8 and 9 are discussed. Special attention is given to the analysis of the product spectrum, which includes on- and off-line gas chromatography (GC-TCD, GC-FID). More importantly, the methodology and use of comprehensive two-dimensional gas chromatography (GC×GC-TOF/MS), which yielded several important sets of results in this thesis is discussed.

Theoretical method and model

Theoretical background

The following discussion of the theoretical background is aimed at highlighting the most important conceptual aspects for the computational approaches that are applied in the calculations performed in this thesis. It is therefore *not* the intention of this discussion to provide an exhaustive review of first principles calculations or density functional theory. For a thorough review of these topics, the interested reader is directed to references [1–3].

First principles calculations

The basis of many *ab initio* (i.e. “from first principles ”) calculations is the approximation to the solution of the time independent non-relativistic Schrödinger equation (Eq. 4.1),

$$\hat{H}\Psi_n = E_n\Psi_n \tag{4.1}$$

where the time-independent Hamiltonian ($\hat{H}$) operates on the many particle wavefunction (Ψ_n) and produces the numerical value for the energy (E_n) associated to the energy level n. This equation, developed by the Austrian physicist Erwin Schrödinger, contains all the properties of electrons and nuclei, and can only be solved for small systems such as the hydrogen atom. Due to the vast difference in mass between electrons and nuclei, it is universally approximated that the motions of these entities can be separated, this is known as the *Born-Oppenheimer approximation*. The Hamiltonian ($\hat{H}$) that operates on the electronic wavefunction can be expanded (see Eq. 4.2, given in atomic units i.e. $e^2 = \hbar = m = 1$) into operators for the kinetic energy ($\hat{T}$) and potential energy ($\hat{V}$),

$$\hat{H} = \hat{T} + \hat{V}_{ne} + \hat{V}_{ee} = \sum_{i=1}^{N}(-\frac{1}{2}\nabla_i^2) - \sum_{i=1}^{N}\sum_{\alpha=1}^{n}\frac{Z_\alpha}{r_{i\alpha}} + \sum_{i<j}^{N}\frac{1}{r_{ij}} \tag{4.2}$$

where $\hat{T} \rightarrow \sum\limits_{i=1}^{N}(-\frac{1}{2}\nabla_i^2)$ is the kinetic energy operator for electron i, $\hat{V}_{ne} \rightarrow \sum\limits_{i=1}^{N}\sum\limits_{\alpha=1}^{n}\frac{Z_\alpha}{r_{i\alpha}}$ is the electron-nucleus attraction energy operator and $\hat{V}_{ee} \rightarrow \sum\limits_{i<j}^{N}\frac{1}{r_{ij}}$ is the repulsion energy operator of two electrons i and j.

The Hartree-Fock theory (HF) is a traditional molecular computational technique that is used to approximate the determination of the wave function and energy for a complicated many body system. There are several computational approaches or techniques used in DFT that resemble those used in the HF theory. In HF theory the variational principle of the electronic wavefunction is applied to find the ground state energy. By using a self-consistent field approach, a linear combination of atomic orbitals are sought that minimizes the energy with respect to variations in the antisymmetric wavefunction. A key difference in the two theoretical methods (HF and DFT) is the inclusion of electron correlation effects, where these interactions are by definition excluded in HF theory, but are approximated in DFT through the exchange-correlation functional. The HF approximation gave rise to significant progress towards the calculation of the total energy. However, finding approximate solutions to the electronic wavefunctions with modern computational techniques such as the Hartree-Fock or post-Hartree-Fock techniques is computationally demanding for larger systems. DFT has improved the capabilities to find the ground state energies and wavefunctions of more complex systems.

Density functional theory

In DFT an entirely different, formally rigorous approach is followed compared to other *ab initio* computational techniques (e.g. Hartree-Fock theory). The important difference is the promotion of the electron density (ρ) from many other obervables to the key variable. Hohenberg and Kohn (HK) showed in their paper [4] that the external potential, $v(\mathbf{r})$, is a unique functional of the ground state electron density, ρ_0. Moreover, it allowed them to show that the ground state energy (E_0), and all other ground state properties, are uniquely determined by the electron density.

$$E_0 = E[\rho_0] \tag{4.3}$$

The second important piece of information provided by Honenberg and Kohn, sometimes referred to as the *second HK theorem*, is that the variational principle applies to the ground state energy obtained from the electron density (ρ_0),

$$E[\rho_0(\mathbf{r})] < E[\rho'] \tag{4.4}$$

where ρ_0 represents the ground state electron density and ρ' is a different density. In other words, similar to the variational principle for wavefunctions, the total energy ($E[\rho']$) corresponding to electron density ρ' will never be lower than the true ground state energy ($E_0[\rho]$) associated with the ground state density ρ_0. The energy can be expanded in two terms

$$E[\rho(r)] = \int v(\mathbf{r})\rho(\mathbf{r})d\mathbf{r} + F[\rho(\mathbf{r})] \tag{4.5}$$

where the first term ($\int v(\mathbf{r})\rho(\mathbf{r})d\mathbf{r}$), which represents the interaction between the electrons and the external potential, is readily calculated once the system (i.e. nuclear coordinates) has been specified. The second term ($F[\rho]$), can be decoupled (see Eq. 4.6) to give the sum of the kinetic energy ($T[\rho]$) and the Coulomb electron-electron repulsion energy ($V_{ee}[\rho]$) and represents a universal functional that can now be minimized independently from the external potential.

$$F[\rho] = T[\rho] + V_{ee}[\rho] \tag{4.6}$$

In principle, if the explicit expressions for $T[\rho]$ and $V_{ee}[\rho]$ are known, mimization of the energy with respect to the density would yield the ground state energy. Such expressions for the energy functionals do however not exist.

Kohn and Sham (KS) [5] approached the calculation of the unknown functional $F[\rho(r)]$, by replacing the interactive problem and mapping it onto a fictitious non-interacting reference system of N electrons. In the KS formulation one thus have,

$$F[\rho] = T_s[\rho] + E_H[\rho(r)] + E_{XC}[\rho(r)] \tag{4.7}$$

where $T_s[\rho]$ represents the kinetic energy of the non-interacting reference system and $E_H[\rho(r)]$) is the classic Hartree interaction energy, which can both be calculated in a similar fashion as established in Hartree-Fock theory. The third term, the exchange-correlation energy ($E_{XC}[\rho(r)]$), contains all the "many particle" information such as the exchange energy of spin (which stems from the Pauli exclusion principle) and the correlation energy of the electrons. Kohn and Sham expressed the density as the sum of the square moduli of N "artificial " one-electron orthonormal orbitals, or Kohn-Sham orbitals ($\phi_i(r)$).

$$\rho(r) = \sum_{i=1}^{N} |\phi_i(r)|^2 \tag{4.8}$$

The relationship in Eq. 4.8 has the necessary condition to reproduce the ground state denstity (ρ_0), which is in turn dependent on the choice of the correct effective potential ($V_{eff}(r)$).

The Kohn-Sham equations (see Eq. 4.9)

$$\left\{-\frac{\nabla_1^2}{2}+V_{eff}\right\}\phi_i(r_1)=\varepsilon_i\phi_i(r_1) \tag{4.9}$$

are thus solved self-consistently via the following sequence:

1. A trial electron density is determined ($\rho(r)$).
2. An approximate exchange-correlation energy functional is used on the trial electron density to obtain $V_{XC}[r]$, and in so doing $\mathrm{V}_{eff}(r)$.
3. The Kohn-Sham equations are then solved to obtain an initial set of Kohn-Sham orbitals ϕ_i.
4. These orbitals are then used to calculate an improved electron density, $\rho(r)'$.
5. The process is repeated until convergence between the ρ_{input} and ρ_{output} is reached, and hence the final ρ_{output} is accociated with a converged E_{XC}.
6. And finally, the electronic energy $E[\rho(r)]$ is calculated.

Exchange-correlation functionals

The accuracy of DFT calculations lies within the approximation to the exchange-correlation energy functional.

The most basic approximation is the *Local Density Approximation* (LDA), which is based on the Uniform Electron Gas model, in which the local electron density is constant. The exchange energy density of an inhomogeneous system is thus replaced, within a local space (dr), with the exchange energy of a homogeneous electron gas. This approximation is successful in describing systems where there is minimal change in the electron densities, such as metals. However, since positive or electronic charges in actual molecules are rarely uniformly distributed, the LDA tends to lead to unreliable binding energies [6]. An example of this functional is the functional developed by Vosko, Wilk and Nusair (VWN) [7], which specifically refers to the correlation energy contribution.

The more commonly used alternative approximation to the exchange-correlation energy functional is the *Generalized Gradient Approximation* (GGA), which is an improvement to the LDA by extending the dependence to the gradient of the electron density ($\nabla\rho(r)$). With the inclusion of the dependence on the gradient of the electron density, these functionals become more computationally demanding, but yield much improved binding energies. Several GGA exchange-correlation energy functionals have been developed, such as the Perdew-Wang 91 (PW91) [8], the Perdew-Burke-Enzerhof (PBE) and the revised form of the Perdew-Burke-Enzerhof (RPBE) [9, 10] functionals. The RPBE functional is used throughout this work, except where comparisons are made with the PW91 exchange-correlation energy functional.

VASP

The software package used to perform periodic DFT calculations throughout this work is the Vienna *ab initio* Simulation Package (VASP). An important aspect of VASP is that the equations of motions of the system are separated from the calculation of the electronic wavefunctions. Two loops are utilized, where the inner loop involves the minimization of the electronic wavefunction by solving the Kohn-Sham equations, while the geometry optimization is solved within the outter loops. VASP is designed for the treatment of periodic systems and is therefore widely used to study properties of bulk materials and heterogeneous catalysis in general. VASP makes use of ultra-soft pseudopotentials (USPP) or the projector-augmented wave method (PAW) to describe electron-ion interactions and a plane wave basis set. The PAW method was employed in this thesis as implemented by Kresse and Joubert [11] as it is more reliable for magnetic systems, such as the metallic iron slab (Fe(100)) used in the catalytic reactions considered in this work, with the exception of the comparative calculations with the PW91 exchange-correlation energy functionals where USPPs were used. For accurate computational results several parameters need to be optimized. The most important parameters will be discussed in the subsequent subsections.

Optimization of key parameters

For this model surface to provide accurate results several key parameters (e.g. kinetic cut-off energy, k-points, vacuum gap etc.) had to be optimized.

Kinetic cut-off energy (E_k): In this work, plane waves are utlized as basis set functions to expand the Kohn-Sham orbitals. Using Bloch's theorem, the wavefunction can be expressed as the product of a plane wave function ($e^{i(\mathbf{k}+\mathbf{r})}$) and a periodic function ($u_{n\mathbf{k}}(\mathbf{r})$) with the same periodicity of the lattice (see Eq. 4.10).

$$\psi_{n\mathbf{k}}(\mathbf{r}) = e^{i\mathbf{k}\cdot\mathbf{r}}u_{n\mathbf{k}}(\mathbf{r}) \tag{4.10}$$

where $\mathbf{r}$ is a position vector and $\mathbf{k}$ is a "wave-vector" that is dependent on the size of the unit cell. When introducing the reciprocal lattice vector $\mathbf{G}$, Eq. 4.10 can be written as the sum of plane waves (see Eq. 4.11)

$$\psi_{n\mathbf{k}}(\mathbf{r}) = \sum_{G} c_{n,\mathbf{G}}(\mathbf{k})e^{i(\mathbf{k}+\mathbf{G})\cdot\mathbf{r}} \tag{4.11}$$

where the co-efficients $c_{n,\mathbf{G}}$ can be minimized to find the lowest energy solution. For a perfect expansion of the KS orbitals, an infinite number of plane waves is needed. However, the short plane wave (or high kinetic energy) terms do not play a significant role in the description of the valence density ($\rho(\mathbf{r})$). This provides the justification for truncating the plane wave basis sets above a kinetic cut-off energy (E_{cut}).

k-points: The k-points can be viewed as a "sampling grid" for the first Brillouin zone in reciprocal space. These grids are generated via the use of the Monkhorst Pack scheme [12]. When setting up the model, the k-points sampling density is optimized by sequentially increasing the number of k-points used within a particular system, and calculating the associated energy (by performing a single point energy calculation). When the energy difference with further increase in the sampling density is within ± 1 meV per atom, the k-points are sufficiently converged to ensure that enough k-points were used to describe the system. Furthermore, the aforementioned convergence criteria conforms to the inherent accuracy of DFT to calculate energies. The minimum number of k-points is desired, since more k-points results in increased computational expense. The optimization of these parameters are further described in the subsequent sections.

Computational setup

Bulk phase optimization

Before finding the cell parameter of the bulk bcc Fe structure, a choice for a well converged cut-off energy and k-point grid had to be determined. An extended discussion on the procedure followed and the results for the aforementioned optimization calculations can be found in Appendix B (see Figures B.1 and B.2). Every pseudopotential in VASP has a default recommended cut-off energy. These values serve as a good reference, but it is also important that a set of calculations is performed to make sure that the energy is well converged for the chosen cut-off energy. The methodology followed during convergence tests for the kinetic energy (E_{cut}) was to keep the number of k-points constant and vary the cut-off energy from 200 to 500 eV until the energy calculated of the bcc Fe bulk conventional unit cell was within an error of ± 1 meV/atom. A similar procedure was followed to find a suitable k-point mesh. A Monkhorst-Pack scheme [12] was used and the k-point sampling grid was varied from 1×1×1 to 19×19×19. A cut-off energy of $E_{cut} = 380$ eV and k-point grid of 11×11×11 were determined to be sufficient values to be used for the calculation of bulk bcc iron for both the RPBE and PW91 E_{xc}-functionals. The parameters evaluated for the bulk phase, such as the lattice parameter, the corresponding bulk modulus (B = 161 GPa) and magnetic moment of (M = 2.31 μB), correlate well with experimentally-determined values (a = 2.86 Å, and B = 168 GPa and M = 2.24 μB respectively) [13].

Model Fe(100) surface

The model Fe(100) surface used to perform the study of CO and NH_3 adsorption and co-adsorption is illustrated in Figure 4.1. Similar to the case in crystallography, a unit cell and the structural and symmetry information it contains is used to construct the crystal lattice (or metal lattice) into three infinite dimensions. To generate the model Fe(100) surface, the bulk catalyst is cleaved along the (100) Miller plane, and a sufficient volume of empty space (i.e. a vacuum gap) is introduced in the z-direction. The model surface thus contains a predetermined number of Fe(100) layers which extend to infinity in the x-y direction, and the infinite slabs thus formed are separated by a predetermined vacuum gap so that no interaction between the top and bottom layers of neighbouring slabs occurs.

Similar to the optimizations performed for the bulk phase of bcc Fe, the ideal k-point sampling and kinetic cut-off energy had to be determined for the model Fe(100) surface. In addition, the number of atomic layers used to model the surface, the number of atomic layers that were allowed to translate or were constrained during geometry optimizations and the size of the vacuum layer

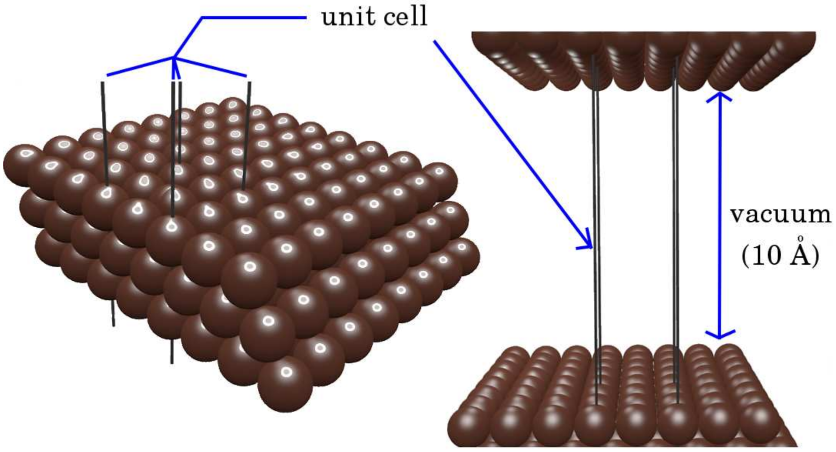

Figure 4.1: Schematic illustration of the periodic Fe(100) surface model generated for the calculations in this work.

between the atomic layers had to be evaluated. The results for the aforementioned tests is presented in Appendix B (see Figures B.3, B.4, B.6 and B.7). Based on these calculations, a model surface with 5 atomic layers, where the top two layers were allowed "relax" was chosen for the 2×2 unit cell that was predominantly used in the DFT calculations. A 10 Å vacuum gap in the z-direction was found to be sufficient to eliminate any interaction between the model Fe(100) surfaces. Furthermore, a k-point mesh of 5×5×1 and a kinetic cut-off energy of 400 eV was found to be the suitable values for these parameters when using the 2×2 unit cell. The adsorbates were generally configured to have the initial geometries situated on the high symmetry sites (atop - at, bridge - br and fourfold hollow fh) of the Fe(100) surface as shown in Figure 4.2. If one ignores stoichiometry, the adsorption energy (E_{ads}) for the adsorbates is calculated with Eq. 4.12

$$E_{ads} = E_{X+slab} - (E_{slab} + E_{X(g)}) \tag{4.12}$$

where E_{X+slab} is the energy calculated for adsorbate X (e.g. X = CO/NH$_3$) on the model Fe(100) slab, E_{slab} is the energy calculated for the empty slab and $E_{X(g)}$ is the energy calculated for the gas phase molecule or radical. A correction was added to account for the magnetic moment of Ferromagnetic Fe atoms. To account for the net dipole moment generated due to only adsorbing the adatoms and adsorbates on one side of the slab, a dipole correction was

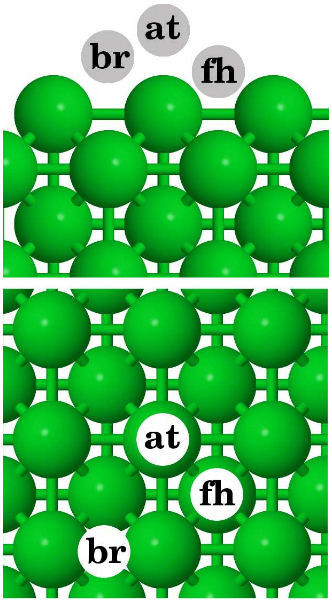

Figure 4.2: Top and side view of the Fe(100) surface that illustrates the positions of the high symmetry adsorption sites: atop - *at*, bridge - *br* and fourfold hollow *fh*.

added to the total energy by setting the flag ("IDIPOL") in the VASP software.

Vibrational analysis

The VASP code allows for the determination of the Hessian matrix and the vibrational frequencies of a particular system. To simplify the calculation only a partial Hessian vibrational analysis (PHVA) was performed on the adsorbed systems, by only considering the forces due to the displacement (0.02 Å) of the adsorbates (e.g. NH_3, CO) and "freezing" the surface coordinates, i.e. the vibrational analyses were performed under the frozen phonon approximation. The vibrational frequencies were subsequently used to validate that the optimized geometry or transition state structures were at a local minimum, or first order saddle point on the potential energy surface. Futhermore, the calculated vibrational frequencies allowed for the calculation of partition functions, vibrational contribution to the enthalpy and entropy (H_v and S_v, see Appendix B) and zero-point vibrational corrections to the energy ($ZPVE$) using standard equations from statistical mechanics. The energies calculated via DFT is at the minimum of a potential well, and do not include its $ZPVE$, which is calculated using Eq. 4.13

$$ZPVE = \sum \frac{1}{2} hv \tag{4.13}$$

where h is Planck's constant and v is the vibrational frequency. The adsorption energy is thus corrected by adding the change in the zero point energy (ΔZPE) to the calculated adsorption energy (see Eq. 4.14).

$$\Delta E_{ads} = E_{ads} + \Delta ZPE \tag{4.14}$$

A similar procedure is followed for transition state structures, with the ommission of the imaginary vibrational mode when calculating the $ZPVE$.

Locating transition state structures

The nudged elastic band (NEB) method [14] was used to locate the transition state structures. If the initial (x_R) and final (x_P) coordinates of the reaction being considered are known, the NEB method can be used to locate the transition state structure and the minimum energy path (MEP) connecting those points on the PES. To initiate the NEB algorithm, a set of images (x_n, with n between 6 and 8 images for this work) is generated via linear interpolation of the reaction coordinates between the reactant and product. The NEB originates from the chain-of-states method where the gradient of the energy with respect to the reaction coordinates is optimized through the use of a spring constant k. The target function to be optimized would thus be

$$F^{EB} = \sum_{i=0}^{n} E(x_i) + \sum_{i=1}^{n} \frac{n \cdot k}{2}(x_i - x_{i-1}) \tag{4.15}$$

Optimization of F^{EB} does however fail to accurately find the MEP due to the tendency of the spring force to make the path straight. Jonsson et al. [15] solved this problem in the NEB method, by only considering the normal component of the potential force, and the tangential component of the spring force to move the chain of states. For the image along the MEP with the highest energy, a vibrational analysis was performed to confirm that only one imaginary mode (which would indicate a transition state structure based on harmonic TST) was present. A Quasi-Newton algorithm was further applied to this structure to minimize the forces (with convergence criteria: 0.03 eV/Å) acting on the atoms.

Statistical thermodynamics

Statistical mechanics or atomistic thermodynamics is a powerful tool, that can aid the interpretation of results obtained via DFT calculations. In this thesis, a basic model (presented in Appendix B) is used to construct a free energy diagram (ΔG) of the decomposition of NH_3 on Fe(100). Furthermore, a model proposed by Ciobîcă et al. [16] is followed to calculate the Gibbs free energy of mixing (ΔG_{mix}) for CO + NH_3 on the Fe(100) surface. A full description for the calculation of all partition functions, as well as enthalpy and entropy contributions to the free energy is documented in Appendix B.

Experimental methods

Catalyst preparation and characterization

Preparing Fe-based catalysts

The unsupported K promoted Fe-based catalysts used throughout this study was prepared via a discontinuous precipitation method as described by Claeys [17]. A 1 molar solution of $Fe(NO_3)_3 \cdot 9H_2O$ (Sigma Aldrich) was prepared, combined to the desired ratio and subsequently brought to the boil whilst being stirred at 24 000 rpm with a mechanical stirrer (IKA ULTRA-TURRAX, T 25 digital with a S25N-25G dispersion element). A separate 2 l beaker containing an aqueous solution of 5 vol% NH_4OH (Kimix Chemical Supplies) was brought to the boil and swiftly added to the metal nitrate solution. An estimate for the volume of the NH_4OH solution needed to achieve a pH of 7 was pre-determined in a smaller scale cold test. To assure that a pH of 7 was achieved, a separate smaller beaker (500 ml) containing the 5 vol% NH_4OH solution was heated on a hot plate and added while measuring the pH with a ThermoOrion 410Aplus pH meter equipped with a 91065NWP electrode (Thermo electron corporation, USA). The solution containing the precipitated catalyst was then left on a hot plate for an additional 15 minutes of stirring and subsequently filtered. The filtrate was washed with ca. 4 liters of boiling, deionized H_2O until it was free of all nitrates, which was followed by a drying step (in air) in an oven held at 130 ℃ for 18 hours. The catalysts were crushed to a fraction below 125 μm to avoid intra-particle mass-transfer limitations in the catalytic tests, and transferred to a fluidized bed reactor (20 mm I.D.) for a calcination step. The calcination was achieved as follows: synthetic air was allowed to flow through a quartz fluidized bed reactor at 900 ml/g_{Fe}/h (NTP) while ramping the catalyst temperature from ambient temperature to 400 ℃ at a heating rate of 10 ℃/min and held constant at this temperature for an additional 3 hours. A 1 molar aqueous solution of KNO_3 (Sigma Aldrich) was prepared and used to impregnate the catalyst with the desired loading (100:2 g/g weight ratio). After impregnation a rotary evaporator was used to dry the catalyst, but to ensure that the catalyst was free of all nitrates an additional calcination step (which follows the same procedure as described above) was performed.

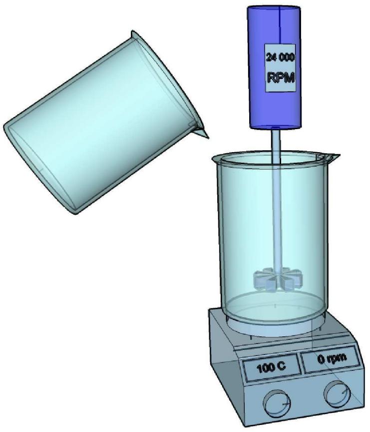

1. Precipitation
2. Washing and filtration
3. Drying at 130 ^oC
4. Crushing to $< 125\mu m$
5. Calcination
6. Impregnation
7. Calcination

Figure 4.3: Schematic showing the preparation procedure for the precipitated Fe-based catalyst.

Preparing Rh-based catalyst

The incipient wetness technique was employed to synthesize a 10 wt% Rh/Al_2O_3 catalyst. In this technique, a metal-containing solution is applied to the support, which corresponds to the total pore volume of the support material. Capillary forces provide the driving force for the introduction of the impregnation solution into the support [18]. The pore volume of the Al_2O_3 (Sasol Puralox SSCa 5/150) support was determined to be 0.5 ml/g. An aqueous solution with the required amount of $Rh(NO_3)_3$ (Sigma Aldrich) to result in a 10 wt% Rh catalyst was prepared and added to the support until incipient wetness was reached. The sample was dried at room temperature for 24 hours and subsequently calcined in air at 350 ℃ for 5 hours in a fluidized bed reactor.

Atomic absorption spectroscopy (AAS) and inductively coupled plasma (ICP) analysis

Atomic absorption spectroscopy (AAS) and inductively coupled plasma (ICP) analyses were used to determine the Fe and K weight ratios of the catalyst. A micro-wave technique was used to digest the sample, which was then analyzed with the AAS and ICP instruments. Since it was initially desired to reproduce the catalyst composition that was used by Sango [19], a 100:2 (g/g) Fe to K weight ratio was targeted. The analysis revealed that the K content was slightly lower (100: 1.82 (g/g) Fe to K weight ratio) than the desired loading, but sufficient for the purpose of this study. Cairns [20] reports an uneven distribution of K on the various iron-based catalyst samples that he prepared in a similar fashion.

ICP analysis was also used to confirm the loading of the Rh-based catalyst (9.6 wt % Rh/Al_2O_3).

Powder X-ray diffraction (PXRD)

Powder X-ray diffraction (PXRD, Bruker D8 Advanced laboratory X-ray diffractometer) was used for the phase identification of the prepared catalysts (Fe_2O_3), the spent catalyst (Fe_3O_4, χ-Fe_5C_2, ε-Fe_2C) and the white solid (NH_4CO_3) formed during NH_3 co-feeding FTS reactions. A cobalt X-ray source ($\lambda = 1.78897$) was used, with the optics set to make use of a parallel beam. Diffraction patterns of aforementioned phases were identified via comparison of the diffraction patterns available in the International Center for Diffraction Data PDF-2 database. The analysis of the calcined catalyst confirmed the preparation of Fe_2O_3 (hematite, Figure 4.4). Some unidentified peaks were present in the XRD pattern, which could not be identified based on the XRD patterns available in the database but were assumed to be due to bulk phases associated with K. The XRD results for the characterization of the spent catalyst and NH_4CO_3 are presented and discussed in Chapter 7.

The average crystallite size (d_c) was calculated from the XRD scans via the use of the Scherrer equation (Eq. 4.16),

$$d_c = \frac{K\lambda}{\beta \times cos\theta} \tag{4.16}$$

where K is the shape factor (0.9), λ is the wavelength of the X-ray, β is the line broadening at half the maximum intensity (FWHM) and θ is the Bragg angle.

Temperature programmed reduction (TPR)

To establish the degree of reduction, temperature programmed reduction (TPR) experiments were conducted on an Autochem 2910 (Micromeritics Instrument Corp., USA). Approximately 30 mg of the catalyst sample was weighed and loaded into a U-type quartz reactor and subsequently placed inside the furnace of the instrument. The thermocouple was situated 2 mm above the catalyst bed. The hydrogen consumption was measured via the change of signal of a thermal conductivity detector (TCD).

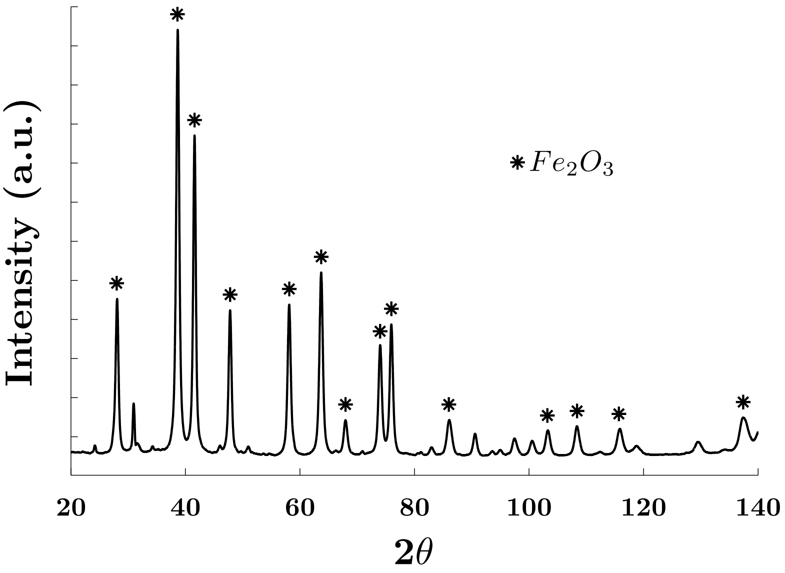

Figure 4.4: Confirmation of Fe_2O_3 (hematite) via analysis of the XRD pattern obtained.

In order to determine the degree of reduction, the catalyst was first reduced using the same reduction procedure that was used for the FTS reactions conducted with the Fe-based catalysts. That is, a H_2 flow rate of 45 ml/g_{cat}/min (NTP) was initiated and the furnace ramped at a rate of 1 ℃/min from 25 ℃ to 400 ℃ where it was held for 16 hours. In the second step, the catalyst was exposed to argon and cooled to 50 ℃. As soon as the TCD signal was stable the gases were switched from Ar to a gas containing 4.9 vol% H_2 in Ar and the furnace ramped from 50 ℃ to 950 ℃ with a 10 ℃/min ramp rate. Based on the measured H_2 consumption, it was calculated that the Fe/K catalyst had a degree of reduction of 95 % (± 2 %), i.e. 95 % of Fe was available as metallic Fe (α-Fe).

In-situ reduction of Fe-based catalyst (in-situ PXRD)

For the confirmation of the TPR experiments and to gain additional information on the reduction behaviour of the catalyst, a reduction of the catalyst was conducted while recording XRD patterns (in-situ PXRD). For an in-situ PXRD experiment, the catalyst was placed in the sample holder of a XRK-900 reaction chamber (Anton-Paar, Austria) attached to the laboratory XRD instrument (described above, Section 4.2.1.4). The XRD patterns were recorded without any interruption of the reduction procedure (e.g. temperature and H_2 flow rate). To obtain the maximum "resolution", relatively fast scans were taken, with the scan range set to $20 \leq 2\theta \leq 85$ and the step sizes set to 0.01151626 degrees, allowing 0.2 seconds of acquisition per step, which results in 19 minutes of scanning time per diffractorgram. The results obtained for the in-situ PXRD pre-treatment experiments with the Fe-based catalyst that was only promoted with K (Fe:K, 100/2 (g/g)), which was used in all Fe-based FTS reactions, is presented in Figure 4.5 (*Top*). These results would suggest that the catalyst is in fact completely reduced to metallic Fe at the final stage of the pre-treatment, while the TPR results suggest that 5 ± 2 wt% was not reduced. One would expect the XRD analysis to be more accurate in this respect. In the bottom part of Figure 4.5 the crystallite size (calculated via the Scherrer equation) of the catalyst plotted as a function of the time (in hours) is presented. These sizes are considerably higher than the crystallite sizes (ps, ca. 30 nm) reported by Cairns [20] who used a similar Fe-based catalyst preparation technique. The way that Cairns determined these values was based on ex-situ characterization of the catalyst reduced in a fluidized bed reactor, followed by a passivation process with CO_2. The difference in the values obtained here could be due to the different methodologies followed.

Laboratory test scale unit

General test unit setup

The general setup for the laboratory scale test unit will briefly be discussed while the use of the fixed bed and slurry phase reactors, either one of which can be used at a time, will be detailed in the following subsections. The test unit used throughout this study was specifically designed and constructed as part of the experimental part of this project, since very specific requirements are needed when co-feeding NH_3 during FTS. A full diagram of the setup is given in Figure 4.6 and a picture accompanied with further information of the reactor system can be found in Appendix C and Figure C.2. The following gases, CO, CO_2, H_2, N_2, 0.0018 vol % C_6H_{12} (cyclo-hexane) in N_2 and 10.1 vol % NH_3 in H_2 were passed through in-line filters to protect the mass flow controllers further downstream. As an additional precautionary measure, a carbonyl decomposer was situated after the in-line filter for the CO gas. The pressures of the aforementioned gases were then reduced via pressure regulators to appropriate levels (typically 10 - 15 bar) and was

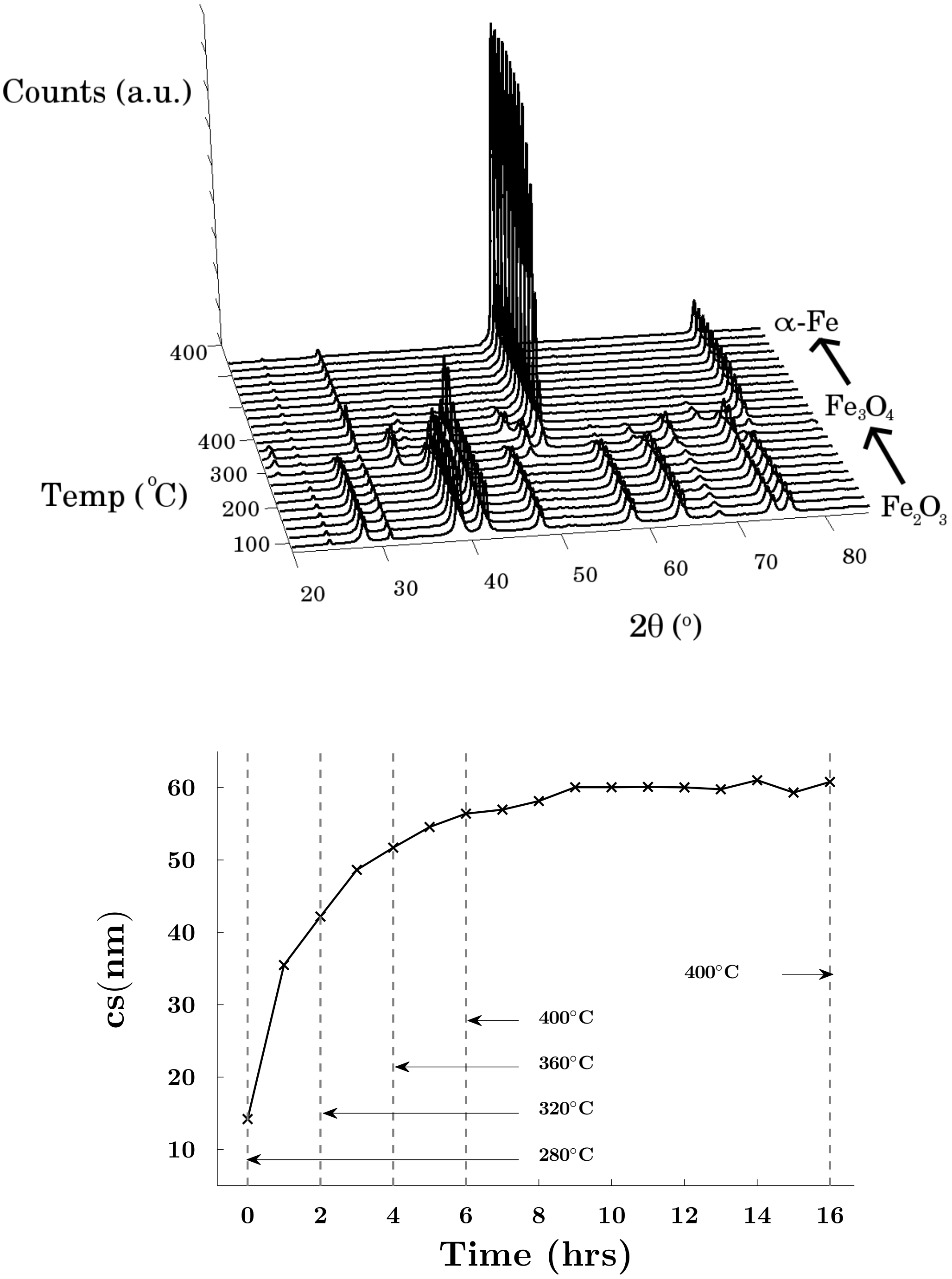

Figure 4.5: (*Top*) PXRD patterns obtained during TPR experiments conducted in the XRK-900, with the temperature, 2θ (with θ the Bragg angle) and intensity as x, y and z co-ordinates respectively. (*Bottom*) The iron crystallite size (cs) as a function of time (where t = 0 is the onset of the formation of α-Fe). After 2 hours at 400 °C, the crystallite size remains constant.

regulated via thermal mass flow controllers (Brooks Instrument). After the combination of the relevant gases, they were sent through a coil for adequate mixing. For the co-feeding of the $C_{8/9}$ liquid products in Chapter 8, it was important to keep the inlet pipelines heated to 120 ℃. The downstream lines were kept at 220 ℃, to ensure that all gaseous FTS products remained in the gas phase before the condensation vessels and on-line gas chromatographs. These heated lines are indicated in red in Figure 4.6. All pressurized vessels with a volume larger than 100 cm^3 were connected to pressure release valves, which were configured to release pressures above 10 bar to the ventilation pipeline for safety purposes (not indicated in figure). Prior to the inlet section of the reactors, a three-way valve is located to allow the by-passing of the reactors. A second three-way valve allowed for the choice between the fixed bed reactor and the slurry phase reactor, essentially allowing dual operation of the test unit. The gases that enter (by-pass mode) or exit the reactors can finally be combined with the reference gas (0.0018 vol % C_6H_{12} (cyclo-hexane) in N_2) that is indicated by the green line in Figure 4.6. The organic compounds can be analyzed via three techniques. Firstly, an ampoule sampling device (see further details in Section 4.2.3.4 is connected to allow for analysis via off-line GC-FID or GC×GC-TOF/FID. Secondly, an on-line GC-FID is connected further downstream that provides certain benefits over the ampoule sampling technique as described in subsequent sections. Finally, a "cold trap" is located before the backpressure regulator, where the liquid FTS products that condense at ca. 10 ℃ (5 bar) can be collected. A spring loaded backpressure regulator (Go Regulator) that operates through a diaphragm mechanism was used for accurate pressure regulation. The inorganic compounds can be analyzed via an on-line gas chromatograph equipped with a TCD that is directly connected to the line exiting the backpressure regulator.

Slurry phase reactor

A slurry phase reactor (see Figure 4.7 - (*Top*)) was used for most of the reactions reported in Chapters 7 and 8. This continuously stirred-tank reactor (CSTR) can be assumed to be gradientless with respect to temperature and concentrations of reactants and product [21, 22]. The major components of the slurry phase reactor and the general operational procedure is outlined below.

The stainless-steel reactor (Parr Instruments) with a volume of 600 cm^3, is equipped with a

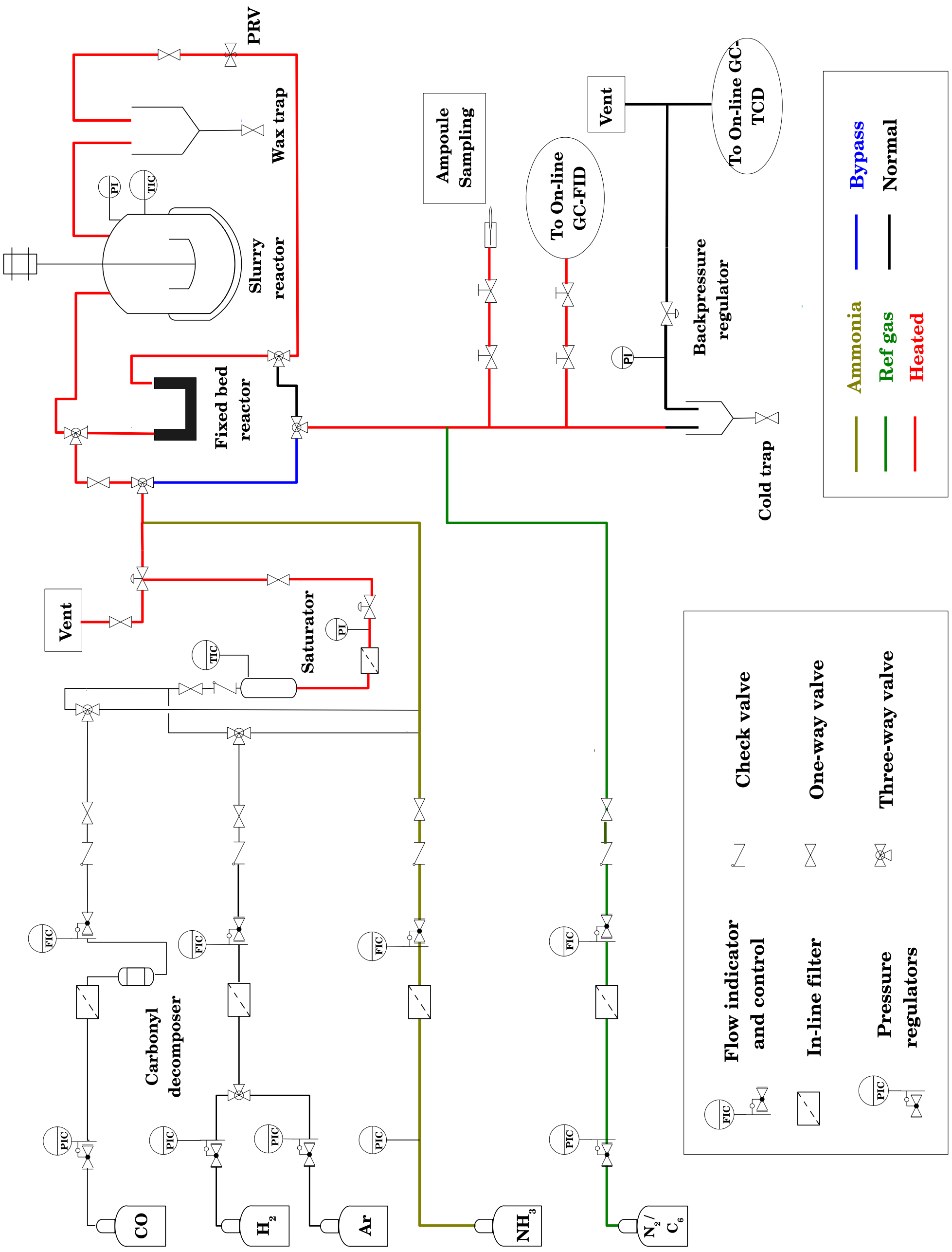

Figure 4.6: General process flow sheet for the laboratory scale test unit used for the Fischer-Tropsch synthesis experiments.

thermocouple, magnetic stirrer (IKA EUROSTAR Power Control) and a wax leveler. The gases enter the reactor via an 1/8" stainless steel tube that terminates 1 cm from the bottom of the reactor. The liquid and gas phase products leave the reactor via a wax leveler (see Figure C.3 in Appendix C), which has a filter with a pore diameter of 2 μm and is designed to avoid the catalyst from moving downstream and to keep the liquid volume in the reactor constant.

In the start up of the reactions reported, the reactor was heated to 130 ℃ while allowing N_2 to pass through the system at a low flow rate (10-20 ml(NTP)/min). An amount of 300 g of wax (Sasol, C_{30-60}) was melted and subsequently added to the reactor. The liquid wax was purged with the inert gas flowing through it for 30 minutes. In order to obtain a final mass of 2.00 g of the reduced catalyst, 2.86 g of the Fe oxide catalyst was reduced externally and transferred under an inert atmosphere into a small amount (8 g) of wax. This wax pellet was then added to the reactor, whilst slowly stirring (ca. 50 rpm) with the stirrer. After the wax of the pellet melted and the reduced catalyst was introduced to the wax medium, the reactor was closed up and the stirring speed was brought to 500 rpm, the temperature was increased to 250 ℃ and the flow rate of the inert gas (N_2) was increased to 100 ml (NTP)/min. Via the use of a spring-loaded back-pressure regulator (Go Regulator) the system was pressurized to 5 bar. The reactor valves were then switched to by-pass mode and left for another hour at 5 bar to assure that the reactor remained pressurized, which served as an indicator that there were no leaks in the system. Whilst the flow configuration was in by-pass mode, the reactant gases CO, H_2 (with or without NH_3) were set to the desired flow rates ($\dot{n}_{i,in}$) and confirmed via GC-TCD using N_2, which was added together with the organic internal standard (cyclohexane). As soon as all aforementioned procedures were completed, the reaction was initiated by switching the relevant valves to initiate the reaction. For these procedures, safety was of paramount importance and the relevant safety protocols were followed (e.g. the use of face shields, thermal gloves etc.).

Fixed bed reactor setup

In Chapter 9 the results obtained with the use of a fixed bed reactor (which is depicted in Figure 4.7 - (*Bottom*)) are reported. The reactor consists of a 1/4" stainless steel U-tube with an internal diameter of 3.8 mm embedded in an aluminium casing. The heating elements are situated directly next to the catalyst bed with the thermocouple placed at the center of the

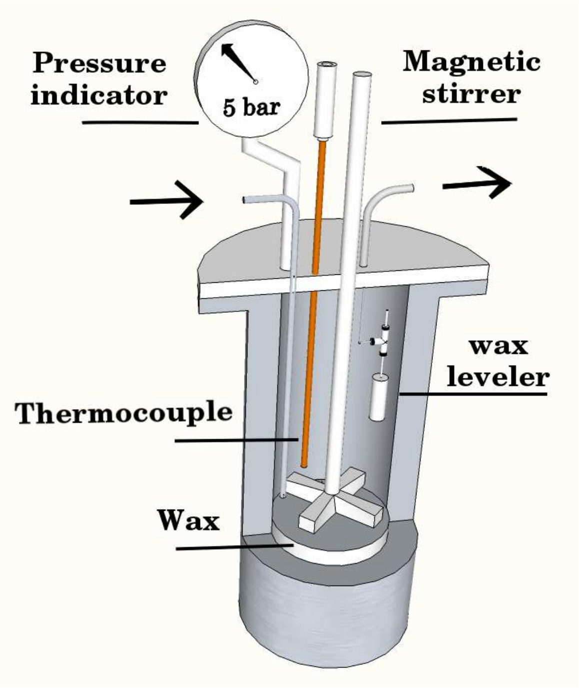

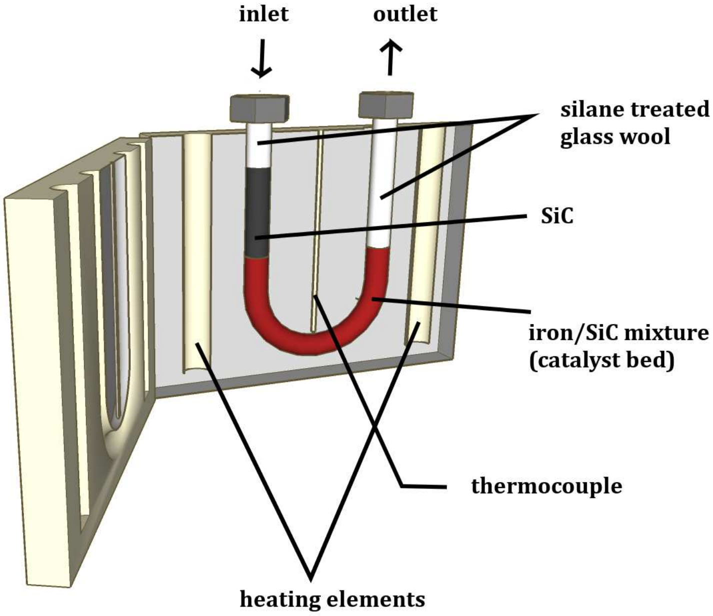

Figure 4.7: Schematic showing important components of the (*Top*) slurry phase reactor and the (*Bottom*) "u-tube" fixed bed reactor used in the results Chapters 7, 8 and 9

casing for accurate temperature control. The amount of catalyst that could be loaded to the reactor was limited (approximately 0.75 g of catalyst could be loaded). To avoid a pressure drop over the catalyst bed and in order to minimise exotherms due to the reaction heat, the iron-based catalysts had to be diluted (0.75 g_{cat}/g_{SiC}) with silicon carbide with a mesh size of 200 - 250 μm. An additional amount of SiC (ca. 3 cm^3) was added to the inlet to act as a pre-heating zone for the gases entering the reactor. Both ends were tightly packed with silane treated glass wool to prevent the catalyst bed from shifting. Contrary to the experiments in the slurry reactor, the catalysts used in the fixed bed reactor were pretreated in the reactor itself and not externally.

Product analysis

The FTS product distribution contains information that may assist in "monitoring" events taking place on the surface and could contribute to the understanding of the pathway to product formation. An accurate description of the product spectrum is thus desired to compare the performance of the catalysts, to evaluate the effects that stem from certain gases in this study (NH_3) and to probe the kinetics of certain reactions. The efforts to identify and quantify the inorganic and organic compounds of interest are described below.

Analysis of inorganic products

The inorganic gases (H_2, CO, CO_2, CH_4 and NH_3) in the feed and the exit of the reactor as well as the internal standard (N_2), were monitored via an on-line gas chromatograph equipped with thermal conductivity detectors (GC-TCD).

The final results reported in this thesis makes use of a "modern" micro gas chromatograph (micro-GC, Varion, CP-4900). One of the major advantages of this instrument is its fast sampling time. A sampling frequency of 5-7 minutes could be achieved, whereas the analysis on an older gas chromatograph (HP 5810) required approximately 20 - 30 minutes for the same separation (see Figure C.5 in Appendix C). This was particularly useful during the initial stages of the FTS reactions with or without the addition of NH_3 where temporal changes of the catalyst performance were monitored. This improvement in signal-to-noise ratio is a result of splitting the sample into three channels operating at separate, specified conditions (see Table

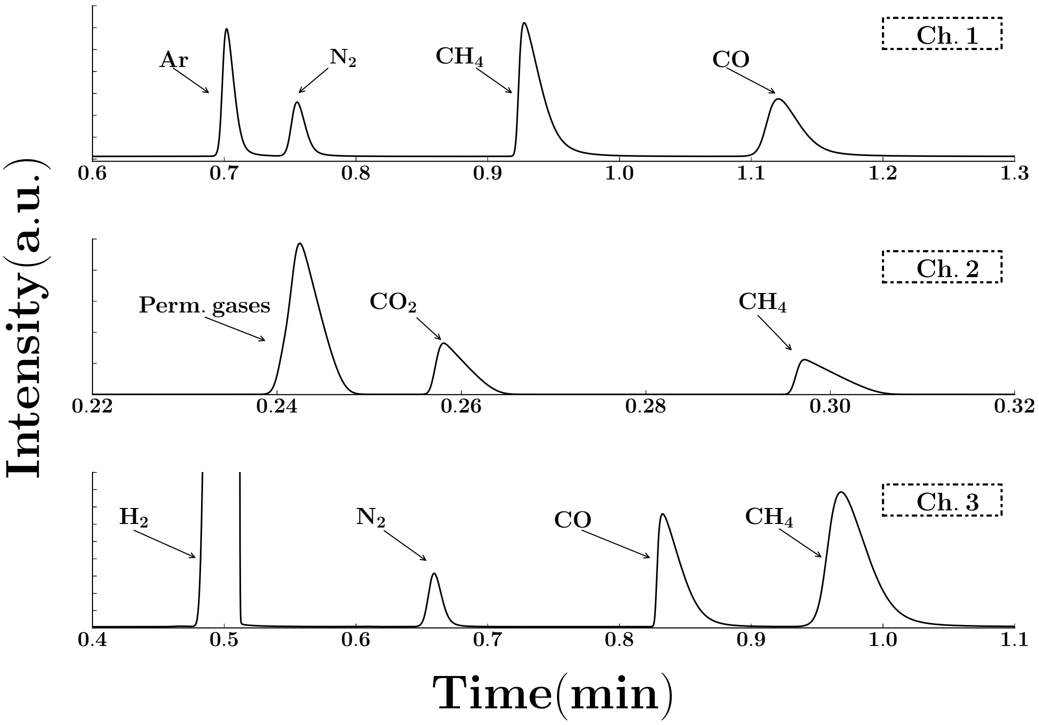

Figure 4.8: An example of an analysis (of the calibration gas) when using the on-line micro-GC (Varion, CP-4900).

4.1 for details). All data processing and instrumental control was handled with the Galaxie chromatography software.

For quantification purposes, the gas chromatograph was calibrated using gases with known concentrations (e.g. 6 % Ar, 5 % N_2, 15 % CO, 10 % CH_4, 20 % CO_2, 44 % H_2; Afrox RSA). For the calibration of NH_3, a combination of a gas containing 10.1 vol% NH_3 in H_2 and a gas containing the internal standard N_2 were used. A typical set of (three) chromatograms obtained after analysing the calibration gas with the (three channels of the) micro-GC is presented in Fig.4.8. These calibrations were periodically (every 2-3 months) performed to determine the calibration factors (cf_i) to use for quantification with the TCD. The calibration factors relative to N_2, which was used as an internal standard, were obtained via the use of Eq. 4.17:

$$\frac{A_i}{A_{N_2}} = cf_i \frac{\dot{n}_i}{\dot{n}_{N_2}} \tag{4.17}$$

where A_i is the area under the peak, $\dot{n}_i$ is the flow rate of compound i, $\dot{n}_{N_2}$ is the flow rate of the internal standard N_2 (which is known), and cf_i is the calibration factor for the respective gases (i = H_2, CO, CO_2, CH_4 and NH_3).

The conversion of the reactants (CO and H_2) was determined by applying Eq. 4.18

$$X_i = \frac{\dot{n}_{i,in} - \dot{n}_{i,out}}{\dot{n}_{i,in}} \tag{4.18}$$

where $\dot{n}_{i,in}$ is the flow rate of compound i measured before initiating reaction, $\dot{n}_{i,out}$ flow rate of compound i measured during reaction.

The yields of the products were calculated on a molar (Y_i) or carbon ($Y_{i,C}$) basis using Eq.'s 4.19 and 4.20

$$Y_i = \frac{\dot{n}_i}{\dot{n}_{CO,in}} \tag{4.19}$$

$$Y_{i,C} = \frac{\dot{n}_{i,C}}{\dot{n}_{CO,in}} \tag{4.20}$$

where:

$\dot{n}_i$	is the molar flow rate
$\dot{n}_{i,c}$	is the flow rate on a carbon basis
$\dot{n}_{CO,in}$	is the molar flow rate of CO into the reactor

Then, by using the CO conversion (X_{CO}) and the yield of compound i, the selectivity (S_i) for compound i can be calculated using Eq. 4.21.

$$S_i = \frac{Y_i}{X_{CO}} \tag{4.21}$$

The analysis of NH_3, as mentioned before, presents challenges when separation from all other permanent gases is required. NH_3 gas has the tendency to adhere to the walls of the gas lines. This particular problem does not pose a significant problem in this work, since the constant feed of NH_3 would saturate the gas lines. Furthermore, the acidic surface species of conventional packing material has the tendency to interact with the NH_3, due to its polarity and basicity. This makes the separation without applying deconvolution techniques difficult. In Appendix C, the efforts for achieving complete separation of NH_3 and the other inorganic gases (H_2, CO, N_2, CO_2, CH_4) are summarized. NH_3 could be detected and quantified in the second channel

Table 4.1: All important settings used with the micro-GC (Varian, CP-4900). Each channel is described in detail to include information about its stationary phase, column head pressure, oven temperature, carrier gas and the gases that are detectable in that particular channel.

Gas chromatograph	**Varian, CP-4900 (micro-GC)**
Detectors	Thermal conductivity detectors
$T_{Detectors}$	110 ℃
Ref gas	N_2
Injection time	300 ms
Channel 1	
Stationary phase	20 m Molsieve 5
Column head pressure	150 kPa
Oven temperature	80 ℃
Carrier gas	H_2
Gases detected	N_2, CH_4, CO
Channel 2	
Stationary phase	10 m Porapak Q (PLOT)
Column head pressure	100 kPa
Oven temperature	60 ℃
Carrier gas	H_2
Gases detected	CH_4, CO_2, NH_3
Channel 3	
Stationary phase	10 m Molsieve 5
Column head pressure	150 kPa
Oven temperature	80 ℃
Carrier gas	Ar
Gases detected	H_2, N_2, CH_4, CO

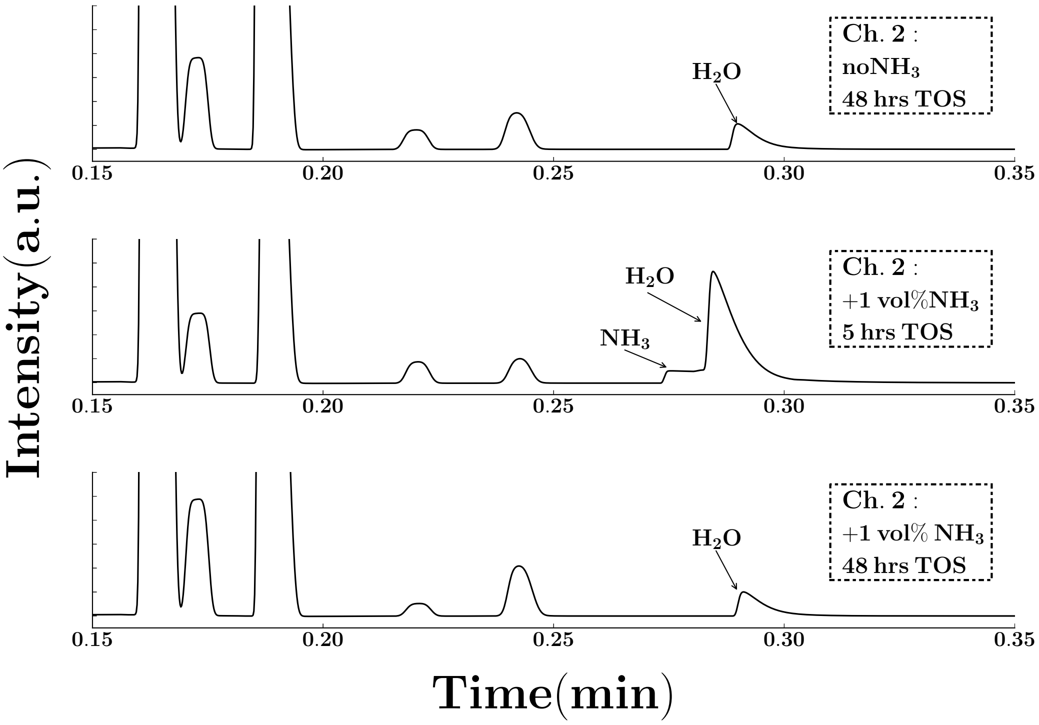

Figure 4.9: Chromatograms obtained via channel 2 using the micro-GC (Varion, CP-4900) for FTS reactions with or without NH_3 addition. During the initial stage NH_3 is present whereas at steady state no NH_3 can be detected.

using the micro-GC, but becomes convoluted with the H_2O produced during FTS (see Figure 4.9). Note that a different method was used (compared to the calibration chromatogram given in Figure 4.8) in order to achieve a maximum resolution for the separation between NH_3 and H_2O. In the top part of Figure 4.9, the chromatogram for the reaction where no NH_3 was added during FTS, shows the formation of H_2O, which elutes in a similar region as NH_3. This can be seen in the second chromatogram, where 1 vol% NH_3 is added during the initial stages (5 hours TOS) of the FTS reaction. At steady state, however, no NH_3 can be detected. This was due to the consumption of NH_3 via a side reaction to produce NH_4CO_3, which is discussed in more detail in Chapter 7. Therefore, for most of the reactions discussed in this work, it was not possible to provide quantitative data for the conversion of NH_3.

Analysis of organic products

The analysis of the organic compounds produced during FTS and the co-feeding experiments conducted in this work is of prime importance and benefits from an extensive analytical protocol. It was possible to analyze the organic compounds in the gas phase via a GC-FID (Varian, GC-430) that was connected on-line, downstream from the reactor and to subsequently compare those results with data obtained from off-line GC-FID (Varian, GC-430) analysis. The off-line GC-FID analysis was performed by analyzing ampoule samples taken via the ampoule sampling technique (as described in sections below). In addition, the liquid product that was collected from the cold trap (i.e. the oil and water phases) could be analyzed via similar off-line sampling using the aforementioned GC-FID. More importantly, these samples (oil and water phases) could be analyzed via comprehensive two-dimensional gas chromatography (LECO, Pegasus 4D). As intricate as the analytical system was, some difficulties were encountered throughout this study. In the following subsection the analytical techniques used is elaborated, and also include discussions on the challenges encountered when analyzing the organic FTS product spectrum, paying particular attention to the analysis of oxygenates and N-containing aliphatic hydrocarbons.

Condensation of organic compounds

In FTS operations, the phase of the organic product is an important parameter to consider. In Figure 4.10 (taken from reference [23]) the partial pressure as a function of carbon number is plotted for two chain growth probabilities ($\alpha = 0.6$ and 0.9) for normal paraffins in a FTS product. These variables were used to model potential fluid formation on catalyst particles in the Shell Middle Distillate Synthesis (SMDS). In their model, the constant β, is a function of temperature (e.g. here 280 ℃ corresponds to $\beta = 0.71$) and is related to the incremental energy of vaporization per segment of the carbon chain length. If $\beta < \alpha$, condensation is predicted. The total pressure, reaction temperature, chain growth probabilities and vapor pressures of hydrocarbons are some of the parameters that dictate if a product of certain chain length n would be in the oil or gas phase (or both) at a relevant sampling point. When considering the samples that were analyzed in this work, it can be predicted that a fraction of the product may be lost due to condensation for higher carbon numbers. The considerations taken with

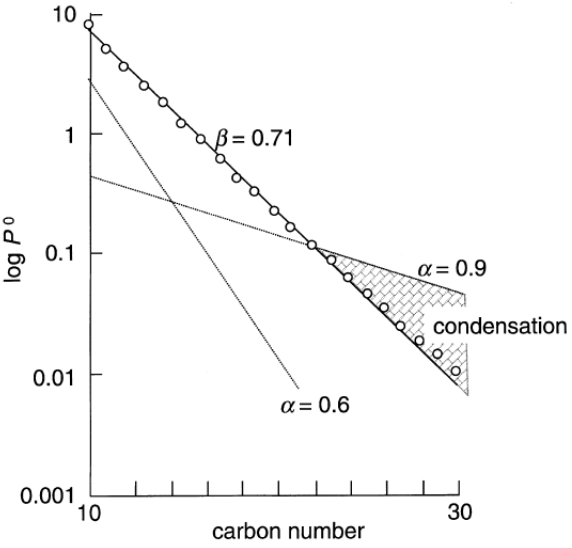

Figure 4.10: Condensation predicted at T = 280 ℃ for two chain growth probabilities (α = 0.6 and 0.9). Taken from Ref. [23].

this work with respect to condensation are discussed and highlighted throughout the following subsections.

Ampoule sampling technique

Introduction:

The ampoule sampling technique developed by Schulz [24] is an extremely powerful tool for the analysis of the organic compounds produced in the FTS. In particular when information for the initial stages of the FTS is required [24–26], rapid sampling using the ampoule technique can "store" these results to be analyzed at a later stage via off-line gas chromatography.

Ampoule sampling during FTS reactions:

Figure 4.11 shows a schematic of the device attached to the reactor system that was used for ampoule sampling. The products that exit the reactor which were not trapped in the first condensation vessel travel towards the ampoule sampling section, gas chromatographs and second condensation vessel. The procedure for ampoule sampling is as follows: the evacuated ampoule

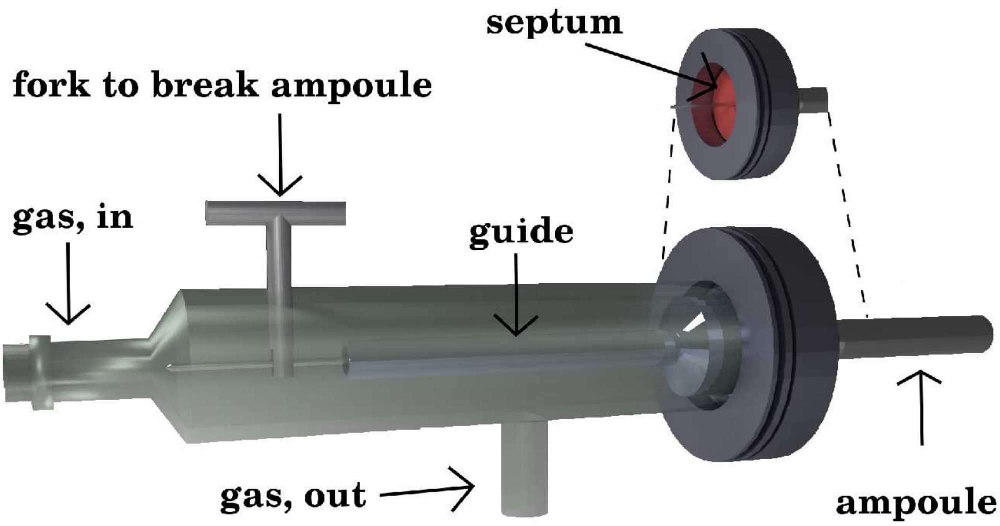

Figure 4.11: Schematic drawing of the ampoule sampling instrument attached downstream of the reactor that was used to sample the gas phase products.

is inserted into the ampoule sampling device (while the reactor pressure is maintained through the use of a septum), a fork is then used to break the ampoule and the gases are drawn into the ampoule cavity due to the vacuum. The ampoule is then sealed with a laboratory gas torch.

Ampoule delivery to GC-FID:

The glass ampoule containing the sample is subsequently placed in an ampoule breaking device (see Figure C.1 in Appendix C for a detailed sketch). The breaker itself was heated (220 ℃) to avoid any condensation before sampling. A schematic of the ampoule delivery system used to inject the contents of the ampoule into the gas chromatograph for the analysis of the organic compounds is presented in Figure 4.12. When the ampoule system was in use, a constant flow of the carrier gas (H_2) and an inert gas (N_2) were maintained for purging purposes. As soon as the gas-chromatograph (GC-FID) reached a steady state with regards to temperature and head pressure, a signal was sent to the pneumatically controlled plunger that subsequently crushed the ampoule and allowed for the organic compounds to be introduced via a six-port valve.

A very specific problem encountered with the ampoule sampling device during this work was

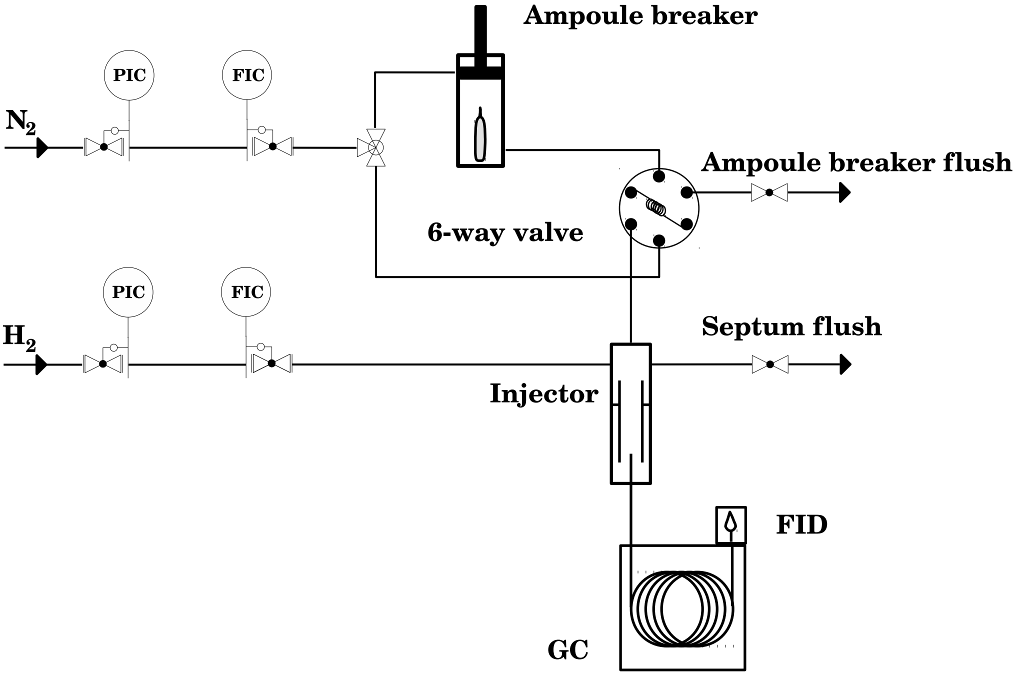

Figure 4.12: A simplified flow diagram for the ampoule breaking device that illustrates the introduction of the samples to the GC-FID.

its ability to analyze certain oxygen- and nitrogen-containing compounds. When analyzing aliphatic acids, only a fraction (ca. 10 wt%) of the products could be observed via ampoule sampling (i.e. off-line GC-FID analysis), compared to on-line GC-FID analysis. A similar observation was made when analyzing the products obtained when NH_3 was co-fed during FTS, in particular for the aliphatic amines. Almost none of the primary amines could be observed using the ampoule technique, while the on-line GC-FID analysis clearly allowed for the detection and quantification of this class of organic compounds. Sango [19, 27] was able to detect primary amines, but only from liquid samples and at higher concentrations of NH_3 ($\geq$ 2 vol % NH_3). The loss of these product classes (acids and amines) during off-line analysis is believed to be due to their adsorption in the ampoule breaking system and may be mitigated by the use of on-line analysis.

On-line GC-FID

Similar chromatographic equipment (e.g. Varian, GC-430 with a Varian capillary column CPSil 5CB) was used for both on- and off-line analysis. The details for the gas chromatograph used for the on-line and off-line gas chromatography of the organic compounds are presented in Table 4.2. All data processing and instrumental control was handled with the Galaxie chromatography software (Agilent). All variables (e.g. column head pressure, injector and detector temperatures etc.) were synchronized for both on- and off-line analysis in order to facilitate a comparative analysis, with the exceptions of the split ratios and initial heating/cooling of the GC ovens that depended on the sample being analyzed or the system used. For example, to achieve an ideal separation of the primary amines in the on-line GC-FID, either -30 or 30 ℃ was desired as an initial temperature. With the use of the ampoule delivery system, -50 ℃ was found to be sufficient initial temperature for the GC oven for ideal separation of the FT product spectrum. The injectors of the off-line and on-line GC-FIDs were set to a split ratio of 50:1, 100:1 respectively and both had a sample loop of 250 μl. When an oil or water based sample was analyzed, a 1 μl syringe was used and the split for the injector was set to a ratio of 500:1. An additional similarity shared by the on- and off-line GC-FIDs is the use of a 6-port (VICI) valve, which was used to inject the samples. In Figure 4.13 a schematic is given that shows the 6-port valve in its loading (A) and injecting (B) positions. When configured in the loading position

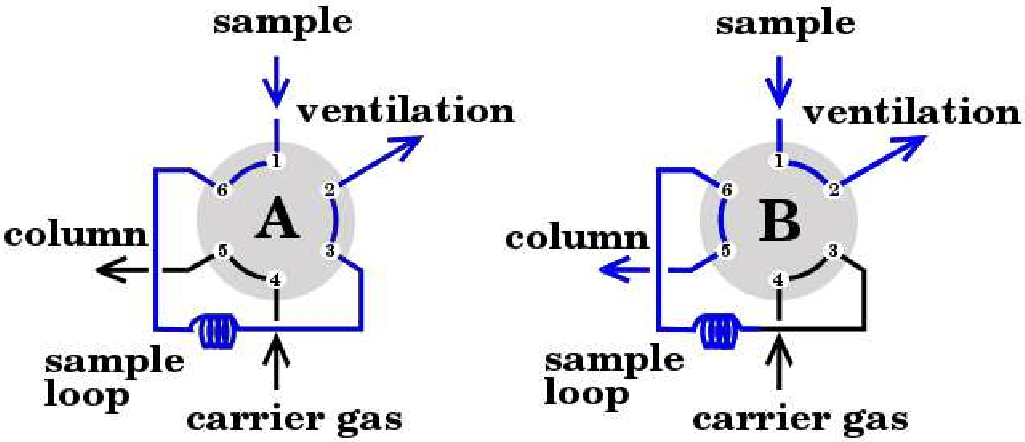

Figure 4.13: A schematic of the technique used to sample the gas phase via an ampoule.

(A), the carrier gas is constantly flowing through the column and thus purges the system. This configuration (A) in addition allows for a constant flow of the sample through the sample loop. The content of the sample loop is then introduced onto the capillary collumn as soon as the valve is switched to the injecting position (B). During the time period (45 seconds) that the sample is in the injection position, the sample line (that is, for example the downstream flow from the reactor) flows toward the ventilation unit.

Identification of organic compounds in FTS product spectrum

Identification of the products detected via GC-FID analysis was achieved via a combination of using Kovats indices [28], comparison with analyses from previous studies [20, 26] as well as GC-TOF analysis (Pegasus 4D in 1D-mode). For certain compounds of interest, pure standards (e.g. 99 % acetic acid, Sigma) were analyzed to estimate the retention times of these compounds. Kovats indices (see equation 4.22) provide a way of normalizing the retention times and allow for a system-independent identification of the products that elute between the linear alkanes with carbon numbers n and $n+1$.

$$KI_X = 100 \cdot [n + \frac{log(RT_X) - log(RT_n)}{log(RT_{n+1}) - log(RT_n)}] \tag{4.22}$$

Table 4.2: The general method used for on- and off-line GC-FID analysis.

Gas chromatograph	**Varian, GC-430 (on- and off-line)**
Injector	split/splitless
	split ratio - 50:1 (system/sample dependent)
	T_{inj} = 225 ^{o}C
Detector	flame ionisation detector (FID)
	T_{det} = 250 ^{o}C
Column head pressure	10 psi (isobaric)
Stat phase	Varian Capillary Column CPSil 5CB (25 m; 0.15 mm; 2 μm)
Cryogenic cooling	liquid CO_2
Temp program	T_1 = -30 ^{o}C (isothermal for 1 min, system/sample dependent)
	T_1 = -30 ^{o}C → T_2 = 150 ^{o}C (ramped @ 7 ^{o}C/min)
	T_2 = 150 ^{o}C → T_3 = 280 ^{o}C (ramped @ 10 ^{o}C/min)
	T_3 = 280 ^{o}C (isothermal for 15 min)

where KI_X is the Kovats index of a compound X, RT_X is the retention time of the unknown peak and RT_{n+1} and RT_n are the retention times of the linear alkanes with carbon numbers n and $n+1$.

In addition to the Kovats indices, the GG×GC instrument (Pegasus 4D, LECO) was operated in 1D-mode when possible. In order to obtain similar separation to the on- and off-line GC-FID analysis, the polar column in the first dimension of the GC×GC-TOF/FID was exchanged for the capillary column used in the GC-FID. When operating in 1D-mode, no modulation or data manipulation was applied. The short (1.8 m) apolar secondary column had a negligible effect on the separation of the analytes. A chromatogram obtained during this analysis can be found in Appendix C (see Figure C.6).

Quantification of the results from the various chromatograms is discussed in more detail in the following section. As anticipated, product identification in general was substantially improved via the use of comprehensive two-dimensional chromatography, which is discussed in Section 4.3.

Quantifying organic compounds via flame ionization detection (FID)

The flame ionization detector (FID) is one of the most widely used detectors for quantifying the organic products of the Fischer-Tropsch synthesis, when analyzed via gas chromatography. It benefits from high sensitivity, a broad linear range and uniform response to hydrocarbons [29]. These advantages can easily be understood by evaluating the mechanism of the FID. A full description of the mechanism falls outside the scope of this project; the interested reader is directed to an insightful review given by Holm [30]. The important features of the FID that has relevance to the quantifying procedures used throughout this thesis will briefly be discussed.

Several aspects of the mechanism are not yet fully understood, but the most important aspects can be related to chemical processes taking place in the flame. Degradation is assumed to take place in a pre-combustion zone, leading to the formation C_1 units.[1] Via experimental evaluations [31] of the reactions occurring inside the flame, it was concluded that the chemi-ionization of the $CHO\cdot$ radical would produce the CHO^+ ion (see Equation 4.23).

---

[1] Statement is simplified for brevity, see [30].

$$CH + O \rightarrow CHO\cdot \rightarrow CHO^{+} + e^{-} \tag{4.23}$$

These ions are accelerated towards an anode, while the flame acts as the cathode, and is subsequently subjected to an ion counter.

Holm [30] describes the FID as a ”carbon counting device”, since the FID response is generally proportional to the mass of carbon present in the sample [29]. The predictability of FID response for these hydrocarbons is essential when quantifying the organic compounds in the FTS product spectrum, as it is practically impossible to calibrate such a complex matrix of molecules. It is known that compounds that have carbon atoms bonded to heteroatoms (e.g. N, O, S, Cl) significantly reduce the FID response for the analyte [29, 30, 32–34]. These deviations are however also predictable (to a certain extent), based on the functional group present in the organic molecule. It has become a custom, when quantifying oxygenates produced during FTS, to make of the methodology proposed by Kaiser [33]. In this incrementation method the contributions of carbon atoms with a single bond to an oxygen atom, and a carboxyl carbon are “corrected” by multiplying with constants lower than unity (0.55 and 0.00 respectively) in the denominator as opposed to 1.00 for all other carbon atoms (see Figure 4.14). The response factor is then calculated with the use of Eq. 4.24

$$f_i = \frac{N_{c,i}}{1.00 * N_{c,C-C} + 0.55 * N_{c,C-O} + 0.00 * N_{c,C=O}} \tag{4.24}$$

where $N_{c,i}$ is the number of carbon atoms in molecule i, $N_{c,C-C}$ is the number of carbon atoms with carbon-carbon bonds (including double bonds), $N_{c,C-O}$ is the number of carbon atoms with one oxygen bond and $N_{c,C=O}$ is the number of carboxyl carbon atoms.

An alternative technique for predicting the FID response of compounds containing carbon atoms bonded to heteroatoms is via the effective carbon number (ECN) technique [34]. These values are obtained by evaluating the response of the FID for ranges of hydrocarbons based on a reference compound. Kallai et al. [34] reviewed a homologous series of various groups of hydrocarbons that included linear alkanes, primary amines and terminal alcohols. Selected results from this study is presented in Table 4.3. A crude assumption based on these results (presented in Ref. [34]) is that the oxygen and nitrogen atoms have a similar effect on the response factors (f_i) for N- or O-containing hydrocarbons. In this work it is assumed that the response factors for

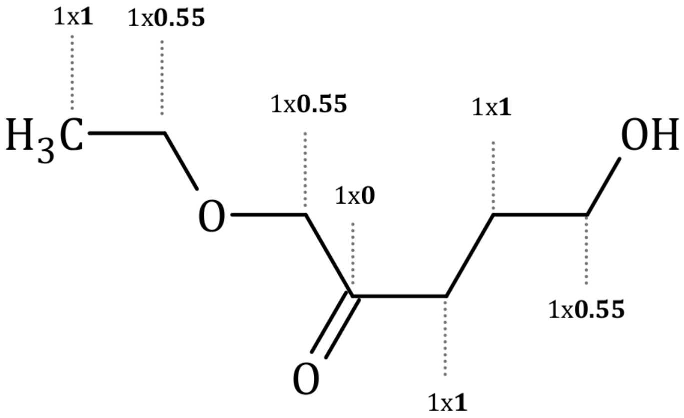

1-ethoxy-5-hydroxypentan-2-one

Figure 4.14: An example of Kaiser's model [33] to account for the loss of intensity due to C-O and C=O bonds. (Please note that 1-ethoxy-5-hydroxypentan-2-one is not likely to form during FTS, and is only used for illustration purposes.)

Table 4.3: The effective carbon numbers (ECN) given reported by Kallai et al. [34]

Name	CN	ECN
n-octane	8	7.83
n-nonane	9	8.95
n-decane	10	10.05
n-tridecane	13	13.08
n-hexadecane	16	15.28
n-heptadecane	17	16.40
1-butanol	4	3.24
1-pentanol	5	4.56
1-hexanol	6	5.41
1-heptanol	7	6.15
1-octanol	8	7.25
1-decanol	10	9.03
1-dodecanol	12	10.18
1-tetradecanol	14	11.8
n-butylamine	4	3.20
n-pentylamine	5	4.31
n-hexylamine	6	5.36
n-heptylamine	7	6.11
n-octylamine	8	7.04
n-decylamine	10	8.40
n-dodecylamine	12	10.11
n-tetradecylamine	14	12.88

N-containing compounds produced during the FTS experiments can be calculated via Kaisers methodology [33] by treating the N atoms in a similar way as the O atoms in Eq. 4.22. A list of calculated response factors for various compounds produced during the experiments is presented in Figure C.4 in Appendix C.

A reference gas containing 0.015 vol % cyclohexane (C_6H_{12}) in nitrogen, which does not form during FTS, was added at the exit of the reactor as a reference gas. The flow rates are then calculated on a molar and carbon weight bases using equations 4.25 and 4.26 respectively

$$\dot{n}_i = \left(\frac{N_{c,C_6H_{12}}}{N_{c,i}}\right) \times \left(\frac{f_i \times A_i}{A_{C_6H_{12}}}\right) \times \dot{n}_{C_6H_{12}} \tag{4.25}$$

$$\dot{n}_{i,c} = N_{c,C_6H_{12}} \times \left(\frac{f_i \times A_i}{A_{C_6H_{12}}}\right) \times \dot{n}_{C_6H_{12}} \tag{4.26}$$

$\dot{n}_i$	molar flow rate
$\dot{n}_{i,c}$	flow rate on a carbon basis
$N_{c,C_6H_{12}}$	number of carbon atoms in reference gas
$N_{c,i}$	number of carbon atoms in compound i
f_i	response factor of compound i
A_i	area under peak for compound $_i$
$A_{C_6H_{12}}$	area under peak for reference gas
$\dot{n}_{C_6H_{12}}$	molar flow rate of the reference gas

Combining of gas and oil samples

The products which were in the gas phase at sampling conditions were quantified via the use of a reference gas (cyclohexane, C_6H_{12}) added to the product stream, as mentioned above. The products collected in the oil phase in the “cold trap” do not contain the full fraction of the cyclohexane that was added as reference gas due to partial condensation at room temperature. To allow for the quantification of the oil phase products, the ASF product distribution of the FTS products is utilized. Initially, the “flow rate” ($\dot{n}_i$, $\dot{n}_{i,c}$) on a molar or carbon basis for the oil phase products is estimated by employing an arbitrary constant T_f in Eq. 4.27 and 4.28

$$\dot{n}_i = \frac{T_f \times f_i \times A_i}{N_{c,i}} \tag{4.27}$$

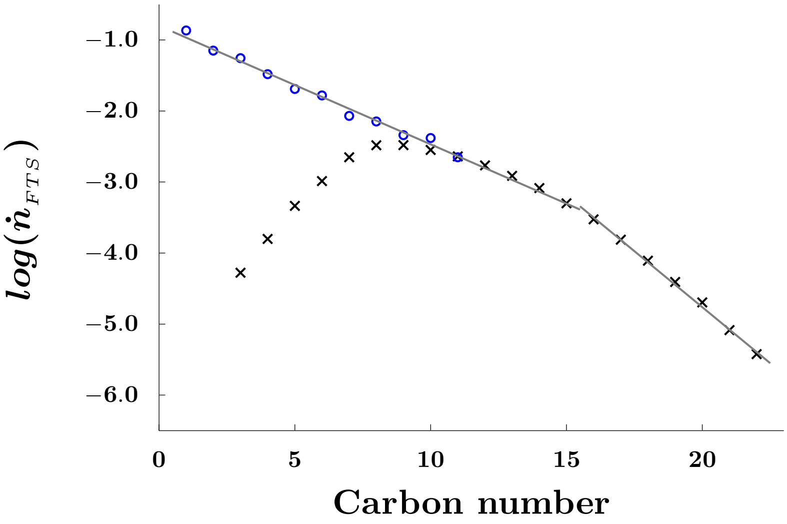

Figure 4.15: A linear regression technique was used to combine the oil and gas phase products (this example is taken from a slurry phase FT experiment where no NH_3 was added (SPR^1, T = 250 ℃, P = 5 bar, GHSV = 2250 ml/hr/g_{cat}, $H_2/CO = 2$), as discussed in Chapter 7)

$$\dot{n}_{i,c} = T_f \times f_i \times A_i \tag{4.28}$$

where T_f is a tying factor, f_i is the FID response factor, A_i is the area under the peak and $N_{c,i}$ is the number of carbon atoms for compound i. By varying the value for T_f, a point is reached where the chain growth probability (α) of the FTS products as a function of carbon number of the gas and oil sample (analyzed by on/off-line GC-FID or GC×GC-FID respectively) have the same value. A plot of the logarithm for the total flow rate of FTS product (where no NH_3 is added) samples (oil and gas) as a function of carbon number is shown in Figure 4.15. Here it can be seen that the chain growth probabilities (α) for the hydrocarbons corresponds throughout the C_{10-16} carbon number range for the oil (C_{1-11}) and gas phase (C_{3-23}) samples.

The flow rates can thus be adjusted (by setting T_f) to allow for the flow rate of the C_{10} products of the gas products to be equal to the flow rate of the C_{10} oil products. In other words, a C_{10} product (e.g. *n*-decane) can serve as a tying compound between the two samples. Beyond C_{17+} the log($\dot{n}_{FTS}$) values start to decline. This is due to the temperature (180 ℃) in the first condensation vessel that allows condensation of these higher carbon number products. The condensation at that carbon number range does not pose any problems for the work discussed

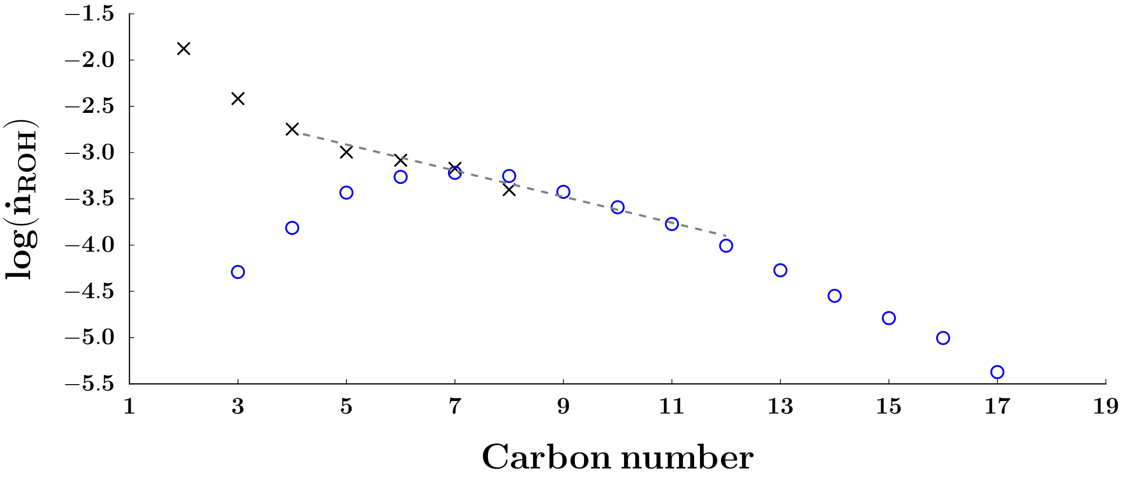

Figure 4.16: The semi-logarithmic plot of the flow rate ($\dot{n}_i$) as a function of carbon number (n) for the linear alcohols suggests that C_{7-8} oxygen containing compounds are fully immersed in oil phase (Oil and gas samples taken from reaction SPR^1, T = 250 ^{o}C, p_T = 5 bar, GHSV = 2250 ml/hr/g_{cat}, H_2/CO = 2)

in this thesis, as the full spectrum can be obtained by extrapolating the ASF distribution, and the O- and N-containing compounds of interest can reliably be quantified in the desired carbon number range (C_{1-16}).

It should however be noted that even though it seems from the analysis described above that only the C_{10+}-fractions are fully represented in the oil phase, O- and N-containing compounds are fully immersed in the oil phase at lower carbon number ranges. This is due to their low vapour pressures compared to the alkanes and alkenes as a function of carbon number (see Section C.1.5.1 in Appendix C for a detailed discussion). For example, if the same methodology (using Eq. 4.28) is used to plot a semi-logarithmic plot for the flow rate of the linear alcohols as a function of carbon number, for the oil and gas phase samples, equivalent chain growth probabilities are observed at a lower carbon number range (c.a. C_{8+}) compared to the full FTS product (see Figure 4.16). It can therefore be assumed that the full fraction of C_{8+} for linear alcohols (and other O- and N-containing compounds) is present in the oil phase, which is an important requirement for the results presented in Chapter 8.

Table 4.4: Summary of the analytical techniques used for the analyses (quantification and identification) of the organic FTS product spectrum obtained from various sources (e.g. ampoule or on-line sampling). *GC-TOF and GC×GC-TOF could be used to aid identification for organic products in ampoule samples.

CN	Source	Product	Quantification	Identification
C_{1-10}	ampoule, on-line	*n*-alkanes/alkenes	GC-FID	Kovats indices
C_{1-7}	ampoule, on-line	N/O-containing HC's	GC-FID	(GC-TOF and GC×GC-TOF*)
C_{11-20}	oil sample	*n*-alkanes/alkenes	GC×GC-FID	GC×GC-TOF
C_{8-17}	oil sample	N/O-containing HC's	GC×GC-FID	GC×GC-TOF
C_{1-7}	water sample	N/O-containing HC's	GC×GC-FID	GC×GC-TOF

Summary: Organic compound analyses

In summary, organic compounds that formed as products during the FTS reactions discussed in Chapters 7, 8 and 9 were analyzed from samples taken via on-line-, ampoule- or liquid- (oil and water phase) sampling. The analytical tools used to separate, identify and quantify the products obtained from these samples are tabulated in Table 4.4. C_{10} hydrocarbons could be used to tie the gas and oil phase samples. Due to the lower vapor pressures of the hydrocarbons containing hetero-atoms (O and N) compared to the other hydrocarbons, GC×GC analyses of the oil phase could be used to quantify these compounds from C_8 and higher carbon numbers.

Kaiser's method [33] was used to calculate response factors for the hydrocarbons in the FTS product spectrum. The assumption was made that N- and O-containing compounds have a similar effect on the FID response based on the effective carbon numbers (ECN) reported by Kallai et al. [34]. Comprehensive two-dimensional gas chromatography (GC×GC-FID/TOF) is mentioned throughout this section as it was an important tool for identification and quantification of the hydrocarbons, and due to the novelty of the technique it is discussed in more elaborate detail (with respect to literature, mechanism and instrumentation) in the following section.

Comprehensive two-dimensional gas chromatography

Introduction

The advent of comprehensive two-dimensional gas chromatography (ca. 20 years ago) has substantially improved the potential to separate, identify and quantify compounds found in complex samples (e.g. food, drugs, petrochemicals and contaminated water) [35]. In all reports of the analyses of complex Fischer-Tropsch synthesis or petrochemical products, mention is made of the major improvement of comprehensive GC×GC techniques over classic 1D-GC techniques [36–41]. Van der Westhuizen et al. [38] were able to separate dienes formed during HTFT from the rest of the FTS product spectrum. These compounds are believed to undergo Diels-Alder polymerization, which is partially responsible for gum formation in HTFT derived fuels. In one of the few cases where the GC×GC technique was insufficient, a liquid chromatography (LC) pre-fractionation procedure was used to separate saturated from unsaturated compounds [39]. This extensive procedure in turn provided them with confirmation of the presence of cyclics, that were likely formed via secondary reactions of HTFT oligomerization products.

The complexity of the product spectra from cobalt-based FTS can mostly be overcome by employing a "longer" column (e.g. 150 m) with a thin film (e.g. 0.01 μm) and applying a slow temperature program. An example of such an analysis is given in Figure 4.17 (Data taken from [17]).

The product spectrum originating from Fe-based FTS however is significantly complex. By employing a similar analytical technique when analyzing products obtained during this project (Fe-based FTS), a very poor separation is achieved (see Figure 4.18 *Top*). In particular, when considering the compounds of interest, the oxygenates, these compounds are often present in small quantities and co-elute with the branched paraffins and olefins (see Figure 4.18 (*Bottom*)). Grobler et al. [37] compared one dimensional GC-FID over comprehensive GC×GC-FID analyses when investigating the selectivity of Fe-based LTFT products (CSTR, T = 225 ℃, P = 27 bar, $H_2/CO = 1.5$, SV = 4800 ml/g_{cat}/h). They were able to identify and quantify the linear acids, ketones, aldehydes, secondary alcohols as well as branched - paraffins, olefins, alcohols and acids. The improved and accurate quantitative data obtained via comprehensive GC×GC analysis automatically improves the construction of ASF selectivity models that correlate FT

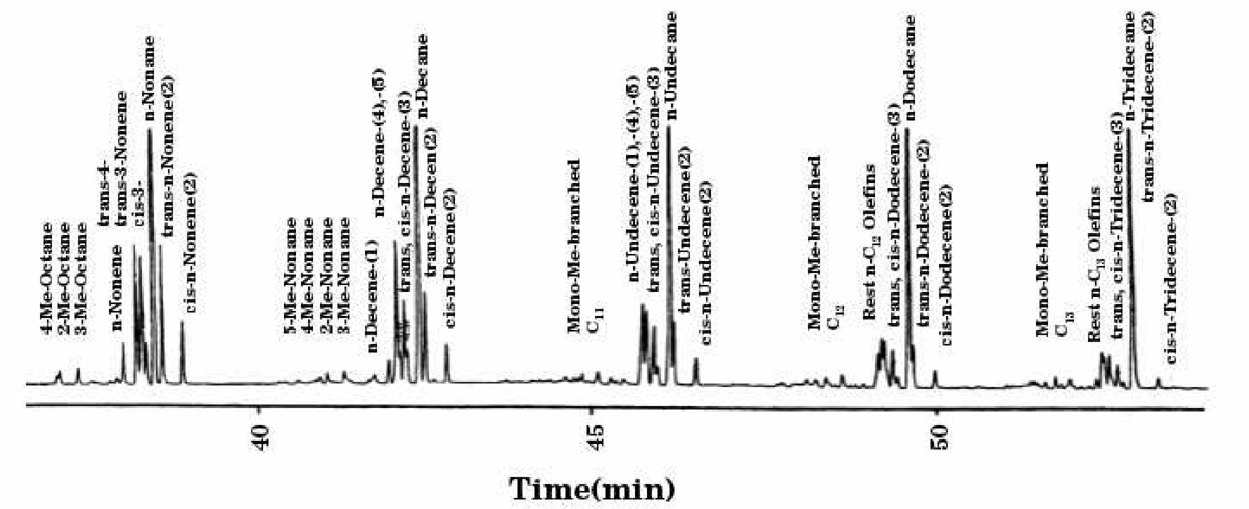

Figure 4.17: Example of a chromatogram obtained from the analysis (GC-FID) of an FT product (C_{9-13}) conducted on a Co-based catalyst. (Chromatogram taken from the PhD thesis of Claeys [17].)

product distributions with reaction variables [40].

The addition of ammonia during FTS in a slurry phase reactor as to be reported in this thesis, leads to the formation of N-containing compounds, which also need to be identified and quantified, a task virtually impossible with conventional gas chromatography. Wang et al. [41] made use of a GC×GC-NCD technique and showed that they could quantify N-containing compounds that were present in very low concentrations (10 wppm) in Diesel fuel. This was in part due to the application of a nitrogen chemiluminescence detector (NPD), but they ascribe their success in separation and quantification of this complex matrix due to the increased separation and sensitivity afforded by comprehensive two-dimensional gas chromatography (GC×GC).

Two-dimensional gas chromatography was pivotal for the work conducted here (see Chapters 7 and 8). The mechanism of the GC×GC analyses will be further discussed in the following section. Furthermore, the specific instrumentation used for the experimental part of this work will be introduced.

GCxGC-FID/TOF: Mechanism and instrumentation

A brief discussion of the important aspects of comprehensive two-dimensional gas chromatography (GC×GC) will be presented in conjunction with a description of the system that was used

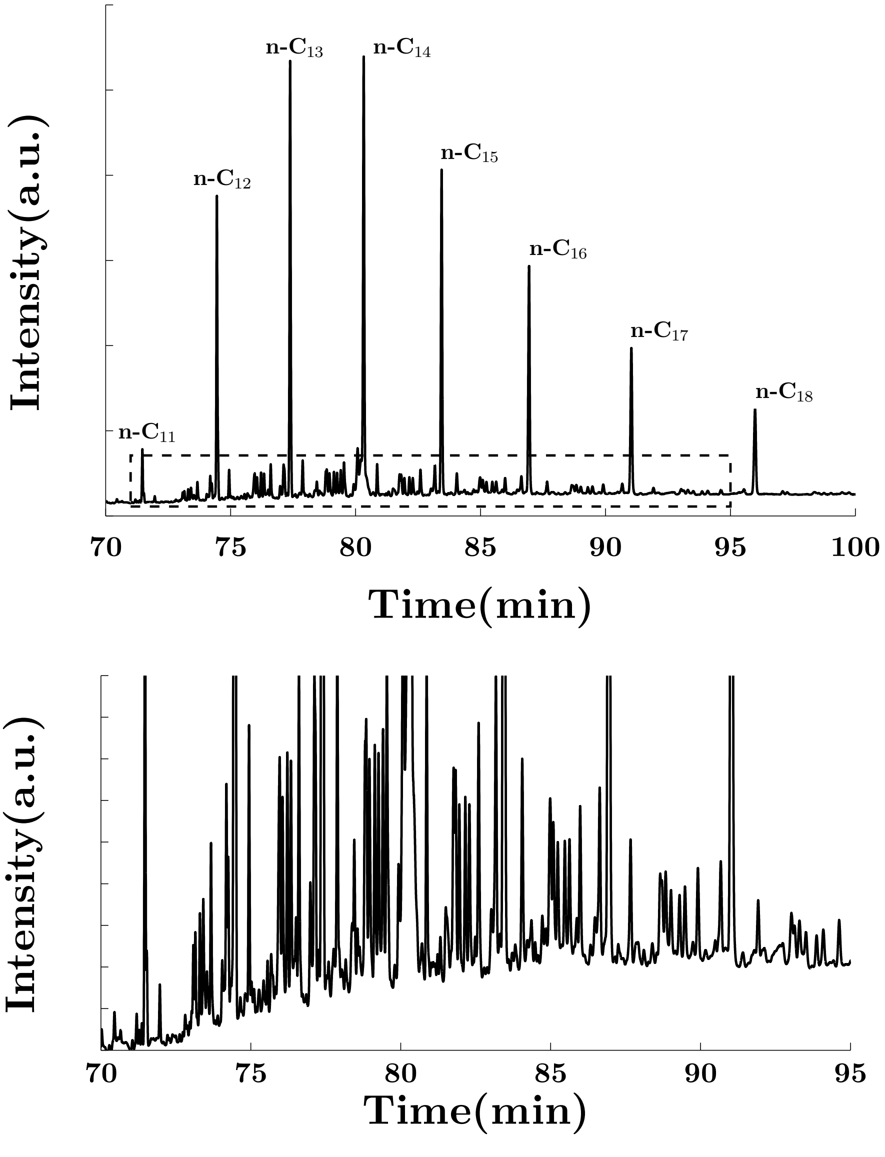

Figure 4.18: (*Top:*) An example of a chromatogram obtained during the analysis (GC-FID) of an oil drained during FTS conducted on an Fe-based catalyst. (Oil taken from reaction SPR^1, see Chapter 7) (*Bottom:*) The difference in selectivities increases with increasing carbon number. (SPR^1, T = 250 ℃, P = 5 bar, GHSV = 2250 ml/hr/g$_{cat}$, H_2/CO = 2)

(LECO, Pegasus 4D) in this study. For a more in-depth review of the mechanism, the interested reader is directed to the paper of Dallüge et al. [35].

A schematic (see Figure 4.19) is given to illustrate the important parts of the instrument used for the GC×GC-TOF/MS analyses. Two important aspects are required when performing two-dimensional gas chromatography. Firstly, the separation required between two dimensions has to be orthogonal, this is to say that the two modes of separation need to be fundamentally different. The two columns that were used in this work were a polar stationary phase (Varian, CP-WAX 52 CB, 30 m × 0.25 mm × 0.25 μm) for separation in the first dimension, while an apolar stationary phase was employed in the secondary phase (Varian, CP-Sil 8CB, 1.6 m × 0.10 mm × 0.10 μm). The second separation thus occurs over a much shorter time-span in comparison to the first, when considering the differences in column length and diameter (first - 30 m × 0.25 mm, second - 1.6 m × 0.10 mm). In fact the second dimension separation time was set between 3-8 seconds, while the first dimension separation was completed in ca. 60-80 minutes. The second important aspect when conducting GC×GC analyses is known as "modulation", which is a focusing technique that is used to control the injection of multiple fractions of the analyte that was separated on the first column onto the secondary column.

The modulator is thus used to retard the motion of fractions of the analyte for the duration of the secondary separation. In the system used throughout this work (LECO, Pegasus 4D), a double jet system is used, the mechanism of which is depicted in Figure 4.19 (*Bottom*). The schematic is divided into four stages, during which three separate fractions (B1-3) are involved. The first fraction B1 enters the modulator, and is "frozen" for the duration of the separation by passing a jet with 7 l/min flow rate of N_2 gas which has been cooled by liquid nitrogen over a small section of the primary column. Fraction B1 is then released by switching the air-flow to 7 l/min N_2 air that has been heated. At the same time a similar cooling procedure is followed by the second jet to "freeze" the second jet for a second period. Alternating the flow of the cold and hot streams then allows for the second fraction B2 to enter the cold stage and the simultaneous injection of B1 onto the secondary column. This modulation is thus repeated throughout the analysis to inject fractions B1 → BN onto the second column with this sophisticated focusing mechanism. The N_2 gas consumption used in these analyses is relatively high, which is why a N_2 generator were used in the setup reported in this thesis.

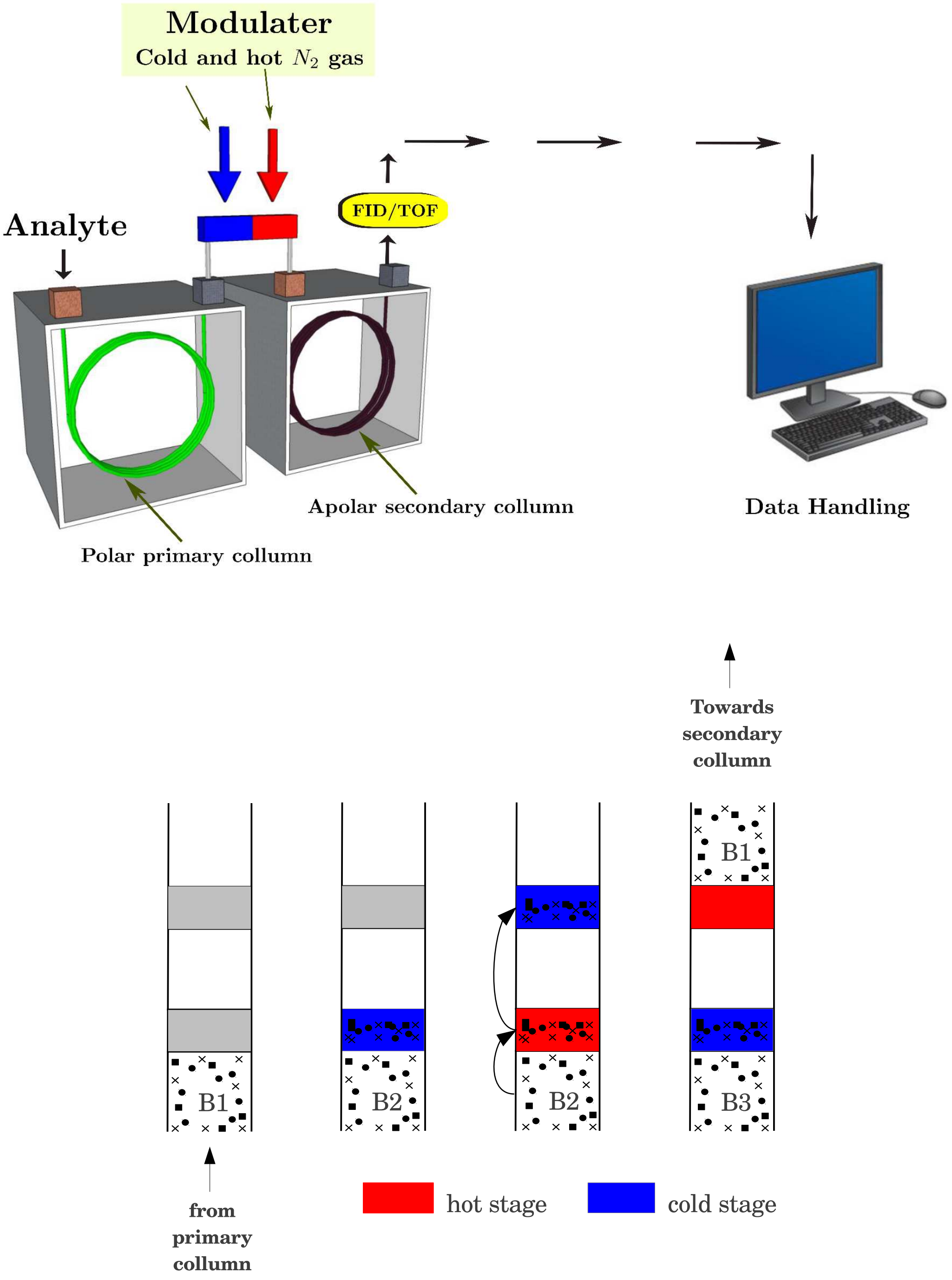

Figure 4.19: (*Top*) A general setup is schematically displayed to show the important components needed for two-dimensional chromatography. (*Bottom*) The mechanism of operation for the double stage modulator used in the LECO, Pegasus 4D is presented by this schematic.

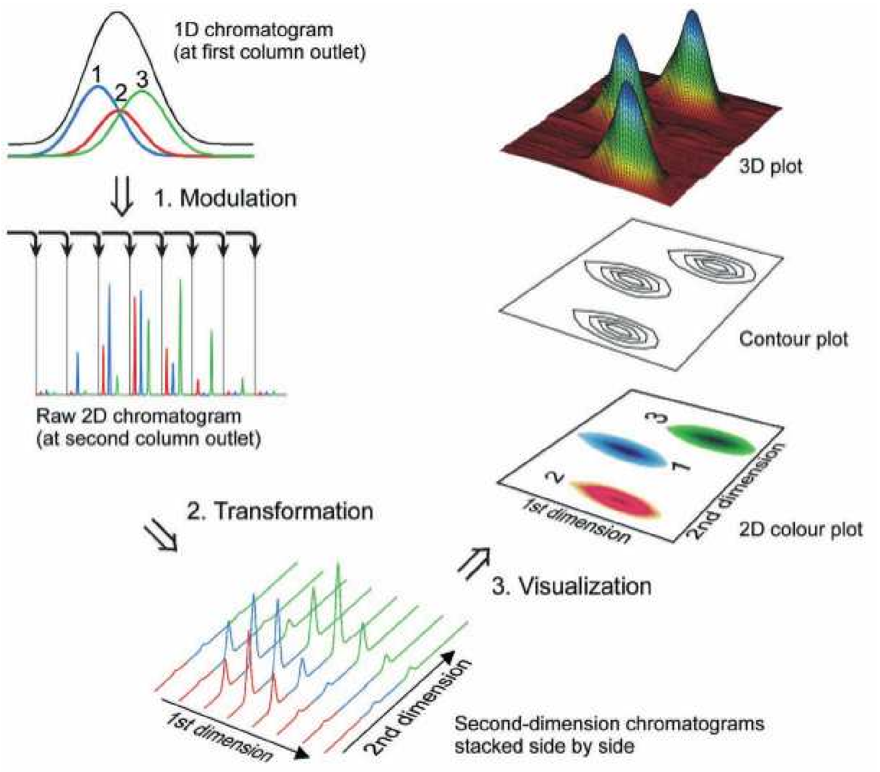

Figure 4.20: Process of constructing the visualization of the results obtained from two-dimensional gas chromatography. Taken from Reference [35]

The detectors (an FID and TOF detector in the system used in this work) thus collects the N 1-D chromatograms, which are stacked parallel to each other to eventually generate a topographic plot, if viewed from the top or a 3-D plot with the z-axis indicating intensity or M/Z ratios. For a schematic of how this is accomplished, a figure (see Figure 4.20) from reference [35] is given. The Pegasus 4D (LECO) system used in this work is equipped with both a time-of-flight (TOF) mass spectrometer and a flame ionization detector (FID). Both could however not be in use simultaneously. When the FID was in use, the TOF was shut off at the transfer line port, in order to maintain its low pressure. The use of an FID was discussed in detail in Section 4.2.3.7 and only the TOF detector will be discussed here. A TOF detector follows the same principle as all mass spectrometers, that is the compounds present in a sample is ionized (electron impact ionization used in this work) and in most cases de-fragmented. In the case of TOF detectors, the time that it takes for an accelerated ion to travel a known distance between the ionization and detection points is measured. With all parameters known (e.g. distance traveled, strength of the electric field), the only unknown variables (mass-to-charge ratios (M/Z)) are readily calculated via Newton's laws. The resulting mass-to-charge ratios (M/Z) are used to construct a mass spectrum that presents a unique fingerprint for the molecule. A unique feature of the TOF detector used in this work (Pegasus HT Mass Spectrometer, LECO), is that it can collect up to 500 spectra per second, which allows for deconvolution of the M/Z ratios of multiple compounds in a complex sample. To achieve a vacuum of ca. 1.0×10^{-8} Torr (1.3×10^{-11} bar) and thus minimize interference from gases present in the air, two (200 and 600 l/s) molecular turbo pumps (Varian) were used in conjunction with a 14.2 m^3/h mechanical pump (BOC Edwards). The transfer line that leads from the secondary oven to the TOF detector houses an additional 0.18 cm of the secondary column, which is not taken into account when specifying the secondary column length. The separation at that stage is negligible since the distance of the column is short and the temperature of the transfer line is kept constant at 350 ℃. All the final data analyses were performed with the use of ChromaTOF software (LECO). The gas chromatograph housing the two ovens was an Agilent 7890. The general parameters used for the GC×GC-TOF/FID analysis is presented in Table 4.5.

The result for a typical analysis of an oil phase sample obtained after Fe-based FTS (SPR^1, T = 250 ℃, P = 5 bar, GHSV = 2250 ml/hr/g$_{cat}$, $H_2/CO = 2$) can be seen in Figure 4.21. By virtue of conducting two-dimensional gas chromatography the various groups of FTS products are grouped in certain regions on the topographic plot, better known as classes. The paraffins and olefins elute in the top two "rows" of the spectrum, while the oxygenates are grouped between 0 and 3 seconds in the secondary dimension. The carboxilic acids, linear alcohols, iso-alcohols, ketones and aldehydes are separated, identified and quantified in a straightforward manner as opposed to the case in the one-dimensional chromatography. The respective classes for the N-containing compounds, i.e. the primary, secondary and tertiary amines, aliphatic nitriles and amides were similarly treated as discussed in the results Chapters 7, 8 and 9.

Table 4.5: The general method used for comprehensive two-dimensional chromatography.

Gas chromatograph	**Leco Pegasus 4D (Agilent7890)**
Injector	split/splitless
	injection volume = 250 μl (gas phase analysis)
	injection volume = 0.1 μl (oil phase analysis)
	split ratio - 20:1 (gas phase analysis)
	split ratio - 400:1 (oil phase analysis)
	T_{inj} = 225 ℃
Transfer line temp.	350 ℃
Carrier gases	He (0.6 ml/min - Leco column calculator)
Column head pressure	Varying head pressure to maintain flow rate
Stat phase - polar	Varian, CP-WAX 52 CB, 30 m x 0.25 mm x 0.25 μm
Stat phase - apolar	Varian, CP-Sil 8CB, 1.6 m x 0.10 mm x 0.10 μm
Cryogenic cooling	liquid CO_2
Primary oven	T_1 = 40 ℃ (isothermal for 1 min)
	T_1 = 40 ℃ → T_2 = 215 ℃ (ramped @ 3 ℃/min)
Secondary oven	T_1 = 60 ℃ (isothermal for 1 min)
	T_1 = 60 ℃ → T_2 = 235 ℃ (ramped @ 3 ℃/min)
Modulator Temp offset	+ 15 ℃ w.r.t. primary oven
Modulation	5 s
Cooling (C) and heating (H) pulses	C : 1.2 s, H 0.6 s, (dependent on modulation period)
Detector # 1	Time-of-flight mass spectrometer (TOF)
	T_{det} = 250 ℃
Detector # 2	Flame ionisation detector (FID)
	T_{det} = 250 ℃

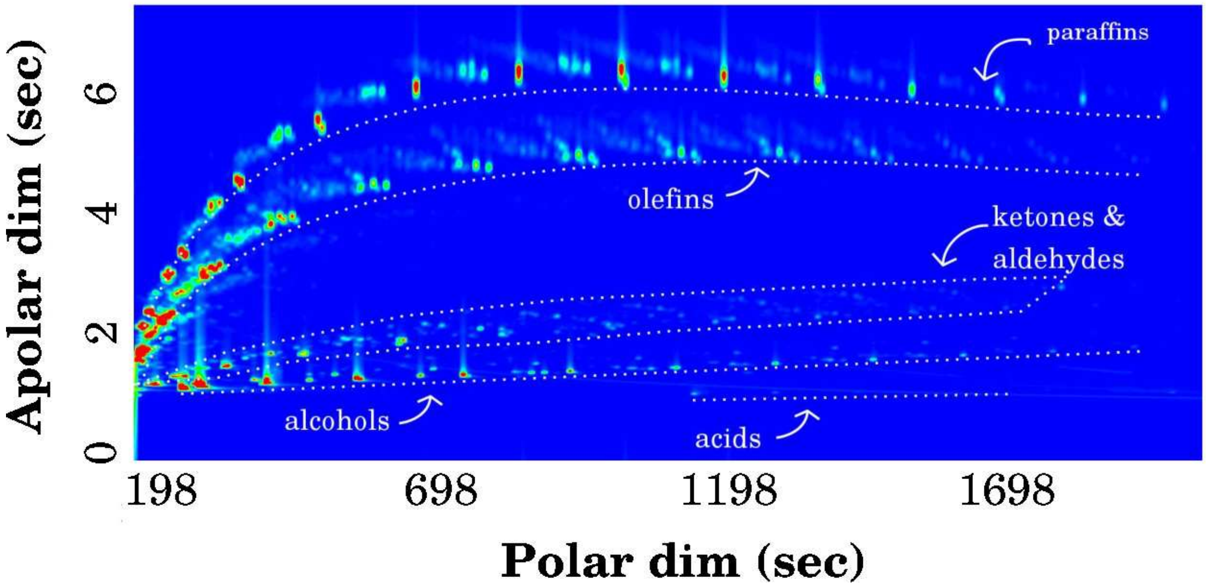

Figure 4.21: The chromatogram obtained after performing comprehensive two-dimensional gas chromatography on an oil sample obtained during FTS. The classes, paraffins, olefins and selected oxygenates are indicated.

References

[1] R.G. Parr and W. Yang, Density-Functional Theory of Atoms and Molecules, Oxford University Press, Oxford, 1989.

[2] R.M. Dreizler and E.K.U. Gross, Density Functional Theory: An Approach to the Quantum Many-Body Problem, Springer-Verlag, Berlin, Berlin Heidelberg, 1990.

[3] W. Koch and M.C. Holthausen, A Chemist's Guide to Density Functional Theory, John Wiley & Sons, New York, Weinheim, 2001.

[4] P. Hohenberg and W. Kohn, Phys. Rev. 136 (1964) B864–B871.

[5] W. Kohn and L. J. Sham, Phys. Rev. 140 (1965) A1133–A1138.

[6] R.O. Jones and O. Gunnarsson, Rev. Mod. Phys. 61 (1989) 689–746.

[7] S.H. Vosko, L. Wilk and M. Nusair, Can. J. Phys. 58 (1980) 1200.

[8] J.P. Perdew, J.A. Chevary, S.H. Vosko, K.A. Jackson, M.R. Pederson, D.J. Singh and C. Fiohais, Phys. Rev. B 46 (1992) 6671–87.

[9] J.P. Perdew, K. Burke and M. Ernzerhof, Phys. Rev. Lett. 77 (1996) 3865.

[10] B. Hammer, L.B. Hansen and J.K. Nørskov, Phys. Rev. B 59 (1999) 7413–7421.

[11] G. Kresse and J. Joubert, Phys. Rev. B 59 (1999) 1758–84.

[12] H.J. Monkhorst and J.D. Pack, Phys. Rev. B 13 (1976) 5188.

[13] C. Kittel, Introduction to Solid State Physics, Wiley & Sons, 1996.

[14] G. Henkelman, B.P. Uberuaga and H. Jónsson, J. Chem. Phys. 113 (2000) 9901–9904.

[15] H. Jonsson, G. Mills and K.W. Jacobsen, 'Nudged Elastic Band Method for Finding Minimum Energy Paths of Transitions' in 'Classical and Quantum Dynamics in Condensed Phase Simulations', World Scientific, 1998.

[16] I.M. Ciobîcă, A.W. Kleyn and R.A. van Santen, Journal of Phys. Chem. B 107 (2003) 164–172.

[17] M. Claeys, Selektivität, Elementarschritte und kinetische Modellierung bei der Fischer-Tropsch-Synthese, Ph.D. thesis, Unversität Fridericiana Karlsruhe, Germany (1997).

[18] K.P. de Jong, Synthesis of Solid Catalysts, WILEY-VCH, Weinheim, 2009.

[19] T. Sango, *Nitrogen-containing compounds from ammonia co-feed to the Fischer-Tropsch synthesis*, Master's thesis, University of Cape Town, South Africa (2013).

[20] P. Cairns, Oxygenates in iron Fischer-Tropsch Synthesis: is copper a selectivity promoter?, Ph.D. thesis, University of Cape Town, South Africa (2008).

[21] A.P. Steynberg, M.E. Dry, B.H. Davis and B.B. Breman, Chapter 2 - Fischer-Tropsch Reactors, in: A.P. Steynberg and M.E. Dry (Eds.), Fischer-Tropsch Technology, Vol. 152 of Stud. Surf. Sci. Catal., Elsevier, 2004, pp. 64 – 195.

[22] R.L. Espinoza, A.P. Steynberg, B. Jager and A.C. Vosloo, Appl. Catal., A 186 (1999) 13.

[23] S.T. Sie and R. Krishna, Appl. Catal., A 186 (1999) 55–70.

[24] H. Schulz, Catal. Today 178 (2011) 151 – 156.

[25] H. Schulz, G. Schaub, M. Claeys and T. Riedel, Appl. Catal., A 186 (1999) 215–227.

[26] N. Fischer, Preparation of nano and angstrom sized cobalt ensembles and their performance in the Fischer-Tropsch synthesis, Ph.D. thesis, University of Cape Town (2011).

[27] T. Sango, N. Fischer, R. Henkel, F. Roessner, E. van Steen and M. Claeys, Appl. Catal., A 502 (2015) 150–156.

[28] E.S. Kovats, Zeitschrift für analytische Chemie 181 (1961) 351.

[29] A.D. Jorgensen, K.C. Picel and V.C. Stamoudis, Anal. Chem. 62:7 (1990) 683–689.

[30] T. Holm, J. Chromatogr. A 842 (1999) 221–227.

[31] H.F. Calcote, in: 8^{th} Int. Symp. Combust., 1962.

[32] J.C. Sternberg, W.S. Gallaway and D.T.L. Jones, Gas Chromatography, Academic Press, New York, 1962, p. 261.

[33] R. Kaiser, Bibliographisches Institut, Manheim.

[34] M. Kállai, Z. Veres and J. Balla, Chromatographia 54 (2001) 511–517.

[35] J. Dallüge, J. Beens and U.A.Th. Brinkman, J. Chromatogr. A 1000 (2003) 69–108.

[36] C. Vendeuvre, F. Bertoncini, L. Duval, J.L. Duplan, D. Thieèbaut and M.C. Hennion, J. Chromatogr. A 1056 (2004) 155–162.

[37] T. Grobler, M. Claeys, E. van Steen and M.J. Janse van Vuuren, Catal. Commun. 10 (2009) 1674–1680.

[38] R. van der Westhuizen, A. Crouch and P. Sandra, J. Sep. Sci. 31 (2008) 3423–3428.

[39] R. van der Westhuizen, H. Potgieter, N. Prinsloo, A. de Villiers and P. Sandra, J. Chromatogr. A 1218 (2010) 3173–3179.

[40] R. van der Westhuizen, R. Crous, A. de Villiers and P. Sandra, J. Chromatogr. A 1217 (2010) 8334–8339.

[41] F.C. Wang, W. Robbins and M.A. Greaney, J. Sep. Sci. 27 (2004) 468–472.

CHAPTER 5

INDIVIDUAL ADSORPTION AND DISSOCIATION OF CO AND NH_3 ON FE(100)

This chapter makes use of spin-polarized periodic density functional theory (DFT) calculations to investigate aspects of the individual surface chemistries of CO and NH_3 *adsorbed on a model Fe(100) surface. Optimizing CO conversion into higher hydrocarbons is usually key to ideal Fischer-Tropsch synthesis. CO adsorption and dissociation reactions have been identified as important elementary reactions in FTS.* NH_3 *has, in turn, been evaluated as a potential co-reactant in FTS reactions for the production of N-containing hydrocarbons. To shed light on the possible* NH_x *surface species involved in the pathway to the formation of these N-containing compounds, an improved understanding of the decomposition of* NH_3 *at FTS conditions was sought. In addition,* NH_3 *is present in biomass-derived synthesis gas (CO +* H_2*), which is classically grouped with the FTS catalyst poisons. It was therefore desired to gain an improved understanding of the elementary reactions of CO in the presence of* NH_x *surface species on a model catalyst (Fe(100)) surface, which is the subject of Chapter 6. This chapter thus initiates the study by evaluating and comparing the individual decomposition reactions of CO and* NH_3 *on the Fe(100) surface.*

The adsorption and dissociation of CO on the Fe(100) surface is evaluated and compared to *theoretical and experimental results reported in literature. A similar procedure is followed for* NH_3 *adsorption and its subsequent decomposition reactions. The computed results (i.e. adsorption energies, geometries, site preferences and activation energies), generally compare well with what has been reported in literature. Discrepencies are however found when other computational methodologies have been employed, in particular with DFT calculations where other exchange correlation energy functionals have been used. A comparison is made between the potential energy surfaces (PES) obtained for the two sets of reactions.*

The DFT results are subsequently used to study the NH_3 *decomposition reaction at relevant reaction conditions (*$T = 523$ *K,* $P = 5.2$ *bar and* $p^{*}(NH_3) = 0.2$ *bar) through the use of harmonic transition state theory and statistical mechanics. The free energy profile for* NH_3 *decomposition suggests that the* NH_2 *dehydrogenation would be the rate limiting step, and additionally implies that* NH_2 *could be the dominant surface species for this reaction on the Fe(100) surface. A basic microkinetic model for the decomposition of* NH_3 *on a model Fe(100) surface in an isothermal plug-flow reactor at these conditions further supports this hypothesis.*

Importantly, the individual decomposition reactions of CO and NH_3 *through the use of one exchange correlation function (*E_{xc}*), serve as an ideal platform to study the co-existence of CO and* NH_x *on the Fe(100) surface.*

Introduction

In this chapter the results obtained after investigating the individual adsorption and decomposition profiles of CO, NH_3 and its derivative fragments (NH_2, NH, and N) on a model Fe(100) surface by means of spin-polarized DFT calculations are presented. The primary interest throughout the theoretical part of this thesis is the co-adsorption of these surface species on a model Fe surface (i.e. CO + NH_x on the Fe(100) surface). It is however pivotal to have a clear understanding of the individual adsorption and decomposition profiles for these adsorbates before embarking on the study of their co-existence on the Fe(100) catalyst surface.

Both CO and NH_3 are industrially relevant reactants and products in several processes (e.g. ammonia synthesis and FTS) and have thus been studied in great detail, both theoretically and experimentally [1–5]. The results from DFT calculations are however not necessarily directly comparable (see Table 5.1), which is mainly due to the choice of exchange-correlation energy functional, and can also be influenced by several parameters chosen for the DFT calculations. For example, the number of atomic layers used to model the surface can vary or the choice of ultrasoft pseudo-potentials (USPP) or the projector augmented wave (PAW) method to describe the electron-ion interaction, can affect the adsorption energy calculated. Moreover, one E_{xc}-functional is sometimes used in a full self-consistent calculation to find the optimized structure, while another is used in a static calculation to determine the adsorption energy. Sorescu et al. [1] used spin-polarized DFT calculations to investigate CO adsorption and dissociation on Fe(100). They calculated the adsorption energy of CO adsorbed in the fourfold-hollow site in a tilted configuration (denoted as *ft*) to be -2.02 eV (46.7 kcal/mol) at $\theta = 0.25$ ML when treating the exchange-correlation energy with the generalized gradient approximation of Perdew et al. (PW91) [6] as implemented in VASP. However, when they used the revised form of the Perdew, Burke, and Ernzerhof (RPBE), as introduced by Hammer et al. [7] and implemented in the software package CASTEP (Cambridge serial total energy package), an adsorption energy of -1.90 eV was obtained. The adsorption energy calculated by Sorescu et al. [1] for CO in the *ft*-configuration on the Fe(100) surface, using the RPBE E_{xc}-functional, was calculated using a geometry previously optimized using the PW91 E_{xc}-functional. Bromfield et al. [2] performed a similar set of calculations, and reported an adsorption energy for CO (*ft*) of -2.56 eV at

$\theta = 0.25$ ML CO on the Fe(100) facet when using the PW91 as exchange correlation energy functional as implemented in VASP. Van Helden and Van Steen [3] used the RPBE functional as implemented in CASTEP and reported an adsorption energy for CO (*ft*) at $\theta = 0.25$ ML of -1.89 eV. The potential for improved agreement with experimental adsorption energies is a known feature of the RPBE exchange-correlation energy functional [8]. Jiang and Carter [4] performed a geometry optimization with the PBE functional, then performed a static calculation using the RPBE E_{xc}-functional using VASP and reported a value of -1.49 eV for CO(ft) at $\theta = 0.25$ ML on Fe(100) when using the implemention of the VASP software package. The adsorption energy reported by Jiang and Carter [4], is in closest agreement with the experimentally determined adsorption energy ($E_{ads} = -1.13$ eV, assuming a pre-exponential factor A = 10^{13} s^{-1}) reported by Moon et al. [5] who conducted ultra high vacuum (UHV) temperature programmed desorption (TPD) experiments with CO on a Fe(100) surface. This is likely to be a fortuitous result based on the variation (~ 0.40 eV) in adsorption energies reported by other authors [1, 3] using the RPBE E_{xc}-functional. If one assumes that E_{ads} is only dependent on the parameters compared in Table 5.1, it would indicate that the use of USPP or the PAW method gives rise to the aforementioned variation in adsorption energy, since this is the only major parameter changed for the adsorption energies calculated with the RPBE E_{xc} functional. The results reported by van Helden and van Steen [3] correlates well with that of Soresecu [1] who used a similar methodology (RPBE, $E_{ads} = -1.89$ and -1.90 eV respectively). In contrast however, Bromfield et al. [2] and Sorescu [1] compute significantly different adsorption energies ($E_{ads} = -2.02$ and -2.56 eV), even though they both made use of the PW91 E_{xc}-functional, which is indicative of a strong influence by either the methodology used to treat the electron-ion interaction (USPP/PAW) or the implementation of the methodologies in the relevant source codes (VASP/CASTEP).

A similar argument can be made when evaluating the results from spin-polarized DFT calculations, where the adsorption and decomposition energetics of NH_3 on model Fe surfaces have been investigated [9–13] (see Section 5.3.3 for a detailed discussion). In summary, even though the individual adsorption and decomposition of CO and NH_3 on Fe(100) have been studied previously with periodic DFT calculations, inconsistencies in the reported results due to variations in the theoretical methodologies (e.g. E_{xc}, USPP/PAW etc.) motivates the need to obtain a

Table 5.1: Adsorption energies calculated using DFT (with varying methodologies) for CO adsorbed in the most stable four-fold hollow (tilted) configuration on Fe(100) at $\theta = 0.25$ ML calculated by various authors [1–4]. *Full SCF* indicates if a full self-consistent field optimization was performed or only a static calculation with the tabulated E_{xc}-functional.

Author	**Full SCF**	**E_{xc}**	**USPP/PAW**	**Software**	**At. layers**	**E_{ads} (eV)**
Sorescu et al. [1]	Yes	PW91	USPP	CASTEP	6	−2.02
Sorescu et al. [1]	No	RPBE	USPP	VASP	6	−1.90
Bromfield et al. [2]	Yes	PW91	PAW	VASP	4	−2.56
van Helden and van Steen [3]	Yes	RPBE	USPP	CASTEP	7	−1.89
Jiang and Carter [4]	Yes	PBE	PAW	VASP	5	−2.08
Jiang and Carter [4]	No	RPBE	PAW	VASP	5	−1.49

consistent set of results in the current work.

The individual decomposition of NH_3 is of further importance when considering the formation of N-containing compounds, as it has been proposed that NH_x ($x = 3,\ 2,\ 0$) surface species are incorporated into the hydrocarbon chain at the desorption step to produce N-containing compounds [14–17] when NH_3 is co-fed during FTS. Based on pathways proposed by others, it is thus desired to know what the dominant NH_x surface species would be when NH_3 is exposed to a model Fe surface.

Grunze et al. [18] made use of ultraviolet photoelectron spectroscopy (UPS), Auger electron spectroscopy (AES), low energy electron diffraction (LEED), work function measurements and TPD experiments to characterize the decomposition of NH_3 on the Fe(111) and Fe(100) surfaces. It should be pointed out that NH_3 TPD experiments inherently suffer from slow diffusion and adsorption of NH_3 on the walls of the equipment used [18, 19]. To circumvent this problem Grunze et al. [18] designed a technique where the NH_3 gas was dosed from a capillary in front of the Fe(111) surface during the NH_3 TPD experiments. For their NH_3 TPD experiments on the Fe(100) facet, only preliminary results was reported that did not employ the capillary technique. Furthermore, no figures was published for the NH_3 TPD experiments on a clean Fe(100) surface, and it was only stated that the results was similar to that of the Fe(111) surface. The adsorption energies deduced from these results should thus be considered to be qualitative in nature. Note that it was not possible for the authors to report on the exact surface coverage of the adsorbates in their study. Grunze et al. [18] reported that NH_3 is weakly bound between -0.43 and -0.52 eV on the Fe(100) surface and starts to transform to NH_2 + H at temperatures as low as 140 - 160 K. For Fe(111), the two peaks (β_1, β_2) observed in the TPD spectra at 160 and 210 K were associated with adsorbed NH_3 states and considered to be reactions of first order, while the third peak (β_3) was concluded to be second order and related to the reaction $NH_x + (3 - x)\ H \rightarrow NH_3$ followed by desorption of NH_3. Two distinct adsorbed NH_3 states (β_1 and β_2) was not discernible in the TPD spectra of NH_3 on the Fe(100) surface. Based on the β_3 peak, the overall activation energy was estimated to be $E_a = 0.87$ eV [18]. Yeo et al. [13] recently published a DFT-based study for the decomposition of NH_3 on the Fe(100) surface with $\theta = 0.11$ ML, the result for NH_3 adsorption ($E_{ads} = -0.92$ eV) is however not consistent with the adsorption energies deduced experimentally, but serves as comparison for the NH_3 PES calculated in the current work at $\theta = 0.25$ ML.

In this work, an extensive study of the individual surface chemistry of CO and NH_x ($x = 3$, 2, 1, 0) on the Fe(100) surface is made using the RPBE exchange-correlation functional as implemented in VASP, and is subsequently used to evaluate the changes or interactions generated when both species are present on the surface in Chapter 6. By applying harmonic transition state theory (TST) and statistical mechanics using the DFT results computed for the decomposition of NH_3, a surface free energy profile is used to evaluate the elementary reactions at the FTS reaction conditions applied in the experimental work (T = 523 K and $p^*(NH_3) = 0.2$ bar). Furthermore, these results are implemented in a basic microkinetic model that is used to estimate the concentration of the various NH_x surface species (θ_{NH_x}) on the Fe(100) surface in a plug-flow reactor.

Computational method

Calculations based on periodic DFT with the PAW method in the implementation of Kresse and Joubert [20, 21] were performed using VASP [22–25]. The RPBE exchange-correlation functional [7] was used in the electronic structure calculations. For comparison, the PW91 functional described by Perdew and Wang [6] (with the PAW method) was tested in preliminary calculations. To aid the electronic energy convergence, a Methfessel-Paxton [26] smearing method with a smearing width $\sigma = 0.15$ eV was employed. For k-point sampling of the Brillouin zone the Monkhort-Pack [27] scheme was used. The sampling density (k-point: 5×5×1) and kinetic energy cutoff for the plane wave basis set ($E_{cut} \leq 400$ eV) converged (see Chapter 4) within an error of ± 1 meV per atom. The convergence tests (see Appendix B) for the number of atomic layers used to model the surface and the vacuum gap revealed an uncertainty of $\sim$ 0.03 eV/(for CO and NH_3 adsorption at $\theta = 0.25$ ML), which has previously been reported when a similar computational method was used [28]. The GGA-RPBE calculations reported make use of p(2×2), p(3×3) and p(4×4) surface unit cells, with the Fe(100) surface represented by 5 atomic surface layers, where the adsorbates and the top two layers were allowed to relax and the bottom three layers were kept fixed. Geometry optimizations were terminated after the maximum forces on the atoms were below 0.03 eV/Å. A dipole correction was added to account for the artificial net dipole moment generated by adsorbing the molecules on only one side of the slab. By varying the lattice parameter (a) of the unit cell for bulk bcc iron and fitting the calculated energy to the Birch-Murnaghan equation of state [29] an optimum lattice parameter of $a = 2.87$ Å were obtained (see Figure B.5 in Appendix B). The lattice parameter, as well as the corresponding bulk modulus of $B = 161$ GPa and magnetic moment of $M = 2.31$ μB, correlate well with experimentally-determined values ($a = 2.86$ Å, and $B = 168$ GPa and $M = 2.24$ μB respectively) [30]. A partial Hessian vibrational analysis (PHVA) was performed in the frozen phonon approximation by diagonolizing the Hessian matrix arising from finite differences of the adsorbates displaced 0.02 Å in the x, y and z directions, when using Cartesian coordinates. The normal modes calculated for the optimized and transition state configurations were used to verify that the structures correspond to a local minimum or first order saddle point, respectively, on the potential energy surface. The gas phase molecules were optimized in a cubic box of 10 × 10 × 10 Å sampled at the gamma-point and compared with their equilibrium properties in the gas phase using the RPBE E_{xc}-functional and the same cutoff parameters used for the slab calculations. For CO, the equilibrium bond length, $r_e = 1.146$ Å (1.147 Å), and vibrational frequency for CO, $v_{CO} = 2165$ cm^{-1} (2143 cm^{-1}), correlate well with what has been measured experimentally [31]. For gaseous NH_3, the vibrational spectra compared well with experimental values 3511 cm^{-1}(3444 cm^{-1}), 3384 cm^{-1}(3336 cm^{-1}), 1631 cm^{-1}(1626 cm^{-1}), 1020 cm^{-1}(968 cm^{-1}) [32]. The N-H bond distance is found to be $r_e = 1.03$ (1.02 Å). N_2 in

Table 5.2: Calculated adsorption energies (ΔE_{ads}), change in zero point energies (ΔZPE) and the heat of adsorption (ΔE_{ads} at 0 K) for CO and NH_x on Fe(100) at $\theta = 0.25$ ML is tabulated. Note the influence of the ΔZPE on the dehydrogenated NH(fh) and N(fh).

Adsorbates ($\theta = 0.25$ML)	**ΔE_{ads} (eV)**	**ΔZPE (eV)**	**ΔE_{ads} (eV)**
CO(ft)	−1.51	0.02	−1.49
NH_3(at)	−0.25	0.08	−0.17
NH_2(br)	−0.67	−0.14	−0.81
NH(fh)	−0.63	−0.40	−1.02
N(fh)	−0.98	−0.56	−1.55

the gas phase had a stretching frequency of 1631 cm^{-1}(1626 cm^{-1}) and a bond distance of r_e = 1.03 Å (1.02 Å). Similarly the H_2 vibrational mode in the gas phase was calculated to be v_{H-H} = 4401 cm^{-1} (4401 cm^{-1}) with an equilibrium bond distance r_e = 0.749 Å (0.749 Å) [31]. All energies reported includes zero point vibrational energy corrections ($ZPVE_c$) and the change in zero point energy ΔZPE unless otherwise stated. ΔZPE-values were found to significantly influence the heat of adsorption for the NH_x adsorbed species (as can be seen in the selected results in Tabel 5.2), which can be expected due to the loss of the N-H vibrational modes upon the decomposition of NH_3.

The nudged elastic-band method (NEB) [33] was used to locate transition states for the CO dissociation and the sequential NH_x dehydrogenation reactions. The transition states obtained in this way were further refined by minimizing the forces on the atoms until they were relaxed below 0.03 eV/Å, by making use of a quasi-newton algorithm. Additional experimental data available for CO, NH_x (with $x = 3, 2, 1, 0$) and H adsorption on the Fe(100) surface will be discussed in the relevant sections.

Results and discussion

During the initial calculations performed on the model Fe(100) surface with the RPBE and PW91 E_{xc}-functionals, stronger binding energies (ca. 0.25 - 0.50 eV) was calculated with the

Table 5.3: Comparing the adsorption energies for CO and NH_3 on Fe(100) calculated with the PW91 and RPBE functionals. ($E_{cut} < 400\,eV$, k-points: 5x5x1)

Adsorbate	**Coverage (θ)**	**ΔH$_{ads}$ (eV)**	
		RPBE	PW91
NH_3 (at)	0.25 ML	-0.17	-0.44
	0.11 ML	-0.28	-0.59
	0.063 ML	-0.35	-
CO (ft)	0.25 ML	-1.49	-2.00

PW91 E_{xc}-functional when compared to the binding energies obtained with the RPBE E_{xc}-functional (see Tabel 5.3). These tendencies are known for these functionals [8], and are reported in previous DFT studies that are relevant to this work [1, 11].

CO adsorption on Fe(100)

CO adsorption at 0.25 and 0.50 ML coverage was probed at the high symmetry sites (at, br and fh - see Chapter 4) of the Fe(100) surface. It has been shown that the CO adsorbed in a tilted configuration results in increased bonding between the metal surface and CO surface species [1]. These configurations are therefore calculated in addition to the adsorbates bonded with the CO bond orthogonal to the surface plane (see Figure 5.1). To calculate the adsorption energy for the adsorbates the general form of equation 5.1 was used,

$$E_{ads} = E_{ads+slab} - E_{slab} - E_{ads} \tag{5.1}$$

where E_{ads} is the adsorption energy of the adsorbate , $E_{ads+slab}$ is the energy calculated for the geometry optimized structure of the adsorbate on the Fe(100) surface, E_{slab} is the energy calcualted for the empty slab and E_{ads} is the energy value for the corresponding gas phase molecule. To maintain an average energy per mole of the relevant gas phase molecule at higher coverages (e.g. $\theta = 0.50$ ML), the energy were calculated using equation 5.2

$$E_{ads} = (1/n) \times E_{ads+slab} - (1/n) \times E_{slab} - E_{ads} \tag{5.2}$$

for a system containing n molecules. A top and side view of all the optimized geometries for the respective configurations of CO^* is given in Figure 5.1. The heats of adsorption ($E_{ads,CO}$ at 0 K), CO bond distance (d_{C-O}), the shortest metal-carbon bond distances to the first and second Fe layers (d_{Fe^1-C} and d_{Fe^2-C}), the shortest distance between the bonding metal-oxygen atoms (d_{Fe-O}) and the angle that the CO adsorbates bond makes with the surface normal (ϕ) are tabulated in Table 5.4. Furthermore, the vibrational modes calculated for these structures and the number of imaginary frequencies are tabulated in Table 5.5. From the vibrational analysis it was found that CO bonded in vertical orientation on the bridge and fourfold hollow sites were not at stable minima, as it contained imaginary frequencies. In both the $\theta_{CO} = 0.25$ and 0.50 ML coverages, the fourfold hollow site with the CO in the tilted configuration (ft) was found to be the most stable ($E_{ads,CO} = -1.49$ and -1.46 at $\theta = 0.25$ and 0.50 ML respectively). When CO is configured to have only one oxygen atom bonded to an iron atom, tilted in a similar configuration (denoted as ft'), a stable geometry was calculated (with $E_{ads,CO} = -1.48$ and -1.45 eV at $\theta = 0.25$ and 0.50 ML respectively). Analysis of the vibrational modes for CO adsorbed in this configuration (ft') yielded no imaginary frequencies and this geometry is thus at a local minimum on PES. This stable configuration of CO was not reported in previous DFT studies [1, 2, 28, 34], which could be due to the force convergence criteria in this work (forces smaller than 0.03 eV/Å). For example, Bromfield et al. [2] terminated their geometry optimizations when forces of smaller than 0.01 eV/Å acted on the atoms, while Jiang and Carter's [28] geometry optimizations were terminated when the forces were below 0.025 eV/Å. The differential adsorption of CO can be calculated using Eq. 5.3

$$E_{ads}^{diff} = E_{n\times ads} - E_{(n-1)\times ads} - E_{ads} \tag{5.3}$$

where E_{ads}^{diff} is the differenial adsorption energy, $E_{n\times ads}$ is the adsorption energy for n adsorbates on the surface unit cell and E_{ads} is the energy calculated with reference the gas phase molecule associated with ads. For the most stable configurations, CO(ft) and CO(ft') at the coverages considered ($\theta = 0.25$ and 0.50 ML), the differenial adsorption energy is $E_{ads}^{diff} = -1.47$ and -1.48 respectively. These values would suggests that it would require minimal energy to increase the coverage from $\theta = 0.25$ to 0.50 ML. When CO is bonded in the ”conventional” fourfold tilted configuration, it makes a 47°angle with the surface normal, while CO tilted with one oxygen bonded to iron (ft') has a higher inclination ($\phi = 43°$). Both of these calculated angles for CO are in agreement with what was determined experimentally ($\phi = 45 \pm 10°$) using near edge X-ray absorption fine structure (NEXAFS) [35]. When Moon et al. [5] exposed a clean Fe(100) surface to various exposures of CO at 150 K, four desorption peaks (α_1, α_2, α_3 and β) were identified with peak temperatures at 220 K, 305 K, 440 K and 820 K during TPD experiments. The first three peaks were attributed to three adsorption sites which were sequentially filled. By employing normal transition state theory, and using a pre-exponential factor of $A = 10^{13}$ s^{-1}, binding energies for α_1, α_2 and α_3 of -0.56 eV (12.8 kcal/mol), -0.78 eV (18.0 kcal/mol) and -1.14 eV (26.2 kcal/mol) respectively were derived. The absolute adsorption energies calculated in this work are significantly lower than the aforementioned values. This can in part be due to the choice of pre-exponential factor in the experimental analysis, which is believed to be inappropriate for the CO desorption system [1]. Larger values between $A = 10^{15}$ - 10^{18} s^{-1}, has been proposed [1, 36], which would bring the experimental values slightly closer (α_1, α_2, α_3: -0.69 eV $\rightarrow$ -1.56 eV) to those calculated here ($E_{ads,CO} = -1.09 \rightarrow -1.49$ eV). Alternatively, it has recently been shown that the GGA-DFT level of theory has the tendency to underestimate the HOMO-LUMO gap in gas phase CO [37–39]. The underestimation of the energy value for the antibonding $2\pi^*$ orbitals of CO, has the consequence that increased backdonation from the metal surface can take place upon adsorption, and hence unrealistically "strong" bonds are calculated by DFT. Mason et al. [37] adressed the overbinding tendency of DFT, by extrapolating the adsorption energy to the value that would be obtained for the correct singlet-triplet excitation energy. Correcting their adsorption energies calculated via DFT (E_{xc} = PBE) using this technique led to energies that are in better agreement with experimental values for a number of metal systems, and has shown succes elsewhere [38, 39]. Abild-Pedersen and Andersson [39] showed that these corrections could in addition improve the DFT results obtained when using the RPBE as E_{xc}-functional on various metals, including Fe (i.e. a Fe(110) surface). If we employ the correction suggested by Mason et al. [37], using equation 5.4, derived from their data,

$$E^{corr}_{ads,CO} = E_{ads} - 1.8 + 0.0008 * v \tag{5.4}$$

where $E^{corr}_{ads,CO}$ is the corrected adsorption energy (in eV), E_{ads} is our GGA-DFT calculated

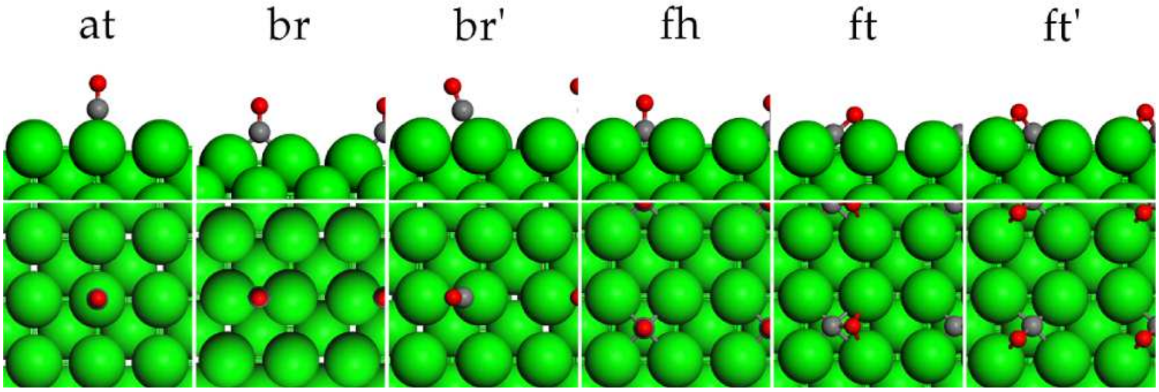

Figure 5.1: CO adsorption geometries at $\theta = 0.25ML$ are displayed in a top and side view for all the configurations calculated on the Fe(100) surface. (Color scheme: Fe - green, C - grey , O - red)

energy and v is the stretching frequency of CO (in cm^{-1}), our calculated values falls between $E_{ads,CO} = -0.58 \rightarrow -0.80\ eV$. This leads to an overcorrection when compared to the experimentally determined values [5] and the proposition that the site preference is different to what has been determined via the DFT calculations in this work. The association of the α_3 peak with CO adsorbed in the fourfold tilted configuration is however supported by various surface science studies [35, 40, 41]. It should in addition be borne in mind that there is a variation in CO adsorption energies (between $E_{ads,CO} = -1.49$ and -2.54 eV) calculated via plane wave DFT as discussed in the introduction, which can be assigned to the choice of exchange-correlation functionals (e.g. RPBE or PW91). The RPBE functional does, in this case provide adsorption energies that are in closer agreement to experimental values, which is a well-known feature for this exchange-correlation functional [8].

CO dissociation pathway

The PES of CO dissociation on Fe(100) at $\theta = 0.25$ ML was calculated to allow for comparison with the activation energies for the NH_3 decomposition reactions. In addition, in Chapter 6 we use these results to compare against the case where CO dissociation takes place in the presence of the NH_x (x = 3, 2, 1, 0) adsorbates. The adsorption energies calculated for the C and O atoms showed their preference for the fourfold hollow sites (see Table B.4 in Appendix B). Previous DFT [1, 2] and experimental studies [5, 35, 40, 41] have shown that the α_3-CO structure (i.e.

Table 5.4: Average, CO adsorption energies calculated ($E_{ads,CO}$), their corrected DFT values via the method proposed by Mason et al. [37] ($E_{ads,CO}$), calculated distances and angles for the configurations of CO adsorbed on Fe(100) considered at $\theta = 0.25$ and 0.50 ML coverages. Experimentally derived adsorption values are appended using pre-exponential factors (A) between 10^{13-18} s^{-1}.(GGA-RPBE, $E_{cut} = 400\,eV$, k-points: 5x5x1)

Config	θ	$\mathbf{E_{ads,CO}}$(eV)	$\mathbf{E^{corr}_{ads,CO}}$(eV)	$\mathbf{d_{C-O}}$ (Å)	$\mathbf{d_{Fe^1-C}}$ (Å)	$\mathbf{d_{Fe^2-C}}$ (Å)	$\mathbf{d_{Fe-O}}$ (Å)	ϕ (°)
(at)	0.25	−1.09	−0.74	1.18	1.77	–	2.95	0
	0.50	−0.94	−0.62	1.18	1.78	–	2.96	0
(br)	0.25	−0.96	−0.54	1.20	1.96	–	2.93	0
	0.50	−0.83	−0.44	1.18	1.78	–	2.94	0
(br')	0.25	−1.11	−0.77	1.19	1.78	–	3.10	20
	0.50	−0.74	−0.44	1.18	1.81	–	3.16	10
(fh)	0.25	−1.14	−0.48	1.26	2.14	2.10	2.81	0
	0.50	−1.07	−0.43	1.25	2.15	2.10	2.82	0
(ft)	0.25	−1.49	−0.66	1.31	1.97, 2.24	2.09	2.17	47
	0.50	−1.46	−0.63	1.31	1.99, 2.23	2.07	2.18, 2.19	48
(ft')	0.25	−1.48	−0.71	1.29	1.91, 2.16	2.07	2.06,	43
	0.50	−1.45	−0.69	1.29	1.93, 2.14	2.08	2.06, 2.12	42

Exp. Ref. [5]		$\mathbf{E_{ads}}$ (eV)	
	$A = 10^{13}$ s^{-1}	$A = 10^{15}$ s^{-1}	$A = 10^{18}$ s^{-1}
α_1	−0.56	−0.64	−0.78
α_2	−0.78	−0.90	−1.08
α_3	−1.14	−1.31	−1.58

Table 5.5: Vibrational frequencies (cm^{-1}) calculated for CO adsorbed on Fe(100) at $\theta = 0.25$ and 0.50 ML coverages. (i) and n(i) are used to indicate imaginary frequencies and the number of the imaginary frequencies respectively.(GGA-RPBE, $E_{cut} < 400\,eV$, k-points: 5x5x1)

Config	θ	**v(cm^{-1})**	**n(i)**	**ΔZPE (eV)**
(at)	0.25 ML	1808, 446, 320, 301, 206, 147	0	0.03
	0.50 M	1911, 1846, 404, 401, 383, 378,...	0	0.06
		370, 368, 67, 57, 57, 53		
(br)	0.25 ML	1730, 331, 302, 199, 33, 126 (i)	1	0.04
	0.50 ML	1795, 1732, 348, 345, 308, 305,...	1	0.03
		203, 188, 47, 40, 31, 153 (i)		
(br')	0.25 ML	1831, 389, 380, 339, 62, 55	0	0.06
	0.50 ML	1912, 1824, 380, 373, 354, 351,...	0	0.05
		296, 260, 127, 58, 51, 50		
(fh)	0.25 ML	1426, 247, 166, 145, 193 (i), 237 (i)	2	-0.01
	0.50 ML	1472, 1437, 290, 245, 176, 156,...	4	-0.01
		138, 109, 170 (i), 188 (i), 221 (i), 274 (i)		
(ft)	0.25 ML	1210, 344, 325, 302, 204, 144	0	0.03
	0.50 ML	1224, 1211, 384, 354, 315, 310,...	0	0.03
		282, 267, 223, 215, 171, 156		
(ft')	0.25 ML	1286, 355, 317, 255, 234, 109	0	0.03
	0.50 ML	1311, 1293, 398, 365, 320, 307,...	0	0.03
		285, 265, 259, 253, 91, 83		

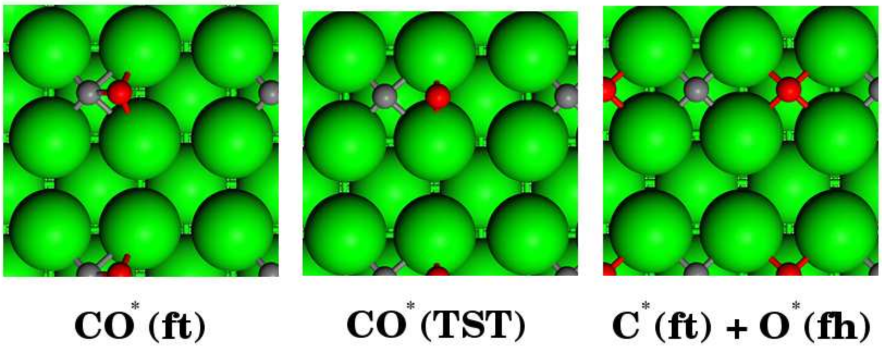

Figure 5.2: The initial, transition and final state structures for the dissociation of CO → C + O on Fe(100) ($\theta = 0.25$ ML, GGA-RPBE, $E_{cut} < 400\,eV$, k-points: 5x5x1; Color scheme: Fe - green, C - grey , O - red)

the fourfold tilted configuration) is the precursor state for the CO dissociation pathway. The E_a value reported is the energy difference calculated between the energy of the transition state structure (with $d_{C-O} = 1.96$ Å and an imaginary vibrational mode of $v_i = 309$ cm^{-1}) and the energy of the initial state structure that has CO in the ft configuration. The final state structure has C and O coadsorbed in their most stable sites (see Figure 5.2), the fourfold hollow (fh) sites. For the CO dissociation reaction, an activation barrier of $E_a = 1.19$ eV and an exothermic value for the reaction $E_{CO\rightarrow C+O} = -0.35$ eV was calculated. These calculations are in close agreement with previous theoretical DFT studies. Soresecu [1] calculated these pathways with the PW91 E$_{xc}$-functional and reports an activation barrier of $E_a = 1.06$ eV with the heat of reaction exothermic ($E_{CO\rightarrow C+O} = -0.43$ eV (10 kcal/mol)), while Bromfield et al. [2], using the RPBE as E_{xc}-functional, reports a higher barrier of $E_a = 1.16$ eV and $E_{CO\rightarrow C+O} = -0.34$ eV at $\theta = 0.25$ ML.

NH_3 adsorption on Fe(100)

The adsorption of NH_3 and its decomposition fragments NH_2, NH and N on Fe(100) was evaluated at various coverages (see Table 5.8 and Figure 5.3) and are discussed in the following subsections. The dehydrogenated fragments NH_2, NH and N can be calculated with reference to the radicals in the gas phase ($NH_2\cdot$, $NH\cdot$ and $N\cdot$). In this work an alternative route is however

Table 5.6: Adsorption energies calculated for the adsorbates NH$_3$, NH$_2$, NH and N on the high symmetry sites (at - atop, br - bridge and fh - fourfold hollow) on the Fe(100) surface at a coverage of $\theta = 0.25ML$. ZPVE$_c$ are not included. (GGA-RPBE, $E_{cut} = 400\,eV$, k-points: 5x5x1)

	$\mathbf{E_{ads}^{no-ZPE}}$ **(eV)** $\theta = \mathbf{0.25ML}$			
Site	**NH$_3$**	**NH$_2$**	**NH**	**N**
(at)	-0.25	-0.11	0.91	1.09
(br)	n/a	-0.67	0.07	0.46
(fh)	n/a	0.27	-0.63	-0.98

followed, where the adsorption energy for these fragments are calculated by incorporating the adsorption of a H atom on a distinct Fe(100) surface. The adsorption energy is thus calculated by using Eq. 5.5

$$E_{ads_{NH_x}} = E_{NH_x+slab} + (3-x)E_{H+slab} - (4-x)E_{slab} - E_{NH_3(g)} \tag{5.5}$$

where E_{NH_x} is the adsorption energy of the NH$_x$ fragment, E_{NH_x+slab} is the optimized energy of the NH$_x$ fragment on the slab, E_{H+slab} is the adsorption energy of a hydrogen atom on its favored site on a distinct Fe(100) surface and $E_{NH_3(g)}$ is the gas phase energy of NH$_3$. To get an overall view of the NH$_3$ synthesis reaction, the calculation of the adsorption of molecular N$_2$ are inluded at $\theta = 0.25$ ML on Fe(100). The coadsorption of NH$_x$ and H are included a section below, and its results are further elaborated on in Appendix B. In Table 5.6, the energies calcualted for the NH$_x$ ($x = 3$, 2, 1, 0) at the at, br and fh sites with $\theta = 0.25$ ML on Fe(100) are presented without any zero point energy corrections. For all the NH$_x$ adsorbates a strong preference for their respective stable adsorption sites is calculated. The vibrational analysis (see Table 5.7) showed that some of the vibrational modes contained one or more imaginary modes, indicating that not all the optimized structures were at a local minimum on the PES.

NH$_3$ adsorption

At $\theta = 0.25$ ML, stable adsorption for NH$_3$ was found only at the atop site (see Table 5.6 in Appendix B) with a weak adsorption energy of $E_{ads,NH_3} = -0.17$ eV. Attempts to adsorb NH$_3$

Table 5.7: The vibrational modes calculated for NH_x with x = 3, 2, 1, 0, when adsorbed on the Fe(100) surface at a coverage of $\theta = 0.25$ ML.

Adsθ	**Site**	**v(cm^{-1})**	**n(i)**	**ΔZPE(eV)**
NH_3	(at)	3501, 3500, 3368, 1608, 1603, 1097, 434, ... 426, 224, 101, 89, 83	0	0.08
NH_2	(at)	3539, 3436, 1488, 501, 494, 287, 110, 96, 49(i)	1	-0.20
	(br)	3482, 3385, 1488, 626, 612, 531, 402, 293, 142	0	-0.14
	(fh)	3252, 3175, 1513, 587, 452, 350, 244, 154, 126	0	-0.21
NH	(at)	3415, 655, 35, 41(i), 279(i), 290(i)	3	-0.47
	(br)	3342, 611, 507, 392, 380, 71(i)	1	-0.40
	(fh)	3234, 573, 570, 355, 263, 261	0	-0.40
N	(at)	946, 113, 53	0	-0.57
	(br)	577, 423, 91(i)	1	-0.58
	(fh)	409, 407, 395	0	-0.56

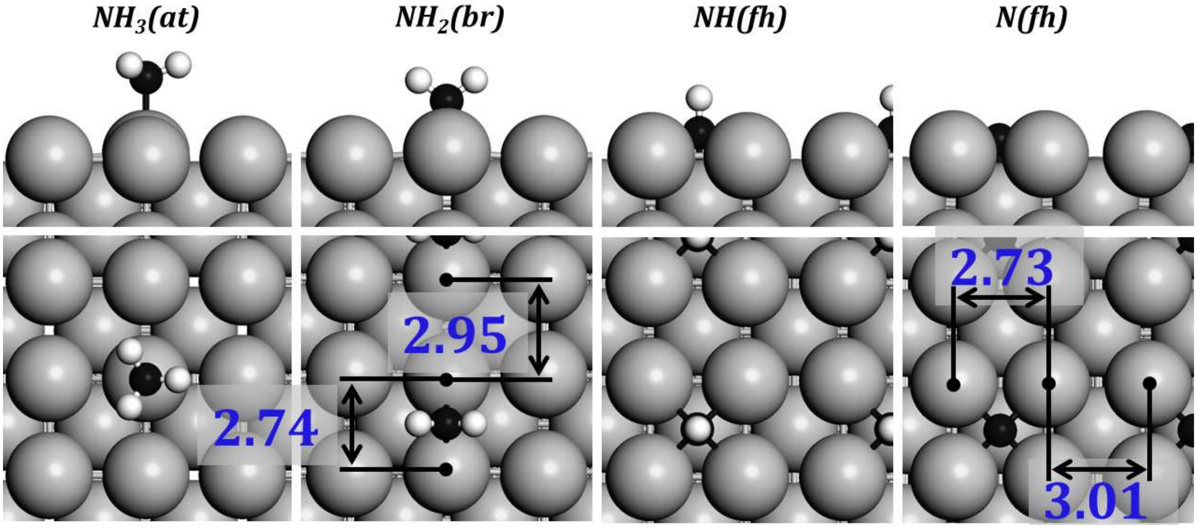

Figure 5.3: The most stable configurations obtained for NH_3, NH_2, NH and N on the Fe(100) surface with $\theta = 0.25$ ML. Note how the d_{Fe-Fe}-values are influenced by the presence of the NH_x surface species.

Table 5.8: Most stable site, coverage, average adsorption energies and geometry for NH_x on Fe(100). (GGA-RPBE, $E_{cut} = 400\,eV$, k-points: 5x5x1)

Species	Site	θ	cell	$\Delta H_{ads,NH_x}$ (eV)	d_{N-H} (Å)	d_{N-Fe} (Å)
NH_3	(at)	0.063 ML	1/16[f]	-0.35 ($-0.43 \leftrightarrow -0.52$)[c]	1.01	2.20
	(at)	0.11 ML	1/9	-0.28	1.02	2.22
	(at)	0.25 ML	1/4	-0.17	1.03	2.25
	(at)	0.50 ML	1/4	-0.04	1.03	2.29
NH_2	(br)	0.11 ML	1/9	-0.75	1.02	2.04
	(br)	0.25 ML	1/4	-0.77	1.02	2.05
	(br)	0.50 ML	1/4	-0.74	1.03	2.01
NH	(fh)	0.11 ML	1/9	-0.98	1.03	2.06; 2.48[b]
	(fh)	0.25 ML	1/4	-1.03	1.03	2.12; 2.17[b]
$(trans)$	(fh)	0.50 ML	1/4	-0.97	1.03	2.11; 2.10[b]
N	(fh)	0.11 ML	1/9	-1.44	–	1.96; 2.01[b]
	(fh)	0.25 ML	1/4	-1.54	–	1.98; 1.98[b]
$(trans)$	(fh)	0.50 ML	1/4	-1.45	–	1.90; 1.90[b]
N[a]	(fh)	0.25 ML	1/4	-2.26 (-2.26)[d]	–	1.98; 1.98[b]
$(trans)$	(fh)	0.50 ML	1/4	-2.26	–	1.90; 1.90[b]
N_2	(fh)	0.25 ML	1/4	-0.28 (-0.21)[e]	–	1.98; 1.98[b]
H	(fh)	0.25 ML	1/4	-0.39	–	2.12, 1.73[b]

[a] Nitrogen atom adsorbed with respect to nitrogen in the gas-phase (N_2(g)).

[b] Nitrogen atom bonded to second layer Fe atom.

[c] Exp. reference [8].

[d] Exp. reference [9].

[e] Exp. reference [9].

[f] 1/16, 1/9 and 1/4 refers to the use of p(4x4), p(3x3) or p(2x2) surface unit cells respectively.

at the remaining two sites resulted in the molecule migrating away from the surface during the geometry optimization calculation. The calculated N–H bond length is the same as for ammonia in the gas phase (1.03 Å) while the newly formed bond distance (Fe–N) is 2.25 Å. This optimized structure, where ammonia bonds via the lone pair of the nitrogen atom to the atop site, is consistent with what has been deduced experimentally [18] and calculated theoretically [9–12] on Fe surfaces. Temperature programmed desorption (TPD) spectra obtained by Grunze et al. [18] for Fe(111) and Fe(100) surfaces is characterized by three peaks with maxima at 160 K, 210 K and 310 K (β_1, β_2, β_3) respectively. It should be noted that the aforementioned experimental work was complicated by non-ideal experimental conditions as stressed by the authors [18]. The TPD spectra for the Fe(100) were reported to be similar to that of the Fe(111) surface, and a broad peak was observed between 160 to 210 K, leading Grunze et al [18] to estimate a similar adsorption energy that ranges between −0.43 and −0.52 eV for this surface (Fe(100)). The third peak, β_3, resembled a second order reaction and was associated with the recombination of NH_2 and H and subsequent desorption as NH_3. The deviation between our calculated adsorption energy ($E_{ads,NH_3} = -0.17$ eV at $\theta = 0.25$ ML) and the experimentally obtained values (between $E_{ads,NH_3} = -0.43$ and −0.52 eV and) could in part be explained by considering lower coverages. Based on the preference for the NH_3 to be adsorbed at the atop site at $\theta = 0.25$ ML, only this configuration were evaluated at lower coverages. At the lowest coverage ($\theta = 0.063$ ML) an adsorption energy of $E_{ads,NH_3} = -0.35\, eV$ was calculated, which is considerably closer to that inferred experimentally. If one now consider NH_3 adsorption at the various coverages, including $\theta = 0.50$ ML, a dramatic coverage dependence (see Table 5.8) is found, which could be expected due to NH_3-NH_3 lateral interactions [42]. Calculating the differential heat of adsorption for NH_3 using Eq. 5.3 and the energies calculated at the coverages $\theta = 0.25$ and 0.50 ML, an endothermic energy value is calculated ($E_{ads}^{diff} = +0.09$ eV). This would suggest that the saturation coverage for NH_3 occurs at $\theta < 0.50$ ML.

In Table 5.9 the NH_3 adsorption energies reported in other DFT and experimental studies for various Fe facets are compared with the results calculated here for NH_3 adsorption on Fe(100). Yeo et al. [13] recently published their investigation of the decomposition of NH_3 on an Fe(100) surface, making use of periodic DFT calculations. They made use of the PBE exchange correlation functional and calculate an adsorption energy of −0.92 eV, which “overbinds” by ∼

Table 5.9: Experimentally- and theoretically-determined values for the average adsorption energy of NH_3 on the atop site on model Fe surfaces available in literature. These values are compared with the current work.

Study	**Surface**	θ	$\mathbf{E_{ads}}$	$\mathbf{E_{xc}}$	**Ref.**
Exp.					
	Fe(100)	$(n.s.)^a$	$\beta_1 \rightarrow -0.43$		[18]
	& Fe(111)		$\beta_2 \rightarrow -0.52$		
	Fe(110)	$(n.s.)$	$\beta_1 \rightarrow -0.43$		[43]
			$\beta_2 \rightarrow -0.74$		
p-DFT^b					
	Fe(100)	0.11 ML	−0.92	PBE	[13]
		0.063 ML	−0.35	RPBE	This work
		0.11 ML	−0.28	RPBE	
		0.11 ML	−0.60	PW91	
		0.25 ML	−0.17	RPBE	
		0.25 ML	−0.44	PW91	
	Fe(111)	0.11 ML	−0.70		[12]
	Fe(211)	0.11 ML	−0.79	PW91	[11]
		0.11 ML	~ -0.34	RPBE	[11]
c-DFT^b					
	Fe_{10} $(Fe(110))$		−0.65	B3LYP	[9]
	Fe_{10} $(Fe(111))$		−0.91	B3LYP	[9]
	Fe_{55}		−0.37	RPBE	[10]

[a] n.s. → information not specified in relevant literature

[b] Periodic or cluster based DFT results respectively

0.40 eV from the experimentally determined value [18] and 0.64 eV compared to calculation with the RPBE-E_{xc} reported in this work at the same coverage ($\theta = 0.11$ ML, $E_{ads,NH_3} = -0.28$ eV). This could be due to their choice of exchange-correlation functional. In addition, they do not report the inclusion of zero point vibrational corrections, which would result in a weaker (~ 0.08 - 0.10 eV) adsorption energy (see Table 5.2 in Chapter 4). The periodic calculations of Mckay et al. [11] on a model Fe(211) surface finds the most stable energy to be $\Delta E_{ads,NH_3} = -0.79\,eV$ at the atop site. This surface plane has an open structure, which would typically contain several high coordination sites to accomodate adsorbates, but adsorption at the atop site should not necessarily result in a more stable adsorption energy for this plane. They however make use of the PW91 functional as exchange correlation functional, which is notorious to overestimate adosrbate-metal binding energies. It is therefore important to note, that when they recalculated the heats of adsorption for their most stable configurations with the use of the RPBE functional to treat the exchange correlation energy, they found a difference of $\sim$ 0.45 eV, which indicates that their heats of adsorption is closer to the values calculated in the present study. To verify this assumption, a similar procedure was followed by recalculating $\Delta E_{ads,NH_3}$ using the PW91 functional. The use of the PW91 to the calculate NH_3 adsorption on Fe(100) produced a value of $\Delta E_{ads,NH_3} = -0.44$ eV at $\theta = 0.25$ ML which falls within the experimentally obtained value. However, at $\theta = 0.11$ ML coverage, NH_3 overbinds with the Fe surface ($\Delta E_{ads,NH_3} = -0.60\,$eV) when compared to the experimentally determined value (between -0.43 and -0.52 eV [18]), which would expected to be even lower at at a lower coverage (e.g. $\theta = 0.062$ ML). On the other open and corregated Fe(111) plane, Lin et al. [12] calculates $\Delta E_{ads,NH_3} = -0.70$ eV, which deviates from the experimentally determined value. This is interesting since, unlike the Fe(211), these calculations were obtained with the same E_{xc} functional employed in the current paper. On a nanosized cluster Lanzani and Laasonen [10] find the most stable adsorption at the atop site with $\Delta E_{ads,NH_3} = -0.37\,eV$ and the cluster work communicated by Satoh et al. [9] which represents the Fe(110) and Fe(111) facets are found to be $\Delta H_{ads,NH_3} = -0.65$ eV and $\Delta E_{ads,NH_3} = -0.97$ eV respectively.

In summary, the adsorption energy values calculated for NH_3 adsorption on the Fe(100) facet is similar to that reported in previous studies. The error introduced as a consequence of the chosen computational methodology (in particular the choice of exchange-correlation energy functional) is evident from reviewing the various studies.

NH_2 adsorption

After evaluating all the high symmetry sites, the NH_2 fragment were found to be stable on both the atop and bridge sites on the Fe(100) surface (see Table 5.6 in Appendix B). The bridge site was energetically favored for NH_2 adsorption at both $\theta = 0.25$ and 0.50 ML coverages with adsorption energies of $\Delta E_{ads,NH_2} = -0.77$ and -0.74 eV respectively and Fe-N bond lengths of 2.05 Å, indicative of pronounced Fe-N interaction when compared to NH_3 adsorption (see Table 5.8). When NH_2 is adsorbed in the bridge position, the iron atoms bound to the adsorbate are shifted by ~ 0.10 Å towards the nitrogen atoms and has the consequence of creating a site for coadsorbed hydrogen (see Figure 5.4) that is analogous to the three-fold hollow site adsorption of H on the Fe(111) surface [4]. This coadsorbed state has a slightly weaker bonding energy ($\Delta E_{ads,NH_2+H} = -0.72$ eV) than NH_2 on its own. When hydrogen is coadsorbed in the bridge site, the same adsorption energy is calculated. Mckay et al. [11] calculate the heat of adsorption for NH_2 to be $\Delta E_{ads,NH_2} = -2.00$ eV for the Fe(211) facet. They however report a ~ 0.45 eV additional discrepancy as a result of the choice of functional (PW91). Their Fe-N bond lengths (1.94 and 1.96 Å) also suggest that the Fe(211) surface allows for increased bonding interaction between the nitrogen and iron atoms. Lin et al. [12] calculated their adsorption energies with reference to the NH_2 radicals, which results in an adsorption energy of -2.81 eV. This value deviates significantly from the bonding energies estimated by Ertl [44] for NH_2 adsorption on an iron surface ($\Delta E_{ads,NH_2} = ca - 0.94$ eV), which was based on a body of experimental surface science studies that investigated the interaction of NH_3 with the lower Miller indices of Fe.

NH adsorption

The NH fragment was found to be the most stable in the fourfold hollow position and it is important to note that the other sites (bridge and atop) were much less stable (by 0.70 eV and 1.5 eV respectively, see Table 5.6 in Appendix B). This was true for both coverages investigated (i.e. $\theta = 0.25$ and 0.50 ML) where similar adsorption energies were calculated ($\Delta H_{ads,NH} = -1.03$ and -0.97 eV respectively). In the fourfold-hollow site the nitrogen atom is co-ordinated to four iron atoms, thus interrupting the preferred quasi-tetrahedral geometry. The Fe-N bond lengths

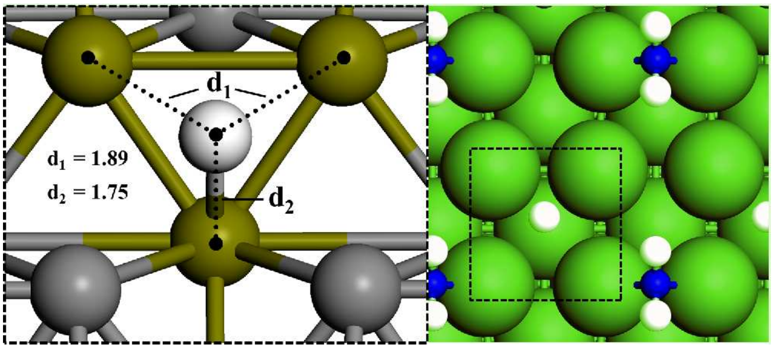

Figure 5.4: (Left) The iron atoms (color: brown) and their distances to H are indicated on an enlarged view to illustrate the three-fold-like adsorption site. (Right) H adsorbed in a quasi three-fold adsorption site when adsorbed in the presence of NH_2. (GGA-RPBE, $E_{cut} = 400\,eV$, k-points: 5x5x1)

varied between 2.11 and 2.17 Å and the N–H bond remained unchanged ($d_{N-H} = 1.03$) when compared to NH_3 in the gas phase. When NH is coadsorbed with hydrogen, it is calculated that H situated in the fh site is the most stable ($\Delta H_{ads,NH+H} = -1.00$ eV), but here the NH bond was found to be slightly tilted from the higher symmetrical perpendicular configuration. Mckay et al. [11] showed that the NH fragment would preferentially bond in a three-fold hollow site on the 'open' Fe(211) surface with a bonding energy of $\Delta E_{ads,NH} = -2.04$ eV. Preferential adsorption in the three-fold co-ordinated site were corroberated by work of Lin et al. [12]. However, even though the Fe(211) and (111) are assumed to have similar reactivity [45], they calculate the adorption energy to be $\Delta E_{ads,NH} = -4.03$ eV, deviating from the experimentally estimated [44] bonding energy ($\Delta E_{ads,NH} = -1.29$ eV) for NH on iron surfaces.

N adsorption

Similar to NH adsorption, the fourfold hollow site were found to be the most stable for N adsorption on the Fe(100) surface (see Table 5.6 in Appendix B). In a detailed theoretical study performed by Mortensen et al. [46], they show the superior despriction of the RPBE over PW91 for nitrogen adsorption on Fe(111),(100) and (110) surfaces as well as the accuracy with which one can predict the geometry of the experimentally determined configuration by comparing their calculated results with that of Bozso et al. [47]. When ΔZPE is included, the adsorption energy of N is found to be $\Delta H_{ads,NH} = -1.03$ and -0.97 eV at $\theta = 0.25$ and 0.50 ML coverages respectively (see Table 5.8). Similar to NH_2 adsorption, the iron atoms are moved towards the nitrogen atom and in doing so providing a three-fold co-ordinated configuration for hydrogen adsorption. In this case an adsorption energy that is 0.11 eV lower ($\Delta H_{ads,N+H} = -1.55$ eV) is calculated compared to the case where the N atom is present on its own ($\Delta H_{ads,N} = -1.44$ eV). The most stable configuration of N on the Fe(211) surface were calculated to be $\Delta H_{ads,N} = -1.72$ eV [11]. If the nitrogen adsorption is calculated with respect to molecular nitrogen (N_2) as apposed to ammonia in the gas phase an adsorption energy of $\Delta H_{ads,N_2} = -2.26$ eV is obtained. This result is consistent with the experimental value obtained by Bozso et al. [47] ($\Delta H_{ads,N_2} = -2.26$ eV) and close to that calculated by Norskov et al. [46] $\Delta H_{ads,N_2} = -2.43$ eV.

Molecular N_2 and H adsorption

Calculations for the adsorption of molecular N_2 and atomic hydrogen on the Fe(100) surface at $\theta = 0.25$ ML coverage is included in this study in order to construct the full PES for the ammonia synthesis reaction (see Figure 5.8 in Section 5.3.5).

For N_2 adsorption, three stable configurations were calculated, where the vertically adsorbed N_2 is not activated ($d_{N-N} = 1.14$ Å) and the two tilted configurations have the nitrogen bond elongated ($d_{N-N} = 1.28$ Å). The heat of adsorption were $\Delta E_{ads,N_2} = -0.07 eV$ for the vertically adsorbed molecule and $\Delta E_{ads,N_2} = -0.28\, eV$ for the tilted configurations. Mortensen et al. [48] extended their study of the Fe(111) facet to include N_2 adsorption, diffusion and dissociation. Their results corresponds to what was calculated here, that is they find perpendicularly adsorbed as well tilted configurations with $\Delta E_{ads,N_2} = -0.01 \leftrightarrow -0.41\, eV$. It is interesting to note that Mckay et al. [11] find a strong heat of adsorption ($\Delta E_{ads,N_2} = -1.84\, eV$) for molecular nitrogen on Fe(211), which differs from experimentally determined results [47, 49].

The surface chemistry of hydrogen adsorbed on Fe(100) were thoroughly investigated by Sorescu [50]. Similar to his work a slight preference is calculated for H adsorption in the fourfold hollow site (with $\Delta E_{ads,H} = -0.39\, eV$) over the bridge site. Furthermore, the atop site was found to be unstable with the atomic hydrogen moving away from the Fe(100) surface during the geometry optimization.

NH_3 decomposition

In the following subsections a description is given of the PES calculated for the decomposition reactions of NH_x (with x = 3, 2, 1) on the Fe(100) surface at $\theta = 0.25$ ML.

NH_3 dehydrogenation pathway

As discussed before, NH_3 preferentially adsorbs at the atop site at a coverage of $\theta = 0.25$ ML, which was taken as the initial structure. Several possible configurations for hydrogen coadsorbed with NH_2 were found to be stable (see Table B.5 and Figure B.8 in Appendix B). All the possible routes were investigated and activation barriers (E_a) ranging between 0.70 eV and 1.10 eV were calculated. The lowest activation barrier ($E_a = 0.70$ eV) were found when the NH_2 molecule twisted and moved towards the bridge site to facilitate the bond breaking process as depicted in Figure 5.5, with $d_{N-H} = 1.44$ Å. The reaction was exothermic with $\Delta H_{NH_3 \rightarrow NH_2+H} =$ -0.56 eV. One imaginary mode were calculated confirming the transition state (v_i = 1235 cm^{-1}). For the reverse (hydrogenation) route an activation barrier of $E_a = 1.27$ eV was calculated. These results deviates from what was calculated in the recent paper for NH_3 decomposition on the Fe(100) surface by Yeo et al. [13]. They find the forward energy barrier to be $E_a =$ 0.95 eV while their reaction is less exothermic $\Delta H_{NH_3 \rightarrow NH_2+H} =$ -0.26 eV. This can again be due to their choice of exchange-correlation functional (PBE) or the possible exclusion of zero-point vibrational frequencies. It could in addition be an effect of surface coverage, i.e. that different transition state structures exists when the surface is less populated. Mckay et al. [11] used a robust approach and studied the decomposition route with an eigenvector following technique. On the more corrugated Fe(211) surface they find a barrier of $E_a = 0.42$ eV for the dehydrogenation reaction ($NH_3 \rightarrow NH_2 + H$) and 1.40 eV for the reverse/hydrogenation reaction. Lin et al. [12] assumed that nitrogen would remain at the atop site which results in an endothermic reaction. They find the activation barrier for NH_3 ($\rightarrow NH_2 + H$) dehydrogenation to be 1.23 eV.

NH_2 dehydrogenation pathway

The reactions considered for NH_2 dehydrogenation had NH_2 adsorbed in the bridge site in the initial structure and H in either the (1) bridge, (2) *cis* or (3) *trans* fourfold hollow positions for

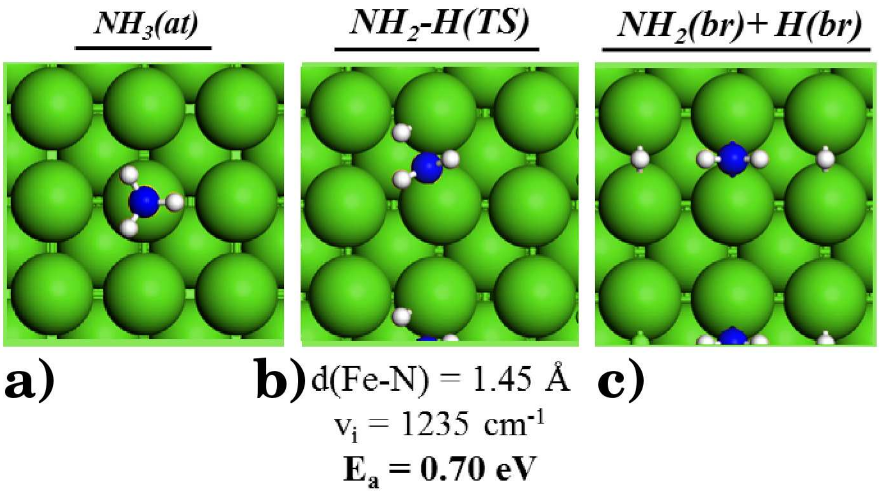

Figure 5.5: The initial, transition state and final structures for the dehydrogenation of NH_3 to NH_2 + H on Fe(100) ($\theta = 0.25$ ML, GGA-RPBE, $E_{cut} < 400\,eV$, k-points: 5x5x1; Color scheme: Fe - green, N - blue, H - white)

the decomposed NH(fh) + H products (see Fig. B.8 in Appendix B). For the NH_2 dehydrogenation routes that were calculated, activation barriers ranging between $E_a = 1.43$ and 1.60 eV was calculated. The lowest activation barrier of 1.43 eV and $d_{N-H} = 1.45$ Å had H coadsorbed in the *cis* fourfold hollow position with respect to NH on the (2 × 2) surface unit cell in the final structure (see Figure 5.6). As mentioned before the NH fragment is very unstable at the bridge and atop sites. There is no other route to avoid surface NH moving through one of these sites, leading to these high activation barriers. The reverse barrier is similarly large ($E_a = 1.63$ eV), as the product state has NH and H adsorbed in their most favored site, the fourfold hollow site. For the Fe(100) surface, Yeo et al. [13] finds an activation barrier of $E_a = 1.14$ eV, which is considerably smaller than our calculated result. The Fe(211) and Fe(111) facets similarly resulted in high dehydrogenation activation barriers ($E_a = 1.35$ eV and 1.24 eV respectively) as reported in the relevant studies [11, 12]. The hydrogenation reaction had an even higher activation barrier ($E_a = 1.43$ eV) on Fe(211). It is questionable to compare the reversed route for the Fe(111) facet, considering the endothermicity imposed by the assumptions made by Lin et al. [12].

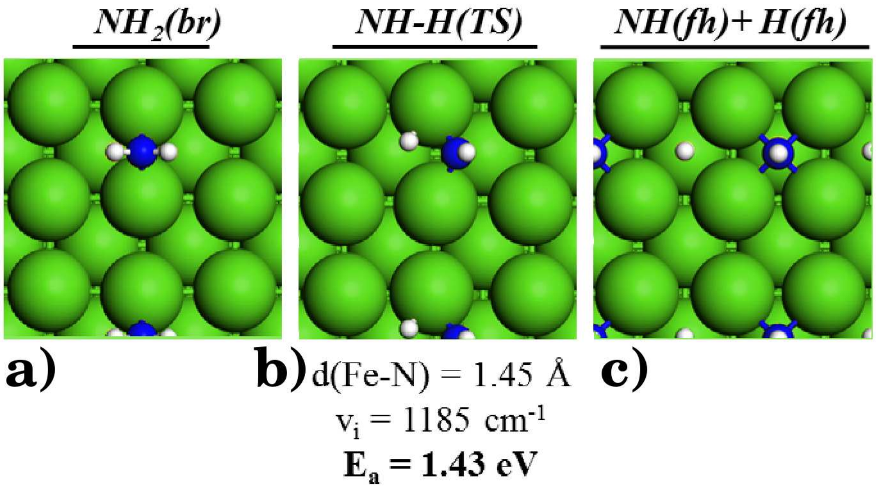

Figure 5.6: The initial, transition state and final structures for the dehydrogenation of NH_2 to NH + H on Fe(100) ($\theta = 0.25$ ML, GGA-RPBE, $E_{cut} < 400\, eV$, k-points: 5x5x1; Color scheme: Fe - green, N - blue, H - white)

NH dehydrogenation pathway

Similar to NH_2, three possible routes were investigated, with NH adsorbed in the fourfold hollow site as our initial structure and as final structures with H in the (1) bridge, (2) cis and (3) trans fourfold hollow positions for the decomposed N(fh) + H products (see Fig. B.8 in Appendix B). The activation barriers calculated varied between $E_a = 0.66$ and 1.03 eV. The MEP had the surface hydrogen product coadsorbed in the fourfold hollow site in the *cis* position with respect to the N adatom on the (2×2) unit cell, with an activation barrier of $E_a = 0.66$ eV and $d_{N-H} = 1.45$. This lower energy barrier can be attributed to surface NH and H being situated in preffered sites for the transition state structure, with N in the fourfold hollow and H in the bridge site (the bridge site is 0.03 eV less stable than the fourfold hollow site for H) respectively (see Figure 5.7). The activation barrier calculated by Yeo et al. [13] for the Fe(100) surface is higher than what is calculated here ($E_a = 0.78$ eV). The lowest activation route for the dehydrogenation of NH on the Fe(211) surface involved migration to different sites which had an overall activation barrier of 0.89 eV [11]. The periodic calculations on Fe(111) find an dehydrogenation activation barrier for NH to be 1.09 eV [12].

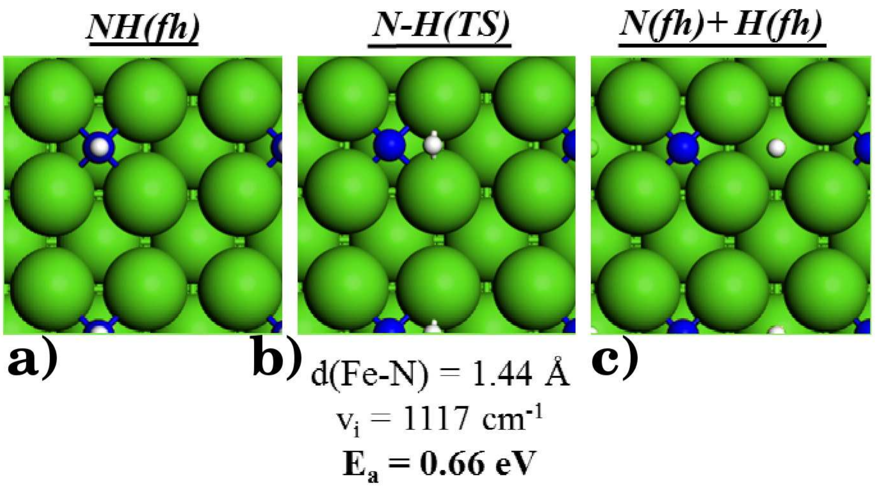

Figure 5.7: The initial, transition state and final structures for the dehydrogenation of NH to N + H on Fe(100) ($\theta = 0.25$ ML, GGA-RPBE, $E_{cut} < 400\,eV$, k-points: 5x5x1; Color scheme: Fe - green, N - blue, H - white)

PES for NH_3 synthesis

Considering the proposition that Fe-based catalysts can be used to decompose NH_3 to afford N_2, the full PES for this reaction was included in the DFT calculations (see Figure 5.8). The construction of aforementioned PES required the calculation of the adsorption and dissociation of N_2 on the Fe(100) surface. The most stable N_2 configuration resulted in a weak adsorption energy of $\Delta H_{ads,N_2} = 0.28$ eV, while the lowest N_2 dissociation activation barrier were found to be $E_a = 2.53$ eV. The N_2 decomposition reaction with the lowest barrier has the two N adatoms in a *cis* configuration, which is 0.63 eV less stable than the *trans* configuration. To cross this migration barrier an activation energy of $E_a = 1.20$ eV was calculated. In Figure 5.8 a full PES diagram for the decomposition of two NH_3 molecules to combine and form N_2 (+ 3 H_2) is presented. From these calculations it can be suggested that no appreciable N_2 formation would occur (on a model Fe(100) catalyst) at the temperatures and pressures applied during the relevant NH_3 co-feeding FTS reaction conditions (e.g. T = 523 K, P = 5 bar).

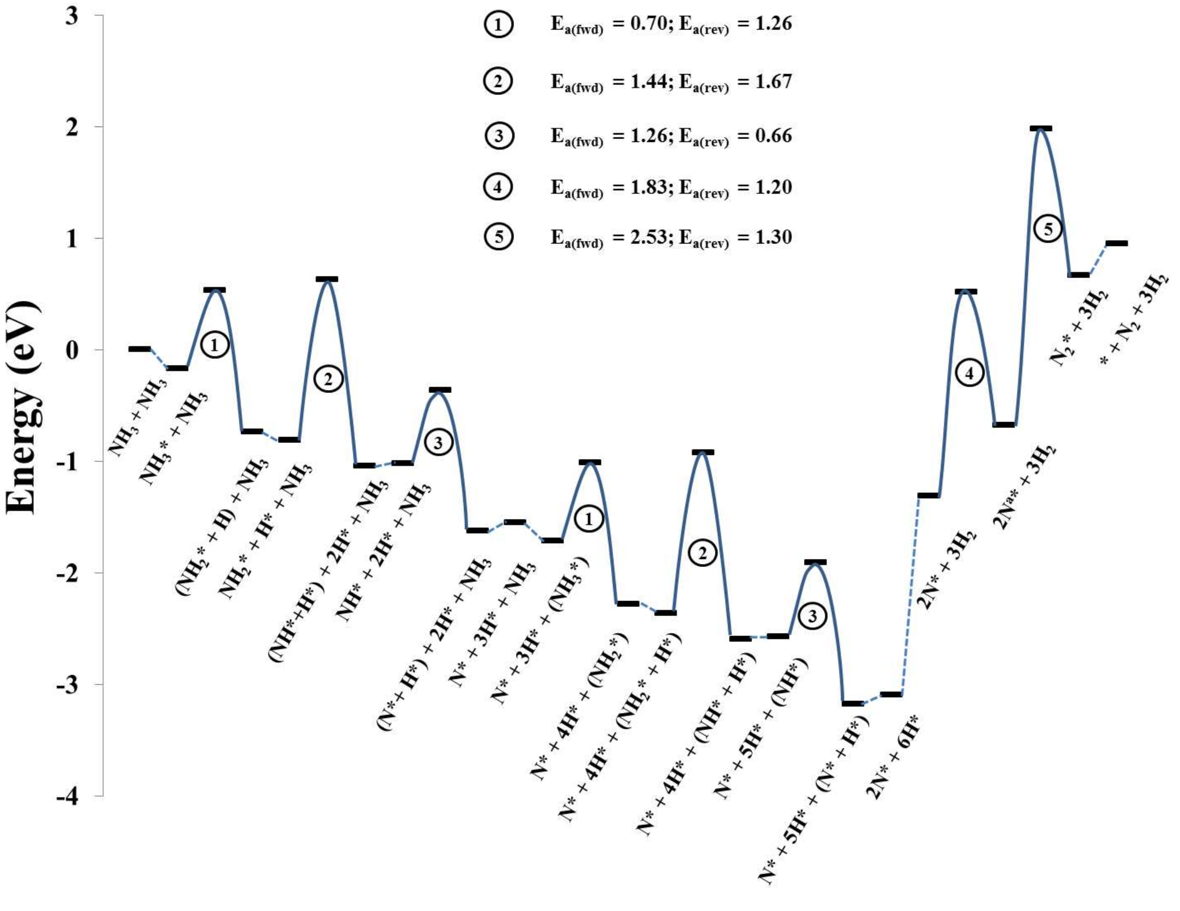

Figure 5.8: PES for NH_3 synthesis with $\theta = 0.25$ ML on Fe(100). (GGA-RPBE, $E_{cut} < 400\,eV$, k-points: 5x5x1)

PES for NH_3 and CO decomposition

The primary aim of Chapter 5 was to generate data for the individual decomposition reactions of NH_3 and CO on a model Fe(100) surface, which is then subsequently used to study their coadsorption on Fe(100) in Chapter 6. In Figure 5.9 the potential energy surfaces (PES) for the decomposition of CO (right) and NH_3 (left) on an Fe(100) surface are superimposed. Two important observations can be made by comparing the two energy profiles. Firstly, the decomposed adatom N and adsorbate CO have similar adsorption energies and prefer adsorption in the fourfold hollow site. One may thus speculate that the decomposed product N could block sites available for CO adsorption and in doing so retard the FTS reaction rate. Secondly, the highest activation barrier for NH_3 decomposition, the NH_2 dehydrogenation step is considerably high, when compared to the activation barrier of CO dissociation. The applicability of the DFT results does however benefit from analysis at higher temperatures and pressures via the use of statistical thermodynamics and microkinetic models. The remainder of this chapter makes use of these techniques to further investigate the NH_3 decomposition on Fe(100) at relevant temperatures and pressures. [3] Similar techniques were employed in a comprehensive study evaluating CO adsorption and decomposition on the Fe(100) surface were conducted by van Helden [34].

NH_3 PES at higher temperatures and pressures

In this section the calculated DFT results in combination with transition state theory (TST), stastical mechanics and microkinetic modeling were used to further probe the NH_3 decomposition at higher temperatures and or pressures. Firstly, the individual adsorption of NH_3 on a model Fe(100) surface is considered at various reaction conditions including the conditions used in the experimental part of this thesis. Secondly the DFT results for the NH_3 decomposition reaction is evaluated at $T = 523$ K and $p^*(NH_3) = 0.2$ bar, including two lower and higher temperatures ($T = 323, 423, 623$ and 723 K), to shed light on the rate limiting step if it was extended to these reaction conditions. Finally, a basic microkinetic model is developed to predict what the possible surface coverage of a catalyst in a plug flow reactor would be based on the DFT results for the PES of NH_3 decomposition on the Fe(100) surface. The general methodologies for the calculations will be discussed in the relevant subsections, but further supporting information can be found in Appendix B.

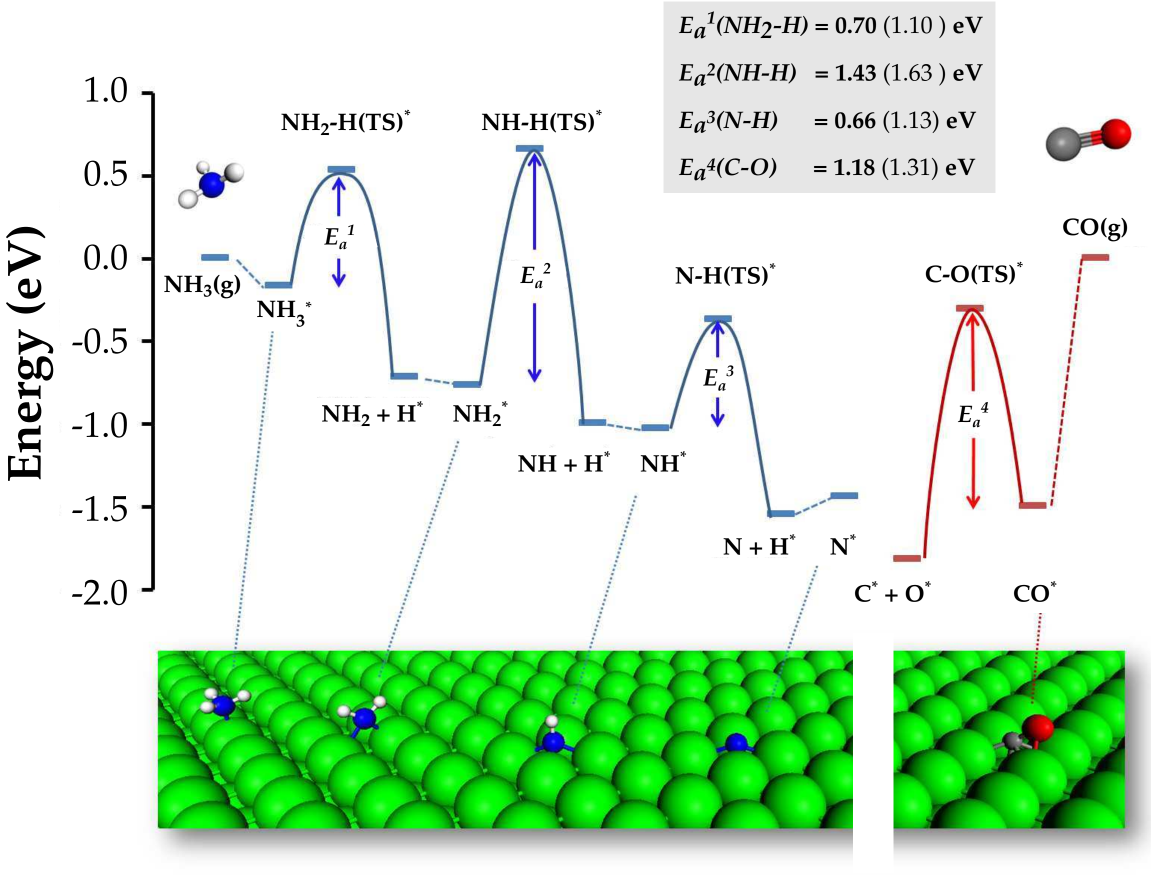

Figure 5.9: (Left - blue) Potential energy surface (PES) constructed for NH_3 adsorption and decomposition on Fe(100).; (Right - red) CO adsorption and dissociation reactions on Fe(100). Activation energy barriers for the reverse reaction are given in paranthesis. ($\theta = 0.25$ ML, GGA-RPBE, k-points: 5x5x1, Ek = 400 eV; Color scheme: Fe - green, C - grey, O - red, N - blue, H - white)

Free energy for NH_3 adsorption on Fe(100)

Since it is of interest to produce N-containing compounds, it would be beneficial to control the amount of NH_3 that adsorbs onto the catalyst surface. Parameters such as the temperature and pressure of the reaction could provide such control over this elementary reaction. To extend the DFT results obtained for the adsorption of NH_3 at 0 K at the various coverages ($\theta = 0.0625$, 0.11, 0.25 and 0.50 ML) to higher temperatures and pressures, the free energy of adsorption ($\Delta G_{ads,NH_3}$) for NH_3 on the Fe(100) surface is calculated using Eq. 5.6

$$\Delta G_{ads,NH_3} = \Delta H - (T \times \Delta S) + RTln(\frac{P}{P_0}) \tag{5.6}$$

where ΔH and ΔS are the changes in enthalpy and entropy between the gas phase and adsorbed NH_3 respectively, R is the universal gas constant and P_0 is the standard pressure (1 bar). The methodology for calculating ΔH and ΔS are outlined in Appendix B. In Figure 5.10 the results are given for the $\Delta G_{ads,NH_3}$-values as a function of increasing temperature for the four coverages calculated ($\theta = 0.0625$, 0.11, 0.25 and 0.50 ML) at two (low = 1^{-6} mbar and high = 5 bar) different partial pressures of NH_3. Since it is expected that NH_3 would loose some degree of freedom during the adsorption process, this model predicts that adsorption of NH_3 would be thermodynamically favored at lower temperatures and higher partial pressures. Many other factors could ultimately influence the adsorption of NH_3, but it is interesting to point out here that Sango [17] saw a concomitant increase in N-containing compounds with an increase in NH_3 partial pressure when co-feeding NH_3 during FTS reactions (NH_3 added: 0 - 25 vol % NH_3, CSTR, T = 270 ℃, P = 4 bar, H_2/CO = 2, GHSV = 2250 ml/hr/g_{cat}).

Free energy for NH_3 decomposition on Fe(100)

Using a similar methodology as were used for the Gibbs free energy of adsorption of NH_3, the free energy profile for the decomposition of NH_3 on Fe(100) was calculated at T = 523 K and P = 5 bar. In order to see how ΔG-values change with a change in temperature, two temperatures ± 100 and 200 K were added to the plot. If the harmonic transition state theory is applied, then the rate of the reaction (r) can be described by Eq. 5.7

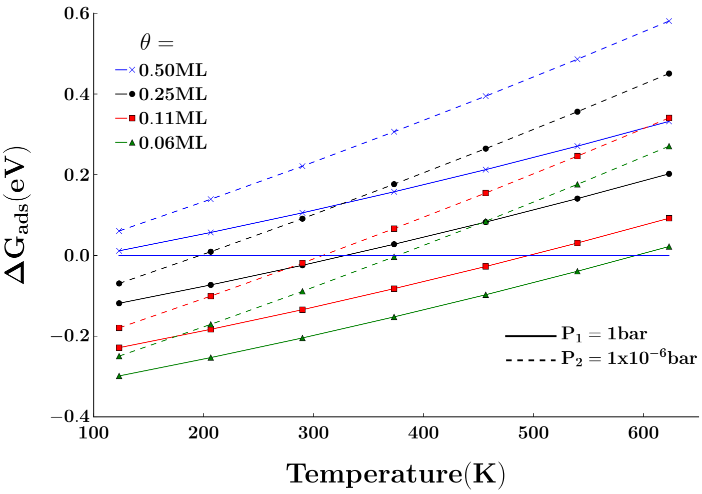

Figure 5.10: Gibbs free energy for NH_3 adsorption on Fe(100) surface as a function of coverage and pressure (low = 1^{-6} mbar and high = 5 bar)

$$r = \frac{k_b \cdot T}{h} \cdot e^{\frac{\Delta G}{k_b \cdot T}} \tag{5.7}$$

, where T is the temperature, k_b is Boltzman's constant and h is Planck's constant. These energy values can therefore serve as an indication of the potential rate limiting step for the decomposition of NH_3 on the Fe(100) surface at the temperatures and pressures used for the NH_3 co-feeding during FTS reactions. In Figure 5.11 the ΔG value for the NH_2 dehydrogenation reaction ($NH_2 \rightarrow NH + H$) would be the limiting rate at all temperatures evaluated. This would furthermore suggest that the dominant NH_x surface species could be NH_2 on a model Fe(100) surface. Evaluation of a microkinetic model would however shed further light on aforementioned assumption.

Surface species during NH_3 decomposition on Fe(100)

A basic microkinetic model was developed (see Appendix B) to estimate the population of the NH_x surface species on a model Fe(100) surface in a plug flow reactor (PFR) at the temeperatures and pressures where the NH_3 co-feeding reactions were conducted (T = 523 K, P = 5 bar). The model is based on the results calculated using DFT for the NH_3 decomposition reaction

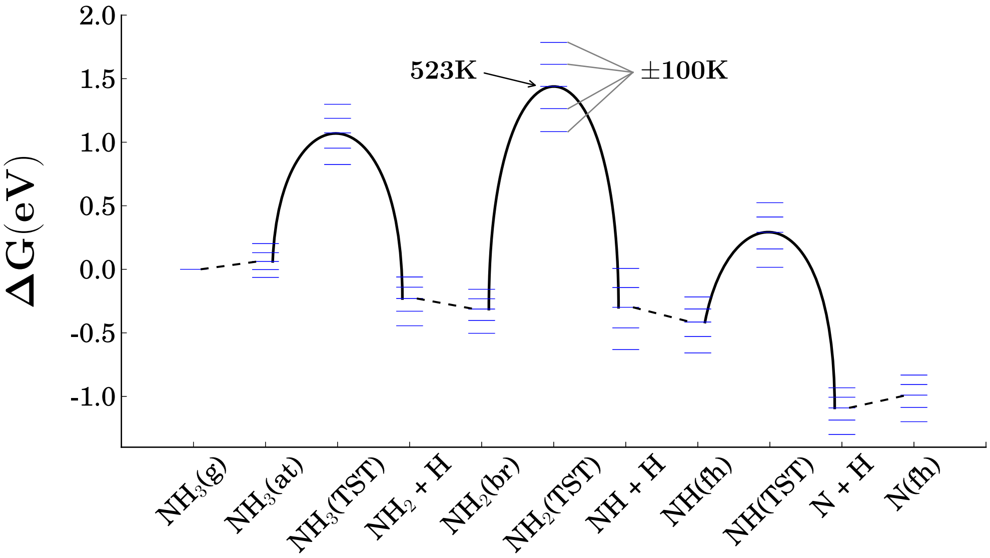

Figure 5.11: Free energy potential energy surface for the decomposition of NH_3 on a model Fe(100) surface at T = 523 K (with T ± 100 K added for comparison) and P = 5 bar. ($\theta = 0.25$ ML, GGA-RPBE, $E_{cut} < 400\, eV$, k-points: 5x5x1)

on a model Fe(100) surface at $\theta = 0.25$ ML. No assumptions were made with regards to the rate limiting step or potential site blocking. Also note that the model does not incorporate the maximum coverage for the NH_x adsorbates on the surface, which would for example be between $\theta = 0.25$ and 0.50 ML for NH_3 adsorption as inferred from the results calculated with DFT. The intention is thus only to relatively quantify the composition of the coverages for the NH_x surface species at elevated temperatures and pressures. In Figure 5.12 the results calculated for NH_3 reacting in a dimensionless reactor at four different temperatures (T = 160, 300, 523 and 700 K) is presented. At 160 K the model predicts that the Fe(100) surface would predominantly be covered with NH_3. The reaction at 300 K would predict that NH_3 initially adsorbs at a slow rate and the formation of NH_2 + H occurs towards the exit of the reactor. At 523 K the surface would predominantly be covered with NH_2 and H, while at 700 K it would mostly be covered with NH, N and H. When Henkel [16] used an iron based catalyst in a fixed bed reactor (which would behave like a PFR), the predominant N-containing compound formed during NH_3 co-feeding FTS (T = 523 K, P = 5 bar) reactions were primary amines [16]. The formation of primary amines would require NH_2 as a key reactant based on the mechanisms proposed by

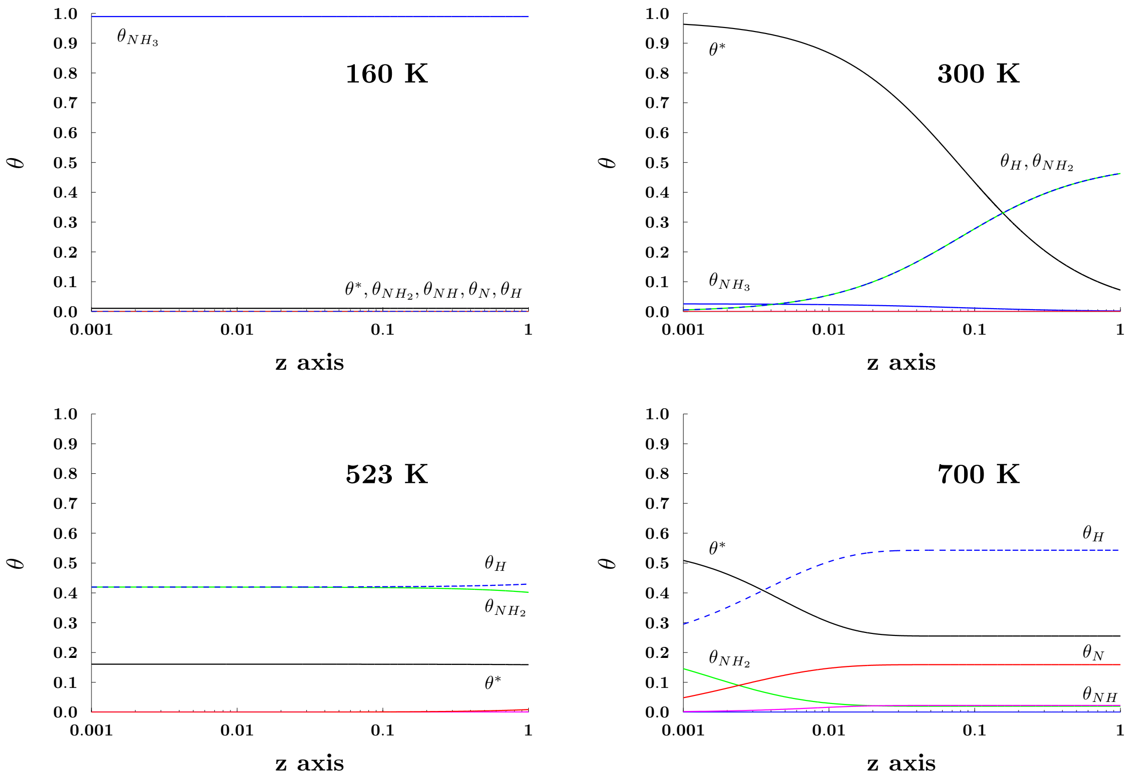

Figure 5.12: The coverage of NH_x, H and free sites (θ) as a function of dimensionless z-axis of a plug flow reactor (T = 160 K, 300 K, 523 K, 700 K, P = 5.2 bar, p_{NH_3} = 0.2 bar).

Henkel [16] and Sango [17].

Conclusions

The individual adsorption and decomposition profiles of CO and NH_x (with $x = 3, 2, 1, 0$) on a model Fe(100) surface was evaluated. The site prefferences and geometries of the adsorbates calculated were in general agreement with what has been reported in literature when DFT were used to study CO [1, 2, 28, 34] and NH_x ($x = 3, 2, 1, 0$) [13] interaction with the Fe(100) surface.

A tilted adsorbate configuration where the oxygen of CO was bonded to one Fe atom, as opposed to two were found to be stable at both the $\theta = 0.25$ ML and 0.50 ML coverages, which has not been reported in previous studies [1, 2, 34]. The heat of adsorption calculated for CO deviated from certain results obtained via DFT [1, 2, 34], but corresponded well with the values found by Jiang and Carter [28], who made use of a similar computational methodology as were employed in this work. The activation barrier calculated for CO dissociation ($E_a = 1.19$) were similar to those found by Sorescu [1] and Bromfield et al. [2], $E_a = 1.10$ and $E_a = 1.16$ respectively. Similar to the reports of lattice distortions by Pederson et al. [51] for N on the Fe(100) surface, it was calculated here that NH_2 and NH has similar effects on the Fe(100) surface. This leads to perturbations in the available sites, creating a pseudo three-fold hollow site when some of the NH_x adsorbates are coadsorbed with H. These effects play an important role when the coadsorption of CO and NH_x is considered in Chapter 6. The values calculated for the heat of adsorption of NH_3 on the Fe(100) ($\Delta E_{ads,NH_3} = -0.35$ eV) did however not correspond to the values ($\Delta E_{ads,NH_3} = -0.92$ eV) reported in a recent paper by Yeo et al. [13]. These values could in addition not be reconsiled by evaluating the adsorption energies via the use of other exchange-correlation functionals. The adsorption energy for NH_3 calculated in this study was however in closer agreement with what was determined experimentally (between $\Delta H_{ads,NH_3} = -0.43$ and $-0.52eV$) [18]. Furthermore, the activation barriers calculate here for the reactions $NH_x \pm H$, did not correspond to the values reported by Yeo et al. [13], which could be due to different pathways available on a lower coverage, as their decomposition reactions were evaluated at $\theta = 0.11$ ML, compared to the coverage considered here ($\theta = 0.25$ ML). By calculating the full PES for the NH_3 synthesis reaction, that is by including the molecular N_2 adsorption and dissociation, it was possible to speculate that N_2 formation is unlikely on the Fe(100) surface under the conditions where NH_3 are co-fed during FTS in the experimental part of this study. Comparing the PES of NH_3 and CO decomposition reactions revealed that the decomposed products, NH and N could lead to site blocking for CO during FTS on an Fe(100) surface, since these adsorbates had similar adsorption energies and they all preferred adsorption in the fourfold hollow site.

Importantly, the initial goal of this study was accomplished, which was to perform calculations for the individual decomposition of CO and NH_3 using the RPBE exchange correlation functional in order to provide a solid basis to draw comparisons between individual and coadsorption of CO and NH_3 on the Fe(100) surface, which is discussed in Chapter 6. Furthermore, these DFT results were used to explore the elementary reactions for NH_3 adsorption and decomposition at higher temperatures and pressures by combining it with transition state theory, statistical mechanics and microkinetic modelling. From the aforementioned analysis it can be suggested that NH_2 would be the rate limiting step (at $T = 523$ K and $p^* = 0.2$ bar when $\theta = 0.25$ ML NH_3 decomposition is considered on the Fe(100) facet). This is particularly interesting when considering the observation that primary amines are the dominant product in most NH_3 co-feeding FTS reactions [14, 16, 17], which led some authors [16, 17] to propose the incorporation of NH_2 adsorbates during the final desorption step in the pathway to the formation of primary amines.

REFERENCES

[1] D.C. Sorescu, D.L. Thompson, M.M. Hurley and C.F. Chabalowski, Phys. Rev. B 66 (2002) 035416–1–13.

[2] T.C. Bromfield, D.C. Ferré and J.W. Niemantsverdriet, ChemPhysChem 6 (2005) 254–260.

[3] P. van Helden and E. van Steen, J. Phys. Chem. C 112 (2008) 16505–16513.

[4] D.E. Jiang and E.A. Carter, Surf. Sci. 547 (2003) 85–98.

[5] D.W. Moon, D.J. Dwyer and S.L. Bernasek, Surf. Sci. 163 (1985) 215–229.

[6] J.P. Perdew, J.A. Chevary, S.H. Vosko, K.A. Jackson, M.R. Pederson, D.J. Singh and C. Fiohais, Phys. Rev. B 46 (1992) 6671–87.

[7] B. Hammer, L.B. Hansen and J.K. Nørskov, Phys. Rev. B 59 (1999) 7413.

[8] B. Hammer, L.B. Hansen and J.K. Nørskov, Phys. Rev. B 59 (1999) 7413–7421.

[9] S. Satoh, H. Fujimoto and H. Kobayashi, J. Phys. Chem. B 110(10) (2006) 4846–52.

[10] G. Lanzani and K. Laasonen, Int. J. Hydrogen Energy 35 (2010) 6572–77.

[11] H.L. Mckay, S.J. Jenkins and D.J. Wales, J. Phys. Chem. C 113 (2009) 15274–15287.

[12] R.J. Lin, Li F.Y. and Chen H.L., J. Phys. Chem. C 115 (2011) 521–28.

[13] S.C. Yeo, S.S. Han and H.M. Lee, J. Phys. Chem. C 118 (2014) 5309 – 5316.

[14] H. Kölbel and J. Trapper, Angew. Chem. Int. Ed. 5 (1966) 843–844.

[15] A. Rausch, C-N-kopplungen an heterogenen kobalthaltigen katalysatoren, Ph.D. thesis, Carl von Ossietzky Universität, Germany (2008).

[16] R. Henkel, The influence of ammonia on fischer-tropch synthesis and formation of N-containing compounds, Ph.D. thesis, Carl von Ossietzky Universität, Germany (2012).

[17] T. Sango, Nitrogen-containing from ammonia compounds co-feed to the Fischer-Tropsch synthesis, Master's thesis, University of Cape Town, South Africa (2013).

[18] M. Grunze, F. Bozso, G. Ertl and M. Weiss, App. of Surface Science 1 (1978) 241–265.

[19] N.D. Spencer, R.C. Schoonmaker and G. A. Somorjai, J. Catal. 74 (1982) 129–135.

[20] P.E. Blöchl, Phys. Rev. B 50 (1994) 17953 –17975.

[21] G. Kresse and J. Joubert, J. Phys. Rev. B 59 (1999) 1758–84.

[22] G. Kresse and J. Hafner, Phys. Rev. B 47 (1993) 558.

[23] G. Kresse and J. Hafner, Phys. Rev. B 49 (1994) 14251.

[24] G. Kresse and J. Furthmuller, Phys. Rev. B 11 (1996) 169.

[25] G. Kresse and J. Furthmuller, Comput. Mater. Sci. 6 (1996) 15.

[26] M. Methfessel and A.T. Paxton, Phys. Rev. B 40 (1989) 3616.

[27] H.J. Monkhorst and J.D. Pack, Phys. Rev. B 80 (1976) 890.

[28] D.E. Jiang and E.A. Carter, J. Phys. Chem. B. 110 (2006) 22213–22219.

[29] F. Birch, Phys. Rev. 71 (11) (1947) 809 –824.

[30] Kittel, Introduction to Solid State Physics, John Wiley and Sons, 1996.

[31] K.P. Huber and G. Herzberg, Molecular Spectra and Molecular Structure 4: Constants of Diatomic Molecules., Van Norstrand Reinhold Co., New York, New York, 1979.

[32] J.O.P. McBride and R.W. Nicholls, J. Phys. B: Atom. Molec. Phys. 5 (1972) 408–417.

[33] E. Weinen and E. Vanden-Eijnden, Annu. Rev. Phys. Chem. 61 (2010) 391–420.

[34] P. van Helden, Initial steps of the Fischer-Tropsch synthesis on Fe(100): The role of hydrogen, Ph.D. thesis, University of Cape Town, South Africa (2008).

[35] D.W. Moon, S. Cameron, F. Zaera, W. Eberhardt, S.L. Carr, R. Bernasek, J.L. Gland and D.J. Dwyer, Surf. Sci. 180 (1987) 123–128.

[36] L.J. Whitman, L.J. Richter, B.A. Gurney, J.S. Villarrubia and W. Ho, J. Chem. Phys. 90 (3) (1989) 2050–2062.

[37] S.E. Mason, I. Grinberg and A.M. Rappe, Phys. Rev. B 69 (2004) 161401.

[38] S. Pick, Surf. Sci. 601 (2007) 5571–5575.

[39] F. Abild-Pedersen and M.P. Andersson, Surf. Sci. 601 (2007) 1747 – 1753.

[40] D.W. Moon, S.L. Bernasek, D.J. Dwyer and J.L. Gland, J. Am. Chem. Soc. 107 (1985) 4363–64.

[41] S.D. Cameron and D.J. Dwyer, Langmuir 4 (1988) 282–288.

[42] Z. Ulissi, V. Prasad and D.G. Vlachos, J. Catal. 281 (2011) 339–344.

[43] M. Weiss, G. Ertl and F. Nitschké, App. Surf. Sci. 00 (1979) 614 – 635.

[44] G. Ertl, Angew. Chem. Int. Ed. Eng. 29 (1990) 1219–1227.

[45] P. Iyngaran, D.C. Madden, S.J. Jenkins and D.A. King, PNAS 108 (2011) 925–930.

[46] J.J. Mortensen, M.V. Ganduglia-Priovano, L.B. Hansen, B. Hammer, P. Stoltze and J.K. Nørskov, Surf. Sci. 422 (1999) 8–16.

[47] F. Bozso, G. Ertl, M. Grunze and M. Weiss, J. Catal. 49 (1977) 18–41.

[48] J.J. Mortensen, L.B. Hansen, B. Hammer and J.K. Nørskov, J. Catal. 182 (1999) 479–488.

[49] D. Haneman, Surf. Sci. 375 (1997) 71–80.

[50] D. Sorescu, Catal. Today 105 (2005) 44–65.

[51] M.O Pederson, L. Osterlund, J. Mortensen, M. Mavrikakis, L.B. Hansen, I. Stengaard, E. Laegsgaard, J.K. Nørskov and Besenbacher F., Phys. Rev. Letters 84 (2000) 4898–4901.

CHAPTER 6

COADSORPTION OF CO AND NH$_x$ ON A MODEL FE(100) SURFACE

CO adsorption and dissociation are considered by many to be important elementary reactions for Fischer-Tropsch synthesis (FTS) pathways. In this chapter the influence that NH_x *(with* $x = 3, 2, 1, 0$*) adsorbates have on these elementary reactions is studied through periodic density functional theory (DFT). A comprehensive set of DFT calculations for the individual adsorption and decomposition of CO and* NH_3 *on Fe(100) was presented in Chapter 5 and is used here to study the changes that occur upon coadsorption. A geometry optimized (2 × 2) Fe(100) surface unit cell containing* $\theta = 0.25$ *ML* NH_x *surface species is used to perform a geometry optimization with CO adsorbed in its favored sites as calculated in Chapter 5. In order to gain additional information, a (3 × 3) surface unit cell was used to calculate some of the most stable coadsorption structures at* $\theta = 0.11 + 0.11$ *ML CO +* NH_3 *on Fe(100). Furthermore, the 0.25 + 0.25 ML CO +* NH_x *on Fe(100) coadsorption is compared with the individual adsorption of CO and* NH_x *at* $\theta = 0.50$ *ML. Adsorbed CO is stabilised in tn the presence of* NH_x *adsorbates, with the exception of* NH_2*. The heat of mixing (*ΔE_{mix}*) at a coverage of* $\theta = 0.25 + 0.25$ *ML is exothermic and further supports the notion of stabilization by* NH_3*, NH and N, while repulsive lateral interactions and island formation is predicted for* NH_2 *adsorption. The evaluation of the changes in the electronic structure by calculation of the Bader charges, the projected density of*

states (PDOS) and electron redistribution plots provide insight into the stabilization or destabilization predicted by the ΔE_{mix} *values. Finally, by calculating the CO dissociation reaction in the presence and absence of* NH_x *adsorbates on the Fe(100) surface, it is possible to compare the effect these adsorbates have with previous DFT studies where CO was coadsorbed with a promoter (K) [1] or a poison(S) [2] on the Fe(100) surface. This evaluation suggests that the overall effect on CO adsorption and dissociation is complex and that* NH_3 *and its decomposed fragments can behave like a promoter or a poison in certain cases.*

Introduction

The deliberate introduction of NH_3 with a conventional synthesis gas feed ($CO + H_2$) during Fischer-Tropsch synthesis (FTS) leads to the formation of valuable N-containing compounds [3–8] in addition to the conventional FTS products. Despite the interest in this route to produce valuable N-containing chemicals, little is known about the underlying mechanisms that are responsible for the formation of the N-containing compounds. Based on the observation that the primary amines were the major N-containing products reported in most NH_3 co-feeding (during FTS) studies [3–8], Henkel [7] and Sango [8] suggested the incorporation of an NH_2 surface species into the growing chain during the desorption step. It was shown in Chapter 5 that NH_2 might have a longer lifespan on a model Fe(100) catalyst surface compared to the other NH_x surface species, and may thus be readily available during the latter stages of the pathway to the formation of N-containing compounds. By studying the coadsorption of CO and NH_x on Fe(100), an improved view can be gained of the role that the NH_x surface species have during the initial stages of the pathway towards the formation of N-containing compounds. For example, an important aspect to consider when NH_x surface species are present during FTS, is that certain surface species (e.g. H, K, Na, Cl, S, NH_3) coadsorbed with CO on transition metal surfaces can influence the adsorption and dissociation of CO, which are important elementary reactions in several proposed FTS mechanisms [2, 9–12]. NH_3 is generally grouped with the FTS catalyst poisons [13]. Conversely, Henkel [7] compared FTS reactions (using a precipitated Fe-based catalyst, fixed bed reactor, $T = 270$ °C, $P = 4.0$ bar, $H_2/CO = 2.0$, GHSV = 1920 ml/hr/g_{cat}) with either potassium promotion or NH_3 co-feeding during FTS, and concluded that the presence of K and NH_3 during FTS leads to the same trends in CO consumption and FTS product formation. It is known that K addition to a model Fe(100) surface stabilizes CO adsorption and lowers the activation energy for CO dissociation.

An indication of the degree and nature of the interaction between coadsorbates can be obtained by looking at the changes in the bond lengths, adsorption energies and electron densities. Experimental surface science techniques, such as temperature programmed desorption experiments (TPD), can often provide insight that can indicate how the coadsorbed surface species may influence the CO$-$metal (i.e. the modified transition metal) interaction. However, the determination of the heat of adsorption for CO on an NH_3-modified surface ($\Delta E_{ads,CO'}$) via experiment proves to be problematic, since the desorption of NH_3 occurs at much lower temperatures than that of CO [16].

Theoretical studies present an alternative route to investigate possible lateral interactions that exist between coadsorbates present on a metal surface. In previous density functional theory (DFT) studies, for example, the heat of adsorption for CO on K [11] and S [2] precovered Fe(100) surfaces has been calculated by subtracting the energies calculated for the sum of the precovered surface (E_{Ads}, $Ads = K, S$) and the gaseous CO ($E_{CO(g)}$), from the energy of the optimized coadsorbed structure (E_{CO+Ads}).

$$\Delta E_{ads,CO'} = E_{CO+Ads} - (E_{CO(g)} + E_{Ads}) \tag{6.1}$$

These calculated energies can in turn be used to quantify the lateral interactions between the coadsorbates [17, 18].

In addition to quantifying the lateral interactions between CO and NH_x, it is also possible to use the computational results to predict if it is thermodynamically feasible for adsorbates to mix on the Fe(100) surface, or if segregation into islands of CO and NH_x is preferred. Ciobîcă et al. [17] made use of periodic DFT calculations to calculate the Gibbs free energy of mixing for CO and H on a Ru(0001) surface and showed that mixed states are not thermodynamically feasible for these coadsorbates. A similar approach was followed by van Helden and van Steen [12] when they studied the coadsorption of CO and H on an Fe(100) surface. They proposed that the formation of mixed layers of CO + H on Fe(100) would be favored above island formation for certain configurations of CO and H ($\theta_{CO} = 0.25/0.50$ ML + $\theta_H = 0.00/0.25/0.50/0.75/1.00$ ML) [12]. These calculations allowed for an improved understanding of the role of H in FTS [19]. To the knowledge of the author, no experimental results are available that would suggest the feasibility of CO and NH_x coadsorption on the Fe(100) or other model Fe surfaces. The surface chemistry of CO + NH_3 on other model surfaces has however been probed experimentally via various surface science techniques [16, 20–23]. These studies generally concluded that a synergistic effect occurs when these adsorbates are both present on the surface. Sasaki et al. [20] investigated the coadsorption of CO and NH_3 on a Ru(001) facet via the use of low-energy electron diffraction (LEED), TPD and high-resolution electron energy-loss spectroscopy (HREELS). The LEED spectra indicated that mixed ordered overlayers of CO and NH_3 formed within p(2 × 2) unit cells when exposing a CO pre-covered Ru(001) surface to NH_3 at 100 K. Depending on the CO surface coverage, a two to one NH_3/CO (α-phase) or CO/NH_3 (β-phase) coverage ratio was observed within the (2 × 2) structures. The presence and surface coverage of CO seemed to influence the NH_3 decomposition rate, where the β-phase (0.50 ML CO + 0.25 ML NH_3 within a p(2 × 2) unit cell) allowed 4-6 times faster NH_3 decomposition than the α-phase (0.25 ML CO + 0.50 ML NH_3 within a p(2 × 2) unit cell). The differences in the NH_3-decomposition rates were attributed to a tilting of the C_{3v} axis of the NH_3 molecule derived from the HREELS spectra, which was in turn ascribed to an increased electron donation between CO and NH_3 via the Ru(001) surface. The tilting of the NH_3 molecule's C_{3v} axis was corroborated in a separate study by Sasaki and Iwasawa [24], where an electron stimulated desorption ion angular distribution (ESDIAD/TOF) technique was employed to monitor coadsorption of CO and NH_3 on Ru(001). In order to fundamentally probe questions regarding the extreme poisoning effect of NH_3 during cobalt catalyzed FTS, Kizilkaya et. al [23] used UHV experiments (including TPD, work function measurements, Reflection-absorption infrared spectroscopy (RAIRS) and LEED) and DFT calculations to evaluate individual NH_3/CO adsorption and CO + NH_3 coadsorption on a model Co(0001) surface. Similar to the Ru(001) surface, the coadsorption of CO and NH_3 on the Co(0001) surface resulted in the formation of a stable coadsorbed layer [23]. The authors ascribed the attractive lateral interactions revealed by their experiments to be due to a combination of electrostatic interactions between CO and NH_3 and changes brought about within the electronic structure upon coadsorption.

Theoretical studies that investigate the coadsorption of CO and NH_x on metal surfaces are less populated, and appear to be non-existant for the Fe(100) surface. Curulla-Ferré et al. [25] made use of periodic DFT calculations of coadsorbed CO + N on a Rh(100) surface to demonstrate the adequate accuracy of the pairwise additive potential approximation for representing adsorbate-adsorbate interactions. After they calculated several permutations and combinations of CO and N on the Rh(100) facet, they report that CO and N have repulsive lateral interactions on the Rh(100) surface.

Moon and co-workers [10] experimentally determined that S preadsorbed on the Fe(100) surface, slows down the kinetics for CO dissociation by blocking sites needed for CO dissociation. These results were corroberated by the periodic DFT calculations performed by Curulla-Ferrè et al. [2]

that was performed to study the direct activation of CO on an Fe(100) surface covered with θ_S = 0.25 or 0.50 ML of sulfur. They calculated similar activation energies for CO dissociation in the presence and absence of the sulfur on the Fe(100) surface. However, the exothermic dissociation reaction became slightly endothermic due to the presence of the S adatoms.

In this chapter, periodic density functional theory calculations were employed to study the influence of a NH_x ($x = 3, 2, 1, 0$) precovered Fe(100) surface on CO adsorption and dissociation. The individual adsorption of $\theta = 0.25$ ML CO and NH_x on Fe(100) as reported in Chapter 5 is directly compared to the coadsorbed state where $\theta = 0.25 + 0.25$ ML CO and NH_x are both present in the (2 × 2) surface unit cell. These values are subsequently used to calculate the mixing energy and thus quantify the stabilizing or destabilizing effect upon coadsorption of CO + NH_x. The calculation of mixing energies is extended to a lower coverage ($\theta = 0.11$ ML) by comparing the most stable individual and coadsorbed states in a (3 × 3) unit cell and a higher coverage ($\theta = 0.50$ ML) by comparing the energies calculated for coadsorption at $\theta = 0.25 + 0.25$ ML CO and NH_x with the individual adsorption at $\theta = 0.50$ ML on Fe(100). In order to provide further insight to the de-/stabilization upon coadsorption, the electronic structure of the coadsorbates with $\theta = 0.25 + 0.25$ ML CO + NH_x is studied by calculating their localized density of states (LDOS) and electron redistribution plots and comparing it with that of the individually adsorbed CO and NH_x at $\theta = 0.25$ ML. Finally, the individual CO dissociation reaction on the Fe(100) surface with a coverage of $\theta = 0.25$ ML is compared to the reaction ($CO \rightarrow C + O$) in the presence of $\theta = 0.25$ ML NH_x. The results obtained after studying these elementary reactions are subsequently used to discuss the possible roles of the NH_x adsorbates in the formation of FTS products. Furthermore, to address some of the questions that exist around the promotional or poisoning effect of NH_3 during FTS, these results are compared to the calculations reported for S and K coadsorption with CO on the Fe(100) facet [1, 2], which are generally grouped with the FTS catalyst poisons and promoters respectively [13].

Computational method

The periodic DFT calculations used in this work have been performed using the Vienna *ab-initio* simulation package (VASP) [26–29]. The Kohn-Sham equations that makes use of a basis set of plane waves in periodic DFT, were solved iteratively with the projector augmented wave

(PAW) method in the implementation of Kresse and Joubert [30, 31]. The generalized gradient approximation (GGA) with the revised Perdew Burke Enzerhof (RPBE) exchange-correlation functional [32] was used in the electronic structure calculations. A Methfessel-Paxton [33] smearing method with a smearing width $\sigma = 0.15$ eV was used to treat the electron distribution at the Fermi level. For k-point sampling of the Brillouin zone a Monkhort-Pack [34] grid was used. The sampling density (k-point mesh of 11×11×11 for the bulk bcc Fe and a 5×5×1 for the p(2 × 2) or 3×3×1 for the p(3 × 3) unit cells on the Fe(100) surface), kinetic energy cutoff for the plane wave basis set ($E_{cut} = 400$ eV), slab thickness and vacuum gap (10 Å) were optimized such that the total energy was converged within an error margin of ± 1 meV. All gaseous molecules (CO, NH_3 and H_2) were optimized within a 10 × 10 × 10 Å unit cell. (Please refer to Chapters 4 and Chapter 5 for a comprehensive validation of the model used here.) A p(2 × 2) surface unit cell was generally used, but additional calculations were also performed in a p(3 × 3) surface unit cell. The optimization of the number of atomic layers in the slab revealed an uncertainty ($\sim$ 0.03 eV) in the calculated adsorption energies for the 5 layer slab used in these calculations, which is the same magnitude of error reported by authors that used a similar methodology [35]. The adsorbates were placed on one side of the slab prior to the geometry optimization calculation and a correction for the dipole was subsequently applied. All adsorbates as well as the top two layers were allowed to relax. The nudged elastic band method (NEB) [36] was used to locate transition states of CO dissociation reactions in the presence of the NH_x adsorbates. A partial hessian vibrational analysis (PHVA) was performed after each geometry optimization to confirm that the structure was at a local minimum and for each transition state structure to confirm that it was a first order saddle point on the potential energy surface (PES). All energies reported contains corrections for the zero point vibrational energies (ΔZPE). The methodology used for calculating the adsorption energy of CO in the presence of the NH_x species, the mixing energy and electron redistribution is discussed at the beginning of each relevant section.

Results and discussion

CO adsorption on a NH$_x$ precovered Fe(100) surface

The adsorption of CO on the NH$_x$ pre-covered Fe(100) surface is in part investigated using the results obtained in Chapter 5, where the most stable individual NH$_x$/CO adsorption on Fe(100) is reported. In the calculations to be discussed here, CO is placed on the optimized NH$_x$ + Fe(100) surface. For efficiency, CO was only coadsorbed in its favored adsorption site, the fourfold hollow (fh) site. In Chapter 5 it was determined that CO can exist in the fh site with two non-equivalent configurations (see Fig. 5.1 in Chapter 5), with the tilted CO bonding through the oxygen atom to either two or one Fe atom(s). The aforementioned two structures will henceforth be denoted as ft and ft' respectively. The adsorption energies of 0.25 ML CO on a Fe(100) surface pre-covered with 0.25 ML NH$_x$, with x = 3, 2, 1, 0 ($\Delta E_{ads,CO'}$), were calculated using equation 6.2

$$\Delta E_{ads,CO'} = E_{ads,CO+NH_x} - E_{ads,NH_x} - E_{CO(g)} \tag{6.2}$$

where $E_{ads,CO+NH_x}$ is the energy of the geometry optimized structure with both CO and NH$_x$ in the (2 × 2) surface unit cell, E_{ads,NH_x} is the energy of the NH$_x$ adsorbate (as reported in Chapter 5) in its respective most stable site on the Fe(100) surface and $E_{CO(g)}$ is the energy of CO in the gas phase. In Table 6.1 the CO adsorption energies ($\Delta E_{ads,CO'}(eV)$) on a NH$_x$ precovered Fe(100) surface, together with structural information can be found. The changes in CO's structural properties are mainly reported in Table 6.1, as it is the prime interest of this work to evaluate how CO is influenced by the presence of the NH$_x$ surface species. The details of the structural changes for NH$_x$ incurred upon CO + NH$_x$ coadsorption is however reported in Table 6.2. Note that similar to the definition in Chapter 5, the coadsorption of two adsorbates adjacent to each other in the (2 × 2) unit cell is denoted as a *cis* configuration, while the configuration with the adsorbates located diagonally from each other is denoted as the *trans* configuration.

Table 6.1: CO adsorption energies ($\Delta E_{ads,CO'}(eV)$) and geometries for the most stable configuration of CO co-adsorbed with NH$_x$ on Fe(100). d_{C-O} is the C-O bond length, d_{Fe^1-C} and d_{Fe^2-C}, the bond length between carbon and the 1st and 2nd layer Fe atoms, d_{Fe^1-O} the bond length between Fe and O and ϕ is the angle that the C-0O bond makes with the surface nomal.

Ads.	$\Delta E_{ads,CO'}(eV)$	d_{C-O} (Å)	d_{Fe^1-C} (Å)	d_{Fe^2-C} (Å)	d_{Fe^1-O} (Å)	ϕ (°)	v_{C-O} (cm^{-1})
CO(ft')	-1.48	*1.29*	*1.91; 2.16*	*2.07*	*2.12*	*53*	*1286*
+ NH_3	-1.65	1.31	1.94; 2.14	2.04	2.11	59	1219
CO(ft)	*−1.49*	*1.31*	*1.94; 2.24*	*2.09*	*2.16*	*45*	*1210*
+ NH_2(i)	-1.36	1.32	1.97; 2.27	2.09	2.16	48	1161
+ NH_2(ii)	-1.27	1.31	1.94; 2.22	2.07	2.15	49	1236
+ NH(cis)	-1.21	1.30	1.97; 2.27	2.13	2.25	48	1266
+ NH(trans)	-1.70	1.32	1.98; 2.27	2.00	2.18	49	1171
+ N(cis)	-1.13	1.29	1.98; 2.24	2.16	2.26	51	1312
+ N(trans)	-1.66	1.33	1.99; 2.36	1.99	2.12	41	1155

Table 6.2: NH_x (with $x = 3, 2, 1, 0$) geometries for the most stable configuration of NH_x co-adsorbed with CO on Fe(100) compared to their individual adsorption data taken from Chapter 5. d_{Fe_1-C} and d_{Fe_2-C} are the bond lengths between N and the 1^{st} and 2^{nd} layer Fe atoms, $d_{Fe_1-Fe_1}$ is the distance between the top layer Fe atoms directly bonded to N, d_{N-H} is the bond length between N and H and ϕ is the angle that the Fe-N (or the N-H bond in NH(fh)) bond makes with the surface plane.

Ads.	d_{Fe_1-N} (Å)	d_{Fe_2-N} (Å)	$d_{Fe_1-Fe_1}$ (Å)	d_{N-H} (Å)	ϕ (°)
NH_3(at)	2.25			1.02	90
NH_3(at) in CO + NH_3	2.21			1.02	84
NH_2(br)	2.04		2.74	1.02	
NH_2(br)i in CO + NH_2	2.03/2.04		2.81	1.02	
NH_2(br)ii in CO + NH_2	2.00/2.06		2.76	1.02	
NH(fh)	2.12	2.17	2.84	1.03	90
NH$(fh)_{trans}$ in CO + NH	2.13	2.17	2.77/2.85	1.03	
NH$(fh)_{cis}$ in CO + NH	2.18/2.01	2.16	2.79/2.88	1.03	83
N(fh)	1.98	1.98	2.73		
N$(fh)_{trans}$ in CO + N	1.96/1.98	1.94	2.72/2.83		
N$(fh)_{cis}$ in CO + N	1.95/1.99	1.92	2.71/2.85		

CO + NH_3 on Fe(100)

For coadsorbed CO and NH_3 on Fe(100), NH_3 was adsorbed in its atop configuration at the start of the optimization, thus in the initial structure the Fe-N bond was 90° with respect to the surface. For the first calculation, CO was orientated such that the oxygen is bonded to two Fe atoms (ft). (These initial and final structures are presented in Fig. B.10 of Appendix B). The adsorption energy calculated for CO in the presence of 0.25 ML pre-adsorbed NH_3 ($\Delta E_{ads,CO'} = -1.65\, eV$) is 0.16 eV more stable than in the absence of NH_3 ($\Delta E_{ads,CO} = -1.49\, eV$). The geometry optimized structure for the coadsorbed CO and NH_3, together with the individually adsorbed structures (of CO and NH_3), taken from Chapter 5 are given in Figure 6.1. These optimized structures will be used to compare the changes upon coadsorption. CO rotates horizontally from the ft configuration during the geometry optimization, so that the final structure has the oxygen of CO bonded to only one Fe atom (ft', see Figure 6.1). There is a slight increase ($\Delta d_{C-O} = 0.02$ Å) in CO bond length and the CO bond tilt is increased by 6° (see Table 6.1). The C-O bond elongation is accompanied by a decreased CO stretching frequency ($v_{C-O} = 1286$ cm^{-1} vs $v_{C-O}^{+NH_3} = 1219$ cm^{-1}), which would suggest weakening of the CO bond. A 0.03 Å Fe-C bond elongation is observed between the first layer Fe atom that is situated within the N-Fe-C-O bonding sequence. The remaining two Fe-C bonds for the first layer Fe atoms, the second layer Fe-C bond as well as the Fe-O bond are reduced by 0.02, 0.03 and 0.01 Å respectively. After optimization NH_3 tilts by 6° towards the opposite side of the coadsorbed CO, thus making a 84° angle with the surface normal (see Table 6.2). The Fe-N bond is reduced by 0.04 Å when coadsorbed with CO, and if the slight tilt of the Fe-N bond is considered, the N is 0.05 Å closer to the Fe(100) surface. The N-H bonds are all reduced by 0.01 Å. In summary, the coadsorption energy calculated indicates an attractive interaction between the CO and NH_3 adsorbed on the Fe(100) surface. This is further supported by a change in the geometries that has several bonds (of CO and NH_3) closer to the catalytic surface and a weakened CO bond.

CO + NH_2 on Fe(100)

The most stable configuration for individually adsorbed NH_2 on the Fe(100) surface is the bridged configuration (see Figure 5.3 in Chapter 5). Two inequivalent structures were initially

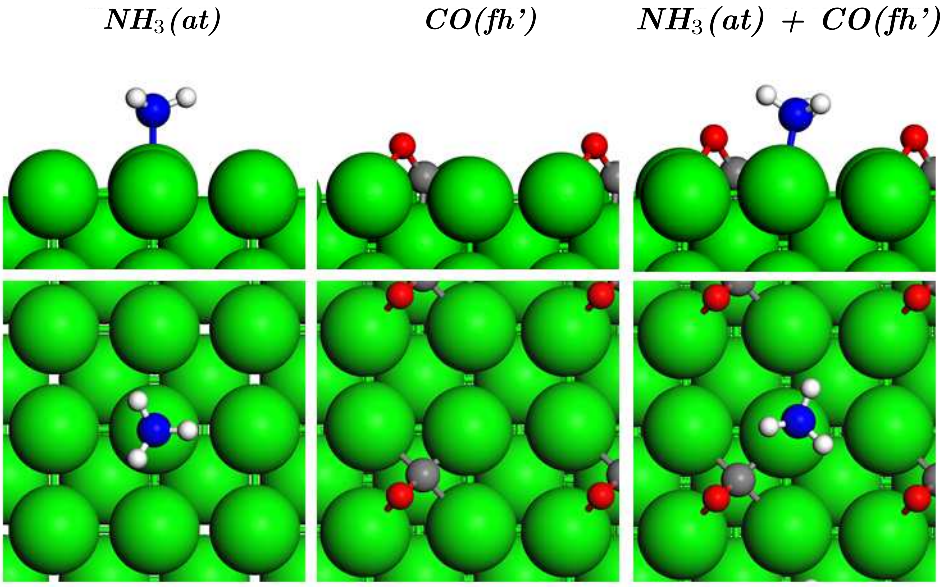

Figure 6.1: Top and side views of CO, NH$_3$ and CO+NH$_3$ on the Fe(100) surface with $\theta = 0.25$ ML for the individual adsorption and $\theta = 0.25$ ML + 0.25 ML for the coadsorbed states (Color scheme: Fe - green, O - red, C - grey , N - blue, H - white)

calculated with 0.25 ML NH_2 adsorbed in the bridge site of the (2×2) unit cell. Other non-nequivalent structures were ruled out during the optimization of these two initial structures, as the CO rotated horizontally from the initial configurations, passing through the configuration where the oxygen of CO is bonded to one Fe atom (ft'), and finally resulting with the optimized structures as shown in Fig. B.11 of Appendix B. The most stable of the two configurations has NH_2 in a bridge site, which is situated between the two carbon atoms as indicated in Fig. 6.2. The geometries for the most stable configurations of $NH_2(br)$ and $CO(ft)$ on the Fe(100) surface (with $\theta = 0.25$ ML) that is used to compare between the individual and coadsorbed structures are also given in Figure 6.2. The adsorption energy ($\Delta E_{ads,CO'}$ = -1.36 eV) calculated for CO coadsorbed with NH_2 in its most stable state is 0.13 eV less stable than the individually adsorbed CO (ft, $\Delta E_{ads,CO'}$= -1.49 eV). This is indicative of repulsive lateral interactions when 0.25 ML CO is co-adsorbed with 0.25 ML NH_2 on Fe(100), which is further explored in following subsections. A 0.03 Å increase for the Fe_1-C bonds in the first layer is calculated. The distance between the second layer Fe atom and C remains unchanged at $d_{Fe_2-C} = 2.09$ Å. The slight (0.01 Å) increase in CO bond length as well as a lower CO stretching frequency would suggest that the presence of NH_2 on the Fe(100) surface does weaken the CO bond. There is small changes in the geometry of the NH_2 adsorbate upon coadsorption with CO as reported in Table 6.2. The most notable difference for the NH_2 geometry in CO + NH_2 on the Fe(100) surface would be the distance between the Fe atoms directly bonded to N ($\Delta d_{Fe_1-Fe_1} = +0.07$ Å). It is highlighted in Chapter 5 how the top layer Fe-Fe bond distances either increase or contracts in order to facilitate the NH_x (in particular $x = 2, 0$) bonding on the Fe(100) surface.

CO + NH on Fe(100)

Three structures were initially considered for the coadsorption of CO and NH, two configurations with the NH adsorbates located in a *cis* and one in a *trans* configuration. A supplementary discussion of the geometry optimization for $CO(ft) + NH(fh)$ on Fe(100) including the relevant figures can be found in Appendix B. The summary of the calculated adsorption energies for CO + NH on Fe(100) and structural properties is given in Table 6.1.

Both configurations with CO placed in a *cis* position with respect to the NH adsorbate were significantly less stable (by 0.49 and 0.71 eV) than the CO coadsorbed in a *trans* position ,

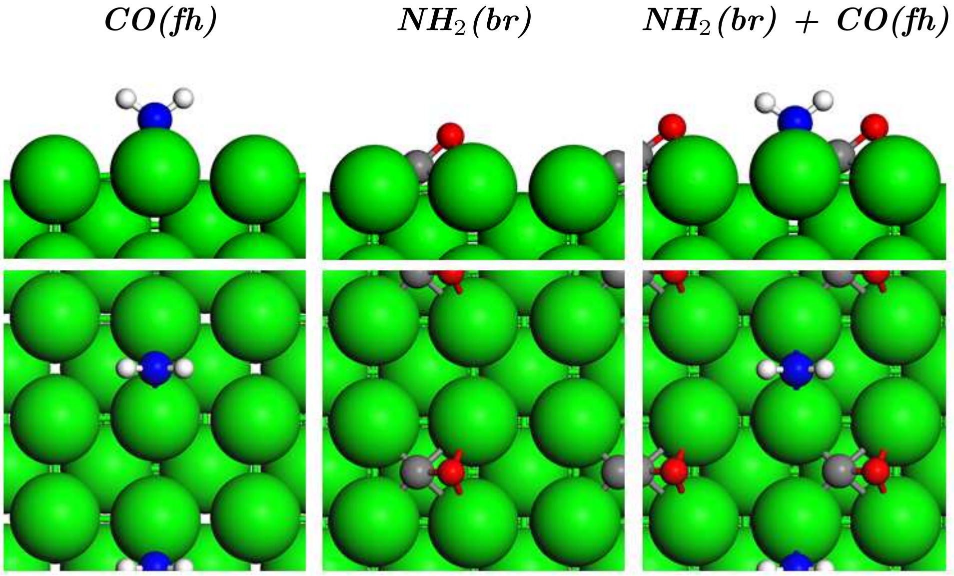

Figure 6.2: Top and side views of CO, NH$_2$ and CO+NH$_2$ on the Fe(100) surface with θ = 0.25 ML for the individual adsorption and θ = 0.25 ML + 0.25 ML for the coadsorbed states (Color scheme: Fe - green, O - red, C - grey , N - blue, H - white)

which resulted in a markedly stable adsorption energy $\Delta E_{ads,CO'}(eV)$ = -1.70 eV. Based on a vibrational analysis, one of the *cis* configurations was located at a transition state on the PES (i.e. it was characterized by having one imaginary vibrational frequency). Therefore, the discussion is predominantly focused on the *trans* configuration (see Fig. 6.3), but further attention is given to the *cis* configuration that was at a local minimum, as it is included in sections that follow to shed light on the possible factors that leads to the destabilizing nature of this configuration. Again, for the sake of comparison the geometry optimized structures of CO(ft) and NH(fh) with θ = 0.25 ML from the results calculated in Chapter 5 are given in Fig. 6.3. A small (Δd_{C-O} = 0.01 Å) C-O bond elongation and reduction are calculated for CO in the *trans* and *cis* coadsorbed structures respectively, when compared to the individually adsorbed CO(ft). The C-O stretching frequency for CO in the *trans* and *cis* configurations are $v_{C-O}^{+NH_{trans}}$ = 1171 cm^{-1} and $v_{C-O}^{+NH_{cis}}$ = 1266 cm^{-1}, which respectively results in a 39 cm^{-1} lower and 56 cm^{-1} higher vibrational mode compared to the individually adsorbed CO (v_{C-O} = 1210 cm^{-1}). Both *trans* and *cis* configurations have the C-O bond more inclined (3 and 4°) relative to the surface compared to the case when 0.25 ML CO is individually adsorbed. In Chapter 5, it was noted that the adsorption of NH_2, NH and N have a major influence on the positions of the top layer Fe atoms, and in doing so create a pseudo-threefold hollow site for H coadsorption on the Fe(100) surface. In both the *cis* and *trans* coadsorbed structures, the first layer Fe atoms bonded to carbon are elongated by approximately 0.03 Å, which could be a result of the aforementioned deformation caused by the coadsorbed NH. A major difference can furthermore be seen in the O distance to the first layer Fe atom in the *cis* configuration (d_{Fe_1-O}= 2.25 Å), which is 0.07 Å and 0.09 Å longer than for CO in the *trans* configuration and the individually adsorbed CO, respectively.

There are practically no structural changes for the NH adsorbate when coadsorbed diagonally (*trans*) to the CO(ft), whereas a disproportion of the N-Fe_1 bonds is calculated for NH coadsorbed in the *cis* position. The N-Fe_1 bonds closer to the carbon become significantly shorter (d_{Fe_1-N}= 2.01 Å), while the N-Fe_1 bonds closer to the oxygen atom are elongated (d_{Fe_1-N}= 2.18 Å) in comparison to the individually adsorbed NH(fh), where d_{Fe_1-N}= 2.13 Å. The overall effect indicates that the stability for the coadsorption of CO(ft) + NH(fh) in the *trans* configuration occurs in conjunction with increased CO-Fe interaction via the second layer atom

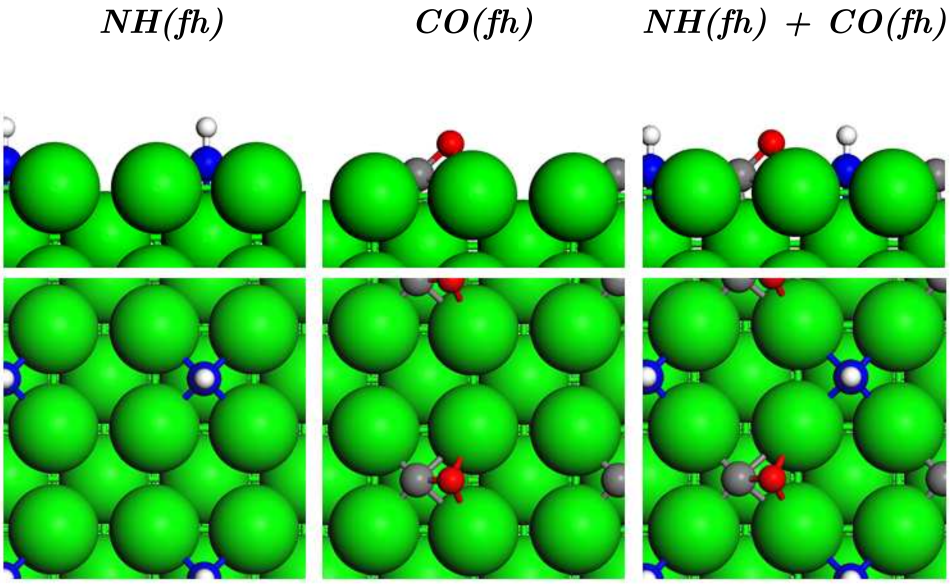

Figure 6.3: Top and side views of CO, NH and CO+NH (*trans*) on the Fe(100) surface with $\theta = 0.25$ ML for the individual adsorption and $\theta = 0.25$ ML + 0.25 ML for the coadsorbed states (Color scheme: Fe - green, O - red, C - grey , N - blue, H - white)

and a weakening of the CO bond. Conversely, the less stable *cis* configuration for CO + NH shows less interaction between CO and Fe, based on the elongated Fe$_1$-C, Fe$_2$-C and Fe$_1$-O bonds and exhibits a slightly stronger CO bond.

CO + N on Fe(100)

The coadsorption of CO + N yielded similar results to those reported for CO + NH coadsorption on Fe(100). Three non-equivalent initial structures were constructed as shown in Fig. B.13 of Appendix B. The results for the final structures that are discussed here are essentially the same as the *cis* and *trans* configurations discussed for CO + NH, with the absence of an N-H bond. Top and side views of the most stable coadsorbed CO + N configuration, that is the *trans* configuration, as well as the geometry optimized structures of CO(ft) and N(fh) individually adsorbed on Fe(100) (with $\theta = 0.25$ ML) are presented in Fig. 6.4. Table 6.1 contains the results for the calculated CO adsorption energies and structural properties that are discussed for the coadsorption of CO + N on Fe(100).

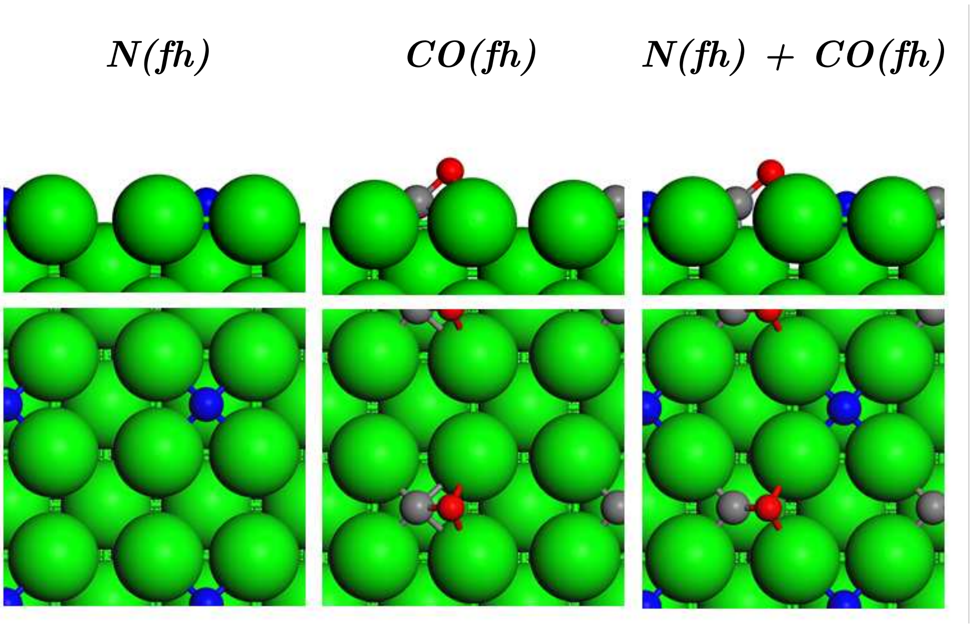

Figure 6.4: Top and side views of CO, N and CO+N (*trans*) on the Fe(100) surface with $\theta = 0.25$ ML for the individual adsorption and $\theta = 0.25$ ML + 0.25 ML for the coadsorbed states (GGA-RPBE; $E_{cut} < 400$ eV; k-points: 5x5x1; Color scheme: Fe - green, O - red, C - grey , N - blue)

Similar to the CO + NH coadsorption, the CO adsorption energy calculated with N in an adjacent fh site with respect to CO was significantly less stable ($\Delta E_{ads,CO'} = -1.13$ eV) than when coadsorbed diagonally from CO ($\Delta E_{ads,CO'} = -1.66$ eV), with the former CO adsorption energy being 0.36 eV less stable, and the latter 0.17 eV more stable when compared to the adsorption energy ($\Delta E_{ads,CO'} = -1.49$ eV) of $\theta = 0.25$ ML individually adsorbed CO(ft) on the Fe(100) facet. The C-O bond is increased by 0.02 Å and reduced by 0.02 Å upon coadsorption with N in the *trans* and *cis* configurations, respectively. Compared to the calculated C-O stretching frequency of individually adsorbed CO ($v_{C-O} = 1210$ cm^{-1}), a lower C-O stretching frequency ($v_{C-O}^{+NH_{trans}} = 1155$ cm^{-1}) is obtained for CO + N *trans* coadsorption, whereas a higher C-O stretching frequency ($v_{C-O}^{+NH_{cis}} = 1312$ cm^{-1}) is calculated when CO and N is coadsorbed in a *cis* configuration. The CO bond makes a 41° and 51° angle with the surface plane when coadsorbed in a *cis* or *trans* configuration with N respectively, while a 45 ° angle is calculated for individually adsorbed CO(ft). For the CO coadsorbed with N in the *trans* configuration, the bond distance between carbon and the top layer Fe atoms is significantly increased compared to the individually adsorbed CO ($d_{Fe_1-C} = 1.99$ and 2.36Å for CO(ft) + N(fh)($trans$) compared to $d_{Fe_1-C} = 1.94$ and 2.24Å for CO(ft)). Furthermore, the coadsorption of CO and N in the *trans* configuration leads to a $\Delta d_{Fe_2-C} = -0.10$ Å reduction in Fe$_2$-C bond length. Such a pronounced change for the distance between the first layer Fe and carbon atoms is not obtained in the configuration where CO + N are coadsorbed adjacent to each other in the (2 × 2) unit cell. The opposite effect is found for the Fe$_2$-C bond length within the *cis* CO + N configuration, with an increase of Δd_{Fe_2-C}= +0.07 Å compared to the individually adsorbed CO. The distance between the Fe atom in the first layer and the O atom is slightly reduced when CO + N are coadsorbed in the *trans* configuration (Δd_{Fe_2-C}= −0.04 Å), but is significantly elongated upon coadsorption in the *cis* configuration Δd_{Fe_1-O}= +0.10 Å. In Chapter 5 it was determined that for N(fh) adsorption (with $\theta = 0.25$ ML) on Fe(100), the adsorbates reconstructed the topmost Fe layer so that the distance between surface Fe atoms were either reduced to $d_{Fe_1-Fe_1} = 2.73$Å or expanded to $d_{Fe_1-Fe_1} = 3.01$Å (see Fig. 5.3 in Chapter 5). Conversely, it has been shown via DFT calculations that oxygen bonding on the Fe(100) leads to an expansion of the top layer Fe atoms [37]. These properties of N and O is maintained upon coadsorption of CO+N on Fe(100) (see Figure 6.5) and creates a markedly different cavity for the CO adsorption on the Fe(100)

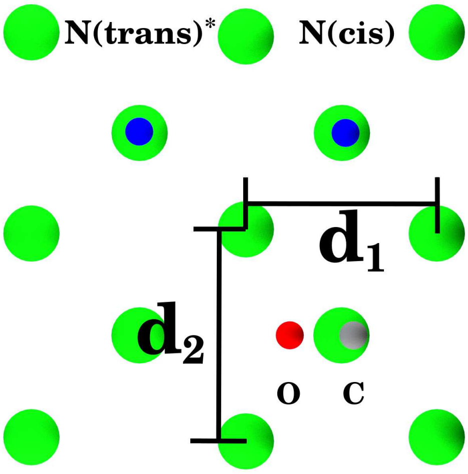

	CO(ft)	N(fh)	cis	trans
d_1(Å)	**2.87**	2.73	**2.71**	**3.02**
d_2(Å)	2.93		3.01	3.01

Figure 6.5: (*Left:*) A top view of the stable geometry for CO(ft) + N(fh) in the *cis* configuration is given, with the *trans* configuration superimposed as a visual aid. Important deviations in the distances between certain top layer Fe atoms is indicated (d_1, d_2). (*Left:*) The values for the $Fe - Fe$ distances indicated in the figure is summarized.

surface. The most pronounced change in the CO + N($trans/cis$) coadsorbed configurations would be the distances between the Fe atoms that are parallel to the CO bond (d_2 in Figure 6.5), which changes from $d^{cis}_{Fe_1-Fe_1} = 2.73$ Å in the in the individually adsorbed CO(ft) to $d^{trans}_{Fe_1-Fe_1} = 3.01$ Å and $d^{cis}_{Fe_1-Fe_1} = 2.73$ Å for the *trans* and *cis* configurations, respectively. Some of the observed changes in the geometry of the CO adsorbate in the two configurations ($cis/trans$) can most likely be ascribed to the reconstruction of the top layer, which in turn is due to the presence of the N adatom on the Fe(100) surface.

In summary, when comparing individual CO adsorption with CO + N($trans$) coadsorption on Fe(100), a more stable adsorption energy is calculated that exhibits a weakened CO bond that makes a less tilted angle with the surface. Conversely, it can be generalized that most properties discussed for CO adsorption were found to be reversed when CO was coadsorbed in a *cis* configuration to N on the Fe(100) surface. The changes between in the geometry of the CO adsorbates in the coadsorbed configurations (CO + N($cis/trans$) on Fe(100)) can in part be explained due to the reconstruction of the top layer induced by N adsorption on the Fe(100) surface.

As a general remark for the coadsorption of CO with NH_x on the Fe(100) surface species, it should be pointed out that all the stable configurations would predict a redshift in the CO stretching vibrational frequency.

Heat of mixing (ΔE_{mix}) for CO + NH_x on Fe(100)

To calculate the heat of mixing, the methodology proposed by Ciobîcă et al. [17] is used.

$$X = a - b - c - d \tag{6.3}$$

$$Y = e + f - 2b - c - d \tag{6.4}$$

In Eq.'s 6.3 and 6.4:

- a is the energy of the coadsorbed system
- b is the energy calculated for the clean Fe(100) slab
- c and d is the energy for CO and NH_3 in the gas phase, respectively
- e and f is the energy for CO and NH_3 individually adsorbed on an Fe(100) surface, respectively
- X is the adsorption of CO + NH_3 in the coadsorbed state on the Fe(100) surface
- Y is the sum of the adsorption energies calculated for CO and NH_3, individually adsorbed (or segregated) on Fe(100) surfaces

The heat of mixing for the remaining NH_x (with x = 2, 1, 0) adsorbates is treated as discussed above, with the exception that the loss of the hydrogen atoms are accounted for by including the energy of (x ×) H atoms adsorbed on a distinct surface. (The interested reader is directed to Chapter 5 for more information on the approach followed for the calculation of the NH_x (x = 2, 1, 0) surface species on Fe(100).) The energy for the mixing reactions are obtained by calculating the difference between X and Y ($\Delta E_{mix} = X - Y$) for the surface mixing reactions given in Table 6.3. Even though most of the results and discussion is based on the coadsorption of $\theta = 0.25$ ML CO with an equivalent coverage of NH_3, the influence of coverage on these results

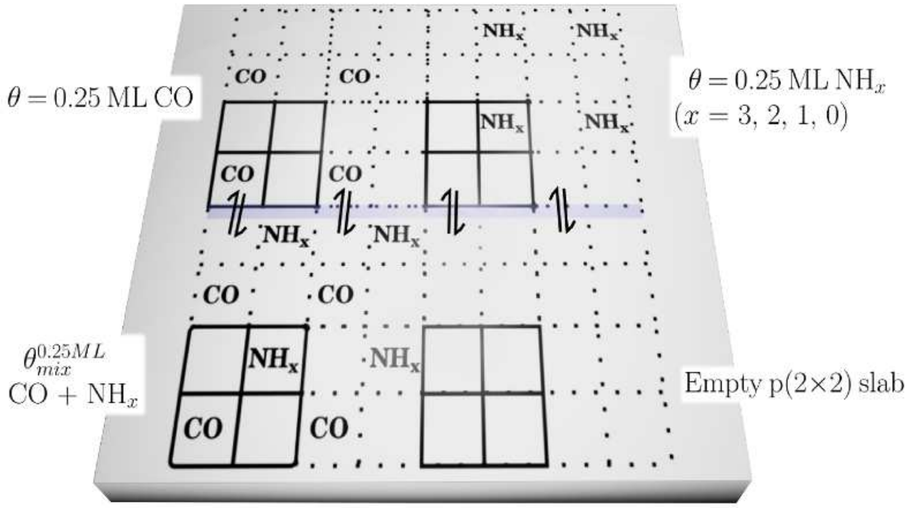

Figure 6.6: Schematic to illustrate the mixing reactions considered for CO and NH$_x$ (x = 3, 2, 1, 0) on the Fe(100) surface at $\theta_{mix}^{0.11/0.25ML}$.

are verified by including the calculations for ΔE_{mix} at the lower and higher coverages of θ = 0.11 and 0.50 ML on the Fe(100) facet, respectively. The three different coverages represent θ = x + x ML (with x = 0.11, 0.25 or 0.50 ML) will henceforth be denoted as θ_{mix}^{xML}. To facilitate the discussion a schematic for the mixing reaction with $\theta_{mix}^{0.25ML}$ is presented in Fig. 6.6. For $\theta_{mix}^{0.11ML}$, a (3 × 3) unit cell was used to calculate the coadsorbed structures and subsequently compared in a similar fashion as described for $\theta_{mix}^{0.25ML}$. The adsorption energy for CO at θ = 0.11 ML does not change ($\Delta E_{ads,CO} = -1.49$ eV) at this coverage. The results obtained for the individual adsorption of NH$_x$ on Fe(100) with θ = 0.11 ML is reported in Table 5.8 of Chapter 5. The $\theta_{mix}^{0.50ML}$ coadsorption energies involve a direct comparison of the CO + NH$_x$ coadsorption energies with θ = 0.25 + 0.25 ML coverages calculated here with the average adsorption energy for the θ = 0.50 ML for the individual adsorptions reported in Chapter5, and is therefore better represented by the schematic given in Fig. B.14 of Appendix B. The segregation for CO + NH$_3$ with $\theta_{mix}^{0.50ML}$ is not likely to occur, since the differential adsorption energy of NH$_3$ at 0.50 ML (E^{diff} = + 0.09 eV) calculated in Chapter 5 indicates that NH$_3$ on the Fe(100) surface would not build up to θ = 0.50 ML. The aforementioned calculation does however aid the discussion of the lateral interactions between CO and NH$_3$ on Fe(100) and is therefore included in Table 6.3. The reactions considered for these calculations provide information about the

Table 6.3: The heat of mixing calculated for CO and NH_x (x = 3, 2, 1, 0) on Fe(100) at the various coverages (θ = 0.11, 0.25 and 0.50 ML).

Adsorbates	ΔE_{mix} (eV)		
		θ	
	0.11 ML	0.25 ML	0.50 ML
$NH_3(at)$ + $CO(ft')$	−0.08	−0.16	−0.32
$NH_2(br)$ + $CO(ft)$	0.03	0.13	0.07
$NH(fh)$ + $CO(ft)$ - *trans*	0.03	−0.21	−0.21
- *cis*		0.28	
$N(fh)$ + $CO(ft)$ - *trans*	0.02	−0.17	−0.19
- *cis*		0.36	

preference of these coadsorbates to form mixed states (if ΔE_{mix} is exothermic) or if it would instead be thermodynamically favorable for NH_x and CO to segregate into islands (if ΔE_{mix} is endothermic). Furthermore, the mixing energy calculated here is essentially equivalent to quantifying the lateral interactions between CO and NH_x when coadsorbed on Fe(100). The use of the methodology employed by Curulla-Feré et. al [18] to quantify the lateral interactions between CO and N on a Rh(100) surface based on their DFT results, is equivalent to the ΔE_{mix} defined here. A positive or negative ΔE_{mix} respectively corresponds to either a repulsive or attractive lateral interaction between adsorbates. Note that configurational entropy is not included in this discussion.

ΔE_{mix} for CO + NH_3 on Fe(100)

For the $\theta_{mix}^{0.25ML}$ mixing reaction an exothermic heat of mixing ($\Delta E_{mix} = -0.16$ eV) is calculated, which indicates that the formation of a mixed state is thermodynamically feasible and that attractive interactions exist between CO and NH_3 for this coverage. It should be borne in mind that part of the comparison made here includes NH_3 adsorption on Fe(100) at θ = 0.25 ML, which was determined in Chapter 5 to exhibit repulsive NH_3-NH_3 lateral interactions.

The heat of mixing as a function of coverage indicates that the attractive lateral interactions become more pronounced at higher coverages ($\Delta E_{mix} = -0.08$, -0.16 and -0.32 eV for $\theta = 0.11$, 0.25 and 0.50 ML respectively). It is therefore interesting to point out that Kizilkaya et. al [23] reports the observation of an increase of the NH_3 saturation coverage (from $\theta = 0.25$ ML to 0.34 ML) when performing TPD experiments for individual NH_3 and coadsorbed CO + NH_3 adsorption on the Co(0001), respectively. The attractive lateral interaction is consistent with the changes observed in the geometry optimized structures upon coadsorption of CO + NH_3 on Fe(100), where a lower C-O stretching frequency, a weakened C-O bond, and reduced Fe-N, Fe-C and Fe-O bond lengths were obtained for the adsorbates in the coadsorbed state. In order to provide further insight from the DFT results reported here, the calculated projected density of states (PDOS), Bader charge analysis and electron redistribution plots are reported in the following section (see Section 6.3.3).

$\Delta \mathbf{E_{mix}}$ for CO + NH_2 on Fe(100)

As alluded to in the previous section, coadsorption of CO with NH_2 on the Fe(100) surface (with $\theta = 0.25 + 0.25$ ML) leads to a less stable structure. For CO coadsorbed with NH_2, the calculated heat of mixing ($\Delta E_{mix} = 0.13$ eV) at $\theta_{mix}^{0.25ML}$ reveals repulsive lateral interactions, which indicates that segregation is thermodynamically preferred at this coverage. It is interesting to note that repulsive interactions is calculated here even though a redshift would be predicted based on the lower vibrational stretching frequency of CO and the elongated C-O bond. Lower repulsive interactions were calculated for the CO + NH_2 mixing reactions at $\theta_{mix}^{0.11ML}$ and $\theta_{mix}^{0.50ML}$, with $\Delta E_{mix} = 0.03$ eV and $\Delta E_{mix} = 0.07$ eV for the respective coverages. NH_2 is the only adsorbate that leads to repulsive interactions at all coverages calculated here upon coadsorption with CO on the Fe(100) surface. In Chapter 5 the calculated PES for the NH_3 decomposition at $\theta = 0.25$ ML and the kinetic analysis thereof were indicative of kinetic trapping of the NH_2 adsorbate on the Fe(100) facet. It is therefore interesting to point out here that the predominant N-containing compound formed when NH_3 is co-fed during FTS is primary amines [3–8], which in some postulated pathways [7, 8] to the formation of these compounds require the insertion of NH_2 adsorbates at the desorption stage of the mechanism. The electronic structure of CO + NH$_2$ on Fe(100) for $\theta_{mix}^{0.25ML}$ is further studied in a Section 6.3.3 below to provide further information on the underlying interactions that lead to the destabilization.

$\mathbf{\Delta E_{mix}}$ for CO + NH on Fe(100)

The mixing energy calculations for coadsorbed CO and NH on Fe(100) with $\theta_{mix}^{0.25ML}$ was performed for both the *cis* and *trans* configurations. At $\theta_{mix}^{0.25ML}$ the *trans* configuration of CO + NH on Fe(100) led to the most pronounced stabilization (ΔE_{mix} = -0.21 eV), while a significant repulsive lateral interaction can be extracted from the mixing energy in a *cis* configuration (ΔE_{mix} = 0.28 eV). It is interesting to see that the attractive lateral interaction of CO + NH in the *trans* configuration seems to be particularly prevalent at higher coverages since ΔE_{mix} = -0.21 eV at $\theta_{mix}^{0.50ML}$ and ΔE_{mix} = 0.03 eV at $\theta_{mix}^{0.11ML}$.

$\mathbf{\Delta E_{mix}}$ for CO + N on Fe(100)

The similarities between the coadsorption of CO + NH and CO + N on Fe(100) extends to their calculated mixing energies. An exothermic mixing energy (ΔE_{mix} = -0.17 eV) for CO and N in the *trans* configuration is calculated while an endothermic mixing (ΔE_{mix} = 0.36 eV) energy is found for the *cis* configuration at $\theta_{mix}^{0.25ML}$. Again, these calculations are in close agreement with the structural properties discussed in the previous section. Similar to CO + NH(*trans*) on Fe(100), the attractive lateral interaction for the *trans* configuration of CO + N on Fe(100) seems to be absent at the lower coverage of $\theta_{mix}^{0.11ML}$ with ΔE_{mix} = 0.02 eV, while it remains present at $\theta_{mix}^{0.50ML}$ where ΔE_{mix} = -0.19 eV.

$\mathbf{\Delta E_{mix}}$ at higher temperatures

The ΔH_{mix} values for the mixing reactions of CO and NH$_x$ on Fe(100) are calculated at 0 K. To evaluate these reactions at higher reaction temperatures and to incorporate entropy (see equations 6.5 and 6.6), use is made of the vibrational frequencies calulated and the simplified methodology of Loffreda [38].

$$\Delta S_{vib} = -Rln(\frac{Q^{vib}_{product}}{Q^{vib}_{reactant}}) \tag{6.5}$$

$$\Delta G_{mix} = \Delta H_{mix} - T\Delta S^{vib}_{mix} \tag{6.6}$$

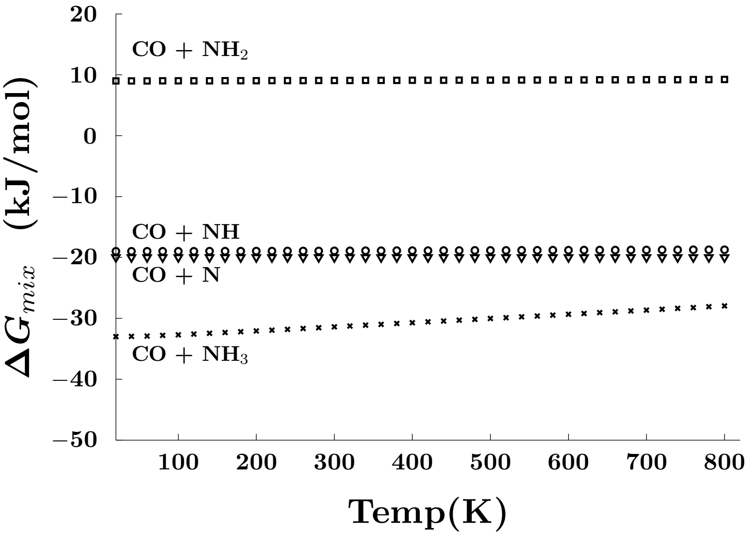

Figure 6.7: The ΔG_{mix} calculated in the temperature range 0 - 800 K for the CO and NH$_x$ (x = 3, 2, 1, 0) on the Fe(100) surface. (GGA-RPBE, $E_{cut} \leq 400$ eV, k-points: 5x5x1)

If the temperature range 0 - 800 K (see Figure 6.7) is considered, only minor deviations from the Gibbs free energy calculated at 0 K are observed. One can therefore predict from these results that mixing of the adsorbates may occur, but to a lesser extent at higher temperatures for CO + NH$_3$.

Electronic structure (CO + NH$_x$ on Fe(100))

To further study the changes incurred by the presence of either adsorbate (CO/NH$_x$) upon adsorption on the Fe(100) surface, a Bader charge analysis, projected density of states (PDOS) and electron redistribution plots of the individually adsorbed structures are compared to that of the most stable coadsorbed configurations. The charge densities was obtained in single point energy calculations (i.e. a static calculations) for the optimized structures, from which the PDOS was derived. In order to calculate well defined PDOS, all parameters remained unchanged with the exception of the k-points, where a 19×19×1 k-points grid was found to be sufficient for these calculations. The electron redistribution plots for the individually adsorbed CO or NH$_x$ on the Fe(100) surface ($\Delta\rho_{ind}$) was calculated with Eq. 6.7,

$$\Delta\rho_{ind} = \rho_{ads+Fe} - \rho_{ads} - \rho_{Fe} \tag{6.7}$$

where ρ_{ads+Fe}, ρ_{ads} and ρ_{Fe} are the electron densities of the geometry optimized structure for the adsorbate on the Fe(100) surface, the reference adsorbate and reference surface, respectively. The electron redistribution plots for the adsorbates in the coadsorbed configurations ($\Delta\rho_{coads}$) was calculated with a similar method (see Eq. 6.8).

$$\Delta\rho_{coads} = \rho_{ads_1+ads_2+Fe} - \rho_{ads_1+Fe} - \rho_{ads_2+Fe} + \rho_{Fe} \tag{6.8}$$

The electron redistribution plots for the coadsorbed structure (ρ_{coads}) was calculated by subtracting the electron density of the coadsorbed configuration ($\rho_{ads_1+ads_2+Fe}$) from the electron density of the individually adsorbed CO/NH$_x$ + Fe(100) ($\rho_{ads_{1/2}+Fe}$) configurations, and the subsequent addition of a clean Fe(100) surface (ρ_{Fe}) to account for the extra slab. For all the reference configurations, the cartesian coordinates of the geometry optimized configurations were used for the calculations. For brevity, the PDOS and electron redistribution for only a selected set of coadsorbed structures (NH$_3$ + CO, NH$_2$ + CO and NH(*trans*/*cis*) + CO) are discussed. In all the electron redistribution plots reported in the following subsections, the isosurfaces for the accumulation and depletion of electrons are drawn in yellow and blue respectively, while the z axis color assignment is given for the cuts through the surface.

Bader charge analysis

To evaluate the charge density changes upon coadsorption of CO and NH$_3$ on the Fe(100), we make use of Bader charge analysis through the use of algorithms and code provided by the Henkelman group [39]. Bader charge analysis, developed by Richard Bader [40], provides a way of partitioning atoms in molecules via the changes in fluxes of the electron densities.

The changes in the Bader charge upon coadsorption of CO + NH$_x$ on Fe(100) is tabulated in Table 6.4. The changes in the electronic charge of CO calculated for this series is relatively small, with the exception of NH and N in the *cis* configuration which leads to electron accumulation on the CO (Δq = +0.09 and +0.13 e respectively). CO coadsorbed with NH/N in the *cis* configuration resulted in a destabilizing effect based on their calculated heat of mixing. NH$_3$, NH(*trans*) and N(*trans*) effects a Δq = −0.05, −0.05 and −0.03 e change for CO upon

Table 6.4: A summary for the changes in the Bader charges upon coadsorption for CO and the NH_x (x = 3, 2, 1, 0) is presented.

CO +	**NH_3**	**NH_2**	**NH (t)**	**NH (c)**	**N (t)**	**N (c)**
Δq (NH_x) (e)	+0.06	+0.08	+0.01	+0.10	+0.01	+0.13
Δq (CO) (e)	−0.05	+0.01	−0.05	+0.09	−0.03	+0.13

coadsorption respectively, which is indicative of electron donation to CO from NH_3 and associated with a promotional effect [1, 11]. These values are however smaller in magnitude than the values (between $\Delta q = -0.07$ and -0.24 (e)) calculated for CO in (CO + K on Fe(100)) reported by Sorescu [1]. It was calculated for the aforementioned coadsorption structures (CO + NH_3/NH/N on Fe(100)) to have exothermic heats of mixing. With the exception of the CO + NH/N in the *trans* configurations, there is an increase in the charge (between $\Delta q = +0.06$ and +0.13) on the NH_x surface species. All of these NH_x adsorbates (in their relevant configurations), except NH_2 was calculated to have an endothermic heat of mixing in the current work. These findings are combined with some PDOS and electron redistribution plots in order to shed light on the changes in the electronic structure when both CO and NH_x is coadsorbed on the surface.

NH_3/CO in (CO + NH_3) on Fe(100)

In Figure 6.8 the PDOS for the s+p orbitals of CO and NH_3 that was calculated for the geometry optimized structure of CO + NH_3 on Fe(100) is given. The enlarged plots added at the bottom of the figure serves as a visual aid. From this analysis it can be deduced that CO and NH_3 interacts directly through the formation of linear combinations of their atomic orbitals. The rehybridization that is required for this newly formed bonds could lead to a stronger or weaker adsorption energy for the individual adsorbates. This observation was made for all the coadsorbed (CO +NH_x) structures and is discussed below for CO + N (*cis*/*trans*), while that of CO + NH_2/NH is presented in Appendix B (see Figure B.15).

In Figure 6.9 the electron redistribution plot for $\theta = 0.25$ ML covered $NH_3(at)$ adsorbed on Fe(100) is given. The cut through the plane that contains the Fe-NH_3 bond reveals the major

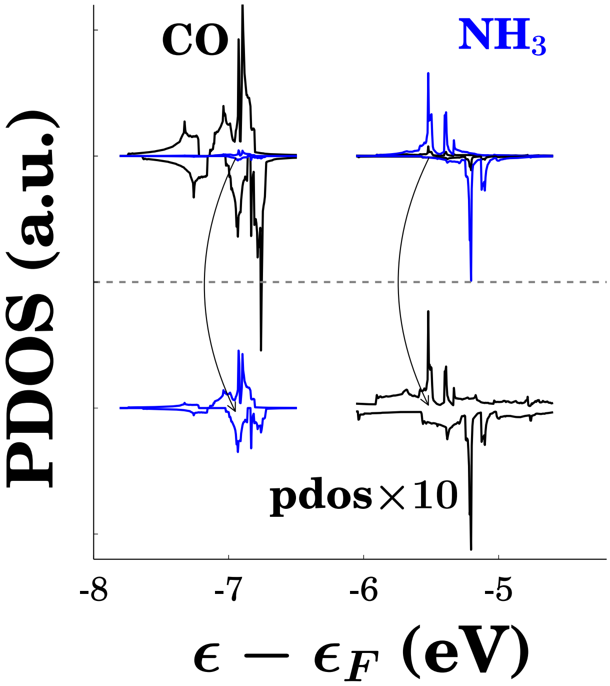

Figure 6.8: The PDOS for CO and NH$_3$ when coadsorbed on the Fe(100) surface is plotted as a function of the energy below the Fermi level ($\epsilon_F - \epsilon$). Enlarging the PDOS at the bottom part of the figure illustrates the linear combination of their individual orbitals at certain energy levels.

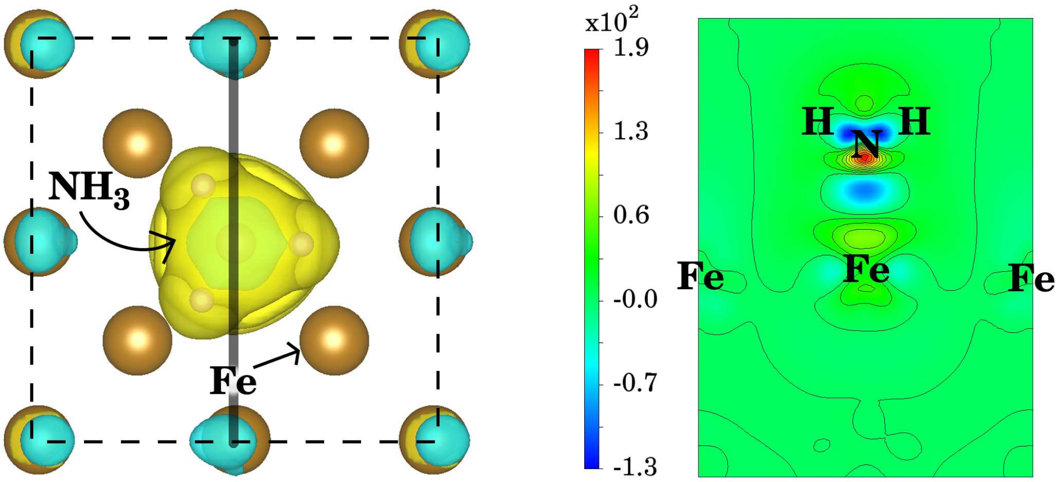

Figure 6.9: (*Left:*) Top view for the electron redistribution plot when NH_3 adsorbs on Fe(100) at a $\theta = 0.25$ ML coverage. The line indicates the position of the plane that cuts through NH_3 and the surface. Electron accumulation and depletion is shown in yellow and blue respectively. (*Right:*) The electron delocalization does not only occur between the Fe atom directly below the NH_3, but also the neighbouring Fe atoms.

electron redistribution here, which is mainly a rehybridization of the orbitals of NH_3 in order for the NH_3 adsorbate to share its lone pair with the Fe atom. In the context of the coadsorption of NH_3 with CO, it is interesting to note that it is not only the Fe atom directly bonded with the NH_3 adsorbate where the electron density changes, but an accumulation of electrons can be seen in the region above the remaining three Fe atoms in the top layer (see the top view in (Figure 6.9: *Left*) and the cut through the plane (*Right*)). A similar electron redistribution pattern was calculated for K on Fe(100) at a lower coverage ($\theta = 0.11$ ML) [1].

The electron redistribution plot (see Figure 6.10) calculated for CO + NH_3 on the Fe(100) surface reveals several aspects of the electronic structure that are at play when these adsorbates are both present on the Fe(100) surface. Most notably would be the polarization that occurs around the oxygen atom. An electron redistribution plot with a similar polarization effect around the oxygen atom was calculated by Sorescu [1] for CO + K on Fe(100) using DFT. In accordance with the Bader charge analysis discussed above, a depletion of electrons can be seen between the Fe-N bond which could lead to a higher charge on the NH_3 adsorbate or N atom. The depletion of the electrons around the N atom are to some extent directed toward the

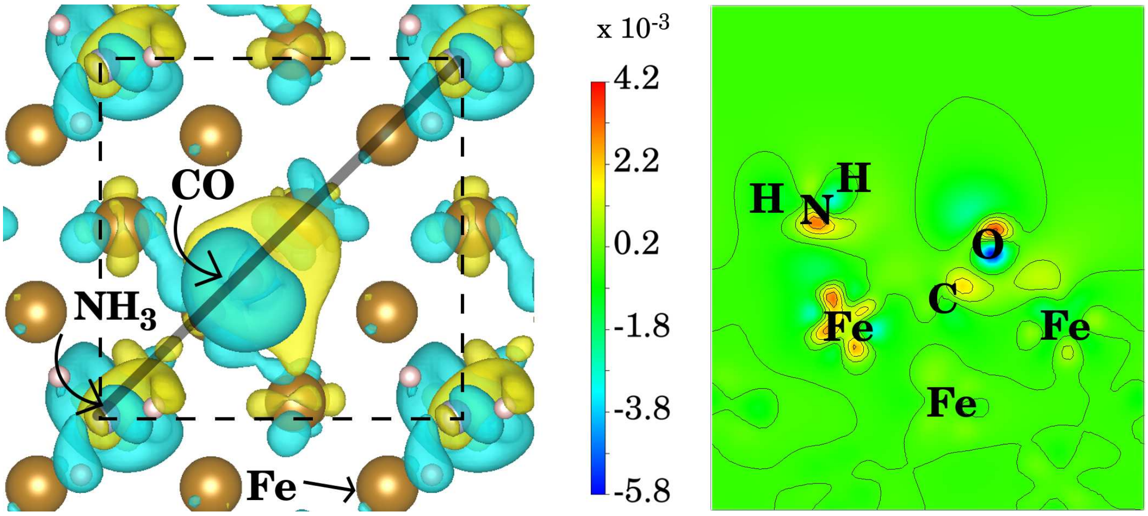

Figure 6.10: (*Left:*) Top view for the electron redistribution plot when CO(ft') + NH$_3$(at) coadsorbs on Fe(100) at a $\theta = 0.25 + 0.25$ ML coverage. The line indicates the position of the plane that cuts through NH$_3$ and the surface. Electron accumulation and depletion is shown in yellow and blue respectively. (*Right:*) There is electron depletion between Fe-N and polarization of electrons around the oxygen atom. A slight increase in electrons can be seen between the oxygen and hydrogen atom.

CO adsorbate, which corroborates the direct interactions between CO and NH$_3$ suggested by the PDOS (see Figure 6.8). It is also interesting to note that there is a slight accumulation of electrons in the region of the H atoms. Moreover, there is a region of accumulation of electrons between the H and O atom. When studying the coadsorption of Na/K + CO on the Fe(100) facet using DFT, Mahyuddin et al. [11] assigned the promotional effects of the alkali adatoms on CO adsorption to electrostatic interactions between the electronegative oxygen atom and the electropositive K/Na atoms based on their LDOS and Bader charge analysis. It was also suggested in this study [11] that K has a larger stabilization effect than Na, due to the direct hybridization of K with O which was not the case for Na. The electron redistribution observed between the H and O atoms could thus contribute to the favorable heat of mixing calculated for CO + NH$_3$ on Fe(100).

To shed light on possible electrostatic interactions between CO and NH$_3$ on the Fe(100) surface, the Bader charge of individually adsorbed CO and NH$_3$ and that of the coadsorbed structure (CO + NH$_3$ on Fe(100)) are further deconvoluted by considering the Bader charges of the atoms

(See Figure 6.11). If the Bader charge of the three hydrogen atoms are added (3H), the dipole moment that exists within the NH_3 adsorbate is revealed. Even though the change in the overall charge of the NH_3 adsorbate does not change significantly as discussed above, the charge on the hydrogen atoms decrease by $\Delta q = -0.10\ e$ and increase by $\Delta q = +0.15\ e$ for the N atom. The combination of the polarization of electrons observed around the oxygen atom in the electron redistribution plot (see Figure 6.10), and the Bader charge analysis in Figure 6.11 would suggest that a dipole-dipole interaction occurs between NH_3 and O when CO and NH_3 are coadsorbed on the Fe(100) surface. If the electrostatic interaction is contributing to the stabilization for the coadsorbed state of CO + NH_3 on the Fe(100) facet, it could be possible that such dipole-dipole effects occur on other transition metal surfaces, such as the Co(0001) and Ru(001) surfaces where mixed ordered states of CO + NH_3 was experimentally observed [20, 23].

A final result that sheds light on the favorable heat of mixing calculated for CO and NH_3 on Fe(100) is the rehybridization calculated within the $p_{x/y/z}$-orbitals of the oxygen atom. In Figure 6.12 the PDOS of the $p_{x/y/z}$-orbitals for oxygen in the individually adsorbed (*black*) and coadsorbed (*blue*) structure are superimposed and plotted as a function of energy below the Fermi level (ϵ - ϵ_F). The first observation that can be made here is the shift from the sharp peak (at approximately −6.7 eV) of the p_x-orbital in CO(*ft'*) to a broader distribution at lower energy levels for O in the in the coadsorbed structure, which would lead to a lower adsorption energy. This sharp peak in the CO(ft') structure presumably originates due to the direct bonding of the oxygen atom with the Fe atom as discussed in Appendix B. It is possible that the additional electrons located on the Fe atoms that is not directly bonded to NH_3 (as a consequence of NH_3 adsorption on Fe(100) (see Figure 6.9)) contribute to this new hybridization. The polarization effect discussed above could also contribute to the change in the electronic structure predicted by the PDOS of the oxygen p_x-orbitals. Secondly, it should be pointed out that the three $p_{x/y/z}$-orbitals change their contributions towards the formation 1π and 5σ orbitals for the O in the two environments, which could again be due to the additional electrons on the Fe atoms bonded to O or the polarization effect that arise as a consequence of NH_3 adsorption on the Fe(100) surface.

In summary, the electronic structure analysis (conducted via Bader charge analysis, PDOS and

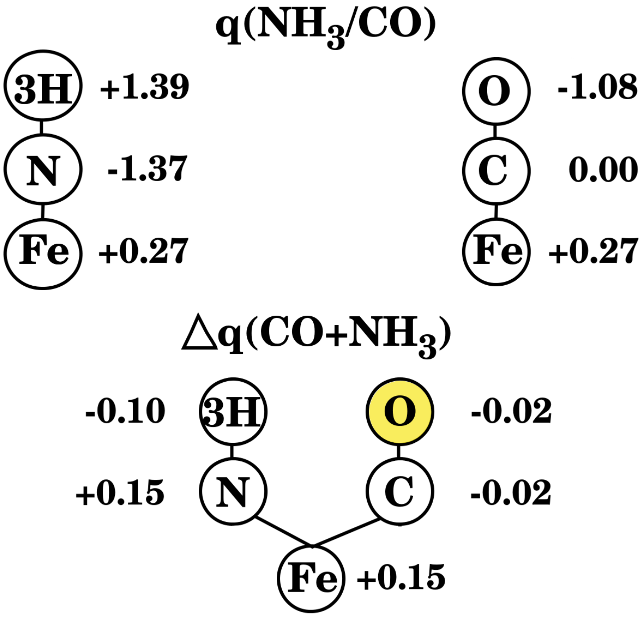

Figure 6.11: Schematic accompanied by a Bader charge analysis that illustrates the possible electrostatic interactions between CO and NH_3 when individually (*Top*) adsorbed or coadsorbed (*Bottom*) on the Fe(100) surface. The Bader charge and change in charge per atom (or sum of atoms, e.g. 3 × H) is denoted by $q/\Delta q$ respectively. Oxygen is highlighted in the figure to indicate the polarization observed in its electron redistribution plot (see Figure 6.10)

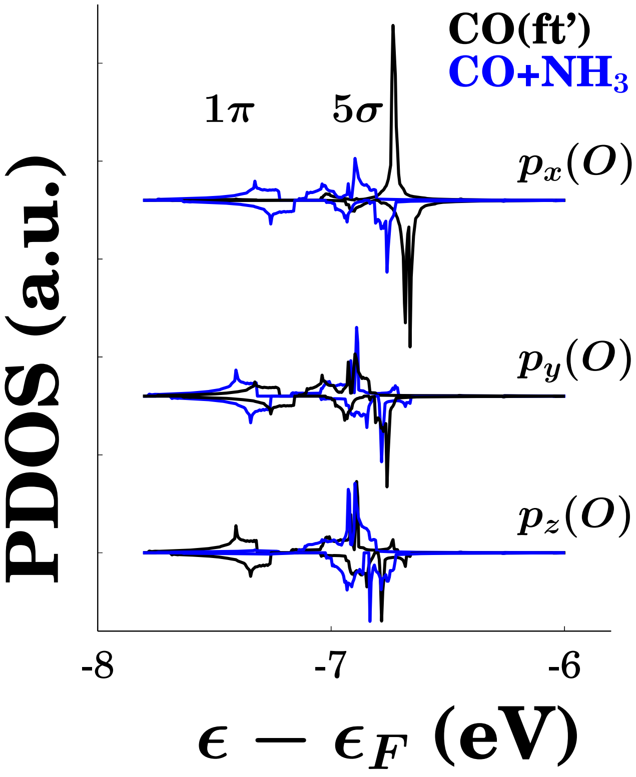

Figure 6.12: (*Top:*) PDOS for $p_{x/y/z}$-orbitals of oxygen in CO(ft') (*black*) and (CO(ft') + NH$_3$(at)) (*blue*) as a function of energy from the Fermi level (ϵ - ϵ_F). When NH$_3$ is present on the surface, the hybridization of the $p_{x/y/z}$-orbitals for oxygen changes in a way that has a net stabilizing effect.

electron redistribution plots) points toward an energetically feasible configuration for CO + NH_3 on Fe(100). The underlying mechanism for this stable coadsorbed system is likely due to a combination of the change in the electronic structure upon coadsorption and electrostatic interactions between the adsorbates. In contradiction to the view of NH_3 acting as a poison in the FTS regime, the electronic structure analysis reported here resembles those calculated in DFT studies of FTS catalyst promoters (K/Na) on Fe(100) [1, 11]. It is therefore interesting to remark that in an experimental study, Henkel [7] reported that the addition of NH_3 during FTS when using an unpromoted Fe-based catalyst led to similar promotional effects on the FTS product spectrum as one would expect when promoting the catalyst with potassium (see Chapter 5 for a detailed discussion).

NH_2/CO + CO on Fe(100)

In Figure 6.13 the electron redistribution plot for the coadsorbed structure of CO + NH_2 on Fe(100) is presented. To get a detailed picture of the changes in the electronic structure, the slab is cut through four planes as indicated on the right of the figure (*A, B, C, D*). The accumulation of electrons in the Fe-N bonding regions (see Figure 6.13: *A, B*) seems consistent with the increased charge ($\Delta q = +0.08$) calculated for NH_2 in the Bader charge analysis in NH_2 + CO on Fe(100). Unlike the case for NH_3, minimal changes are seen around the carbon and oxygen atoms, which also corresponds to the electronic charge reported earlier ($\Delta q = +0.01$) for CO in CO + NH_2. This analysis thus seems to suggest that the NH_2 bonding is disturbed by the presence of CO, and CO bonding is unperturbed by the presence of NH_2. Importantly, this analysis is in agreement with the endothermic heat of mixing calculated for CO + NH_2 on Fe(100).

N/CO on Fe(100)

Based on the PES for NH_3 decomposition discussed in Chapter 5, it is predicted that N adsorbed in the fh site would be the most thermodynamically stable among the NH_x surface species and could potentially block the CO adsorption reaction. Furthermore, the CO + N in the *trans* and *cis* configurations was calculated to have exothermic and endothermic heats of mixing respectively. It is therefore important to understand the mechanistic detail that leads to this

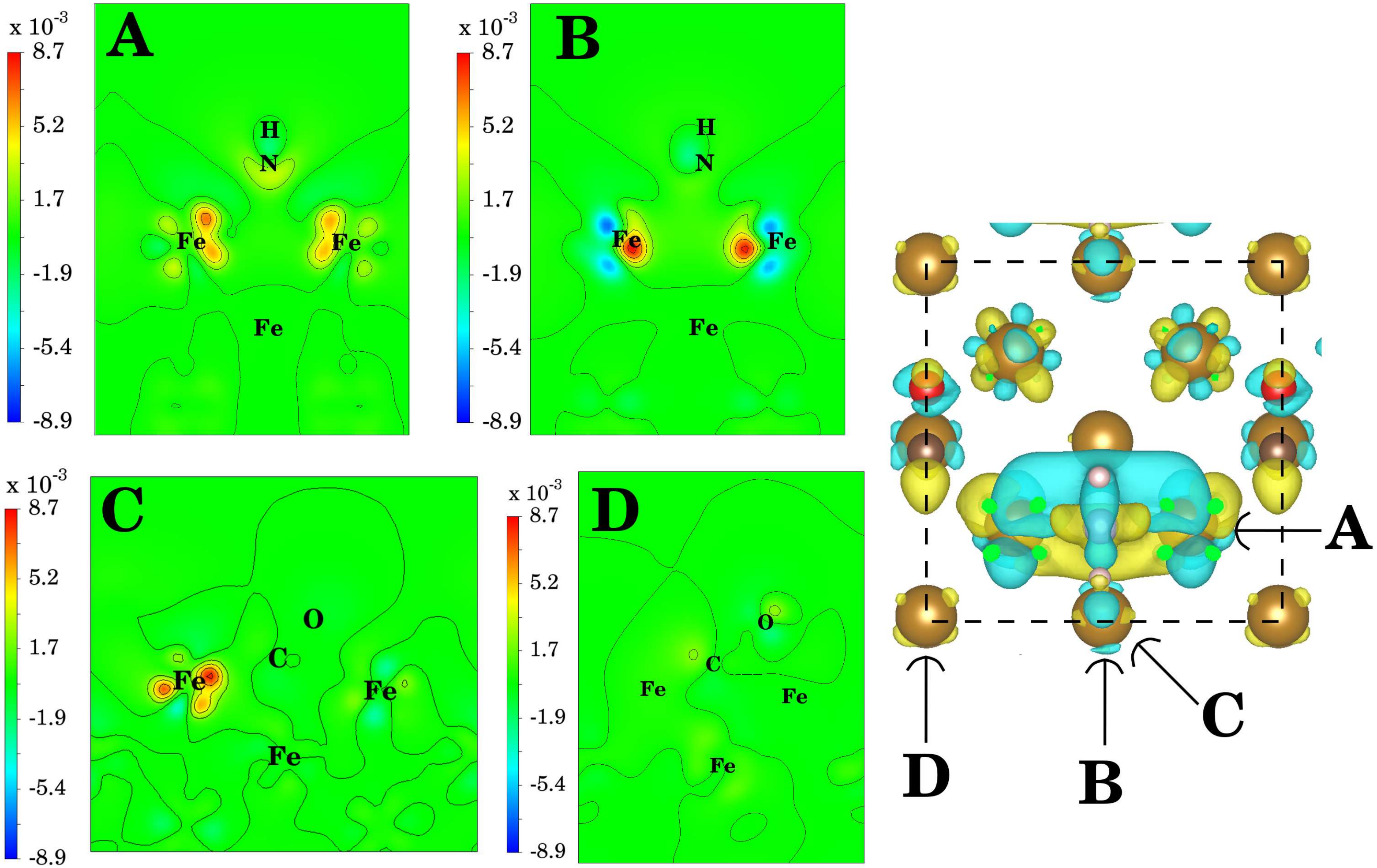

Figure 6.13: *Top:* Electron redistribution plots for 0.25 + 0.25 ML of CO(ft) + NH_2(at) on Fe(100) where the slab has been cut through the plane at the positions *A* - *D* indicated on the right. Electron accumulation and depletion is shown in yellow and blue respectively. Minimal changes occur on the CO adsorbate, but electron depletion is observed in areas between the Fe-N bonds.

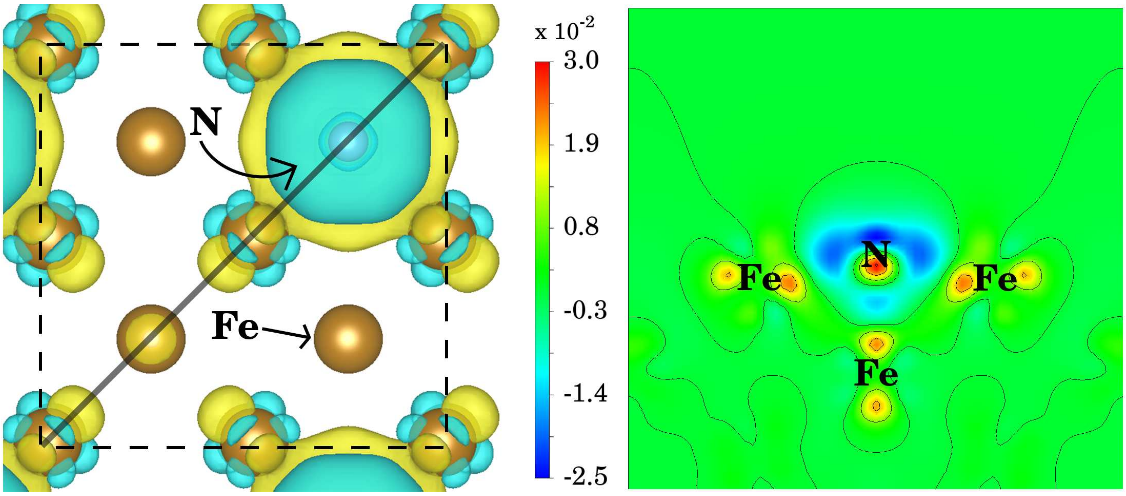

Figure 6.14: (*Left:*) Top view for the electron redistribution plot when N adsorbs at the fh site on Fe(100) at a $\theta = 0.25$ ML coverage. The line indicates the position of the plane that cuts through the N adatom and the surface. Electron accumulation and depletion is shown in yellow and blue respectively. (*Right:*) The electron delocalization does not only occur between the Fe atom directly below the NH$_3$, but also the neighbouring Fe atoms.

(de-)stabilization. In Figure 6.14 the electron redistribution plot for individually adsorbed N in the fh site is given. The (solid) line that passes through the diagonal of the unit cell (dotted line) in the top view indicates the plane that cuts through the surface to produce the 2D plot. From this plot (Figure 6.14: *Right*) it is easy to see the stabilization afforded by the interaction of N and its neighbouring Fe atoms. More importantly, when considering the fh sites now available for CO adsorption (best observed in the top view Figure 6.14: *Left*), a distinct difference in the electronic structure can be seen in the *cis* and *trans* configurations. The different environments created by N(fh) on Fe(100) could thus contribute to the difference in heats of mixing calculated in these configurations.

In Figure 6.15 the PDOS for oxygen in the individually adsorbed state CO(ft) and coadsorbed states CO(ft) + N(*trans*)/N(*cis*) is compared. In order to assist the argument, the PDOS is subdivided into three areas (R1, R2 and R3) which correspond to the regions where the $1\pi/5\sigma$, the newly formed O+N orbitals and the $2\pi^*$ orbitals are respectively located. When integrating over these areas (Figure 6.15: *Bottom*), one can see that the overall effect would be stabilization for CO + N(*trans*) and destabilization for CO + N(*cis*). This finding is consistent with the longer Fe-O bonds ($\Delta d_{Fe^1-O} = 0.14$ Å) in the *cis* configuration It was mentioned in the discussion of the geometry of the CO + N (*trans*/*cis*) configurations above, that the drive for N to reconstruct the surface leads to a smaller cavity for the CO to bond in the *fh* site. It is thus likely that the decreased interaction with O in the CO + N(*cis*) configuration is due to the shorter distances between the Fe atoms ($\Delta d_{Fe-Fe} = 0.14$ Å) parallel to the CO bond, which in turn is a consequence of the presence of N adatoms.

CO dissociation in the presence of NH_x (with x = 3, 2, 1, 0) on Fe(100)

In Chapter 5, the calculated potential energy surface for the CO dissociation reaction at $\theta = 0.25$ ML on the Fe(100) surface was reported, which will be compared here to the CO dissociation reaction in a (2 × 2) supercell that is preadsorbed with $\theta = 0.25$ ML of the NH_x adsorbates (i.e. NH_3, NH_2, NH or N). The geometry optimized structures of the coadsorbed CO + NH_x on Fe(100) (see Fig. 6.1 - 6.4) were used in each case as the initial structure, while the relevant final states (C + O + NH_x) were calculated prior to the searches for the transition states. Based on the redshift in the stretch frequency of the tilted CO in the presence of the NH_x adsorbates, it is reasonable to assume that the CO dissociation pathway proceeds from the ft/ft' geometries analogous to CO dissociation on the Fe(100) facet in the absence of NH_x. This presents the added advantage of allowing for a direct comparison between CO dissociation in the presence and absence of the NH_x adsorbates on Fe(100). For the aforementioned reason and efficiency no further searches were carried out for other possible CO dissociation routes. The initial, transition and final state of the pathway for CO dissociation (at $\theta = 0.25$ ML) in the absence of NH_x on Fe(100) can be seen in Fig. 5.2 of Chapter 5. In this route the carbon atom remains in the original fourfold hollow site, while the C-O bond elongates until the transition state is reached where the oxygen atom is situated in a quasi bridge position. The oxygen atom then finally diffuses to the adjacent fourfold hollow site. The initial, transition and final state of the pathway for ($\theta = 0.25$ ML) CO dissociation in the presence of ($\theta = 0.25$ ML) NH_x on Fe(100) are presented in Fig. B.20 - B.23 of Appendix B. In order to gain an overall view of the CO dissociation reaction with the addition of the NH_x adsorbates on the Fe(100) surface, it is important to consider the relative stability of the coadsorption at the initial state, which can be quantified via the mixing energy (ΔE_{mix}). To visualize the comparison made for the

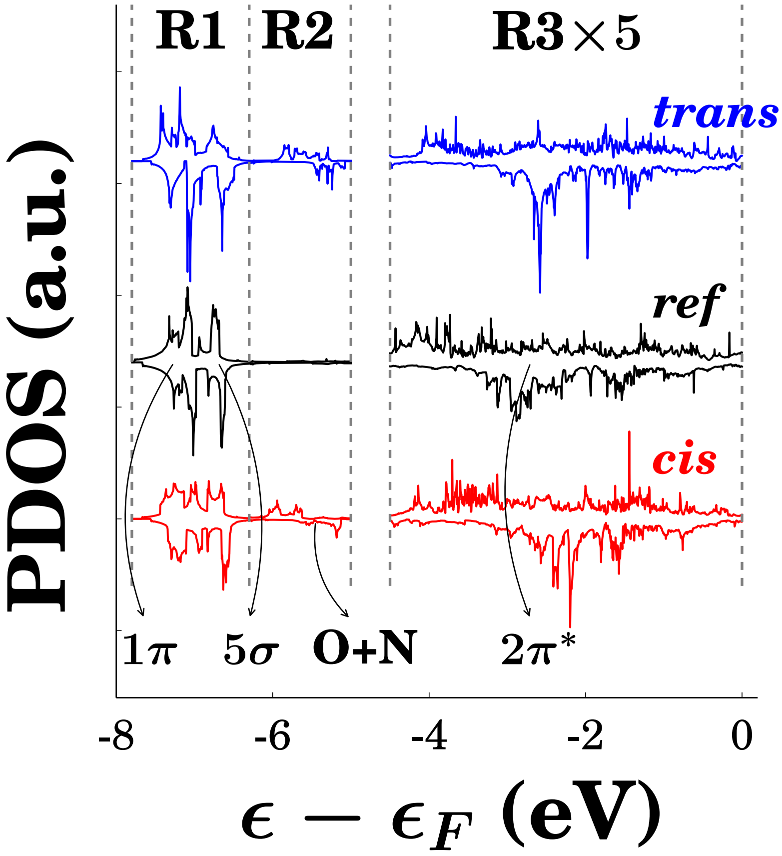

Distribution of e^{-}s (%)			
	ref	*cis*	*trans*
R1	63	57	60
R2	2.9	10	11
R3	34	33	29

Figure 6.15: (*Top:*) Localized density of states (LDOS) as a function of energy from the Fermi level (E - E$_f$) and (*Bottom:*) electron redistribution plots for 0.25 ML CO(ft) adsorbed on the Fe(100) surface and when coadsorbed with 0.25 ML N(fh, *trans*) on the same surface. Electron accumulation and depletion is shown in blue and yellow respectively. (E$_{cut}$ $\leq$ 400 eV, k-points: 11x11x1 for LDOS)

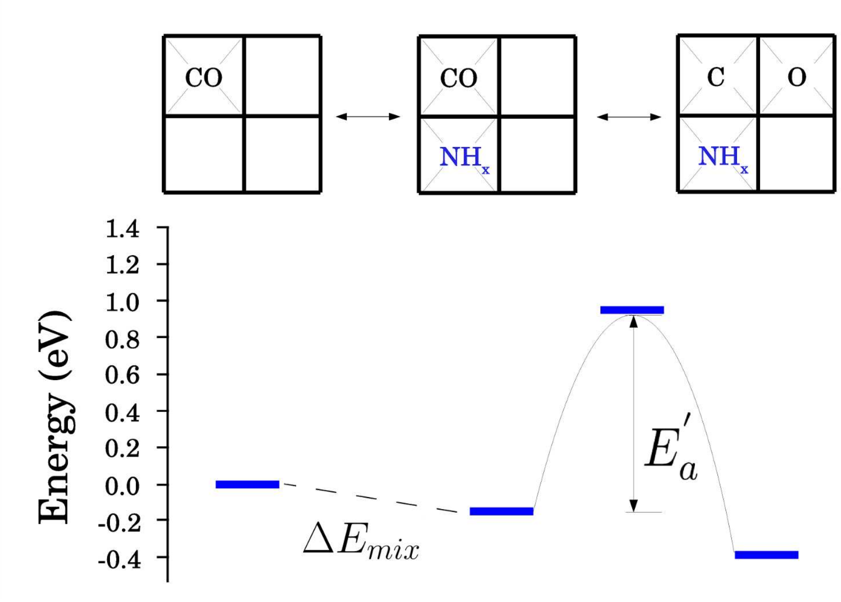

Figure 6.16: Schematic to to illustrate the overall comparison for the CO dissociation in the presence of the NH$_x$ adsorbates, which includes the effect upon coadsorption of the NH$_x$ adsorbates which is quantified via the heat of mixing (ΔE_{mix}) with θ = 0.25 + 0.25 ML for CO + NH$_x$ on Fe(100) as calculated in the Section 6.3.2. The activation energy E_a' refers to the CO dissociation in the absence and presence of the NH$_x$ adsorbates respectively.

CO dissociation reaction on an NH$_x$ precovered Fe(100) surface, a schematic is given in Fig. 6.16. The calculated mixing energy (ΔE_{mix}), activation energy (E_a), the changes incurred on the activation energy by the presence of the coadsorbates (ΔE_a) and the heats of the reaction (ΔE_{rxn}) are tabulated in Tabel 6.5.

NH_3 + CO → NH_3 + C + O

For the CO dissociation reaction where CO is coadsorbed with NH$_3$ on Fe(100) (see Fig. B.20 of Appendix B), the initial structure has the CO adsorbate bonded in the fourfold tilted position with oxygen bonded to only one Fe atom (ft') and the final structure with C and O in two fourfold hollow sites. The minimum energy pathway (MEP) calculated for this reaction initially proceeds with a horizontal rotation of the CO bond to take on the CO(ft) configuration with CO bonded to two Fe atoms. It then follows a similar route as the pathway described for the CO dissociation of the individually adsorbed CO on Fe(100) with θ = 0.25 ML. The CO bond

Table 6.5: Calculated activation energies (E_a) for the CO dissociation on a clean and NH_x precovered Fe(100) surface, the difference between the aforementioned activation energies (ΔE_a), the heat of mixing for the initial coadsorption configuration (E_{mix}) and the heat of the CO → C + O reaction (ΔE_{rxn}) is tabulated below.

Surface reactions	$\Delta E_{mix}(eV)$	E_a (eV)	ΔE_a (eV)	d_{CO} (Å)	ΔE_{rxn} (eV)
CO → C + O	0.00	1.19	0.00	1.96	−0.35
NH_3 + CO → NH_3 + C + O	−0.16	1.11	−0.08	1.95	−0.24
NH_2 + CO → NH_2 + C + O	0.13	1.07	−0.12	1.99	−0.21
NH + CO → NH + C + O	−0.21	1.26	0.07	2.05	0.11
N + CO → N + C + O	−0.17	1.38	0.19	2.20	0.35

length (d_{C-O} = 1.95 Å) and imaginary vibrational mode ($v_i = 303i$ cm^{-1}) calculated for the transition state structure is similar to that calculated in the absence of NH_3 (d_{C-O} = 1.96 Å and $v_i = 309i$ cm^{-1}). As discussed before, there is a stabilizing effect ($\Delta E_{mix} = -0.16$ eV) when NH_3 and CO are coadsorbed on Fe(100). The calculated CO dissociation energy barrier in the presence of NH_3 of E_a = 1.11 eV, is lower (ΔE_a = -0.08 eV) than in its absence (E_a = 1.19 eV). The exothermicity for the heat of the reaction (ΔE_{rxn} = -0.24 eV) when CO and NH_3 are coadsorbed is however reduced by 0.11 eV when compared to the CO dissociation reaction for the individually adsorbed CO (ΔE_{rxn} = -0.35 eV).

NH_2 + CO → NH_2 + C + O

Only one pathway was considered for the CO dissociation reaction of CO coadsorbed with NH_2 on Fe(100). Figures for the initial, transition and final state configurations are given in Fig. B.21 of Appendix B. The calculated CO dissociation reaction pathway in the presence of NH_2 proceeds as described for the reaction in the absence of the NH_2. Furthermore, the C-O bond length (d_{C-O} = 1.99 Å) and imaginary vibrational frequency ($v_i = 299i$ cm^{-1}) at the transition state structure could be indicative of a ‘later ’transition state along the PES when compared to these parameters calculated in the absence of NH_2 (d_{C-O} = 1.96 Å and v_i = 309 cm^{-1}). Even though the lateral interaction between NH_2 and CO is repulsive (ΔE_{mix} = 0.13 eV), a lower activation energy (E_a = 1.07 eV, $\Delta E_a = -0.12$ eV) is obtained when comparing the CO dissociation reaction in the presence and absence of NH_2. Similar to NH_3, the exothermicity ($\Delta E_{rxn} = -0.21$ eV) for the CO dissociation reaction calculated when NH_2 is coadsorbed with CO is reduced when compared to the heat of the reaction of individually adsorbed CO ($\Delta E_{rxn} = -0.35$ eV).

NH + CO → NH + C + O

Two possible pathways were considered for CO dissociation in the presence of NH (see Fig. B.22 of Appendix B). The first reaction pathway was set up with the CO and NH situated diagonally across the (2 × 2) Fe(100) surface unit cell (*trans*) for the initial structure. The final structure therefore has the carbon atom in a *trans* position, while the oxygen is in a *cis* position with respect to the NH adsorbate. The second route was set up in the opposite configuration, with the initial CO + NH in adjacent (*cis*) positions in the (2 × 2) supercell and the final structure thus having the carbon and oxygen atoms situated in *cis* and *trans* configurations respectively. The C-O bonds ($d^{trans}_{C-O} = 2.05$ Å and $d^{cis}_{C-O} = 2.03$ Å) and imaginary vibrational frequency ($v_i^{trans} = 248i$ cm^{-1} and $v_i^{cis} = 296i$ cm^{-1}) for the TS structures suggests a 'later 'transition state for both paths compared to the case for the individual CO dissociation on Fe(100) ($d_{C-O} = 1.96$ Å and $v_i = 309i$ cm^{-1}). Even though the mixing energy for CO + NH in the *trans* configuration is energetically favorable ($\Delta E_{mix} = -0.21$ eV), the calculated activation energy for this pathway is $E_a = 1.26$ eV, which is 0.07 eV higher than in the absence of NH ($E_a = 1.19$ eV). Furthermore, the overall CO dissociation reaction is not favored for this pathway, since the calculated heat of the reaction is endothermic with $\Delta E_{rxn} = 0.11$ eV. The calculated activation energy for CO + NH on Fe(100) coadsorbed in the energetically unfavored *cis* configuration ($\Delta E_{mix} = 0.28$ eV) as the initial structure is even higher with $E_a = 1.42$ eV. The heat of the reaction for dissociation in the CO + NH *cis* configuration is similar to all previous calculations less exothermic with $\Delta E_{rxn} = -0.11$ eV.

N + CO → N + C + O

Analogous to CO dissociation in the presence of NH, two paths were investigated for CO + N coadsorbed in the (2 × 2) surface unit cell. That is, the initial structures were set up with CO and N either in *trans* or *cis* configurations and their final structures with the C and O atoms situated in the fh sites as shown in Fig. B.23 of Appendix B. When CO + N on Fe(100) has N in the $trans$ configuration initially, the C-O bond is significantly elongated d^{trans}_{C-O} = 2.20 Å, indicating a much later transition state for dissociation if the C-O bond length is taken as the dominant component of the reaction coordinate. A slightly reduced C-O bond (d^{cis}_{C-O} = 1.94 Å) was calculated for cis configuration at the TS compared to the CO bond (d_{C-O} = 1.96 Å) for the TS structure calculated in the individual CO dissociation reaction on Fe(100). For CO + N in the $trans$ configuration, the initial structure is calculated to be stabilized by the presence of N (ΔE_{mix}) so that mixing of CO and N is predicted to be favourable, but the activation energy for this pathway is E_a = 1.38 eV, which is 0.19 eV higher than in the absence of N. Moreover, a high endothermic heat of reaction (ΔE_{rxn} = 0.35 eV) is obtained for the CO + N ($trans$) CO dissociation reaction, that has N and O located adjacent to each other in the final structure in the (2 × 2) unit cell. The activation energy when the initial structure has the two adsorbates (CO + N) in a cis configuration also results in a similar increase in the activation barrier (E_a = 1.39 eV), but the reaction remains exothermic. Nevertheless, this initial structure where CO is adsorbed adjacent to N on the Fe(100) surface, is highly destabilizing (ΔE_{mix} = 0.36 eV). Overall there does not seem to be a direct correlation between the CO vibrational stretching frequency or the C-O bond lengths in the initial state and the activation energies calculated here (E_a). The activation energy could however potentially be predicted by a Brønsted-Evans-Polanyi (BEP) type relation. Such a correlation is further investigated and discussed in Section B.3.4.1 of Appendix B. Based on this analysis, one can hypothesize that a BEP relation may exist, however, an account may have to be made for the electrostatic interactions of the coadsorbed surface species at the transition state of the PES.

Pathway to FTS products

Based on the results reported here, the possible role that NH$_x$ adsorbates may play in the formation of FTS products is further discussed in this section. Here, FTS products include the formation of N-containing compounds upon the co-feeding of NH$_3$ during FTS.

The role of NH_2

Various authors have reported that the predominant N-containing compounds formed when co-feeding NH_3 during FTS are primary amines [3–8]. Both Henkel [7] and Sango [8] postulated that NH_2 could be inserted into a growing chain during the final step to form primary amines. It is therefore interesting to note that different properties for NH_2 compared to the other adsorbates NH_3, NH, and N were obtained. Firstly, it is inferred from Chapter 5 that NH_2 could be kinetically trapped on the Fe(100) catalytic surface based on its significantly higher activation barrier ($E_a = 1.44$ eV) for the reaction $NH_2 \rightarrow NH + N$. Furthermore, it was reported here that unlike the other adsorbates, NH_2 and CO are likely to form islands on the Fe(100) surface at the coverages investigated. This could potentially lead to the availability of NH_2 adsorbates in regions on the catalytic surface to react with growing carbon chains. It has been shown via a combination of DFT and microkinetic modelling that it is likely that certain stages of FTS pathways occur on different types of catalytic surfaces [41]. Significantly more DFT computation and a microkinetic analysis thereof would however be required to confirm the hypothesis put forward above. A final hypothesis one can make based on these results is that the lower activation energy for CO dissociation when CO and NH_2 are in close proximity would increase the rate of formation of C atoms on the surface. If this could be coupled with rapid O removal, the formation of primary amines may be enhanced.

NH_x as promoter or poison

Promotion or poisoning of a FTS based catalyst is a complex aspect of FTS catalysis that can be subdivided into several modes of deactivation [13]. In Fe-based FTS catalysis, K and S are generally regarded as key examples of chemical promoters or poisons, respectively. As mentioned before, CO adsorption and dissociation reactions are considered to be important elementary reactions in FTS mechanisms [42]. It is therefore interesting to compare the results obtained here with studies where similar periodic DFT methods have been used to investigate CO adsorption and dissociation in the presence of K and S on Fe(100) surfaces, respectively. In Table 6.6 a summary is given of the results reported by Sorescu [1] and Curulla-Ferré et al. [2] who performed calculations for CO adsorption and dissociation in the presence of K and S in (2 × 2) periodic surface unit cells, respectively. An extensive investigation was performed by

Table 6.6: Calculated activation energies (E_a) for CO dissociation on a clean and K/S precovered Fe(100) surface, the difference between the aforementioned activation energies (ΔE_a), the heat of mixing for the initial coadsorption configuration (E_{mix}) and the heat of the CO → C + O reaction (ΔE_{rxn}). Results are derived from data in Ref. [1] and [2].

Surface reactions	$\Delta E_{mix}(eV)$	E_a (eV)	ΔE_a (eV)	ΔE_{rxn} (eV)
Results from Soresco [1] DFT calculations				
K(*trans*) + CO → K + C + O	−0.23	0.78	−0.24	0.00
K(*cis*) + CO → K + C + O	−0.45	0.83	−0.27	0.05
Results from Curulla-Ferré et al. [2] DFT calculations				
S(*trans*) + CO → S + C + O	0.27	1.29	0.15	0.32
S(*cis*) + CO → S + C + O	1.01	1.25	0.11	−0.44

Sorescu [1] to study K coadsorption with CO, but only the information that corresponds to the results here (0.25 + 0.25 ML CO + K on Fe(100)) are discussed. In both studies, unique nomenclature was used to describe the coadsorption of CO + K/S on Fe(100), however in order to facilitate the argument being made here, the nomenclature (e.g. *cis* and *trans*) that has been defined in this work is used to describe the coadsorbed structures in Table 6.6. Two basic trends can be observed. Firstly, the presence of K and S leads to a stabilization or a destabilization for CO adsorption, respectively. Secondly, the CO activation energy is lower in the presence of K and higher in the presence of S. The endo-/exothermicity of the overall reaction (ΔE_{rxn}) remains unchanged for K coadsorption while the reaction is endothermic for *trans* coadsorption of CO + S on Fe(100).

NH_3 as promoter or poison

Based on the aforementioned breakdown of the CO coadsorption with a promoter and poison on Fe(100), NH_3 surprisingly exhibits similar trends to those that were reported for the coadsorption of CO with a promoter (K). It is therefore interesting to revisit the results obtained by Henkel [7], who found that NH_3 co-feeding during FTS (using an Fe-based catalyst in a fixed bed reactor) seemed to “mimic” the effects that were observed for K promotion during Fe-based FTS.

NH/N as promoter or poison

It was reported in Chapter 5 that N and possibly (NH) adsorbates will block the fourfold hollow sites based on the their relative stability compared to CO and preference for adsorption in the fourfold hollow site. The heat of mixing reported here for CO + N on Fe(100) predicts that it is not thermodynamically favored for CO to adsorb in the position adjacent to a pre-adsorbed N, which would therefore not only block CO adsorption at one site but effectively three sites in a (2×2) Fe(100) surface unit cell. If one considers NH and N coadsorption with CO on Fe(100) in comparison to the promoter and poison, it seems as if their effect on the coadsorption of CO in the *trans* configuration would be similar to the promoter for the stabilization of CO adsorption. However, the increase in CO activation energy and the endothermic heats of the reaction are similar to those of S + CO on Fe(100). This in fact presents a unique problem, since the mixed coadsorbed state would be preferred (based on the calculated ΔE_{mix} values), but its presence in that configuration would inhibit CO dissociation, which is necessary for the production of hydrocarbons. Sango [8, 43] reports on the deactivation of the Fe-based catalyst that he used when co-feeding NH_3 during FTS in a slurry phase reactor at higher concentrations of NH_3 (5 - 20 vol %). At these NH_3 concentrations a significant formation of aliphatic nitriles were observed which could be indicative of the formation of surface N species.

Conclusions

In this chapter the coadsorption of CO and NH_x (with $x = 3, 2, 1, 0$) on the Fe(100) surface were studied via spin-polarized DFT calculations. Attention was specifically given to the mechanisms by which the NH_x adsorbates influence the important CO adsorption and dissociation reactions on the Fe(100) facet. The calculation of the adsorption energies of $\theta = 0.25$ ML CO on $\theta = 0.25$ ML NH_x pre-covered Fe(100) surfaces ($E'_{ads,CO}$) allowed for the calculation of the mixing energies ΔE_{mix}. The calculation of mixing energies was extended to a lower and higher coverage ($\theta = 0.11$ and 0.50 ML) respectively to gain additional information about the lateral interactions between CO and NH_3 on Fe(100). The stabilization or destabilization that was predicted by the mixing energies and structural changes upon coadsorption were then further elucidated by calculating Bader charges, PDOS and electron redistribution plots for some of the individual and coadsorbed structures. In order to evaluate the effects the NH_x adsorbates have on the important CO dissociation reaction, transition states for the CO dissociation reaction were located using the climbing image NEB method in a (2 × 2) Fe(100) surface unit cell that was pre-adsorbed with $\theta = 0.25$ ML NH_x. The geometry optimization for CO coadsorbed with NH_3 on Fe(100) resulted in a tilting (from 90° to 84°) of the Fe-N bond with the Fe(100) surface, which is an interesting observation if one considers the tilting observed during surface science studies of the mixed CO + NH_3 phases on a Ru(001) surface [20, 24]. Furthermore, mixed phases of CO and NH_3 was reported by Kizilkaya et. al [23] during their UHV experiments used to probe the coadsorption of CO and NH_3 on Co(0001). If the results reported in these respective studies can be extended from the Ru(001) or Co(0001) surfaces, an enhanced electron exchange between CO and NH_3 and the transition metal surface predicted by these authors [20, 23, 24] is corroborated by this first principle study based on the results discussed for the Bader charges, PDOS and electron redistribution between CO and NH_3 on Fe(100). A comparison between the results calculated here for CO + NH_x on Fe(100) with that reported [1, 2] for CO adsorption and dissociation in the presence of poison (S) and a promoter (K), respectively revealed mixed results. NH_3 coadsorption exhibits the same stabilizing effects on CO coadsorption and a lowering of the CO activation energy as was found for K + CO coadsorption on the Fe(100) surface at the same coverages considered ($\theta = 0.25 + 0.25$ ML CO + K). Coadsorption of CO with N or NH on Fe(100) however increased the activation energy and made the overall CO dissociation reaction endothermic. Even though it has been shown that the carbide phase would be the dominant bulk phase during Fe-based FTS [14, 15], it is interesting to note that Henkel [7] found similarities between K promotion and NH_3 addition during his NH_3 co-feeding FTS reactions . Conversely Sango [8] reports on significant poisoning at higher concentrations of NH_3 during his NH_3 co-feeding reactions, at which high selectivities for aliphatic nitriles were found. In Chapter 5 it was shown that NH_2 could be the dominant surface species based on the calculation of the individual NH_3 decomposition on Fe(100). The calculations in this chapter reveal that NH_2 is the only adsorbate that does would not form a mixed state in the presence of CO on the Fe(100) surface for the coverages considered. It is finally thus important to point out that the dominant N-containing compound in most reports for the co-feeding of NH_3 during FTS is primary amines, which would be indicative of NH_2 surface reactions during the final desorption steps [7, 8]. These observations could merely be a coincidence, but this study provides a solid basis for understanding the elementary reactions where NH_x are present on an Fe surface and provides a basis to further explore the effects caused by their presence during FTS.

REFERENCES

[1] D.C. Sorescu. *Surf. Sci.*, 605:401–414, 2011.

[2] D. Curulla-Ferré, A. Govender, T.C. Bromfield, and J.W. Niemantsverdriet. *J. Phys. Chem. B*, 110:13897–13904, 2006.

[3] A. Clark. Process of synthesizing aliphatic amines, us 2,518,754., 1950.

[4] H. Kölbel and J. Trapper. *Angew. Chem. Int. Ed.*, 4:981, 1965.

[5] H. Kölbel and J. Trapper. *Angew. Chem. Int. Ed.*, 5:843–844, 1966.

[6] W. Röttig. Catalytic hydrogenation of carbon monoxide with addition of ammonia or methylamine, us 2,821,537., 1958.

[7] R. Henkel. *The influence of ammonia on Fischer-Tropch synthesis and formation of N-containing compounds.* PhD thesis, Carl von Ossietzky Universität, Germany, 2012.

[8] T. Sango. Nitrogen-containing compounds from ammonia co-feed to the Fischer-Tropsch synthesis. MSc thesis, University of Cape Town, South Africa, 2013.

[9] J.K. Nørskov. *Prog. Surf. Sci.*, 38:103–144, 1991.

[10] D.W. Moon, D.J. Dwyer, and S.L. Bernasek. *Surf. Sci.*, 163:215–229, 1985.

[11] M.H. Mahyuddin, R.V. Belosludov, M. Khazaei, H. Mizuseki, and Y. Kawazoe. *J. Phys. Chem. C*, 115:23893–23901, 2011.

[12] P. van Helden and E. van Steen. *J. Phys. Chem. C*, 112:16505–16513, 2008.

[13] C.H. Bartholomew. *Appl. Catal., A*, 212:17–60, 2001.

[14] E. de Smit, A.M. Beale, S. Nikitenko, and B.M. Weckhuysen. *J. Catal.*, 262:244–256, 2009.

[15] E. de Smit, F. Cinquini, A.M. Beale, O.V. Safonova, W. van Beek, P. Sautet, and B.M. Weckhuysen. *J. Am. Chem. Soc.*, 132:14928–14941, 2010.

[16] C. Xu and D.W. Goodman. *J. Phys. Chem. B*, 102:4392–4400, 1998.

[17] I.M. Ciobîcă, A.W. Kleyn, and R.A. van Santen. *J. Phys. Chem. B*, 107:164–172, 2003.

[18] D. Currula Ferrè, A.P. van Bavel, and J.W. Niemantsverdriet. *ChemPhysChem*, 6:473–480, 2005.

[19] P. van Helden. *Initial steps of the Fischer-Tropsch synthesis on Fe(100): The role of hydrogen.* PhD thesis, University of Cape Town, South Africa, 2008.

[20] T. Sasaki, T. Aruga, H. Kuroda, and Y. Iwasawa. *Surf. Sci.*, 240:223–244, 1990.

[21] S. Akhter, Y. Zhou, and White J.M. *J. Chem. Soc. Faraday Trans.*, 86:2271–2275, 1990.

[22] J.T. Ranney, A.J. Franz, and J.L. Gland. *Surf. Sci. Lett.*, 384:L865–L868, 1997.

[23] A.C. Kizilkaya, J.W. Niemantsverdriet, and Weststrate C.J. *J. Phys. Chem. C*, 120:3834–3845, 2016.

[24] T. Sasaki and Y. Iwasawa. *Surf. Sci.*, 384:L798 – L804, 1997.

[25] D.C. Curulla-Ferrè, A.P. van Bavel, and J.W. Niemantsverdriet. *ChemPhysChem*, 6:473–480, 2005.

[26] G. Kresse and J. Hafner. *Phys. Rev. B*, 47:558, 1993.

[27] G. Kresse and J. Hafner. *Phys. Rev. B*, 49:14251, 1994.

[28] G. Kresse and J. Furthmuller. *Phys. Rev. B*, 11:169, 1996.

[29] G. Kresse and J. Furthmuller. *Comput. Mater. Sci.*, 6:15, 1996.

[30] P.E. Blöchl. *Phys. Rev. B*, 50:17953–17975, 1994.

[31] G. Kresse and J. Joubert. *J. Phys. Rev. B*, 59:1758–1784, 1999.

[32] B. Hammer, L.B. Hansen, and J.K. Nørskov. *Phys. Rev. B*, 59:7413, 1999.

[33] M. Methfessel and A.T. Paxton. *Phys. Rev. B*, 40:3616, 1989.

[34] H.J. Monkhorst and Pack J.D. *Phys. Rev. B*, 80:890, 1976.

[35] D.E. Jiang and E.A. Carter. *J. Phys. Chem. B.*, 110:22213–22219, 2006.

[36] E. Weinen and E. Vanden-Eijnden. *Annu. Rev. Phys. Chem.*, 61:391–420, 2010.

[37] P. Błoński, A. Kiejna, and J. Hafner. *Surf. Sci.*, 590, 2005.

[38] D. Loffreda. *Surf. Sci.*, 600:2103–2112, 2006.

[39] W. Tang, E. Sanville, and G. Henkelman. *J. Phys.: Condens. Matter*, 21:084204:1–7, 2009.

[40] R.F. Bader. *Chem. Rev.*, 91:893–928, 1991.

[41] I.A.W. Filot, R.A. van Santen, and E.J.M. Hensen. *Angew. Chem.*, 126:12960–12964, 2014.

[42] M. Claeys and E. van Steen. Chapter 8 - basic studies. In A.P. Steynberg and M.E. Dry, editors, *Fischer-Tropsch Technology*, volume 152 of *Stud. Surf. Sci. Catal.*, pages 601 – 680. Elsevier, 2004.

[43] T. Sango, N. Fischer, R. Henkel, F. Roessner, E. van Steen, and M. Claeys. *Appl. Catal., A*, 502:150–156, 2015.

CHAPTER 7

ADDING 1 VOL % NH_3 DURING FISCHER-TROPSCH SYNTHESIS

In this chapter an evaluation of the effects incurred via the addition of 1 vol % NH_3 *during Fe-based Fischer-Tropsch synthesis is presented. The deliberate addition of* NH_3 *during FTS has shown potential to produce valuable N-containing chemicals, for example aliphatic primary amines, nitriles and amides. Conversely,* NH_3 *is classically grouped with the FTS catalyst poisons, which necessitates its removal prior to FTS reactions. The results for the FTS reactions discussed here were conducted over a K promoted Fe-based catalyst, operated in a slurry phase reactor at 250* ℃ *and 5 bar total pressure. The analysis of the FTS product spectrum that is produced through Fe-based catalysis is complex and becomes more convoluted with the introduction of an additional class of organic compounds, the N-containing aliphatic hydrocarbons. To assist in the identification and quantification of the organic products, comprehensive two-dimensional gas chromatography (GC×GC-TOF/FID) was employed. When comparing the synthesis gas* (CO/H_2) *conversion data for the reaction where 1 vol%* NH_3 *was present with the reaction where no ammonia was added, no clear evidence for catalyst deactivation was observed. Even though the steady-state conversion data was similar, when drawing comparisons between the initial stages of the FTS experiments with or without the addition of* NH_3*, the* H_2/CO *conversion rates and* CO_2 *selectivity points towards a retardation of the formation of the* *working catalyst (Fe-carbide) due to the presence of* NH_3 *in the synthesis gas. Post run XRD analysis of the spent catalysts did not provide any evidence of severe phase changes and/or the formation of nitrides, upon the addition of ammonia. The use of the GC×GC-TOF/FID analysis of the organic products was pivotal in detecting a homologous series of secondary and tertiary amines, which has not been reported in previous studies. Similar to previous reports, a significant decline in the selectivity of oxygenates was observed, which suggests that FTS oxygenates are being suppressed or could act as precursors to the formation of the N-containing compounds when ammonia is added to the syngas.*

Introduction

If ammonia is deliberately added as reactant during Fischer-Tropsch synthesis, a range of N-containing compounds is produced, which includes aliphatic amines, nitriles and amides [1–7]. The conventional industrial route to produce various N-containing compounds such as primary amines and nitriles is through the amination of oxygenates with NH_3 or other amines, which are relatively expensive starting materials [8]. The incentive to directly produce these valuable chemicals from less expensive starting materials ($CO + H_2 + NH_3$) has thus led to several studies that evaluated the potential of this alternative route to the formation of N-containing compounds [2–7]. It should however be noted that NH_3 is typically considered a FTS catalyst poison [9]. Biomass-derived synthesis gas usually contains approximately 1000-14000 ppm (0.1-1.4 vol %) NH_3 and thus necessitates a cleaning step prior to conducting FTS reactions [10]. To resist over-design of the cleaning section, limits need to be determined for catalyst poisons such as NH_3 [11]. Studies for the case where NH_3 is present as a reactant therefore does not only shed light on the potential to produce valuable chemicals in this way, but they also provide information regarding the potential of NH_3 to act as FTS catalyst poison.

The first report of producing valuable N-containing chemicals via the addition of NH_3 during FTS was presented in a form of a patent by Clark in 1947 [2]. No quantitative information was included to describe the composition of the FTS product spectra obtained during Clarks' attempt to produce primary amines in addition to the FTS products. In Clark's design and at the conditions applied (Fe- and Co-catalysts, slurry phase reactor, $T = \sim 200$ and ~ 300 ℃, $P = 10$ bar, $H_2/CO = 2$, 15.6 mol % NH_3) identification of various products (e.g. primary amines, light FTS products etc.) was achieved and ammonium bicarbonate was reported to be present in the aqueous product [2]. Röttig [3] added 0.5 to 2.0 vol % NH_3 to the synthesis gas during FTS (Fe/Cu/K, fixed bed reactor, $T = 188$ ℃, $P = 30$ bar, $H_2/CO = 2$), employing a copper promoted Fe-based catalyst and achieved 12-17 wt % selectivity towards primary amines. Kölbel and Trapper [4] conducted their NH_3 co-feeding experiments (Fe/Cu/K, fixed bed, $T = 250$ ℃, $P = 11$ bar, $CO/H_2O = 3$) with the use of H_2O, as opposed to H_2 and achieved a selectivity of up to 25 wt% towards N-containing compounds (predominantly primary amines). It was also shown by Kölbel and Trapper (see [1] and references therein) that co-feeding aliphatic amines such as ethylamine, piperidine and pyrrolidine with synthesis gas during FTS leads to the incorporation of these N-containing compounds into growing alkyl chains. Henkel [5, 7] recently conducted similar NH_3 co-feeding experiments (Fe/K, fixed bed reactor, T = 270 ℃, P = 4 bar, H_2/CO - 2:1, GHSV = 1920 ml/g_{cat}/hr) with various K-containing Fe-based catalysts (0/2/5:100 (g/g), K/Fe ratios) and observed a decline in the oxygenate selectivity upon the addition of ammonia or the formation of the N-containing compounds respectively. Based on mass balances stemming from these results, Henkel noted that the loss of the oxygenates quantitatively matches the amount of the N-containing compounds formed (mainly linear primary amines). Furthermore, the results from NH_3 co-feeding during FTS experiments showed that a lower potassium loading on an Fe-based catalyst led to a significant increase in the FTS activity when NH_3 is present in the inlet. Sango et al. [6, 7] probed the effects of increasing the NH_3 concentration during FTS (Fe/K, slurry phase reactor, T = 270 ℃, P = 5 bar, H_2/CO - 2:1, GHSV = 2250 ml/g_{cat}/hr) while keeping the CO and H_2 partial pressures constant. At higher concentrations of NH_3 (5 - 20 vol%) present in the synthesis gas a high selectivity towards aliphatic nitriles was achieved as well as smaller quantities of aliphatic amides, and a decline in oxygenate selectivity was observed. A concomitant decrease in oxygenate selectivity was thus reported by both Henkel et al. [5, 7] and Sango et al. [6, 7], which strongly suggests that N-containing compounds form to the detriment of the oxygenates. Product analysis in the aforementioned studies has thus revealed several aspects of the pathway towards the formation of the N-containing compounds. The introduction of this new class of organic chemicals (aliphatic amines, nitriles and amides) due to the incorporation of N further complicates the separation, identification and quantification of the products. The analysis of N-containing organic products in the studies of Henkel et al. [5, 7] and Sango et al. [6, 7] relied extensively on the extraction of mass to charge ratios (via GC-MS) to estimate the quantities of N-containing compounds that formed. Analysis of more complex FTS product spectra, such as the products obtained during high temperature FTS has recently been simplified via the use of two-dimensional gas chromatography [12–15], which is an integral part of the present study.

To improve upon the analysis of the organic products obtained during the reaction where 1 vol % NH_3 is added during FTS (Fe/K, slurry phase reactor, T = 250 ℃, P = 5 bar, H_2/CO = 2, SV = 2250 ml/hr/g_{cat}), comprehensive two-dimensional gas chromatography (GC×GC-TOF/FID) is employed in this work. Furthermore, to evaluate NH_3 as a potential catalyst poison during FTS reaction, the FTS activity (CO + H_2 conversion) and product selectivities (CH_4, CO_2, oxygenates, olefin/paraffin ratios, chain-growth probabilities) were compared for the two cases, where 1 vol % NH_3 is present or absent in the reactor feed. Some final remarks are also made for the differences observed in the spent catalysts and the spent reaction wax media for the NH_3 co-fed and NH_3-free FTS reactions.

Experimental Setup

Catalyst preparation

A potassium promoted iron-based catalyst was prepared via a discontinuous co-precipitation method (see Chapter 4 for details). The desired Fe:K weight ratio was 100:2 (g/g), which was confirmed by means of atomic absorption spectroscopy (AAS) and inductively coupled plasma (ICP) analysis. The catalyst used for the slurry phase reactions was externally reduced in a fluidized bed reactor. The reduction was conducted in hydrogen (45 ml(NTP)/g_{cat}/min) following a temperature program (heating from room temperature to 400 ℃, with a holding time of 16 hours; heating rate: 1 ℃/min) that ensured a fully reduced catalyst as evidenced by in-situ X-ray diffraction (XRD) measurements (see Chapter 4). After pre-treatment the reduced catalyst was transferred under inert atmosphere into Sasol paraffin wax (C_{30-60}, with melting point ca. 112 ℃) in order to protect if from oxidation. The catalyst-in-wax pellet was then transferred into the slurry reactor, which contained 300 g of molten wax for the start up of the FT synthesis.

Reactor setup and reaction conditions

In Figure 7.1 a simplified schematic drawing is given for the reactor setup used to perform the FT reactions discussed in this chapter. (A more detailed setup can be found in Chapter 4.) The gases CO, H_2, NH_3 (10.1 vol % NH_3 in H_2) and the reference gas (a mixture of 0.0018 vol % cyclohexane in N_2) were introduced via mass-flow controllers (Brooks). The reactor system is equipped with both a slurry phase and a fixed bed ("u-tube") reactor, in this section the slurry

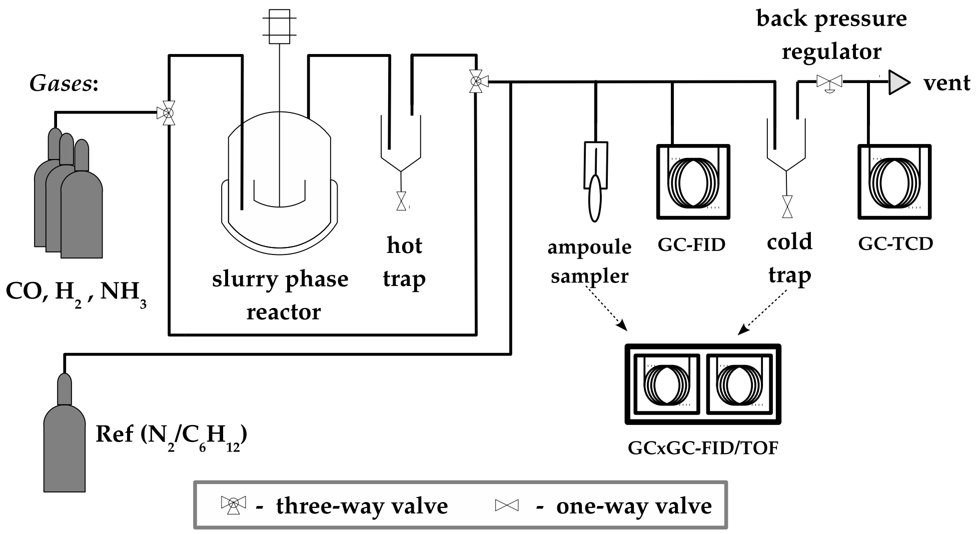

Figure 7.1: Schematic drawing of reactor setup for FTS reactions performed in slurry phase reactors.

phase reactor was employed. A condensation trap ("hot trap") is situated directly after the exit line. This vessel was maintained at 180 ℃ to ensure that all "high-boiling" organic products (wax) does not enter the ampoule sampler or the on-line GC-FID. A second condensation vessel ("cold trap") was maintained at approximately 10 ℃ and this was used to collect the oil and water phase products, which were analyzed off-line. The cold trap was positioned before the back pressure regulator, which increases the efficiency of product condensation. Both the products collected in the cold trap and the gas phase samples obtained via the ampoule sampling technique were analyzed via off-line GC-FID and GC×GC-TOF/FID analyses.

Three experiments were conducted in order to study changes in the product spectrum when adding NH_3 to the synthesis gas during FTS. The first two reactions SPR^1 and SPR^2 were compared directly, where no NH_3 and 1 vol% NH_3 was added respectively with the syngas during FT experiments. Each of these reactions were conducted with a freshly loaded catalyst. In a third experiment (SPR^3) the reaction was started up in the absence of NH_3 and ran for a period of 24 hours, which was sufficient to reach steady state This was then followed by an additional 12 hours where 1 vol % ammonia was added to the synthesis gas. The reaction conditions are given in Table 7.1. For this the reactor was pressurized to 5 bar in argon at the beginning of the experiment and subsequently replaced with synthesis gas or synthesis gas plus ammonia respectively. In the latter case the total pressure was raised to 5.1 bar in order to

Table 7.1: Summary of experimental conditions. Temperature and total pressures remained constant for all experiments: $T = 250$ ℃, and $P = 5$ or 5.1 bar (NTP) with or without ammonia addition respectively

Experiment	**Feed**	**GHSV (ml/hr/g$_{cat}$)**	**TOS (hrs)**
SPR^1	$H_2/CO = 2$ (no NH_3)	2250	90
SPR^2	$H_2/CO = 2$ (+1 vol% NH_3)	2250	90
SPR^3	$H_2/CO = 2$, (no/+1 vol% NH_3)	2250	0-24 (FTS) 24-36 (NH_3-FTS)

account for the 1 vol % ammonia in the feed.

Note that insufficient oil and water phase products was collected during the third FT experiment (SPR^3) and the analysis of the heavier products is therefore limited.

Analysis of reactants and products

As previously mentioned, the analysis of the reactants and products was important for the current work. A detailed discussion of the setup and methodologies for the analytical techniques can be found in Chapter 4 (see Sections 4.2.3 and 4.3). In Table 7.2 a summary of the methods used to analyze the various analytes are given in conjunction with the relevant instrumentation. Furthermore, a reference to the location in Chapter 4 is included in Table 7.2 to direct the interested reader to the relevant tables where the key parameters is discussed for the various analytical techniques.

Results and Discussion

Catalyst activity (CO/H_2 conversion)

The steady state conversion (24 hours TOS) in the reaction where 1 vol% NH_3 was added and in the reaction where no ammonia was added (see Figure 7.2 (*Top*)) are similar, suggesting that ammonia does not act as a catalyst poison at these conditions. Even a slight increase in the

Table 7.2: Summary of the analytical techniques used for the identification and quantification of the inorganic and organic reactants and products in the FT synthesis experiments.

Method (Instrument)	**Analyte**	**Ref.**
on-line GC-TCD	inorganic gases	Table 4.1
(Varian, CP-4900)	(e.g. CO, H_2, NH_3)	
on/off-line GC-FID	organic gases	Table 4.2
(Varian, GC-430)	(e.g. paraffins, olefins, oxygenates)	
off-line GC×GC-TOF/FID	organic gases	Table 4.5
(Leco, Pegasus 4D (Agilent 7890))	(e.g. paraffins, olefins, oxygenates)	

activity was observed for the reaction SPR^3 where NH_3 was introduced to the reactant feed after 24 hours TOS (see Figure 7.2 (*Bottom*)). Sango et al. [6, 7] did not observe any deactivation of the Fe-based catalyst when increasing the concentration of NH_3 from 0 to 2 vol % during FTS, but at higher NH_3 concentrations (5 - 20 vol %), a decline in activity was observed (see Appendix C, Figure C.14). Henkel [5], who similar to this work and that of Sango et al. [6, 7] made use of an unsupported iron based catalyst promoted with potassium (2 and 5 wt %) reports on an initial decline in FT activity without any NH_3 added, which is commonly observed in Fe-based FTS due to carbon deposition from the Boudoard reaction. Minimal changes in the catalytic activity (CO and H_2 conversion) was reported to be due to the addition of NH_3 (2 vol %) in his FT experiments that was conducted in a fixed bed reactor with the potassium promoted catalysts. The unpromoted catalysts brought about a CO conversion that did not exhibit an initial deactivation and remained stable after adding NH_3 to the feed, while the H_2 conversion was lowered ($\Delta X_{H_2} = 10$ mol %) upon the addition of NH_3. In Henkels [5] FT experiments, both before and after NH_3 addition, a lower potassium content resulted in a higher activity which he ascribes to site blocking from the potassium [16] and a possible promotional effect of the added NH_3.

A closer inspection of the conversion data collected at the initial stages of SPR^1 and SPR^2 reveals that the addition of NH_3 seems to have an effect on the carburization process, as the CO conversion was much lower during the first 24 hours of this experiment. It should be noted that reduced metallic iron catalysts undergo significant initial phase changes and a considerable fraction of CO is consumed to form iron carbides [17, 18]. Furthermore, it is important to point out that it has been shown that by pre-sulfiding an Fe-based catalyst with high concentrations (20 000 ppm) of sulfur the carburization of the Fe-based catalyst was significantly retarded [19]. This observation could not be made by either Henkel [5] or Sango et al. [6, 7] due to the fact that their FT experiments was never initiated via the immediate addition of NH_3 to the synthesis gas feed.

CH_4 selectivity

A CH_4 selectivity of 10.5 C wt% was calculated for the FT reaction where no NH_3 was added to the feed, whereas the reaction that had 1 vol% NH_3 present in the synthesis gas was higher at 14.5 C wt% (SPR^{1-2}, see Figure 7.3). The methane selectivity increased only marginally (from 11.5 to 12.6 C wt%) for the FT reaction (SPR^3) where the 1 vol% NH_3 was added after 24 hours of normal FTS activity (see Figure 7.3). A similar increase in methane selectivity was reported in the work of Sango et al. [6, 7] where an increase in methane selectivity ($S_{CH_4} = 3.7$ to 4.2 C wt%) was observed when increasing the NH_3 concentration from 0 to 2 vol % of the total reactant feed. Henkel [5] did not observe any changes in methane selectivity ($S_{CH_4} = 5$ C wt%) upon the addition of NH_3 during his NH_3 co-feeding FT reactions when using catalysts with potassium promotion (2 and 5 wt%). However, when using an Fe-based catalyst that was not promoted with potassium, he reports a decline in methane selectivity from approximately 20 to 16 C wt% upon the addition of NH_3 to the synthesis gas feed. This finding is thus in line with the notion that NH_3 can act as a promoter in a similar way as potassium, as introduced by Henkel [5]. Note that the methane selectivity values reported by Sango et al. [6, 7] and Henkel [5, 7] is lower than those reported here, since these authors included the formation of CO_2 in their definition of methane selectivity. It is furthermore interesting to note that the sulfur and sodium promoted nano-sized Fe catalysts synthesized by Torres-Galvis et al. [20, 21] for the production of short chain olefins lowers the methane selectivity during FTS (from ca. 40 to 25 C wt%). Based on the 'carbide' mechanism (discussed in Chapter 2), both Henkel [5] and Torres-Galvis et al. [20, 21] argues that the NH_3 addition to the feed or sulfur and sodium catalyst promotion in the respective studies acts to limit hydrogenation reactions of the monomer CH_2^*

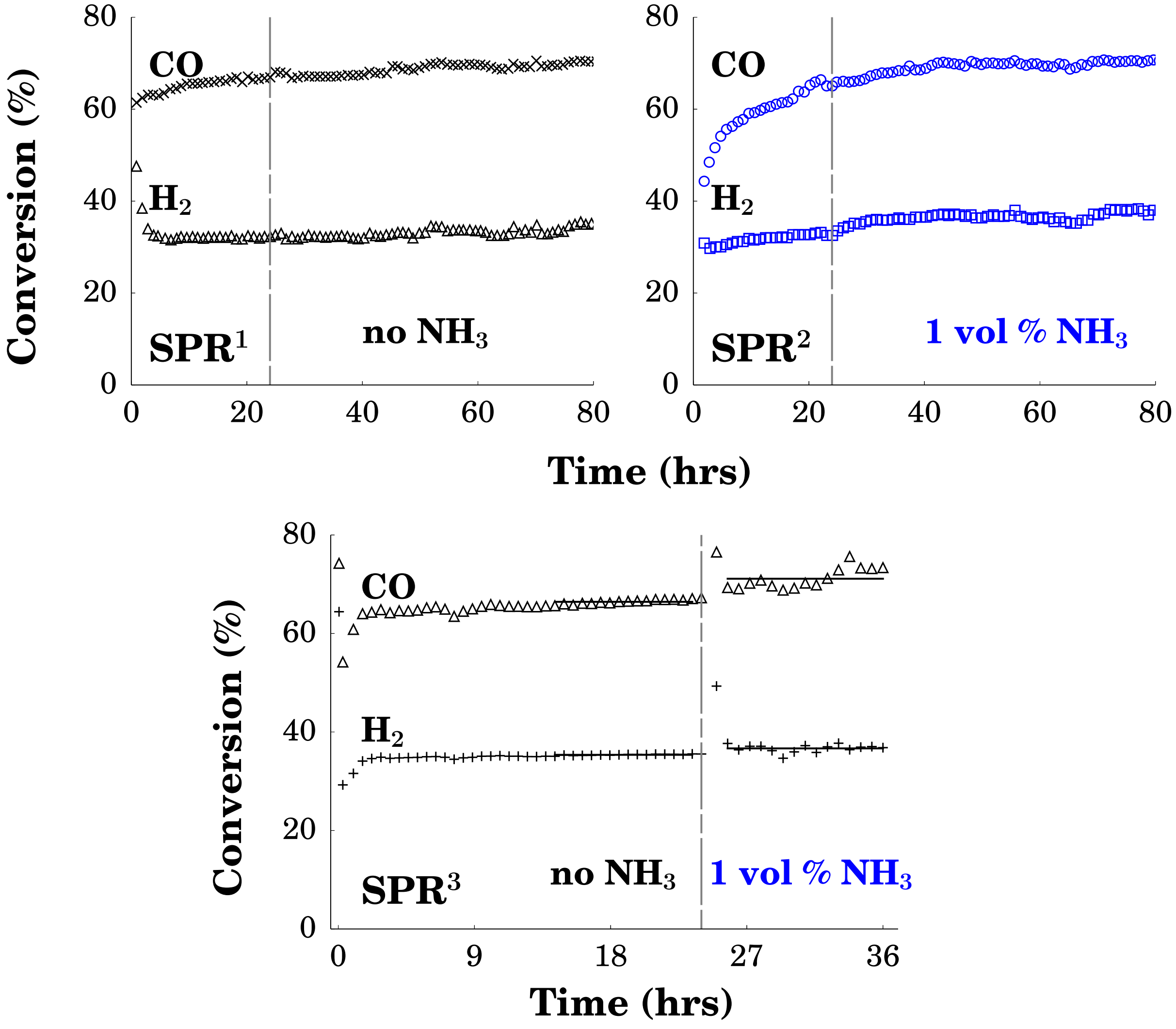

Figure 7.2: *Top:* H_2 and CO conversion as a function of time on stream (TOS) for the reactions where 1 vol% NH_3 were present/absent during the whole duration of the FTS reaction. *Bottom:* H_2 and CO conversion as a function of time on stream (TOS) for the reactions where 1 vol% NH_3 were added after 24 hours TOS (SPR^{1-3}, T = 250 ℃, P = 5 bar(NTP), GHSV = 2250 ml/hr/g_{cat}, H_2/CO = 2, +0/1 vol% NH_3)

surface species, and promotes β-hydride elimination and in doing so leads to lower methane selectivity.

CO_2 selectivity

CO_2 formation in iron-based FTS is due to WGS activity [16]. When studying the influence of NH_3 addition during FTS in this work, a significant decline in CO_2 selectivity was observed. This observation was made in both cases, firstly a 5 C wt% decline was calculated for the comparison between the NH_3-free syngas and the reaction where 1 vol % NH_3 gas was added during the FTS reaction (see Figure (*Top*) 7.4). A similar, yet smaller (ca. 2-3 C%) decline in CO_2 selectivity was observed when switching from the syngas with no NH_3 after 24 hours to the condition where 1 vol % was present in the syngas feed (see Figure (*Bottom*) 7.4).

During the NH_3 co-feeding reaction (feed: CO + H_2 + 1 vol % NH_3), large volumes (ca. 4-5 cm^3) of a white solid that formed at the entrance of the second condensation vessel ('cold trap '- 10 °C) could be isolated. The formation of a similar solid material was reported by Sango [6], who confirmed the formation of ammonium bicarbonate reported by Clark [2], by characterizing it via Raman spectroscopy. The solid produced in this work was subjected to XRD analysis (see Figure 7.5) and the results corroborates the finding obtained by Sango [6] and Clark [2]. It is likely that NH_4HCO_3 forms via a reaction of water, NH_3 and CO_2 (as indicated in Eq. 7.1). Its formation preferably occurs at conditions of high pressure and low temperature as applied in the cold trap in this work and could therefore explain the lower CO_2 selectivity observed when adding NH_3 during the FT experiment.

The increase in CO_2 selectivity for the reaction where 1 vol % NH_3 was added during FTS from the start (SPR^2) was significantly slower to reach a steady state compared to the corresponding NH_3-free FTS reaction. In addition to the consumption of CO, it has been shown that CO_2 formation is suppressed during the initial phase changes from metallic iron to the working catalyst, the iron carbide [17, 18]. This observation therefore further supports the view of a retarded carburization process when NH_3 is added during FTS.

$$CO_2 + H_2O + NH_3 \rightleftharpoons NH_4HCO_3 \qquad (7.1)$$

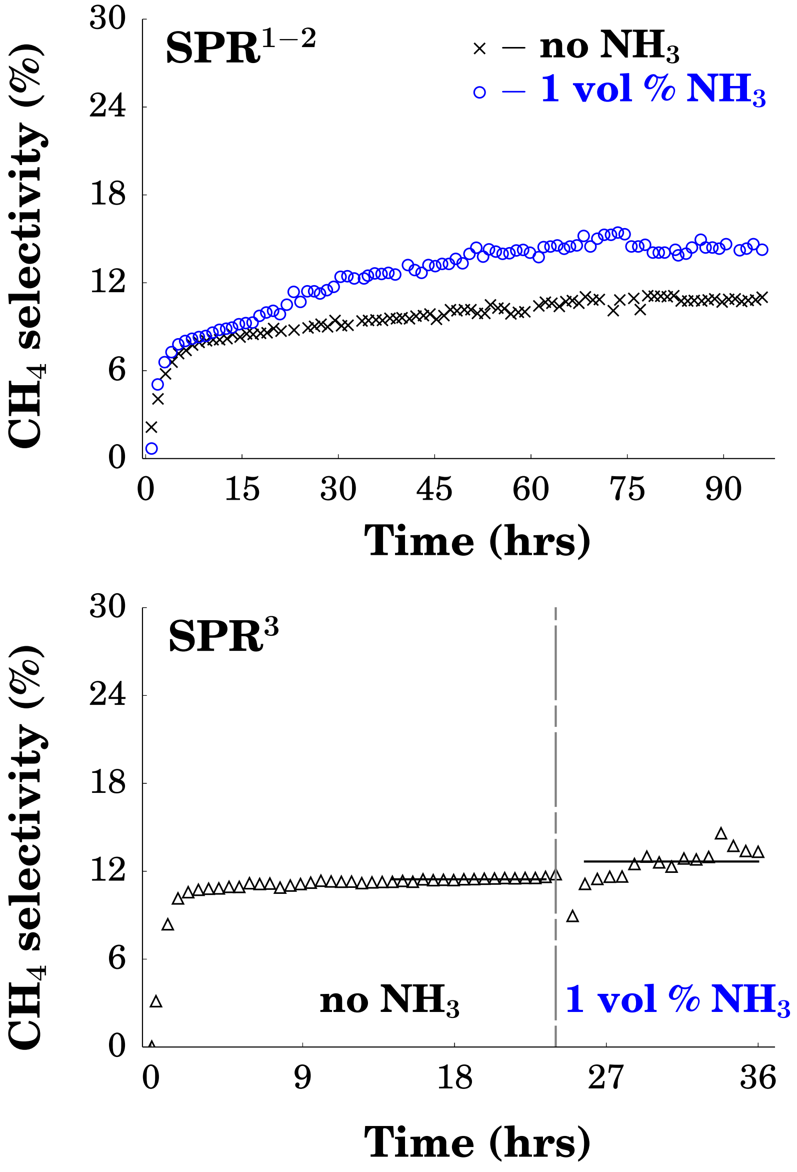

Figure 7.3: *Top:* CH_4 selectivity as a function of time on stream (TOS) for the reactions where 1 vol% NH_3 were present/absent during the whole duration of the FTS reaction. *Bottom:* CH_4 selectivity as a function of time on stream (TOS) for the reactions where 1 vol% NH_3 were added after 24 hours TOS (SPR$^{1-3}$, T = 250 °C, P = 5 bar, GHSV = 2250 ml/hr/g_{cat}, H_2/CO = 2, +0/1 vol% NH_3)

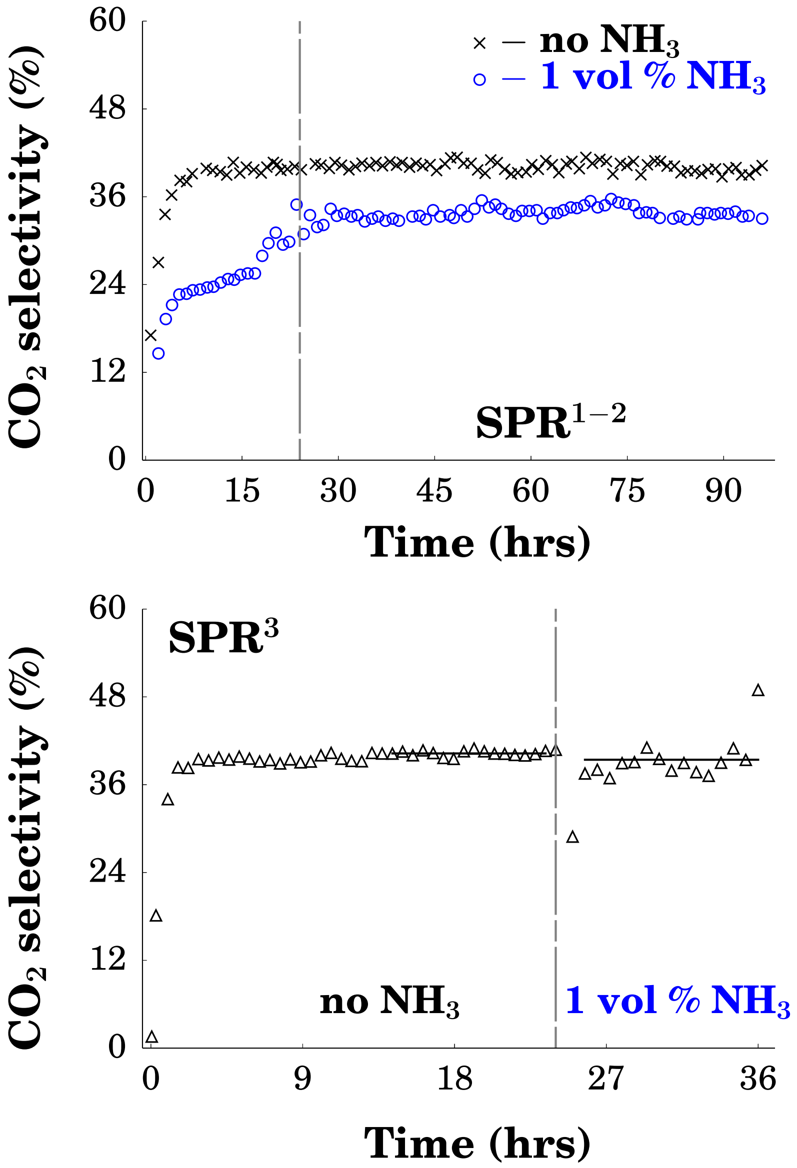

Figure 7.4: *Top:* CO$_2$ selectivity as a function of time on stream (TOS) for the reactions where 1 vol% NH$_3$ were present/absent during the whole duration of the FTS reaction. *Bottom:* CO$_2$ selectivity as a function of time on stream (TOS) for the reactions where 1 vol% NH$_3$ were added after 24 hours TOS (SPR$^{1-3}$, T = 250 °C, P = 5 bar, GHSV = 2250 ml/hr/g$_{cat}$, H$_2$/CO = 2, +0/1 vol% NH$_3$)

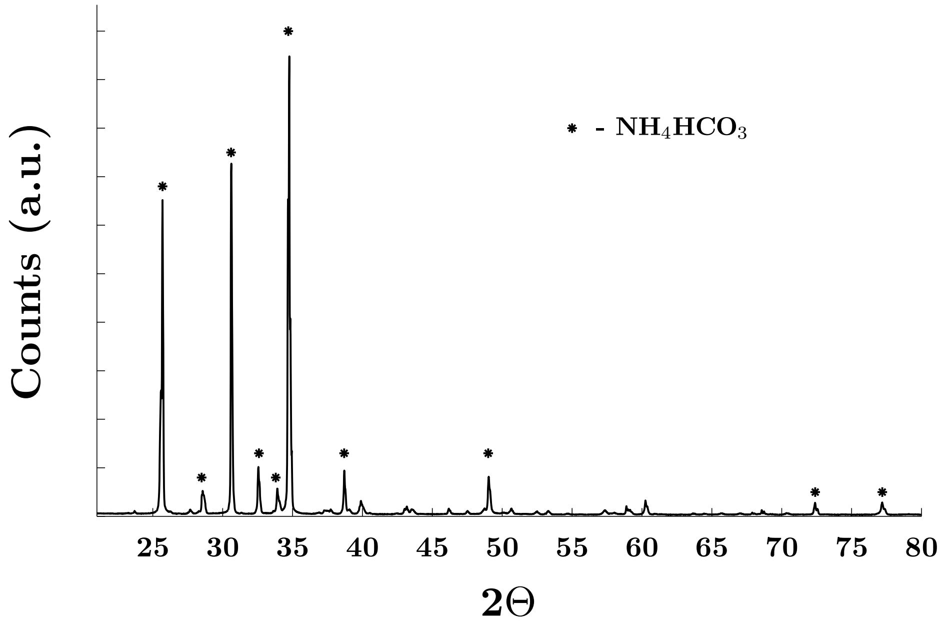

Figure 7.5: XRD pattern obtained when analyzing white solid formed during reaction. This pattern corresponds to that of NH_4CO_3

Product distribution

The ASF distributions of the FT products that are plotted in Figure 7.6 was calculated with the use of Eq. 7.2

$$log(w_f/n) = n\,log(\alpha) + c \tag{7.2}$$

where w_f is the weight fraction, n the carbon number and α is the chain growth probability. These figures show a linear behaviour over a wide carbon number range, indicating largely carbon number independent chain growth probabilities (α). The slope in the carbon number range C_{1-17} was used to determine chain growth probabilities. Visually inspecting these distributions one can see that the presence of 1 vol % NH_3 in the syngas feed does not affect the distribution by much. The chain growth for the carbon number range C_{1-17}, were α = 69 % for the FT experiment had 1 vol % NH_3 added to the reactant feed (SPR^2). A similar chain growth probability (α = 69 %) was calculated for the reaction with no NH_3 added (SPR^1) for the carbon number range between C_{1-10}, but there may be a slight deviation from this straight line between carbon numbers C_{11-17} (α = 66 %). For the organic product with carbon numbers above C_{18} the plot of $log(w_f/n)$ decreases rapidly. This is due to the fact that the heavy products, with their high boiling points, were partially contained in the first condensation vessel (T = 180 ℃).

Olefin selectivity

α-Olefins are the main primary products of the FTS [22]. They are believed to be formed via β-hydrogen elimination upon desorption of surface alkyl chains. They can undergo secondary reactions [22], including hydrogenation to parafins, double bond shift and incorporation into growing chains. A schematic of the proposed pathways of the secondary reactions of olefins are presented in Figure 7.7 [23].

In order to assess the extent of hydrogenation the molar olefin content in the fraction of linear hydrocarbons is plotted as a function of carbon number in Figure 7.8. These curves peaks at $C_{3/4}$ and olefin contents decrease with increasing carbon number and are lower for C_2, due to increased residence times of longer chain products and higher reactivity of ethene, respectively [22]. Figure 7.8 only considers the C_{1-12} product range in order to directly compare between the three FT experiments (SPR^{1-3}). These plots are extended to products with car-

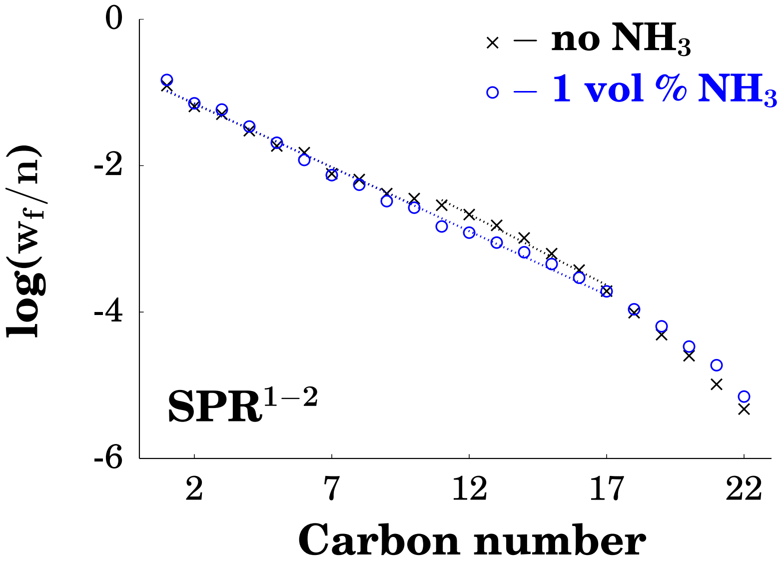

Figure 7.6: Semi-logarithmic plots ($log(w_f/n)$ as a function of carbon number) for SPR$^{1-2}$, where the slope of the line yields the chain growth probabilities (α) based on the ASF model. (T = 250 °C, P = 5 bar, GHSV = 2250 ml/hr/g$_{cat}$, H$_2$/CO = 2, 0/1 vol% NH$_3$)

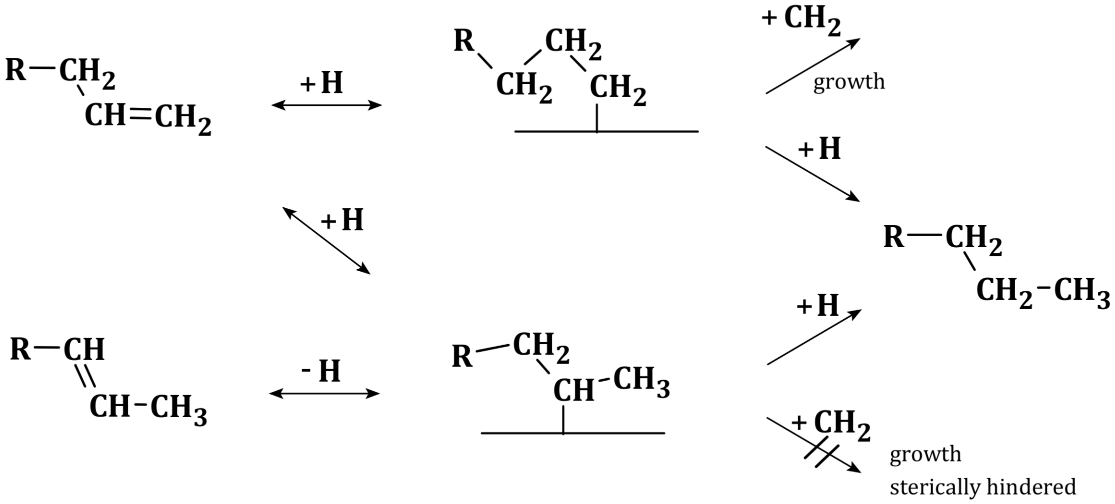

Figure 7.7: Schematic illustrating the proposed mechanistic pathways for the hydrogenation, double bond shift and incorporation secondary reactions of olefins, based on Ref. [23]

bon numbers up to C_{20} in Figure C.15 of Appendix C. These results are in agreement with both Henkel [5] and Sango et al. [6, 7] for the C_{2-12} carbon number range, as they reported no changes in the olefin-parafin ratios upon NH_3 addition during their FT experiments when using K promoted Fe-based catalysts. Interestingly however a lower olefin selectivity ($S_{o/p}$ = 28 % with 1 vol % added compared to $S_{o/p}$ = 35 % without NH_3 addition) was observed for the products in the C_{13-20} carbon number range in the current work.

A rapid increase in olefin parafin ratios (from $S_{o/p}$ = 14 to 65 % with or without NH_3 addition respectively) when using un-promoted Fe-based catalysts during Henkels FT experiments, further supports his claim of NH_3 acting like a promoter in a way that K does.

The formation of olefins with internal double bonds is predominantly via secondary reactions and believed to occur as illustrated in the schematic of Figure 7.7 [22]. The degree of double bond shift isomerization can be deduced by comparing the α-olefin molar percentage in the total olefin fraction, which is plotted as a function of carbon number in Figure 7.9. No major changes can be seen from the curves when comparing the reactions with or without NH_3 addition (SPR^{1-3}), nor for FT experiments where the carbon number range C_{2-20} are included (see Figure C.16 of Appendix C). This finding is consistent with previous NH_3 co-feeding FT experiments [5–7].

Degree of branching

α-Olefins formed via a primary route can re-adsorb on the catalyst surface with the penultimate carbon atom and subsequently grow to a minor extent to form branched hydrocarbons [22]. The schematic in Figure 7.10 illustrates the secondary route to the formation of branched hydrocarbons.

The results calculated for the degree of branching in this work is tabulated in Table 7.3. When considering the $C_{4/5}$ fractions, there seems to be negligible impact on the degree of branching when adding NH_3 during FTS. The iso/n ratio for the C_4 fraction remains approximately 2 mol % with or without NH_3 addition (SPR^{1-3}), while it remains ca. 6 mol % for the C_5 fraction. For the heavier products (C_{10-20}) however, 1 vol % addition of NH_3 led to a 5 mol % increase (from 16.5 to 21.5 mol %) when comparing the NH_3-free FTS reaction with the FT experiment where NH_3 was added (SPR^{1-2}, see Figure C.17 of Appendix C). It is possible that the lower olefin-parafin ratios calculated in the C_{13-20} carbon number range of SPR^2 (where 1 vol % was

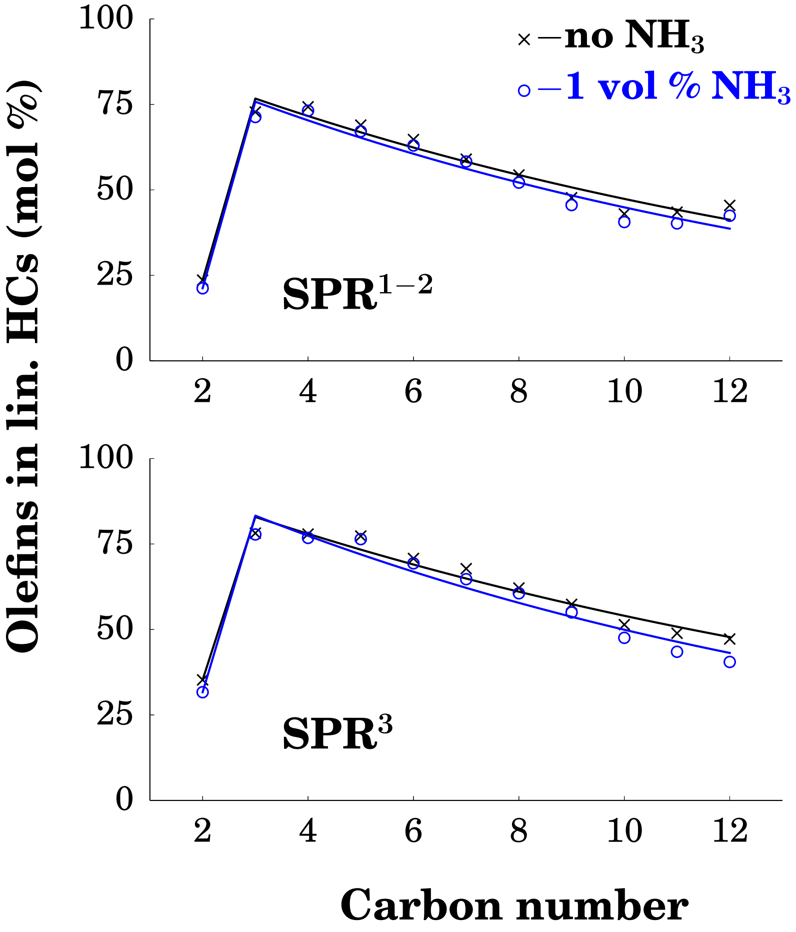

Figure 7.8: Olefin selectivity expressed as the molar percentage present in the linear hydrocarbon products. (SPR^{1-3}, T = 250 ^oC, p_T = 5 bar, GHSV = 2250 ml/hr/g_{cat}, H_2/CO = 2, 1 vol% NH_3)

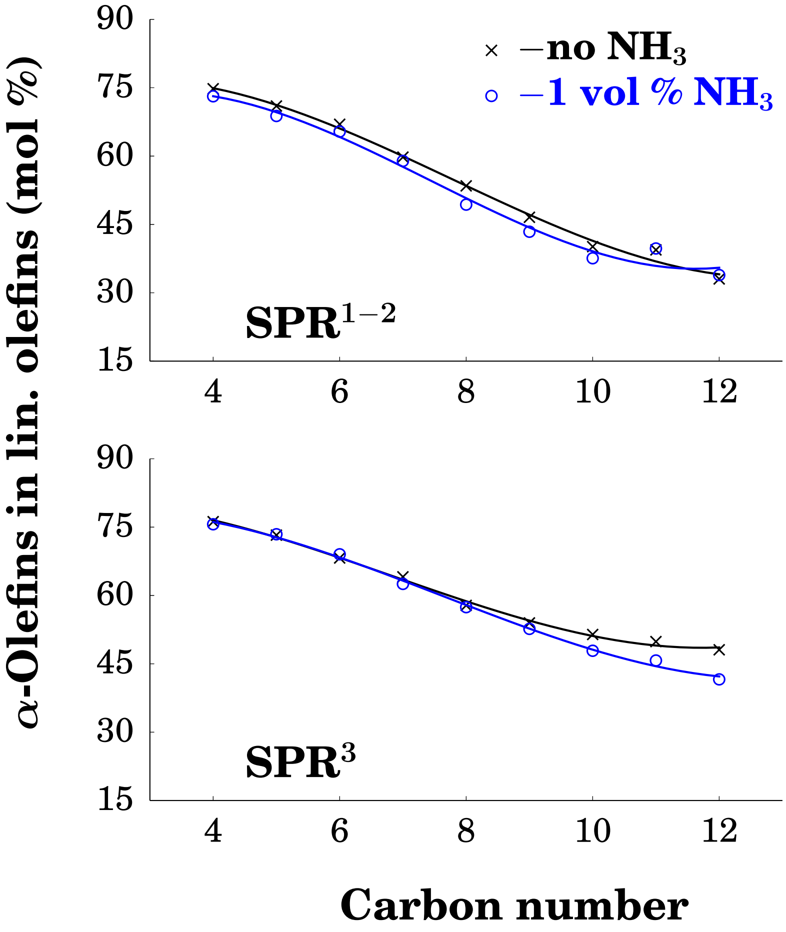

Figure 7.9: α-Olefins present in linear olefins as a function of carbon number. (SPR^{1-3}, T = 250 ℃, P = 5 bar, GHSV = 2250 ml/hr/g_{cat}, H_2/CO = 2, 0/1 vol% NH_3)

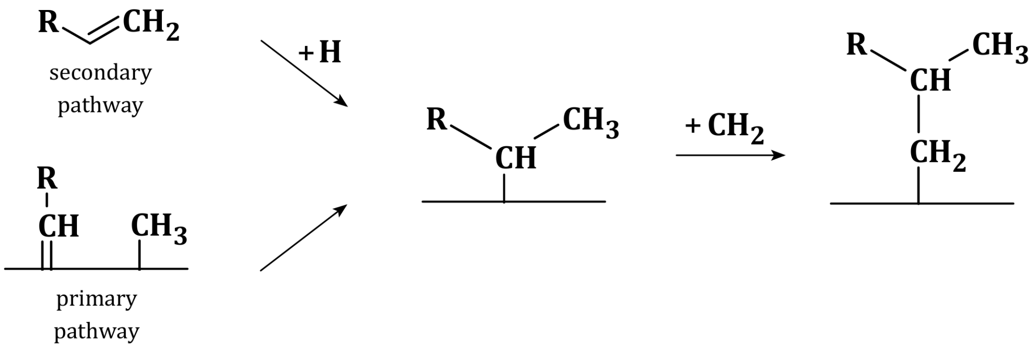

Figure 7.10: Schematic illustrating the formation of methyl branched hydrocarbon via primary or secondary pathways. Adapted from Ref. [6]

added) could be due to secondary reactions of α-olefins to form branched hydrocarbons.

To estimate the effect that NH_3 has on the degree of branching, Sango et al. [6, 7] calculated the iso/n ratios for the C_5 fraction. Sango reports that the extent of branching is independent of NH_3 concentration based on the iso/n ratios (21 - 27 mol %) that he reported for the FT experiments where the NH_3 concentrations were increased from 0 to 20 vol %, but at the highest NH_3 concentration tested (35 vol %) a higher value of 36 mol % was calculated. It should be pointed out that the high iso/n ratios reported by Sango [6] is questionable, since a high degree of branching is not typically associated with lower temperature FT [16] and considering the 20 mol % iso/n ratio that was reported by Cairns [24] for the C_5 fraction when using a similar Fe-based catalyst during his FT experiments that he conducted at HTFT conditions (T = 350 °C). Henkel [5] used the C_4 fraction to estimate the degree of branching and reported a 2 mol % iso/n ratio for the FTS reactions (before and after NH_3 addition) that was conducted with Fe based catalysts containing 2 and 5 wt % potassium. When using an un-promoted K-based catalyst, Henkel [5] reports on a decline in the degree of branching (from 9.0 to 2.0 mol %). Thus, similar to the chain growth, methane selectivity and olefin selectivity, Henkel argues that when NH_3 is added to the synthesis gas feed and an unpromoted Fe-based catalyst is used, the NH_3 can exhibit similar promotional effects as potassium does in Fe-catalyzed FTS.

Table 7.3: Degree of branching expressed by the iso/n ratios for the $C_{4/5}$ fractions, obtained during reactions with and without NH_3 addition during FTS. (SPR^{1-3}, T = 250 °C, P = 5 bar, GHSV = 2250 ml/hr/g_{cat}, H_2/CO = 2, 0/1 vol% NH_3)

Carbon number	**iso/n ratios (mol %)**	
	SPR^1 (no NH_3)	SPR^2 (1 vol % NH_3)
4	1.67	1.70
5	5.53	5.63
10-20	16.5	21.5
	SPR^3 (no NH_3)	SPR^3 (1 vol % NH_3)
4	2.00	1.78
5	5.78	6.20

Analyses of N- and O-containing products

The analyses of the N- and O-containing compounds with the GC×GC-TOF and -FID brought about significant benefits in quantifying the changes and formation of these chemicals, which will be highlighted in this section. In addition, some challenges that was encountered when analyzing these compounds will be discussed. In Figure 7.11 a comparison is made between the GC×GC-TOF chromatograms for the oil samples collected at steady state from the reactions SPR^1 and SPR^2, where no NH_3 and 1 vol % NH_3 was added during the FT experiments respectively. At the time of the analysis, some minor differences in the analytical methodologies makes it challenging to directly compare these chromatograms based on their separation in the first dimension. Therefore, the first and second dimensions of the 2D chromatogram is constructed so that the compounds of interest is highlighted and the exact quantities for these dimensions are omitted for clarity. In order to emphasize the loss of oxygenates and the formation of the N-containing compounds the z-axis (which represents the total ion current) is qualitatively normalized. It is evident from these chromatograms that the separability of these compounds are far superior to what is possible via one-dimensional chromatography. Furthermore, one can easily detect the lower signals for the oxygenates (a/f, c/h, d) and in particular the complete

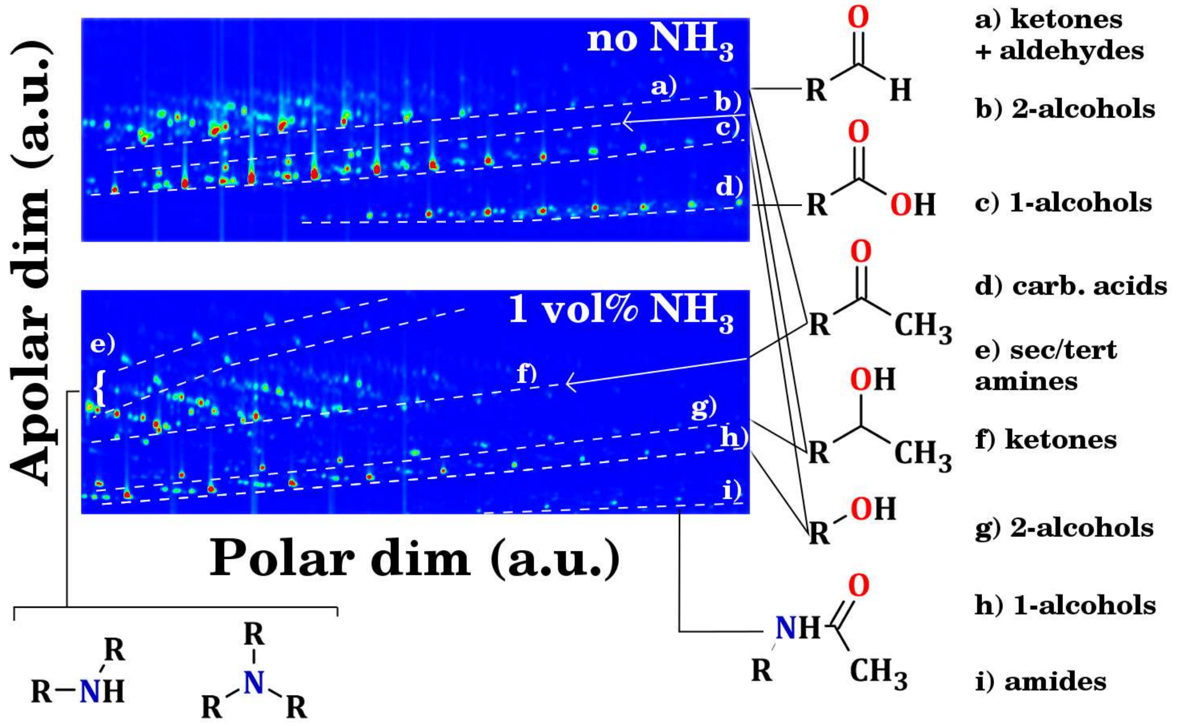

Figure 7.11: Two dimensional chromatograms obtained after GC×GC-TOF analysis of the oil samples taken from the reactions where *(Top:)* no or *(Bottom:)* 1 vol% NH$_3$ was added during Fe-catalyzed FTS reactions conducted in a slurry phase reactor. Note that retention times are omitted to simplify the figure. (T = 250 °C, P = 5 bar, GHSV = 2250 ml/hr/g$_{cat}$, H$_2$/CO = 2)

suppression of the carboxylic acids (*d*).

A group of secondary and tertiary amines were detected in the oil sample of SPR^2 (with NH$_3$ co-feeding) and is indicated in Figure 7.11 *(Bottom:)* - *(e)*. The formation of this class of N-containing compounds has not been reported in previous NH$_3$ co-feeding FT experiments where an Fe-based catalyst was used [2–7]. Kölbel and Trapper [4] showed that by deliberately adding other N-containing hydrocarbons such as ethylamine, piperidine and pyrrolidine, the surface alkyl groups from the FT reaction would react with these amines to form secondary and tertiary amines. The significance in observing the formation of secondary and tertiary amines in this work thus reveals that these group of N-containing compounds can form directly from CO, H$_2$ and NH$_3$, without the need for the addition of a primary amine.

The sec/tert amines was present in smaller quantities, which could in part be why the formation of these N-containing compounds has not yet been reported. Even with the use of the GC×GC-TOF/FID as analytical tool, the formation of these N-containing compounds is challenging. In Figure 7.12, a 2D chromatogram is presented in a topographic view that was produced when analyzing the FTS products present in the oil phase during the 1 vol% NH_3 co-feeding FTS experiment (SPR^2, sample taken at steady state, 48 hrs TOS). In the top part of Figure 7.12, the results using the total ion current (z-axis intensity in black) is plotted, while in the bottom part the results are overlayed with the chromatogram where only the $m/z = 72$ ion current is extracted (z-axis intensity in blue). Since the $m/z = 72$ ion current ratio corresponds to the defragmentation of the secondary and tertiary amines, it facilitates the identification of the region where the secondary and tertiary amines elutes on the 2D chromatogram. Furthermore, it shows that a whole range of these N-containing hydrocarbons are present in the oil sample.

A much improved separation could be achieved for the formation of amides. In Figure 7.13 the area where the amides elutes is enlarged and shows how complete isolation of this group of N-containing compounds could be achieved (sample analyzed from oil phase SPR^2, 48 hours TOS). Furthermore, the amides that was submersed in the water phase could be identified in the water phase collected after 48 hours TOS during the 1 vol % NH_3 co-feeding FT experiment (see Figure 7.14.

The quantification of the water phase products was challenging since it was not possible to accurately quantify the exact fraction of the compounds present in the water and oil phases for the water soluble oxygenates and N-containing compounds. The results from these analyses are therefore an underestimate for the O- and N-containing compounds, and to a large extent qualitative. In the 2D chromatogram (see Figure 7.14) obtained after GC×GC-TOF analysis of the water sample (taken 48 hrs TOS, SPR^2) it is possible to see the formation of a significant quantity of diethylamine (a secondary amine), the primary amines dissolved in the water phase as well as a range of amides. Furthermore, the formation of NH_4HCO_3 is indicated in Figure 7.14. The formation of NH_4HCO_3 was only confirmed after dissolving some of the solid NH_4HCO_3 collected during the FT experiment and analyzing it using the same GC method, since the identity of the compound was not discernible from its mass spectrum.

The formation of primary amines presented a unique problem during the GC×GC-TOF/FID analyses. This class of organic compounds, in particular the higher carbon number ranges

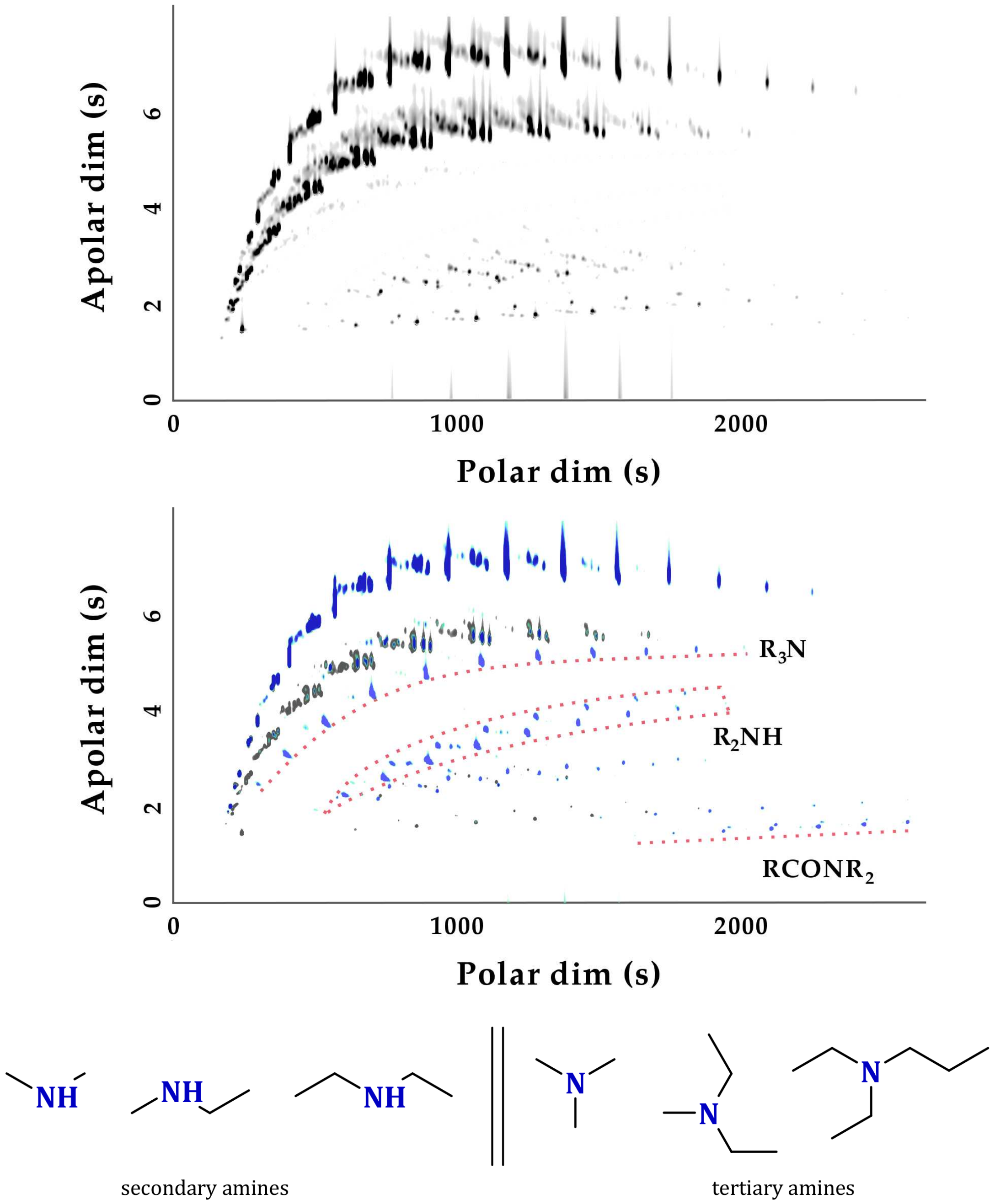

Figure 7.12: A topographic view of the FT product spectrum when the (*Top:*) total ion current (black) is compared to the case where the M/Z = 72 ratio (blue) is extracted and superimposed (*Middle:*). The mass to charge ratio of 72 represents a characteristic fragment for this class of compound which is present in its TOF spectra and simplifies its identification. Some examples of the typical secondary and tertiary amines detected are added at the bottom of the figure. (SPR^2, T = 250 ℃, P = 5 bar, GHSV = 2250 ml/hr/g_{cat}, $H_2/CO = 2$, 1 vol% NH_3, sample taken at steady state - 48 hrs TOS)

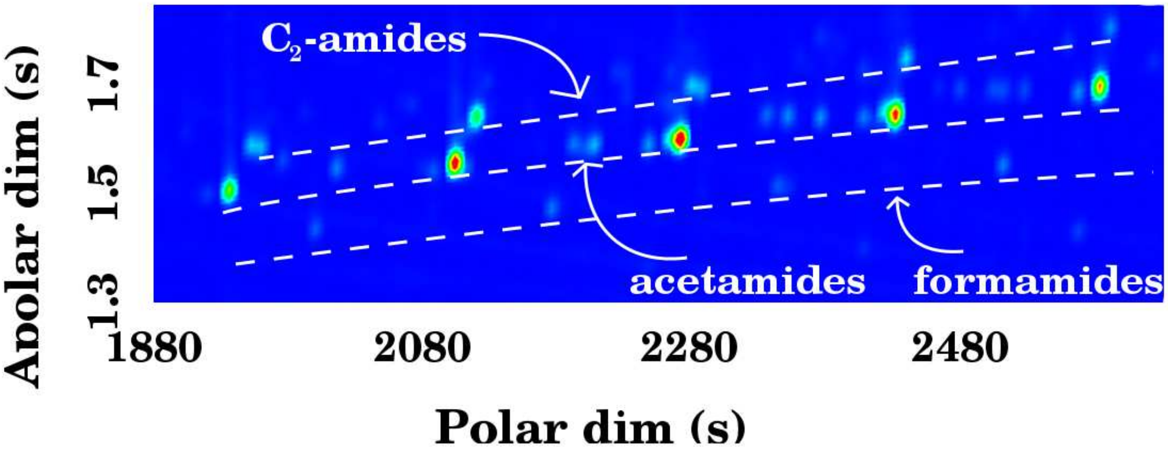

Figure 7.13: 2D chromatogram showing the formation of the formmides, acetamides and C_2-amides that are produced when NH_3 was co-fed during FTS. (SPR^2, T = 250 ^oC, p_T = 5 bar, GHSV = 2250 ml/hr/g_{cat}, H_2/CO = 2, 1 vol% NH_3)

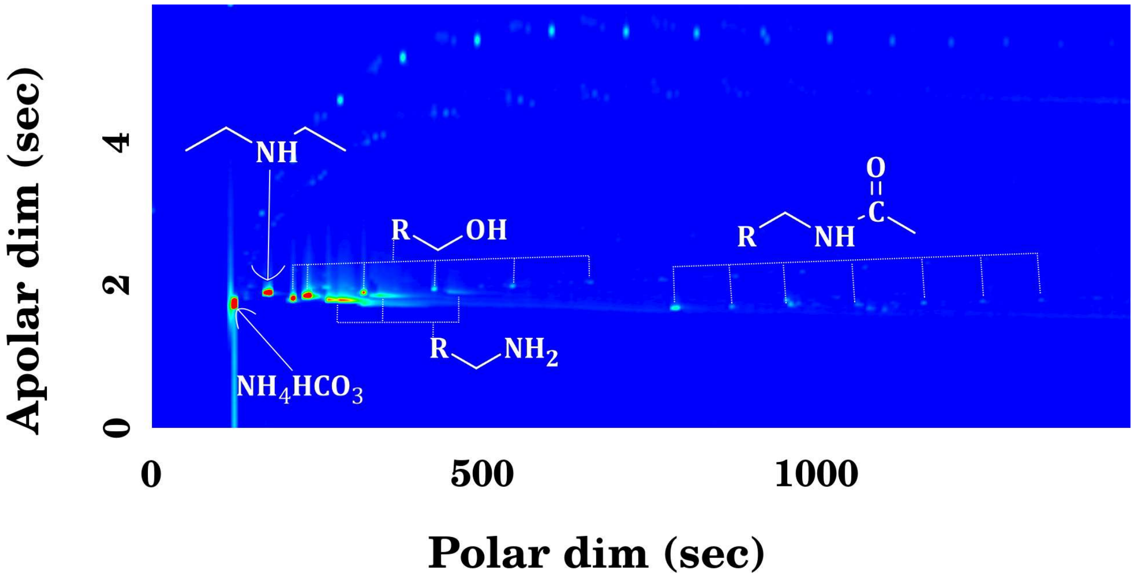

Figure 7.14: (Top) GC×GC chromatogram obtained when analyzing the water phase, where no % NH_3 were added (Bottom) and where 1 vol% NH_3 were added during FTS. (SPR^1, T = 250 ^oC, p_T = 5 bar, GHSV = 2250 ml/hr/g_{cat}, H_2/CO = 2, 1 vol% NH_3)

Table 7.4: The oxygenate selectivity with and without NH_3 addition is tabulated. (SPR[1], T = 250 ^oC, p_T = 5 bar, GHSV = 2250 ml/hr/g_{cat}, H_2/CO = 2, 1 vol% NH_3)

Oxygenates	**Selectivity (C wt%)**	
	$no\ NH_3$	FTS_{NH_3}
n-alcohols (C_{1-17})	7.89	3.43
carboxylic acids (C_{2-12})	0.50	0.02
ketones (C_{3-11})	1.20	0.84
aldehydes (C_{2-11})	0.88	0.00

(C_{6+}) interacted to a great extent with the polar ('wax') column and made their identification and quantification impossible via this particular analytical technique. Fortunately, however, the primary amines in the C_{2-7} carbon number range could very accurately be quantified via the on-line GC-FID technique (see the discussion in Section C.1.7.1 of Appendix C for further information).

After identification of these compounds with the GC×GC-TOF analysis, it was possible to quantify all the organic products with the GC×GC-FID and subsequently calculate the desired product selectivities. The quantitative analysis of the O- and N-containing compounds is discussed in the following sections.

Oxygenate selectivity

An important aspect of this study, was to evaluate the changes in selectivity of the oxygenates produced in the absence and presence of NH_3 (1 vol%) during FTS. The change in oxygenates selectivities (see Table 7.4), when comparing the case where 1 vol % of NH_3 was added during FTS reaction and the NH_3-free FTS reaction, were significant. The loss in oxygenate selectivities were most pronounced for the aldehydes, which were completely suppressed, followed by the carboxylic acids, ketones and the linear alcohols.

The results reported here are therefore in general agreement with previous work where a concomitant decline in oxygenate selectivity were observed with the formation of N-containing hydrocarbons [5, 6]. (The formation of N-containing compounds are discussed in subsequent section.) The pathways of oxygenate formation during FTS is not easily tested and the exact pathways are debated in literature [25, 26]. When considering primary routes to oxygenate formation, the 'CO-insertion' mechanism developed by Pichler and Schulz [27] provides the most adequate description for the pathway to the formation of the oxygenates present in the FTS product spectra. Evidence does however exist for the formation of various oxygenates (aliphatic alcohols, aldehydes, ketones and carboxylic acids) via both primary and secondary routes [16, 28]. The final oxygenate product observed in the product distribution, is thus a contribution of both primary and secondary pathways, and both routes needs to be considered to account for the loss of oxygenate formation when NH_3 are co-fed during FTS.

In Chapter 8 a linear alcohol, 1-octanol, is co-fed with the feed ($CO + 2\ H_2 + 1$ vol % NH_3) to evaluate its potential to form N-containing compounds via secondary reactions. It is therefore important to have a good account of the selectivities of the alcohols, and how it is influenced when 1 vol% NH_3 is added during the reaction. If one looks at the 1-ROH selectivities as a function of carbon number (see Figure 7.15 - top), it can be seen that the loss in oxygenate selectivities occurs for all the linear alcohols. The change in selectivities (ΔS_{n-ROH}) as a function of carbon number, however seems to indicate that the higher carbon number linear alcohols have a greater propensity to be suppressed when 1 vol % NH_3 is added. When Schulz and Claeys [18] studied the secondary reactions of α-olefins, in a slurry phase reactor, they found that the higher carbon number olefins, had a greater potential to undergo secondary reactions. The aforementioned observation could thus suggest that secondary consumption of the (primary) produced FTS oxygenates are to some extent being consumed during secondary reactions to form the N-containing compounds.

N-containing compounds

N-containing compounds were observed to be present in smaller quantities than the oxygenates. The highest selectivity were that of the primary amines ($S_{RNH_2} = 0.94$ C wt%). When analyzing the primary amines (in order to determine S_{RNH_2}) using the ampoule technique, a much lower selectivity is obtained ($S_{RNH_2} = 0.34$ C wt%), which is similar to the problem encountered during the analysis of carboxylic acids [24]. In Figure 7.19 a chromatogram that was obtained during the analysis of the product spectrum when 1 vol % NH_3 was added to

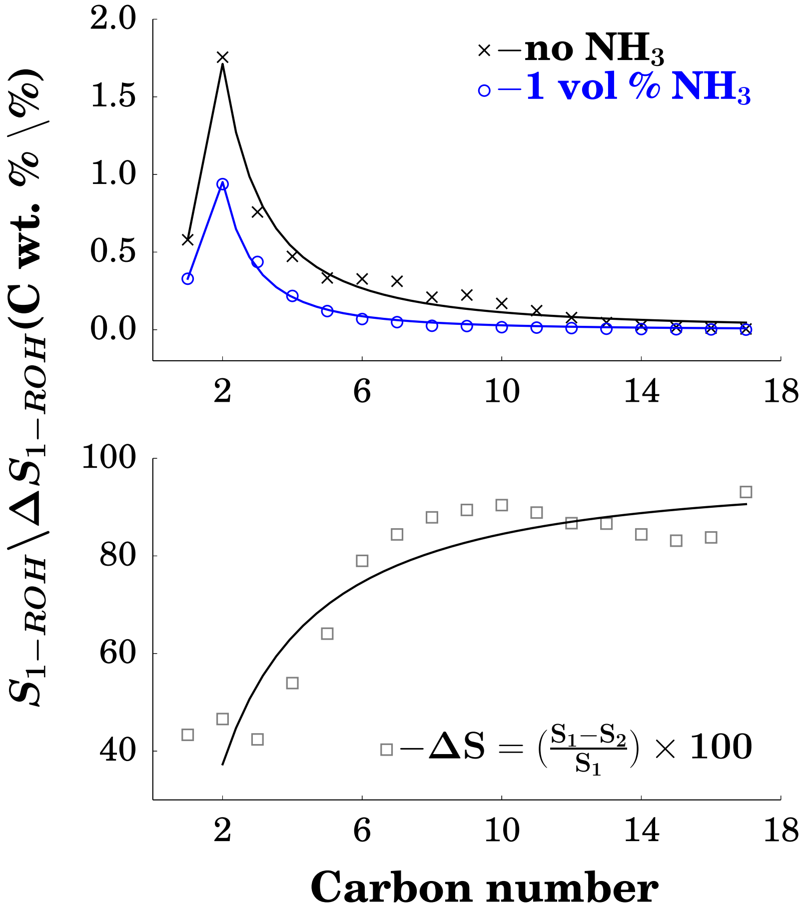

Figure 7.15: Carboxylic acid selectivity calculated as the (carbon weight) percentage as a function of carbon number present in the total hydrocarbon product with and without the addition of 1 vol % of NH_3. (T = 250 °C, P = 5.0/5.1 bar, GHSV = 2250 ml/hr/g_{cat}, $H_2/CO = 2$)

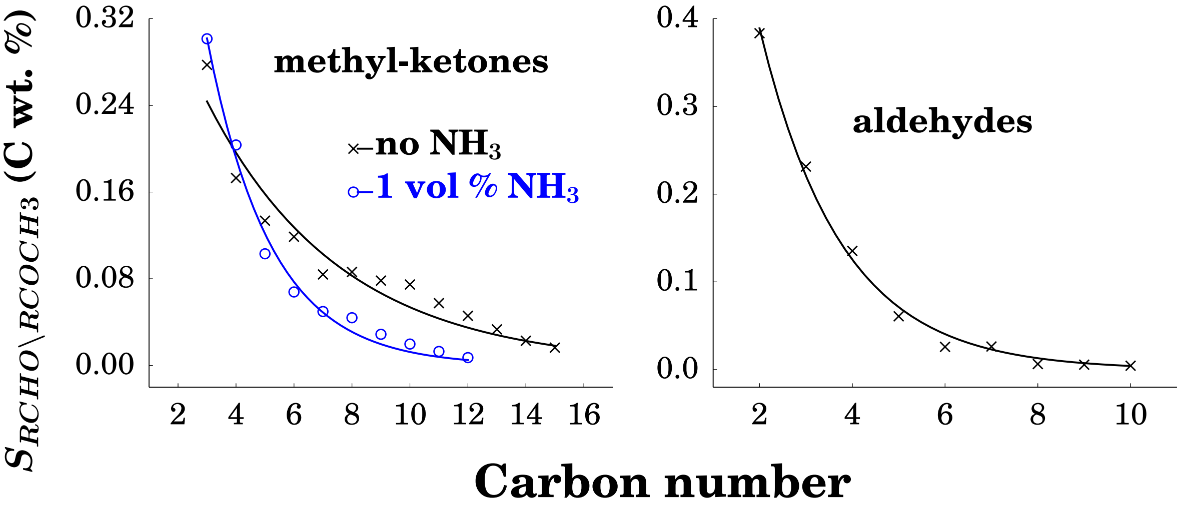

Figure 7.16: Aldehyde and ketone selectivity calculated as the (carbon weight) percentage present in the total hydrocarbon product with and without the addition of 1 vol % of NH_3. (T = 250 °C, P = 5.0/5.1 bar, GHSV = 2250 ml/hr/g_{cat}, H_2/CO = 2)

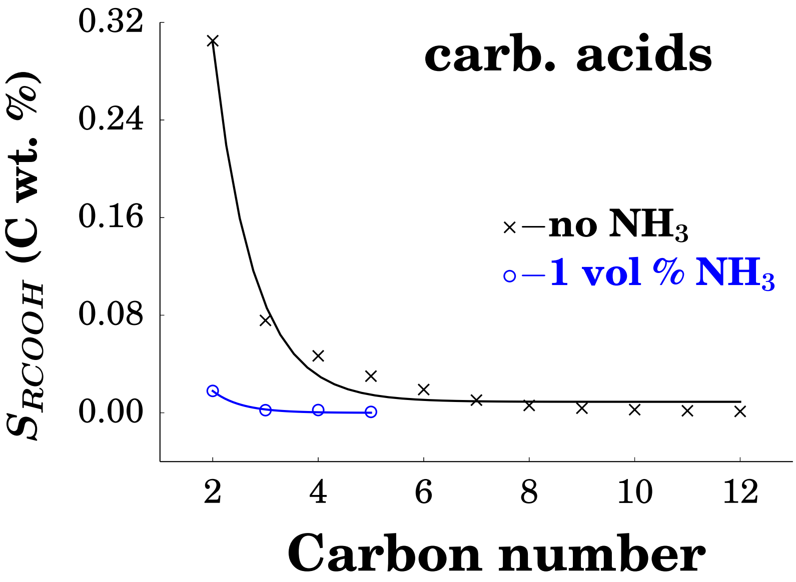

Figure 7.17: Carboxylic acid selectivity calculated as the (carbon weight) percentage as a function of carbon number present in the total hydrocarbon product with and without the addition of 1 vol % of NH_3. (T = 250 °C, P = 5.0/5.1 bar, GHSV = 2250 ml/hr/g_{cat}, H_2/CO = 2)

Table 7.5: The selectivity for the N-containing compounds when NH_3 is added during FTS. (SPR^1, T = 250 ^{o}C, p_T = 5 bar, GHSV = 2250 ml/hr/g_{cat}, H_2/CO = 2, 1 vol% NH_3)

N-containing compounds	**Selectivity (%)**
primary amines (C_{2-7})	0.97
secondary amines (C_{4-11})	0.20
amides (C_{4-11})	0.15
nitriles	0.00

synthesis gas feed during FTS are presented. From this figure (and an enlarged section of the chromatogram) it can be seen how the primary amines could be captured via on-line GC-FID analysis. The separation for the peaks corresponding to the primary amines could be further deconvoluted by varying the initial GC oven temperature (starting at ambient temperatures or -30 ℃ using cryogenic cooling) during the on-line sampling of the organic product at steady state FTS reactions. When using the off-line ampoule gas sampling technique, most of these peaks were not present or not discernible.

The formation of secondary and tertiary amines accompanied by the absence of any detectable aliphatic nitriles brings into question the stability of this group of N-containing compounds. Based on aforementioned observations, a mechanistic scheme (see Figure 7.20) can now be put forward where the primary amines and nitriles undergoes secondary reactions to form secondary or tertiary amines. This hypothesis is tested in Chapter 8 by co-feeding octanitrile with the feed (CO + 2 H_2 + 1 vol NH_3 %) using a saturator.

The higher carbon (C_4+) number aliphatic amides that were present in the oil phase were analyzed via the GC×GC-TOF/FID system, and eluted in a similar region as the carboxylic acids (see the Figures 7.12 and 7.13). Homologous series' of formamides, acetamides and C_2-amides were clearly separable and detectable when analysis were conducted with GG×GC-TOF system and extracting the 72 m/z ion ratio. When using flame ionization as detector for quantification purposes, it becomes complicated to accurately identify this series of compounds amongst the other organic compounds. When combining the use of the deconvoluted total ion current and the FID analysis to quantify the yield of amides, it can qualitatively be calculated

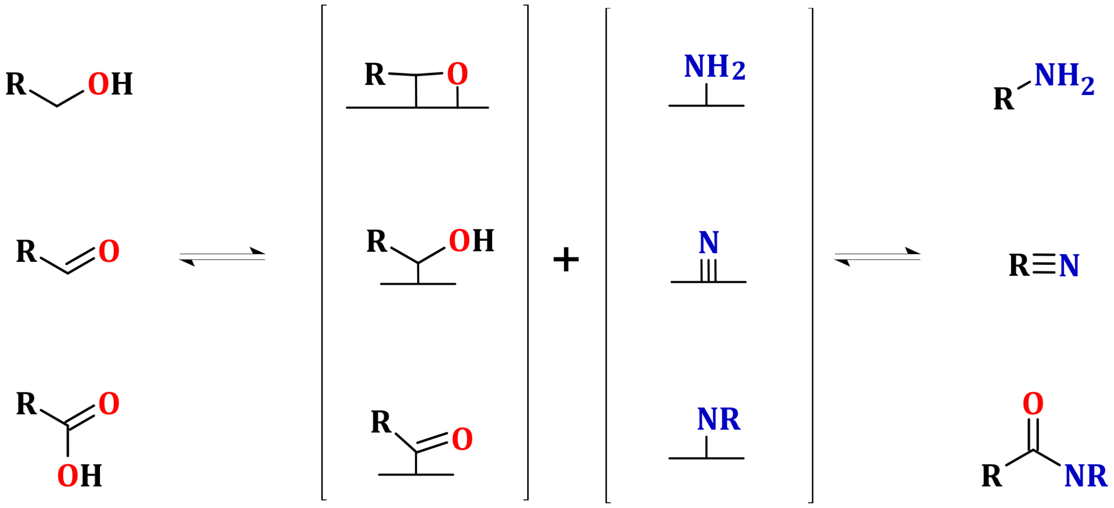

Figure 7.18: Schematic that illustrates the hypothesized route to the formation of N-containing compounds via secondary conversion of oxygenates. Note that the oxygen surface species are omitted in the final state to simplify the schematic.

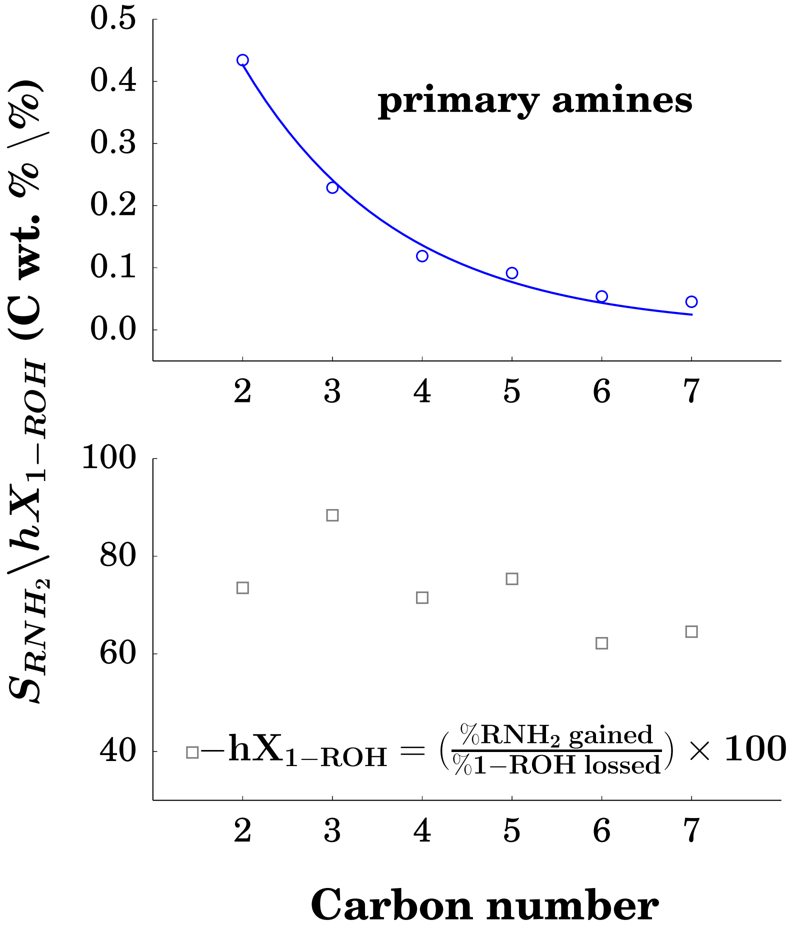

Figure 7.19: *Top:* Selectivity for the formation of primary amines and *Bottom* the hypothetical conversion of 1-alcohols to these N-containing compounds, if they were formed via secondary reactions. (SPR[1], T = 250 ^oC, p_T = 5 bar, GHSV = 2250 ml/hr/g_{cat}, H_2/CO = 2, 1 vol% NH_3)

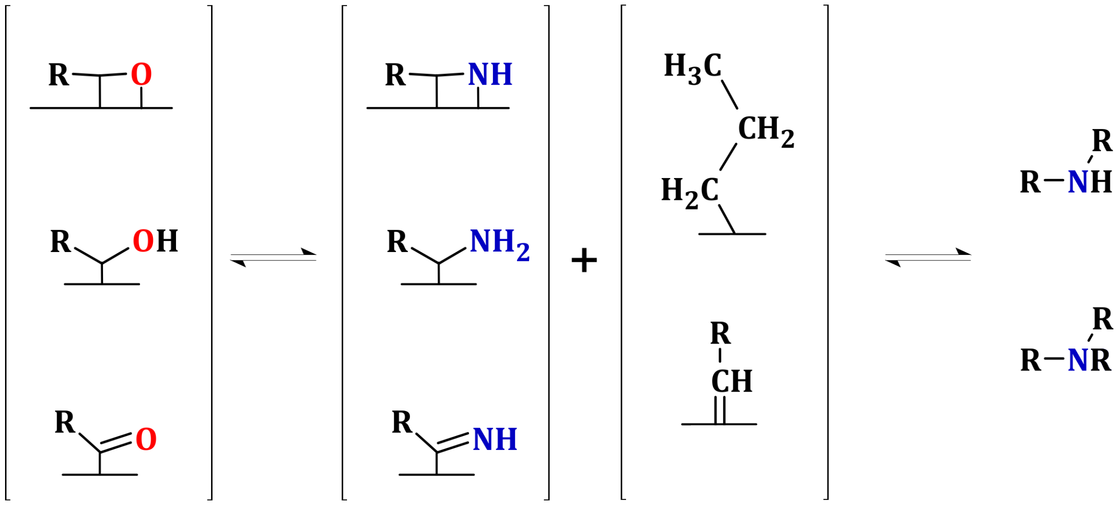

Figure 7.20: Schematic that illustrates the hypothesized route to the formation of secondary and tertiary amines. Oxygenated hydrocarbon surface species are initially converted to N-containing surface species that subsequently scavenges other hydrocarbons surface products to produce the final product. Note that the oxygen surface species are omitted in the final state to simplify the schematic.

that the selectivity for the amides is 0.15 C wt%. The relative carbon weight distribution between the groups acetamides/formamides/C_2-amides would be approximately 10:1:1 (g/g). From this observation one can postulate that an amide-type surface species kinetically favors the incorporation of the methyl surface species as opposed to hydrogen or the ethyl surface species.

The alcohols and carboxylic acids that were present in the water phase, were analyzed via GC×GC-TOF analysis (see Figure 7.14 - top). The water phase of the FTS reaction where 1 vol % NH_3 were co-fed (see Figure 7.14 - bottom) contained, in addition, the lower carbon number primary amines, amides, formamides as well as some dissolved ammonium bicarbonate. In a similar way as it was shown with the more quantitatively accurate techniques (on/off-line GC-FID, GC×GC-FID), it can qualitatively be assessed from the analysis of the water phase using GC×GC-TOF that that a decrease of oxygenate selectivity is a result of having 1 vol % NH_3 in the FTS feed.

Spent catalysts

After 96 hours spent on stream (for SPR^{1-2}), the catalysts that were trapped in the hardened wax were removed and analyzed via powder X-Ray Diffraction (XRD). The identification of the bulk phases present in these spent catalysts were achieved by comparing the XRD patterns with the diffraction patterns provided by the International Centre for Diffraction Data PDF-2 database. When analyzing both catalysts, the Fe_3O_4, $\chi - Fe_5C_2$ and $\epsilon - Fe_2C$ phases were present, which are commonly observed for FTS spent catalysts [29, 30]. The diffractogram generated for the catalyst analyzed after the reaction where 1 vol% NH_3 were added with the synthesis gas did not show any clear patterns that would indicate the presence of any Fe-nitrides. The XRD pattern of the spent catalyst generated after NH_3 were co-fed during FTS did in fact seem to be very similar to the spent catalyst analyzed after the NH_3 free FTS reaction (see Figure 7.21). It can therefore be assumed that the possible different carburization processes suggested by the H_2/CO conversions and CO_2 selectivities, essentially leads to the same bulk phase catalyst for the working catalyst. In-situ XRD analysis of the initial stages for the Fe-based catalyst when NH_3 are present during FTS would surely be an interesting study. A special reactor system would however have to be designed and commissioned to protect the specialized equipment used in XRD experiments against the corrosive nature of NH_3.

Wax

An interesting observation when comparing these experiments, were a clear difference in the color of the wax removed from the reactors after the FTS reactions. An exact "shutdown" procedure were followed for the two reactions, but when the wax solidified, the resulting color for the NH_3 co-feeding reactions were significantly lighter in color than that of the normal FTS reaction. Figure 7.22 shows the spent waxes taken from various reactions where no NH_3 (left) were added and some where 1 vol % NH_3 (right) were added during FTS. Co-based FTS reactions generally produces a white wax with the dark catalyst submerged at the bottom of the solidified wax, while Fe-based catalysts have the bulk of the catalyst at the bottom but a much darker color for the top part of the wax. It is well-known that Co-based catalyst have a significantly lower oxygenate selectivity than Fe-based catalysts [16]. A possible reason for the difference in color could therefore be the absence of certain oxygenates observed when 1 vol % NH_3 is added during FTS. In particular the organic carboxylic acids, which may have the metal particles suspended in the wax at the point where the reaction is allowed to cool down. One can however not rule out the possibility that fines were still present even after sieving the catalyst to a diameter below 2μm, and are hence suspended in the wax.

Conclusions

An investigation of the changes (w.r.t. activity and selectivity) incurred apon 1 vol% NH_3 addition to synthesis gas during FTS, when using a precipitated Fe-based catalyst in a slurry phase reactor, were conducted. The CO and H_2 conversions data did not seem to point to any deactivation of the catalyst at this concentration. The initial activity and CO_2 selectivity data did however suggest that the NH_3 plays a role in retarding the carburization process of the Fe-based catalyst. Methane selectivity increased from 11 to 14 % and the CO_2 selectivity were lowered from 40 % to 35 %. The significant decline in CO_2 selectivity were ascribed to the formation of ammonium bicarbonate (NH_4CO_3) by reaction of H_2O, NH_3 and CO_2, which were subsequently confirmed via PXRD analysis of a solid formed during the reaction. Since the oil and water phase collection vessel (i.e. the cold trap) were held at a low temperature and high

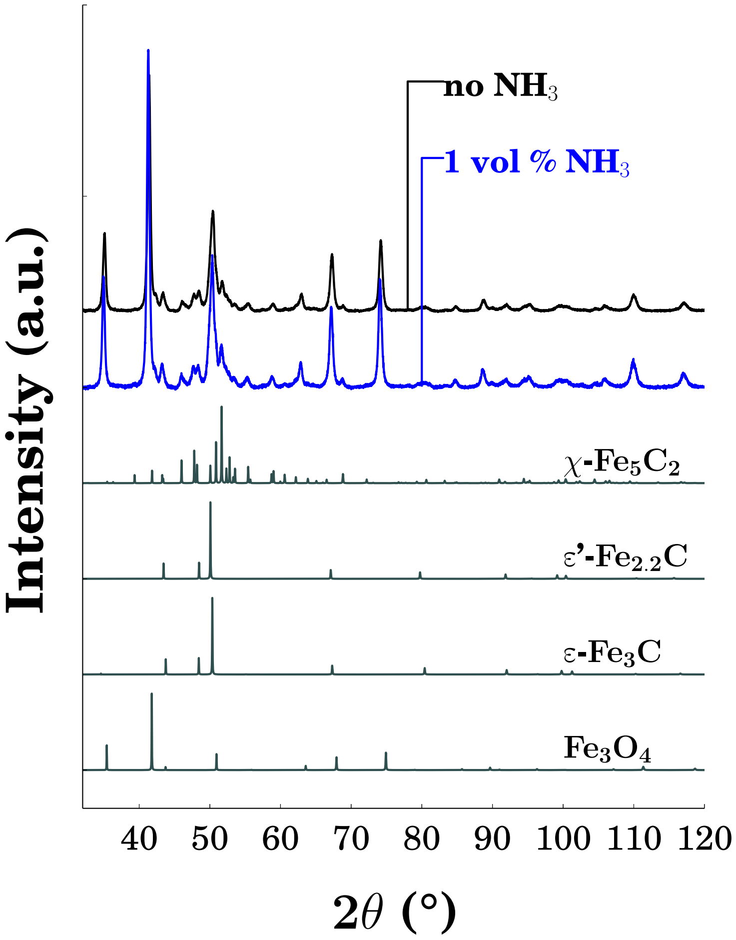

Figure 7.21: Spent catalyst for the FTS reactions conducted with and without the addition of NH_3. Reference spectra were drawn based on the parameters given in Ref [31]

Figure 7.22: The spent, solidified waxes taken from reactions where no NH_3 (left) and 1 vol % NH_3 (right) were added during FTS which shows the marked differences in color. This observation could indicative of the absence of certain oxygenates.

pressure (273 K, 5 bar, NTP), large quantities of the NH_4CO_3 were collected. A significant loss in oxygenate selectivities were observed when 1 vol % NH_3 were added during FTS, which is in agreement with previous studies [5, 6]. By analyzing the oil and water phase products with two-dimensional chromatography (GC×GC-TOF/FID) it was possible to identify a range of secondary and tertiary amines formed during the reaction in addition to those reported in previous studies (primary amines and amides). The formation of aliphatic nitriles were however not observed at this concentration and is postulated to undergo secondary reactions to form secondary/tertiary amines. The spent catalysts of both reactions yielded similar results, indicating that the formation of the Fe_3O_4, χ-Fe_5C_2 and ϵ-Fe_2C phases were present during these reactions. It was not possible to identify the formation of any Fe-nitrides present in the bulk phase when analyzing the spent catalysts from the NH_3 co-feeding FTS reaction with PXRD. When shutting down the respective reactions, a difference in the color of the wax obtained were observed on several occasions when NH_3 were present in the synthesis gas feed. The color were similar to wax usually obtained after Co-based FTS slurry phase reactions, which does not produce much oxygenates. This observation could be due to the reduction in the formation of oxygenates (in particular carboxylic acids) when NH_3 are present in the synthesis gas feed.

REFERENCES

[1] R.B. Anderson, H. Kölbel and M. Rálek, The Fischer-Tropsch synthesis, Academic Press, Orlando, Orlando, 1984.

[2] A. Clark, Process of synthesizing aliphatic amines (1950).

[3] W. Röttig, Catalytic hydrogenation of carbon monoxide with addition of ammonia or methylamine (1958).

[4] H. Kölbel and J. Trapper, Angew. Chem. Internat. Edit 5 (1966) 843–844.

[5] R. Henkel, The influence of ammonia on fischer-tropch synthesis and formation of N-containing compounds, Ph.D. thesis, Carl von Ossietzky Universität, Germany (2012).

[6] T. Sango, Nitrogen-containing from compounds ammonia co-feed to the fischer-tropsch synthesis, Master's thesis, University of Cape Town, South Africa (2013).

[7] T. Sango, N. Fischer, R. Henkel, F. Roessner, E. van Steen and M. Claeys, Appl. Catal., A 502 (2015) 150–156.

[8] J. M. Pommersheim and J. Coull, AIChE Journal 17 (5) (1971) 1075–1080.

[9] C.H. Bartholomew, Appl. Catal., A 212 (2001) 17–60.

[10] W. Torres, S. Pansare and J. Goodwin, J. Catal. 49 (2007) 407–456.

[11] E. van Steen and M. Claeys, Chem. Eng. Technol. 31 (2008) 655–666.

[12] T. Grobler, M. Claeys, E. van Steen and M.J. Janse van Vuuren, Catal. Commun. 10 (2009) 1674–1680.

[13] J. Dallüge, J. Beens and U.A.Th. Brinkman, J. Chromatogr. A 1000 (2003) 69–108.

[14] R. van der Westhuizen, H. Potgieter, N. Prinsloo, A. de Villiers and P. Sandra, J. Chromatogr. A 1218 (2010) 3173–3179.

[15] R. van der Westhuizen, R. Crous, A. de Villiers and P. Sandra, J. Chromatogr. A 1217 (2010) 8334–8339.

[16] M.E. Dry, Chapter 3 - chemical concepts used for engineering purposes, in: A.P. Steynberg and M.E. Dry (Eds.), Fischer-Tropsch Technology, Vol. 152 of Stud. Surf. Sci. Catal., Elsevier, 2004, pp. 196 – 257.

[17] H. Schulz, Z. Nie and M. Claeys, Initial episodes of Fischer-Tropsch synthesis with cobalt catalysts, in: A. Parmaliana, D. Sanfilippo, F. Frusteri, A. Vaccari and F. Arena (Eds.), Natural Gas Conversion V Proceedings of the 5th International Natural Gas Conversion Symposium, Vol. 119 of Studies in Surface Science and Catalysis, Elsevier, 1998, pp. 191 – 196.

[18] H. Schulz, G. Schaub, M.E. CDry and T. Riedel, Appl. Catal., A 186 (1999) 215–227.

[19] T.C. Bromfield and N.J. Coville, Appl. Catal., A 186 (1999) 297–307.

[20] H.M. Torres Galvis, J.H. Bitter, C.B. Khare, M. Ruitenbeek, A. Iulian Dugulan and K.P. de Jong, Science 335 (2012) 835–838.

[21] H.M. Torres Galvis, A.C.J. Koeken, J.H. Bitter, T. Davidian, M. Ruitenbeek, A. Dugulan, Iulian Dugulan and K.P. de Jong, J. Catal. 303 (2013) 22–30.

[22] H. Schulz and M. Claeys, Appl. Catal., A 186 (1999) 71–90.

[23] H. Schulz, Erdöl und Köhle 30 (1977) 123.

[24] P. Cairns, Oxygenates in iron Fischer-Tropsch Synthesis: is copper a selectivity promoter?, Ph.D. thesis, University of Cape Town, South Africa (2008).

[25] M. Claeys and E. van Steen, Chapter 8 - basic studies, in: A.P. Steynberg and M.E. Dry (Eds.), Fischer-Tropsch Technology, Vol. 152 of Stud. Surf. Sci. Catal., Elsevier, 2004, pp. 601 – 680.

[26] B.H. Davis, Catal. Today 141 (2009) 25–33.

[27] H. Pichler and H. Schulz, Chem. Ing. Tech. 42 (1970) 1162.

[28] M. Claeys, Selektivität, Elementarschritte und kinetische Modellierung bei der Fischer-Tropsch-Synthese, Ph.D. thesis, Unversität Fridericiana Karlsruhe, Germany (1997).

[29] M.E. Dry, Catalysis Science and Technology, Vol. 1, Springer Verlag, New York, 1981.

[30] E. de Smit, Iron-based fischer-tropch synthesis: New insights from in-situ (micro)spectroscopy, diffraction and theory, Ph.D. thesis, Universiteit Utrecht, The Netherlands (2010).

[31] H.E. du Plessis, Structures of carbides, Ph.D. thesis, University of Johannesburg, South Africa (2007).

CHAPTER 8

SECONDARY REACTIONS: CO-FEEDING OF OXYGENATES AND N-CONTAINING COMPOUNDS

The role of secondary reactions of oxygenates and N-containing compounds when 1 vol % NH_3 is present in the synthesis gas feed ($CO + H_2$) during low temperature, Fe-catalyzed Fischer-Tropsch synthesis (FTS) is discussed. Previous studies, where NH_3 was co-fed during FTS, a concomitant loss in oxygenate selectivity was observed with the formation of N-containing compounds, which suggests that the latter compounds form to the detriment of the oxygenates or originates from them, respectively. Experimental studies have been reported that suggest that the formation of oxygenates could follow primary and/or secondary FTS pathways when using Fe-based catalysts. The observed loss of oxygenates could thus also occur via primary or secondary pathways, where the latter reactions seem particularly feasible when considering the possibility of amination reactions of oxygenates to form N-containing compounds. It is however not clear if these types of secondary reactions could take place under FTS reaction conditions. In this work the hypothesis that primary produced FTS oxygenates are consumed via secondary reactions to form N-containing compounds is tested via co-feeding a probe molecule (1-octanol) with the feed $CO + 2\ H_2 + 1$ vol % NH_3 during Fe-based FTS in a gradientless slurry phase reactor.

Furthermore, the formation of secondary and tertiary amines, and the absence of aliphatic nitriles observed when co-feeding NH_3 *during FTS in Chapter 7, posed questions regarding the stability of the aliphatic nitriles, and subsequently motivated the co-feeding of nonanitrile under similar reaction conditions. The volatilization of the* $C_{8/9}$*-hydrocarbons was achieved via the use of a saturator, and the product analysis was simplified through the use of comprehensive two-dimensional gas chromatography (GC×GC-TOF/FID). When co-feeding 1-octanol, a significant increase in the formation of secondary and tertiary amines and smaller quantities of amides were observed, clearly showing the potential for these secondary reactions to occur under these reaction conditions. Furthermore, it is suggested that nonanitrile is likely to re-adsorb onto the catalyst surface and undergo secondary reactions, based on its high conversion (67.0 %) to N-containing compounds during the nonanitrile co-feeding FT experiment. An increase in the 1-nonanol fraction was observed when co-feeding nonanitrile, indicating the reversibility of the terminal alcohols and nitriles when* NH_3 *is co-fed during FTS. These findings thus highly suggest that secondary pathways plays an important role in shaping selectivity for the N-containing compounds present in the FT product spectrum when* NH_3 *is added.*

Introduction

The Fischer-Tropsch synthesis (FTS) is an industrial process that is capable of producing various petroleum products (e.g. diesel, jet fuel etc.) and it can in addition be used to produce chemicals such as α-olefins and oxygen-containing organic products (oxygenates) [1]. Earlier experimental Fischer-Tropsch (FT) studies that considered the addition of NH_3 to the synthesis gas ($CO + H_2$) feed during Fe-catalyzed FTS revealed that valuable N-containing compounds, amines, can be formed under these conditions [2–5]. A decrease in oxygenate selectivity was reported in more recent studies [6–9] where NH_3 was co-fed with synthesis gas feeds during FTS conducted over Fe- and Co- based catalysts in slurry and/or fixed bed reactors. Sango et al. [7, 8] co-fed increasing concentrations (0 - 35 vol %) of NH_3 during Fe-catalyzed FTS (slurry phase, T = 250 ℃, P = 5.0 - 8.0 bar, $H_2/CO = 2.0$, GHSV = 2250 ml/g_{cat}/hr) in order to improve the selectivity of N-containing compounds and reported a significant decline in oxygenate selectivity upon increased formation of N-containing compounds. Furthermore thermodynamic calculations was reported that predicts that the (C_{1-6}) oxygenates and N-containing compounds have similar potentials for formation from the reaction of CO, H_2 and NH_3 at the relevant reaction conditions (T = 500 K). Henkel [6] added 2 vol % NH_3 during FTS (Fe/K 100/0-10 (g/g), fixed bed, T = 270 ℃, P = 4.0 bar, $H_2/CO = 2.0$, GHSV = 1920 ml/g_{cat}/hr) and was able to tie the loss of the oxygenate selectivities observed to the molar quantities of the N-containing compounds that formed. Rausch et al. [9] added between 0 - 26 vol % NH_3 during FT experiments (slurry phase, T = 240 ℃, P = 11 bar, $H_2/CO = 1.2\text{-}2.0$, GHSV = 545 ml/g_{cat}/hr) conducted over Co-based catalysts (15 wt% Co/SiO_2). When they compared the FT product distributions for the reactions with and without NH_3 addition, they find that the addition of NH_3 led to a complete suppression of the alcohols (C_{3-9}), a significant decline in the formation of carboxylic acids (C_{2-7}) and the formation of small quantities of amines and amides. The concomitant loss of oxygenates with the production of N-containing compounds was confirmed in Chapter 7 when analyzing the organic products obtained when co-feeding 1 vol % NH_3 during FTS (slurry phase, T = 250 ℃, P = 5.1 bar, $H_2/CO = 2.0$, GHSV = 2250 ml/g_{cat}/hr) with the GC×GC-TOF/FID analytical technique. Based on the observed loss of oxygenates and the formation of the N-containing compounds during the NH_3 co-feeding FT experiments, it has been postulated that the pathway to the formation of the oxygenates are impeded in some way, and that the route to the formation of the N-containing compounds and oxygenates could be interrelated [6–9].

The pathways to the formation of oxygenates that form during FTS is not as well-defined as that of the α-olefins or paraffins, but various proposals for these mechanistic routes have been reported [5, 10–12]. The products obtained during FTS are generally not observed to be in thermodynamic equilibrium, which allows for the deduction of mechanistic information by evaluation of the FTS product spectrum [5]. Dry [11] reports on the concentrations (ratios) for selected products, including the oxygenates - ethanol, acetic acid and acetaldehyde, observed at the exit of a reactor, where FTS was conducted over Fe-based catalysts at typical FTS conditions (T = 237/327 °C). He subsequently compared these concentration ratios with the thermodynamically predicted concentration ratios that would be expected if they formed via secondary reactions (e.g. the formation of ethanol from the hydrolysis of ethene). The possibility for these oxygenates to have formed via secondary reactions of α-olefins was refuted by the significantly higher concentration ratios of the oxygenates observed in the product spectrum, compared to their thermodynamically predicted concentration ratios [11]. The feasibility for small quantities ($<$ 4 mol %) of oxygenates to form via hydroformylation reactions of α-olefins was demonstrated by Claeys [13] when he co-fed various α-olefins during Fe-based FTS. Schulz and Claeys [14] however ruled out the exclusive formation of oxygenates in this way and point out that the formation of C_{1-2}-oxygenates could not be explained via the hydroformylation route. Based on these experimental results [11, 13, 14] it is predicted that the oxygenates can form as primary FTS products. The most plausible or accepted primary route to oxygenate formation is via termination steps that involve the ‘CO-insertion’ mechanism proposed by Pichler and Schulz [15] or alternatively termination steps that involve the reaction of growing alkyl chains with OH surface species [16].

Dry [11] mentions that once these primary FTS oxygenates are formed, they could re-adsorb on the catalyst surface and undergo secondary reactions, which was evidenced by the deliberate co-feeding of ethanol, acetic acid and acetaldehyde during FTS. When one of these oxygenates (ethanol, acetic acid and acetaldehyde) were co-fed during Fe-based FTS, two of the other oxygenates were produced, which suggested that these oxygenates are interrelated via secondary reactions. Several other oxygenate co-feeding experiments during FTS have been reported in literature to elucidate the role of secondary reactions of oxygenates in FTS [17–24]. Emmet [17] reported on experiments where ^{14}C-labeled oxygenates are co-fed during FTS, and similar studies where radioactive oxygenates were co-fed during FTS were extended by the group of Davis et al. [10]. These studies generally revealed that many of the shorter chain C_{2-5}-oxygenates readsorb during FTS and can, in some cases, be incorporated into the growing chain [10]. A study conducted by Cairns [24] included co-feeding of C_8-oxygenates during FTS to study their role in secondary reactions during Fe-catalyzed FTS. These co-feeding reactions were conducted in a Berty reactor using a similar catalyst (precipitated Fe/K 100/5 (g/g)) to the one used in the present study, albeit at a higher temperature (T = 300 °C, P = 21 bar, $H_2/CO/CO_2$ = 4:1:1, GHSV = 4000 ml/g_{cat}/hr). A schematic that represents some of the key findings of his co-feeding study is presented in Figure 8.1. When one of the three oxygenates (octanal, 1-octanol or octanoic acid) was co-fed with a synthesis gas feed, an increase in two of the other C_8-oxygenates was observed, which corroborates the results obtained for the shorter chains by Dry [11]. This observation led him to believe that these oxygenates undergo secondary reactions via a common surface acyl intermediate. In addition, when these oxygenates were co-fed, an increase in the formation of the C_9-ketone and -iso-alcohol was observed. These reactions are assumed to be irreversible, since the co-feeding of the ketone did not result in an increase in yields for the C_8-aldehyde, -alcohol or -carboxylic acid. The formation of the C_9-iso-alcohol was presumed to occur via hydrogen addition to the C_9-ketone. No chain initiation was observed when any of the oxygenates were co-fed during Cairns' [24] co-feeding experiments. Considering the potential for the amination of oxygenates [25] and their feasibility to undergo secondary reactions during FTS [17–24], it is proposed that a significant conversion of primarily produced oxygenates are consumed via secondary reactions, which leads to an increased selectivity for the N-containing compounds when NH_3 is present in the synthesis gas feed during FTS.

To test this hypothesis, a C_8-oxygenate (1-octanol) was added via a saturator during the FTS reaction with co-feeding of NH_3 conducted in a slurry phase reactor (T = 250 °C, P = 5 bar, GHSV = 2250 ml/hr/g_{cat}, $H_2/CO = 2$, 1 vol % NH_3). The results obtained from the FT experiments where 0 or 1 vol% NH_3 was added during FTS, as reported in Chapter 7, are inferred here and serve as base case studies for these co-feeding experiments. The current study benefits from off-line analysis of the oil phase via the use of comprehensive two-dimensional gas chromatography (GC×GC-TOF/FID) which has been shown to drastically improve the ability to analyze complex FTS product spectra [26–28]. The results obtained in Chapter 7 and the initial (1-octanol) co-feeding experiment led to questions regarding the stability of primary amines and aliphatic nitriles. Therefore, nonanitrile was co-fed during a separate FT experiment ($T = 250$ ℃, $P = 5$ bar, GHSV = 2250 ml/hr/g_{cat}, $H_2/CO = 2$, 1 vol% NH_3), following a similar procedure as described above.

Experimental setup

Catalyst preparation

An unsupported Fe-based catalyst precursor was prepared via a precipitation technique described by Claeys [13]. For a full description of the preparation and characterization of the catalyst, the reader is directed to the relevant sections in Chapter 4. The catalyst was promoted with potassium (via an aqueous KNO_3 solution, Sigma Aldrich) by making use of an impregnation technique. A 100:2 (g/g) ratio for Fe/K was targeted and a 100:1.8 (g/g) ratio was confirmed via atomic absorption spectroscopy (AAS). Calcination of the catalyst was conducted in air (900 ml/g_{cat}/hr) in a fluidized bed reactor that was ramped from ambient temperature to 400 ℃(heating rate - 10 ℃/min), where it was kept constant for a further 3 hours. This calcination procedure was performed before and after potassium promotion to ensure that the catalyst was in its oxidic form and free of any nitrates. The catalyst was crushed and sieved to obtain particle sizes below 125 μm in order to avoid intra-particle mass-transfer limitations [13, 29]. A quantity of 2.86 g of the K promoted Fe_2O_3 (hematite phase as confirmed by X-ray diffraction (XRD) spectroscopy) was transferred to a fluidized bed reactor where it was reduced externally. The reduced catalyst (ca. 2.00 g) was transferred into a beaker containing hot molten wax (Sasol grade, C_{30-60}) under inert conditions (argon blanket) and allowed to cool down. The pellet that formed could then transferred to the slurry reactor for FT testing.

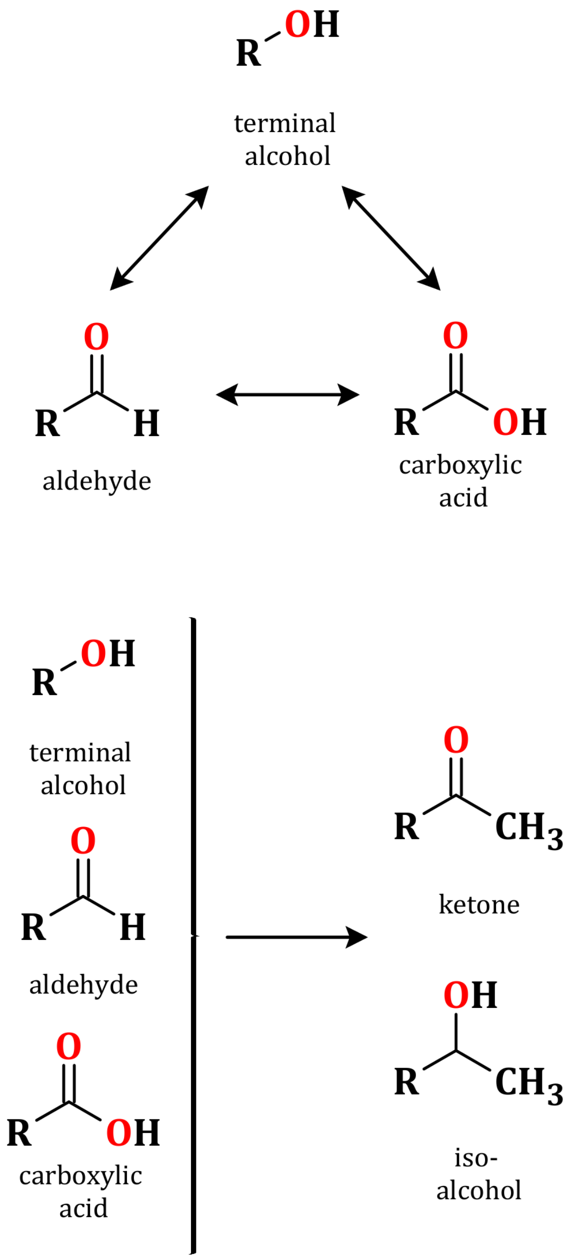

Figure 8.1: Results obtained by Cairns [24] when co-feeding C_8 oxygenates during FTS using an Fe-based catalyst. *(Top)* The C_8 aliphatic aldehydes, linear alcohols and carboxylic acids were found to reproduce each other during this study. *(Bottom)* The secondary reactions of aforementioned oxygenates also yielded the C_9 ketone and iso-alcohol in an irreversible reaction as demonstrated via co-feeding those compounds. (Berty reactor, T = 300 °C, $p_T = 21$ bar, GHSV = 4000 ml/hr/g_{cat}, $H_2/CO/CO_2 = 4:1:1$).

FTS reactions

A schematic that illustrates the important reactor units and analytical techniques relevant for the reactions discussed here is given in Fig. C.18 of Appendix C. The co-feeding experiments was performed in a slurry phase reactor, which can be considered to be gradientless w.r.t. temperature and concentrations of reactants and products [14, 30, 31]. The flow rates of all gases (CO, H_2, C_6H_{12} in N_2 and NH_3 in H_2) were controlled with mass flow controllers (Brooks) and their signal in the GC-TCD calibrated with a reference gas of known concentrations (6 % Ar, 5 % N_2, 15 % CO, 10 % CH_4, 20 % CO_2, 44 % H_2; Afrox RSA). The gases CO and H_2 could be set to flow in a direction that combined directly with NH_3, which was the configuration used during the first 48 hours of the experiment. After 48 hours, a three-way valve was set such that CO + H_2 first passed through a temperature controlled (T = 80, and 40 ℃, respectively) saturator containing the 1-octanol and nonanitrile respectively, which then followed heated lines (> 120 ℃) and were combined with the NH_3/H_2 mixture prior to entering the reactor. The reference gas (0.0018 vol % cyclohexane in N_2), used for quantification of the organic products, was added directly after a hot trap that was set to 180 ℃. All gas lines between the reactor, ampoule sampling device and on-line GC-FID were kept at 220 ℃ in order to avoid condensation of the products. A cold trap, situated after the ampoule sampler and on-line GC-FID was maintained at 0 ℃ with the intention of maximizing the amount of products obtained via condensation in the oil and water phases.

Product analysis

Analysis of the organic and inorganic products formed during these co-feeding reactions was accomplished via both on- and off-line gas chromatography as well as the GC×GC-TOF/FID technique. A summary of the analytical techniques that was used for the various reactants and products is summarized in Table 8.1. Note that NH_3 could not be detected during the reaction as it was consumed in a side reaction with CO_2 and H_2O (see relevant discussion in Chapter 7). The choice that Cairns [24] made to use oxygenates with a carbon chain length of eight (C_8) was motivated by the fact that the C_8-fraction are completely immersed in the oil phase, which simplifies the analysis of the product spectrum. This was an important parameter that was employed in the present work, since the GC×GC analysis was only possible with the oil phase

Table 8.1: Summary of the techniques used to analyze the organic and inorganic reactants and products.

Products	Analytical method
H_2, CO, CO_2, CH_4, N_2	on-line GC-TCD analysis of feed/ cold tail gas
C_{1-10} olefins and paraffins	on- and off-line GC-FID analysis of hot tail gas
C_{11-17} olefins and paraffins	GC×GC-TOF/FID analysis of product oil phase
C_{1-7} oxygenates and N-cont cmpds	on- and off-line GC-FID analysis of hot tail gas
C_{8-17} oxygenates and N-cont cmpds	GC×GC-TOF/FID analysis of product oil phase
C_{18+} organic FTS products	via extrapolation assuming ASF kinetics

product. The GC×GC-TOF/FID system was not equipped with an ampoule breaker. The ampoule samples that were taken during these experiments was however used, by directly injecting these gaseous samples into the GC×GC-TOF/FID, in order to estimate if similar patterns for the formation of oxygenates and N-containing compounds (C_{1-7}) were observed.

On- and off-line gas chromatography

The complete data and discussion of the parameters chosen (e.g. oven temperature profiles, columns used, detector/injector temperatures) for the analytical techniques used throughout this study is reported in Chapter 4, and only the most important aspects are highlighted here. On-line analysis of the inorganic gases (H_2, CO, CO_2, CH_4 and N_2) was achieved via the use of a GC-TCD ("micro-GC", Varion, CP-4900), which was sampled at the exit of the reactor and before the ventilation unit. The micro-GC is set up to split the sample into three channels that have their individual carrier gases, columns and detectors. This design thus allows for reduced separation time and increased signals for the relevant gases. On-line GC-FID (Varian, GC-430 fitted with a Varian capillary column CP-Sil-5CB) analysis was achieved by directly sampling the product line that exits the hot trap. The flow rate of the gaseous product that flowed towards the on-line GC-FID was kept at a low flow rate (1 ml/min) and when it was in use passed through a smaller cold trap, which effluent was then allowed to flow towards the ventilation unit. Sampling of this line was achieved via a 6-port (VICI) valve that was kept at 250 °C. Off-line analysis of the gaseous product was performed via the ampoule sampling technique developed by Schulz [32]. The content of these glass ampoules, which includes the volatile organic compounds was analyzed in a GC-FID using similar parameters as those used for the on-line GC-FID. The reactor was designed with a bypassing system, which allowed to measure the flow rates of the organic compounds (1-octanol and nonanitrile) that was added via the saturator. For this on-line GC-FID measurements were employed using the internal organic standard, cyclohexane, for quantification purposes.

Comprehensive GC×GC-TOF/FID analysis

Comprehensive two-dimensional gas chromatography (GC×GC-TOF/FID) was performed on the liquid products using a Pegasus 4D instrument (Leco Corporation, St. Joseph, MI, USA), equipped with both time-of-flight (TOF) and flame ionization detectors (FID). A reversed phase configuration was utilized, with a polar wax column (Varian, CP-WAX 52 CB, 30 m × 0.25mm × 0.25 μm) in the first dimension and an apolar column (Varian, CP-Sil 8CB, 1.6 m × 0.10mm × 0.10 μm) in the second dimension. The primary oven was held at 40 ℃ for 1 minute and then heated up to to 220 ℃ at 3 ℃/min. A 20 ℃ difference between the primary and secondary oven was maintained and a 30 ℃ temperature off-set (relative to primary oven) was applied for the modulator. A modulation period that ranged between 4 and 8 seconds, which depended on the detector and separation achieved, was sufficient to avoid any ‘wrap-around’ errors. The flow rate of the carrier gas (helium) was kept constant at 0.6 ml/min for the duration of the analysis. A volume of 0.1 μL of the oil sample was manually injected and the split valve set to achieve a 500:1 split ratio. The mass spectrometer was set to collect 200 spectra per second, which was sufficient for the purposes of this study. Identification of the organic compounds was achieved by comparing the collected TOF spectra with the National Institute of Standards and Technology (NIST) libraries included in the ChromaTOF (Leco, v4.24) software. For quantification purposes the analysis was repeated with the use of a similar setup (with variations in the modulation frequency), but by reconfiguring the system by using the TOF detector and use the FID detector instead. The data were processed with ChromaTOF software and only peaks with a S/N ratio $\geq$ 20 were considered.

Table 8.2: Thermodynamic data used to calculate the partial pressure of 1-octanol that was sourced from Daubert et al. [33]

Constant	Value
A	1.562×10^{2}
B	-1.430×10^{4}
C	-1.859×10
D	1.332×10^{-17}
E	6.000

Saturator setup

The saturator setup (see Figure 8.2) consisted of a jacketed stainless steel tube (*i.d.* = 10 mm, $l = 20$ cm). Accurate temperature control of the saturator was achieved via continuously circulating an antifreeze/water mixture and a water bath equipped with a pump. To insure the liquid (1-octanol and nonanitrile) remained in the designated area, the saturator was filled with highly porous Chromosorb-P (Sigma Aldrich) which rested on a frit (5 μm) with a frit with a mesh size. For co-feeding, the synthesis gas was then passed through the liquid wetted Chromosorb-P (downwards flow) and saturated with the respective compound according to the saturator temperature or compound vapour pressure, respectively. The theoretical flow rate for 1-octanol was obtained by making use of thermodynamic data provided by Daubert et al. [33], and subsequently solving Eq.'s 8.1 and 8.2 simultaneously.

$$p^{*} = exp\left(A + \frac{B}{T} + ClnT + DT^{E}\right) \tag{8.1}$$

$$n_i = \frac{p^{*}}{p_{total}} \times \frac{(V_{CO} + V_{H_2})_{in}}{V_A} \tag{8.2}$$

where p^{*} is the vapor pressure of 1-octanol in Pascal, T is the temperature in Kelvin, V_{CO} and V_{H_2} are the volumetric flow rates of CO and H_2 respectively and V_A is the molar volume of a gas. The saturator temperature was 80 and 70 °C for 1-octanol and nonanitrile, respectively. As previously mentioned, a by-pass system was used to confirm the flow rates estimated from

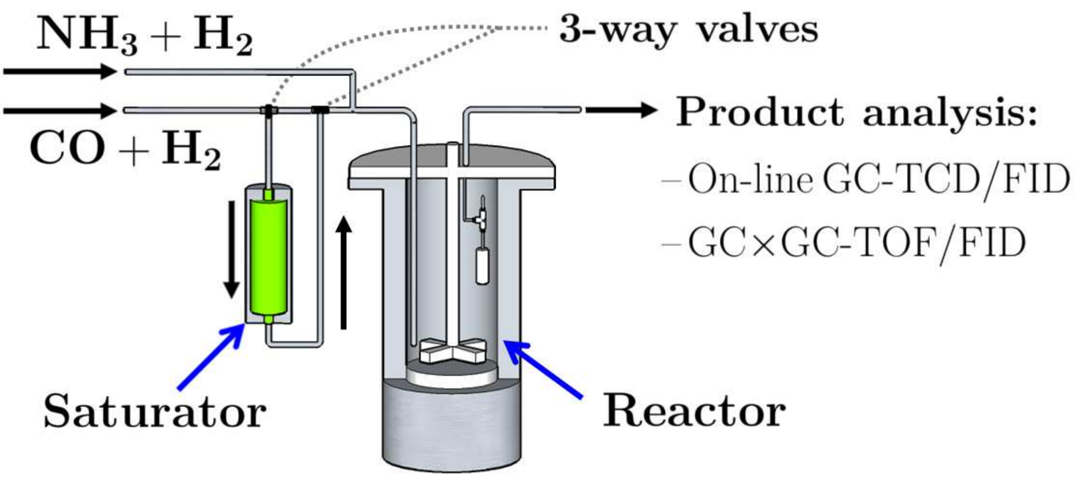

Figure 8.2: Schematic that illustrates the addition of 1-octanol and nonanitrile through the use of a saturator. (T = 250 °C, P = 5 bar, GHSV = 2250 ml/hr/g_{cat}, $H_2/CO = 2$, 1 vol% NH_3, $T_{sat} = 70$ °C)

the thermodynamic data. All the pipelines was kept at high enough temperatures (> 120 °C) to ensure no condensation occurred prior to the reactor or on-line GC-FID.

The flow rate of the converted 1-octanol ($\dot{n}_{1-oct,conv}$) was calculated with Eq. 8.3 and its conversion (X_{1-oct}) via the use of Eq. 8.4

$$\dot{n}_{n-oct,conv} = \dot{n}_{1-oct,in} - \dot{n}_{1-oct,out} - \dot{n}_{1-oct,FTS} \tag{8.3}$$

$$X_{n-oct} = \frac{\dot{n}_{1-oct,in} - \dot{n}_{1-oct,out} - \dot{n}_{1-oct,FTS}}{\dot{n}_{1-oct,in}} \times 100 \tag{8.4}$$

where $\dot{n}_{1-oct,in}$ is the measured flow rate of co-fed 1-octanol, $\dot{n}_{1-oct,out}$ is the flow rate of 1-octanol during co-feeding (derived from the oil phase analysis after 96 hours TOS) and $\dot{n}_{1-oct,FTS}$ is the flow rate before co-feeding commenced (i.e. after 48 hours TOS). The preference for certain secondary reactions to take place was expressed by calculating the selectivity for the secondary reactions of 1-oct (S_x^{oct}) with Eq. 8.5

$$S_x^{oct} = \frac{\dot{n}_{x,out} - \dot{n}_{x,FTS}}{\dot{n}_{1-oct,conv}} \times 100 \tag{8.5}$$

where $\dot{n}_{x,out}$ is the flow rate of product x (e.g. x = octanal, octanoic acid, 2-nontanol, 2-nonanone) measured at the outlet and $\dot{n}_{x,FTS}$ is the flow rate of product x measured after 48 hours TOS. The selectivity and conversion values for the co-feeding of nonanitrile is trivially calculated by substituting the relevant flow rates and making use of equations 8.3, 8.4 and 8.5.

Results

Co-feeding 1-octanol

The general concept of the 1-octanol co-feeding experiment is relatively straight-forward if the assumption is made that the 1-octanol that was co-fed represents an oxygenate that formed via a primary FTS pathway. If it is feasible for 1-octanol produced via a primary FTS reaction to be converted to N-containing compounds via a secondary pathway, a decrease in the concentration of 1-octanol should result in a concomitant increase in the formation of the N-containing compounds. Since a slurry phase reactor (that is assumed to be gradientless with respect to temperature and concentrations) was used, the changes in concentration observed in the product spectrum are representative of the kinetic reactions taking place on the catalytic surface. In order to simplify the analysis, it was targeted to add 2.6 μmol/min of 1-octanol (which is 100 × the molar flow rate measured during the base case study where 1 vol % NH_3 was added to the synthesis gas and approximately 10× the molar flow rate when no NH_3 was added). It is however important to ensure that the co-feeding experiments does not impede on the FTS reaction itself. The activity and selectivities for the reactants and products of the FTS reaction with the feed (n CO + $2n$ H_2 + 1 vol % NH_3) were therefore closely monitored, in particular after the 1-octanol was added (after 48 hours time one stream (TOS)). In Figure 8.3 one can see that after addition of 1-octanol, the CO/H_2 conversions and the CO_2/CH_4 selectivities was not significantly influenced by the addition of 1-octanol to the feed. These results correspond well to the activity and selectivity results obtained for CO/H_2 and CO_2/CH_4 respectively reported for the addition of 1 vol% NH_3 with a synthesis gas feed during FTS in Chapter 7.

Another important selectivity indicator of the FTS reaction is the chain growth probability (α) which is extracted from the slope in the Anderson-Schulz-Flory (ASF) distribution [11]. The ASF model is a mathematical description that can be used to predict the FTS product distribution if ideal surface polymerization is assumed through the use of Eq. 8.6 .

$$log(W_n/n) = nlog(\alpha) + K \tag{8.6}$$

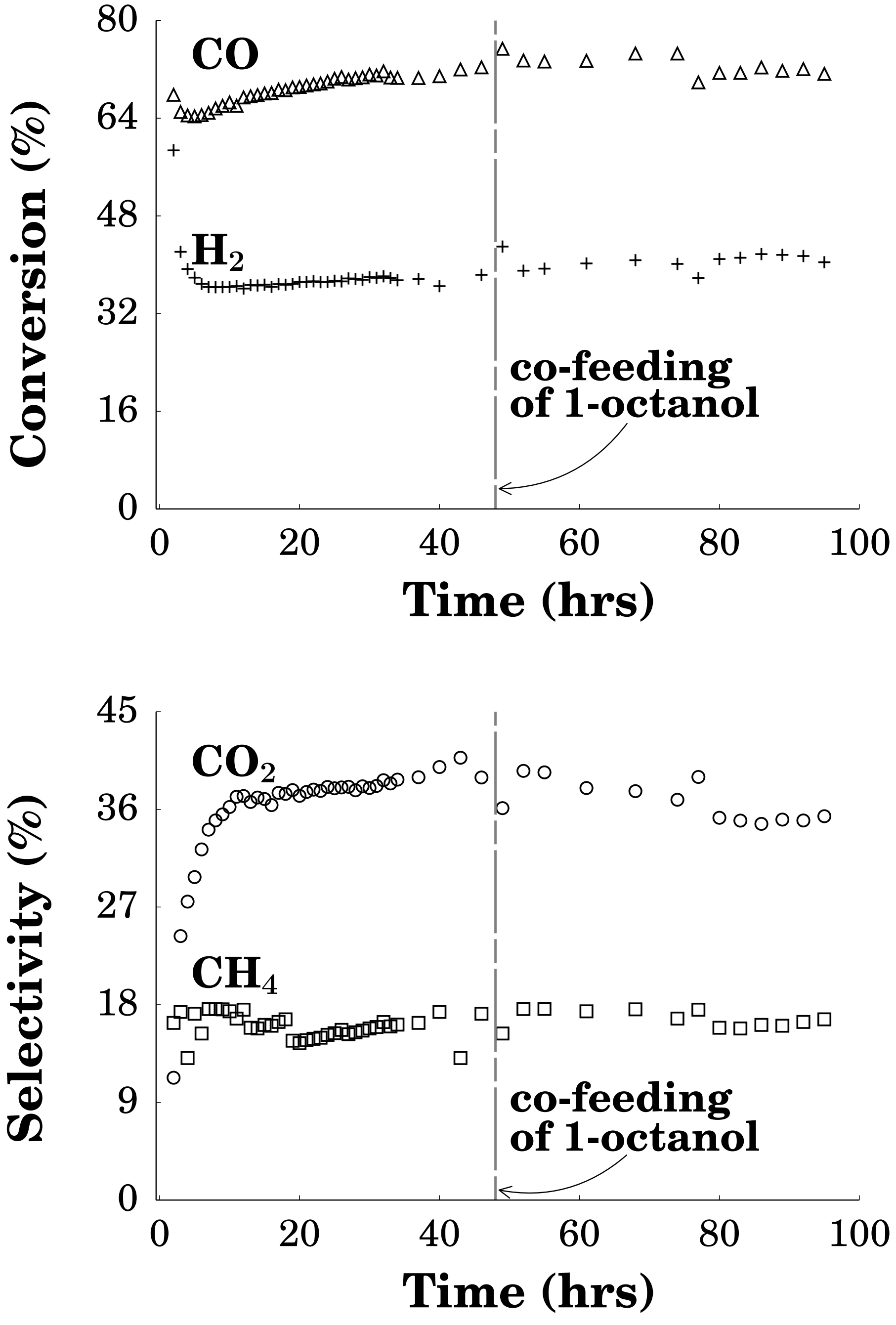

Figure 8.3: (Top:) Both the conversion of CO/H_2 and the *(Bottom:)* CO_2/CH_4 selectivities were not influenced after the addition of the 1-C_8OH. (T = 250 ℃, p_T = 5 bar, GHSV = 2250 hr^{-1}, H_2/CO = 2, +1 vol% NH_3).

where W_n is the mass fraction of products with a carbon number n and K is a constant. Furthermore, an increase in the ASF distribution from the carbon number range C_{9+}, would indicate possible chain-initiation incurred by the presence of increased concentration of 1-octanol. When comparing the ASF plot (see Figure 8.4) calculated from the FTS products in the reaction where 1 vol % NH_3 is added during FTS at steady state (i.e. after 48 hours TOS) with an ASF plot generated for the products after 96 hours TOS when 1-octanol was co-fed, no major deviations was observed. A slight increase in the C_{8-11}-fraction can be seen, but no major changes is detected for the C_{12-16}-range. This suggests that the co-feeding of 1-octanol did not impede on chain growth for the FTS reaction where 1-octanol was co-fed with the feed and did not initiate chain growth after. This finding is consistent with the results reported by Cairns [24], who conducted 1-octanol co-feeding during Fe-catalyzed FTS in the absence of NH_3 at an elevated temperature (T = 300 °C) and observed no chain growth. When adding short chain linear and iso-alcohols (C_{2-3}), some chain initiation was however observed in previous studies [34–36].

Oil phase analysis with GC×GC-TOF/FID

The general results for the co-feeding of 1-octanol can easily be explained by the topographic view of the 2D chromatogram that is presented in Fig. 8.5, which was obtained after GC×GC-TOF analysis of the oil phase product collected after 96 hours TOS. A 3d view is superimposed in as a visual aid. As indicated on the figure (A), some of the co-fed 1-octanol (39 mol %) was not converted, but a clear increase in some of the N-containing compounds was observed. The formation of the methyl ketone (B) and and 2-nonanol (C) is also easily detectable. Based on Cairns work, one would furthermore expect the formation of octanal and octanoic acid, but these compounds was not detected. A formation of whole range of secondary and tertiary amines (F) can be seen in the chromatogram. A significant concentration of N,N-dimethyl-octylamine (E) was detected in the chromatogram. To further shed light on the extent to which these reactions take place, the quantification of the oxygenates and N-containing compounds is discussed in the following subsections.

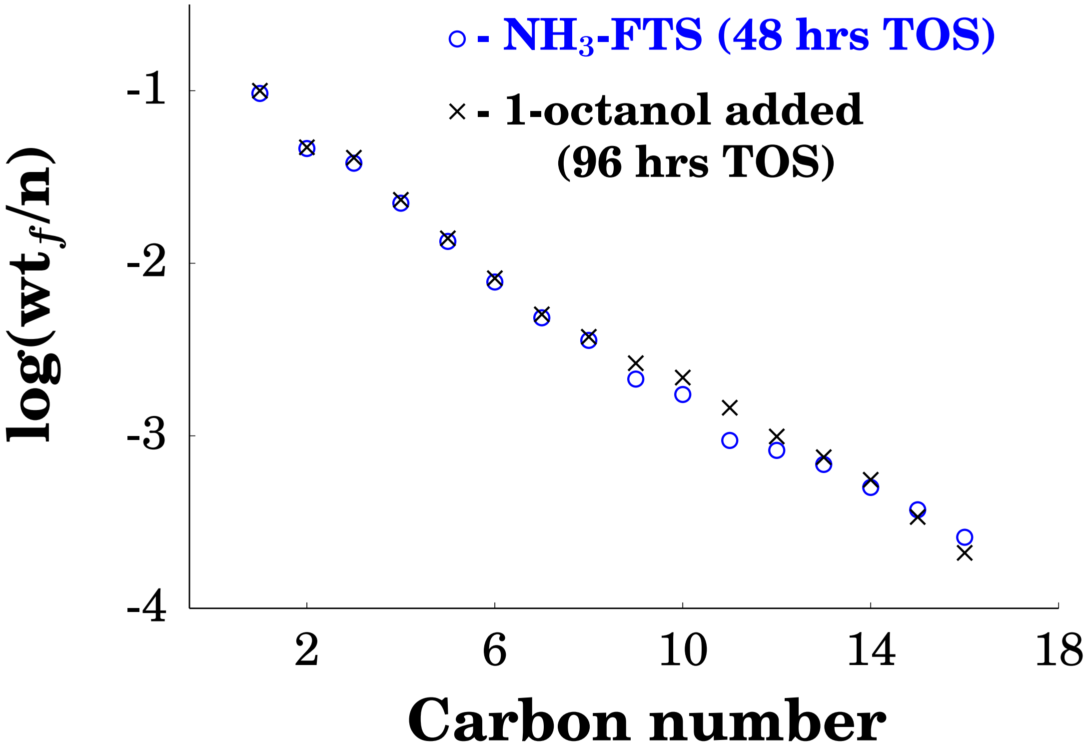

Figure 8.4: The ASF plots without (feed CO + 2 H_2 + 1 vol % NH_3) and with addition of the n-C_8OH. (T = 250 °C, p_T = 5 bar, GHSV = 2250 ml/hr/g_{cat}, H_2/CO = 2, 1 vol% NH_3)

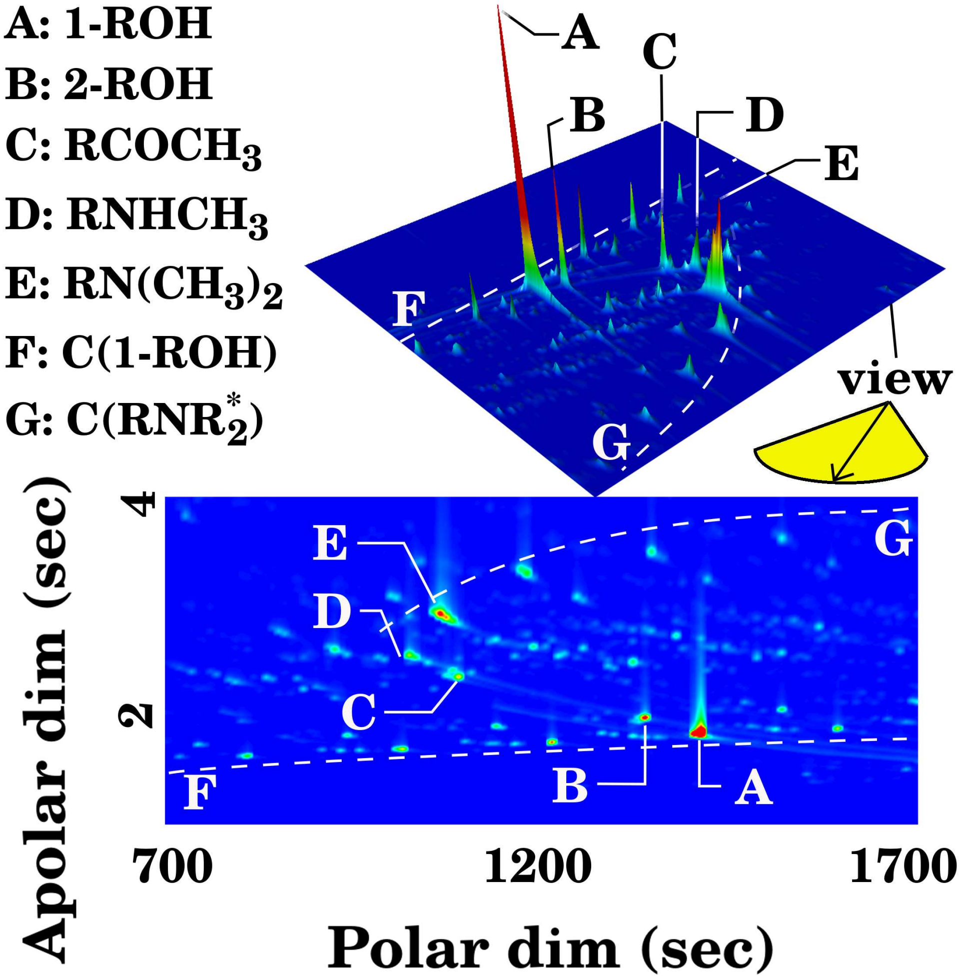

Figure 8.5: Topographic view of the 2D chromatogram obtained when analyzing the oil phase sample that was collected after co-feeding 1-octanol (i.e. after 96 hours TOS) with GC×GC-TOF.

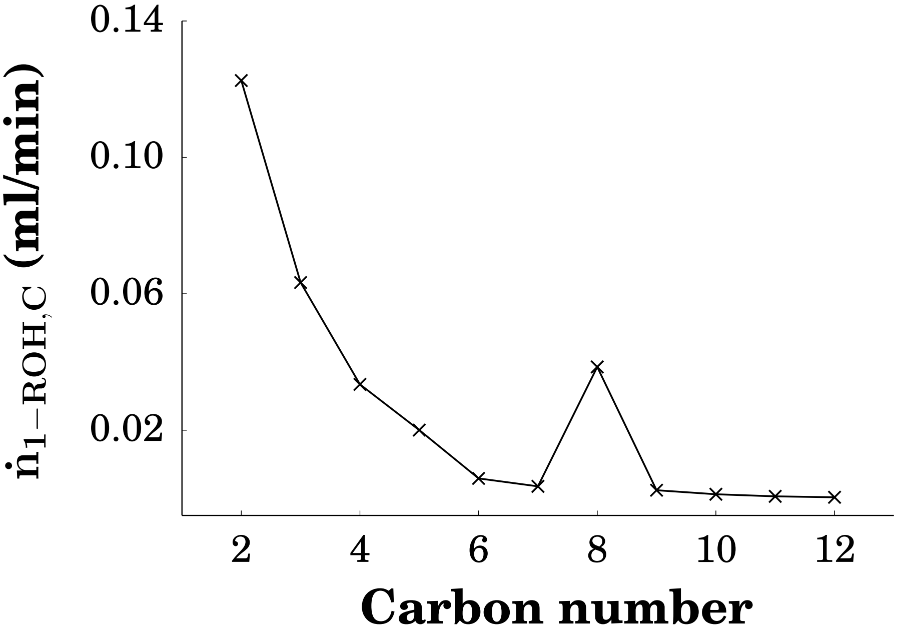

Figure 8.6: Flow rates of the linear alcohols (1-oct) when 1-octanol was co-fed to probe secondary reactions. (T = 250 ℃, P = 5 bar, GHSV = 2250 ml/hr/g_{cat}, H_2/CO = 2, 1 vol% NH_3)

Formation of oxygenates

The flow rates calculated for the linear alcohols obtained after 96 hours TOS is presented in Fig. 8.6. Not all of the added 1-octanol was converted as can be seen in Figures 8.5, 8.6 and C.19. The total conversion of 1-octanol was calculated to be 61.0 %, which was based on the theoretically predicted flow rate of 1-octanol. At least 58 % of the converted 1-octanol led to the formation of N-containing compounds. Cairns [24] report a conversion of ca. 4.3 wt% for the co-fed 1-octanol (assuming that the additional oxygenates was the only products). It is thus possible that secondary reactions of 1-octanol take place more readily under the conditions applied here compared to that particular study. This is possibly due to the use of a slurry reactor which has a large hold-up compared to the Berty reactor system used by Cairns [31].

There were several oxygenates and N-containing compounds that increased in formation rate when 1-octanol was co-fed. The discussion will however be limited to the compounds that showed the most significant increases upon co-feeding of 1-octanol. The C_9 iso-alcohol and ketone were found to be present in considerably higher quantities (see Fig. 8.7 and Tabel 8.3)

Table 8.3: Selectivities calculated for the major compounds found when co-feeding octanol to study the role of secondary reactions when NH_3 is present in a syngas feed during FTS in a slurry phase reactor. (T = 250 °C, P = 5 bar, GHSV = 2250 ml/hr/g_{cat}, $H_2/CO = 2$, 1 vol% NH_3). * The detection and quantification was complicated by the GC×GC technique (see section 8.3.1.4).

Product/Reactant	**Selectivity/Conversion (%)**
1-octanol	61.0
2-nonanol	6.6
2-nonanone	3.2
di-methyl-octanamine	24.3
methyl-octanamine	10.4
sec/tert amines (C_{9-12})	6.5
octyl acetamide	2.2
(octanamine*)	36.0

compared to what was calculated prior to 1-octanol addition, i.e. 48 hours TOS. Approximately 6.6 and 3.2 % of the co-fed 1-octanol was converted to the iso-alcohol and ketone respectively. This was observed in the co-feeding work of Cairns [24] when there was no NH_3 present in the syngas feed, and could thus have been expected. What is important to note, is that there was no increase in the formation of the C_8-aliphatic aldehyde or carboxylic acid, which strongly suggests that the presence of NH_3 leads to the complete suppression of these secondary reactions.

N-containing compound formation

The results for the selectivities of the N-containing compounds formed during the co-feeding of 1-octanol is tabulated in Tabel 8.3. The flow rates calculated for series of tertiary amines and amides are presented in Fig. 8.8. The formation of nitriles in the C_{8-10} fractions could not be detected.

This does not necessarily suggest that these compounds does not form via secondary reactions. A plausible alternative route, is that octanitrile is converted in secondary (or perhaps) tertiary reactions to form the observed secondary and tertiary amines. A significant increase in the

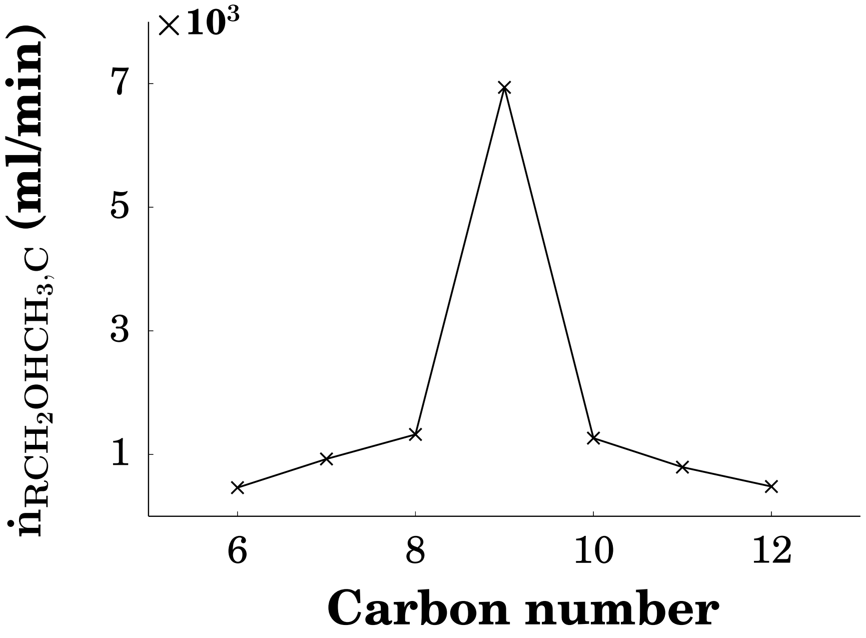

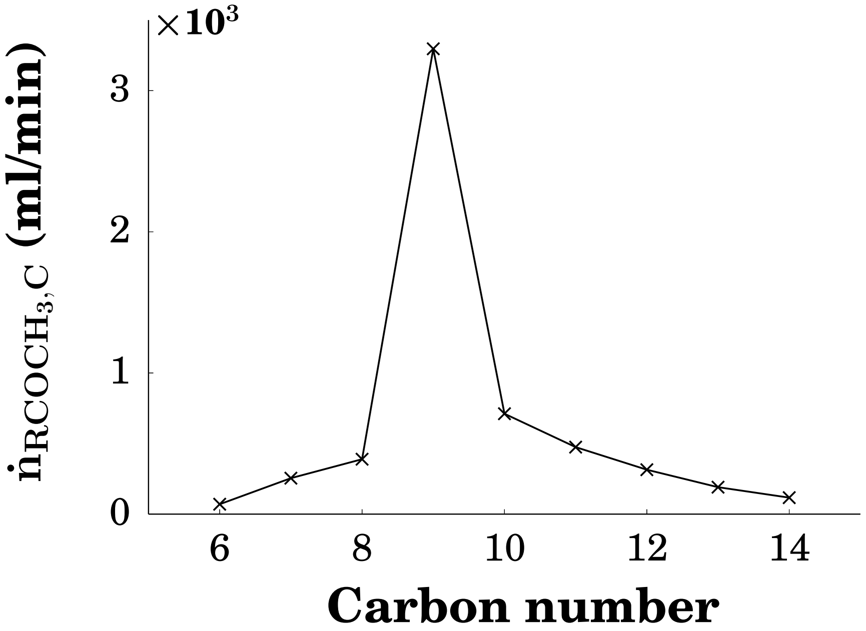

Figure 8.7: Flow rates of the iso-alcohols (top, i-oct) and ketones (bottom, $RCOCH_3$) found in the oil phase when n-C_8OH were co-fed. (T = 250 ℃, p_T = 5 bar, GHSV = 2250 ml/hr/g_{cat}, $H_2/CO = 2$, 1 vol% NH_3)

flow rate for the C_{10} tertiary amine N,N-dimethyl-octylamine was observed, which had the highest selectivity ($S^{oct}_{R_3N}$ = 24.3 %) of all other products that formed during the co-feeding of 1-octanol. N-methyl-octylamine formed to significant extent too as indicated in Figure 8.5. Other secondary and tertiary amines with the C_8N- fraction of the molecule substituted with combinations of methyl or ethyl groups was observed to have higher selectivities. In addition, an increase in the C_{10} flow rate of the amides was observed. The selectivity for the amides were much lower ($S^{oct}_{RNCOCH_3}$ = 2.2 %), but sheds light on the formation of these class of compounds. Considering the structures of the N-containing compounds formed via these co-feeding reactions, it seems as if the 1-octanol are first converted to a C_8N^* surface species, which then scavenges various surface products to produce compounds with the relevant alkyl or acyl groups attached. It can not be ruled out that the conversion of the 1-octanol leads to the formation of C_8^*-alkyl surface species, which can then further interact with N-containing surface species, such as -$N(CH_3)_2^*$ or -$NCOCH_3^*$. Even though the former pathway seems mechanistically unlikely due to possible steric hindrance, it is one of many possible routes that should be considered. The secondary reactions of nonanitrile should help to distinguish between these aforementioned pathways and provide information regarding the stability of these compounds during slurry phase NH_3-FTS reactions.

Inspecting Table 8.3 (without the selectivity of octanamine added), it is clear that the mass balance does not account for all the 1-octanol co-fed during the experiment. The formation of octanamine as the likely source is discussed below.

Formation of octanamine

As discussed in Chapter 7, the formation of primary amines was complicated by the GC×GC-TOF/FID analysis. The polar 'wax' column used in the first dimension interacts to such an extent with the primary amines, that they only elute much later in the chromatogram. From the GC×GC-TOF chromatogram shown below, it can however be seen that octanamine is the only peak that form in the region indicated. Analysis of this peak with GC×GC-FID analysis shows that the selectivity towards octanamine would have a lower limit of $S^{oct}_{RNH_2}$ = 36 %. This is only a lower limit, since not all of the octanamine has eluted at the end of the temperature program. This does however offer the most likely explanation for the problem associated with

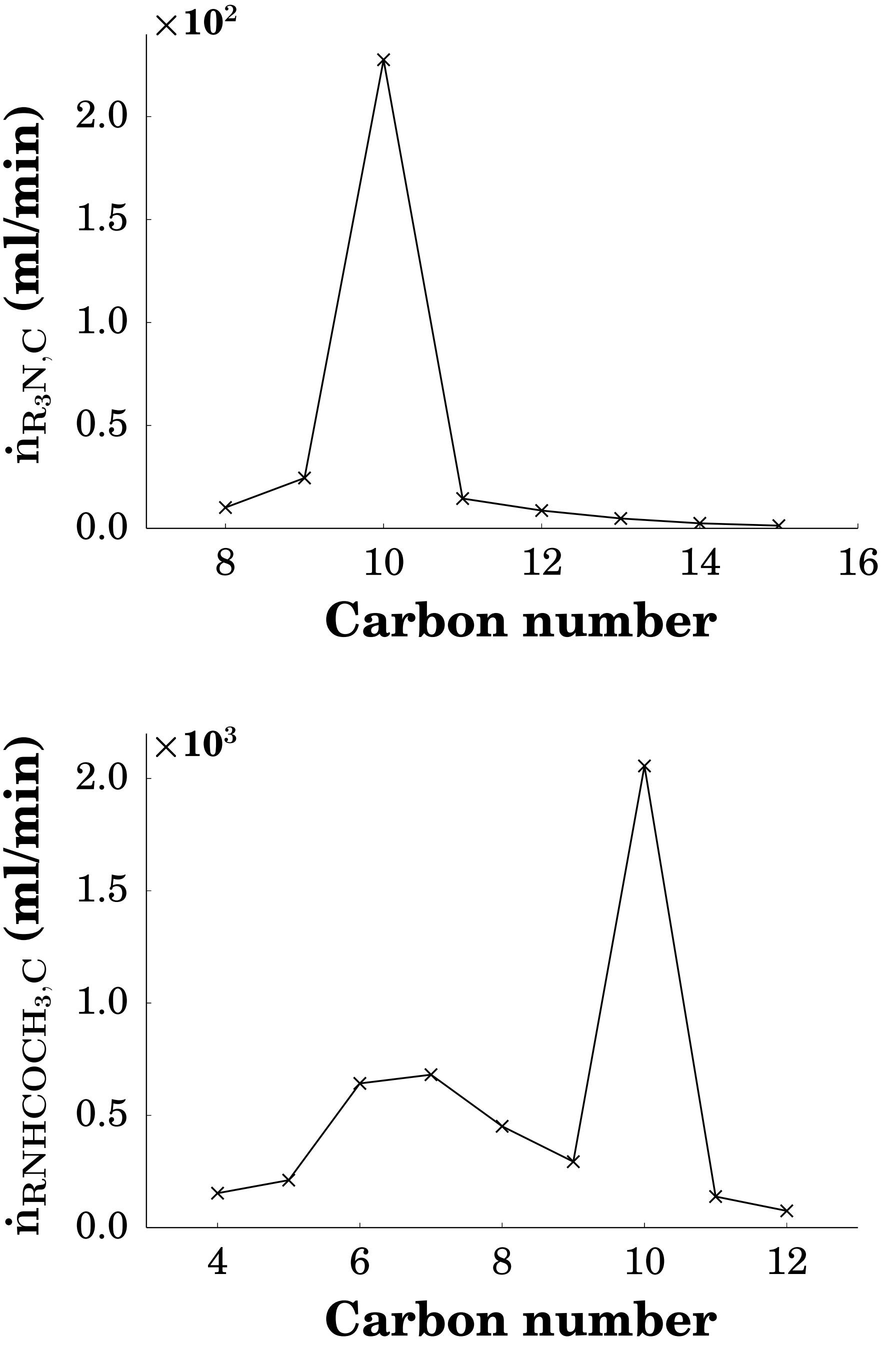

Figure 8.8: Flow rates of the tertiary amines (top, R_3N) and acetamides (bottom, $RNHCOCH_3$) found in the oil phase when n-C_8OH were co-fed. (T = 250 °C, P = 5 bar, GHSV = 2250 ml/hr/g_{cat}, H_2/CO = 2, 1 vol% NH_3)

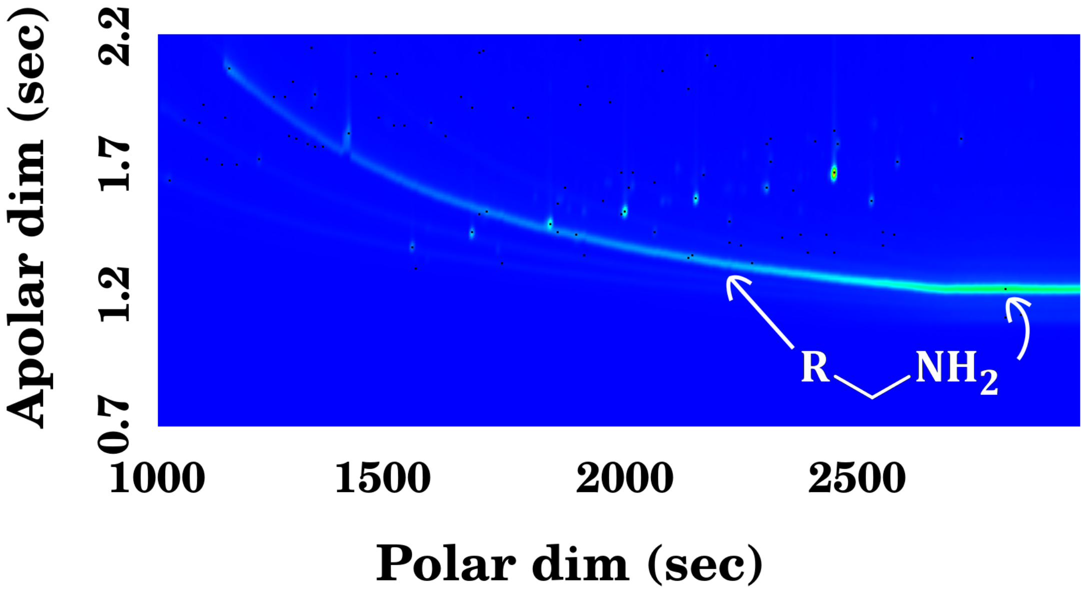

Figure 8.9: Chromatogram obtained from the analysis of the oil phase after 48 hrs of 1-octanol co-feeding that shows the formation of octanamine that interacts with the polar 'wax 'column. (T = 250 ℃, P = 5 bar, GHSV = 2250 ml/hr/g_{cat}, $H_2/CO = 2$, 1 vol% NH_3)

the mass balance discussed above.

Co-feeding nonanitrile

The results of Chapter 7 and the observed secondary reactions when co-feeding 1-octanol led to questions regarding the stability of aliphatic nitriles and amines when NH_3 are present in syngas during FTS. To further shed light on these properties, nonanitrile was co-fed during FTS with the feed: CO + 2 H_2 + 1 vol % NH_3. Approximately 82 % of the co-fed nonanitrile was consumed (see Fig. 8.10 and Tabel 8.4), which suggests that these compounds readily undergo secondary reactions under the conditions applied. The dominant product that formed upon co-feeding of nonanitrile was N,N dimethyl nonylamine which was calculated to have a selectivity of $S_{R_3N}^{RCN} = 51.3$ %. Furthermore, 7.9 % was distributed amongst secondary/tertiary amines with the C_9N fraction combined with combinations of C_{1-3} alkyl groups. The formation of small quantities ($S_{RNH_2}^{RCN} = 1.1$ %) of the primary amine, nonylamine, could have resulted from hydrogenation of the nonanitrile surface species. Similar to the co-feeding of 1-octanol,

Table 8.4: Selectivities calculated for the major compounds found when co-feeding octanol to study the role of secondary reactions when NH_3 is present in a syngas feed during FTS in a slurry phase reactor. (T = 250 ℃, P = 5 bar, GHSV = 2250 ml/hr/g_{cat}, H_2/CO = 2, 1 vol% NH_3)

Product/Reactant	Selectivity/Conversion (%)
nonanitrile	82.0
nonylamine	1.1
1-nonanol	15.3
N,N-dimethylnonylamine	51.3
sec/tert amines (C_{10-13})	7.9
nonyl acetamide	4.2

an increase in the associated acetamide (C_{11}) was observed as depicted in Fig. 8.11. These results suggests that the N-containing compounds could have formed from secondary produced nitriles via primary produced FTS oxygenates, which then scavenges various surface products to produce compounds with the relevant alkyl or acyl groups attached.

An important observation made during this experiment was an increase in the selectivity of 1-nonanol upon the co-feeding of nonanitrile during FTS with NH_3 in the synthesis gas feed. A three dimensional view (see Fig. 8.12) for a selected area of the chromatogram obtained after GC×GC-TOF analysis clearly shows the increased formation of 1-nonanol after 96 hours TOS. This observation is indicative of the reversibility of the secondary reactions between aliphatic alcohols and nitriles. A schematic is given in Fig. 8.13 that illustrates how the combination of these co-feeding experiments allow for the aforementioned hypothesis. When 1-octanol and nonanitrile was respectively co-fed during FTS (with the feed $2n$ H_2 + nCO + 1 vol% NH_3), an increase in the formation of secondary and tertiary amines was observed. The conversion of nonanitrile to the corresponding alkyl and acyl substituted N-containing compounds seemed to be facile. Based on the observation that some of the nonanitrile was converted to 1-nonanol during this co-feeding experiment, it is suggested that nitriles and alcohols are at thermodynamic equilibrium. These results therefore corroborates the thermodynamic calculations of Sango [7] (see Chapter 2, Fig. 2.5).

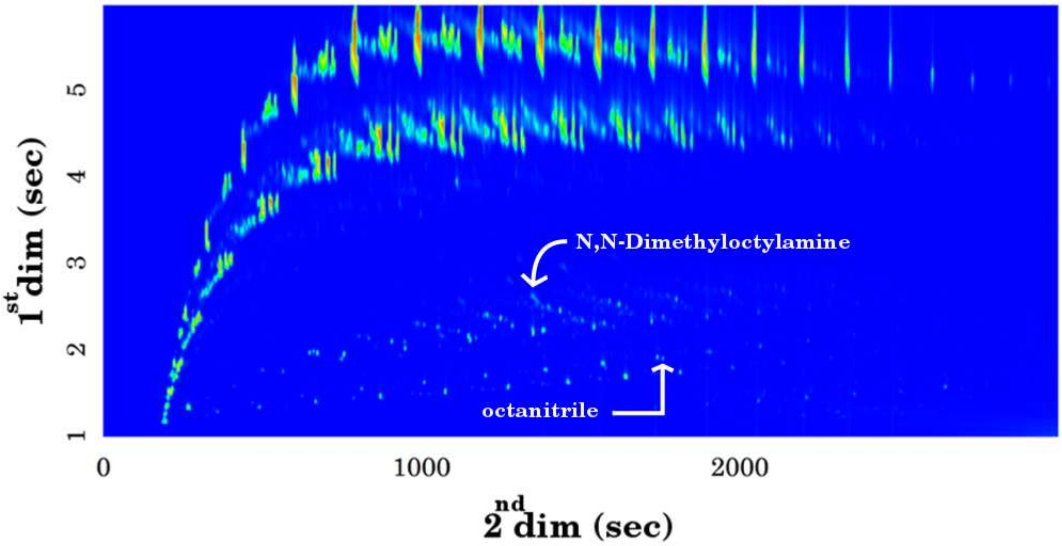

Figure 8.10: Topographic view of the 2D chromatogram obtained from GC×GC-TOF analysis of the oil sample collected 96 hours TOS, 48 hours after initiating co-feeding of nonanitrile.

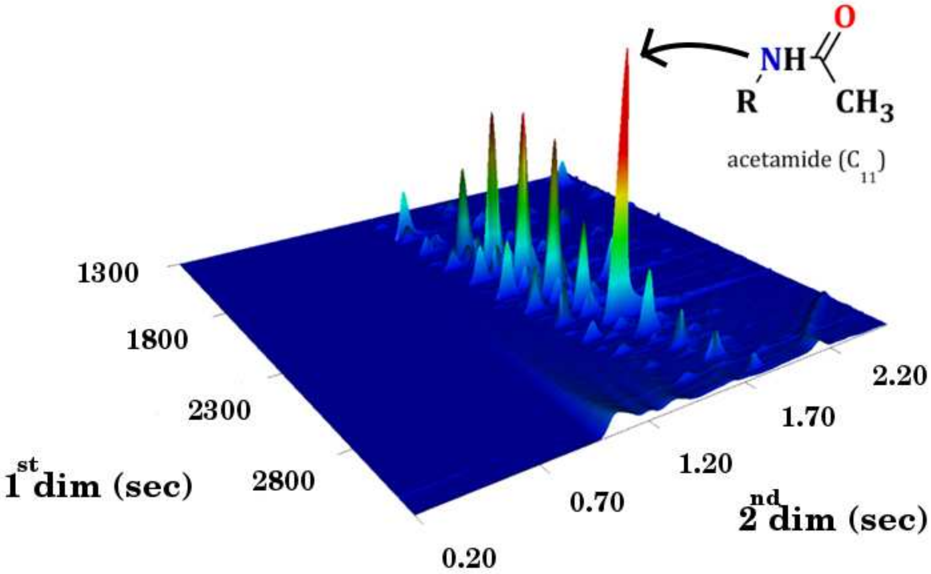

Figure 8.11: An enlarged three-dimensional image, obtained from GC×GC-TOF analysis, showing the increased selectivity towards the C_{11} amide when nonanitrile were co-fed during the reaction.

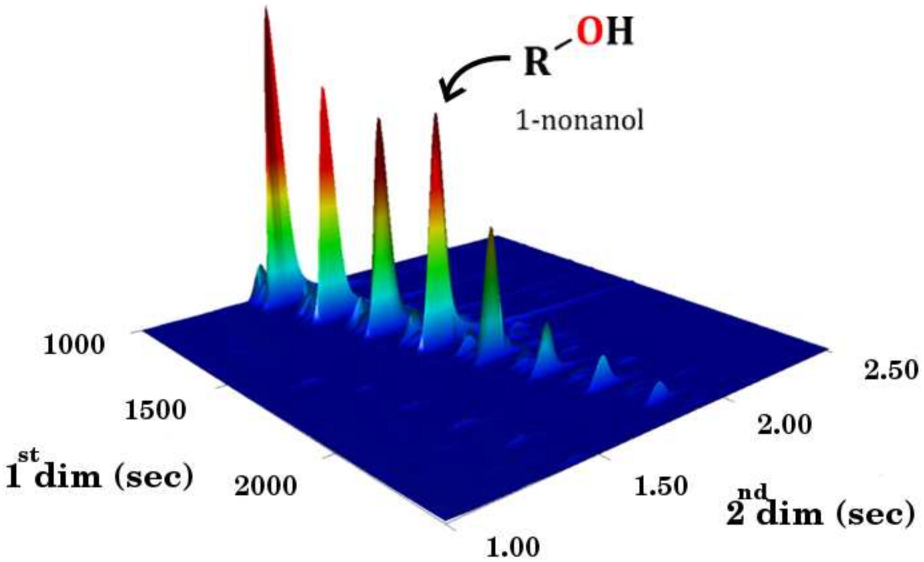

Figure 8.12: An enlarged three-dimensional image, obtained from GC×GC-TOF analysis, showing the increased selectivity towards 1-nonanol when nonanitrile were co-fed during the reaction.

Conclusions

1-octanol and nonanitrile was co-fed during two separate experiments via the use of a saturator, with a syngas containing 1 vol % NH_3, during FTS to study their respective roles in secondary reactions under these conditions. To ensure that an account was made for the activity of the reaction and selectivities of the entire product spectrum, an extensive analytical procedure for the analysis of the product spectrum was followed, which included on-line GC-TCD, on- and off-line GC-FID analysis and the use of comprehensive two-dimensional chromatography (GC×GC-TOF/MS). After steady state was reached (48 hours spent TOS), the co-feeding of the 1-octanol or nonanitrile was initiated. The catalyst activity data (expressed as H_2/CO conversion) suggested that these compounds did not impede on the FTS catalyst performance. In addition, the product distribution did not change upon co-feeding, with the exception of the formation of C_{8-11} oxygenates and N-containing compounds.

The addition of 1-octanol led to the formation of some C_9-oxygenates, 2-nonanol and 2-nonanone, which were expected when considering results obtained from Cairns [24], who observed the for-

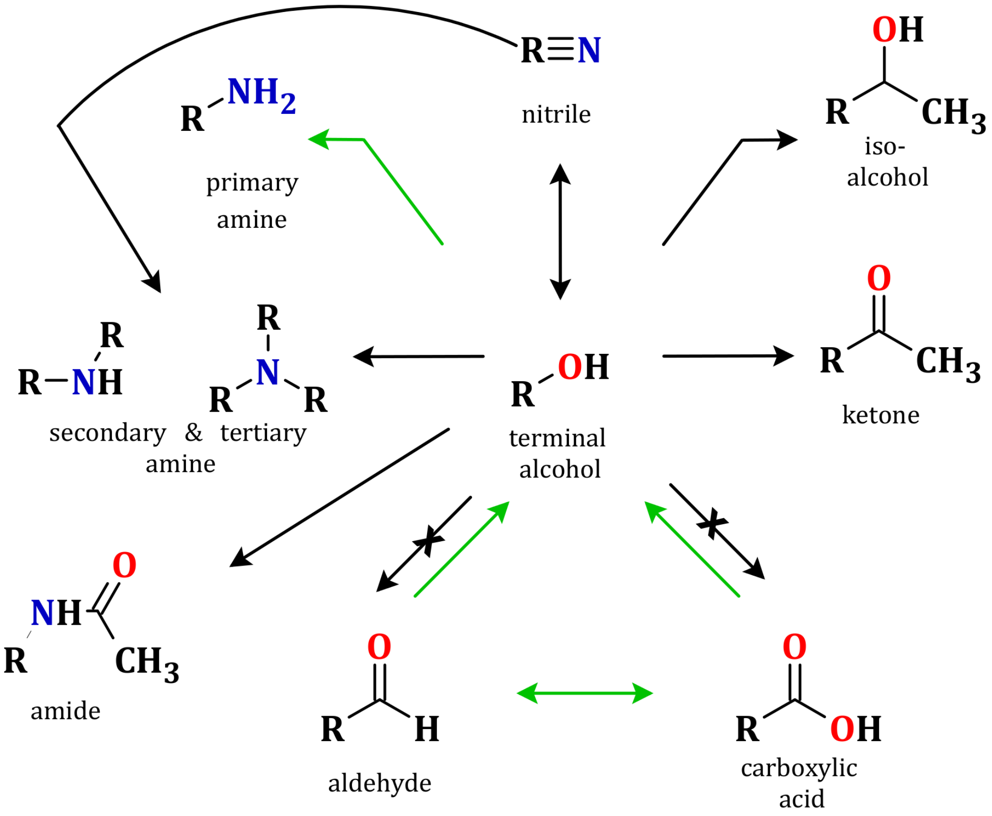

Figure 8.13: Schematic summarizing the view of secondary reactions based on the results of the co-feeding experiments. The green arrows are used to indicate the assumptions made that does not directly stem from the co-feeding results reported in this work.

mation of similar products when co-feeding 1-octanol during FTS (i.e. in the absence of NH_3). Importantly however, the formation of the C_8 aldehyde or carboxylic acid was not observed, which was the major oxygenates that formed when Cairns co-fed 1-octanol in the absence of NH_3, suggesting the complete suppression of these secondary reactions when NH_3 is present during FTS. Several N-containing compounds formed during the 1-octanol co-feeding experiment which provide clear evidence in support of the hypothesis that oxygenates are consumed to the detriment of N-containing compounds. The formation of nonanitrile was not detected, which questioned the stability of these compounds under the conditions applied here that in fact favors secondary reactions. These observations and the absence of these compounds in the product spectra when 1 vol% NH_3 was added in Chapter 7, prompted the co-feeding of nonanitrile.

The co-feeding of nonanitrile revealed that the secondary reactions of nitriles leads to the formation of formamides, acetamides and secondary/tertiary amines. It also suggests that 1-octanol could first converted to a surface nitrile species, which then scavenges surface alkyl or acyl species to afford the amides and secondary/tertiary amines. It was very interesting to note an increase in the formation of 1-nonanol upon the co-feeding of nonanitrile (C_9) in the aforementioned reactions, which is indicative of the reversibility of the nitriles and alcohols. In addition, the reversibility of this reaction corroborates the thermodynamic calculations of [7], which suggests an equilibrium between these products at these conditions. A much improved view of secondary reactions can therefore now be made as is depicted in the schematic given in Figure 8.13.

REFERENCES

[1] A.P. Steynberg, Chapter 1 - Introduction to Fischer-Tropsch Technology, in: A.P. Steynberg and M.E. Dry (Eds.), Fischer-Tropsch Technology, Vol. 152 of Stud. Surf. Sci. Catal., Elsevier, 2004, pp. 1 – 63.

[2] A. Clark, Process of synthesizing aliphatic amines (1950).

[3] H. Kölbel and J. Trapper, Angew. Chem. Int. Ed. 4 (1965) 981.

[4] H. Kölbel and J. Trapper, Angew. Chem. Int. Ed. 5 (1966) 843–844.

[5] R.B. Anderson, H. Kölbel and M. Rálek, The Fischer-Tropsch synthesis, Academic Press, Orlando, Orlando, 1984.

[6] R. Henkel, The influence of ammonia on Fischer-Tropch synthesis and formation of N-containing compounds, Ph.D. thesis, Carl von Ossietzky Universität, Germany (2012).

[7] T. Sango, Nitrogen-containing compounds from ammonia co-feed to the fischer-tropsch synthesis, Master's thesis, University of Cape Town, South Africa (2013).

[8] T. Sango, N. Fischer, R. Henkel, F. Roessner, E. van Steen and M. Claeys, Appl. Catal., A 502 (2015) 150–156.

[9] A.K. Rausch, L. Schubert, R. Henkel, E. van Steen, M. Claeys and F. Roessner, Catal. Today 275 (2016) 94–99.

[10] B.H. Davis, Catal. Today 141 (2009) 25–33.

[11] M.E. Dry, Chapter 3 - Chemical concepts used for engineering purposes, in: A.P. Steynberg and M.E. Dry (Eds.), Fischer-Tropsch Technology, Vol. 152 of Stud. Surf. Sci. Catal., Elsevier, 2004, pp. 196 – 257.

[12] M. Claeys and E. van Steen, Chapter 8 - Basic studies, in: A.P. Steynberg and M.E. Dry (Eds.), Fischer-Tropsch Technology, Vol. 152 of Stud. Surf. Sci. Catal., Elsevier, 2004, pp. 601 – 680.

[13] M. Claeys, Selektivität, Elementarschritte und kinetische Modellierung bei der Fischer-Tropsch-Synthese, Ph.D. thesis, Unversität Fridericiana Karlsruhe, Germany (1997).

[14] H. Schulz and M. Claeys, Appl. Catal., A 186 (1999) 71–90.

[15] H. Pichler and H. Schulz, Chem. Ing. Tech. 42 (1970) 1162.

[16] P. Johnston and R.W. Joyner, Structure-Function Relationships in Heterogeneous Catalysis: the Embedded Surface Molecule Approach and Its Applications, in: F. Solymosi L. Guczi and P. Tétényi (Eds.), New Frontiers in Catalysis - Proceedings of the 10th International Congress on Catalysis, Budapest, 19-24 July 1992, Vol. 75 of Stud. Surf. Sci. Catal., Elsevier, 1993, pp. 165 – 180.

[17] P.H. Emmett, Cat. Rev. - Sci. Eng. 7 (1972) 1–24.

[18] L. Tau, R. Robinson, R.D. Ross and B.H. Davis, J. Catal. 105 (1987) 335–341.

[19] L. Tau, H. Dabbagh and B.H. Davis, Energy Fuels 4 (1989) 94–99.

[20] L. Tau, H. Dabbagh, S. Bao and B.H. Davis, Catal. Lett. 7 (1990) 127–140.

[21] L. Tau, H. Dabbagh and B.H. Davis, Energy Fuels 5 (1991) 174–179.

[22] L. Tau, H. Dabbagh, J. Halasz and B.H. Davis, J. Mol. Catal. 71 (1992) 37–55.

[23] A. Sarkar, R. Keogh, S. Bao and B.H. Davis, Catal. Lett. 120 (2008) 25–33.

[24] P. Cairns, Oxygenates in iron Fischer-Tropsch Synthesis: is copper a selectivity promoter?, Ph.D. thesis, University of Cape Town, South Africa (2008).

[25] T. Mallat and A. Baiker, Handbook of Heterogeneous Catalysis, Wiley-VCH, 2008.

[26] T. Grobler, M. Claeys, E. van Steen and M.J. Janse van Vuuren, Catal. Commun. 10 (2009) 1674–1680.

[27] R. van der Westhuizen, H. Potgieter, N. Prinsloo, A. de Villiers and P. Sandra, J. Chromatogr. A 1218 (2010) 3173–3179.

[28] R. van der Westhuizen, R. Crous, A. de Villiers and P. Sandra, J. Chromatogr. A 1217 (2010) 8334–8339.

[29] M. Claeys and H. Schulz, Prepr. Pap. - Am. Chem. Soc., Div. Pet. Chem. 49 (2) (2004) 195–200.

[30] R.L. Espinoza, A.P. Steynberg, B. Jager and A.C. Vosloo, Appl. Catal., A 186 (1999) 13–26.

[31] A.P. Steynberg, M.E. Dry, B.H. Davis and B.B. Breman, Chapter 2 - Fischer-Tropsch Reactors, in: A.P. Steynberg and M.E. Dry (Eds.), Fischer-Tropsch Technology, Vol. 152 of Stud. Surf. Sci. Catal., Elsevier, 2004, pp. 64 – 195.

[32] H. Schulz, Catal. Today 178 (2011) 151–156.

[33] T. Daubert, Physical and thermodynamic properties of pure chemicals: evaluated process design data, Taylor and Francis, Philadelphia, Pensilvania, USA, 1999.

[34] K.H. Hall, R.J. Kokes and P.H. Emmett, J. Am. Chem. Soc. 79 (1957) 2983–2989.

[35] J.T. Kummer and P.H. Emmett, J. Am. Chem. Soc. 75 (1953) 5177–5184.

[36] J.T. Kummer, H.H. Podgurski, W.B. Spencer and P.H. Emmett, J. Am. Chem. Soc. 73 (1957) 564–570.

CHAPTER 9

THE USE OF CO_2 AND FIXED BED REACTORS

In this chapter results three shorter experiments are discussed that probe some detailed aspects of the pathway to the formation of N-containing compounds. It is firstly of interest to evaluate the role of CO_2 *as a reactant during FTS where 1 vol %* NH_3 *is added. It is hypothesized here that the slow production of CO via the reverse WGS activity would allow for less competitive results between CO and* NH_3 *on the Fe catalyst surface, and therefore result in a higher selectivity for N-containing compounds. In a second set of reactions it was desired to gain a more detailed view of the product spectrum at higher space velocities, as this information could shed light on the potential of primary product formation when* NH_3 *is added during FTS. Finally, based on the thermodynamic data* (ΔG_f) *that suggests similar probabilities for the formation of oxygenates and N-containing compounds (as calculated by Sango [4]) and the relationship that was shown to exist between these products in Chapter 6, it is anticipated that a catalyst that produces a high yield of oxygenates would readily produce N-containing compounds.*

Introduction

Three sets of data were collected to further explore certain concepts w.r.t the use of NH_3 during Fischer-Tropsch synthesis.

It is well established that CO_2 can be used as starting material (see Eq. 9.1) when conducting the FTS reactions with Fe-based catalysts [1, 2]. This occurs via the reverse water-gas-shift (r-WGS) reaction (see Eq. 9.2).

$$CO_2 + 3nH_2 \rightarrow -(CH_2)_n - +2nH_20 \tag{9.1}$$

$$CO_2 + H_2 \rightleftharpoons CO + H_20 \tag{9.2}$$

The dependence of this FTS reaction on r-WGS activity has the consequence that only small partial pressures of CO are obtained. This presents a unique opportunity to study the reaction where higher NH_3 concentrations (relative to CO concentrations) can be obtained, without the limitation of experimental complications regarding high ammonia partial pressures. One could therefore potentially have less competition by CO. CO_2 may not be a major problem within the FTS regime, as it can be used in recycle streams when using iron-based catalysts [1]. If one however move upstream, the gasification of coal and biomass are plagued by the production of CO_2. Finding novel techniques for the use of the greenhouse gas CO_2 are therefore desired, in particular when considering the potential and evolution of biomass-to-liquids (BTL) processes. In order to investigate the role of CO_2 as a carbon source, two slurry phase FT experiments were conducted with an iron based catalyst, where the activity and selectivity of the reactions was monitored in the presence and absence of NH_3 gas.

Secondly, to gain further insight to the N-containing products formed during NH_3 co-feeding FTS reactions, fixed bed reactions was tested at a higher space velocity. If the time that the products spend in the reactor is reduced, the probability of secondary reactions are reduced and one can thus speculate on possible primary products. A full space velocity study was not possible with the experimental setup used throughout this work, but a comparison of these results with the results obtained during the slurry phase reactions (see Chapter 7) did shed light on possible primary products produced during FTS, when NH_3 is present in the syngas feed. Where possible we compare these results with the fixed bed Fe-based work of Henkel [3]. Finally, previous studies seemed to to suggest a correlation between oxygenates and N-containing compounds when NH_3 were co-fed during FTS [3, 4]. If a catalyst that has high selectivities for oxygenates, should theoretically have high selectivity towards the desired N-containing compounds. To explore this hypothesis, we employ a Rh-based catalyst (Rh/Al_2O_3) in a NH_3 co-feeding FTS reaction conducted in a fixed bed reactor.

The combination of the information obtained here provides us with vital mechanistic information and in addition highlights the potential for NH_3 co-feeding during FTS.

Experimental setup

For reactions SPR^{1-2} and FBR^{1-2}, a precipitated Fe-based catalyst (Fe/K 100:2 (g/g)) were prepared as described in Chapter 4 and characterized via XRD, AAS and ICP-MS analysis (see aforementioned chapter). In reaction FBR^3 we make use of a 10 wt % Rh on Al_2O_3, which was prepared via an incipient wetness technique (see Chapter 4). The loading of the catalyst were confirmed via ICP-MS analysis. X-ray diffraction analysis of the prepared Rh/Al_2O_3 was not possible due to the small catalyst particles, low loading and support used (Al_2O_3). We were however able to analyze the spent catalyst via Scanning Transmission Electron Microscopy (STEM) measurements. STEM analysis were performed using a field emissions Tecnai F20 (University of the Western Cape) operated at 200kV which is equipped with a high-angle annular dark-field (HAADF) detector for Z-contrast imaging and coupled with an energy dispersive X-ray spectrometer (EDX) for elemental analysis. Prior to measurements, the catalyst materials were sonicated in ethanol and supported onto lacey carbon coated copper grids (SPI Supplies, 200 mesh).

For the slurry phase reactor, the catalyst were reduced in a fluidized bed, and transferred to the slurry phase reactor in its reduced state via encapsulating it in a wax pellet. The catalyst used during the fixed bed reactions were reduced inside the reactor, prior to the FTS reactions. For more detailed information regarding the operation of these reactors, see Chapter 4. All reactions took place at $T = 250\ ^{o}C$, and $p_T = 5$ during normal FTS operations or 5.1/5.2 bar when NH_3 was added (NTP). In Tabel 9.1 the feed composition, gas hourly space velocity (GHSV) and the time spent on stream for the reactions are summarized. Note that a higher concentration

Table 9.1: Overview of reaction condition to study CO_2 as carbon source, the use of fixed bed reactors, and the use of a Rh-based catalyst. Temperature and total pressures remained constant for all experiments (i.e. T = 250 ^oC, and $p_T = 5$ during normal FTS operations or 5.1/5.2 bar when NH_3 was added (NTP)), catalyst 100g Fe:2g K except FBR[3]

Reaction	**Feed**	**GHSV (ml/hr/g$_{cat}$)**	**Reactor**
SPR[1]	$H_2/CO_2 = 3$	3000	Slurry
	(no NH_3)		
SPR[2]	$H_2/CO_2 = 3$,	3000	Slurry
	(+1 vol% NH_3)		
FBR[1]	$H_2/CO = 2$	4500	Fixed bed
	(+2 vol% NH_3)		
FBR[2]	$H_2/CO = 2$	4500	Fixed bed
	(+2 vol% NH_3)		
FBR[3]	$H_2/CO = 2$,	4500	Fixed bed
(Cat → Rh/Al_2O_3	(+2 vol% NH_3)		

of NH_3 (2 vol%) is used in reactions FB$^{1-3}$. When considering a higher space velocity, it was pre-empted that a higher concentration of NH_3 may be required. Similarly, when using the Rh-based catalyst, one would require higher concentrations of NH_3, if the predicted oxygenate formation were to form as N-containing compounds.

Results and discussion

Using CO_2 as carbon source - SPR$^{1-2}$

The general selectivity and activity results obtained when adding NH_3 during FTS where CO_2 are being used as carbon source are tabulated in Tabel 9.2. The H_2 and CO conversion data suggests that no appreciable deactivation takes place in the presence of 1 vol % NH_3 gas present in the syngas feed ($H_2/CO_2 = 3$). A CO_2 conversion of 22-23 % is consistent with the slurry

Table 9.2: Summary of the results obtained during the FTS reactions conducted with CO_2 as carbon source, with and without 1 vol % NH_3 addition. (SPR^{1-2}, T = 250 °C, p_T = 5 bar, GHSV = 4500 ml/hr/g_{cat}, $H_2/CO_2 = 3$, , and $p_T = 5$ during normal FTS operations or 5.2 bar when NH_3 was added (NTP), catalyst 100g Fe:2g)

Property	**FTS**	**FTS + 1 vol% NH_3**
$X(CO_2)$	23 %	22 %
$X(H_2)$	11 %	11 %
S(CO)	25 %	25 %
α	0.62	0.61
olefin content (C_{2-9})	50 - 60 %	50 - 60 %

phase CO_2-based FTS reactions conducted by Riedel et al. [2]. Approximately 25 % of the CO_2 added were converted to CO that did not react further to form organic products in both the NH_3 containing and NH_3 free syngas FTS reactions. A slightly lower chain growth probability ($\alpha = 0.62/0.61$) were observed for the reactions that had CO_2 as carbon source when compared to $\alpha = 0.67/0.67$ when CO + 2 H_2 were used as syngas. A higher olefin content were observed, suggesting that more primary reactions took place in these reactions.

Oxygenates

An important observation during the FTS reaction where no NH_3 were added, were a high selectivity towards acetic acid (ca 2 wt%) (see Figure 9.1). In Chapter 7 it was observed that the N-containing compounds seem to form to the detriment of the oxygenates (including acetic acid). However, we did not observe a significant increase in the predicted acetamide. This could be due to the difficulty in analyzing this group of organics in the absence of oil phase product. The use of on-line GCxGC-TOF/FID in future work should shed light on the possibility of this reaction. The formation of acetamide was observed in the ampoules collected, but could not accurately be quantified. We did however observe a sever decrease in acetic acid selectivity (ca 0.5 wt%) when NH_3 was added during FTS. Thus, even if the role of NH_3 is merely to suppress the formation of acetic acid, this is a highly desired property since acetic acid has been identified

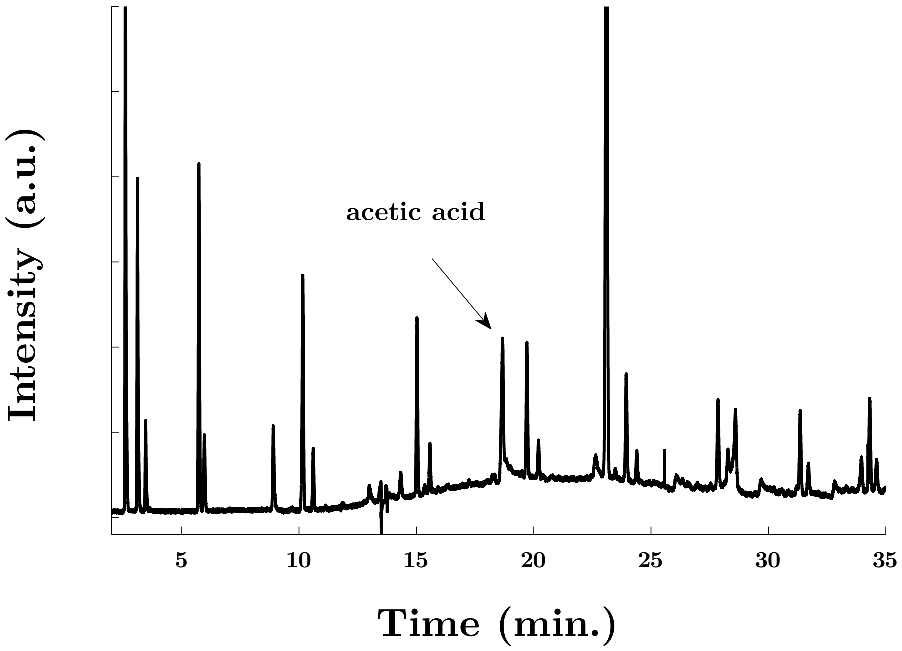

Figure 9.1: A chromatogram obtained from an on-line GC-FID analysis of the product stream when no NH_3 was added. It is easy to see the high selectivity towards acetic acid.

as a major cause of catalyst deactivation for iron-based catalysts.

A similar deactivation in other oxygenates (e.g. aliphatic aldehydes and 1-alcohols) was observed when comparing the two different feeds (SPR^1 and SPR^2, Figure 9.2).

N-containing compounds

One of the major attractive features, when using CO_2 at the conditions applied here, is its selectivity towards nitriles. Analysis by means of two-dimensional gas chromatography, allowed for a thorough investigation of the product spectrum. During the evaluation of the reaction where CO is used as carbon source, the product spectra consisted of a range of aliphatic (1) primary-, (2) secondary-, (3) tertiary -amines, (4) nitriles, (5) amides and (6) formamides. When using CO_2, the selectivity was mainly towards aliphatic nitriles (see Figures 9.3 & 9.4). This set of reactions therefore indicate that CO_2 can be used to produce N-containing compounds. If the selectivity for the N-containing compounds could be optimized, it would be a great feature

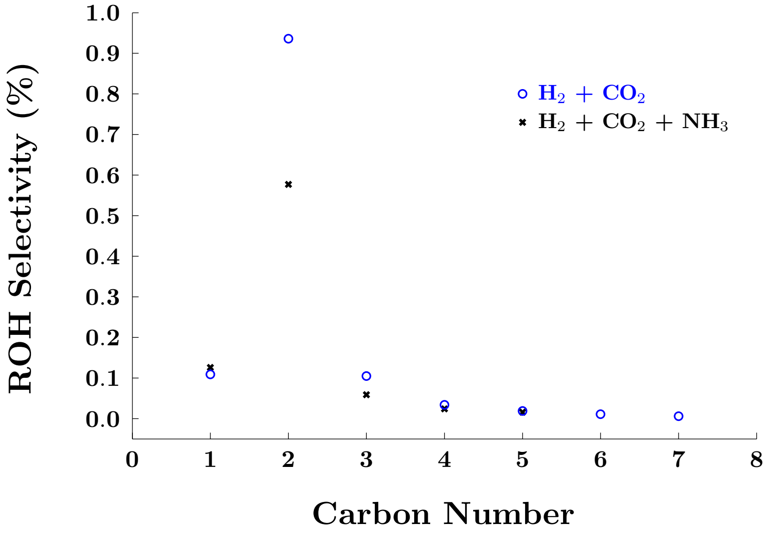

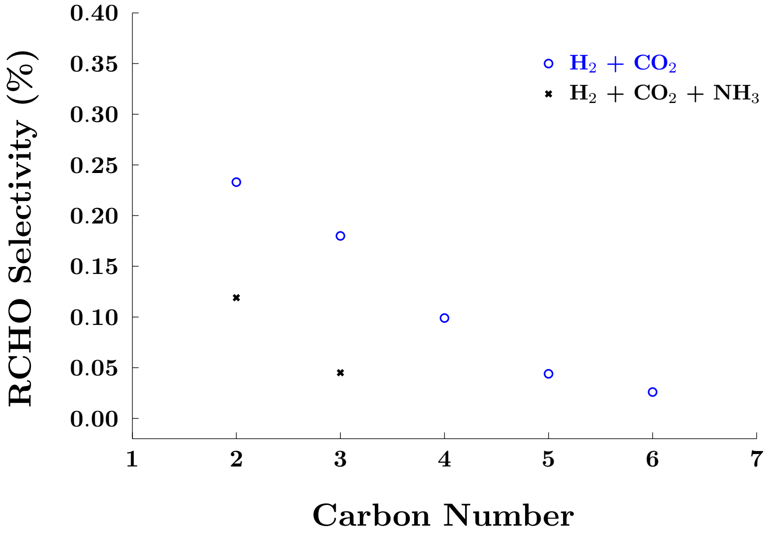

Figure 9.2: (*Top* :) Aliphatic 1-alcohol and (*Bottom* :) aldehyde selectivity as a function of carbon number with/without the addition of NH_3. (SPR^{1-2}, T = 250 ^oC, $p_T = 5$ bar, GHSV = 4500 ml/hr/g_{cat}, $H_2/CO_2 = 3$, , and $p_T = 5$ during normal FTS operations or 5.2 bar when NH_3 was added (NTP))

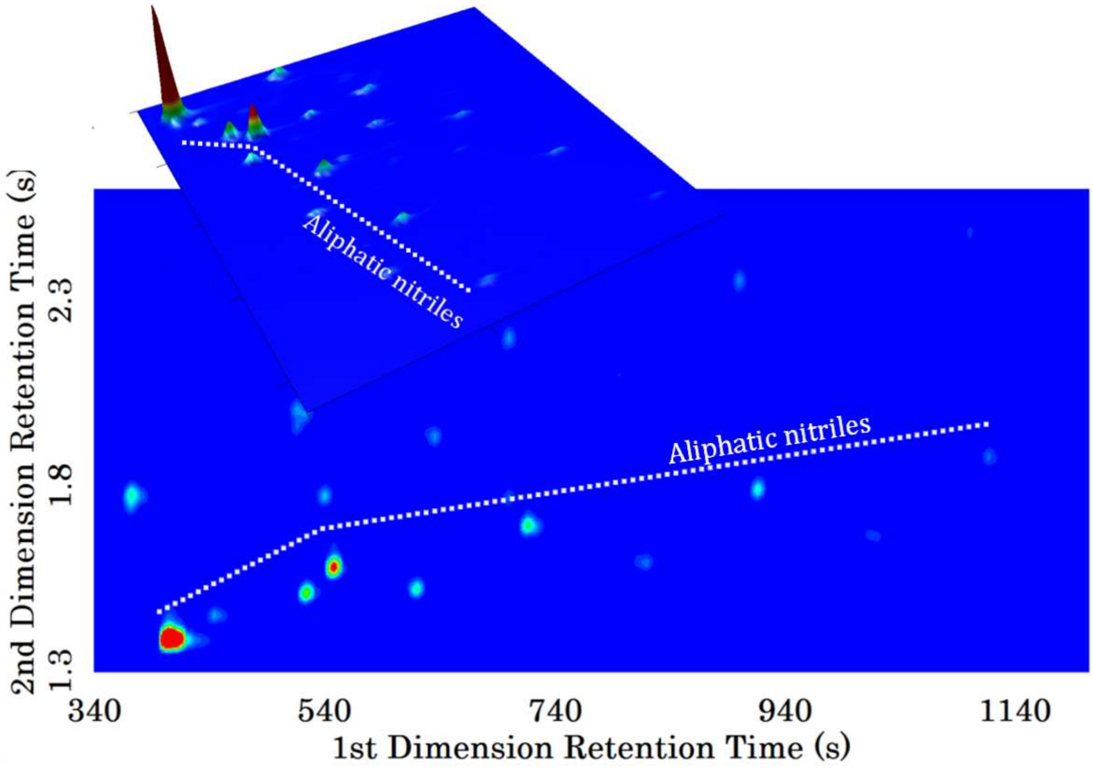

Figure 9.3: A topographic and three-dimensional view of the GCxGC-TOF chromatogram to showcase the formation of the aliphatic nitriles.

if the selectivity for the nitriles are maintained.

Fixed bed reactions with Fe-based catalyst

The iron based catalyst was also tested in a fixed bed reactor with the addition of NH_3 during FTS. The general results are tabulated in Table 9.3. Due to the size of the reactor, only a small quantity of catalyst could be loaded with Si_C which restricts the operation to high space velocities. It is still interesting to note that the CO conversion were not affected after the addition of 2 vol % NH_3 addition. Due to the high space velocities these conversions are to expected to be lower than in the case of the slurry phase reactor ($X(CO)_{slurry} = 70$ % and$X(CO)_{FB} = 19$ %). When considering the chain growth probability (α), it seems that the overall composition of the product spectrum did not change considerably with the addition of the NH_3 to the syngas feed. The chain growth probability, in addition, did not differ significantly

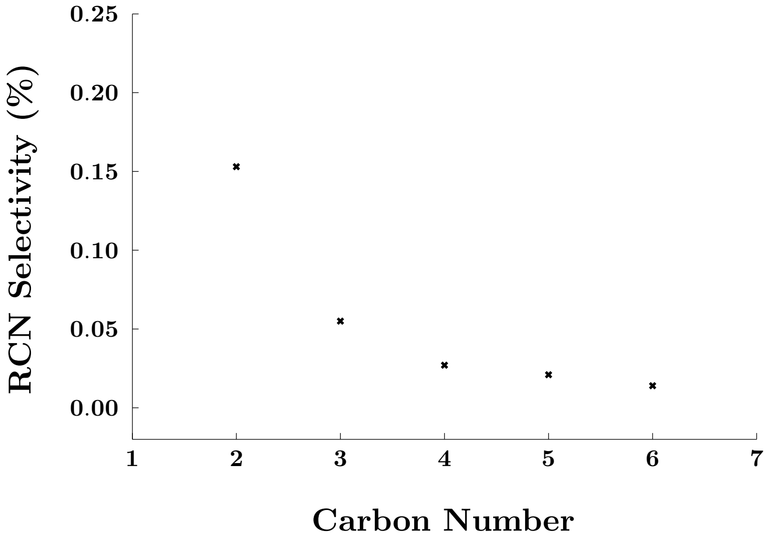

Figure 9.4: The selectivity towards aliphatic nitriles which should increase with increasing NH_3 concentration in the feed.

from the reactions conducted in the slurry phase reactor ($\alpha_{slurry} = 0.69$). One would in addition expect the additional time spent in a slurry phase reactor compared to a fixed bed reactor to lead to a decline in secondary reactions [5]. This can be seen in the high olefin content, but is even more evident when considering that 90 % of these olefins were α-olefins. It is well established that α-olefins are the dominant primary products [6].

Due to the low conversion of CO, it was not possible to obtain sufficient oil phase product to perform a sophisticated analysis of the oxygenates and N-containing compounds produced in these reactions. However, when analyzing the ampoules taken during these reactions some obvious observations could be made. When considering the N-containing compounds formed during these reactions, only aliphatic nitriles were observed. If we extract the relevant ion currents M/Z = 41 or 58 (see (top) Figure 9.5) which would correspond to aliphatic nitriles and the secondary/tertiary amines respectively, there are no traces of the formation of secondary/tertiary amines. If the same procedure is followed for the ampoules obtained during the slurry phase reactions (see (top) Figure 9.5), a converse result is obtained, with no nitrile formation. If we now take into account the fact that a product spectrum rich with primary products (α) are produced during this reaction, it seems as if aliphatic nitriles may form via a primary route

Table 9.3: Summary of the results obtained during the FTS reactions conducted in a fixed bed reactor, with and without 2 vol % NH_3 addition. (SPR^2, T = 250 ^oC, p_T = 5 bar, GHSV = 4500 ml/hr/g_{cat}, $H_2/CO = 2$, , and p_T = 5 during normal FTS operations or 5.2 bar when NH_3 was added (NTP))

Property	**FTS**	**FTS + 2 vol% NH_3**
X(CO)	19 %	19 %
$S(CH_4)$	15 %	14 %
$S(CO_2)$	5.9 %	5.6 %
α	0.64	0.65
olefin content (C_{2-9})	75 - 80 %	75 - 80 %

when NH_3 is present in the syngas feed during FTS.

Fixed bed reaction: Rh-based catalysts

The results obtained when using the Rh-based catalyst ($Rh - Al_2O_3$) are tabulated in Tabel 9.4. A high methane selectivity (S_{CH_4} = 20.33 %) were obtained (see Fig. 9.6), which was the major constituent of the paraffins (S_{paraf} = 27.07 %). A very low olefin selectivity were observed, $S_{olef} = 3.42\%$, since selectivity for the hydrocarbons bonded to heteroatoms were rather high. Oxygenate selectivity of S_{oxyg} = 12.61 % is not particularly high when using Rh-based catalysts, but is considerably high when compared to iron or cobalt-based FTS reactions. The N-containing compounds (mainly aliphatic nitriles) were however the major products produced in this reaction with a selectivity of S_{N-cont} = 42.00 %. The major product acetonitrile made up about two thirds of the N-containing compounds ($S_{acetonitrile}$ = 27.62 %). These results does thus suggest that N-containing compounds can be made to a high selectivity when using Rh-based catalysts.

During the characterization of the freshly prepared catalyst, the problem of analyzing the Rh-based ($Rh - Al_2O_3$) catalyst via scattering techniques (PXRD) were problematic (see Fig. C.4 in Appendix C). However, STEM analysis of the spent catalyst allowed us to characterization of the working catalyst. In top part of Fig. 9.7, one can see that the iron particles are uniformly

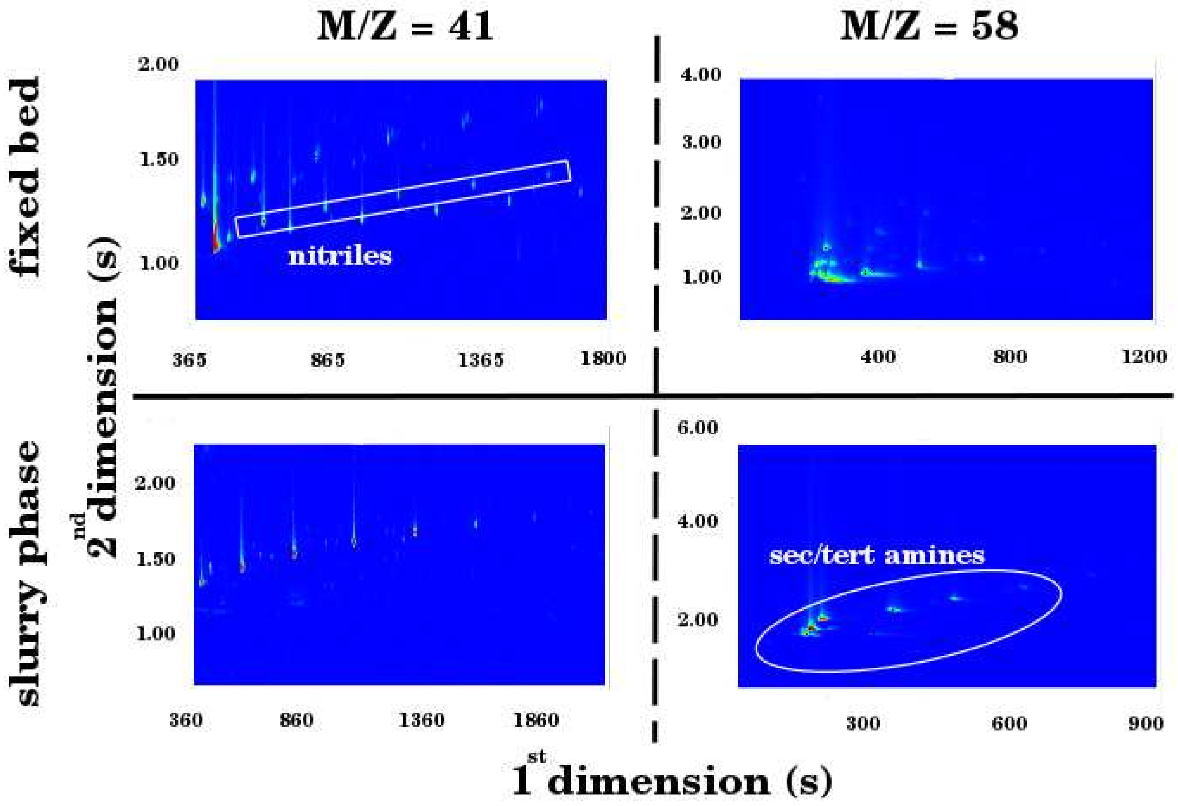

Figure 9.5: A comparison is made between the type of N-containing compounds produced during NH_3 co-feeding in (top) the fixed bed reactions and in the (bottom) slurry phase reacctor.

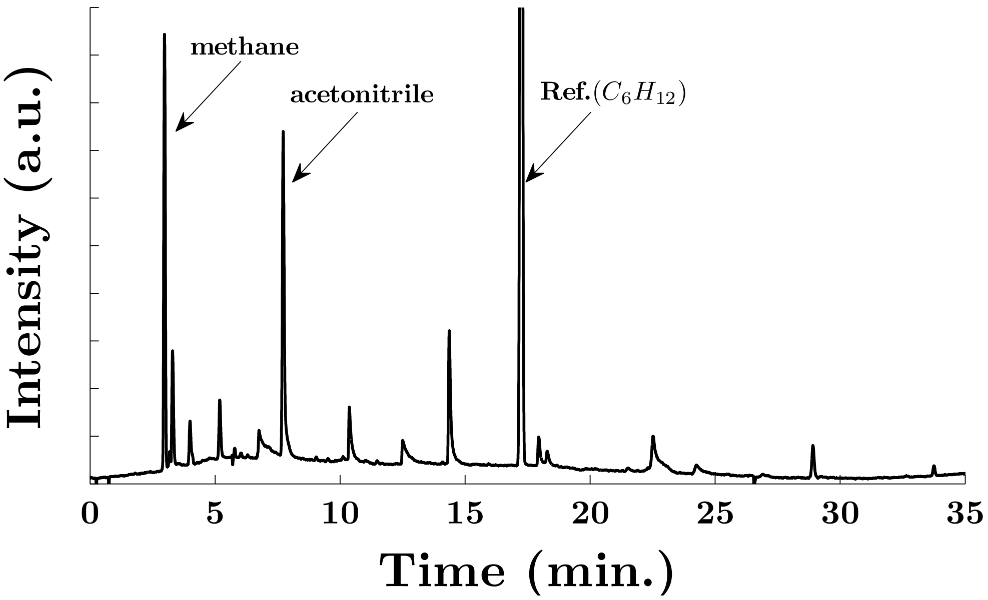

Figure 9.6: A chromatogram obtained when analyzing the gaseous on-line product obtained when conducting reaction with Rh-based ($Rh - Al_2O_3$) catalyst. (FBR^3, T = 250 ^{o}C, p$_T$ = 5 bar, GHSV = 4500 ml/hr/g$_{cat}$, H$_2$/CO = 2, 5 vol% NH$_3$)

Table 9.4: Selectivities calculated for the major compounds found when adding NH$_3$ during FTS and using a Rh-based catalyst. (FBR^3, T = 250 ^{o}C, p$_T$ = 5 bar, GHSV = 4500 ml/hr/g$_{cat}$, H$_2$/CO = 2, 5 vol% NH$_3$)

Product	**Selectivity (%)**
CH_4	20.33
paraf$_{C_{1-4}}$	27.07
olef$_{C_{2-4}}$	3.42
oxyg$_{C_{2-5}}$	12.61
acetonitrile	27.64
N-Cont$_{C_{2-5}}$	42.20

distributed throughout the catalyst. The histogram in the bottom part of Fig. 9.7 shows that the average particle size was 3 ± 1 nm. Please note that some ca. 40 nm clusters were also observed in some of the analyzed STEM micrograms.

Conclusions

It has been shown that the presence of NH_3, when present in 1 vol %, does not have any major effects on te catalyst activity when using CO_2 as a carbon source. A tendency towards the production of primary FTS products were observed (e.g.α-olefins) Similar to the case of CO as carbon source, there is a decline in oxygenate selectivity with the increase in N-containing compounds. The only major group of N-containing compounds produced during these reactions were aliphatic nitriles.

When evaluating these reactions at higher space velocities, higher olefin contents (predominantly α-olefins) were observed, which were to be expected due to the shorter residence time. This is again suggesting a product distribution high in primary FTS products. Amongst these products, only aliphatic nitriles were observed. Even the use of the sensitive GCxGC-TOF could not detect any secondary or tertiary amines, which suggest that these compounds form via secondary reactions.

When testing a catalyst which should have a high selectivity towards oxygenates (Rh/Al_2O_3), a very high N-containing product distribution is obtained. This result suggests that catalyst with a high propensity to produce oxygenates, should yield high N-containing compounds during FTS, should NH_3 be present in the syngas feed.

These results sheds light on several mechanistic questions towards the pathway of N-containing compound formation when NH_3 is co-fed with syngas during FTS. It is however important to confirm many of these observations via co-feeding reactions, which is the topic of investigation in Chapter 8.

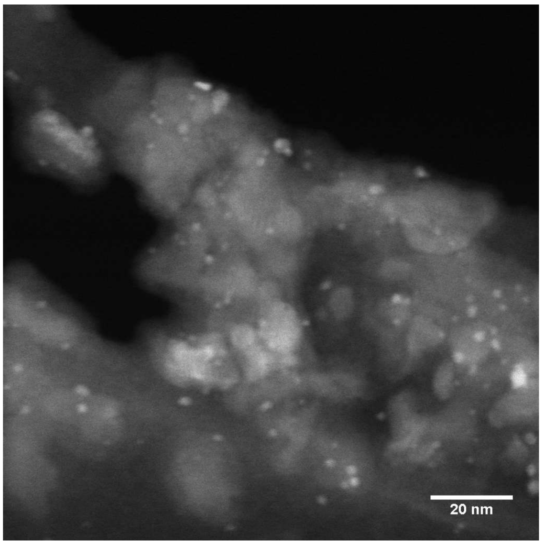

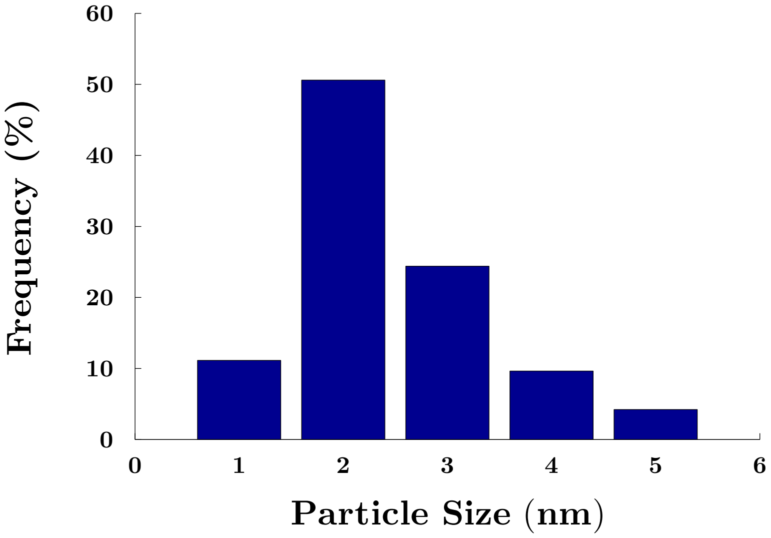

Figure 9.7: *(Top)* A SEM image of the well dispersed spent Rh-based catalyst after conducting FTS where NH_3 were present in the syngas feed. *(Bottom)* The particle size analysis yields that the spent Rh-based catalyst had an average particle size of 3 nm +/-1 (FBR^3, T = 250 ^{o}C, p_T = 5 bar, GHSV = 4500 ml/hr/g_{cat}, H_2/CO = 2, 5 vol% NH_3)

REFERENCES

[1] M Dry. *Chemical concepts used for engineering purposes - In Fischer-Tropsch Technology.* Amsterdam:Elsevier, 2004.

[2] T Riedel, H Schulza, G Schaub, K Jun, J Hwang, and Lee K. Fischer–Tropsch on iron with h_2/co and h_2/co_2 as synthesis gases: the episodes of formation of the Fischer–Tropsch regime and construction of the catalyst. *Topics in Catalysis*, 26:41–54, 2003.

[3] R. Henkel. *The influence of ammonia on Fischer-Tropch synthesis and formation of N-containing compounds*. PhD thesis, Carl von Ossietzky Universität, 2012.

[4] T. Sango. Nitrogen-containing from ammonia compounds co-feed to the fischer-tropsch synthesis. Master's thesis, University of Cape Town, South Africa, 2013.

[5] GP van der Laan and AACM Beenackers. Kinetics and selectivity of the Fischer-Tropsch Synthesis: A literature review. *Catal. Rev. Sci. Eng.*, 3 - 4:255–318, 1999.

[6] H Schulz and M Claeys. Reactions of α -oleins of different chain length added during Fischer-Tropsch synthesis on a cobalt catalyst in a slurry reactor. *Applied Catalysis A: General*, 186:71–90, 1999.

Chapter 10

General conclusions

The general conclusions of the work presented in this thesis is summarized to bring the broader set of findings into context. The key questions set out at the onset of the research project are revisited to identify the progress made in shedding light on those specific areas. Note that each chapter does however contain a subsection at the end of the relevant chapter with a more elaborate conclusion.

Introduction

It has been shown that valuable N-containing compounds (including primary amines, nitriles and amides) form when NH_3 is added during FTS [1–6]. The primary objective of this study was to provide fundemental insight to unresolved questions regarding the mechanistic route to the formation of the products (in particular the N-containing compounds) that form when NH_3 is added during Fe catalyzed FTS. Several of these questions relate to the role of NH_3 (and its dehydrogenated products on the surface) as a reactant and as a promoter or poison.

NH_x (with $x = 3, 2, 1, 0$) as a poison

Even though NH_3 is grouped with the FTS catalyst poisons [7], there is interesting recent literature to consider that provide further mechanistic detail on the role of NH_3 as a poison and the extent to which it occurs during FTS.

Firstly, it can be concluded from the work of Sango et al. [5, 6] that Fe-based catalysts are much more resistant (deactivation observed above 2 vol % NH_3) to poisoning by NH_3 during FTS compared to the detrimental effects observed at low levels (∼ ppm levels) of NH_3 for Co-based [8] catalysts. The stability of the Fe-based catalysts is in agreement with the findings reported in Chapter 7 where 1 vol % NH_3 was added during Fe-based FT experiments (Fe/K, slurry phase reactor, T = 250 ℃, P = 5 bar, $H_2/CO = 2$, SV = 2250 ml/hr/g_{cat}) and no major changes in the activity or selectivity of the FTS products was observed, with the exception of the oxygenates which is discussed below. By comparing separate FT experiments (SPR^{1-2}, discussed in Chapter 7) with or without NH_3 addition, which was not included in the study of Sango et al. [5, 6], it was however revealed here that the presence of NH_3 induce a retardation in the formation rate of the working catalyst (i.e. an Fe carbide that forms during the initial stages of FTS from metallic Fe). In contradiction to the poisoning effect associated with NH_3, Henkel [4] reports that NH_3 has similar effects on the FT product spectrum as the promotional effects observed for K in Fe-based catalysts, which he based on the results of his NH_3 co-feeding FT tests performed on a fixed bed reactor with promoted and unpromoted Fe-based catalysts (0/2/5:100 (g/g), K/Fe ratios).

Most of the proposed pathways, such as the carbide mechanism for FT product formation, neccesitates CO adsorption and bond breaking reactions. These elementary reactions are difficult and perhaps impossible to study at realistic FT conditions. Surface science experiments and theoretical approaches (e.g. DFT) provide a unique tool to study these reactions on model surfaces. In order to evaluate the poisoning effect of NH_3 on cobalt based catalysts during FTS, Kizilkaya et al. [9] reported their results from a set of UHV experiments combined with DFT modelling that focused on the adsorption and coadsorption of CO and NH_3 on the Co(0001) surface. It was experimentally determined in this work that a mixed layer of CO and NH_3 formed on the model cobalt surface, which the authors ascribe to a combination of electrostatic interactions between CO and NH_3 on Co(0001) and changes in the electronic structure of the surface due to the presence of NH_3 (since they expect that NH_3 would donate electrons to the surface). Based on their potential energy surface (PES) for the decomposition of NH_3 calculated with periodic DFT calculations, it is suggested that it is most likely the dehydrogenated surface products NH or N that are the underlying cause for the poisoning effect during cobalt catalyzed FTS as these species would block sites on the surface for CO adsorption. Sasaki et.

al [10] also report on surface science experiments that revealed the formation of ordered mixed layers of CO + NH_3 on Ru(001). In Chapter's 5 and 6 a theoretical (periodic DFT calculations) approach is used to shed light on the influence of NH_x (with $x = 3, 2, 1, 0$) surface species on the CO adsorption and dissociation reactions on a model Fe(100) surface. It can in general be concluded from this work that the presence of NH_3 leads to similar changes (in electronic structure, adsorption energy and CO dissociation activation energy) to that calculated for an Fe catalyst promoter (K + CO on Fe(100), [11]) that was performed for the same surface coverages ($\theta = 0.25 + 0.25$ ML) that was investigated here. The calculated heat of mixing (ΔE_{mix}(CO + NH_3) = -0.08, -0.16 and -0.32 eV at $\theta = 0.11$, 0.25 and 0.50 ML, respectively) were indicative of attractive lateral interactions between CO and NH_3 and predicts the formation of a mixed layer of CO and NH_3 on the Fe(100) surface. Bader charge analysis, PDOS and electron redistribution plots suggests that a similar effect as that proposed by Kizilkaya et al. [9] is responsible for the stabilization, that is that a combination of electrostatic interactions and predominantly surface mediated changes in the electronic structure occur when both CO and NH_3 is present on the Fe(100) surface. The aforementioned result could furthermore provide insight to the promotional effect observed when NH_3 was added during Fe catalyzed FTS [4]. The PES calculated in Chapter 5 for the NH_3 decomposition on Fe(100) predicts that NH and N may form stable surface species in the fourfold hollow (fh) site and thus block sites for CO adsorption. Even though stable heat of mixing energies was calculated in Chapter 6 for CO + NH/N on Fe(100) when these adsorbates are situated in diagonal (*trans*) positions in the (2×2) surface unit cell, this leads to a multiple problems. Firstly, the energies calculated for CO + NH/N on Fe(100) situated in adjacent (*cis*) positions in the (2×2) surface unit cell suggest that repulsive interactions interactions would exist in this configuration. Therefore, the adsorption of one N/NH adatom on Fe(100) would block one site in a (2×2) surface unit cell but will also influence the electronic structure so that CO adsorption is destabilized on $\theta = 0.50$ ML of the remaining $\theta = 0.75$ ML of the model surface. In addition, the products for the CO dissociation reaction, the C and O adatoms prefer the fh site for adsorption, which would also be impeded by the NH/N adsorbates. Most importantly, the calculated CO dissociation activation energy (at $\theta = 0.25$ ML) in the presence of $\theta = 0.25$ ML NH/N is higher ($\Delta E_a = 0.21/0.19$) when compared the CO dissociation on a clean Fe(100) surface and effectively changes the calculated exothermic heat of the reaction ($\Delta E_{rxn} = -0.35$ eV) on the clean surface to an endothermic heat of the reaction ($\Delta E_{rxn} = 0.11/0.35$ eV) when coadsorbed with NH or N on the Fe(100) facet. The aforementioned results therefore suggest that NH/N would adversely affect the important CO adsorption and dissociation reactions. When higher concentrations (5 - 20 vol %) of NH_3 was added during Fe catalyzed FT experiments, Sango et al. [5, 6] report an increase in the formation of aliphatic nitriles. It is therefore interesting to point out that Sango [5] proposed that N adatoms are likely to be more prevalent on the surface at these concentrations of aliphatic nitriles, which coincides with the deactivation of the Fe-based catalysts.

Formation of N-containing compounds

There are two important mechanistic details that can be extracted from previous studies that evaluated the potential of producing N-containing compounds through the addition of NH_3 during Fe-catalyzed FTS [1, 3–6, 12]. Firstly, most studies report that it is predominantly primary amines that form in these FT experiments and it is therefore postulated [4, 5] that NH_2 adsorbates play a key role at the latter stages of the pathway to the formation of N-containing compounds.

Secondly, a concomitant loss of oxygenates and formation of N-containing compounds was reported by Henkel [4] and Sango [5], suggesting that this new class of compounds suppress the primary route to the formation of oxygenates when NH_3 is added during FTS. Alternatively, considering the activity of amination reactions on Fe-based catalysts, there is a plausible route to the formation of N-containing compounds via a secondary pathway. That is, the oxygenates that form via a primary route can be consumed via a secondary reaction to form the N-containing compounds.

In addition to these questions, the initial results obtained in this work presented new questions within the current study. The use of comprehensive two-dimensional gas chromatography (GC×GC-TOF/FID) in Chapter 7 allowed for the detection of a homologous series of secondary and tertiary amines, that was not reported in previous FT experiments where NH_3 was added. These compounds did however raise questions regarding the stability of primary amines and nitriles under the conditions applied in the FT experiments of this work.

NH_2 as a reactant

The calculation (see Chapter 5) of the activation energy for the $NH_x \pm H$ (with $x = 3, 2, 1, 0$) reactions revealed that NH_2 has a significantly higher activation barrier than the other NH_x surface species, which would suggest that the NH_2 surface species may be kinetically trapped on the Fe(100) surface. The calculated PES was subsequently utilized in a mikrokinetic model which predicts that NH_2 would be the dominant surface species in a dimensionless plug flow reactor (with $p_{NH_3} = 0.02$ bar, T = 523 K). In Chapter 6 it was calculated that NH_2 is the only NH_x surface surface species that it is thermodynamically predicted to segregate into islands of CO and NH_2 as opposed to the formation of mixed CO + NH_2 states on the Fe(100) surface. Filot et al. [13] demonstrated through microkinetic modelling that the surface polymerization stages (initiation, propagation and termination) of the pathway could take place on different regions of the catalyst. The island formation predicted for NH_2 thus allow for speculation that these adsorbates are now more readily available in regions of the catalyst where the termination steps, as opposed to the initiation steps take place. Even though the bulk active phase for Fe-based FT catalysts is the Hägg carbide, these results does coincide with what is hypothesized based on experimental FTS reactions where NH_3 is added during FTS.

Secondary reactions of oxygenates and N-containing compounds

In order to shed light on the hypothesis that N-containing compounds can form via secondary reactions of oxygenates, 1-octanol was added through the use of a saturator with the feed (CO + 2 H_2 + 1 vol % NH_3) using an Fe-based catalyst in a slurry phase reactor (see Chapter 8). These studies revealed that 8.8 mol % of the added 1-octanol is converted to 2-nonanone and 1-nonanol, which could be expected based on the formation rates observed for the oxygenates in the base case study presented in Chapter 7 and results reported by Cairns [14] when he co-fed 1-octanol during FTS (T = 300 °C, P = 21 bar, $H_2/CO/CO_2 = 4:1:1$, GHSV = 4000 ml/g_{cat}/hr). The formation of carboxylic acids was significanltly reduced and aldehydes completely supressed in the base case study presented in Chapter 7. The study of Cairns does however predict the formation of significant quantities of aldehydes and carboxylic acids upon co-feeding of 1-octanol (in his NH_3 free FTS reactions), which could not be detected when adding 1-octanol with the feed (CO + 2 H_2 + 1 vol % NH_3) and analyzing the oil product with the sensitive GC×GC-

TOF technique. The absence of these compounds during the co-feeding experiment therefore suggests that the secondary route to the formation of octanal and octanoic acid from 1-octanol is surpressed by the presence of NH_3. Most importantly, the co-feeding of 1-octanol revealed that approximately 43 - 48 mol % of primary formed 1-octanol is likely being consumed via secondary reactions to form N-containing compounds.

In order to gain further information regarding the stability of nitriles when NH_3 is co-fed during FTS, nonanitrle was added to the feed using a similar technique described above. It could be deduced from these results that nitriles are not stable under the conditions employed here and would lead to the formation of secondary and tertiary amines as well as amides. Furthermore, an increase in 1-nonanol was observed upon the co-feeding of nonanitrile, thus indicating the reversibility of the aliphatic nitriles and alcohols. Based on these results a much more detailed depiction of secondary pathways to the formation of N-containing compounds was generated.

In a short study presented in Chapter 9, the information gained in previous Chapters 7 and 8 that suggests a relationship between oxygenates and N-containing compounds is utilized by testing a Rh-based catalyst (Rh/Al_2O_3) which has a high selectivity for oxygenates. Approximately 42 C wt% N-containing compounds selectively formed during this reaction, which demonstrates how the information gained here can be utilized in future work to improve the potential of these reactions.

Primary routes to the formation of N-containing compounds

It is not possible to accurately quantify the extent to which primary products form based on the experiments in this work. Some short studies presented in Chapter 9 did however shed light on the possibility of nitriles forming as primary products. In order to probe the formation of N-containing compounds via a primary route, NH_3 was added during an Fe-catalyzed FT experiment conducted in a fixed bed reactor (which inherently has much lower residence time) at twice the space velocity (4500 ml/hr/g_{cat}) employed in the slurry phase reactions of Chapter 7. The high selectivities for the formation of α-olefins, which is known to be primary products of the FTS, coincided with the formation of aliphatic nitriles. In a second set of reactions that was performed to probe the use of CO_2 as a carbon source, a similar product spectrum with predominantly aliphatic nitriles and a high selectivity for the α-olefins was observed. In combination these results suggests that nitriles can form as a primary product.

Summary

In this project, various aspects of the pathway to the formation of N-containing compounds was investigated. The results employed two diverse techniques (periodic DFT calculations and co-feeding FT experiments) to gain valuable insight into the primary and secondary routes of product formation when NH_3 is present in the synthesis gas during Fe-catalyzed FTS. Novel DFT calculations was presented that rendered important details about the role of the NH_x surface species on the CO adsorption and dissociation reactions on a model Fe(100) surface. This include insightful information about the role of NH_x surface species as a reactant or a poison for Fe based FTS. Experimentally, the use of comprehensive two-dimensional gas chromatography revealed the formation of secondary and tertiary amines during FT experiments where NH_3 was added that has not yet been reported. Clear experimental evidence was provided via the co-feeding of 1-octanol that supports the hypothesis that N-containing compounds form to the detriment of significant quantities of oxygenates via a secondary pathway. In addition to these findings, detailed information is provided throughout the thesis that shapes the route for further improvement of this unconventional route to the formation of N-containing compounds.

REFERENCES

[1] A. Clark, Process of synthesizing aliphatic amines, us 2,518,754. (1950).

[2] H. Kölbel and J. Trapper, Angew. Chem. Int. Ed. 4 (1965) 981.

[3] H. Kölbel and J. Trapper, Angew. Chem. Int. Ed. 5 (1966) 843–844.

[4] R. Henkel, The influence of ammonia on Fischer-Tropch synthesis and formation of N-containing compounds, Ph.D. thesis, Carl von Ossietzky Universität, Germany (2012).

[5] T. Sango, Nitrogen-containing compounds from ammonia co-feed to the Fischer-Tropsch synthesis, Master's thesis, University of Cape Town, South Africa (2013).

[6] T. Sango, N. Fischer, R. Henkel, F. Roessner, E. van Steen and M. Claeys, Appl. Catal., A 502 (2015) 150–156.

[7] C.H. Bartholomew, Appl. Catal., A 212 (2001) 17–60.

[8] J. van der Loosdrecht, F.G. Botes, I.M. Ciobica, A. Ferreira, P. Gibson, D.J. Moodley, A.M. Saib, J.L. Visagie, C.J. Weststrate and J.W. Niemantsverdriet, Fischer-tropch synthesis: Catalysts and chemistry, in: Comprehensive Inorganic Chemistry, 2nd Edition, Vol. 7, Elsevier, 2013, pp. 525–557.

[9] A.C. Kizilkaya, J.W. Niemantsverdriet and Weststrate C.J., J. Phys. Chem. C 120 (2016) 3834–3845.

[10] T. Sasaki, T. Aruga, H. Kuroda and Y. Iwasawa, Surf. Sci. 240 (1990) 223–244.

[11] D.C. Sorescu, Surf. Sci. 605 (2011) 401–414.

[12] W. Röttig, Catalytic hydrogenation of carbon monoxide with addition of ammonia or methylamine, US - 2,821,537 (1958).

[13] I.A.W. Filot, R.A. van Santen and E.J.M. Hensen, Angew. Chem. 126 (2014) 12960–12964.

[14] P. Cairns, Oxygenates in iron Fischer-Tropsch Synthesis: is copper a selectivity promoter?, Ph.D. thesis, University of Cape Town, South Africa (2008).

CHAPTER 11

RECOMMENDATIONS

Introduction

Based on the general conclusions made for the research project, some recommendations are discussed in this chapter. The nature of both the theoretical and experimental research studies conducted throughout this project lends itself to future work, which can shed further light on the problems evaluated here and provide answers to the new questions that developed throughout the study.

Density functional theory

The future of heterogenous catalytic design relies to a large extent on the ability to predict the potential of various catalytic surfaces to increase the rate of important surface reactions. It is therefore vital to acquire the neccesary data, such as those collected in the DFT work presented here on several surfaces. Furthermore, To directly build on this work, it would be useful to apply periodic DFT calculations to evaluate the co-adsorption of CO + NH_x (x = 3, 2, 1, 0) on the more open Fe(110) or the more closed Fe(111) surface. Considering the fact that the working catalyst consists mostly of bulk Fe-carbide phases, and although similar studies on carbide surfaces would require significant computational expense, the information obtained from these computations would serve as valuable tool for direct comparison with experimental findings. Microkinetic models (using transition state theory and statistical thermodynamics), based on

DFT results similar to those presented in this thesis, has on various occasions allowed for the extraction of information that can shed light on these elementary reactions at relevant reaction conditions [1, 2]. It would therefore be useful if the DFT results developed in this study were utilized to the full extent via the incorporation into more sophisticated micro-kinetic models. For the future development of theoretical studies, similar to the work presented here, it is in addition vital to have experimental results that could directly indicate the accuracy of the theoretical results. Future surface science studies (e.g. LEED, TPD, HREELS) to support or refute this work would thus be beneficial.

NH_3 addition during FTS experiments

Several difficulties associated with the analysis of organic compounds formed during the NH_3 addition during FTS were circumvented here via the use of on-line gas chromatography (GC-FID) and off-line comprehensive two-dimensional chromatography (GCxGC-TOF/FID). As much improved as these results were, it only highlighted the need for on-line gas chromatography in conjunction with sophisticated GC×GC-TOF/FID analysis. At the time of writing, these additions were being made to the reactor setup, and will surely improve future studies that does not only improve the NH_3 co-feeding during FTS reactions, but also classical FTS reactions.

It was shown (in Chapter 9) that CO_2 can be used as a carbon source for the production of aliphatic nitriles. In addition, when using CO were used as carbon source, the unconverted NH_3 reacted with the products CO_2 and H_2O to form ammonium bicarbonate (NH_4CO_3). With careful design and additional experimentation, a potential process could thus be developed to serve as means to produce N-containing compounds and serve as a sink for the greenhouse gas CO_2.

In Chapter 7 and 9, a very brief comparison were made between a system that allows for secondary reactions (slurry phase reactor) and one that minimizes secondary reactions (a fixed bed reactor with a high space velocities). A more comprehensive study with a wider range of space velocities should provide additional information with regards to the role of primary FTS reactions in pathway to the formation of N-containing compounds when NH_3 are being added during FTS. Moreover, base case studies (i.e. no NH_3 addition) performed with this analytical approach would surely benefit the elucidation of the formation of oxygenates during FTS.

An important variable to test in future work would be the choice of catalyst used when NH_3 are being added during FTS. The use of Cu-promoted Fe-based catalysts would be of interest, based on the high selectivities reported by Röttig [3] and the differences in oxygenate selectivities reported by Cairns [4] when applying varying loadings of Cu on Fe-based catalysts. Considering the high selectivities for N-containing compounds when doing these NH_3 c-feeding FTS reactions over a Rh-based catalyst, it would be interesting to pursue this genre of catalysts. Dlamini [5] recently varied the Fe-promotion on similar Rh-based catalysts during FTS experiments and found the product spectrum to consist of varying concentrations of oxygenates. The aforementioned catalysts would thus serve as optimization of selectivity and provide additional information w.r.t. the interaction between oxygenates and N-containing compounds.

Co-feeding 1-octanol clearly showed that these products can be converted to secondary and tertiary amines. It is therefore fair to assume that the deliberate addition of a less expensive 1-ethanol with NH_3 and syngas during FTS could lead to the production of valuable C_2-alkyl substituted secondary/tertiary amines. This work would surely have to be optimized, where chain growth would be of particular importance, considering the dominant formation of N, N-dimethyloctylamine during the 1-octanol and octanitrile co-feeding experiments.

REFERENCES

[1] P. van Helden. *Initial steps of the Fishcer-Tropsch synthesis on Fe(100): The role of hydrogen.* PhD thesis, University of Cape Town, 2008.

[2] P. van Helden and E. van Steen. *J. Phys. Chem. C*, 112:16505–16513, 2008.

[3] W. Röttig. Catalytic hydrogenation of carbon monoxide with addition of ammonia or methylamine. US - 2,821,537, 1958.

[4] P. Cairns. *Oxygenates in Iron Fischer Tropsch Synthesis.* PhD thesis, University of Cape Town, 2008.

[5] N. Dumani. Iorn modification of rhodium nano crystallites for CO hydrogenation. MSc thesis, University of Cape Town, South Africa, 2014.

APPENDIX A

SPOT PRICES FOR CHEMICALS

The production of chemicals via FTS

In this section we will briefly summarize the information and spot prices for the most relevant chemical commodities of interest. In all cases we made use of spot prices available in the United States of America (USA). Contract prices are rarely available and would just complicate matters. In some cases the most recent prices could only be found from 2007. But this was mainly for the nitrogen-containing compounds or oxygenates and one would expect higher values for 2011 (especially considering BASF's increased prices for amines in Europe [1]). For the comparative study however "real time" spot prices were used. Where appropriate we will indicate economic impacts from a technical perspective (e.g. cost of gasification).

Reactants

Syngas - The cost for your classic feed (i.e. CO + H_2) to the Fishcer-Tropsch Synthesis (FTS) process is undeniably the most difficult price to estimate. The price is dependent on various factors which would ultimately be determined by the location of the plant. The capital cost for converting coal to syngas would be higher than that for a crude oil refinery. However your "cheap" starting material can make this process more profitable. This is also the driving force behind conversion of biomass to synthetic fuel. Several countries are leaning towards this approach, none more so than in the United States of America. For this reason they conducted several robust studies to investigate the economical feasibility of this process. For more information on the economic feasibility of gasification units I would direct the reader to the study carried out by National Renewable Energy Laboratory which is a national laboratory of the U.S. Department of Energy [2].

Ammonia - It is well known [3] that ammonia is the 2^{nd}largest synthetically produced chemical. Ninety percent of ammonia produced is via the ammonia synthesis reaction developed by Fritz Haber and Carl Bosch. Ammonia is usually handled in liquid form. There is cases where it can be supplied as vapor to downstream consumers, which might help with refrigeration costs.

There are three modes of operation available for storage ([4]):

- Ambient Temperature - This is usually done in cylindrical/spherical vessels and has approximate capacities of 1 500 tonnes
- -33 ^oC - Usually insulated cylindrical tanks with 50 000 t capacity
- 0 ^oC - this reduces the job of pressurized storage and has capacities in the order of 2 500 tonnes

The spot prices for ammonia varies from 400 - 700 USD/tonne (i.e. **0.18 - 0.31 USD/lb**).

Products

Petroleum products - In Table A.1 we tabulate your typical petroleum products and group them via their carbon number distribution. For comparison the price of crude oil is added.
Linear Alpha Olefins (LAO) - Short chain linear alpha olefins are valuable commodities considering their role in the polymer industry. Ethylene and propylene are used as monomers in the production of polyethylene and polypropylene. 1-Butene, 1-hexene and 1-octene are all used as co-monomers in the production of linear low density poly ethylene (LLDPE). These commodities are all subject to the price fluctuations in crude oil. During the middle of 2008 ethylene and propylene prices plummeted from peaks of 0.80 & 0.70 USD/lb to 0.12 & 0.15 USD/lb respectively. For the comparative study done in section we will neglect the contribution of ethylene and propylene, but the values given in Table A.2 should be indicative of the additional profit to be made if these compounds were targeted.

Table A.1: Spot prices for petroleum products

Carbon number range	Petr. product	Price (USD/lb)
C(3-4)	LPG	0.15
C(5-10)	Gasoline	0.45
C(11-12)	Jet Fuel	0.5
C(13-20)	Diesel	0.51
N/A	Crude Oil	0.33

Table A.2: Spot prices for LAO's

LAO	Price (USD/lb)
ethylene	0.65
propylene	0.65
1-butene	0.40
1-hexene	0.6
1-octene	0.88

Table A.3: Spot prices for alcohols

Alcohols	Price (USD/lb)
ethanol	0.38
1-propanol	0.65
1-butanol	0.7
1-hexanol	0.88

Oxygenates - For brevity we will limit ourselves to the production of alcohols (, it should however be noted that aldehydes, acids, esters and ketones produced via FTS is also of higher economic value). Industrially the most important alcohols is methanol, ethanol, 1- propanol, 1-butanol, iso butyl alcohol and fatty alcohols for biodegradable detergents. Crude oil and natural gas predominate as raw material for their manufacture. However production via coal and/or biomass is expected to increase considering worldwide oil and environmental considerations. In Table A.3 we give some spot prices for some alcohols.

Nitrogen-containing compounds - The significance of adding ammonia during FTS to produce nitrogen-containing compounds lies in the economic value of these compounds. They consist of linear amines, nitriles, amides and formamides. These compounds find application in the pesticide industry and are used as precursors for several specialty chemicals. Their high value can easily be explained via their production. For an example, the production of ethyl amine would industrially be achieved via the amination reaction between ethanol and ammonia. In other words a reaction between a high value chemical needs to be produced via a second process to get to these compounds.

Table A.4: Spot prices for nitrogen-containing compounds

N-cont compound	Price (USD/lb)
methyl amine	0.83
ethyl amine	1.3
propyl amine	1.1
acetonitrile	0.8

REFERENCES

[1] www.basf.com, 2011.

[2] Nexant. Equipment design and cost estimation for small modular biomass systems, synthsis gas cleanup, and oxygen separation equipment. Technical report, National Renewable Energy Laboratory, A national laboratory of the U.S. Department of Energy, 2006.

[3] Ullmann. *Ullmann's Encyclopedia of Industrial Chemistry, Seventh Edition*. WILEY-VCH, 2006.

[4] C. Hale. *Nitrogen*, 119:30–36, 1979.

Appendix B

Supplementary information: DFT

Supplementary information: Chapter 4

For theoretical calculations, similar to physical experiments several parameters need to be optimized and justified prior to producing results. The quality of these optimizations have a direct impact on the accuracy of the computational method. Here a discussion of the methods that were used to find and validate a suitable model for the DFT calculations conducted in this thesis is presented.

Optimization of parameters for bulk bcc Fe and Fe(100)

Before optimising the lattice parameter of the bulk bcc Fe structure, a choice for a well converged kinetic cut-off energy and k-point sampling grid density had to be determined. Every pseudopotential that is available in VASP has a recommended default cut-off energy. Table B.1 summarizes the recommended kinetic cut-off energy values provided in the "POTCAR" file for the elements used throughout the DFT calculations.

These values are only a rough estimate to describe the level of accuracy that one is likely to achieve when setting the value for the kinetic cut-off energy. For example, it is pointed out in the VASP manual that a 30 % $\times EMAX$ added to the $EMAX$ values given in Table B.1 (e.g. $E_{cut} = (268 \times 0.3) + 268$ eV for bulk bcc Fe) would lead to an energy convergence of a few meV when performing volume *vs* energy calculations. It is therefore important to perform a set of calculations to confirm that the chosen parameters (kinetic cut-off energy and k-point sampling

Table B.1: Values recommended for the kinetic cut-off energies for the pseudopotentials used in VASP. (Values given for PAW-PBE[1])

	E_{cut} (eV)	
Atom	**EMIN**	**EMAX**
H	200	250
C	300	400
N	300	400
O	300	400
Fe	201	268

grid) lead to well converged total energies. The methodology followed was to keep all other variables constant and vary the cut-off energy from 200 to 500 eV until the energy per atom was converged to within an error of ± 1 meV/atom. A similar procedure was followed to find a suitable k-point mesh, making use of a Monkhorst-Pack scheme [1]. Single point energies were thus calculated using k-points sampling grids that ranged between 3×3×3 and 15×15×15 for the conventional unit cell of bulk bcc Fe. The results for the convergence tests for the k-points and kinetic cut-off energies for bulk bcc iron are presented in Figures B.1 and B.2. Even though it can be seen that convergence of the energy was reached at a energy cut-off value of E_{cut} = 350 eV and a k-point sampling grid of 8×8×8 for the conventional unit cell of bcc Fe, it was decided to use E_{cut} = 380 eV and a k-point sampling grid of 11×11×11 to be sure that any potential errors (e.g. from the Pullay stress calculation in VASP) was avoided during the volume *vs* energy calculations.

A similar procedure were followed for the determination of the paramaters (k-points and E_{cut}) for a cleaved Fe(100) surface consisting of seven layers. The results for the aforementioned convergence tests are presented in figures B.3 and B.4.

One of the most important decisions to make when using DFT, is which exchange-correlation functional to use. We evaluated both the revised Perdew-Burke-Erzerhof (RPBE) [2] and the Perdew-Wang-91 (PW91) [3] functional. By calculating single point (i.e. static) energies for bulk

---

[1] Note that the PBE-PAW pseudopotentials were used for calculations using the RPBE functional

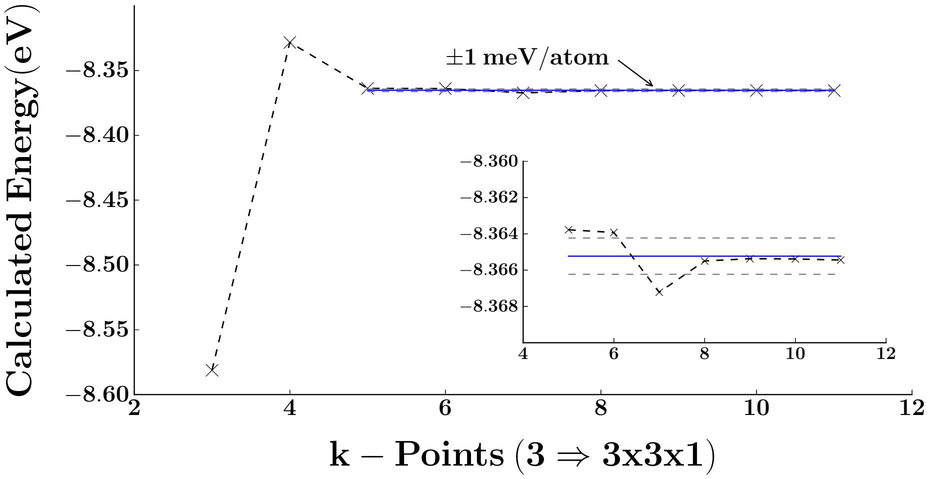

Figure B.1: The energy calculated for bulk bcc iron as a function of increasing k-points. To illustrate how convergence criterea were defined, an expanded view are superimposed. (E_{xc} = RPBE, E_{cut} = 380 eV)

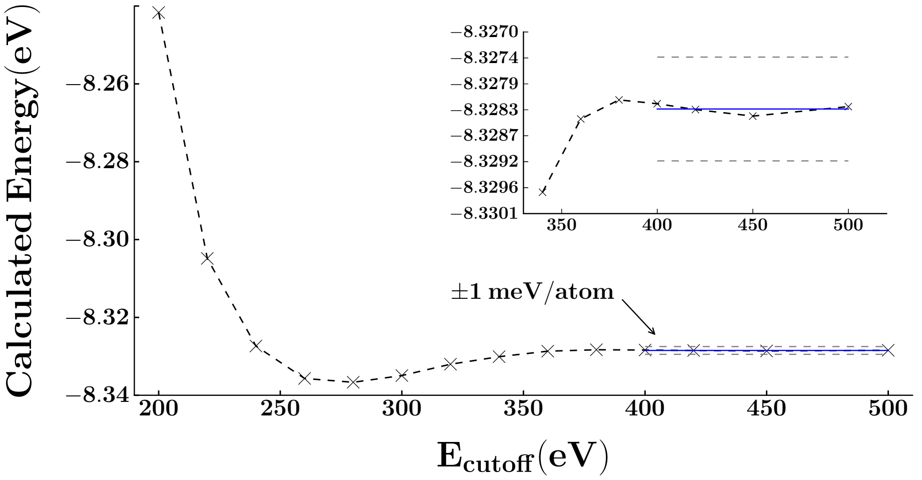

Figure B.2: The energy calculated for bulk bcc iron as a function of increasing kinetic cut-off energy (E_{cut}). To illustrate how convergence criterea were defined, an expanded view are superimposed. Note that the corresponding number of irreducible k-points are given in Table B.2. (E_{xc} = RPBE, k-points = 11x11x11)

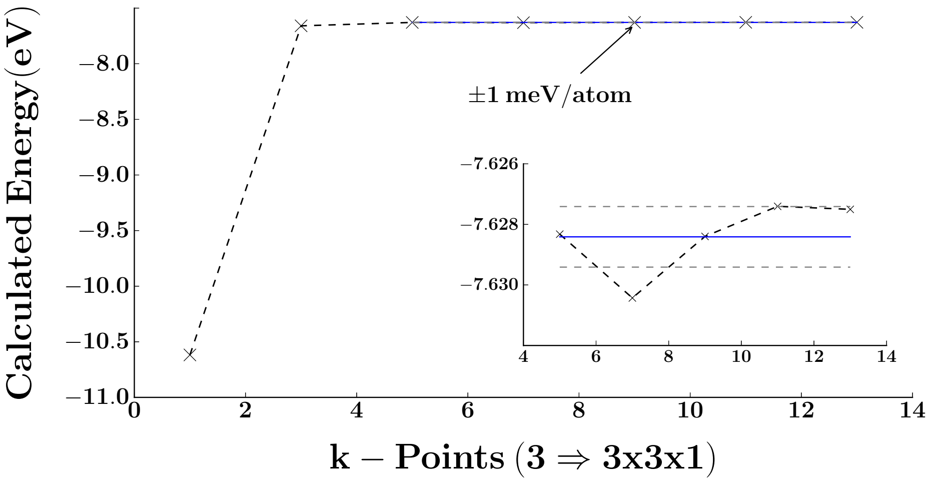

Figure B.3: The energy calculated for an Fe(100) surface consisting of 7 layers as a function of increasing k-points. To illustrate how convergence criterea were defined, an expanded view are superimposed. Note that the corresponding number of irreducible k-points are given in Table B.2. (E_{xc} = RPBE, E_{cut} = 400 eV)

Table B.2: Number of irreducible k-points corresponding to the k-point grids of the bulk Fe phase and the Fe(100) surface from Figures B.1 and B.3

Bulk		Surface unit cell	
3x3x3	4	3x3x1	3
5x5x5	10	5x5x1	6
7x7x7	20	7x7x1	10
9x9x9	35	9x9x1	15
11x11x11	56	11x11x1	21
13x13x13	84	13x13x1	28

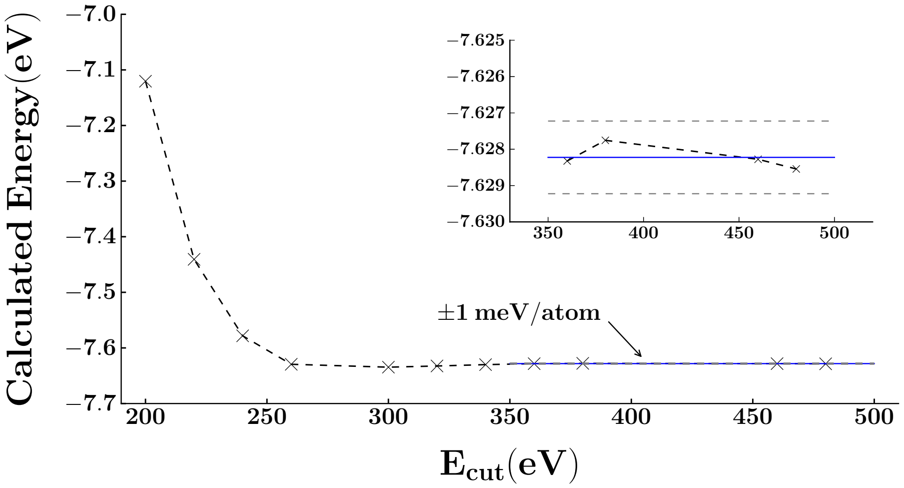

Figure B.4: The energy calculated for bulk bcc iron as a function of increasing kinetic cut-off energy (E_{cut}). To illustrate how convergence criterea were defined, an expanded view are superimposed. (E_{xc} = RPBE, k-points = 5x5x1)

bcc Fe while systematically varying the lattice parameter we were able to find the equilibrium cell parameter (see Figure B.5). Furthermore, by fitting this data to the Birch-Murnaghan equation of state (eq. B.1) we were able to retrieve the bulk modulus B_0. The bulk modulus is the pressure increase needed to cause a given relative decrease in volume. The magnetic moment (μB) for ferromagnetic Fe is included in the DFT calculations and provided in the output files (`OSZICAR`).

$$E(V) = E_0 + \frac{9V_0B_0}{16}\left\{\left[\left(\frac{V_0}{V}\right)^{\frac{2}{3}} - 1\right]^3 B_0' + \left[\left(\frac{V_0}{V}\right)^{\frac{2}{3}} - 1\right]^2 \left[6 - 4\left(\frac{V_0}{V}\right)^{\frac{2}{3}}\right]\right\} \tag{B.1}$$

If we compare the results obtained using two different functionals (Table B.3) it seems that both functionals correspond well with experiment, with the RPBE being slightly better. It has however been shown that the RPBE functional provides improved capabalities for the calculation of adsorption energies [2], which is a key property in the DFT calculations. It was therefore decided to use the RPBE functional for most of the calculations, and only calculate PW91 energies where comparisons were made to literature from previous DFT calculations.

To evaluate the convergence with regards to the number of slabs, the CO adsorption energy in the fourfold hollow site were calculated with Fe slab layer ranging between 3 and 13 layers.

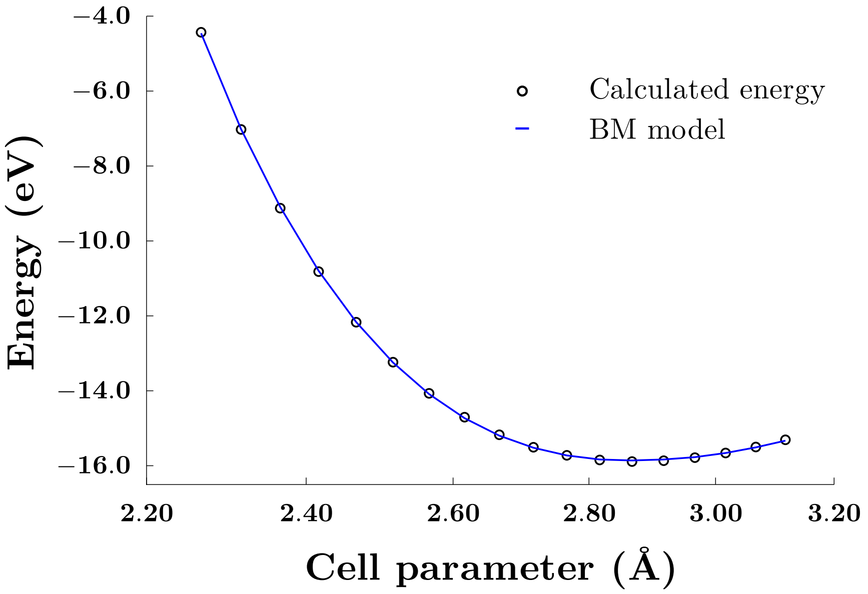

Figure B.5: The change in calculated energy as a function of increasing cell parameter for bulk bcc iron using. The resulting fit of this data to the Birch-Murnaghan equation of state were added to the plot. (E_{xc} = RPBE, k-points = 11x11x11, E_{cut} = 400 eV)

Table B.3: Comparison of the experimentally determined properties with that of our calculated results for bulk bcc Fe.

	Exp	RPBE	PW91
Cell parameter (Å)	2.87	2.87	2.88
Magnetic moment (μB)	2.24	2.31	2.50
Bulk modulus (GPa)	168	161	163

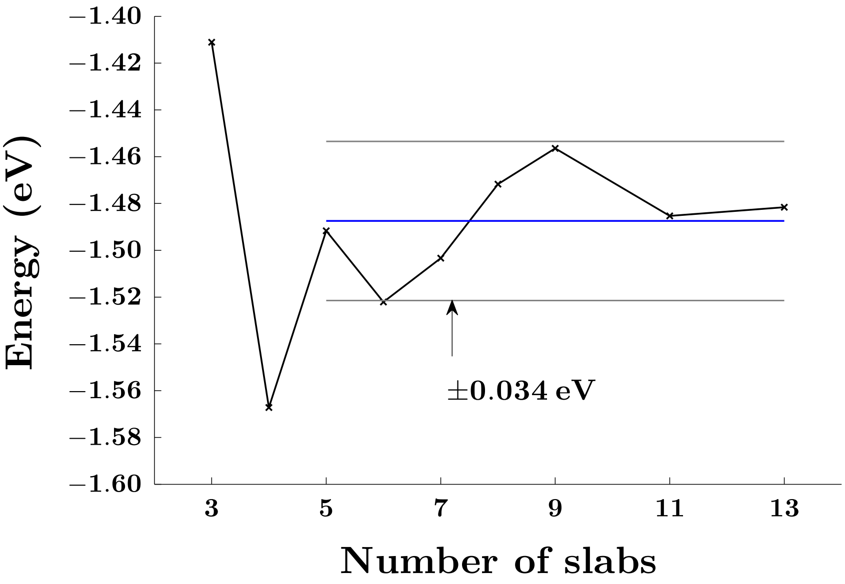

Figure B.6: CO adsorption energy calculated at the fourfold-hollow site on Fe(100) with number of slabs between 3 and 13. (E_{xc} = RPBE, k-points = 5x5x1, E_cut = 400 eV)

As can be see in Figure B.6, between the 5^{th} and 7^{th} layer slab, a ± 0.03 eV error exists. For the consideration of computational expense and the fact that similar errors have been reported when using this methodology [4], 5 layers were chosen for the model Fe(100) surface.

For the purpose of optimizing the vacuum gap, NH_3 adsorbed at the atop site were used as a probe, since this configuration has the adsorbates at the closest distance to the Fe-layer above the vacuum gap. The convergence shows a similar error as were observed for the test of the slab layers. These errors thus has to be considered when evaluating overall results.

Supplementary information: Chapters 5

C and O adsorption on Fe(100)

The results calculated for the adsorption energies after adsorbing C^* and O^* on the high symmetry sites at, br and fh on the Fe(100) are tabulated in Table B.4. The adatoms were calculated with reference to the C and O radicals. Both C^* and O^* were found to be most stable in the fh sites. This information were important for the construction of the PES for CO decomposition.

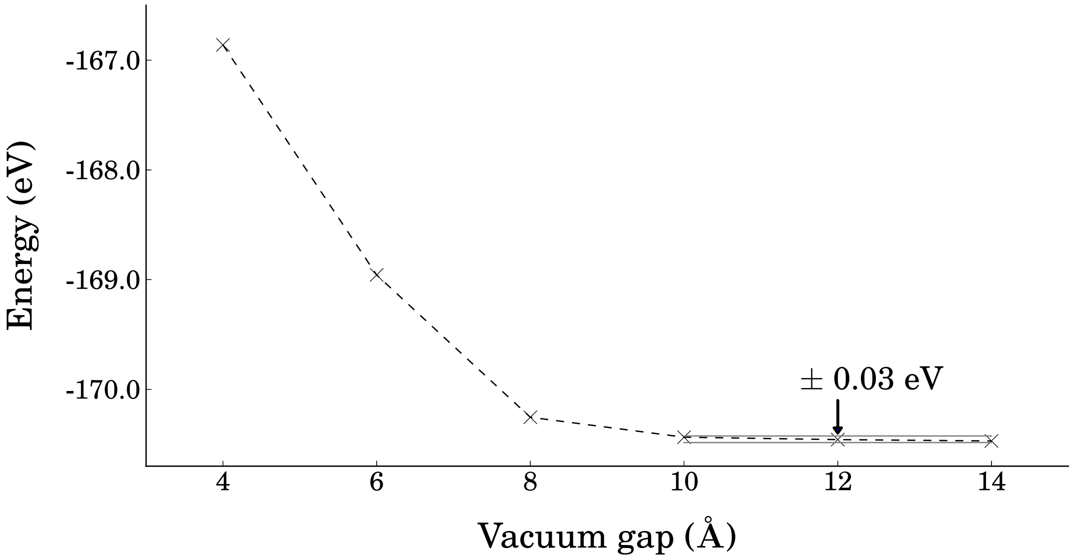

Figure B.7: Total energies obtained after static calculations at various vacuum gaps (in Å) for ammonia adsorption at $\theta = 0.25$ ML on Fe(100). (GGA-RPBE, $E_{cut} < 400\,eV$, k-points: 5x5x1)

Table B.4: Adsorption energies calculated for the adsorbates C* and O* on the high symmetry sites (at - atop, br - bridge and fh - fourfold hollow) on the Fe(100) surface at a coverage of $\theta = 0.25ML$. Energies are calculated w.r.t. the radicals in the gas phase. ZPVE$_c$ are not included. (GGA-RPBE, $E_{cut} < 400\,eV$, k-points: 5x5x1)

	E$_{\mathbf{ads}}$ (eV) $\theta = \mathbf{0.25ML}$	
Site	**C**	**O**
at	-6.15	-6.41
br	-7.63	-7.27
fh	-8.96	-7.84

Table B.5: Stable co-Adsorption energies calculated for NH_x(X) + H(X) (with X = at, br, fh) on Fe(100) with $\theta = 0.25 + 0.25$ ML. $ZPVE_c$ are not included. (GGA-RPBE, $E_{cut} < 400\,eV$, k-points: 5x5x1)

NH_x(X) + H(X)	**co-Adsorption Energies**				**ΔH** (eV)
	E_{ads} (eV) $\theta = 0.25 + 0.25$ML				(most stable conf.)
NH_2(br) + H(X)	br^1	br^2	br^3	fh	
	-0.68	-0.65	-0.45	-0.63	-0.73
NH(fh) + H(X)	br	fh^1	fh^2		
	-0.53	**-0.65**	-0.54		-1.04
N(fh) + H(X)	br	fh^1	fh^2		
	-0.90	**-1.11**	-0.96		-1.63

NH_x + H adsorption on Fe(100)

After finding the most stable adsorption energies for NH_x^* on the Fe(100) surface, we co-adsorbed H^* atoms on the three high symmetry positions. The results for our stable co-adsorptions calculated are tabulated in Table B.5 and depicted in the scheme in Figure B.8. Three unique bridge co-adsorption sites were identified to be stable for NH_2 + H as well as H^* adsorbed in the fourfold hollow site. For NH^* and N^*, both the trans (fh^1) and cis (fh^2) as well as a bridge site were stable co-adsorption sites for H^*. These co-adsorbed states were important when constructing the PES for NH_3 decomposition.

Vibrational analysis

As mentioned in Chapter 4, vibrational analyses were conducted on virtually all structures throughout the thesis. These analysis were then used in turn to evaluate stable adsorption profiles, i.e. to see if the structure were in at a local minimum, saddle point or a transition state. In Table B.6 we give an example of the computed vibrational frequencies for NH_x (x = 3, 2, 1, 0) adsorbed at various coverages (θ = 0.11, 0.25 and 0.50 ML) on the Fe(100) surface.

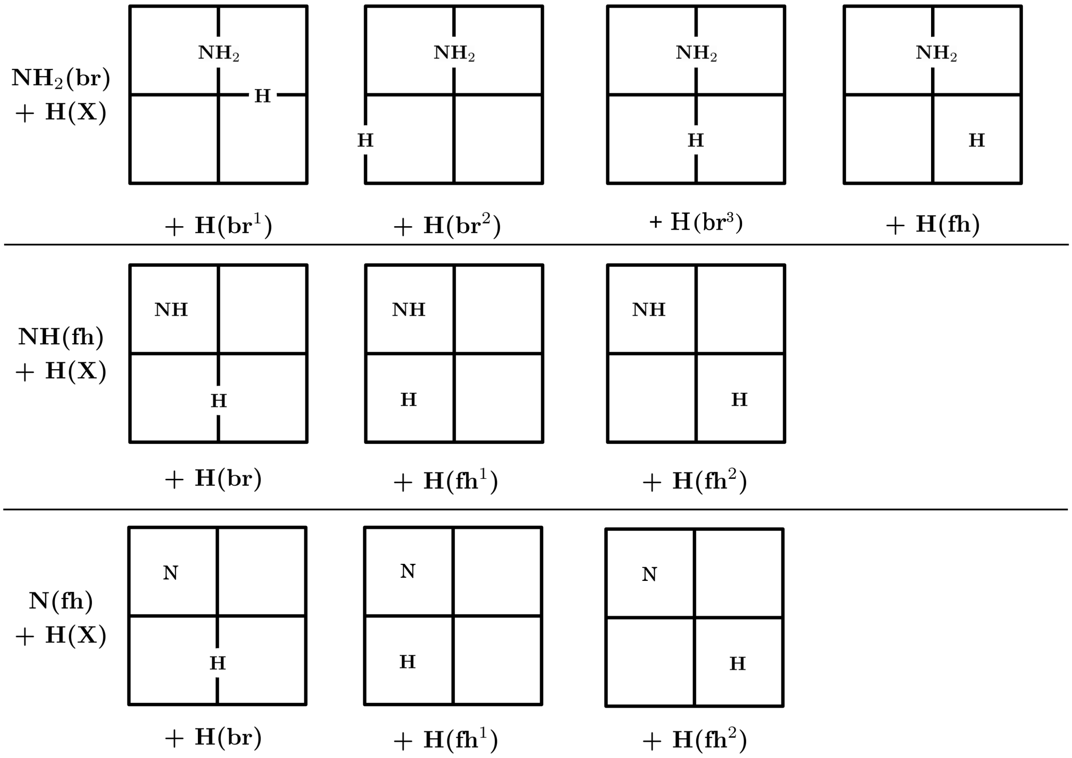

Figure B.8: The different configurations calculated for NH_x + H on the high symmetry positions on Fe(100). In addition, this schematic shows the configurations used as the final states during the search for the minimum energy pathways in the NH_3 decomposition reactions. ($\theta = 0.25$ ML, GGA-RPBE, $E_{cut} < 400\,eV$, k-points: 5x5x1)

Table B.6: Vibrational modes for NH_x adsorption at $\theta = 0.11$, 0.25 and 0.50 ML coverages when adsorbed on the Fe(100) surface. (GGA-RPBE, $E_{cut} < 400\,eV$, k-points: 5x5x1)

NH_3			**NH_2**			**NH**			**N**		
0.11ML	0.25ML	0.50ML	0.11ML	0.25ML	0.50ML	0.11ML	0.25ML	0.50ML	0.11ML	0.25ML	0.50ML
3505	3501	3454	3482	3482	3492	3256	3324	3367	426	409	463
3503	3500	3451	3381	3385	3486	729	573	3357	423	407	439
3373	3368	3444	1490	1488	3388	724	570	585	407	395	334
1615	1608	3427	630	626	3386	362	355	582			332
1608	1603	3306	619	612	1486	331	263	574			319
1130	1097	3300	538	531	1483	327	261	571			316
467	434	1612	400	402	693			389			
460	426	1580	291	293	645			379			
246	224	1578	130	142	591			311			
120	101	1577			552			307			
97	89	1084			550			287			
65	83	1067			548			284			
		363			401						
		359			385						
		350			292						
		345			280						
		193			142						
		182			132						
		166									
		139									
		77									
		66									
		31									

Analysis at higher temperatures and pressures

Statistical thermodynamics

In Chatpers 5 and 6, statistical thermodynamic models were used to aid the disccusion of the DFT results at relevant temperatures and pressures. Here a summary of the key equations and formulations are presented. Transition state theory (TST) can be used to treat surface reaction rates if the activation barriers (E_a) and partition functions (q) for both the reactants and transition states can be computed [5].

For the NH_3(g) molecule, the partition function (q_g) were obtained via Eq.'s B.2 - B.5,

$$q_t = \left(\frac{2\pi MkT}{h^2}\right) V \tag{B.2}$$

$$q_r = \frac{\sqrt{\pi}}{\sigma} \left(\frac{8\pi^2 kT}{h^2}\right)^{3/2} \sqrt{I_1 I_2 I_3} \tag{B.3}$$

$$q_v = \prod_{i=1}^{3N-6(7)} \frac{e^{-hv_i/2kT}}{1 - e^{-hv_i/kT}} \tag{B.4}$$

$$q_g = q_t \times q_r \times q_v \tag{B.5}$$

where: q_t, q_r and q_v are the translational, rotational and vibrational partition functions respectively.

M is the molar mass of NH_3.

v_i are the vibrational modes of NH_3.

I_{1-3} are the moments of inertia for NH_3.

$\sigma = 3$ is the symmetry number for NH_3.

For the partition function of the adsorbates (q_{ads}), the approximation is made that the translational and rotational partition functions does not contribute significantly to the total partition function, i.e. $q_{ads} = q_v$.

The entropy and enthalpy contribution to the Gibbs free energy (G_g) for the gas phase molecule NH_3 were calculated using Eq.'s B.6 - B.13,

$$S_t = \frac{5}{2}R + Rln\left(\frac{V}{N_A}\left(\frac{2\pi MkT}{h^2}\right)^{3/2}\right) \tag{B.6}$$

$$S_r = R\left(\frac{5}{2} + ln\left(\frac{\sqrt{\pi}}{\sigma}\left(\frac{8\pi^2 kT}{h^2}\right)^{3/2}\sqrt{I_1 I_2 I_3}\right)\right) \tag{B.7}$$

$$S_v = R\sum_{i=1}^{3N-6(7)}\left(\frac{hv_i}{kT}\frac{1}{1-e^{-hv_i/kT}} - ln(1-e^{-hv_i/kT})\right) \tag{B.8}$$

$$S_g = S_t + S_r + S_v \tag{B.9}$$

$$H_t = \frac{5}{2}R \tag{B.10}$$

$$H_r = \frac{3}{2}R \tag{B.11}$$

$$H_v = R\sum_{i=1}^{3N-6(7)}\left(\frac{hv_i}{2k} + \frac{hv_i}{kT}\frac{1}{1-e^{-hv_i/kT}}\right) \tag{B.12}$$

$$H_g = H_t + H_r + H_v \tag{B.13}$$

The use of the vibrational frequencies calculated via the partial Hessian vibrational analysis (PVHA) to calculate the vibrational entropy and enthalpy (S_v and H_v), has been shown to reproduce the S_v/H_v-values calculated via the vibrational frequencies calculated via the full Hessian vibrational analysis to within 0.1 - 0.4 kcal/mol [6].

Similar to the partition functions for the adsorbates, the translational and rotational contributions to the enthalpy and entropy for the adsorbates are assumed to be negligable (i.e. $S_{ads} = S_v$ and $H_{ads} = H_v$).

The Gibbs free energy (ΔG) is finally equated using equation B.14.

$$\Delta G = \Delta H - T\Delta S \tag{B.14}$$

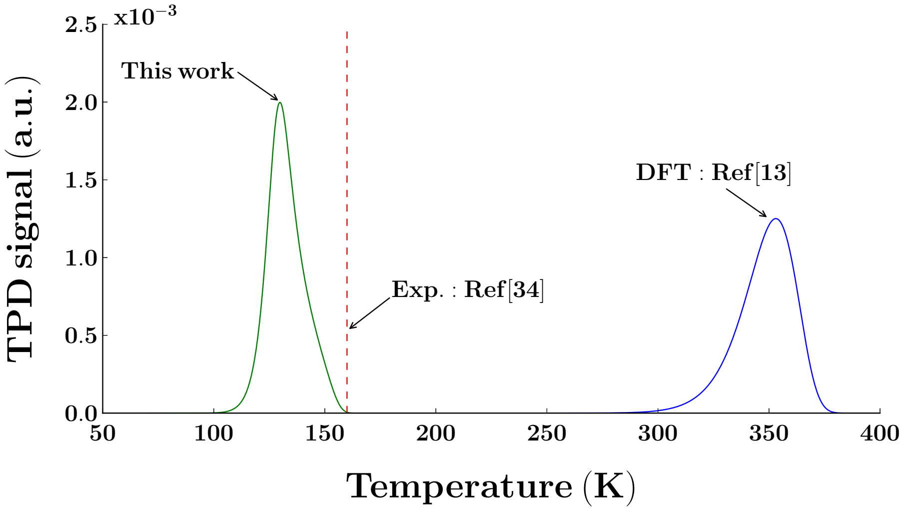

Figure B.9: Simulation of TPD from DFT results calculated in this work, compared with simulated TPD from DFT results from Yeo et al. [8] and experimental TPD results from Grunze et al. [7]

TPD simulation for NH_3 desorption on Fe(100)

To further compare the adsorption energy calculated via DFT with the experimental value obained in the TPD experiment of Grunze et al. [7], a TPD reaction is simulated using Eq. B.15.

$$\frac{d\theta_{NH_3}}{dT} = \frac{A}{\beta} \cdot e^{F/RT} \cdot \theta_{NH_3} \tag{B.15}$$

with E_a the activation barrier, A the pre-exponential factor (taken as $10^{13}\ s^{-1}$), β the ramping rate and F a function ($F = E_a + \theta_{NH_3} \cdot \frac{dE_a}{d\theta_{NH_3}}$) that incorporates the coverage dependency of adsorption energy for NH_3 on the Fe(100) surface. The results for the TPD simulation is presented in Figure B.9, with the maximum peak temperature reported by Grunze et al. [7] indicated on the figure. To compare these results with the NH_3 adsorption energy on Fe(100) calculated by Yeo et al. [8], a simulation (using $F = E_a$) based on their adsorption energy were added to the plot. From this plot it is easy to see the good agreement with the low activation barrier calculated $E_a = 0.35$ eV with the experimental value.

To obtain $\frac{dE_a}{d\theta_{NH_3}}$, the adsorption energies (in kJ/mol) at the coverages $\theta = 0.0625$, 0.11, 0.25 and 0.50 ML, were fitted to the function $1.73{\times}10^4{+}6.15{\times}10^2 \cdot tan(-1.73 + \theta_{NH_3})$. The temperature programmed desorption (TPD) simulation were calculated by solving the ordinary differential equation (ODE) Eq. B.15 using python's 'odeint' function.

Microkinetic analysis

The microkinetic analsis performed in Chapter 5 incorporates transition state theory and statistical mechanics to estimate which surface species are present on the surface at relevant reaction conditions. If one were to consider the decomposition reactions

$$NH_3 + * \underset{k_{f1}}{\overset{k_{r1}}{\rightleftharpoons}} NH_3^* \tag{B.16}$$

$$NH_3^* + * \underset{k_{f2}}{\overset{k_{r2}}{\rightleftharpoons}} NH_2^* + H^* \tag{B.17}$$

$$NH_2^* + * \underset{k_{f3}}{\overset{k_{r3}}{\rightleftharpoons}} NH^* + H^* \tag{B.18}$$

$$NH^* + * \underset{k_{f4}}{\overset{k_{r4}}{\rightleftharpoons}} N^* + H^* \tag{B.19}$$

where k is the rate constants and f/r indicates if the reaction are in the forward/reverse direction for the surface reactions $1-4$. The rate constants (k) is calcualted using TST and in the Arrenhius form of the rate equation

$$k = A \cdot e^{E_a/RT} \tag{B.20}$$

where A is the pre-exponential factor, E_a the activation energy, T the temperature in K and R the universal gas constant.

The pre-exponential factor was calcualted using Eq. B.21

$$A = (k_bT/h) \times (\frac{Q^\ddagger}{Q}) \tag{B.21}$$

where k_b is the Boltzman constant, h is Planck's constant and $Q/Q^\ddagger$ are the partition functions for the reactants and transition states respectively.

The following elementary reactions are thus being considered:

$$\left.\begin{aligned}
f_1 &= k_{f1} \times p(NH_3) \times \theta_* \\
r_1 &= k_{r1} \times \theta_{NH_3^*} \\
f_2 &= k_{f2} \times \theta_{NH_3^*} \times \theta_* \\
r_2 &= k_{r2} \times \theta_{NH_2^*} \times \theta_{H^*} \\
f_3 &= k_{f3} \times \theta_{NH_2^*} \times \theta_* \\
r_3 &= k_{r3} \times \theta_{NH^*} \times \theta_{H^*} \\
f_4 &= k_{f4} \times \theta_{NH^*} \times \theta_* \\
r_4 &= k_{r4} \times \theta_{N^*} \times \theta_{H^*}
\end{aligned}\right\} \quad \text{Elementary Rxs} \tag{B.22}$$

If we now consider implementing these reactions in a plug-flow reactor, the following procedure is taken. Firstly a set of differential equation are defined that describes the change in the partial pressure of $\mathrm{NH_3}$ (p_{NH_3}), adsorbates (θ_{X^*}) and free sites θ_*.

$$\begin{aligned}\frac{d(p_{NH_3})}{dt} &= \frac{1}{v_{NH_3}} \times (r_1 - f_1) \\ &= \frac{1}{v_{NH_3}} \times ([k_{r1} \times \theta_{NH_3^*}] - [k_{f1} \times p(NH_3) \times \theta_*])\end{aligned} \tag{B.23}$$

$$\begin{aligned}\frac{d(\theta_{NH_3^*})}{dt} &= f_1 - r_1 - f_2 + r_2 \\ &= [k_{f1} \times p(NH_3) \times \theta_*] - [k_{r1} \times \theta_{NH_3^*}] - [k_{f2} \times \theta_{NH_3^*} \times \theta_*] + [k_{r2} \times \theta_{NH_2^*} \times \theta_{H^*}]\end{aligned} \tag{B.24}$$

$$\begin{aligned}\frac{d(\theta_{NH_2^*})}{dt} &= f_2 - r_2 - f_3 + r_3 \\ &= [k_{f2} \times \theta_{NH_3^*} \times \theta_*] - [k_{r2} \times \theta_{NH_2^*} \times \theta_{H^*}] - [k_{f3} \times \theta_{NH_2^*} \times \theta_*] + [k_{r3} \times \theta_{NH^*} \times \theta_{H^*}]\end{aligned} \tag{B.25}$$

$$\begin{aligned}\frac{d(\theta_{NH^*})}{dt} &= f_3 - r_3 - f_4 + r_4 \\ &= [k_{f3} \times \theta_{NH_2^*} \times \theta_*] - [k_{r3} \times \theta_{NH^*} \times \theta_{H^*}] - [k_{f4} \times \theta_{NH^*} \times \theta_*] + [k_{r4} \times \theta_{N^*} \times \theta_{H^*}]\end{aligned} \tag{B.26}$$

$$\begin{aligned}\frac{d(\theta_{N^*})}{dt} &= f_4 - r_4 \\ &= [k_{f4} \times \theta_{NH^*} \times \theta_*] - [k_{r4} \times \theta_{N^*} \times \theta_{H^*}]\end{aligned} \tag{B.27}$$

$$\begin{aligned}\frac{d(\theta_{H^*})}{dt} &= f_2 - r_2 + f_3 - r_3 + f_4 - r_4 \\ &= [k_{f2} \times \theta_{NH_3^*} \times \theta_*] - [k_{r2} \times \theta_{NH_2^*} \times \theta_{H^*}] + [k_{f3} \times \theta_{NH_2^*} \times \theta_*] - [k_{r3} \times \theta_{NH^*} \times \theta_{H^*}] \\ &\quad + [k_{f4} \times \theta_{NH^*} \times \theta_*] - [k_{r4} \times \theta_{N^*} \times \theta_{H^*}]\end{aligned} \tag{B.28}$$

and from the site balance, $\theta_* = 1 - (\theta_{NH_3^*} + \theta_{NH_2^*} + \theta_{N^*} + \theta_{H^*})$,

$$
\begin{aligned}
\frac{d(\theta_*)}{dt} &= r_1 - f_1 + r_2 - f_2 + r_3 - f_3 + r_4 - f_4 \\
&= [k_{r1} \times \theta_{NH_3^*}] - [k_{f1} \times p(NH_3) \times \theta_*] + [k_{r2} \times \theta_{NH_2^*} \times \theta_{H^*}] - [k_{f2} \times \theta_{NH_3^*} \times \theta_*] \\
&\quad + [k_{r3} \times \theta_{NH^*} \times \theta_{H^*}] - [k_{f3} \times \theta_{NH_2^*} \times \theta_*] + [k_{r4} \times \theta_{NH^*} \times \theta_*] - [k_{f4} \times \theta_{N^*} \times \theta_{H^*}]
\end{aligned}
\tag{B.29}
$$

This system of ordinary differential equations was then numerically solved in a script written with the *Python* programming code and making use of the *odeint* function from the *scipy.integrate* package.

Supplementary information: Chapter 6

Initial structures for co-adsorption study

CO + NH_3 on Fe(100) geometries

A top view of the initial and final structures that was used and calculated for CO + NH_3 on Fe(100) is presented in Figure B.10. The rotation of the C−O bond in the $x - y$ plane and the change in the geometry of NH_3 is thus due to the co-existence of CO and NH_3 on Fe(100).

CO + NH_2 on Fe(100) geometries

The first NH_2(i) coadsorbed with CO were set up so that the C and N atoms shared Fe atoms, and the second NH_2(ii) where O and N shared the Fe atoms. The heat of CO adsorption with the NH_2(i) configuration (see Figure Fig. B.11) were more stable ($\Delta H_{ads,CO'} = -1.36$ eV) than that of NH_2(ii) ($\Delta H_{ads,CO'} = -1.27$ eV), but both had higher adsorption energies than in the absence of NH_2 ($\Delta H_{ads,CO} = -1.49$ eV).

CO + NH on Fe(100) geometries

For CO coadsorbed with NH, both the *trans* and one of the *cis* structures considered, the geometry does not change significantly between the initial and final structures, which is why only the final structures are given in Figure B.12. The initial two *cis* configurations differ in the direction where the oxygen atoms are directed. When the oxygen faces the NH bond, the CO

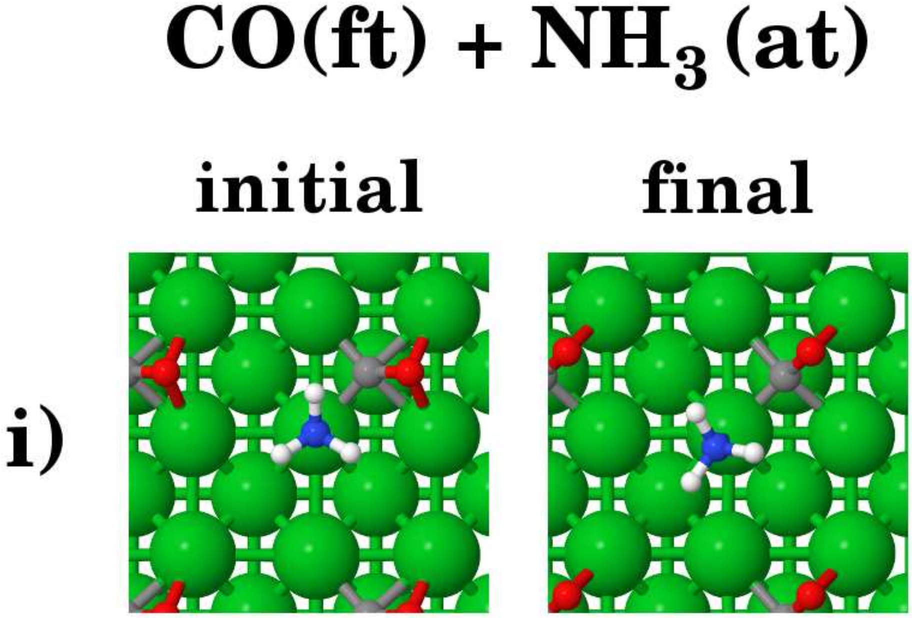

Figure B.10: The initial and final structures for the geometry optimization of (0.25 ML + 0.25 ML) $CO(ft') + NH_3(at)$ on Fe(100).

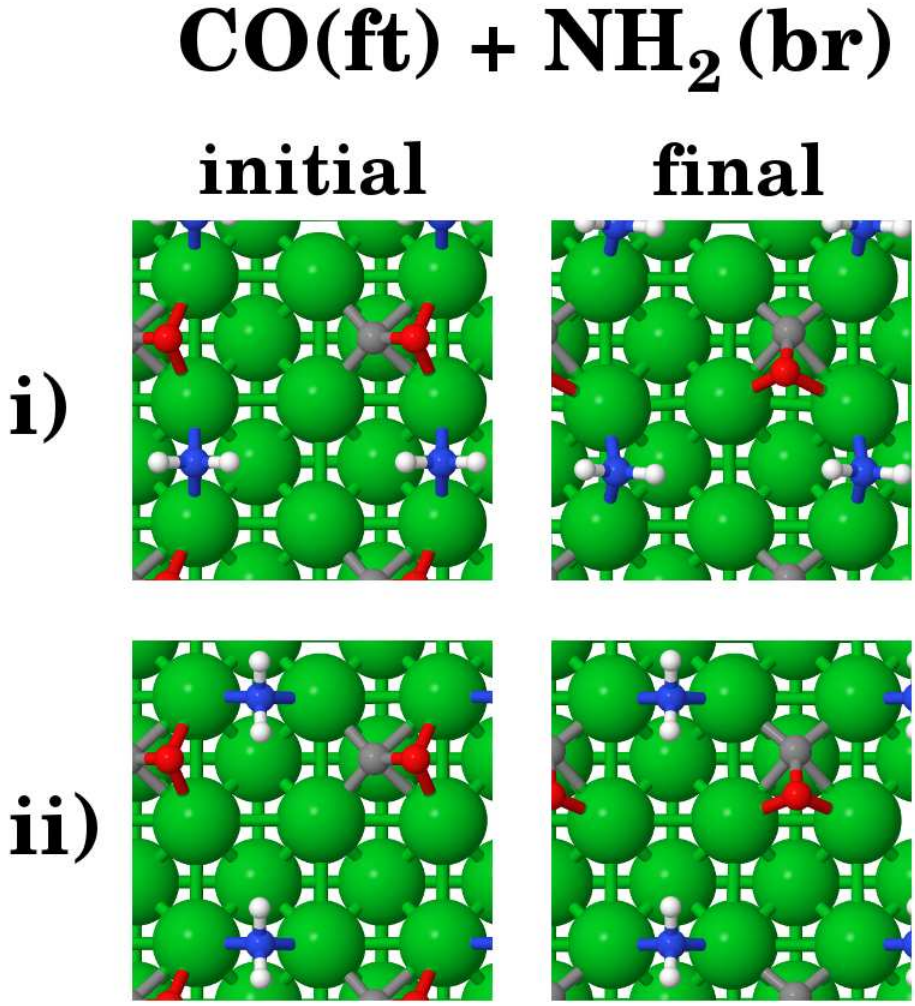

Figure B.11: The initial and final structures for the geometry optimization of (0.25 ML + 0.25 ML) $CO(ft)$ + $NH_2(br)$ on Fe(100).

relaxes so that the final structure has CO in a vertical bonding configuration within the fh site. As mentioned in Chapter 6, the *cis* configurations were both significantly less stable than the *trans* configuration. The vibrational analysis for CO and NH in the *cis* configuration shown in Figure B.12 *i* were however found to be a stable structure (i.e. it contained no imaginary frequencies), while the *cis* configuration of Figure B.12 *ii* contained one imaginary frequency. This frequency is likely to indicate that CO is passing through a transition state, which would finally results in a local minimum where the geometric configuration is that of the *cis* formation shown in Figure B.12 *i*.

CO + N on Fe(100) geometries

The initial and final structures considered for the coadsorption of CO and N on Fe(100) is given Figure B.13. These structures are essentially equivalent to what was discussed for CO + NH on the Fe(100) surface.

Heat of mixing (CO + NH$_X$)

As mentioned in Chapter 6, the geometry optimization for CO coadsorbed with N is essentially equivalent to the CO + NH calculations. The only difference is that the relaxation of CO coadsorbed with NH in a *cis* configuration where the oxygen faces the nitrogen atom (as indicated in Fig. B.13: *iii*) does not end with a vertical CO bond, but essentially converts to the *cis* configuration as shown in Fig. B.13: *ii*)

Since the average adsorption energies with either two CO or NH$_x$ adsorbates on the Fe(100) are compared to the coadsorbed energy with one CO and one NH$_x$ adsorbate on the $p(2 \times 2)$ unit cell, the resulting comparison can be drawn as shown in Figure B.14.

Additional LDOS and electron redistribution plots

In Figure B.15 the PDOS for CO/NH$_2$ (*Top*) and CO/NH (*trans*, *Bottom*) is superimposed and magnified to illustrate the interaction between these adsorbates on the surface. As mentioned in Chapter 6 this combination of their atomic orbitals can lead to both a stabilizing or destabilizing effect.

The individual electron density redistribution plots for CO in the ft and ft' configurations

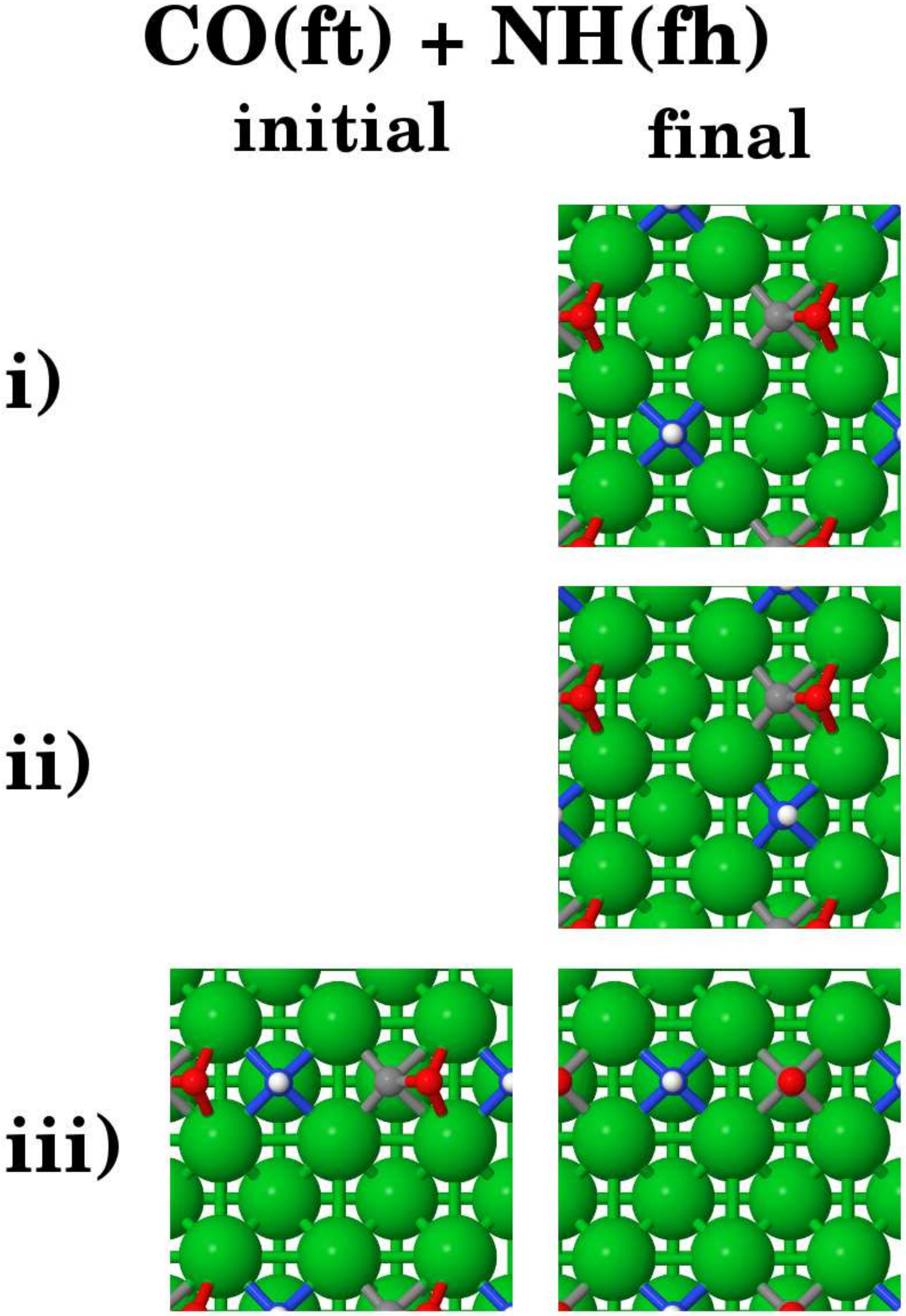

Figure B.12: The initial and final structures for the geometry optimization of (0.25 ML + 0.25 ML) $CO(ft)$ + $NH(fh)$ on Fe(100). Note that only final figures for the $CO + NH$ in *cis* and *trans* configuration that does not change significantly from the initial structure.

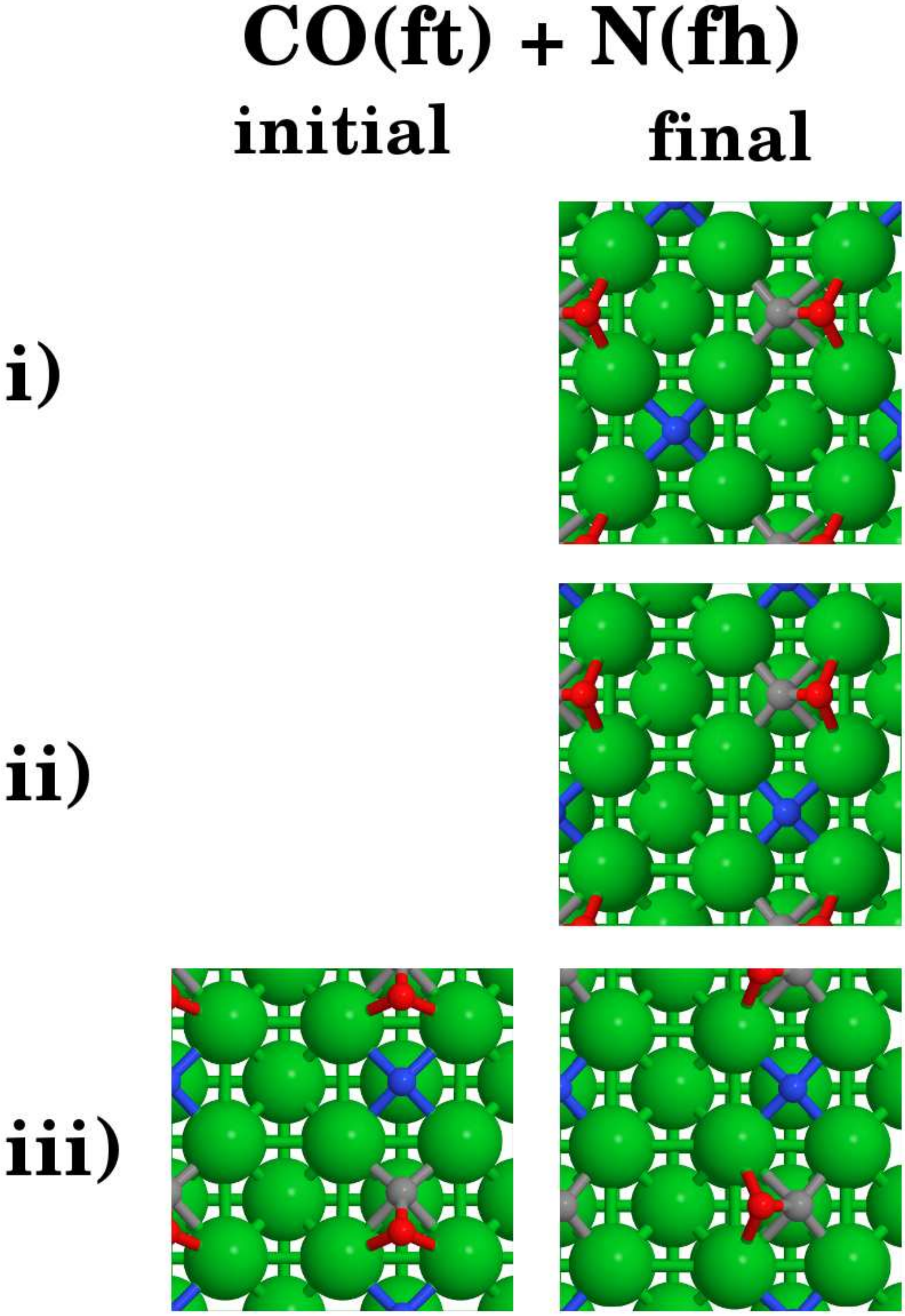

Figure B.13: The initial and final structures for the geometry optimization of (0.25 ML + 0.25 ML) $CO(ft)$ + $N(fh)$ on Fe(100). Note that only final figures are presented for the $CO + N$ in *cis* and *trans* configurations that does not change significantly from the initial structure.

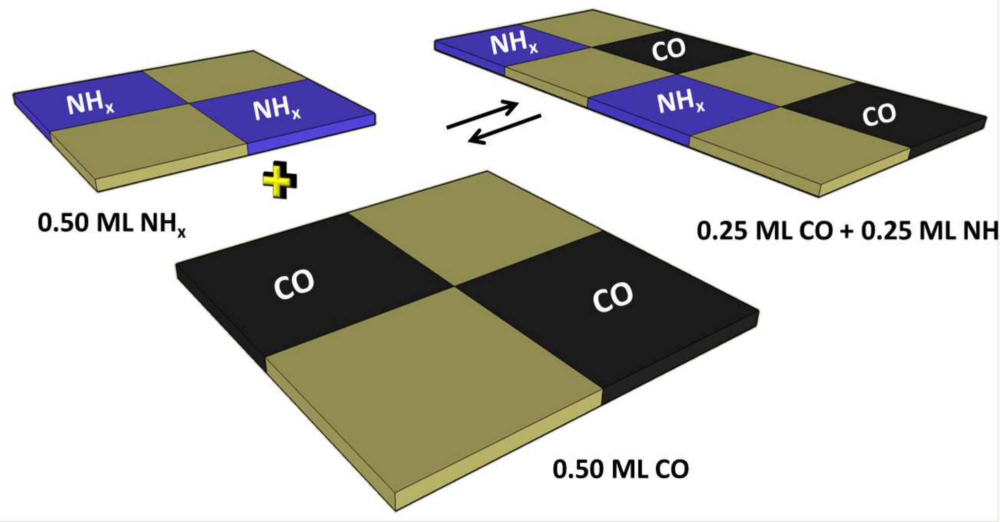

Figure B.14: A schematic is given to illustrate the mixing reactions considered for the CO and NH$_x$ (x = 3, 2, 1, 0) on the Fe(100) surface. (GGA-RPBE, E$_{cut}$ $\leq$ 400 eV, k-points: 5x5x1)

are presented in Figures B.16 and B.16 respectively. It is difficult to see any major difference between CO bonded in these configurations. In the CO(ft') configuration, the O just seems more directed towards the one Fe atom, which could be expected.

Another way of viewing the direct interaction between Fe and the one oxygen atom can be seen if a plane is cut through the Fe−O bonds, as shwon in Figure B.18

The electron redistribution plot of NH$_2$ individually adsorbed in a bridge site on the Fe(100) surface is presented in Figure B.19. From the topographic view obtained after cutting through the plane, one can see that a unique hybridization is formed between NH$_2$ and the Fe(100) surface, compared to that of the other NH$_x$ surface species (discussed in Chapter 6).

CO dissociation in the presence of NH$_x$ on Fe(100)

The initial, transition and final state structures used for the calculation of the CO activation barriers are given in Figures B.20 - B.23 for the CO + NH$_x$ coadsorbates. As discussed in Chapter 6, minimal changes can be seen when compared to CO dissociation in the absence of NH$_x$ (see Chapter 5). The imaginary vibrational mode, C−O bond distance, activation barriers and heat of reactions are reported in the tables below the figures.

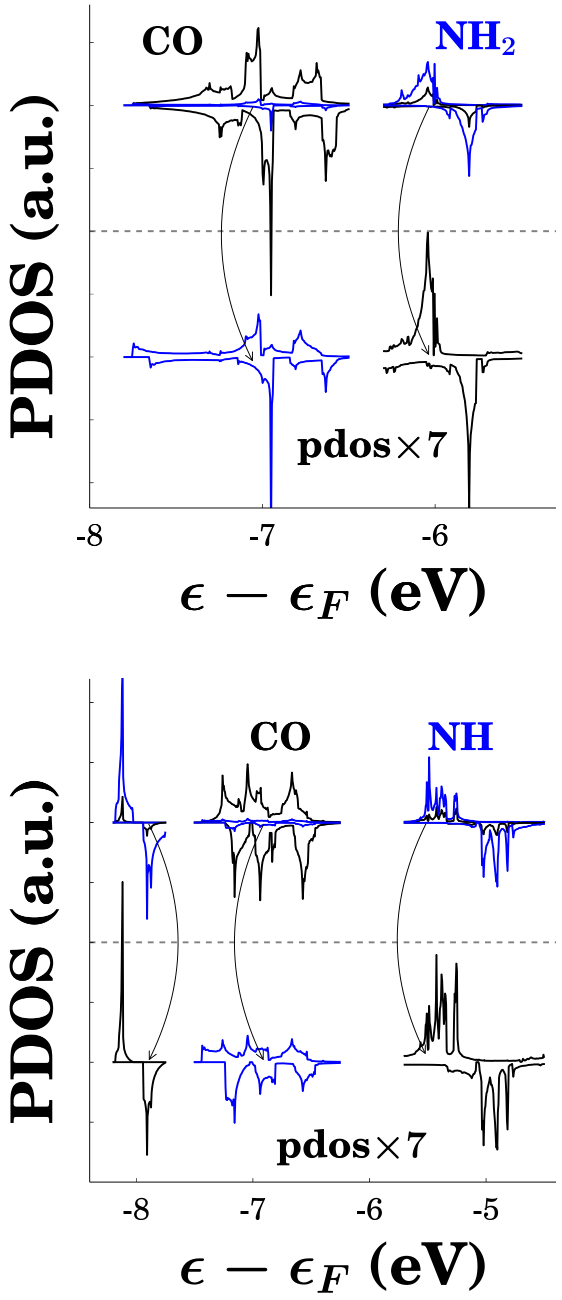

Figure B.15: The PDOS for CO(*ft*) + NH$_2$(*br*) (*Top*)/NH (*Bottom*) on the Fe(100) surface is plotted as a function of the energy below the Fermi level ($\epsilon_F - \epsilon$). Scaling of the PDOS at the bottom part of the figure illustrates the linear combination of their individual orbitals at certain energy levels.

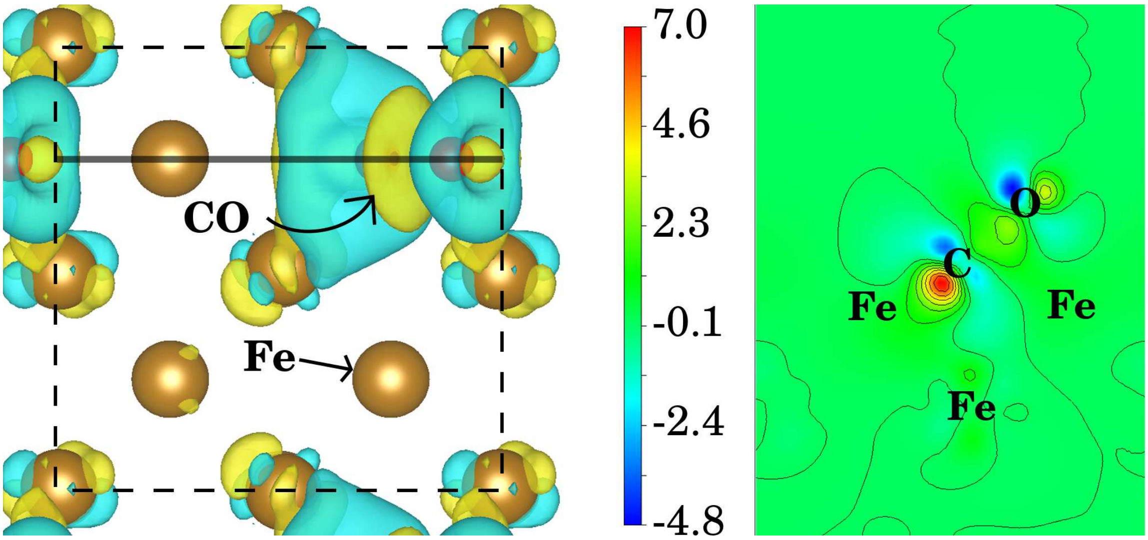

Figure B.16: (*Left:*) Top view for the electron redistribution plot when CO(ft) adsorbs on Fe(100) at a $\theta = 0.25$ ML coverage. The line indicates the position of the plane that cuts through CO and the surface to produce the (*Right:*) topographic view. Electron accumulation and depletion is shown in y ellow and blue respectively.

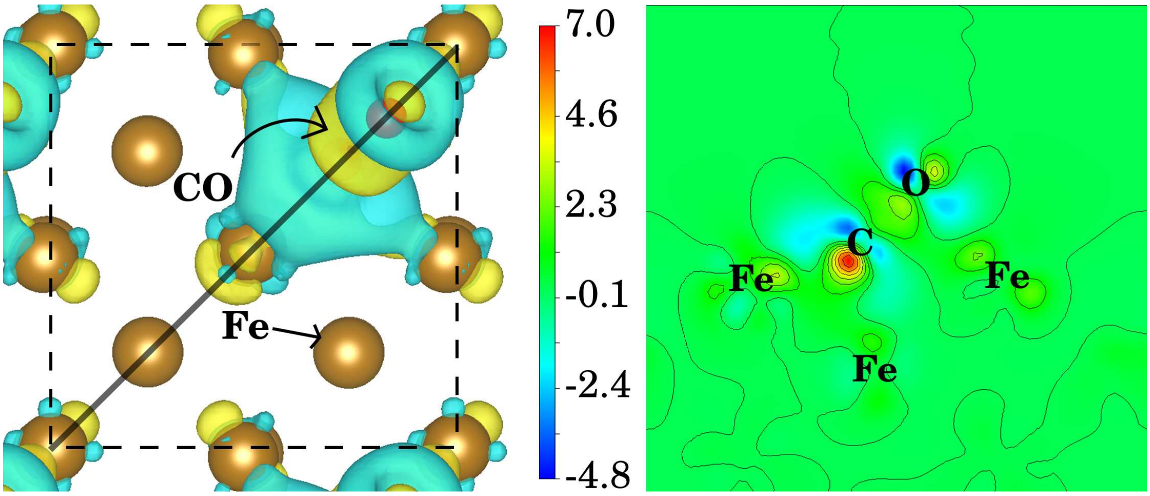

Figure B.17: (*Left:*) Top view for the electron redistribution plot when CO(ft') adsorbs on Fe(100) at a $\theta = 0.25$ ML coverage. The line indicates the position of the plane that cuts through CO and the surface to produce the (*Right:*) topographic view. Electron accumulation and depletion is shown in y ellow and blue respectively.

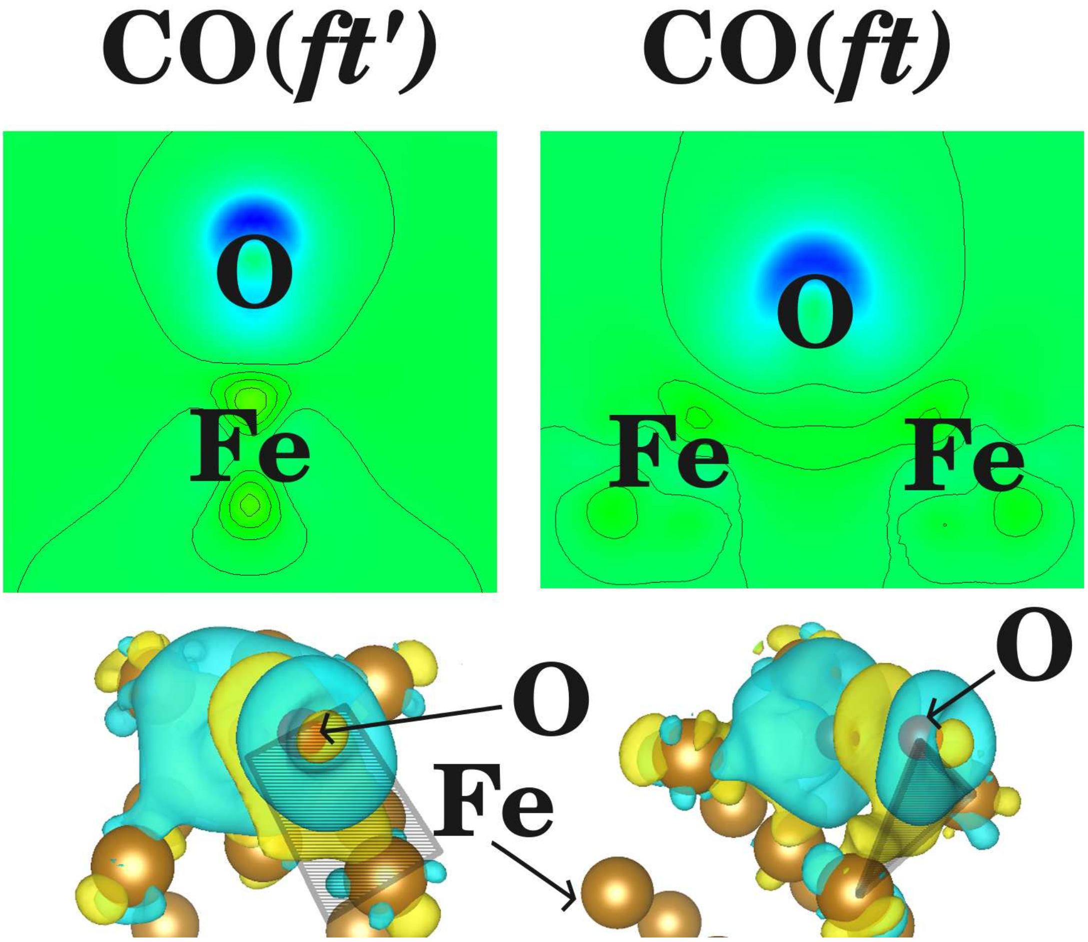

Figure B.18: *Top:* The electron redistribution plots for CO adsorbed in the *ft* or *ft'* orientations when cut through planes that contains the Fe-O bonds as indicated in the bottom part of the figure. Electron accumulation and depletion is shown in blue and yellow respectively

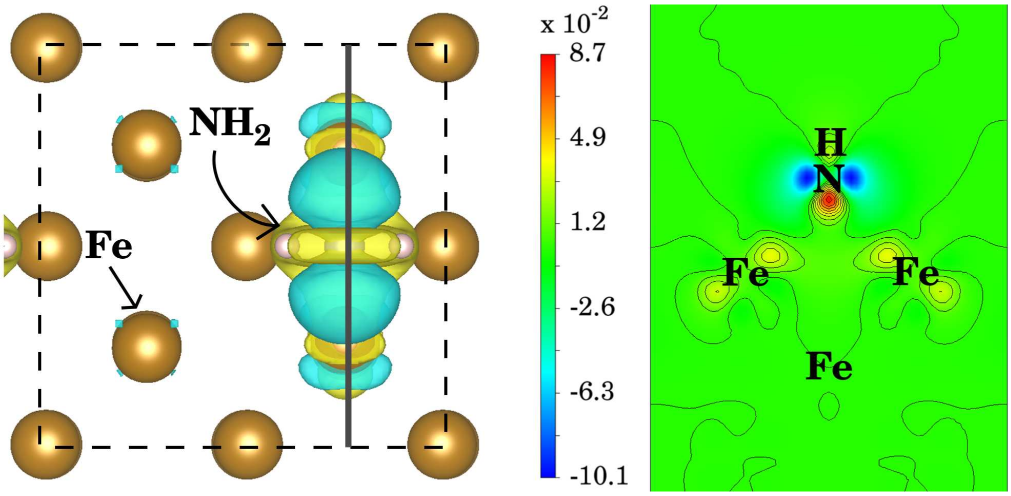

Figure B.19: (*Left:*) Top view for the electron redistribution plot when NH_2 adsorbs on Fe(100) at a θ = 0.25 ML coverage. The line indicates the position of the plane that cuts through NH_2 and the surface. Electron accumulation and depletion is shown in yellow and blue respectively. (*Right:*) Topographic view of cut through the plane.

Trends in CO activation barriers

One can postulate that certain indicators such as the stretching vibrational frequency ($v(CO)$) or the bond length (d_{CO}) of the CO adsorbate in the initial state of the CO dissociation reaction can be used to predict the activation barrier (E_a). That is, if the bond is weaker to start with, it may cost less energy for the bond breaking process. As mentioned in Chapter 6, this did not seem to be the case. In an attempt to further probe this theory, the activation barrier is plotted (in Figure B.24) as a function of the stretching frequency of the CO bond in the fourfold tilted configuration, with and without $\theta = 0.25$ ML NH_x adsorbates coadsorbed on the Fe(100) facet. It is clear from this figure that such a relation can not be made based on this set of calculations. The coefficient of determination ($R^2 = 0.10$), which serves as a statistical measure of the predictability of the dependent variable after a linear regression analysis, highlights the inability of the CO vibrational frequency of the initial state to predict the activation barrier. Even though the results for the CO bond length (d_{CO}) is not explicitly presented here, the results intuitively yields the same conclusion, that is that no clear trend is observed between the activation barrier for the CO dissociation reaction and the CO bond length of the initial

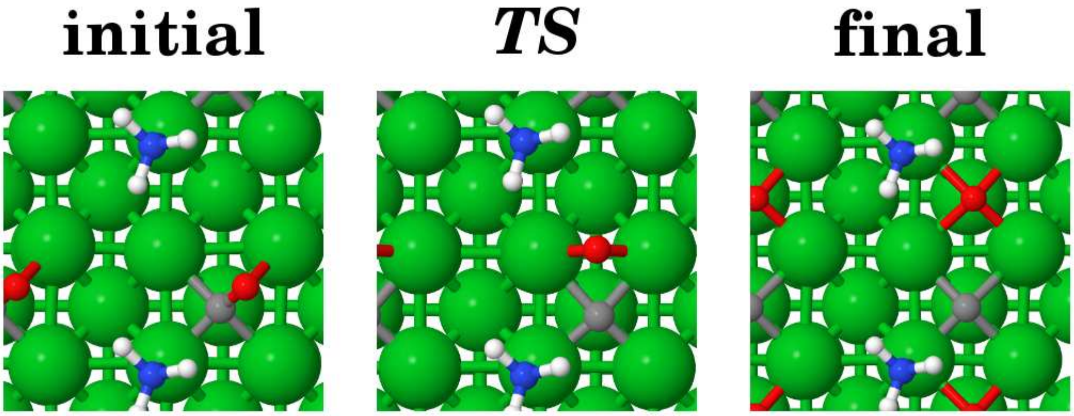

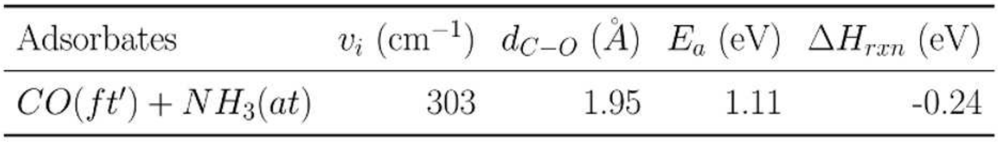

Adsorbates	v_i (cm^{-1})	d_{C-O} ($\mathring{A}$)	E_a (eV)	ΔH_{rxn} (eV)
$CO(ft') + NH_3(at)$	303	1.95	1.11	-0.24

Figure B.20: Top view for the (initial, transition state and final) structures used and calculated for the CO dissociation reactions on a Fe(100) surface covered with $\theta = 0.25$ ML NH_3. Additional information (activation energy (E_a), heat of the reaction (ΔH_{rxn}), imaginary frequency (v_i) and C-O bond distance (d_{C-O})) is tabulated below. ($E_{cut} \leq 400$ eV, k-points: 5x5x1)

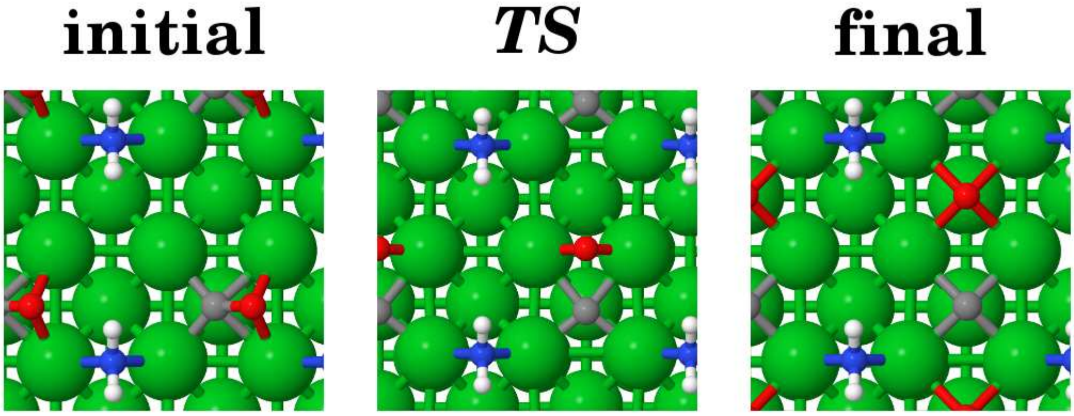

Adsorbates	v_i (cm^{-1})	d_{C-O} ($\AA$)	E_a (eV)	ΔH_{rxn} (eV)
$CO(ft) + NH_2(br)$	299	1.99	1.07	-0.21

Figure B.21: Top view for the (initial, transition state and final) structures used and calculated for the CO dissociation reactions on a Fe(100) surface covered with $\theta = 0.25$ ML NH_2. Additional information (activation energy (E_a), heat of the reaction (ΔH_{rxn}), imaginary frequency (v_i) and C-O bond distance (d_{C-O})) is tabulated below. ($E_{cut} \leq 400$ eV, k-points: 5x5x1)

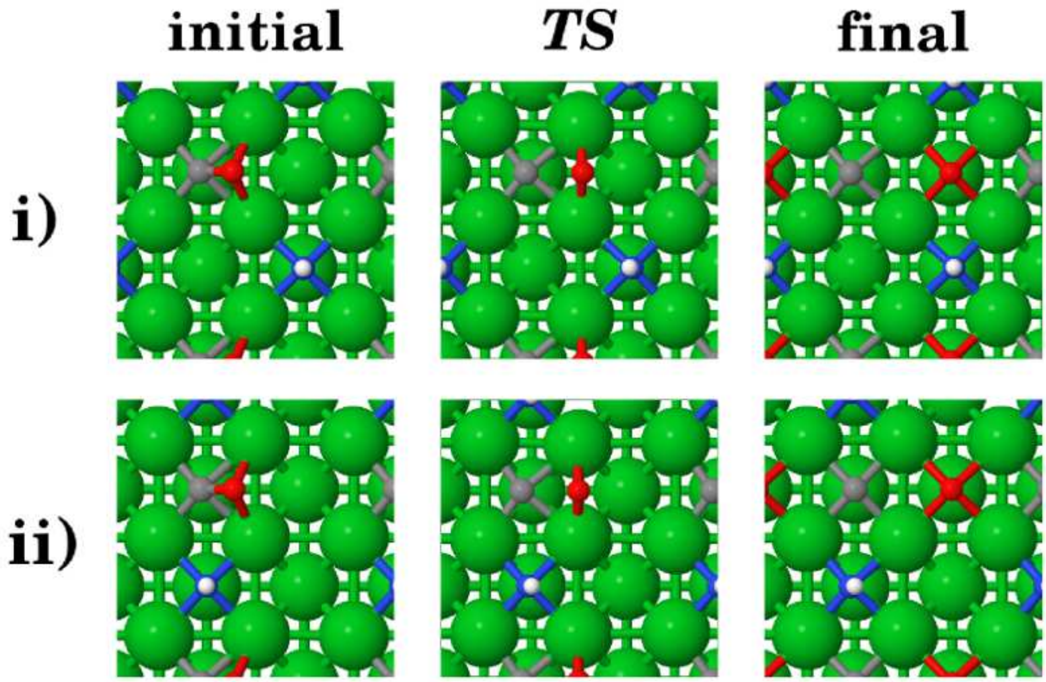

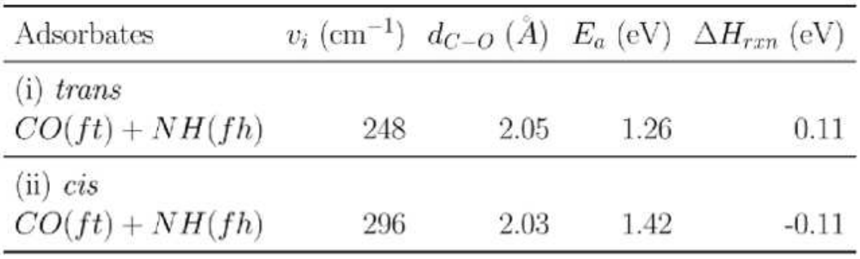

Adsorbates	v_i (cm^{-1})	d_{C-O} (Å)	E_a (eV)	ΔH_{rxn} (eV)
(i) *trans* $CO(ft) + NH(fh)$	248	2.05	1.26	0.11
(ii) *cis* $CO(ft) + NH(fh)$	296	2.03	1.42	-0.11

Figure B.22: Top view for the (initial, transition state and final) structures used and calculated for the CO dissociation reactions with the NH adsorbed in the (*i:*) *trans* (*ii:*) *cis* configurations. Additional information (activation energy (E_a), heat of the reaction (ΔH_{rxn}), imaginary frequency (v_i) and C-O bond distance (d_{C-O})) is tabulated below. ($E_{cut} \leq 400$ eV, k-points: 5x5x1)

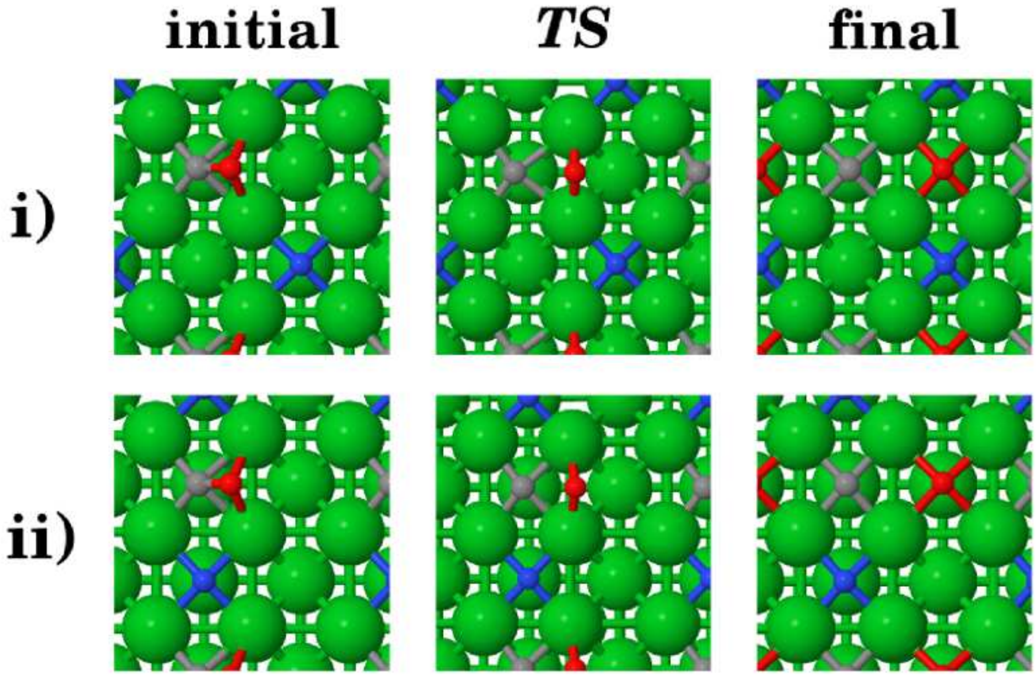

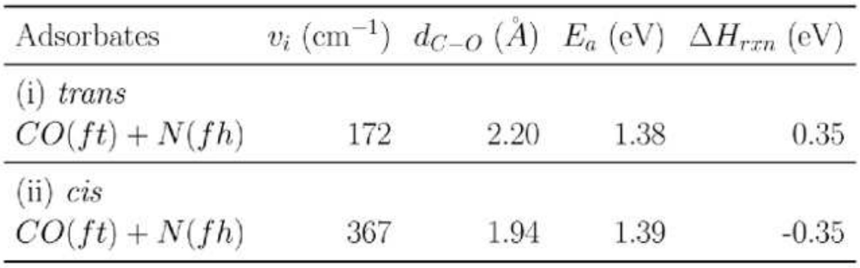

Adsorbates	v_i (cm^{-1})	d_{C-O} (Å)	E_a (eV)	ΔH_{rxn} (eV)
(i) *trans*				
$CO(ft) + N(fh)$	172	2.20	1.38	0.35
(ii) *cis*				
$CO(ft) + N(fh)$	367	1.94	1.39	-0.35

Figure B.23: Top view for the (initial, transition state and final) structures used and calculated for the CO dissociation reactions with the N adsorbed in the (*i:*) *trans* (*ii:*) *cis* configurations. Additional information (activation energy (E_a), heat of the reaction (ΔH_{rxn}), imaginary frequency (v_i) and C-O bond distance (d_{C-O})) is tabulated below. (E$_{cut}$ $\leq$ 400 eV, k-points: 5x5x1)

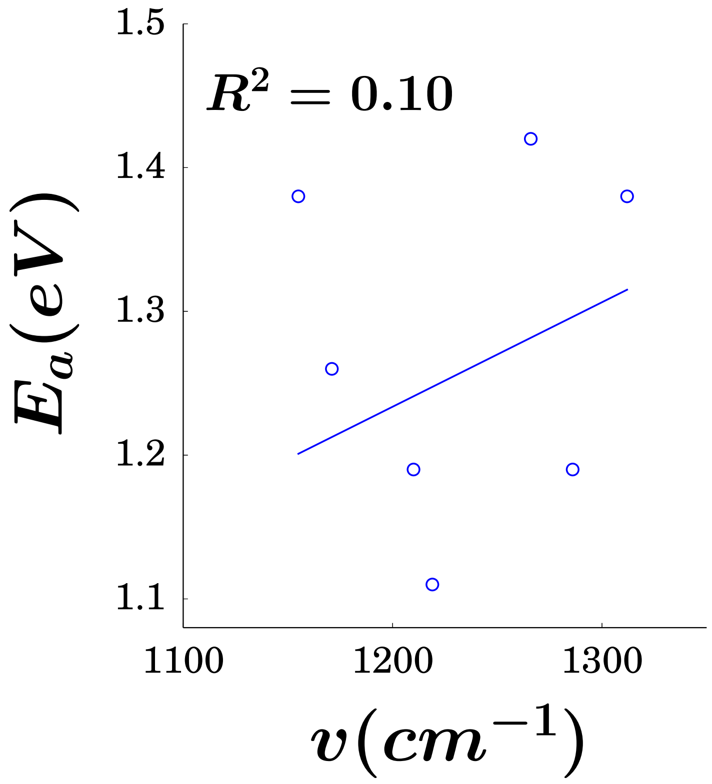

Figure B.24: The CO activation barriers (E_a) is plotted as a function of the stretching frequency of CO ($v(CO)$) in the initial state for the individually adsorbed (CO(ft/ft') and coadsorbed (CO + NH_x) configurations on the Fe(100) surface.

structures.

A second plausible trend that could be used to predict the activation barrier is through a Brønsted-Evans-Polanyi (BEP) relation, which dictates that a linear relationship exists between the reaction energies (i.e. E_{rxn} for CO → C + O) and the transition state energies (E_{TS}) on multiple catalytic surfaces [9]. It has been shown for the CO dissociation reaction on various transition metal surfaces that the energy calculated for the transition state structure will scale with the energy of the final state structure when referenced to gas phase CO [9]. The CO dissociation reaction is thus considered a late transition state due to the fact that the mixing of the adsorbate with the surface at the transition state is similar to that of the final state. To investigate the possibility of extracting a BEP-type relationship between the transition state structure and the CO dissociation reaction on the clean Fe(100) and modified surfaces (NH_x

+ Fe(100)), a similar analysis is presented here. Eq.'s B.30 and B.31 is used to calculate the transition state energy (E_{TS}) and the energy for the reaction (E_{rxn}) respectively,

$$E_{TS} = E_{TST} - E_{(NH_x)+Fe} - E_{CO(g)} \tag{B.30}$$

$$E_{rxn} = E_{(NH_x)+C+O+Fe} - E_{(NH_x)+Fe} - E_{CO(g)} \tag{B.31}$$

where E_{TST} is energy calculated for the transition state, $E_{(NH_x)+Fe}$ is the energy for the clean slab, or the slab with NH$_x$ at its geometry optimized structure, $E_{(NH_x)+C+O+Fe}$ is the energy for the dissociated product on the clean or NH$_x$ covered surface and $E_{CO(g)}$ is the energy for CO in the gas phase. (Note that TST and TS is used to distinguish between the energy calculated for the transition state structures and the transition state relative to the gas phase respectively.) The resulting E_{TS} values is plotted as a function of E_{rxn} values in Figure B.25. Even though it surely seems as if a better trend may exist within the BEP relationship, the R^2 value of 0.37 would suggest that this is not the most accurate way for predicting the activation barrier when NH$_x$ adsorbates are present on the surface.

One possibility for the lack of predictability via a BEP relationship, could be that the lateral interactions of the initial state still exists to some extent in the transition state. In Eq. B.30 the transition state energies (E_{TS}) is modified (E^{ω}_{TS}) to include the lateral interactions (ω) that was calculated for the initial state structures.

$$E^{\omega}_{TS} = E_{TS} + \omega \tag{B.32}$$

The lateral interactions employed in Eq. B.32 is simply the heat of mixing values calculated between CO and NH$_x$ at $\theta = 0.25$ ML in Chapter 6 ($E^{\theta=0.25ML}_{mix} = \omega$). From the modified BEP relationship (see Figure B.26), it thus seem that a better fit is generated ($R^2 = 0.59$). For the coadsorbed structures of CO + NH/N in the *trans* configuration, the heat of mixing is favorable ($\Delta E_{mix} = -0.21$ and -0.17 eV respectively) which suggests attractive lateral interactions. The endothermic heats for the CO dissociation reactions ($\Delta H = 0.11$ and0.35 eV for NH and N respectively) that was in turn calculated for these adsorbates in the final state (NH/N + C + O + Fe) suggests that these configurations now contain repulsive lateral interactions. The opposing lateral interactions in the initial and final states and the results presented in Figures

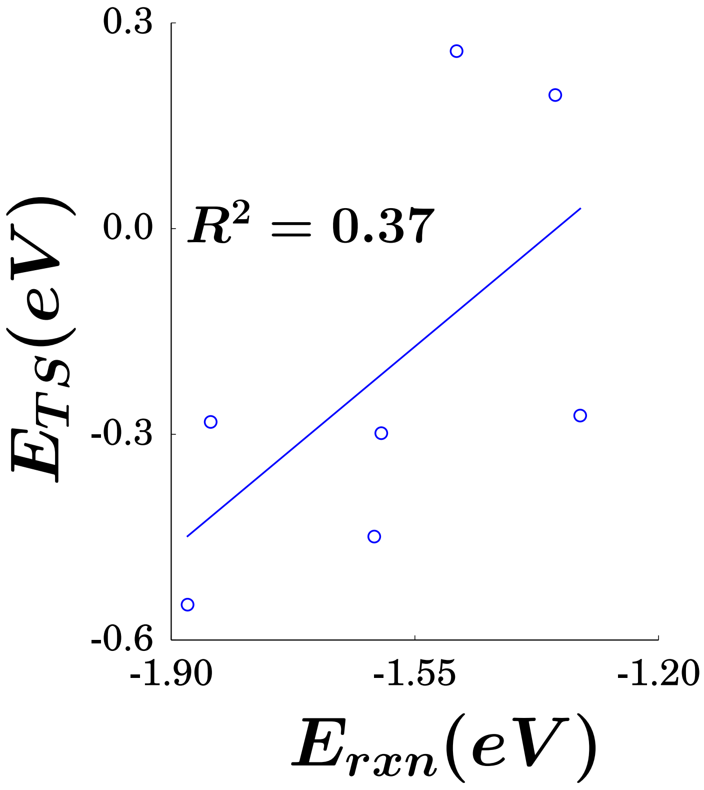

Figure B.25: BEP relation betweenship the transition state and final state structures of the clean and NH_x covered surfaces. The $R^2 = 0.37$ shows that the BEP relation exhibits a better trend than the analysis for the vibrational frequency, but is still not noteworthy.

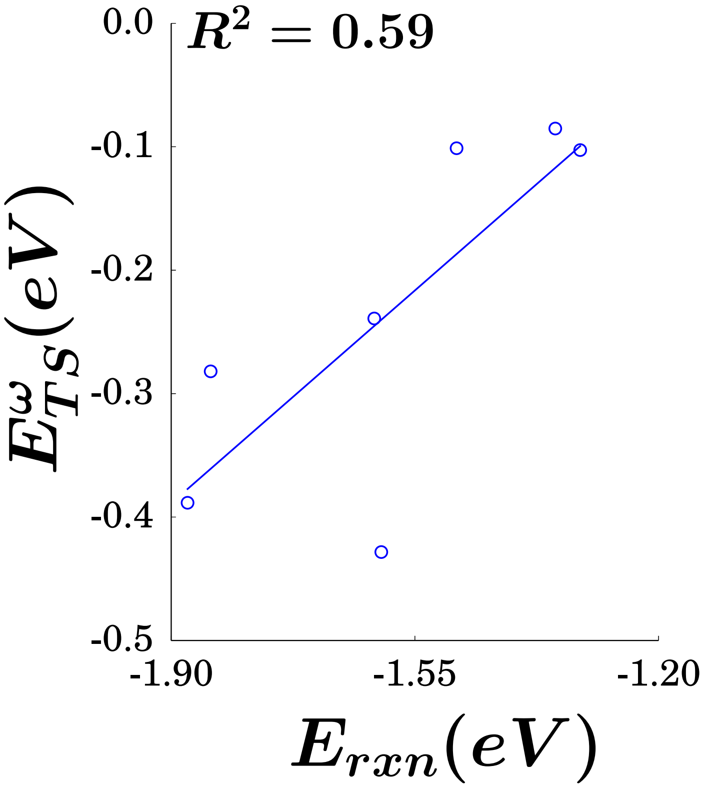

Figure B.26: A modified BEP relationship between the transition state and final state structures of the clean and NH_x covered surfaces is generated by adding the lateral interactions calculated for the initial state (E_{TS}^{ω}). The $R^2 = 0.59$ suggests that the BEP relationship is improved to some extent by accounting for the lateral interactions.

B.25 and B.26 therefore suggests that the deviation from the expected BEP relationship is due to the presence of lateral interactions at the transition state that resemble those of the initial state.

REFERENCES

[1] H.J. Monkhorst and J.D. Pack. *Phys. Rev. B*, 13:5188–5192, 1976.

[2] B. Hammer, L.B. Hansen, and J.K. Nørskov. *Phys. Rev. B*, 59:7413–7421, 1999.

[3] J.P. Perdew, J.A. Chevary, S.H. Vosko, K.A. Jackson, M.R. Pederson, D.J. Singh, and C. Fiohais. *Phys. Rev. B*, 46:6671–6687, 1992.

[4] D.E. Jiang and E.A. Carter. *J. Phys. Chem. B.*, 110:22213–22219, 2006.

[5] K.J. Laidler. *Chemical Kinetics*. Harper & Row, New York, 1987.

[6] H. Li and J.H. Jensen. *Theor. Chem. Acc.*, 107:211–219, 2002.

[7] M. Grunze, F. Bozso, G. Ertl, and M. Weiss. *App. of Surface Science*, 1:241–265, 1978.

[8] S.C. Yeo, S.S. Han, and H.M. Lee. *J. Phys. Chem. C*, 118:5309 – 5316, 2014.

[9] S. Wang, B. Temel, J. Shen, G. Jones, L.C. Grabow, F. Studt, T. Bligaard, F. Abild-Pedersen, C.H. Christensen, and J.K. Nørskov. *Catal. Lett.*, 141:370–373, 2010.

Appendix C

Supplementary results: Experimental

Supplementary information: Chapter 4

Equipment used for experimental studies

Ampoule delivery system

In the experimental part of this thesis, the ampoule system described by Schulz [1] is used to analyze the organic FTS products. As mentioned in Chapters 4 and 7, even though this technique is ideal for most FTS products, our analysis shows that a significantly lower concentration for aliphatic carboxylic acids and amines are detected when analyzing ampoules in this way. This could be due to their interaction with the glass used for the ampoules.

Reactor commissioned for NH_3 co-feeding reactions

The addition of NH_3 during FTS presented unique problems, which called for the commissioning of a reactor specifically for the use of these experiments. NH_3 is a corrosive gas and all analytical tools, such as pressure indicators, valves etc. had to withstand these properties of the new feed gas. In addition, the possibility of forming ammonium bicarbonate had to be anticipated. The aforementioned problem was circumvented by accurate temperature control, so that the solid material only formed in the desired location. The reactor was designed to be connected to

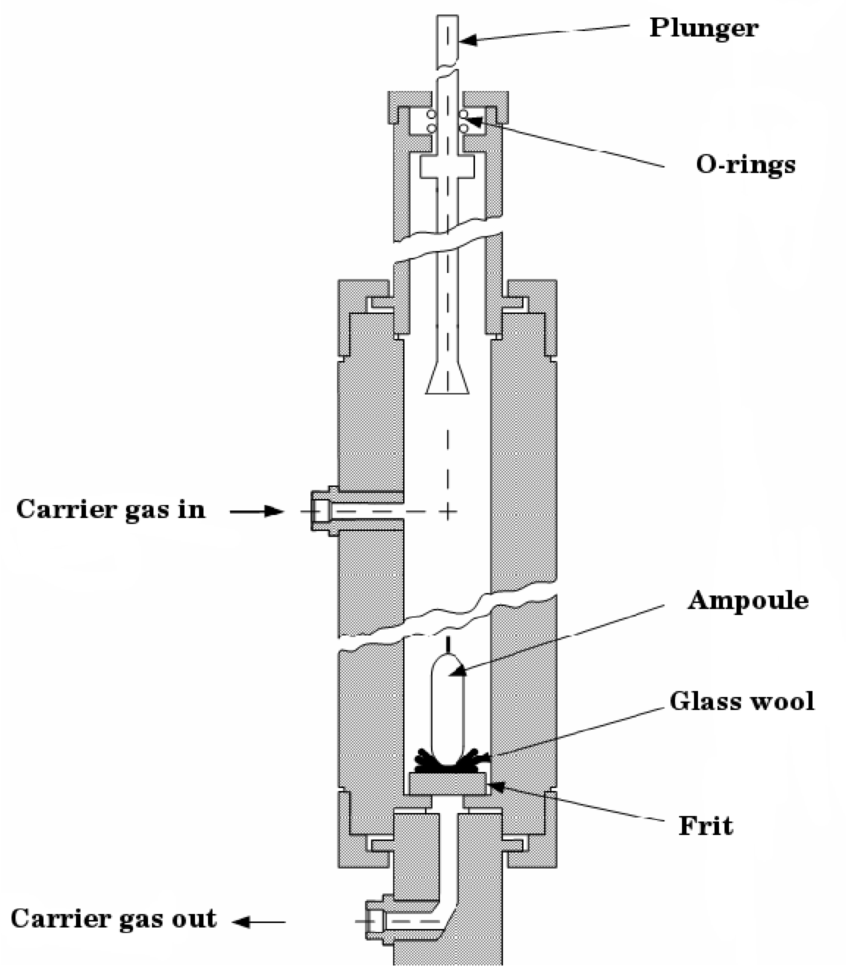

Figure C.1: A schematic representing the important components of the ampoule ”crushing” device. (Figure redrawn from Ref. [1])

Figure C.2: A schematic showing the design of the wax leveler used to avoid catalyst particles moving downstream and maintining liquid/gas phase levels.

an on-line GC-FID and GC-TCD, and will be fitted to an on-line GC×GC-TOF/FID system for future work. In the methodology chapter (Chapter 4) a detailed discussion and the full schematic of the reactor system is given, while a picture of the actual reactor can be seen in Figure C.2.

In Chapter 4, reference is made of the wax leveling system. In Figure C.3 a schematic of the attachment at the exit of the slurry phase reactor is given, which illustrates how catalyst particles were restricted from moving downstream and in addition maintaining the liquid/gas-phase volumes constant. On the left of the figure, it can be seen how the products that are present in the head space are allowed to exit the reactor. A 2 μm frit is used to restrict the flow of the catalyst particles.

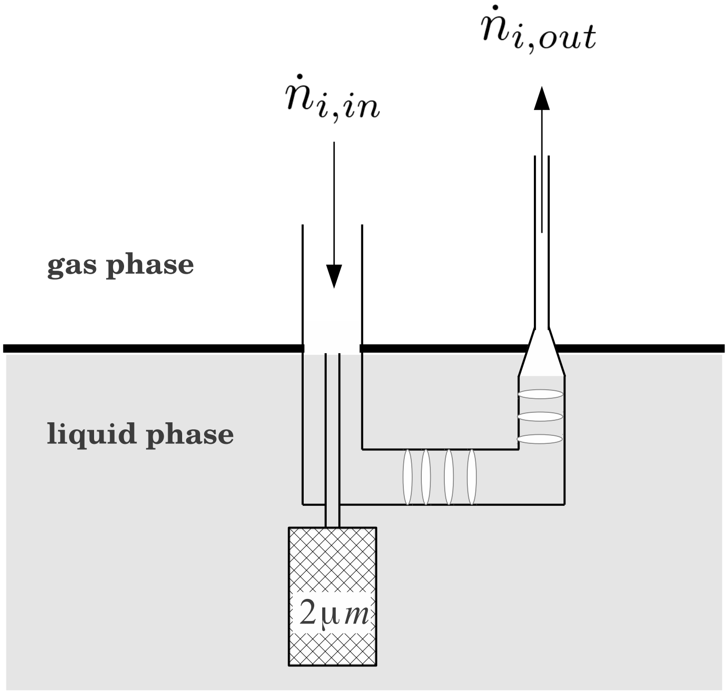

Figure C.3: A schematic showing the design of the wax leveler used to avoid catalyst particles moving downstream and maintaining liquid/gas phase levels.

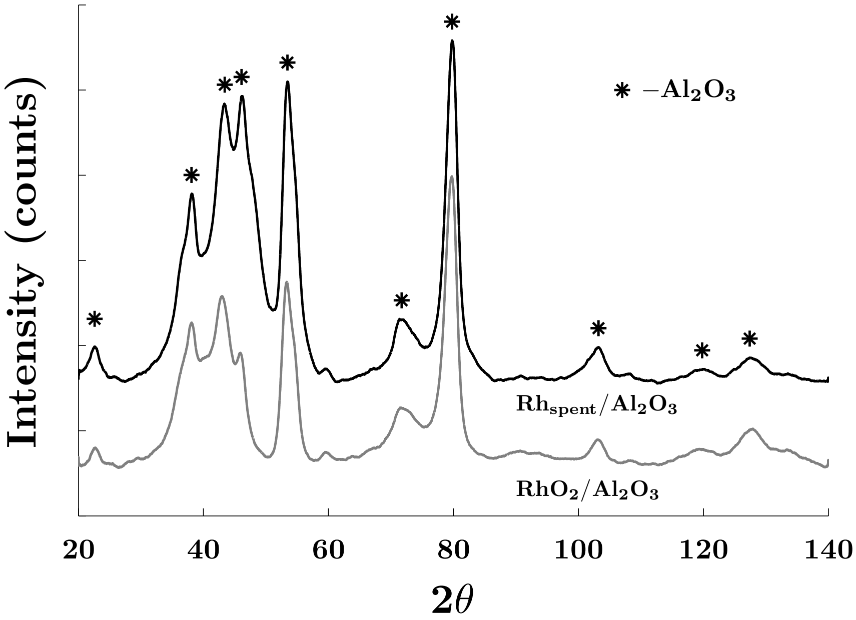

Figure C.4: The x-ray diffractograms obtained after analyzing the prepared Rh oxide catalyst, superimposed with the spent Rh/Al_2O_3 catalyst.

Characterization of catalysts

As mentioned in Chapter 9, the analyses of the bulk phase of the Rh-based catalyst was compromised by its support, which can be seen in Figure C.4.

Separation of NH_3 from other FTS inorganic gases

The separation of NH_3 from the other permanent gases is not straightforward. A combination of cryogenic cooling and a collumn (7 meters in length) packed with a specific packing material (Poropak Q) gave the best results to achieve adequate separation. Figure C.5 shows the resulting chromatogram obtained when optimizing the gas chromatograph in order to gain good separation for NH_3 from the other permanent gases. Unfortunately for most of the slurry phase reactions reported in this work, a side reaction (formation of ammonium carbamate) depleted the unreacted NH_3, rendering its analysis below the limits of detection.

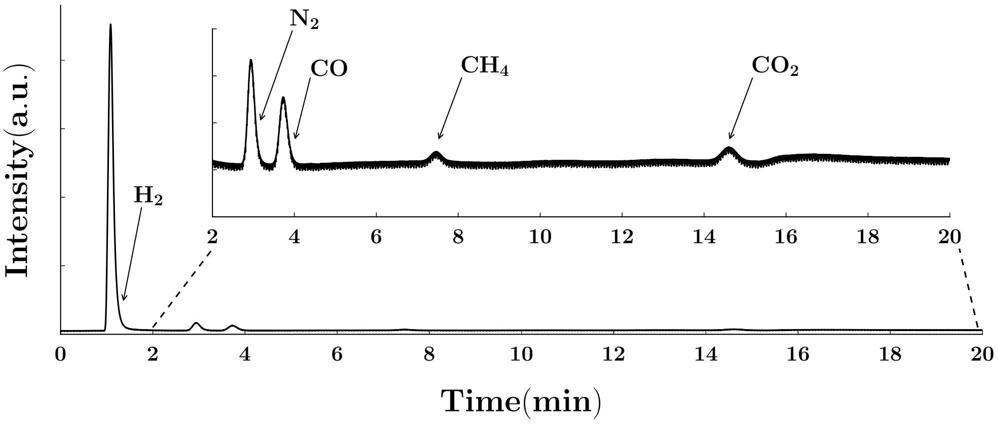

Figure C.5: An older chromatograph was used for early experiments and attempts to separate NH_3 from the other important inorganic gases (H_2, CO, CO_2, CH_4 and N_2)

Identification of organic compounds via GC-FID

GC×GC in 1-D mode

In Chapter 4, the methodology employed for the identification of the FTS products is discussed. One of the techniques used was to operate the LECO Pegasus 4D (comprehensive gas chromatography or GC×GC system) in one dimensional mode. In Figure C.6 an example of a chromatogram is presented that was obtained after analyzing an ampoule sample containing FTS products from an Fe-catalyzed reaction (SPR, T = 250 ℃, P = 5 bar(NTP), GHSV = 2250 ml/hr/g_{cat}, $H_2/CO = 2$). It is pointed out in Chapter 4 that the GC×GC system was not equipped with an ampoule breaker system. The ampoules thus had to be injected manually and at room temperature, which in turn leads to a loss of higher hydrocarbon products. In Figure C.6 this effect can be seen in the region where the C_9 (e.g. 1-nonene and *n*-butane) products elute. Kovats indices and information from previous studies [3, 4] were therefore used to aid in the identification of the FTS products.

Kovats indices

Kovats indices (KI) were used to identify the products that were detected during GC-FID analysis of FTS product samples. The methodology is described in Chapter 4. In Table C.1 a

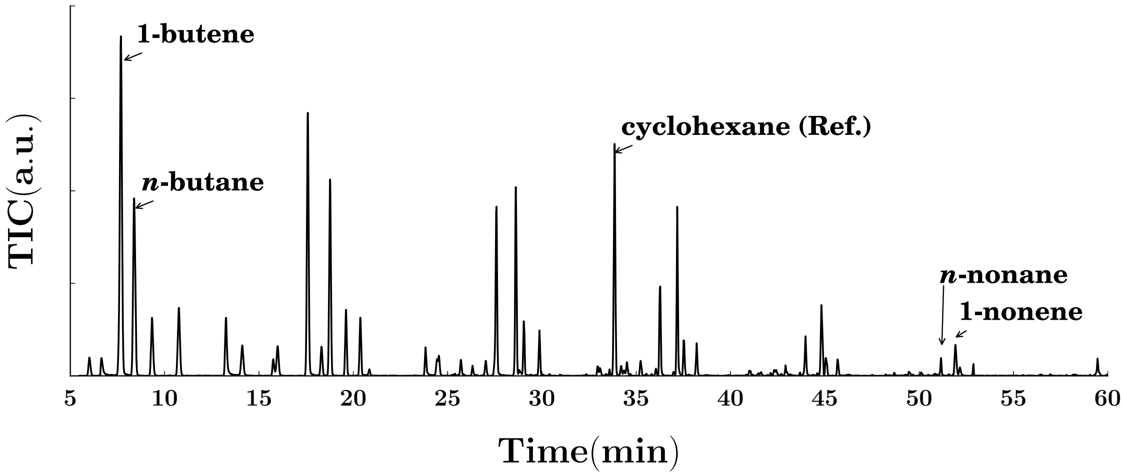

Figure C.6: An example of a GC-TOF chromatogram obtained after analyzing an ampoule sample with the LECO Pegasus 4D in 1-D mode.

table is presented with the Kovats indices obtained after analysis of an Fe-based FTS reaction (SPR, T = 250 ℃, P = 5 bar(NTP), GHSV = 2250 ml/hr/g_{cat}, $H_2/CO = 2$).

In Figure C.7 a chromatogram obtained after GC-FID analysis of a FTS product is presented with labels. These product identification were achieved via the use of Kovats indices, information from previous studies as well as GC-MS analyses. In order facilitate reading the figure, the chromatogram was subdivided into enlarged subplots.

Response factors for quantification

To compensate for a weaker FID response obtained by compounds containing carbon atoms bonded to hetero atoms (e.g. N and O atoms), compared compounds containing only carbon-carbon bonds, Kaisers [5] methodology is used. See Chapter 4 for additional information w.r.t. this technique. In Table C.4 the response factors (f_i) used for selected compounds during quantification of the FTS products are tabulated.

Table C.1: Kovats indices of products produced in this work.

Group	**Name**	**KI**
lin par	methane	100.0
lin olef	ethene	163.9
lin par	ethane	200.0
lin olef	propene	290.3
lin par	propane	300.0
br par	2-Me-propane	367.8
n-ROH	methanol	379.5
lin olef	1-butene	392.3
lin par	**n-butane**	400.0
lin int olef	2-butene-trans	413.3
lin int olef	2-butene-cis	430.9
n-ROH	Ethanol	456.8
lin int olef	3-Pentene_E	464.6
RCHO + RCOR	propanone + acetone	478.3
br par	Butane, 2-methyl	480.1
lin olef	1-pentene	491.9
lin olef	2-pentene_E	497.0
lin par	**n-pentane**	500.0
lin int olef	t-pentene	505.4
lin int olef	c-pentene	510.2
oxygenate	Acetic acid, methyl ester	522.6
br olef	2-butene, methyl	524.9
n-ROH	1-propanol	556.6
br olef	1-pentene, 4-methyl	562.5
br olef	1-pentene, 2-methyl	574.5
br olef	2-pentene, 4-methyl	575.7
RCOR	2-butanone	580.2
br olef	1-pentene,3-methyl	586.4
lin olef	1-hexene	591.3
lin par	**n-hexane**	600.0

Table C.2: Kovats indices of products produced in this work. (Continued)

Group	**Name**	**KI**
lin int olef	3-hexene	601.5
lin int olef	t-hexene	603.5
lin int olef	c-hexene	610.2
br olef	2-pentene, 3-methyl	623.1
RCN	Butanenitrile (app)	641.0
br olef	1-pentene, 2-,4- dimethyl	647.0
ROH	1-butanol	653.8
br olef	1-hexene, 3-methyl	655.4
br olef	1-pentene, 3-methyl	659.0
br par	1-hexane, 5-methyl	661.2
REF	**cyclohexane**	664.2
br olef	1-hexene, 4-me	668.2
RCOR	2-pentanone	669.7
br par	hexane, 2-methyl	671.5
br par	pentane, 2, 3- dimethyl	673.7
br par	hexane, 3-methyl	679.5
br olef	2-hexene, 5-methyl	682.8
int ROH	2-pentanol	685.7
br olef	1-hexene, 2-methyl	688.2
lin olef	1-heptene	690.6
lin int olef	3-heptene	698.3
lin par	**n-heptane**	700.0
t-lin-olef	t-heptene	705.0
c-lin-olef	c-heptene	714.7
br ROH	1-butanol, 3-methyl	720.8
br RCOR	methyl, isobutyl ketone	722.9
br ROH	1-butanol, 2-methyl	724.8
br olef	1-hexene, 3,5-dimethyl	737.8
lin int olef	4-octene (Z)	750.0

Table C.3: Kovats indices of products produced in this work. (Continued)

Group	**Name**	**KI**
br olef	1-heptene, 3-methyl	752.2
ROH	1-pentanol	753.3
br par	hexane, 2,3-dimethyl	764.8
br olef	2-heptene, 5-methyl	766.9
br par	heptane, 2-methyl	769.3
br par	pentane, 3-ethyl	770.6
br olef	2-heptene, 6-methyl	774.0
br olef	1-heptene, 4-methyl	776.8
br olef	1-heptene, 2-methyl	786.4
lin olef	1-octene	789.8
lin int olef	3-octene(Z)	797.3
lin par	**n-octane**	800.0
t-lin-olef	t-octene	803.5
c-lin-olef	c-octene	812.8
br olef	4-octene, 3-methyl	849.8
ROH	1-hexanol	856.2
br par	octane, 4-methyl	866.8
ketone	2-hexanone	870.3
br par	heptane, 3-ethyl	875.8
lin int olef	cis-4-nonene	880.8
br olef	1-octene, 2-methyl	885.3
lin olef	1-nonene	890.0
lin int olef	3-nonene(Z)	895.4
lin int olef	4-nonene(Z)	898.2
lin par	**n-decane**	900.0
t-lin-olef	t-nonene	902.0
c-lin-olef	c-nonene	905.0

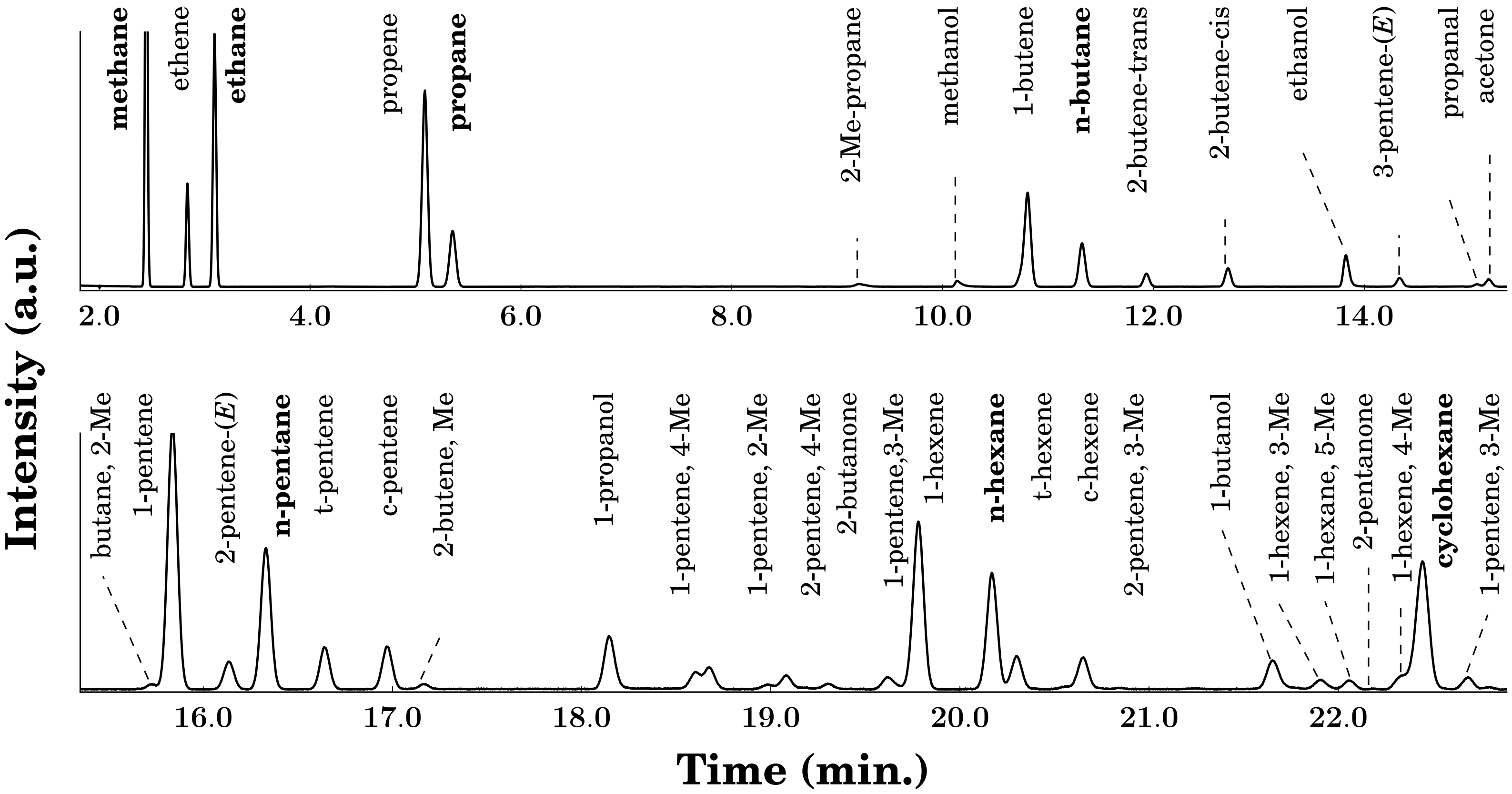

Figure C.7: A GC-FID chromatogram of a typical FTS product sample where the compounds are labeled. Identification of the products were achieved through the use of Kovats indices and GC-MS analyses. (C_{1-7})

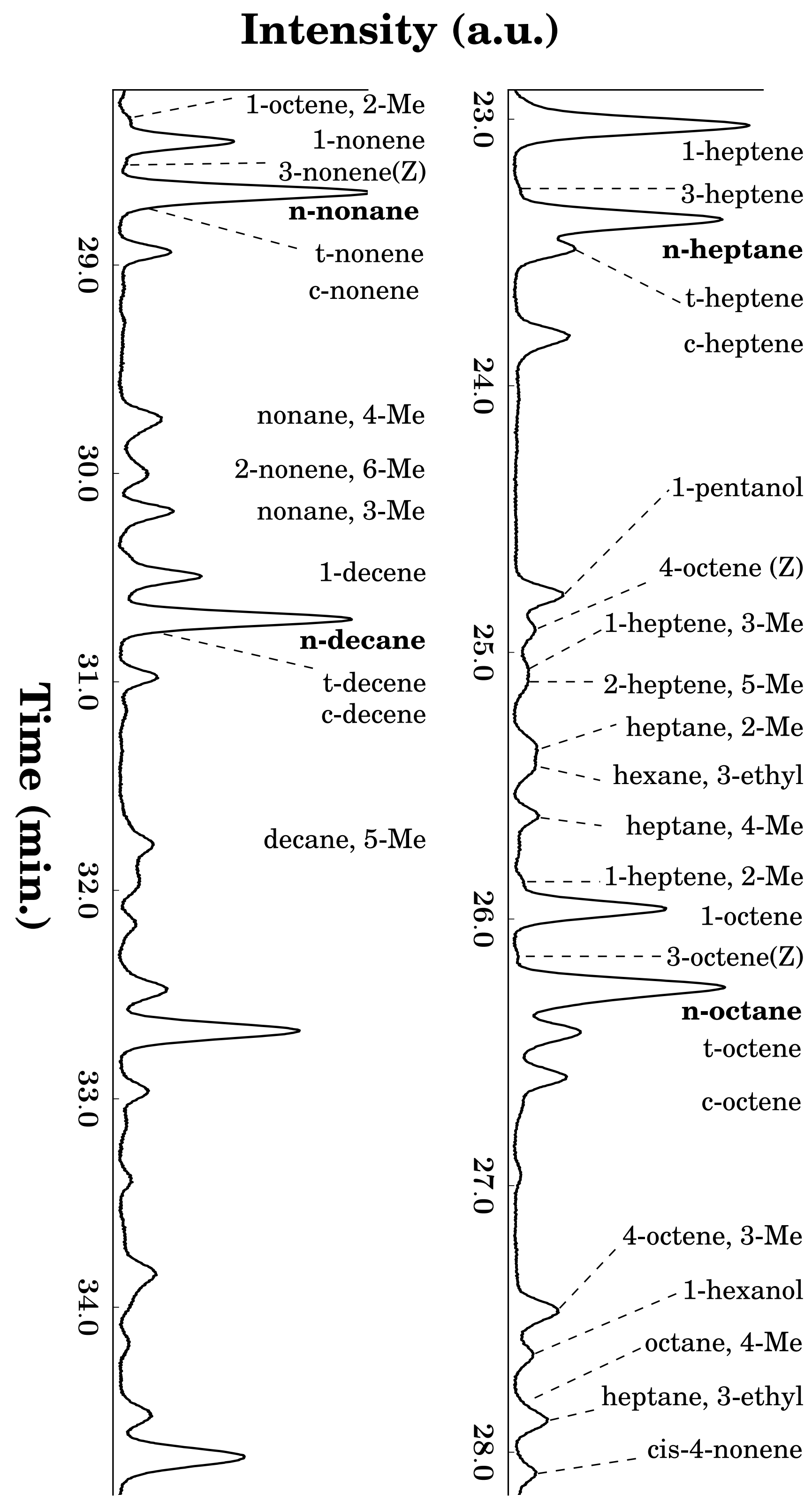

Figure C.8: A GC-FID chromatogram of a typical FTS product sample where the compounds are labeled. Identification of the products were achieved through the use of Kovats indices and GC-MS analyses. (C_{8-12})

Table C.4: Response factors ($\mathbf{f_i}$) calculated for selected compounds via the Kaiser methodology.

Carbon number	Product name	f_i
1	methane	1.00
2	ethane, ethene,	1.00
3	propane, propene	1.00
4	butane, 1-butene	1.00
5	pentane, 1-pentene	1.00
6	hexane, 1-hexene	1.00
7	heptane, 1-heptene	1.00
2	ethanol, ethylamine	1.29
3	propanol, 2-propanol, propylamine	1.17
4	1-butanol, 2-butanol, 1-butylamine	1.13
5	1-pentanol, 2-pentanol, 1-pentylamine	1.10
6	1-hexanol, 2-hexanol, 1-hexylamine	1.08
7	1-heptanol, 2-heptanol, 1-hyptylamine	1.07
2	acetaldehyde	2.00
3	propanal, propanone	1.50
4	butanal, butanone	1.33
5	pentanal, 2-pentanone	1.25
6	hexanal, 2-hexanone	1.20
7	heptanal, 2-heptanone	1.17
2	acetic acid, acetamide	2.00
3	propanoic acid, propanamide, N-methylacetamide	1.50
4	butanoic acid, butanamide, N-methylpropanamide	1.33
5	pentanoic acid, pentanmide, N-methybutanamide	1.25
6	hexanoic acid, hexanamide, N-methylpentanamide	1.20
7	heptanoic acid, heptanamide, N-methylhexanamide	1.17

Condensation of n-alcohols

In Chapter 4 it is mentioned that O- and N-containing compounds are likely to be represented in the oil phase at lower carbon numbers compared to alkanes and alkenes. In order to illustrate this remark, the vapor pressures (p_v) and partial pressures (p^*) of n-alcohols and n-alkanes are discussed here. If $p^* < p_v$, condensation would occur. A rough estimate for the partial pressures can be made by using Eq. C.1

$$p^* = \frac{\dot{n}_{i,c}}{\dot{n}_{total}} \times P_{total} \tag{C.1}$$

where $\dot{n}_{i,c}$ is the flow rate of the n-alcohol/alkane and $\dot{n}_{total}$ is the total flow rate (including the feed, reference gas and products) and P_{total} is the total pressure in the condensation vessel (5 bar). In Figure C.9, the logarithm of the vapor pressures (p_v, in Pa) sourced from Mckay et al. [6] (and references therein) and the logarithm of the partial pressures (p^*, in Pa) for linear alkanes and alcohols are plotted as a function of carbon number. Graphically analyzing this figure, one can see that the n-alcohols undergo condensation at a lower carbon number (c.a. C_7) compared to the n-alkane (c.a. C_9). This analysis therefore supports the suggestion made that C_{7+} O- and N-containing compounds are fully immersed in the oil phase.

Method setup for comprehensive two-dimensional gas chromatography

Comprehensive two-dimensional gas chromatography introduces a problem known as wrap-around errors. These errors arise when all of the compounds contained within the isolated (modulated) fraction is not completely separated within the time span of the secondary separation. This error makes it difficult to construct classifications of organic products that can be reproducible.

When setting up a method for comprehensive two-dimensional gas chromatography (GC×GC-TOF/FID), it is important to avoid wrap-around errors. This is a well-known problem in GC×GC analysis [7] and by avoiding these errors it becomes easier to identify different classes (e.g. paraffin's olefins, and oxygenates) present in the sample. Even though the two-dimensional chromatogram shown in Figure C.10 does at first seem well-separated, especially for those not accustomed to the features of a well-separated chromatogram for FTS products, it contains

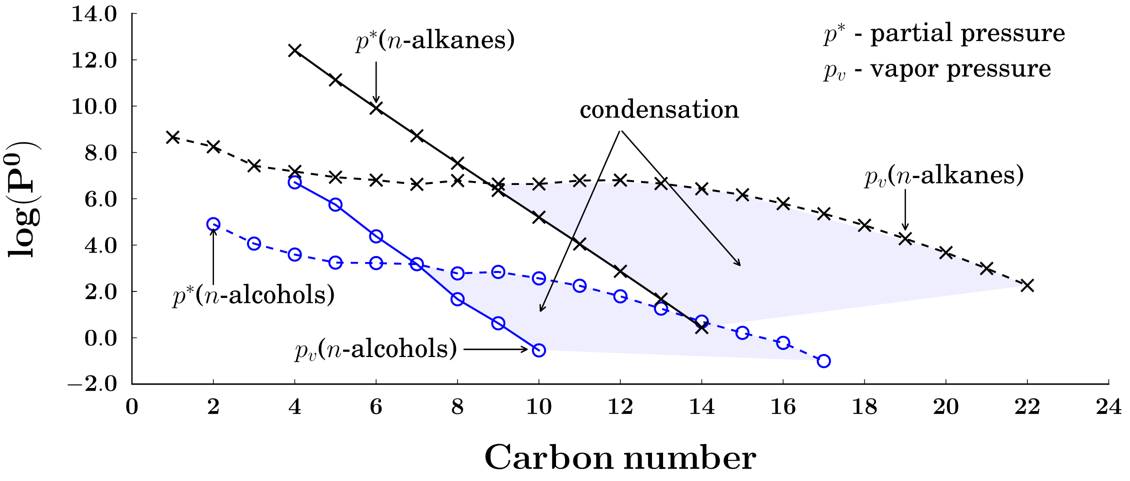

Figure C.9: Condensation of products predicted by comparing the partial pressures (p^*) and vapor pressures (p_v) as a function of carbon number for linear alkanes and alcohols. Data for vapor pressures at 25 °C taken from Ref. [6] and references therein.

wrap-around errors. Wrap-around errors are essentially produced when the fraction of the sample that was isolated in the modulator, is not fully separated within time assigned by or associated with the short modulating period. To visually conceptualize this effect on the 2D chromatogram, one can imagine this fraction subsequently going through the modulator for a second or third time and eluting at a 'pseudo-random location' on the 2D chromatogram. Avoiding wrap-around errors can be approached in several ways, for instances making sure the system is without any leaks or changing certain variables (see below). By allowing for a longer secondary separation (e.g. 8-10 seconds), it was usually possible to evade these errors, but led to non-ideal separations. In Figure C.11 (A) an example of such a chromatogram is given, where the empty space in the bottom 4 seconds (of the secondary dimension) points to inefficiency of the separation. The variation in the temperature of the two ovens (see Figure C.11, B and C), the modulation time (see Figure C.11, A and D) and the length or type of secondary column (with the latter being a last resort) can all be applied to then improve upon this separation, whilst maintaining the goal of avoiding wrap-around errors.

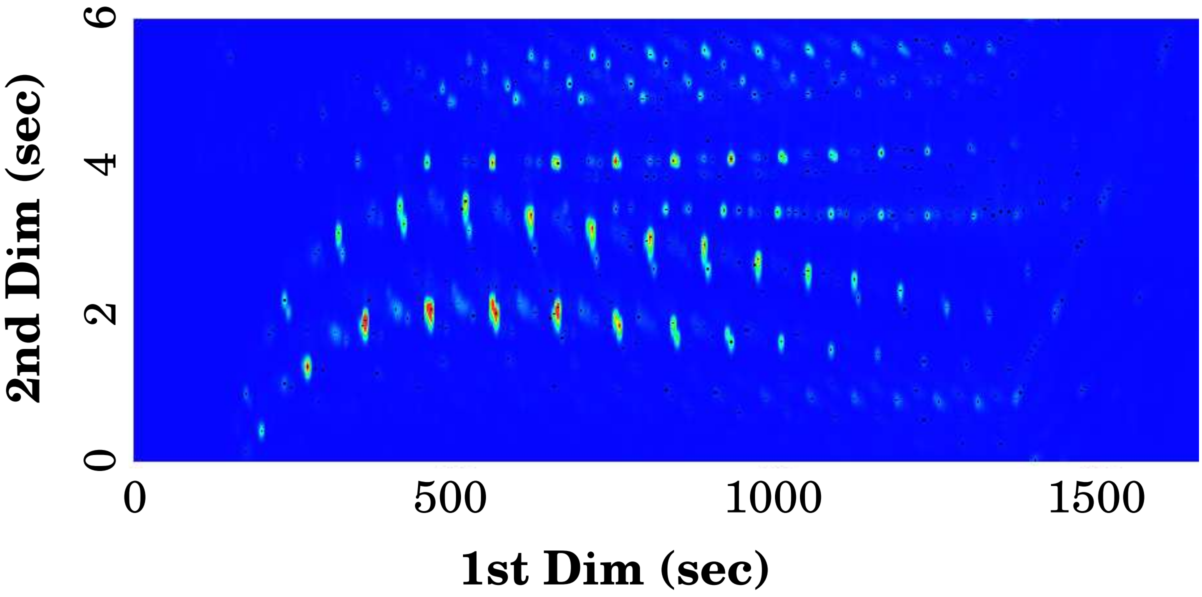

Figure C.10: A chromatogram obtained from GC×GC-TOF/FID analysis that seems to be well separated, but contains wrap-around errors.

Challenges associated with selected organic compounds.

Analysis of primary amines

The analysis of primary amines with the use of comprehensive GC×GC-TOF/FID presented a particular problem. The polar wax column used (as discussed in Chapter 4 to achieve ideal separation for the N- and O-containing compounds, interacted to too great an extent with the primary amines. In particular from the C_{8+} carbon number range, the primary amines became mostly impossible to quantify (See Figure C.12).

Fortunately the C_{1-7} fraction of primary amines could be completely isolated during the on-line GC-FID analyses (as can be seen in Figure C.13).

Supplementary information: Chapter 7

In Chapter 7, reference is made to the activity reported by Sango [4]. A figure that summarizes the activity data is presented in Figure C.14.

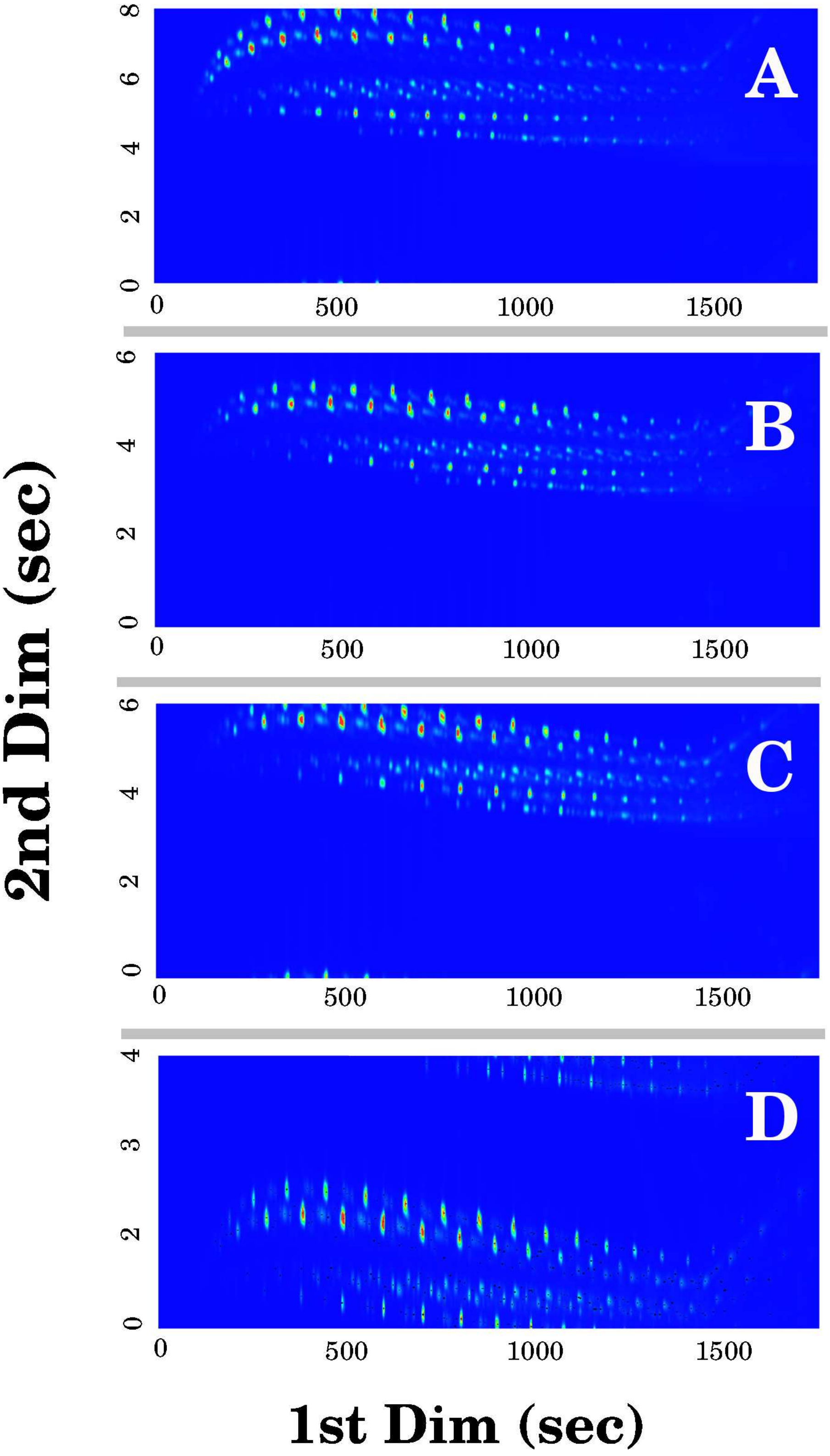

Figure C.11: Chromatograms that illustrate the influence of certain parameters (B and C - Temperature of secondary oven, A and D - retention time in secondary dimension) and how it was adjusted during GC×GC-TOF/FID analysis to achieve ideal separation without any wrap-around errors.

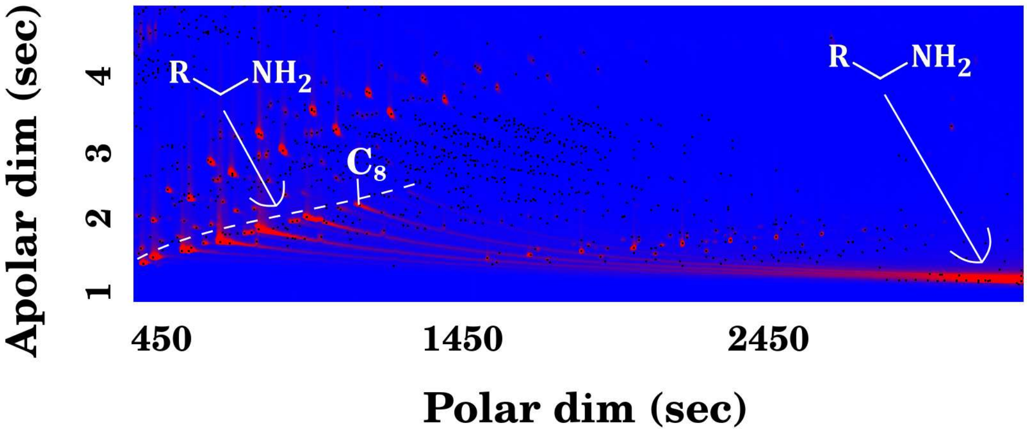

Figure C.12: 2D chromatogram that shows the interaction of the primary amines with the stationary phase of the column used in the first dimension. The amines elutes at the latter stages of the analysis at the higher temperatures (280 ℃) as indicated in the figure.

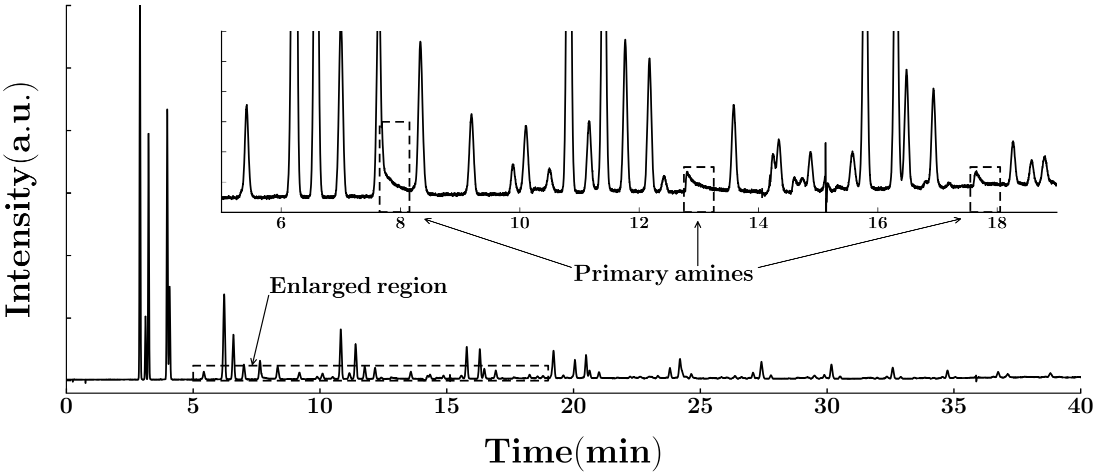

Figure C.13: Chromatogram obtained from on-line GC-FID analysis that was used to quantify the formation of primary amines. (SPR^2, T = 250 ℃, P = 5.1 bar, GHSV = 2250 ml/hr/g$_{cat}$, H_2/CO = 2, 1 vol% NH_3)

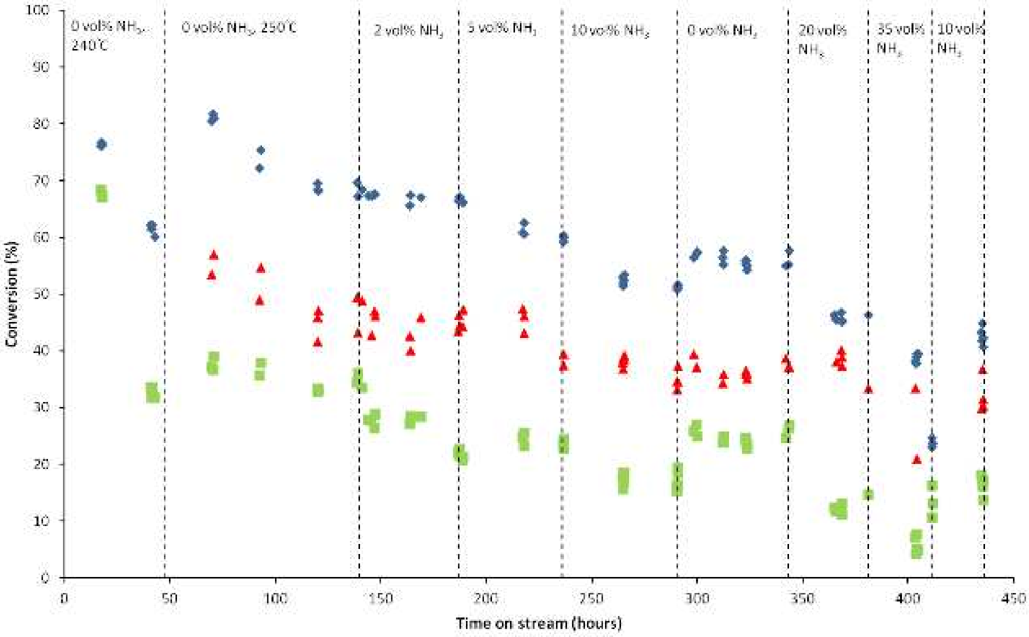

Figure C.14: Acitivity data reported by Sango [4] during his NH_3 co-feeding experiments. (Green - H_2, Blue - CO, Red - CO to HCs

Olefin selectivity

In Chapter 7 it is mentioned that a lower olefin selectivity is observed at higher carbon numbers (e.g. C_{12-20}). The olefin selectivity is plotted in Figure C.15 by reporting the olefins present in the linear hydrocarbon product as a function of carbon number.

The content of α-olefins in the linear olefin products is presented in Figure C.16. The isomerization from the α-olefin to internal olefins does not give any clear indication if significant secondary reactions are taking place.

The Iso/n ratios shown in Figure C.17 as a function of carbon numbers does however indicate that secondary reactions of olefins could be leading to the formation of branched hydrocarbons.

Supplementary information: Chapter 8

To elaborate on the equipment used for the co-feeding reactions, a schematic (see Figure C.18) is provided that shows the important parts of the experimental setup.

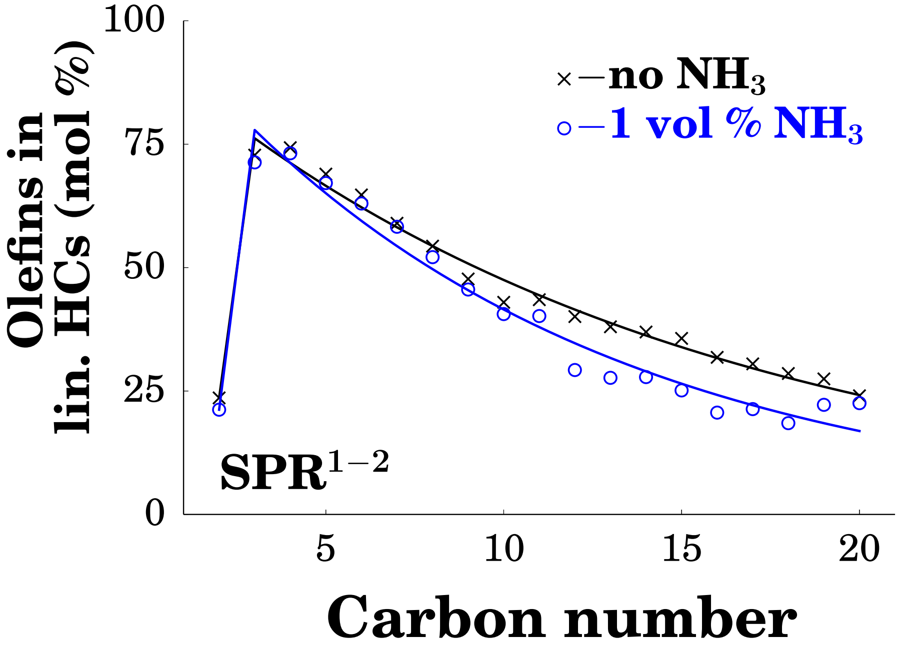

Figure C.15: The olefins in the linear hydrocarbon product (mol %) as a function of carbon number, obtained from the reactions where 0/1 vol % NH_3 was added during FTS. (SPR^1, T = 250 ℃, P = 5 bar, GHSV = 2250 ml/hr/g_{cat}, H_2/CO = 2)

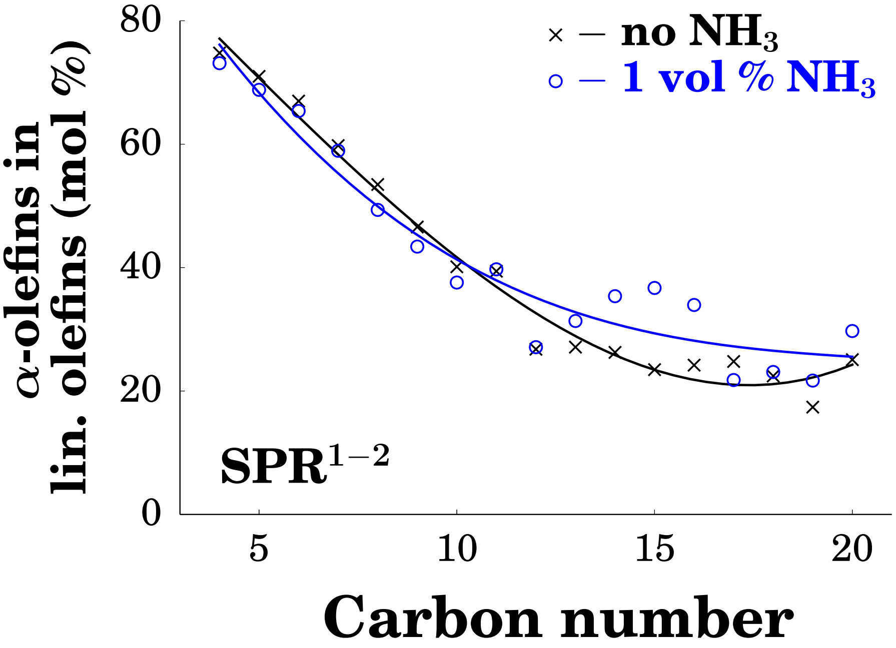

Figure C.16: α-Olefins in the linear olefins (mol %) as a function of carbon number, obtained from the reactions where 0/1 vol % NH_3 was added during FTS. (SPR^1, T = 250 °C, P = 5 bar, GHSV = 2250 ml/hr/g$_{cat}$, $H_2/CO = 2$)

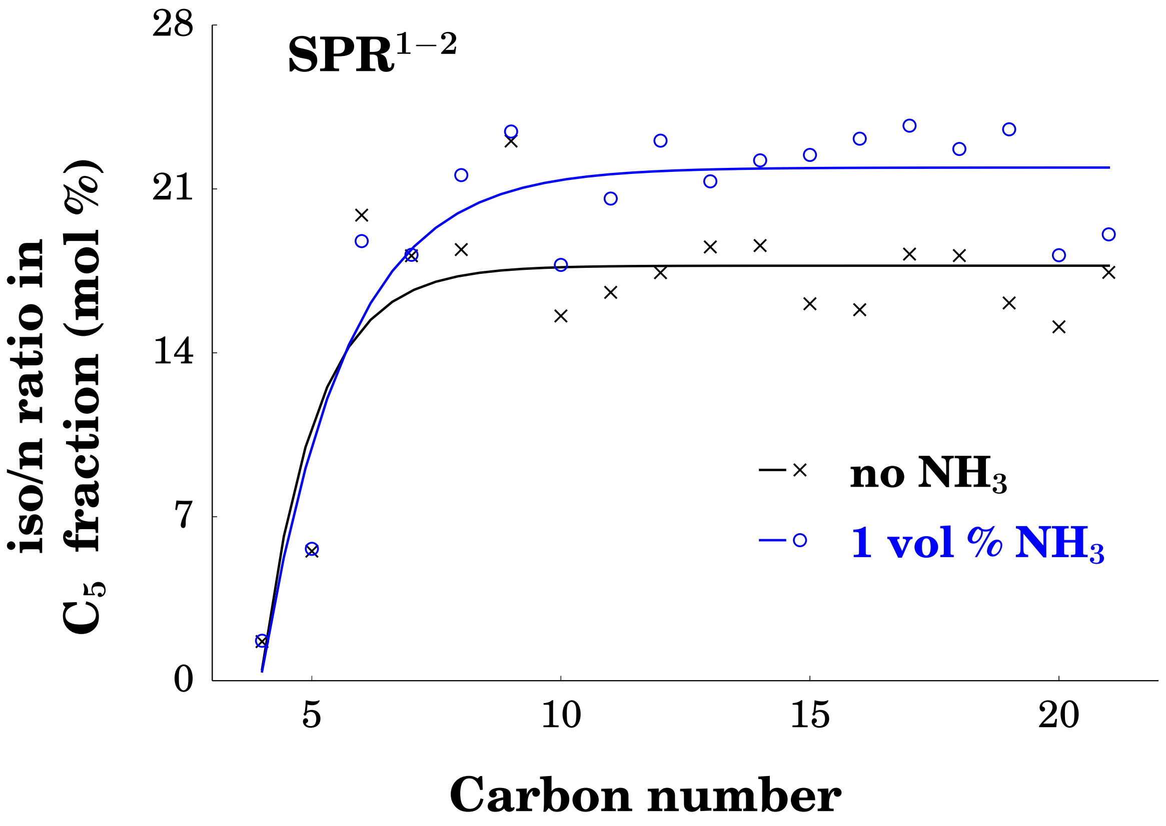

Figure C.17: iso/n ratios (mol %) as a function of carbon number, obtained from the reactions where 0/1 vol % NH_3 was added during FTS. (SPR[1], T = 250 °C, P = 5 bar, GHSV = 2250 ml/hr/g_{cat}, H_2/CO = 2)

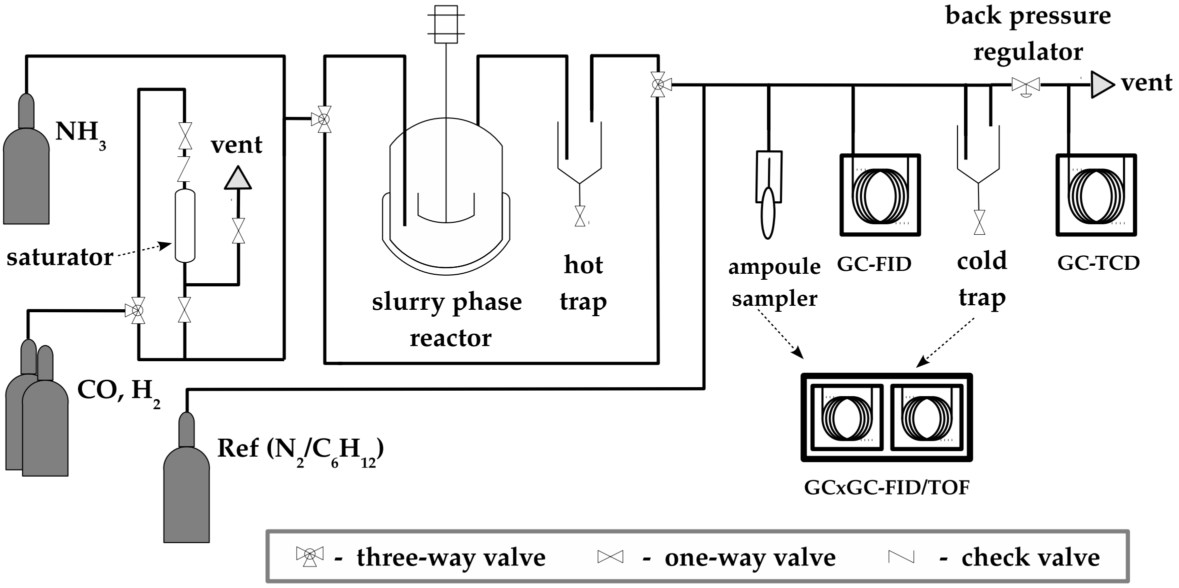

Figure C.18: Simplified schematic that highlights the important experimental units and analytical equipment used during co-feeding experiments discussed in Chapter 8

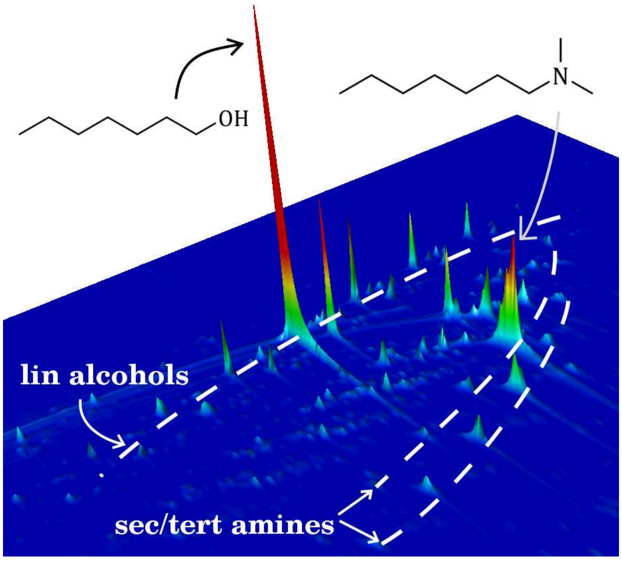

Figure C.19: An enlarged three-dimensional image, obtained from GC×GC-FID analysis, showing the increased selectivity towards secondary and tertiary amines when 1-octanol was co-fed during the FT reaction (slurry phase, T = 250 ℃, P = 5 bar, GHSV = 2250 ml/hr/g_{cat}, $H_2/CO = 2$, 1 vol% NH_3).

A three dimensional view of the products observed during the 1-octanol co-feeding experiment is presented in Figure C.19.

The mass balance in Figure C.20 is constructed based on the 1-octanol co-feeding reaction, which indicates the significant quantities of N-containing compounds that form via a secondary route to the detriment of the oxygenates.

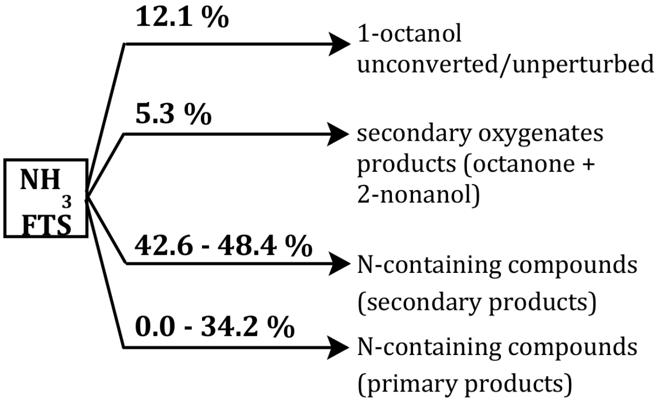

Figure C.20: The mass balance constructed based on the co-feeding of 1-octanol.

REFERENCES

[1] H. Schulz. *Catal. Today*, 178:151–156, 2011.

[2] W. Röttig. Catalytic hydrogenation of carbon monoxide with addition of ammonia or methylamine. US - 2,821,537, 1958.

[3] N. Fischer. *Preparation of nano and angstrom sized cobalt ensembles and their performance in the Fischer-Tropsch Synthesis*. PhD thesis, University of Cape Town, 2011.

[4] T. Sango. Nitrogen-containing from ammonia compounds co-feed to the Fischer-Tropsch synthesis. MSc thesis, University of Cape Town, South Africa, 2013.

[5] R. Kaiser. *Bibliographisches Institut, Manheim*, 1969.

[6] D. Mckay, W.Y. Shiu, K. Ma, and S.C. Lee. *Handbookd of Physical-Chemical Properties and Environmental Fate for Organic Chemicals (Second Edition).* CRC Press, Boca Raton, 2006.

[7] J Dallüge, J Beens, and UAT Udo Brinkman. *Journal of Chromatography A*, 1000:69–108, 2003.

Appendix D

Curricullum Vitae

Christian de Vries

Personal Information

date of birth	15^{th} June, 1982 - Bethal, South Africa
nationality	South African

Education

current	PhD (Chem Eng) Title: "Adding ammonia during Fischer-Tropsh Synthesis: Pathways to product formation" University of Cape Town, Cape Town, RSA
2010	M.Sc. upgraded to PhD status University of Cape Town, Cape Town, RSA
2009	Enrol for M.Sc. (Chem Eng) University of Cape Town, Cape Town, RSA
2008	B.Sc. (Chemistry)(Hons) University of Stellenbosch, Stellenbosch, RSA
2007	B.Sc. (Chemistry & Polymer Science) University of Stellenbosch, Stellenbosch, RSA
2005 - 6	Travel abroad
2001	Enrol B.Sc. (Chemistry & Polymer Science) University of Stellenbosch, Stellenbosch, RSA

2000	High school diploma (Grade 12) Outeniqua high school, George, RSA

International experience

current	Philadelphia, USA
20011-12	Collaboration with Carl von ossietzky Universität Oldenburg, GER
2005-6	Travel abroad Brighton, ENG

Awards and scholarships

2010 - 13	National Research Foundation (NRF) Innovation scholarship for doctoral research
2009 - 13	Department of Science and Technology (DST-NRF) center of excellence in catalysis (c*change) bursary
2012	International student travel grant, (NRF)
	International student travel grant, Catalysis Society of South Africa (CATSA)
2009 - 10	Poster prizes at annual CATSA conferences.
2008	NRF Scarce skill scholarship

Publications

2014

”The co-adsorption of CO^* and NH_x^* (x = 3, 2, 1, 0) on Fe(100):
a DFT study” (To be submitted)

”Adding 1 vol% ammonia during Fischer-Tropsch Synthesis”
(To be submitted)

”Investigating the role of secondary reactions when 1 vol% NH_3 is added during FTS”
(To be submitted)